Exploring diverse solid-state structural assemblies of some organic compounds and metal complexes in the context of crystal engineering

THESIS SUBMITTED FOR THE DEGREE OF DOCTOR OF PHILOSOPHY (SCIENCE)
JADAVPUR UNIVERSITY
2024

BY

SAMIUL ISLAM, M. Sc.

DEPARTMENT OF PHYSICS

JADAVPUR UNIVERSITY

KOLKATA–700032

INDIA

যাদবপুর বিশ্ববিদ্যালয়
কলকাতা-৭০০ ০৩২, ভারত

*JADAVPUR UNIVERSITY
KOLKATA-700 032,INDIA

FACULTY OF SCIENCE : DEPARTMENT OF PHYSICS

CERTIFICATE FROM THE SUPERVISOR

This is to certify that the thesis entitled "**Exploring diverse solid-state structural assemblies of some organic compounds and metal complexes in the context of crystal engineering**" Submitted by Sri **Samiul Islam** who got his name registered on **22/03/2021 (Index No: 34/21/Phys./27; Registration Number: SOPHY1403421)** for the award of Ph.D. (Science) Degree of Jadavpur University, is absolutely based upon his own work under the supervision of **Dr. Saikat Kumar Seth, Associate Professor, Department of Physics, Jadavpur University, Kolkata 700032** and that neither this thesis nor any part of it has been submitted for either any degree / diploma or any other academic award anywhere before.

Saikat Kumar Seth 02/04/2024

Saikat Kumar Seth
Associate Professor of Physics
Jadavpur University

Dr. Saikat Kumar Seth
Associate Professor
Department of Physics
Jadavpur University
Kolkata-700 032, India

Signature of the Supervisor & Date with official seal

Dedicated

to

my beloved parents and my dear wife

Acknowledgement

First and foremost, praises and thanks to the God, the Almighty, for His showers of blessings throughout my research work to complete the research successfully.

I would like to express my deepest and sincere gratitude to my supervisor Dr. Saikat Kumar Seth, Associate Professor, Department of Physics, Jadavpur University, Kolkata-700032, for giving me the opportunity to do research and providing invaluable as well as expert guidance throughout my research work. His dynamism, vision, sincerity and motivation have deeply inspired me. He has taught me the methodology to carry out the research and to present the research works as clearly as possible. It was a great privilege and honour to work under his guidance. I am extremely grateful for what he has offered me. I would also like to thank him for his friendship, empathy, and great sense of humor. I am extending my heartfelt thanks to his family for their acceptance and patience during the discussion I had with him on research work and thesis preparation.

I cordially convey my gratitude to the collaborators, Prof. Partha Pratim Ray and Prof. Subrata Mukhopadhyay of Jadavpur University, India, Prof. Antonio Frontera of the Universitat de les Illes Balears, Spain, Dr. Soumen Ghosh of Chakdaha College, India, and Dr. Samiran Pramanik of Dinabandhu Mahavidyalaya, India.

My heartfelt thanks go to my labmates, Dr. Anower Hossain, Dr. Tripti Mandal, Dr. Suparna Tripathi, Ms. Prantika Das, Mr. Pratik Dey, Mr. Roushan Kabir for their earnest co-operation and support. I especially wish to thank again Prantika and Pratik, not only for their co-operation during my Ph.D. research work but also for making my time at Jadavpur University even more cordial and enjoyable. It has been my pleasure to work in this team that has become an extended family for me.

I am thankful to the University Grants Commission (UGC), Government of India for providing me the fellowship (Ref. No.: 1528/CSIR-UGC NET JUNE 2019).

I would like to thank all the faculty members of Department of Physics for rich academic environment. I would also like to thank central instrument facilities, Department of Physics and single crystal X-ray diffraction facility, Department of Chemistry. I would also like to thank Prof. Deepak Chopra, IISER Bhopal, India for providing me the CSD access. I am grateful to the entire staff of the Faculty of Science and Research Section, for their generous co-operation.

I am grateful to my teachers for their patience, kindness, and support and for imparting valuable life lessons. I cannot forget the contribution of my friends who motivated me highly in my research. I would like to express my special thanks to my dear friend Mr. Nayeem Akhter, who is always there for me in my tough times.

Above all, I would like to express my deepest gratitude to my parents and my sisters. Whatever I am and whatever I aspire to be in the future is because of the goodwill, immense encouragement, and loving blessings I have received from them. They always supported me and encouraged me with their best wishes. I convey my deepest respect, love and affection for the unconditional support by my beloved wife Sadia. I would also like to thank my other family members for their encouragement and kind co-operation.

Last but not the least, I would also like to express my sincere gratitude to those whose names are not included here. Thank you all.

Date: 02/04/2024

Department of Physics

Jadavpur University

Kolkata 700032, India

Samiul Islam

(SAMIUL ISLAM)

ABSTRACT

Title of the thesis: Exploring diverse solid-state structural assemblies of some organic compounds and metal complexes in the context of crystal engineering

Submitted by: Samiul Islam **[Index No: 34/21/Phys./27]**

Department: Physics

X-ray diffraction and crystallography is undoubtedly one of the most powerful analytical technique to elucidate the structure of crystalline materials at the molecular level. The crystallographic study of the solid-state structures of organic compounds and metal complexes has attracted intense attention due to their fascinating structures and properties. The subject, namely crystal engineering, evolved from an intersection of crystallography and chemistry, but nowadays it employs crystallography, spectroscopy, and computation. The study and understanding of weak forces are necessary to develop new applications in supramolecular chemistry across a diversity of fields. The interplay of the cooperative weak noncovalent interactions is certainly of great importance in building multidimensional structures.

In this proposed dissertation, various compounds will be synthesized and structurally characterized by X-ray diffraction. The investigations proposed herein are aimed at systematically studying different noncovalent interactions in building extended solid-state networks to gain knowledge in this nascent field. Therefore, it is aimed to explore the robust feature of non-covalent interactions in building multi-dimensional supramolecular frameworks. Attempts have been made to explore several supramolecular structural diversities for the first time in solid-state. Hirshfeld surface analysis has been performed to quantify non-covalent interactions. The non-covalent interactions have also been successfully characterized by using several theoretical studies, such as DFT calculations, QTAIM analysis, NCI Plot Index, PIXEL calculations, etc.

Saikat Kumar Seth
Signature of the supervisor 02/04/2024

Dr. Saikat Kumar Seth
Associate Professor
Department of Physics
Jadavpur University
Kolkata-700 032, India

Samiul Islam 02/04/2024
Signature of the candidate

CONTENTS

PREFACE

The title of the present thesis is "**Exploring diverse solid-state structural assemblies of some organic compounds and metal complexes in the context of crystal engineering**". The research orientation in the field of crystal engineering mainly focuses on the development of new solids with desired properties as well as the role of non-covalent interactions in the construction of those solids. And the crystalline and molecular structure of grown solids can be effectively done using single crystal X-ray diffraction techniques. However, the structure of the grown crystal is only as good as the crystal used for data collection. The proposed research work focuses on spectroscopic and single crystal X-ray structural studies of various organic compounds as well as metal-organic complexes. The investigation would include structure determination of grown solids using single crystal X-ray diffraction and validation of determined structure through powder X-ray diffraction method, CHN elemental analysis, IR spectroscopic studies etc. The optical property of the grown solids would be determine using UV-Vis spectroscopic study.

Crystallographic research revealed the conformation of the molecules, and also examined the significance of intermolecular interactions in molecular packing, with an emphasis on supramolecular self-assembled structures. The self-assembled supramolecular structures have been explored to observe the role of non-covalent interactions in the formation of crystal structures. Weak interaction-based self-assembly has proven to be a helpful and efficient method for building pre-designed and well-defined architectures. In this proposed research work, the fascinating roles of the most reliable hydrogen bonding interactions as well as interactions involving the aryl ring in the development of supramolecular self-assembly are studied.

In this proposed research work, the non-covalent interactions involved are further characterized using tools based on Hirshfeld surfaces and several theoretical studies, such as DFT calculations, QTAIM analysis, NCI Plot Index, PIXEL calculations, etc. A visual insight into the Hirshfeld surface features non-covalent interactions and corresponding 2D fingerprint plots showing the percentage contribution of interactions involved. DFT calculations can determine the interaction energy of a dimer, and PIXEL calculations can obtain the lattice energy. The topological parameters at the bond critical points indicate the nature of the non-

covalent interaction and further dissociation energy of the interactions can also be obtained. Furthermore, the NCI plot characterize non-covalent interactions visually by colored isosurfaces. Therefore, the proposed research work can help to understand the significance of non-covalent interactions in controlling the crystal structure and designing novel materials in the context of crystal engineering. The present thesis consists of five chapters. The contents of the respective chapters are summarized below.

In **Chapter 1**, the methodology of the proposed research work is discussed. Structure determination from single crystal X-ray data and various methods of characterization of grown solids are covered in detail in this chapter. Phase problems in crystallography, structure solution methods, and structure refinement are briefly described in this chapter. Crystal engineering, molecular recognition, self-assembly, supramolecular synthesis, supramolecular synthons, and other intermolecular interactions (including non-covalent interactions) are all covered in detail. This chapter also covers the concepts of Hirshfeld surface analysis, DFT calculations, QTAIM analysis, NCI plot index, and PIXEL calculation, which are used to to demonstrate the authenticity of the thesis's provided structures.

In **Chapter 2**, the pH-dependent reaction between 2,6-pyridine dicarboxylic acid (PDA) and $Mg(NO_3)_2$ in water leads to the formation of two new complexes (**1**) and (**2**). The grown complexes are structurally characterized through single-crystal X-ray diffraction analyses. The structural investigations show that the hydrogen bonds along with lone-pair···π interactions stabilize the crystal structure of the complex (**1**) whereas complex (**2**) is stabilized only through hydrogen bonds. Non-covalent interactions are characterized using Bader's quantum theory of "Atoms in Molecules" (QTAIM). Topological analysis at the bond critical points revealed that all of the interactions are of closed-shell interactions. The "Non-covalent Interaction" (NCI) plot index was performed to characterize the non-covalent interactions of the structures discussed in this study.

In **Chapter 3**, crystals of penta(carboxymethyl)diethylenetriamine have been characterized using single-crystal X-ray diffraction analysis. X-ray diffraction analysis exhibit that O–H···O and C–H···O hydrogen bonging interactions combine to construct the final solid-state supramolecular structures. Involved intermolecular interactions are quantified through

Hirshfeld surface analysis and fingerprint plots. Molecular energy frameworks have been developed to analyze the dominant interaction forces involved in molecular packing strength. Bader's quantum theory of "Atoms-in-Molecules" (QTAIM) analysis validates the existence of hydrogen bonding contacts, and the topological analysis revealed that all of the interactions are closed-shell interactions. Furthermore, the "Non-covalent Interaction" (NCI) plot index illustrates the solid-state supramolecular networks.

In **Chapter 4**, Two novel Co(II) complexes, {[Co(2,6-pydc)$_2$]·[Co(4,4'-tmdpy)(H$_2$O)$_4$]$_n$·2H$_2$O}(**1**) and {2[Co(2,6-pydc)$_2$]$^{2-}$·[2(4,4′-bpy]$^{2+}$·10(H$_2$O)·O}(**2**) [2,6-pydc = 2,6-pyridinedicarboxylic acid, 4,4'-tmdpy = 4,4'-trimethylenedipyridine, 4,4′-bpy = 4,4'-Bipyridine] have been designed, synthesized, and characterized using elemental analysis, spectroscopic techniques, and single-crystal X-ray diffraction analysis. For complex (**1**), hydrogen bonding, π···π and lone pair (l.p.)···π interactions help in the formation of supramolecular networks, whereas for complex (**2**), hydrogen bonding, π···π, π···π$^+$, π$^+$···π, l.p···π play the pivotal role in building final solid-state structure. A unique 3D supramolecular architecture generated in complex (**1**) through π···π and l.p···π interactions. On the other hand, Complex (**2**) also exhibits a unique (l.p···π/π···π$^+$/π$^+$···π/π···π/π···π$^+$/π$^+$···π/π···l.p)$_n$ self-assembly. The noncovalent interactions were characterized through Bader's quantum theory of "Atoms in Molecules" (QTAIM) and "Non-covalent Interaction" (NCI) plot index. The evaluation of topological parameters at (3, –1) BCPs ensured the 'closed-shell' nature of the intermolecular interactions.

In **Chapter 5**, two polymorphic forms of 2-amino-3-nitropyridine (**Form–I** and **Form–II**) were structurally characterized by single crystal X-ray diffraction analysis and compared with another polymorphic form (**Form–III**) with a detailed analysis of intermolecular interactions. X-ray crystallography reveals that the polymorphs generate completely different network structures through hydrogen bonding interactions. Polymorphic **Form–I** exhibits a layer assembly through cooperative face-to-face π···π and lone pair···π interactions, whereas **Form–II**, and **Form–III** exhibit only hydrogen bonds. Hirshfeld surface analysis reveals a more detailed investigation of the intermolecular interactions experienced by the polymorphic forms of 2-amino-3-nitropyridine. Quantitative analysis of interaction energies involving different noncovalent interactions was calculated and compared to gain deeper insight into the role of

such interactions in stabilizing the polymorphs. The interaction energies of non-covalent interactions are calculated by using theoretical DFT calculations as well as the PIXEL calculations. The PIXEL method provides us precise interaction energy as well as lattice energy with energy decomposition scheme. Bader's quantum theory of "Atoms in Molecules" (QTAIM) expose the nature and strength of these interactions The NCI (Non-covalent Interaction) plots are further employed to characterize the non-covalent interactions.

CHAPTER 1

X-ray Crystallography and Crystal Engineering: Theory and Methodologies

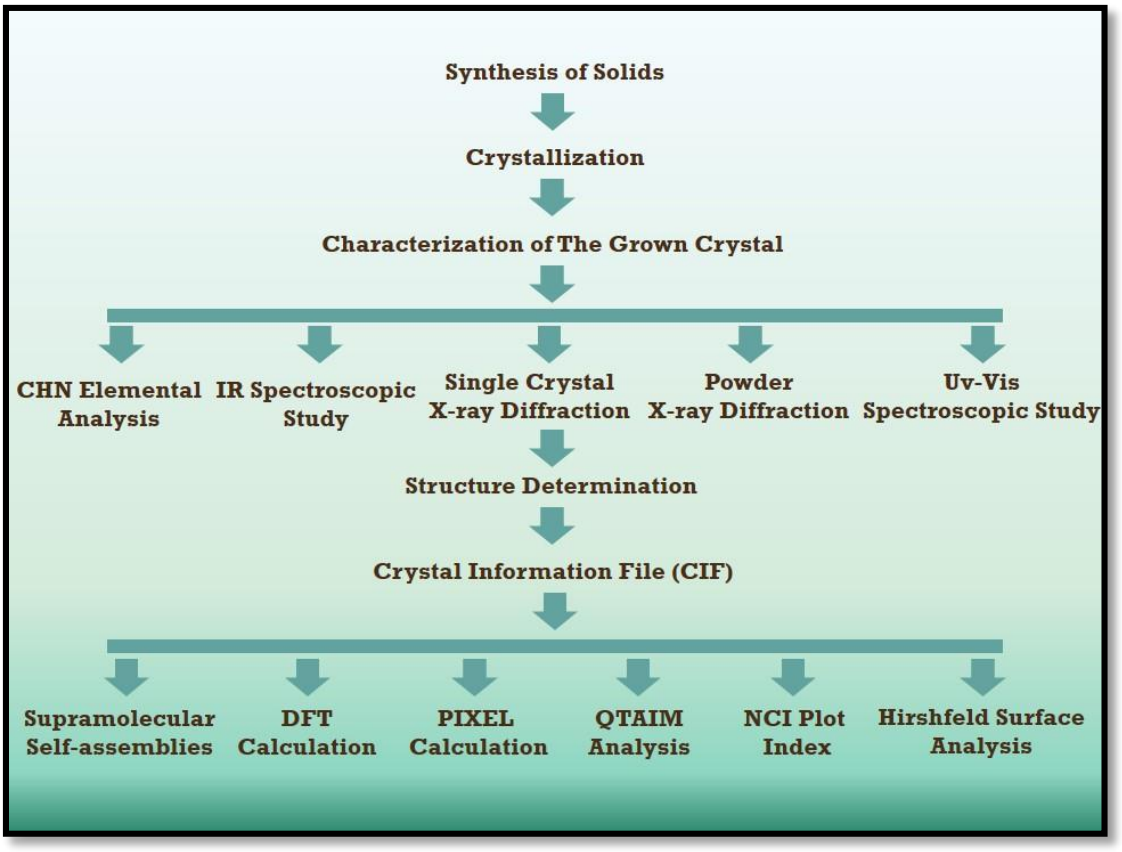

Crystallography is the most powerful analytical method that deals with the structure and properties of crystalline solids, mainly the arrangement and bonding of atoms and molecules in crystalline solids and the geometric structure of the crystal lattices. Crystal structure analysis is based on X-ray diffraction phenomena, where the wavelength of the radiation must be comparable to the inter-atomic spacing. X-ray crystallography determines crystal structure at the atomic and molecular levels, where the crystal atoms diffract X-ray beams. X-ray diffraction is used to investigate the nature of crystalline and noncrystalline materials. X-ray diffraction can provide information about unit cell dimensions. The interior of the unit cell is composed of a collection of atoms and, subsequently, *Z* number of molecules. Because of the periodic nature of crystals, each unit cell and its contents are indistinguishable. The ordered arrangement of atoms, ions, or molecules is related to crystalline materials' physical, chemical, and biological properties. Crystallography has therefore become an interdisciplinary research field. The subsequent sections briefly explain the methods used in the study.

1.1. X-ray Diffraction

Experimental analysis of crystalline materials became possible after Rontgen discovered the X-ray in 1895. In the electromagnetic spectrum, X-rays lie between ultraviolet light and gamma radiation. X-rays have a wavelength in the range of (0.5–2.5) Å. In 1912, Max Von Laue recognized that the wavelength of X-rays is comparable to the typical inter-atomic spacing of the crystal. He further proposed that crystals could be used as the diffraction gratings.

When a crystal is exposed to a monochromatic beam of X-rays, it is reflected. However, the reflection occurs only when the glancing angle θ has specific values. These values depend on the wavelength of the incident beam and lattice constants of the crystal. The crystal is considered a set of parallel lattice planes equidistant from one another in a crystal structure, separated by a distance *d*. The incident X-ray penetrates deep into the crystal and is reflected from the lower planes. Thus several beams of X-rays reflected from each of these planes are obtained. These reflected beams are then collected simultaneously at a distant detector. These reflected radiations may, therefore, undergo constructive or destructive interference producing maxima or minima in specific directions, i.e., experience diffraction phenomena. If the path difference between the two incident wave-fronts is an integral multiple of wavelength λ, constructive interference will take place between the reflected beams. Thus the intensity will be maximum for $n\lambda = 2d\sin\theta$, where *n* is an integer. This is well-known Bragg's law proposed

by W.L. Bragg and W.H. Bragg in 1913. This law reveals that crystals are a periodic array of atoms and open the paths for solid-state physics; hence, a new branch came into existence, i.e., X-ray crystallography [1].

An X-ray diffractometer has an X-ray source, a sample under investigation, and a detector for detecting diffracted X-rays. An automatic counter is there for measuring the intensity of X-ray diffraction. Diffracted intensities are counted directly, and Bragg's law gives the angular information that further helps us achieve the cell geometry and determine crystal structure.

X-ray diffraction is mainly used for two aspects, one is fingerprint characterization of crystalline materials and the other is to determine their structure [2]. Every crystalline solid exhibits a unique characteristic X-ray powder pattern. Consequently, in a given material, the X-ray powder pattern is the "fingerprint" of periodic atomic arrangements [3]. After identifying the material, one can determine its structure in the context of X-ray crystallography, i.e., atomic packing in the crystalline state and the interatomic distance and angle, etc. The size and shape of the unit cell for any compound can be easily determined by X-ray diffraction.

1.2. Structure Determination from Single Crystal X-Ray Diffraction

There are two types of X-ray diffraction techniques, one is powder X-ray diffraction (PXRD), and another is single crystal X-ray diffraction (SCXRD). The main steps in single-crystal X-ray diffraction analysis are presented in the flow chart (Scheme 1.1).

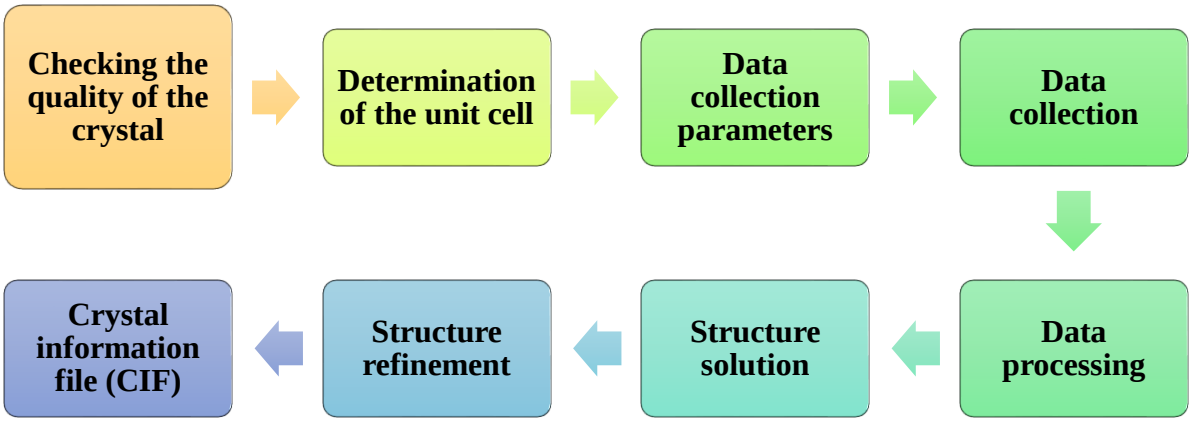

Scheme 1.1. Steps for single crystal X-ray diffraction analysis.

A detailed methodology of the single-crystal X-ray diffraction is attached below.

1.2.1. Sample Selection

The first and most important step for single-crystal X-ray diffraction is sample selection because the quality of the solved crystal structure depends on the crystal selected for data

collection. Therefore, the sample should have smooth surfaces, and the crystal should be optically clear, which can be determined with a polarizing microscope.

1.2.2. Sample Mounting

The selected sample is then mounted to the tip of very thin glass fibre using epoxy or cement. Special care is required to use enough epoxy to secure the sample without embedding the mounting compound. This fibre is attached to a brass mounting pin, usually using modelling clay, and this fibre-pin arrangement is then inserted into the goniometer head. After that, the goniometer head is fitted to the diffractometer. The sample is centered by viewing through a microscope or video camera attached to the diffractometer.

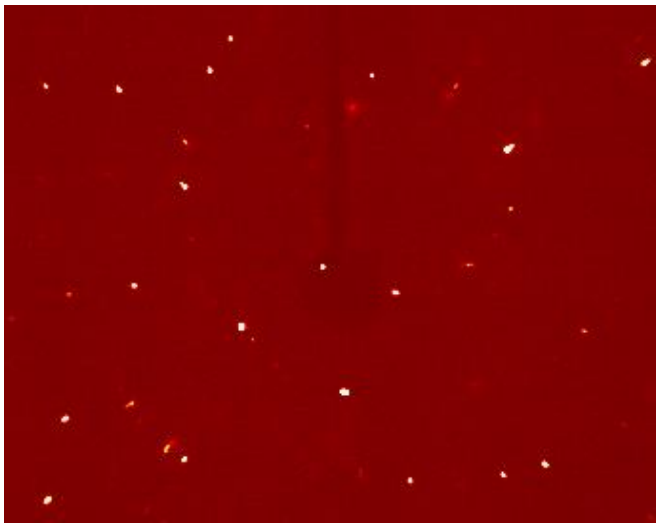

Figure 1.1. Single crystal X-ray diffraction pattern.

1.2.3. Collection of X-Ray Intensity Data

Once the crystal is centered, an enacting rotational image is collected to test the sample's quality and select the parameters for the next steps. An automated collection routine has been used to collect the initial set of frames for unit cell determination. Reflections from these frames are automatically indexed so that the reduced primitive cell is selected and the orientation matrix (which relates the unit cell to the actual crystal position within the beam) is calculated. Primitive unit cells are refined by the least-squares method and then transformed into suitable crystal systems and Bravais lattices. This resulting cell is also refined using the least-squares method to determine the final orientation matrix of the sample. Intensity data are collected after cell refinement and orientation matrix determination. Usually, this is done by accumulating a sphere or hemisphere of data using an incremental scan method, collecting frames in 0.1º– 0.3º increments (at certain angles while keeping others constant). The collection time is reduced for highly symmetric materials because the collection can be constrained symmetrically. For molybdenum (Mo) radiation, data is typically collected between 4º and 60º (2θ). A total run

time of about 6–8 hours is required for a hemisphere of data if the exposure time is 10–30 seconds per frame.

1.2.4. Space Group Determination

Space group determination is the most significant part of crystal structure determination and usually follows the indexing step. The symmetry possessed by crystals can be described by space group theory, one of the triumphs of mathematical crystallography. For example, if a substance has a monoclinic crystal system with an '*n*' number of atoms, then space group theory lists all possible arrangements of '*n*' atoms with monoclinic symmetry. The number of possible space groups can be reduced by noting the missing reflection indices from X-ray diffraction data. Thus, only two or three possible atomic arrangements remain.

Sometimes some space groups can be uniquely determined by applying the missing indices criterion to the diffraction pattern. When this criterion of missing indices fails to determine the correct space group, a number of alternative space groups must be considered and a successful structure solution adopted.

1.2.5. Structure Solution

The structure factor (F_{hkl}) is the mathematical description of the wave scattered by a crystal. The structure factor is a complex quantity, and its magnitude is the amplitude of the wave scattered. The phase angle determined the direction of the structure factor in the complex plane. It is given by the expression

$$F_{hkl} = \sum_{j}^{N} f_j e^{[-2\pi i(hx_j + ky_j + lz_j)]} \tag{1.1}$$

$$\Rightarrow F_{hkl} = |F_{hkl}| e^{i\varphi_{hkl}} \tag{1.2}$$

Where f_j is the atomic scattering factor of the jth atom positioned at (x_j, y_j, z_j) in the unit cell and φ_{hkl} is the phase angle. The scattering intensity is the square of the amplitude of the structure factor and may be expressed as

$$I_{hkl} = |F_{hkl}|^2 \tag{1.3}$$

If the phase angle is known, the structure factor can be represented in terms of electron density distribution function ($\rho(x,y,z)$) and given by the expression

$$F_{hkl} = V \int_{x=0}^{1} \int_{y=0}^{1} \int_{z=0}^{1} \rho(x,y,z) e^{2\pi i(hx+ky+lz)} dx\, dy\, dz \qquad (1.4)$$

The structure factor is the Fourier transform of the electron density distribution function. Hence $\rho(x,y,z)$ can be expressed in terms of F_{hkl} as

$$\rho(x,y,z) = (1/V) \sum_{h} \sum_{k} \sum_{l} F_{hkl} e^{-2\pi i(hx+ky+lz)} \qquad (1.5)$$

Therefore, evaluating the electron density from the set of crystal data and consequently F_{hkl} is mandatory for solving a crystal structure. This operation is known as Fourier synthesis. As the electron density distribution is periodic in nature, it can be represented in terms of the Fourier series. A three-dimensional contour map is usually plotted for $\rho(x,y,z)$, called the electron density map, which includes information on nuclear positions and molecular structure. By considering the phase, electron density distribution for a unit cell can be expressed as

$$\rho(x,y,z) = (1/V) \sum_{h} \sum_{k} \sum_{l} |F_{hkl}| e^{-2\pi i(hx+ky+lz-\varphi_{hkl})} \qquad (1.6)$$

The ultimate goal of an X-ray diffraction experiment is the computation of the electron density function and for this, we need both the magnitude and phase of corresponding structure factors from the relative intensities. However, the diffraction experiment only tells about the intensities of the scattered rays but not about the phases, which are also needed to evaluate electron density function. The interception of the diffracted beam by the intensity recording device leads to the phase problem as the phase information is missing, only the square of the amplitudes of the structure factor is provided by X-ray diffraction experiments.

Elimination of phase problem is vital for structure solution and the solution to the phase problem leads to the initial electron density map. Elements can be imposed to intensity centers, heavier elements are associated with higher intensities. The distances and angles between intensity centers can also be used for atom assignment based on possible coordination. A template may be used for the initial solution for a known sample. The "Patterson method" and the "Direct method" are generally used to overcome the phase problem.

1.2.5a. Patterson Method

In 1934, A.L. Patterson [4] introduce the first systematic approach to determine the structure from experimentally measured intensities. The inability to synthesize an electron density directly from the measured intensities is due to the lack of Fourier coefficients. However, $|F_{hkl}|^2$ does not contain phase information that is fully available. Applying convolution theory to Fourier functions for this particular problem of crystal structure analysis,

a function in Fourier series form is obtained which depends only on $|F_{hkl}|^2$ and is known as the Patterson function. Basically, it is a product of the electron density function. For simplicity, the derivation of the Patterson function in one dimension is achieved, and then it can be extended to two or three dimensions.

In this derivation, it is convenient to use absolute coordinates where fractional coordinates (x) and absolute coordinates (X) are related by

$$x = \left(\frac{X}{a}\right)$$

Where a is the lattice parameter. Let us consider the electron density function for two points X and $X+U$.

$$\rho(X) = \frac{1}{a}\sum_h F_h e^{\frac{-2\pi ihX}{a}} \tag{1.7}$$

$$\rho(X+U) = \frac{1}{a}\sum_h F_h e^{\frac{-2\pi ih(X+U)}{a}} \tag{1.8}$$

The Patterson function can be obtained by multiplying eq(1.7) and eq(1.8), i.e. two electron densities separated by a chosen distance of U inside the same crystal and can be expressed as

$$P(U) = \int_0^a \rho(X)\rho(X+U)\, dX \tag{1.9}$$

$$\Rightarrow P(U) = \int_0^a \left[\frac{1}{a}\sum_h F_h e^{-\frac{2\pi ihX}{a}}\right]\left[\frac{1}{a}\sum_h F_h e^{\frac{-2\pi ih(X+U)}{a}}\right] dX \tag{1.10}$$

It is the integral of the sum of terms. Individual terms of this product, in general, have different indices h. Therefore, denoting these indices as m and n, we have,

$$\Rightarrow P(U) = \int_0^a \left[\frac{1}{a}\sum_m F_m e^{-\frac{2\pi ihX}{a}}\right]\left[\frac{1}{a}\sum_n F_n e^{\frac{-2\pi ih(X+U)}{a}}\right] dX$$

$$\Rightarrow P(U) = \frac{1}{a^2}\sum_m\sum_n F_m F_n e^{-\frac{2\pi inU}{a}} \int_0^a e^{\frac{-2\pi iX(m+n)}{a}} dX \tag{1.11}$$

The integral of eq(1.11) vanishes when $q \neq -m$ except where $q=-m$ the integral of eq(1.11) becomes a.

Eq(1.11) can be written as

$$P(U) = \frac{1}{a^2}\sum_h F_h F_{-h} e^{\frac{-2\pi i(-h)U}{a}}\, a$$

$$\Rightarrow P(U) = \frac{1}{a}\sum_h F_h F_{-h} e^{\frac{2\pi i h U}{a}} \qquad (1.12)$$

Expressing the fractional coordinates $u=U/a$,

$$P(U) = \frac{1}{a}\sum_h |F_h|^2 e^{2\pi i h u} \qquad (1.13)$$

$$\Rightarrow P(U) = \frac{1}{a}\sum_h |F_h|^2\,(cos2\pi hu + isin2\pi hu) \qquad (1.14)$$

Now, according to Friedel's law, $|F_h|^2 = |F_{-h}|^2$

Now the summation over h in eq(1.14) gives to paired terms in $+h$ and $-h$:

For ($-h$), $|F_h|^2\, cos2\pi hu$ becomes

$$|F_{-h}|^2\, cos2\pi(-h)u = |F_h|^2\, cos2\pi hu$$

and, for ($-h$), $i|F_h|^2\, sin2\pi hu$ becomes

$$i|F_{-h}|^2\, sin2\pi(-h)u = -i|F_h|^2\, cos2\pi hu$$

So the sine terms in eq(1.14) cancel in pairs leaving

$$P(U) = \frac{1}{a}\sum_h |F_h|^2\,(cos2\pi hu) \qquad (1.15)$$

This shows that the Patterson function has the same value for $+u$ and $-u$ and is therefore symmetrical in origin. Thus all Patterson functions have a centre of symmetry in origin, regardless of whether the crystal is centrosymmetric or not.

For two and three dimensions, the Patterson function can be expressed as

$$P(uv) = \frac{1}{A}\sum_h\sum_k |F_{hk}|^2\, cos2\pi(hu + kv)$$

$$P(uvw) = \frac{1}{V}\sum_h\sum_k\sum_l |F_{hkl}|^2\, cos2\pi(hu + kv + lw) \qquad (1.16)$$

Where A is the two-dimensional cell's area and V is the three-dimensional cell's volume.

This function shows that each peak in the Patterson map corresponds to an interatomic vector in the crystal structure, and the magnitude of the peak is proportional to the product of the electron density of the corresponding pair of atoms. The Patterson method [4] can be a very useful starting point for solving crystal structures, especially in molecules with few satisfactorily heavier atoms in the molecule. Since the peaks due to heavy atoms – heavy atom interactions will dominate the map calculated from (1.16) and the atomic positions of heavy

atoms can be analyzed. But for lighter atoms, the X-ray intensity is less sensitive to nature and position than for heavy atoms. To overcome this problem, one may go for the 'direct method'. The solution of the Patterson function generally contains only a substructure, whereas direct methods often provide the positions of (almost) all non-hydrogen atoms [5].

1.2.5b. Direct Method

Direct methods are used for phase determination and attempt to derive the structure factor phases using mathematical relationships directly from the observed amplitudes obtained from the study of a single crystal, which implies, direct methods based on reciprocal-space data i.e. the $|F_{hkl}|^2$ values. In this way, direct methods represent an objective series of operations that will yield phase information. The amplitude and the phase of a wave are independent quantities, in the case of X-ray diffraction though, it is possible to make a relationship between these two quantities. Therefore, two important properties of the electron density function should be considered and those are listed below

- Electron density function is everywhere positive, i.e, $\rho(r) > 0$ [positivity];
- Electron density function is composed of discrete atoms [atomicity].

The relation between the positivity of $\rho(r)$ and phase values can be understood by imagining the computation of $\rho(r)$ as a Fourier series of a centrosymmetric structure, first with all signs correct (i.e, as it is) then reverse all the sign, that means phase changing by π. Therefore, in the first case $\rho(r)$ will be positive or zero everywhere, while in the second case $\rho(r)$ will be negative or zero, which is physically unacceptable.

In 1948, Harker and Kasper first introduce mathematical relationships to obtain phase relationships in the form of inequalities [6], and then further developed by Karle and Hauptman and by other scientists. But its implication in practical cases is limited. In 1953, Hauptman and Karle established the basic concepts and the probabilistic foundations of direct methods for solving complex crystal structures [7]. For this great contribution, the mathematician H. Hauptman and the physicist J. Karle were awarded the honorary Noble Prize for Chemistry conferred in 1985.

As the structure factor $F(h)$ and the electron density $\rho(r)$ are related by a Fourier transform, any constraint on the electron density leads to a corresponding constraint imposed on the structure factor. Since the amplitudes of the structures are known, it is sufficient in some favorable cases to determine only the phase values. Some of the constraints imposed on the electron density to determine the crystal structure are listed in Table 1.1.

Table 1.1. Constraints imposed on the electron density**.**

Constraints	**Role**
1. Atomicity of $\rho(r)$	Normalized structure factors [8]
2. Positivity of $\rho(r)$	Inequalities and determinants [9, 10]
3. $\int \rho^3(r)dv = max$	Phase relationship and Tangent formula [11, 12]
4. Equal atoms	Sayre's equation [13]
5. $\int \rho(r)\ ln\rho(r)dv = max$	Maximum entropy methods
6. Partial structure	Modification of probability equations
7. Multiple motifs	Molecular replacement

The condition of the discrete atom is used to define the normalized structure factor, *E* as

$$|E_h|^2 = I_h/\varepsilon_h\langle I\rangle \qquad (1.17)$$

The constraints listed in Table 1.1 give rise to Karle and Hauptman's general inequalities, the probability relation between phases [11], and the tangent formula, which can be expressed as

$$tan\phi_h \approx \frac{\sum_k |E_k E_{(h-k)}|\ sin[\phi_k + \phi_{(h-k)}]}{\sum_k |E_k E_{(h-k)}|\ cos[\phi_k + \phi_{(h-k)}]} \qquad (1.18)$$

The 'equal atoms' constraint used in Sayre's equation [13] gives an exact relationship between the structure factors

$$F_h = \theta_h \sum_k F_k F_{(h-k)} \qquad (1.19)$$

Where, θ_h depends on the shape of the atom. Equations (1.18) and (1.19) can be rewritten as

$$\begin{aligned} \phi_h &\approx phase\ of\ [E_k\ E_{h-k}] \\ \Rightarrow \phi_h &\approx \phi_k + \phi_{h-k} \\ \Rightarrow \phi_h + \phi_k + \phi_{h-k} &\approx 0 \end{aligned} \qquad (1.20)$$

Eq (1.20) is the well-known triple phase relationship.

In general, complete structure solutions of small organic molecules for centrosymmetric crystals are successfully dealt with by direct methods. The structure solution is very complicated for the non-centrosymmetric case, but the tangent formula has proved the most effective. The crystal structure of the smallest molecules is solved by direct methods with a program like SHELXS [14] or SIR [15]. With the help of these computer programs, random phase sets are generated which are further refined using phase annealing and tangent formula methods.

1.2.6. Structure Refinement

The electron density function can be expressed as a Fourier synthesis of structure factors, and the mathematical relationship is given by,

$$\rho(x,y,z) = (1/V)\sum_{h}\sum_{k}\sum_{l} F_{hkl}e^{-2\pi i(hx+ky+lz)}$$

A plot of the electron density function is a contour map of electron density, where peaks are centered at nuclear positions. From this contour map, we can deduce atomic sites, bond length, and all other structural information of crystalline molecules. Hence, obtaining a trial structure of molecules in the crystal is possible. Although, any error in the magnitudes or phases of the structure factors will lead to discrepancies between the calculated electron density and the electron density corresponding to the real structure. These errors have to be minimized in order to produce the real structure. The techniques used to minimize the error involved are called structure refinement methods. The steps for structure refinement are given below:

1.2.6a. Structure Completion

A structure solution provides only a partial set of atoms in the unit cell, which is treated as a trial structure model. However, this partial set of atoms obtained from the structure solution generally contains sufficient phase information that helps the user locate the remaining atoms. A set of structure factors may be calculated using the types of atoms and relative positions of the atoms in the trial structure model. Then, an electron density map can be prepared based on the calculated phase angles and the observed structure factors. The trial structure may not be exactly the same as the real structure. Therefore, the observed structure factor (F_o) derived from the experiment not exactly matches the calculated structure factor (F_c). Therefore, we can calculate a difference electron density map using coefficients of ($|F_o|-|F_c|$) with the calculated phase angles. As a result, difference electron density maps produce peaks indicating missing atoms and produce negative holes or valleys indicating too much electron density has been included in the model (e.g., too heavy of an atom for the site).

Thus, the structure factor is calculated from a partial information model and then a difference electron density map is used to locate the non-hydrogen atoms one by one. This process of structure refinement is repeated until all non-hydrogen atoms are located.

1.2.6b. Cyclic Fourier Refinement

After obtaining the trial structure from a set of atomic positions, we can calculate the structure factor with the expression,

$$F_{hkl} = \sum_{j=1}^{N} f_j e^{[2\pi i(hx_j + ky_j + lz_j)]} \quad (1.21)$$

The trial structure may not be exactly the same as the real structure. Therefore, the observed structure factor (F_o) derived from the experiment not exactly matches the calculated structure factor (F_c). For further refinement, the observed and calculated structure factor phases are compared. The phase angle can be determined using one of the phase-solving techniques. The calculated electron density function can be written as

$$\rho_c(x, y, z) = (1/V) \sum_h \sum_k \sum_l |F_c| e^{-2\pi i(hx + ky + lz - \varphi c)} \quad (1.22)$$

1.2.6c. Difference Fourier Refinement

If we obtain a reliable set of phase data from cyclic Fourier refinement, then we can write observed and calculated electron density as,

$$\rho_o(x, y, z) = (1/V) \sum_h \sum_k \sum_l |F_o| e^{-2\pi i(hx + ky + lz - \varphi c)} \quad (1.23)$$

and,

$$\rho_c(x, y, z) = (1/V) \sum_h \sum_k \sum_l |F_c| e^{-2\pi i(hx + ky + lz - \varphi c)} \quad (1.24)$$

Both expressions will face series termination errors, which may lead to obscure the interpretation of the electron density map. We need to take the difference between $\rho_o(x, y, z)$ and $\rho_c(x, y, z)$ to remove the series termination error. This method of refinement is repeated until the last difference Fourier map shows no further modifications.

1.2.6d. Least-Squares Refinement

The least-square refinement method uses the difference between the square of the observed and calculated structure factors as a measure of their disagreement. This method helps to find out the model having a minimum value of the quantity $[|F_o|^2 - |F_c|^2]$. This refinement method helps obtain a model which represents the best fit with the observed data.

The crystal structure refinement includes the refinement of three positional parameters and six thermal parameters for each atom. In addition to these atomic parameters, the crystal's size to the radiation source's intensity was also refined.

The agreement between the calculated and actual structure is evaluated by the residual factors,

$$R_1 = \frac{\sum_h \big||F_o| - |F_c|\big|}{\sum_h |F_o|} \tag{1.25}$$

and,

$$wR_2 = \left[\frac{\sum_h w_h(|F_o^2| - |F_c^2|)^2}{\sum_h w_h |F_o^2|^2}\right]^{1/2} \tag{1.26}$$

The weight, $w_h = 1/\sigma^2(F_o)$, $\sigma(F_o)$ is the estimated standard deviation of F_o. In a refinement program like SHELXL [16] more complicated weighing scheme is used $w = 1/\{\sigma^2(F_o^2) + (aP)^2 + bP\}$, where $P = [2\,F_c^2 + Max(F_o^2, 0)] / 3$. To give an even distribution of the standard deviations across all groups of data based on the relative intensities, the values for *a* and *b* are chosen.

The goodness of fit,

$$S = \left[\frac{\sum_h w_h(|F_o^2| - |F_c^2|)^2}{\sum_h N_R - N_P}\right]^{1/2} \tag{1.27}$$

(*S* is supposed to be > 1.0)

where N_R and N_P are the number of reflections and the number of refined parameters, respectively. R_1, wR_2, and S values help crystallographers understand structure refinement progress.

1.2.7. Single Crystal X-Ray Diffraction Analysis

Crystallization is the first and probably the most difficult step as there is no choice but to proceed by taking a trial-and-error approach to obtain an adequate crystal. A successful crystallization process may lead to the formation of single crystals, which can be cube-shaped, needle-like, or plate-like shaped. Selected single crystals are placed on a Bruker APEX-II Kappa CCD Single Crystal X-ray diffractometer. The crystals are irradiated using graphite monochromated MoK_α radiation (λ = 0.71073). One can collect diffraction data at different temperatures but of course, low temperature is preferable for data collection and were collected by APEX2 [17]. Data is reduced using the Bruker SAINT program [17]. The multi-scan method was applied for absorption corrections using SADABS [17]. The program SHELXS [14] is used to solve the crystal structure of the compound under investigation, which leads to the trial structure. The trial structure is then refined by full-matrix least-squares technique on F^2 using the program SHELXL [16]. All non-hydrogen atoms are refined anisotropically while all hydrogen atoms can be located from different Fourier maps and considered riding [18]. The structure solution is performed by using the WinGX program V2014.1 [19]. The PLATON

program analyzes the solved structure [20, 21]. Copies of the data are available free of cost when applying to CCDC; E-mail: deposit@ccdc.cam.ac.uk.

1.3. Material Characterization

Material characterization is necessary to obtain a complete description of the physical and chemical properties of the material of interest. Crystals are mandatory for understanding the physics and chemistry of the solid-state. A crystal is thoroughly characterized when its chemical composition, concentration, and structural conformation of all its constituent atoms and other related properties are known. For the characterization of crystals, various methods are available to study the physical and chemical properties of crystals. Some of them are

- Elemental analysis,
- Infrared spectroscopic analysis,
- Powder X-ray diffraction analysis,
- Single crystal X-ray diffraction analysis,
- UV –Vis spectroscopy,
- Thermal analysis.

1.3.1. Elemental Analysis

We need to do an elemental analysis of carbon, hydrogen, and nitrogen to determine the elemental composition of a prepared organic sample. The most preferred elemental analyzer is the CHN analyzer, which helps us determine the amount of carbon, hydrogen, and nitrogen in prepared complexes or compounds. Elemental analyses of our prepared samples were performed on a PerkinElmer 2400 Series-II CHN analyzer, USA, elemental analyzer. Elemental analysis of organic samples requires relatively small sample weights. The nature of the substance, the detection limit, the level of precision required and the type of elemental analyzer used may vary the actual sample weight. It is very important that the sample is weighed accurately, as the final amount of each is usually given as a percentage of the weight of the original sample. So a highly accurate microbalance is required due to the very small sample size. The sample has to be weighed using a tin capsule. The required amount for organic material is 2 to 3 mg, which can hardly exceed 10 mg if inorganic matter with little carbon content is investigated. Excess O_2 is introduced into the reactor chamber before casting the tin capsule enclosing the sample into the reactor chamber. The material is mineralized at about 990˚C. A tungsten trioxide catalyst is passed by the gaseous reaction products, and after that, complete oxidation is reached. The resulting composite should thus consist of CO_2, H_2O, and NO_x. Then the product gas mixture flows through a silica tube packed with copper granules. In this zone remaining oxygen is bound and nitric/nitrous oxides are reduced at about 500˚C. The ejecting gas includes the analytically important species CO_2, H_2O, and N_2. The resulting

products are carried by a constant flow of high-quality carrier gas, helium (Quality 5.0). Finally, the gas mixture achieves a defined pressure condition and then passes to a gas chromatographic system containing a packing material. Depending on the affinity between the analid and the packing material, the packing materials first adsorb and then desorb the gases separately. We measured the thermal conductivity of each eluate from the chromatographic column and then compared it to a standard sample (acetanilide) from which the amount ($\mu V/\mu g$) of each component was obtained.

1.3.2. Infrared Spectroscopic Analysis

Analytical techniques are used to determine a chemical or physical properties of a chemical element, chemical substance, or mixture. Infrared (IR) spectroscopy is one of the most common and widely used analytical techniques mainly employed by inorganic and organic chemists because of its utility in determining the structure of compounds and their identification. IR spectroscopy is nothing but the analysis of infrared light interacting with a molecule. This can be analyzed in three ways by measuring absorption, emission, and reflection. All organic substances possess selective absorption at certain frequencies in the infrared portion of the electromagnetic spectrum. In IR spectroscopy a spectrometer is used to determine the rate of transmission or absorption of the sample at a series of narrow frequency intervals throughout a chosen part of the spectrum. Hence we get a characteristic graph of the sample which is plotted between these transmission or absorption values and frequency or wavelength units. This characteristic graph constitutes an infrared spectrum. We have used a Perkin-Elmer LX-1 FT-IR spectrophotometer to record the infrared spectrum with a modern diamond attenuated total reflectance (ATR) accessory method in the range of 4000–400 cm^{-1}.

A molecule exhibits infrared absorption if and only if it possesses a specific feature i.e. an electric dipole must change during the vibration. Absorption will have more instances for the larger the change. Vibrations can influence either a change in bond length (stretching) or bond angle (bending). There are two types of stretching, symmetrical stretching (bonds can stretch in phase) and asymmetric stretching (bonds can stretch out of phase). A non-linear molecule of N atoms has 3N–6 normal modes of vibration, whereas a linear molecule has 3N–5.

An IR spectrometer consists of three basic components

- A source of radiation
- Optical path and monochromator
- Detector and amplifier

The filament is usually used as the radiation source. Applying an electric current maintains the source at red or white heat. Nernst filament (made of rare-earth oxides) or globar filament (made of carborundum) is mostly used as source filament. The silver-coated mirror is used for focusing the source beam on the sample. A monochromator is an optical device that is based on the separating capability of refraction (prism) or diffraction (diffraction grating), which can transmit a specific band of the electromagnetic spectrum. Therefore, a monochromator can produce radiation of desired frequency. There are mainly two types of detectors used in IR spectroscopy, heat-sensing detectors, and photoconductive detectors. In the case of a heat-sensing detector when radiation falls on a small cell, the air and temperature inside the cell change, and that change are measured in terms of pressure change which can be recorded directly as transmittance. Photoconductive detectors are usually a type of photoconductors that are based on photoconductive semiconducting materials. And PbS which is sensitive to infrared radiation is used as a detector. A photoconductive detector can simply consist of a piece of semiconductor material with two attached metallic electrodes for sensing the resistance. A Wheatstone bridge network is used to measure the conductivity of the material. The sample in fine powder form is pressed into a transparent disk with KBr. Then the disk is placed directly in the infrared beam in a suitable holder.

1.3.3. Powder X-Ray Diffraction Analysis

The powder method is generally used for identifying the sample under test. Powder X-ray diffraction looks at a large sample of polycrystalline material which may appear in many physical forms but is usually a powder; this is the main reason behind the name powder diffraction. A few tenths of a gram (or more) amount of pure sample is taken for grinding into a fine powder. The most preferred powder size is less than ~10 μm (or 200-mesh). The sample is then placed in a groove on a glass or metal plate and the surface of the sample is smoothed by pressing the surface with the help of a glass slide. The sample is then placed inside a goniometer of an X-ray powder diffractometer. The intensity of X-ray diffraction is then recorded on a paper chart recorder. The goniometer and the paper chart recorder are turned on simultaneously and at each Bragg angle, the intensity of diffracted beam appears as a line of a certain width on the paper chart, or the number of counts is recorded directly by a computer. We can easily determine 2θ and d from the positions of these diffraction lines (by applying Bragg's law) and calculate the Miller indices using the computer program POWD [22]. Although each peak consists of two separate reflections ($K_{\alpha 1}$ and $K_{\alpha 2}$), in smaller values of 2θ the peak locations overlap with $K_{\alpha 2}$ appearing as a hump next to $K_{\alpha 1}$. Greater separation occurs

at higher values of θ. Usually, these combined peaks are considered as one. The 2λ position of the diffraction peak is usually measured as the center of the peak at 80% of the peak height. The *d*-spacing of each peak is then obtained by solution of the Bragg equation for the appropriate value of λ.

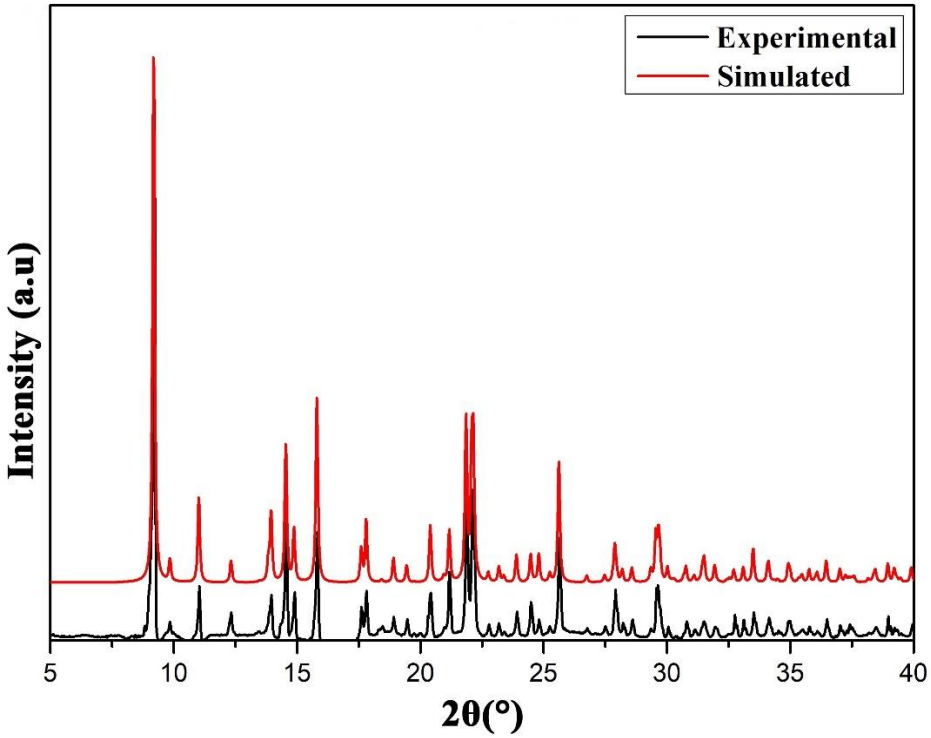

Figure 1.2. Powder X-ray diffraction patterns [23].

1.3.4. Single Crystal X-Ray Diffraction Analysis

A detailed methodology of single crystal X-ray diffraction is appended in Section 1.2.

1.3.5. UV–Vis Spectroscopic Study

UV–Vis spectroscopy is used for the optical characterization of any material. When a molecule absorbs light of a certain wavelength an electron can be raised from its highest occupied molecular orbital resulting in an electronic transition. Many molecules absorb light in the UV–visible region of electromagnetic radiation. Energy absorbed by the molecule leads to a change in the electronic excitation of the molecule. As the attenuation of the beam increases, the absorbance of the solution increases. The energy absorbed (ΔE) in an electronic transition is

$$\Delta E = h\nu = h\frac{c}{\lambda} \tag{1.28}$$

Here, *h* is Plank's constant, *v* is the frequency and λ is the corresponding wavelength of the radiation, and *c* is the speed of light.

In our study, we were optically characterized sample by UV–Vis spectroscopy. The absorption spectra were recorded using UV/Vis lambda 365, Perkin Elmer spectrophotometer. The concentration of the solution prepared for the experiment was kept very low, so the absorbance peak must be within 1.5 a.u. To calculate the optical band gap we have used Tauc's equation [24], which is given by,

$$\alpha h\nu = A(h\nu - E_g)^n \qquad (1.29)$$

where α is the absorption coefficient, h denotes Planck's constant, ν is the frequency of the incident radiation and A is an arbitrary constant that depends on temperature, photo energy, and phonon energy and it is assumed to be 1 for the ideal case. Here, n=1/2 for the allowed direct band gap and n=2 for the indirect band gap [25]. A graph of absorbance vs wavelength was obtained after performing the experiment.

1.3.6. Thermal Analysis

Thermal analysis is used to establish the relationship between the physical and chemical properties of a sample and its temperature. Different thermal analysis methods depend on the property to be measured. Here we mainly discuss Differential thermal analysis (DTA) and thermogravimetric analysis (TGA).

1.3.6a. Differential Thermal Analysis

Differential thermal analysis (DTA) is used to record the temperature difference between a substance and a reference material. As the two samples are heated or cooled at a controlled rate, they are subjected to the same temperature regime. We need to plot the graph between ΔT and T to get the DTA curve. Endotherms are plotted downward whereas exothermic peaks are plotted upward. Experimentally, this is done by employing a furnace. This furnace consists of a sample holder or block and contains two parallel and identical chambers. Each of the chambers has an identical thermocouple (Platinum-Platinum 10% Rhodium) or other temperature detectors. The sample that needs to be investigated is placed in one chamber and a thermally inert substance, which has a similar heat capacity such as α-alumina (Al_2O_3), is placed in the other. In a furnace, the sample and α-alumina are heated at a uniform rate by the temperature difference (ΔT) between them, and this is detected by the temperature detection devices and is recorded as a function of t or T.

1.3.6b. Thermogravimetric Analysis

This branch of thermal analysis investigates the sample's mass change as a function of temperature (in the scanning mode) or as a function of time (in the isothermal mode). The

decomposition and thermal stability of the substances are characterized by thermogravimetric (TG) analysis. The analysis takes place under different conditions to examine the dynamics of the physicochemical processes arising in the sample. There are several experimental conditions that may affect the sample's mass change characteristics. These controlling factors include the mass, volume, and physical form of the sample, the shape and nature of the sample holder, the nature and pressure of the atmosphere in the sample chamber, and the scanning rate. TG curves depict the thermal stability of samples under investigation. The vertical axis represents mass change (Δm) in percentage whereas the horizontal axis represents temperature (T) or time (t).

The thermogravimetric analysis instrument consists mainly of balance, a furnace, and a recorder. The furnace is designed for a linear rise of temperature with time at which the rate of heating can be varied. A small but exactly known sample mass is heated in a crucible on an analytical balance during controlled heating. Simultaneous treatment of an inert reference material (often alumina) ensures that it can be associated with any drift of the instrument. In general, several gas atmospheres (air, N_2, CO_2) can be chosen. Any difference in weight (loss or gain) of the sample during controlled heating is recorded with temperature. The technique is suitable for many solid materials, although there may be limitations in terms of possible reactions with the crucible material, or corrosive gases emitted by the sample.

1.4. Crystal Engineering

Crystal engineering, a subject of vast scope and application, has evolved as the result of fusion of ideas from many other disciplines [26]. Crystal engineering allows us to understand the packing mechanism of molecular crystals [26, 27]. A molecular crystal is one that is composed of molecules. The physical and chemical properties of molecular crystals are related only to the internal periodic structure which is nothing but the crystal structure. The formation of a particular crystal structure is a result of assembling molecules through intermolecular interactions in a particular way [27].

Ray Pepinsky first used the term crystal engineering in 1955 at a meeting of the American Physical Society held in Mexico when he state that "*crystallization of organic ions with metal-containing complex ions of suitable sizes, charges and solubilities results in structures with cells and symmetries determined chiefly by packing of complex ions. These cells and symmetries are to a good extent controllable: hence crystals with advantageous properties can be engineered.*" [28] In the practice of modern crystal engineering, we can clearly see the imprint of Pepinsky's statement because it includes all three vital elements of the subject:

analysis, design, and function. Taken together by this trio of qualities, the subject falls nicely within the scope of engineering. On the other hand, Gerhard M. J. Schmidt and his colleagues at the Weizmann Institute began working in the field of crystal engineering, although Schmidt named the branch *organic solid-state chemistry*. Although the reactivity of the solution is largely a molecular property, the solid-state reactivity of the crystal is characteristic of periodic molecular assembly. Schmidt was the first person who correlated the structure and reactivity in the solid state for a series of photodimerizable alkenes [29]. In the year 1989, G. R. Desiraju provided a proper definition of crystal engineering as "*the understanding of intermolecular interactions in the context of crystal packing and the utilization of such understanding in the design of new solid with desired physical and chemical properties*" [27]. Therefore, there are three distinct activities in this field for continuous consequences (a) study of non-covalent interactions; (b) study of packing modes in the context of these interactions for the purpose of designing a strategy for the construction of crystal and; (c) study of crystal properties. These three stages help us to understand what, how, and why crystal engineering. These features of crystal engineering have greatly influenced the interface of supramolecular and solid-state science [30]. Therefore, crystal engineering is an interdisciplinary area covering crystal growth, organic chemistry, inorganic chemistry and organometallic chemistry, X-ray crystallography, materials sciences, computational chemistry, and pharmaceutics [31].

Although the area of crystal engineering grown a lot, one basic question remains: 'Given the molecular structure of an organic compound, what is its crystal structure?' [31]. In other words, how does one molecule recognize another molecule during a crystallization event? The question may seem simple but there is no proper answer at the present time. However, the answer to this question can be found up to a certain stage. The fact is that a crystal is formed by the assembly of a large number of molecules and this building up (aufbau) does not have to be a smooth and uninterrupted process where the final structure of the crystal is established. A cluster is formed by the assembly of a few molecules, a larger entity is formed with a few clusters and these entities interact with each other through nucleation, which leads to the formation of the first crystal.

Scheme 1.2. Stepwise formation of crystal.

The first one-dimensional chain, then the two-dimensional layer, and then the three-dimensional structure will thus be the crystal formation in the aufbau process [32, 33] described

above, need not necessarily be a simple continuous one. Sometimes a medium-sized cluster may be formed and then may be incapable of growing further when it dissolves again and another pathway for nucleation can be developed. All these difficulties, such as the failure of the functional group approach and the stability and the variable interplay of kinetics and thermodynamics in nucleation invents extreme challenges in the prediction of crystal structure from molecular structures [34]. Therefore, simplification is needed, and the simplification can be provided by the concept of supramolecular synthon [35]. There are various non-covalent interactions, namely, hydrogen bonding, hydrophobic interactions, dispersion interactions, halogen bonding, and the interactions involving the aryl ring such as cation···π, N–H···π, C–H···π, S–H···π, π–π, lone-pair···π, salt bridge···π, etc. interactions are mainly responsible for the formation of supramolecular frameworks in different dimensions [36–42].

Crystal engineering has now entered the stage of maturity by going through the stages of early growth and moving forward toward the goal of consolidated development. A significant portion of structural data has been obtained and analyzed, and generalizations for crystal packing are being formed with this data. Initially, crystal engineering was considered crystal structure engineering, but it has been transformed into crystal property engineering. Therefore, the design of new molecular crystals with various optical, electronic, and chemical properties will play a pivotal role in the advancement of the field of crystal engineering [31]. As well as, understanding new intermolecular interactions will be a fundamental problem that needs to be handled with crystallography, spectroscopy, and computation [43].

1.5. Supramolecular Architectures

1.5.1. Molecular Recognition

Molecular recognition [44–46] at interfaces, self-assembly, nucleation, and growth, are concepts of central importance in physics, chemistry, biology, materials science, nanoscience, and manufacturing. These concepts are manifest in crystals through their different functions and forms. The knowledge of molecular recognition is an exceptionally new field that began in 1967 when C. J. Pedersen discovered crown ethers that were observed to bind alkali metal ions to form highly structured complexes [47]. DJ Cram (1988) also referred to molecular recognition chemistry as 'host-guest' chemistry [48], while Lehn (1988) called it supramolecular chemistry [49]. The term "molecular recognition" became very popular in the early 1980s, including a phenomenon that can be more accurately but less economically depicted as being regulated by specific non-covalent interactions. Such phenomena have

played a very important role in biological systems, and modern chemical research is highly motivated by the possibility that molecular recognition by design can lead to new technologies.

A molecular complex or supramolecule is a remarkably well-organized assembly of host and guest molecules that complement each other sterically and stereo-electronically through multiple contact points on a common surface [47–49]. A complex is formed when a 'host' molecule (a receptor) binds to one or more 'guest' molecules through weak directional forces acting between the component molecules. Molecular recognition is necessary for all supramolecular processes. The key concept of molecular recognition is the “lock and key” theory proposed by Emil Fischer which states that “enzymes have a specific shape that directly correlates to the shape of the substrate.” This mechanism is very crucial due to the structural fit between the recognizing molecule and the recognized molecule [50]. Molecular recognition is further classified into two subdivisions: static molecular recognition and dynamic molecular recognition. Static molecular recognition occurs between a host and a guest binding site. However, in dynamic recognition, the binding of the first guest to the first binding site induces a conformation transformation that influences the second guest's association constant at the second binding site (Figure 1.3). One can anticipate the most common recognition pattern among a set of molecular building blocks as supramolecular materials have a rational design [51]. However, there are many controlling factors that may affect the molecular architectures like metal ions, ligands, metal-ligand ratio, counter ions, pH value, solvents, and temperature.

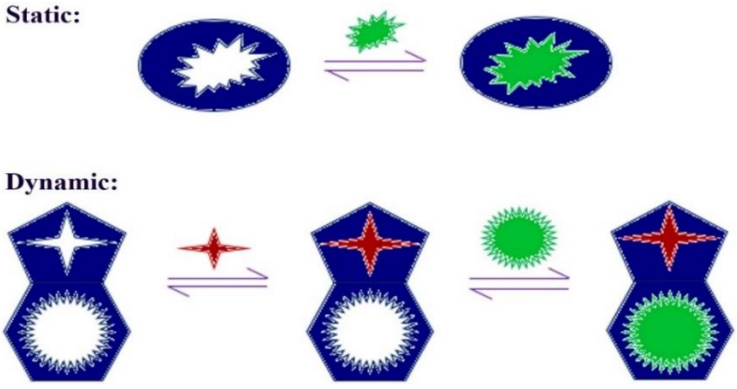

Figure 1.3. Pictorial representation of molecular recognition.

Molecular recognition plays a key role in various areas of science and technology, such as host-guest systems [52], biochemical processes [53, 54], catalysis [55], design of sensor materials [56], surface patterning [57], nanoscale assembly [58], etc. Molecular recognition is responsible for the supramolecular self-assembly of molecular building blocks. The recognition process leads to the design and preparation of functional materials [59, 60]. It is

usually assumed that same recognition patterns exist both in solution and in the crystalline solid-state; in many cases, this has been unequivocally established [61].

1.5.2. Self-Assembly

Self-assembly is the key to achieving supramolecular architectures [62, 63]. As the name suggests, self-assembly is the recognition process of molecules to have definite arrangements without the help of external guidance or management. Small molecules go through spontaneous association and lead to large, stable, and structurally well-defined symmetrical aggregates under equilibrium conditions due to specific, local interactions among the molecules [64]. To design molecular building blocks the concept of self-assembly is used [65]. Spontaneous participation of these artfully designed molecular building blocks acts as a foundation of supramolecular architectures. Self-assembly helps us to understand what will be the crystal structure of a particular molecule.

Self-assembly is scientifically fascinating as well as technologically significant for at least four reasons. Foremost, it is extremely important in life. Biological cells comprise an amazing range of complex structures for instance, lipid membranes, folded proteins, structured nucleic acids, protein aggregates, molecular machines, and many other biomolecules formed due to self-assembly process [66]. Secondly, self-assembly imparts a pathway to a wide-range of materials with well organized structures such as molecular crystals, liquid crystals, semicrystalline and phase-separated polymers [67]. Thirdly, self-assembly is also observed extensively in systems of constituents larger than molecules and exhibited great potential for its utilization in materials and condensed matter science [68–73]. Fourth, one of the most general strategies is offered by self-assembly concepts for generating nanostructure. Therefore, self-assembly is significant in a wide range of fields such as physics, chemistry, biology, materials science, nanoscience, and manufacturing. Hence self-assembly can play a vital role in interdisciplinary research.

The concept of self-assembly can be displayed by certain characteristics of the system i.e., components, interactions, reversibility or adjustability, environment, mass transport, and agitation [74]. In the self-assembly process, a cluster of molecules or parts of a macromolecule that interact among themselves are known as components, where the molecules or parts of macromolecules may be the same or different. In this process of self-association, the components or molecules interact among themselves *via* a balance of attractive and repulsive interactions. These interactions which are involved in the self-association process are generally

weak non-covalent types. During the formation of ordered structures through self-assembly process, the association must be reversible or allow the components to adjust their positions within an aggregate once it has formed.

Self-assembly of organic supramolecular architecture occurs in proteins, nucleic acids, and molecular complexes caused by supramolecular properties, such as weak non-covalent intermolecular forces including hydrogen bonding, electrostatic, van der Waals, stacking or donor-acceptor effects [75–79]. The self-assembly of organic supramolecules is controlled by steric factors associated with organic molecular components.

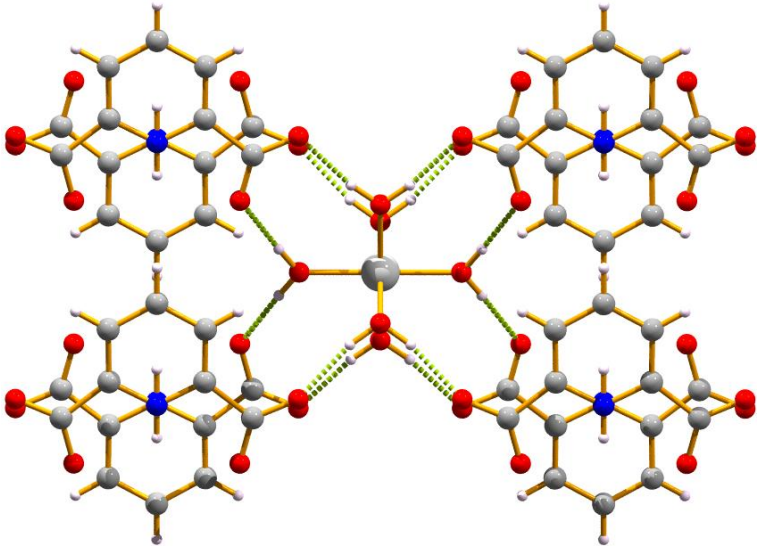

Figure 1.4. Representative example of supramolecular self-assembly [80].

1.5.3. Supramoleculecular Synthesis

According to Webster's Dictionary the term 'supramolecular' originated in 1903 but was first applied in a modern sense in 1978 by Jean-Marie Lehn as "the chemistry of molecular assemblies and intermolecular bonds" [81]. Jean-Marie Lehn explained that atoms link together through covalent bonds to form a molecule, a supramolecule formed with molecules using weaker and reversible intermolecular interactions as connectors. Crystal is a supramolecular entity. Therefore, the design and construction of molecular crystal is a form of supramolecular synthesis in solid-state.

A compound can be distinguished by three levels of structural organization, primary structure, secondary structure, and tertiary structure in accordance with supramolecular synthesis. The primary structure is the molecular level structure. Supramolecular entities generated from intermolecular interactions among molecular precursors are the secondary structure level. And the tertiary structure is the crystal packing of secondary structures or supramolecular entities. Generally, supramolecule synthesis relies on the making and breaking

of non-covalent interactions following an Aufbau strategy integrated into the design of the molecular components.

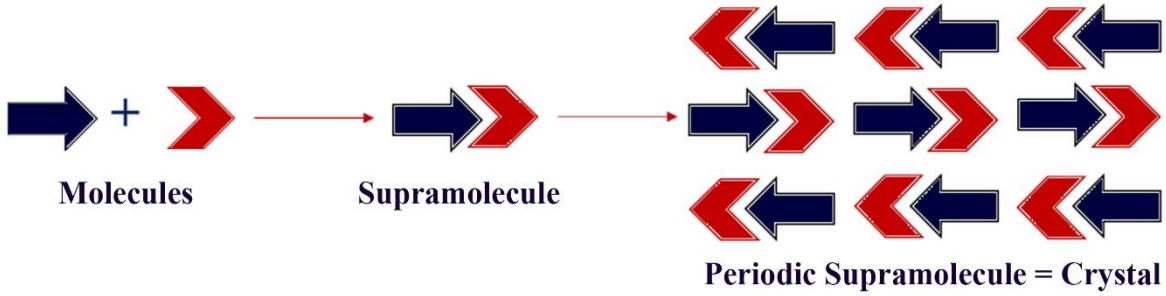

Figure 1.5. Periodic formation of molecule to supramolecule.

1.5.4. Supramolecular Synthon

The term "supramolecular synthon" was introduced by G.R. Desiraju in 1995 as a basic tool in crystal engineering for designing desired supramolecular architectures [82]. The concept of supramolecular synthon has been derived from the definition of "synthons" proposed by Corey [83]. Supramolecular synthon takes a similar fundamental role in supramolecular synthesis as the term synthon does in covalent synthesis. Thus supramolecular synthons are the smallest structural units within supramolecule which include all the information regarding mutual recognition to generate multidimensional supramolecular architectures in solid-state. Therefore, a significant feature of crystal engineering is partitioning a target network into supramolecular synthons and the not-so-critical fragments that connect the supramolecular synthons [82]. Such partitioning facilitates the exploration of the target network and is important in crystal engineering as it differentiates the interchangeability of supramolecular synthons in a family of structures. Critical observations from this type of interchangeability suggest that molecules with extensively divergent functionalities can have rather similar crystal structures.

The weak noncovalent interactions like hydrogen bonds, halogen bonds, and various stacking interactions play a key role in the recognition of supramolecular synthons (Figure 1.6). In this manner, supramolecular synthon permitted structural chemists and crystallographers to utilize the novel concepts of supramolecular approaches, target identification, and synthetic methodology as part of successful crystal engineering.

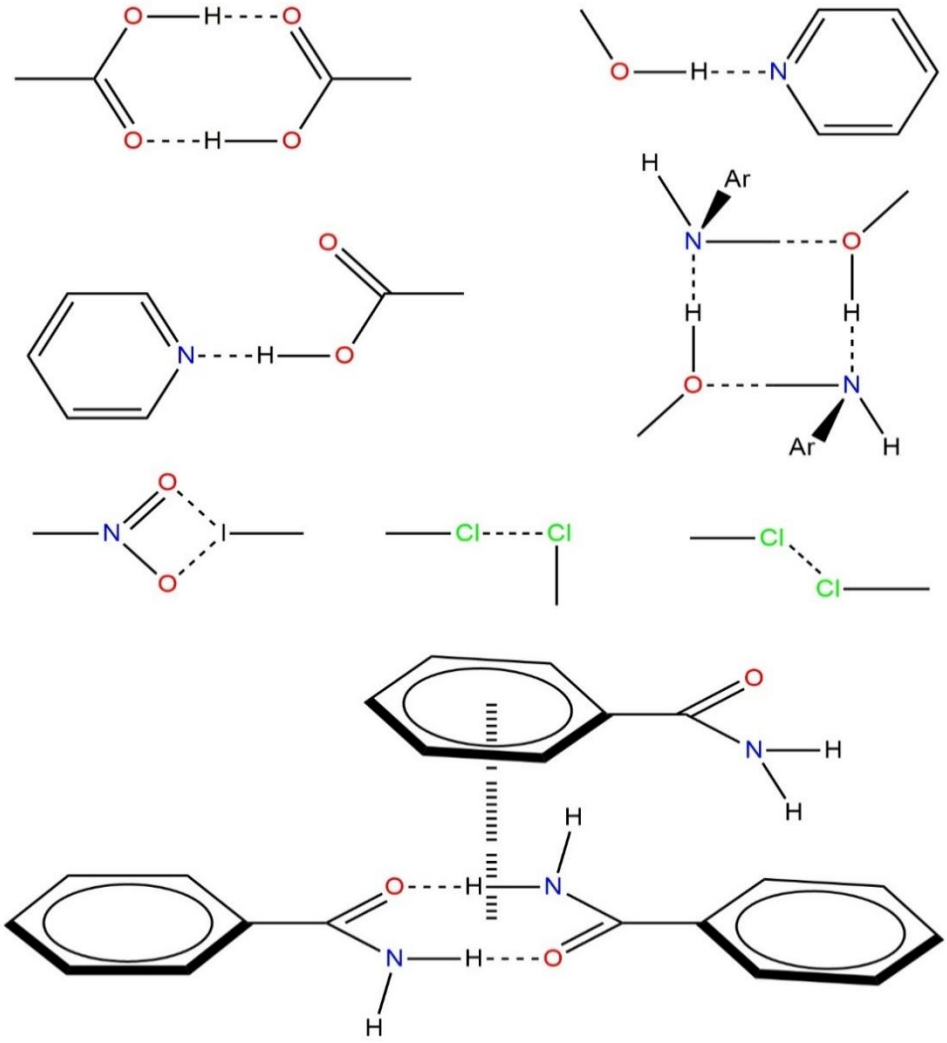

Figure 1.6. Representative examples of some synthons [84].

Supramolecular synthons are of two types, homomeric synthons, and heteromeric synthons. In homomeric synthon, two complementary functional groups interact whereas two different functional groups interact in heteromeric synthon [85]. Supramolecular homosynthons can lead to supramolecular assemblies in which single components form functional groups [86]. Conversely, supramolecular heterosynthons may predominate, when other complementary functional groups are present in the assemblies [87−90] (see Figure 1.7). Supramolecular synthons are characterized by identifying different types of unique intermolecular connections, and this approach is very successful when the molecules have several strong interactions. However, sometimes it can be very challenging to detect, especially in crystals with weak hydrogen bonding contacts. Therefore, the rationalization of association becomes very difficult for these kinds of crystals. An important reason for this situation is a geometric approach to determine the specific intermolecular interactions contributing to supramolecular synthons' formation. It should be noted that the strength of general dispersion

and electrostatic interactions can be comparable to the strength of specific interactions of larger molecules [91]. However, it has become standard practice in recent years to discuss and analyze supramolecular synthons in terms of weak intermolecular interactions. Most interactions are unstable, and their formation behaviour is related to and influenced by small changes in molecular structure and crystallization circumstances. Therefore, the goal should be to discover and design robust synthons to exchange from one network structure to another [92].

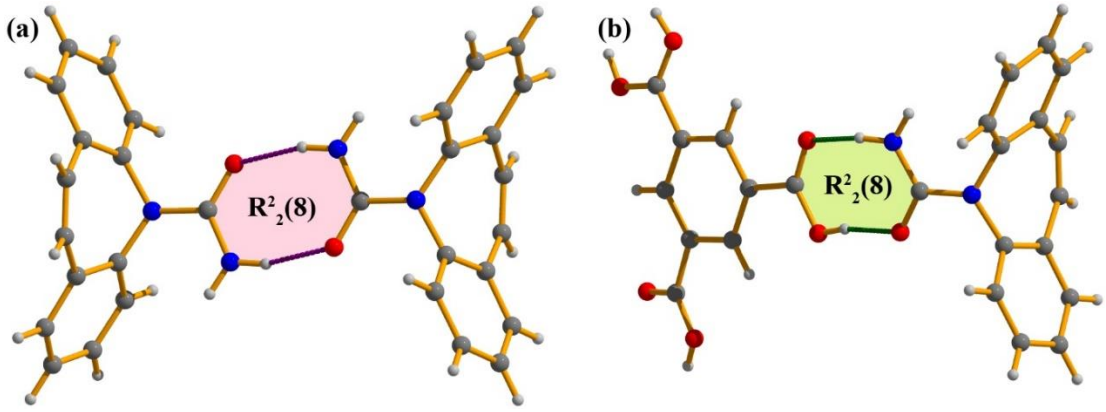

Figure 1.7. (a) Supramolecular homosynthon observed in cocrystal [89]; (b) Supramolecular heterosynthon observed in cocrystal [89].

Supramolecular synthon may lead to the formation of ring motifs denoted as $R_d^a(N)$, where "*a*" is the number of acceptors, "*d*" is the number of donors, and "*N*" is the total number of atoms involved in the formation of the ring motif. Ring motifs may be homomeric or heteromeric types (see Figure 1.7).

1.6. Non-Covalent Interaction

Non-covalent interactions, commonly known as non-covalent bonds, are a chemical bond established between atoms by complete exchange of electrons or no exchange of electrons at all, whereas covalent bonds form by two atoms share their electrons. Therefore, bonding connectivity is the main discrepancy between the non-covalent bonds with the covalent bond. Molecules are formed by covalent bonds whereas non-covalent bonds are the backbone of supramolecular architectures.

Noncovalent interactions are mandatory to maintain the three-dimensional structure of large molecules. In recent years, careful exploration of various non-covalent forces introduced a new variety of non-covalent interactions. These types of interactions include intra and intermolecular hydrogen bonding, hydrophobic interactions, dispersion interactions, halogen bonding, cation···π, N–H···π, C–H···π, S–H···π, π···π, π^+···π, lone pair···π, salt bridge···π, etc. These non-covalent interactions gain great attention due to their pivotal role in controlling

crystal structures and therefore the modes in which molecules arrange themselves greatly influence their properties. Although noncovalent interactions are weak but exhibit significant effects when they work together. Additionally, the sum of the individual bonds has less strength than the combined bond. This is because the sum of the enthalpies of each bond is less than the free energy of multiple bonds due to entropic effects [93−97]. Some notable non-covalent interactions have been discussed in this dissertation.

1.6.1. Hydrogen Bonding Interaction

The hydrogen bond is an exclusive phenomenon in a wide range of chemical systems, from inorganic to biological chemistry, for their structure, function, and dynamics. Many scientific disciplines are involved, such as organic chemistry, molecular medicine, pharmacy, supramolecular chemistry, general inorganic and organic chemistry, mineralogy, and material science. Especially in recent years, research on hydrogen bonds has grown significantly in breadth and depth, new concepts have emerged, and the complexity of the phenomena under consideration has significantly increased [98].

Hydrogen bonding is one type of electrostatic interaction involving a hydrogen atom located between a pair of other atoms with a high electron affinity. The hydrogen atom is covalently bonded with one of those atom pairs, which is an electronegative atom like nitrogen, oxygen, or fluorine that strongly attracts electrons, the remaining atom of the pair preferably has a lone pair of electrons. Hydrogen bonding interactions have been able to exert a great influence on various research fields. Being sufficiently strong and directional, hydrogen bonds can control and dictate the structure of molecular assemblies that help extend supramolecular architectures. The energies of hydrogen bonds lie in between van der Waals interactions and covalent bonds. Hence due to the wide range of energies, hydrogen bonds can be associated as well as dissociate rapidly at ambient temperature. Such dual potential abilities enable hydrogen bonds to establish specific recognition within a short time span, which is necessary for most biological reactions to occur at room temperature.

A D–H···A interaction is called a “hydrogen bond”, where D represents hydrogen bond donor and A represents hydrogen bond acceptor. A generalized definition of the hydrogen bond is proposed in new research as “*the hydrogen bond results from an attractive interaction between the hydrogen from a group or molecule D–H and an atom or a group of atoms A, in the same or a different molecule, where there is evidence of bond formation*” [99]. Pauling coined the concept of hydrogen bonds as electrostatic interaction. According to Pauling, due to

the highly electronegative nature of both the hydrogen bond donor (D) and acceptor (A), they have the ability to induce deshielding of the H atom and thereby increase the electrostatic attraction between the H atom and accepter atom satisfactorily, so this interaction is considered as bond [100].

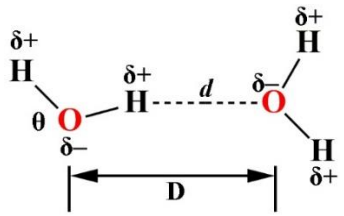

Figure 1.8. Prototype of a hydrogen bond: the water dimer. Definitions of geometrical parameters: d= H···O distance, D= O···O distance, θ= O–H···O angle [101].

The general nature of simple hydrogen bonds is well established. But, when scientists try to delve deeper into the characteristics of hydrogen bonds, such generalizations, and simplistic rationalizations seem completely inadequate. The prototypical hydrogen bond is formed between two water molecules depicted in Figure 1.8 and is represented as $O^{\delta-}$–$H^{\delta+}$···$O^{\delta-}$. The large electronegativity difference between hydrogen and oxygen atoms increases the inherent polarity of the O–H bond of the water molecule, which has a charge distribution of approximately +0.4 on each hydrogen atom and –0.8 on the oxygen atom. As a result, the neighboring water molecules orient themselves in such a way that the local dipoles of $O^{\delta-}$–$H^{\delta+}$ point to the negative partial charge of $O^{\delta-}$, i.e. the lone pair of the filled p-orbital of the negatively polarized oxygen atom. Therefore, the intermolecular separation (i.e. the H···O distance) is compressed by about 1 Å as compared to the sum of corresponding van der Waals radii [102, 103]. Strength of hydrogen bond may vary from weak to very strong. The properties of hydrogen bonding interactions are given in Table 1.2.

Table 1.2. Properties of Hydrogen bonding interactions.

Properties	**Very strong**	**Strong**	**Weak**
Bond energy range (kj mol^{-1})	63–167	17–63	>17
Examples	$[F–H···F]^-$, $[N–H···N]^+$, P–OH···O=P etc.	O–H···O=C, N–H···O=C, O–H···O–H etc.	C–H···O, O–H···O, N/O–H···π etc.
Bond length	D–H equivalent to H···A	D–H is less than H···A	D–H is very less than H···A
Lengthening of D–H (Å)	0.05–0.2	0.01–0.05	≤0.01
D···A range (Å)	2.2–2.5	2.5–3.2	3.0–4.0
H···A range (Å)	1.2–1.5	1.5–2.2	2.0–3.0
D–H···A bond angle range (°)	175–180	130–180	90–180

- **Different kinds of hydrogen bonding**

Different types of hydrogen bonds are based on their geometry (Figure 1.9). The first type is linear type (Figure 1.9 (a)), where the angle between donor atom (D), a hydrogen atom (H), and acceptor atom (A) is ~180°. In second type, the angle deviates from 180° (Figure 1.9 (b)). In addition to these two types of hydrogen bonds, donor atoms can form hydrogen bonds with multiple acceptor atoms at once in multifurcated hydrogen bonds (Figure 1.9 (c–d)). Multifurcated hydrogen bonding requires a high concentration of acceptors, at least locally. Multifurcated hydrogen bonds are widely present in protein molecules [104].

Strong hydrogen bonds correspond to high electronegativity atoms (F, O, and N) act as the donor and acceptor. The energies of strong hydrogen bonding interactions range from 15 to 40 kcal/mole. Weak hydrogen bond corresponds to moderate to low electronegativity of both or one of D and A in the D–H···A format. Interaction energies and geometries for most of the weak hydrogen bonding interactions are given in Table 1.3.

Table 1.3. Interaction energies and geometries of various nob-covalent forces.

Interaction	Energy (kcal/mole)	Typical H···A distance (Å)	Typical D–A distance (Å)
O–H···S	4	2.49	3.25
O–H···O	3–8	1.51	2.78
O–H···C	1.79	2.66	3.30
N–H···O	6	1.80	2.81
N–H···N	6	1.92	2.83
N–H···C	3	2.61	3.30
N–H···S	3	2.60	3.12
N/O–H···π	2–4	2.45	3.30
C–H···F	2.2	2.53	3.47
C–H···F–C	2.2	2.60	3.50
C–H···N	2.0	2.51	3.41
C–H···O	~2.0	2.60	3.50
C–H···Se	1.84	2.81	3.25
C–H···S	1.5	2.70	3.66
C–H···π	~1.0	2.36	3.20
C–H···C	0.33	2.74	3.59
S–H···N	1.5–3.5	2.80	3.70
S–H···S	1.1	2.16	3.48

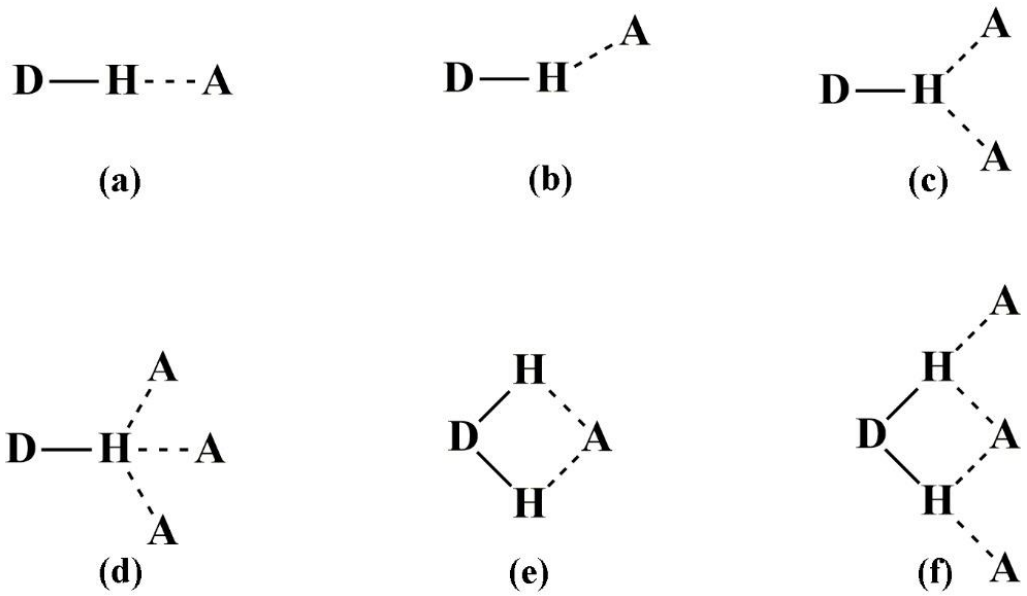

Figure 1.9. Different kinds of hydrogen bonding geometries: (a) linear; (b) bent; (c) donating bifurcated; (d) trifurcated; (e) accepting bifurcated; (f) three-centre bifurcated.

1.6.2. Salt Bridge (SB) Interaction

Salt bridges (SB) are hydrogen-bonded ion pairs and may be defined as interactions between two groups of opposite charges. In salt bridge, protonated and deprotonated residues interact with each other (Figure 1.10), which is important for the stability of the molecular structure [105–107]. Although considerable progress has been made [108, 109], accurately predicting and modelling salt bridges is challenging. Salt-bridge interactions are particularly difficult to predict because combining a basic residue and a carboxylate to form a salt-bridge is difficult. The strict geometrical constraints imposed by electrostatic and hydrogen-bonding interactions also play an important role in salt-bridge formation. Hydrogen bonding of SBs exhibits stronger binding as compared to normal hydrogen bonding interactions as a consequence of zwitterionic charges (charge-assisted hydrogen bonds) [110]. Salt bridge formation is one of the significant non-covalent interactions for the construction of supramolecular self-assembled structures in organic solvents [111, 112]. SBs play an important role in protein chemistry such as substrate binding, catalytic triad activity, secondary-structure stabilization, and stability of thermophilic proteins [113].

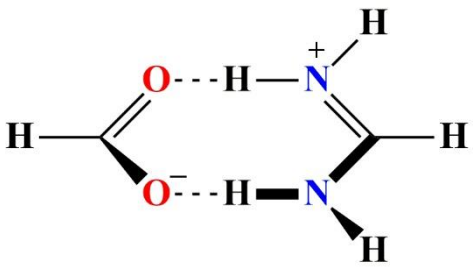

Figure 1.10. Schematic representation of a salt-bridge [114].

1.6.3. C–H···π Interaction

The interaction between an aliphatic/aromatic C–H group and an aromatic π-electron system (or any delocalized π-system) is referred to as a "C–H···π interaction" (Figure 1.11). This phenomenon is observed in several weak nonclassical hydrogen-bonding interactions [115, 116]. Despite the weak character of these interactions, they are ubiquitous. These C–H···π interactions are extensively studied in various branches of science, such as supramolecular chemistry [117], molecular aggregation [118], crystal packing [119], protein and other biomolecule structures [120], and rational drug design [121]. Umezawa et al conducted a close study of the crystal structure database and discovered that about 40% of organic crystals contain C−H···π interactions [122].

The non-classical hydrogen bonding interaction, C–H···π, has a great impact in various fields like self-assembly, structures of proteins and nucleic acids, chiral recognition, and many more [123–127]. C–H···π has been recognized as an attractive molecular force occurring between a non-polar or feebly polar C–H bond and an aromatic π-system [128]. Electrostatic forces are mainly responsible for the attraction in conventional hydrogen bonds, whereas the trivial van-der-Waals force of attraction is responsible for C–H···π interaction. As C–H···π interaction mostly takes place between soft acid and soft bases, which is mainly comprised of electron correlation energy or dispersion energy, although electrostatic forces may have a negligible contribution to some extent [129]. Unlike conventional hydrogen bonds and Coulomb forces, the C–H···π interaction is nonpolar in nature and effective in water and is considered the weakest non-classical hydrogen bond [116].

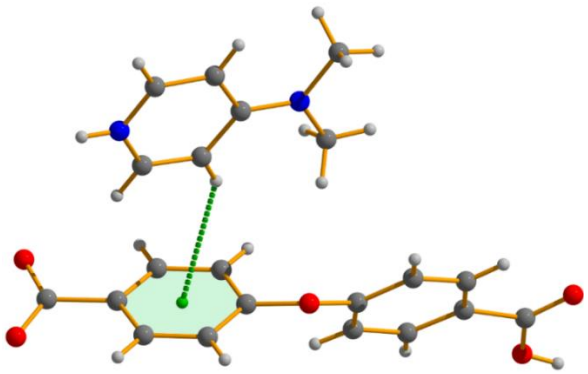

Figure 1.11. C−H···π interaction in a pyridinium-carboxylate salt [130].

1.6.4. π···π Stacking Interaction

The interaction between aryl rings containing π orbitals is widely recognized as π···π stacking interaction (Figure 1.12) which has attracted tremendous attention in various fields of material science, that includes modern chemistry, molecular biology to material designing due to its unique characteristics like strong binding force, non-destructive fabrication process, and

simple operative modes. These interactions are extensively ubiquitous in the crystal packing of an aromatic ring containing organic molecules and in biomolecules and nanomaterials [130−133]. π···π stacking interactions also play a key role in the intercalation of drugs into DNA channels.

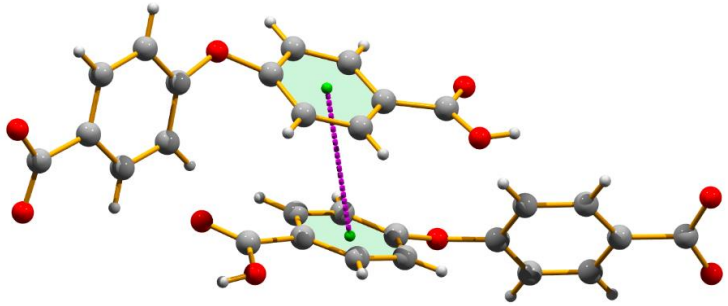

Figure 1.12. π···π interaction in a pyridinium-carboxylate salt [130].

The benzene dimer is the most common type of arene–arene interaction, which can be considered a model system for π···π interactions. Due to its immense importance, a wide range of research is underway, from early gas phase studies to recent computational studies [134−136]. This vast amount of research helps the scientific community gain useful knowledge and understanding of the fundamental properties of π···π interactions. The benzene dimer has a binding energy of 1.6 kcal mol^{-1} (experimentally obtained) [137]. A variety of stacking arrangements are possible for π···π interactions. Aromatic π···π stacking interactions can be divided into two types, the stacked conformation, and the pi-teeing (perpendicular T-shaped) conformation. The stacked conformation of the two aryl rings can either exhibit perfect face-to-face alignment or they can be offset, a parallel displaced packing arrangement (Figure 1.13). Among these three types of conformation, the most common arrangement is offset or slipped packing conformation [138−140]. The interplanar separation distance between two aryl rings involved in the face-to-face parallel alignment is about 3.3–3.8 Å. The edge-on or T-shaped (point-to-face) conformation is for C−H···π interaction (Figure 1.13c) [141].

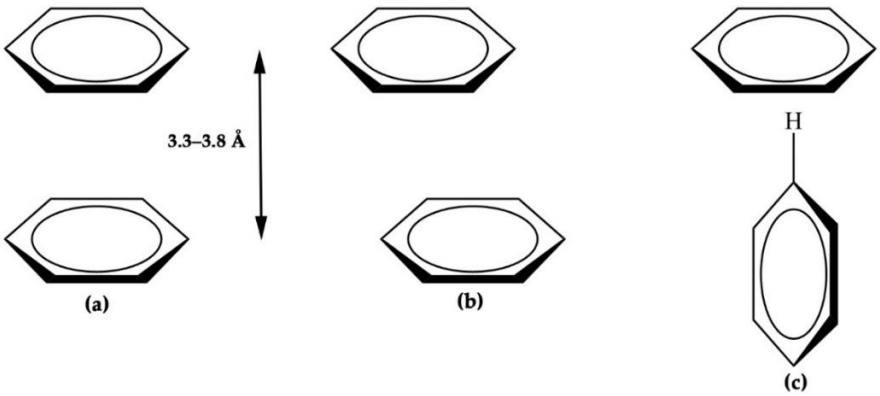

Figure 1.13. Principal orientations of aromatic-aromatic interactions, (a) face-to-face, perfect alignment; (b) offset, slipped, parallel displaced; (c) point-to-face, edge-on, or T-shaped [142].

Despite the great significance of π···π stacking interaction, knowledge of their origin, strength, and orientational dependence took a long time to reveal. A basic charge distribution representation given by Hunter and Sanders attempts to explain the qualitative geometric preferences for interactions between aromatic molecules [143], but in that case, quantitative predictions of geometries and energies are highly desirable. The stability of π···π stacking interactions between closed shell molecules depends mainly on three types of forces, (a) Dipole-dipole forces, (b) Dipole-induced dipole forces, (c) Induced dipole-induced dipole (London) dispersion forces [144].

Hunter and Sanders developed collection of rules depending upon a simple model of charge distribution in a π system to qualitatively understand and analyze aromatic-aromatic interactions. They separated the σ framework and π electrons considering that π···π interactions arise from π···σ attractions that can overcome π···π repulsions [142]. Therefore, for non-polarized π-systems, the "Hunter-Sanders" rules are:

- Rule 1: π···π repulsion becomes important in a face-to-face π-stacked conformation.
- Rule 2: π···σ attraction becomes important in an edge-on or T-shaped conformation.
- Rule 3: π···σ attraction becomes important in an offset π-stacked conformation.

For polarized π systems, there are three additional rules, referred to here as the requirement for face-to-face π stacking.

- Rule 4: Charge–charge interaction becomes important as they cause interactions between highly charged atoms.
- Rule 5: A favorable (face-to-face) interaction with a neutral or weakly polarized site requires as a π polarization a π-deficient atom (in the aromatic ring).
- Rule 6: A favorable (face-to-face) interaction with a neutral or weakly polarized site requires as an σ polarization a positively charged atom (in the aromatic ring).

Experimental results suggest that electron-withdrawing substituents or heteroatoms increase the strength of π···π interactions. The electron density of the π-system is reduced due to electron-withdrawing substituents or heteroatoms, thereby reducing the π···π electron repulsion. Finally, the effectiveness of "π···π interactions" increases the stability of aromatic molecules when both participating aromatic molecules are electron deficient, whereas electron-donating substituents attached to the aromatic system adversely affect the π···π interactions. The sequence of stability of π-interactions between two π-systems is π-deficient···π-deficient

> π-deficient···π-rich > π-rich···π-rich [143, 145]. Consequently, pyridines, bipyridines, and other aromatic nitrogen heterocycles should in principle be suitable for π···π interactions because they are electron deficient, and hence heterocyclic nitrogens exhibit effective π···π interactions [146].

1.6.5. π^+···π Interaction

The π^+···π interaction (Figure 1.14) is one of the recent developments in weak non-covalent interactions. This is similar interaction like π···π stacking interaction. In this case, the positively charged π-aromatic system interacts with the neutral π-aromatic system. The π^+···π interaction differs from the cation···π interaction as there is a strong dispersion force acting between two the stacked aromatic ring systems, although, the extensive investigation revealed that π^+···π interaction is stronger than C–H···π and π···π stacking interaction [147, 148]. There are two main categories of π^+···π interaction, one is displaced stacked (D) another is T-shaped structure (T) conformation. π^+···π systems are mainly stabilized due to both electrostatic and dispersion energy. Binding energies for different orientations of π^+···π interactions have been established by Kim and his co-workers. The characteristic binding energies of the π^+···π(D) structures (~8–11 kcal/mol) and the π^+···π(T) structures (~9–14 kcal/mol) are smaller than the typical cation···π binding energy (~9–23 kcal/mol) [147] but much higher in comparison to the typical H-bonding energy (~5kcal/mol for the water dimer) [149], C– H···π binding energy (~1.5–3 kcal/mol). They also investigated that dispersion and electrostatic forces are the main stabilizing forces responsible for π^+···π interactions.

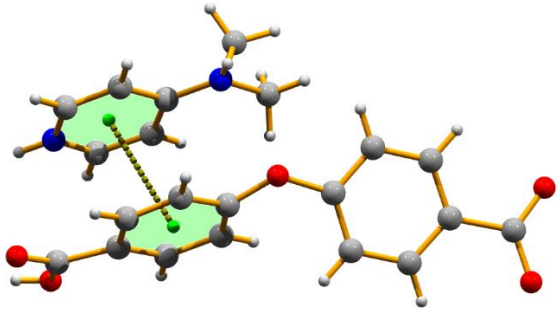

Figure 1.14. π^+···π interaction in a pyridinium-carboxylate salt [130].

1.6.6. Anion···π Interaction

During the last few years, anion-π interaction has attracted great attention as a new supramolecular interaction. Generally, anion···π interactions (Figure 1.15) are called favorable non-covalent interactions involving an electron-deficient (π-acidic) aromatic system and an anion are involved [150]. Several computational studies have shown that electrostatic interactions and anion-induced polarization effects are mainly responsible for the stabilization

of anion···π interactions. Anion-π interaction have many applications in numerous chemical and biological systems, including molecular anion recognition, transport (artificial highly selective anion receptors and channels), and environmental as well as medicinal applications [151, 152].

Any interaction between the anion and the neutral aromatic π-cloud should naturally be repulsive, but once the electron-withdrawing groups are bound to the aromatic π-cloud, the aromatic system becomes acidic (i.e. electron-deficient). Consequently, less repulsive interactions are observed between anions and electron-deficient aromatic systems, under such conditions anion-π interactions are favoured [153]. According to several notable theoretical investigations, these interactions are energetically favorable and fall in the energy range of 20–50 kJ mol^{-1} [154–156], which is also supported by a substantial number of experimental evidence [157–159].

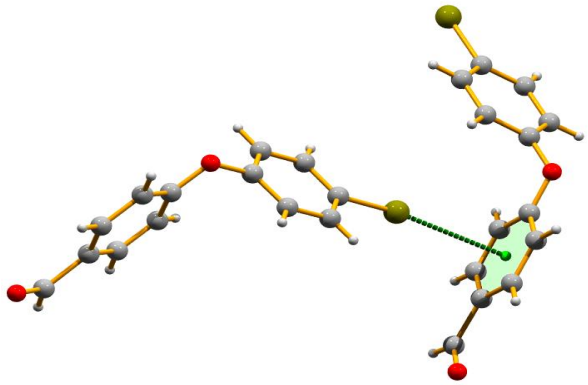

Figure 1.15. Anion···π interaction in solid-state structure of 4-(4-bromophenoxy)benzaldehyde [160].

1.6.7. Lone pair···π Interaction

Lone pair···π interactions (Figure 1.16) have been receiving tremendous attention from the scientific community for the past few years. Lone pair···π Interaction is being recognized as a supramolecular interaction by chemists and crystallographers. Such non-covalent interactions occur between a neutral electron-rich molecule and an electron-poor π-ring, which is assumed to be electrostatically repulsive [161, 162]. Both the anion···π and the lone pair···π, are similar but unusual types of interactions, as the negatively charged elements in both cases tend to position themselves on top of the electron-poor π ring. Lone pair···π interaction is observed in various biological systems [163, 164]. The stability of biological macromolecules is greatly influenced by lone pair···π interactions [165, 166] and it plays an important role in the binding of inhibitors in the binding pocket of biochemical receptors [167]. Sankararamakrishnan and his coworkers performed a detailed investigation of protein

databases of lone pair···π interactions and found that these interactions occur when the lone pair donor atoms are within 3.5 Å of the centroid of the aromatic rings [168]. Lone pair···π interactions play an essential role in forming the crystal structure. [162, 169–171]. Computational studies reveal that the lone pair···π interaction can be energetically favorable [172–174].

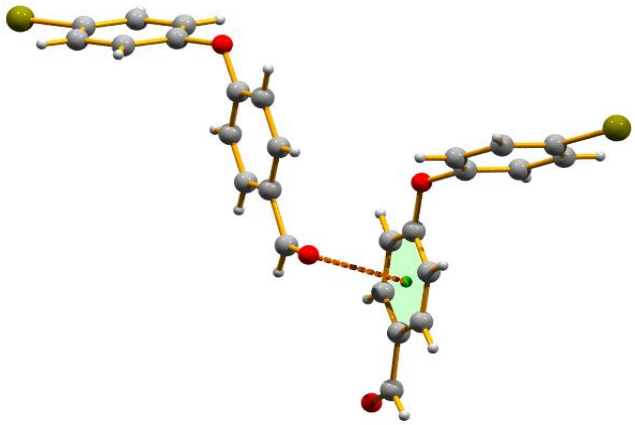

Figure 1.16. Lone pair···π interaction in solid-state structure of 4-(4-bromophenoxy)benzaldehyde [160].

1.7. Hirshfeld Surface Analysis

Hirshfeld surface analysis [175–180] is a quantitative technique to visualize intermolecular interactions of the molecules in a crystal structure and to explore the X-ray information by using *CrystalExplorer* software [181, 182], which can generate them using only Crystallographic Information Files (cifs) [183]. The Hirshfeld surfaces of the crystal structure are fabricated based on electron-distribution calculated as the sum of spherical atomic electron densities. Hirshfeld surfaces are created by dividing the crystal space into different sections where the total electron distribution among the spherical atoms for the molecule (promolecule) dominates the sum of the electron distribution over the crystal (procrystal) [184, 185]. For a particular molecule, weighting function $w(\boldsymbol{r})$ can be defined as,

$$w(\boldsymbol{r}) = \sum_{a \in molecule} \rho_a(\boldsymbol{r}) \Big/ \sum_{a \in crystal} \rho_a(\boldsymbol{r}) \qquad (1.30)$$

$$= \rho_{promolecule}(\boldsymbol{r}) / \rho_{procrystal}(\boldsymbol{r})$$

$$\simeq \rho_{molecule}(\boldsymbol{r}) / \rho_{crystal}(\boldsymbol{r})$$

Since, for Hirshfeld surfaces, $w(\boldsymbol{r})=0.5$; and the electron density of promolecule dominates over the electron density of procrystal when the value of $w(\boldsymbol{r})$ is greater than or equal to 0.5. The ratio between promolecule and procrystal electron densities can be considered an approximation to the ratio between the actual molecule and crystal electron densities in this situation where $\rho(r)$ represents spherically averaged Hartree-Fock atomic electron density

function [186]. Small values of the weight function will cause gaps between adjacent molecules, and larger values will result in the overlap of molecules.

Hirshfeld surface is unique for each crystal structure and a collection of spherical atomic electron densities [185]. Shape of the surface not only depends on the interaction between molecules in the crystal but also on the interaction between atoms in the molecule. Various properties (like d_i, d_e, d_{norm}, shape index, and curvedness) of the surface can be explored by Hirshfeld surface analysis. d_e and d_i denote the distances from the Hirshfeld surface to the closest atoms outside and inside the surface, respectively. The normalized contact distance (d_{norm}) based on both d_e and d_i and the van der Waals (*vdW*) radii of the atoms, is given by

$$d_{norm} = \frac{d_i - r_i^{vdW}}{r_i^{vdW}} + \frac{d_e - r_e^{vdW}}{r_e^{vdW}} \tag{1.31}$$

Shape index (*S*) is the measure of the qualitative shape of the surface. The value of *S* ranges from −1.0 (concave) through 0.0 (minimal surface) to +1.0 (convex). Curvedness (*C*) is the function of the root-mean-square curvature of the Hirshfeld surface. Flat regions of the surface lead to low curvedness whereas sharp curvature indicates high curvedness. High curvedness tends to divide contact patches with the neighboring molecules, hence it is possible to define the coordination number of the crystal with the help of curvedness. The value of *C* ranges from −4.0 (flat) through 0.0 (unit sphere) to +0.4 (singular).

$$S = \frac{2}{\pi}\arctan\left(\frac{k_1 + k_2}{k_1 - k_2}\right) \tag{1.32}$$

$$C = \frac{2}{\pi} ln \sqrt{\frac{{k_1}^2 + {k_2}^2}{2}} \tag{1.33}$$

Where k_1 and k_2 are principal curvature.

Table 1.4. Properties of Hirshfeld surface.

Surface property	**Color on the surface**	**Indication**
$\boldsymbol{d_{norm}}$	Red	Shorter than *vdW* contacts
	White	Equal to *vdW* contacts
	Blue	Longer than *vdW* contacts
$\boldsymbol{d_i}$	Red	H-bond donor region
	Yellow	H-bond acceptor region

d_e	Red Yellow Blue Green	H-bond acceptor region H-bond donor region Stacking region Proximity to atoms in the molecules stacked above
Shape index	Red Blue Red-blue triangle (bow tie)	Hollows Bump π···π stacking
Curvedness	Green Blue Yellow/ Red	R.M.S curvature near unity Large R.M.S curvature Flat region (but not always, sometimes corresponds to H-bond)

The 2D fingerprint plots can be generated for all calculated 3D Hirshfeld Surfaces by using *CrystalExplorer 17* software. 2D Fingerprint plot is the graphical representation of selected or all intermolecular interactions for the crystal structure (based on d_e and d_i) [187, 188]. The window of the fingerprint plot is interconnected with the Hirshfeld surface display. There is a filter for highlighting close contacts by elements inside and outside of the generated surface. Each and every part of the fingerprint plot is unique due to their unique d_e and d_i values. The points with a contribution to the surface are colored red for the greatest contribution through green to blue for a small contribution and the points with no contribution are left uncolored.

Molecular energy framework calculation is carried out using the *CrystalExplorer 17* program and it is useful to understand the topology of overall intermolecular interaction energies between the constituents of a crystal. For calculating interaction energies it is necessary to generate a 3.8Å cluster around the selected fragments [182]. To obtain accurate energy values we have to consider the "B3LYP/6-31G (d,p)" energy model. The cylinders joining the centroids of the pairs of molecules represent the interaction energies. The magnitude of the interaction energy is proportional to the cylinder radius which signifies the energy components of the energy framework. The color of the cylinders corresponding to electrostatic (E_{ele}), dispersion (E_{dis}), and total energy (E_{tot}) are in red, green, and blue color codes, respectively. A scale factor can be used to control the expansion or contraction of the cylinders

in the framework. Keeping the same scale factor, a direct comparison of energy frameworks is possible. An energy threshold can be used to avoid crowded diagrams.

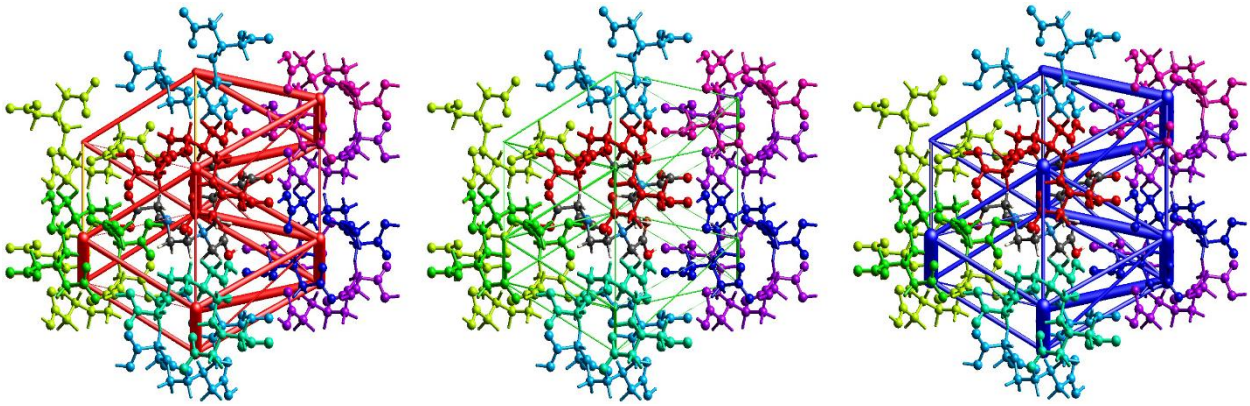

Figure 1.17. Energy framework of Penta(carboxymethyl)diethylenetriamine, the electrostatic potential force (left column), dispersion force (middle column), and total energy (right column) diagrams [189].

1.8. DFT Calculation

The history of the use of electron density instead of the wave function can be traced back to the work of both Llewellyn Thomas and Enrico Fermi in 1927 [190, 191]. The Thomas-Fermi (TF) theory assumes that the electron motion is uncorrelated and that the associated kinetic energy can be described by a local approximation based on the results for free electrons. Although the electron-electron and electron-nucleus interactions are considered classically, the kinetic energy of electrons can be deduced from the quantum statistical theory based on the uniform electron gas according to TF theory, and the kinetic energy of the electrons is defined as,

$$T(\rho) = C_F \int \rho^{5/3}(r)dr \tag{1.34}$$

where,

$$C_F = \frac{3}{10}(3\pi^2)^{2/3} = 2.871 \tag{1.35}$$

Therefore, we can see from the above expression that kinetic energy of electrons is explicitly dependent on electron density. The Thomas-Fermi-Dirac-Weizsacker model (TFDW) for energy functional with the second order gradient correction is [192],

$$E(\rho) = C_F \int \rho^{5/3}(r)dr + \lambda\frac{1}{8}\int \frac{|\nabla(\rho(r)|^2}{\rho(r)}dr - Z\int \frac{\rho(r)}{r}dr + \frac{1}{2}\iint \frac{\rho(r_1)\rho(r_2)}{|r_1 - r_2|}dr_1 dr_2 - C_x \int \rho^{4/3}(r)dr \tag{1.36}$$

The value of λ is 1/9. This model is quite better than Thomas-Fermi and Thomas-Fermi-Dirac models, however, the TFDW model is still very unsatisfactory and cannot be considered as a rigorous approach. Although these models are considered as the approximation of exact density functional theory.

1.8.1. Hohenberg-Kohn Theorem

The establishment of modern DFT is made possible by the existence of two ingeniously simple theorems introduced and proved by Hohenberg and Kohn in 1964 [193]. The Hohenberg-Kohn (HK) theorems prove that minimization of the total energy leads to ground state electron density, which helps to determine all the ground state properties of the system. The first HK theorem states that an external potential ($V_{ext}(r)$) is a unique functional of density for any system of interacting particles. The second HK theorem shows that a universal functional for the energy $E[n]$ can be defined using the variational principle in terms of density. The energy functional tends to a minimum value only for the ground-state electron density. Hence, the global minimum value of energy functional is the exact ground state. These theorems provide rigorous proof that the density can be used as a fundamental variable rather than the wave function but fail to provide any practical approach for performing computations.

1.8.2. The Kohn-Sham Equations

In the year 1965, Kohn and Sham proposed a theory to overcome the shortcomings of HK theory that is able to transform DFT into a practical electronic structure theory [194]. They proposed to work with a system of non-interacting electrons instead of a system of interacting particles. Usually, the wave function as well as the density of the non-interacting electrons is different from that of the interacting ones. Therefore, a hypothetical non-interacting system is constructed in such a way that its density matches the density of the interacting electrons. Consider a system of N non-interacting system of electrons moving in a local effective (fictitious) external potential typically denoted as $V_s(r)$ or $V_{\text{eff}}(r)$, called the Kohn–Sham potential. The Kohn-Sham wavefunction is constructed from a set of orbitals that are the lowest-energy solutions. The Kohn-Sham equation is,

$$\left(-\frac{\hbar^2}{2m}\nabla^2 + V_{eff}(r)\right)\varphi_i(r) = \varepsilon_i\varphi_i(r) \qquad (1.37)$$

where ε_i is the energy of the corresponding Kohn–Sham orbital φ_i. The density for an N-particle system is,

$$\rho(r) = \sum_{i}^{N} |\varphi_i(r)|^2 \tag{1.38}$$

Therefore, the electron density of a Slater determinant wavefunction is simply equal to the sum of the squares of the occupied orbitals.

The energy functional for orbital-free DFT is given by the expression

$$E(\rho) = E_{kin}(\rho) + E_{Hartree}(\rho) + E_{XC}(\rho) + E_{ext}(\rho) \tag{1.39}$$

And the biggest barrier is the lack of an accurate expression for the kinetic energy functional. Khon and Sham treated the kinetic energy functional in a better way. The basic idea is the replacement of the interacting system with an auxiliary non-interacting system having the same particle number density as the interacting system. The energy functional for the Khon-Sham approach is given by the expression

$$E(\rho) = T_s(\rho) + E_{Hartree}(\rho) + E_{XC}(\rho) + E_{ext}(\rho) \tag{1.40}$$

Where $T_S(\rho)$ is the Kohn–Sham kinetic energy, and can be expressed in terms of Khon-Sham orbital as,

$$T_S(\rho) = \sum_{i=1}^{N} d\boldsymbol{r}\, \psi_i^*(\boldsymbol{r}) \left(-\frac{\hbar^2}{2m} \nabla^2 \right) \varphi_i(r) \tag{1.41}$$

For closed-shell molecules, the Khon-Sham orbitals are occupied by two electrons with opposite spins, i.e. no spin polarization. Open-shell systems can be treated using an unrestricted Khon-Sham scheme where each orbital is occupied by one electron. However, the exact form of exchange-correlation potential is not known. The exchange-correlation energy accounts for the residual electron-electron interaction energy along with the kinetic energy component of the real system that is not included in the non-interacting kinetic and electrostatic terms. To perform actual computation with DFT, some approximate form of exchange-correlation functional must be used.

1.8.3. Exchange-Correlation Functional

The practical utility of ground state DFT depends entirely on the approximation of the functional $E_{XC}(\rho)$, which can be obtained and that is sufficiently simple and accurate at the same time. A number of different schemes have been developed to obtain approximate forms of exchange-correlation functional. Errors in DFT generally arise for the approximate nature of E_{XC}. For the *N* electron system, the simplest method which is describing the functional $E_{XC}(\rho)$ is a local-density approximation (LDA). Since the functional $E_{XC}(\rho)$ is mostly contributed by the binding energy calculated from $E_{XC}^{LDA}(\rho)$, the contribution emerging from regions of low-

electron density is underestimated. Hence, the systems with slowly varying densities can be dealt with by LDA but for highly inhomogeneous systems such as atoms and molecules, LDA is inappropriate. Errors in LDA mainly appear in the exchange energy part. It is possible to calculate the exchange energy more precisely by considering the gradient of the density, as well as the value, at a given point. A number of general gradient approximations (GGA) have been proposed that use a fully empirical form to include the gradient of the electron as well as its value in correlation calculations. The general expression for GGA is given by,

$$E_{XC}^{GGA}\big(\rho(r)\big) = \int \rho\,(r)|\nabla\rho(\mathrm{r})|\rho(r)dr \qquad (1.42)$$

The exchange functional has the following form:

$$E_X^{LDA}(\rho) = \left(1 - \frac{\beta}{2^{1/3}A_X}\frac{X^2}{1 + 6\beta X\,\sinh^{-1}(X)}\right) \qquad (1.43)$$

Where, $X = \frac{1.26|\nabla\rho|}{\rho^{1.33}}$, $A_X = 0.7387$, and $\beta = 0.0042$.

There are mainly two types of GGA functionals. The first type contains empirical parameters whose values have been fitted to reproduce experiments or more accurate calculations mostly preferred by the chemists, in which exchange functionals (B (from Becke), CAM, FT97, O, PW, mPW, X) are frequently combined with the correlation functionals (B88, P86, LYP) developed by Lee, Yang, and Parr (LYP) [195], and Perdew and Wang's 91 [196]. A few combined exchange-correlation functionals are BLYP, B3LYP, B3PW91. And the second one does not contain empirically determined parameters and is mostly preferred by Physicists. The exchange functionals are B86, LG, P, PBE, mPBE, and correlation functional PW91 usually used for the second type. The GGA functional yields much better geometrical parameters and relative energies.

1.9. Interaction Energy Calculation

For a chemical system *AB*, composed of two interacting fragments *A* and *B*, the interaction energy (ΔE_{int}) can be expressed as the difference between the energy of complex *AB* and the energies of individual fragments *A* and *B*, and is written as

$$\Delta E_{int}(r_{AB}) = E_{AB}^{AB}(r_{AB}) - (E_A^A + E_B^B) \qquad (1.44)$$

E_{AB} is the energy of the dimer, and E_A and E_B are the energies of monomer *A* and monomer *B* respectively. In our study, crystallographic coordinates were used for theoretical calculations.

- ***Basis Set Superposition Error***

As two atoms approach each other, their basis sets tend to overlap. Each atom therefore "borrows" the basis set functions of other atoms, implying a practical improvement in its basis sets that is further reflected in its energy. This effect increases when the atoms are closer to each other, creating an effectively modified basis set inversely proportional to the interatomic distance. This effect is known as the basis set superposition error (BSSE).

The energy of individual atoms does not depend on the interatomic distance. On the other hand, basis set superposition error varies with interatomic distance. The interaction energy in Eq (1.44) requires correction to BSSE. The most popular way to overcome this error, proposed by Boys and Bernardi, is called the counterpoise (CP) correction [197]. In CP correction, artificial stability is counteracted by allowing individual atoms to enhance their basis sets by borrowing functions from an empty basis set. A ghost atom that has a basis set according to the atom, but no electrons to fill it, is considered an empty basis set. Treating both atoms on the grid in this manner will correct the BSSE. The interaction energy after correcting the basis set superposition error is given by

$$\Delta E_{int}^{CP}(r_{AB}) = E_{AB}^{AB}(r_{AB}) - (E_{A}^{AB}(r_{AB}) + E_{B}^{AB}(r_{AB})) \qquad (1.45)$$

1.10. Quantum Theory of Atoms in Molecules (QTAIM) Analysis

In our studies, Bader's quantum theory of "Atoms in Molecules" (QTAIM) [198–200] was used to analyze non-covalent interactions by the AIMALL calculation package [201]. The QTAIM is based on the concept of partitioning the molecular space into atomic domains with the help of a vanishing gradient of electron density ($\rho(r)$). This theory has proved invaluable not only theoretically but also experimentally in the characterization of various weak non-covalent interactions using electron density obtained. In recent years, the topological parameters derived from the QTAIM theory have been proven to be a powerful tool for investigating the electronic and conformational properties of the molecules [202–204]. Therefore, topological analysis of electron charge density allows for much better insights into the interatomic interactions. The topological properties of electron density and its derivatives are considered to be very useful in describing the concept of bonding through bond paths and bond critical points (BCPs). The gradient of electron density vanishes at special points referred to as Critical Points (CPs), mathematically, $\nabla\rho(r) = 0$ and r is the CP. $\nabla\rho(r)$ is given as

$$\nabla\rho(r) = \hat{\imath}\frac{\partial\rho}{\partial x} + \hat{\jmath}\frac{\partial\rho}{\partial y} + \hat{k}\frac{\partial\rho}{\partial z} \qquad (1.46)$$

To determine a maximum or a minimum or an extremum, it is necessary to explore the second-order derivatives of $\rho(r)$. Nine second-order derivatives are possible for arbitrary coordinate axes. These nine second-order derivatives are represented as 3×3 order real symmetric matrix, which is diagonalizable, known as the Hessian of $\rho(r)$. Therefore, corresponding eigenvalues λ_1, λ_2, and λ_3 are the principal axes of curvature as the magnitude of the three second-order derivatives of $\rho(r)$ evaluated with respect to these axes are extremized.

$$\nabla^2\rho(r) = \frac{\partial^2 \rho(r)}{dx^2} + \frac{\partial^2 \rho(r)}{dy^2} + \frac{\partial^2 \rho(r)}{dz^2} = \lambda_1 + \lambda_2 + \lambda_3 \qquad (1.47)$$

The CPs are stated as (ω, σ), where ω is the rank of CP and σ is its signature. ω is the number of non-zero eigenvalues (non-zero curvatures of $\rho(r)$ at the CPs) and σ is the algebraic sum of the signs of eigenvalues (signs of curvatures of $\rho(r)$ at the CPs). There are four possible combinations for CPs of rank three in the spatial distribution of the electron density.

- (3, –3) → This represents all the curvatures are negative. CP occurs at the nuclear positions which correspond to a local electron density maximum in all directions.
- (3, –1) → Represents two curvatures are negative. CP occurs at a point where the electron density is minimal along the interaction path between two atoms it is maximum in the plane perpendicular to the path line, corresponding to Bond CP (BCP).
- (3, +1) → Represents two curvatures are positive. CP occurs at the interior of the ring and the electron density is a minimum in the ring plane, but it is a maximum along the normal to the ring plane, corresponding to Ring CP (RCP).
- (3, +3) → Represents all curvatures are positive. If the bond paths enclose the interior of a molecule with ring surfaces, CP occurs at a point which is a local minimum is the electron density in all the directions, corresponding to Cage CP (CCP).

The nature of the chemical bond can be understood by characterizing CPs, as each and every CP includes well-to-do chemical information. In terms of topological analysis of electron density, the Laplacian $\nabla^2(\rho(r))$ plays a crucial role in the characterization of a chemical bond. It has been noted that as $\nabla^2(\rho(r)) < 0$, the electron density is concentrated towards the interaction line and hence lowers the potential energy. The magnitude of the potential energy drop is greater than the kinetic energy of the same region resulting in attractive force, which indicates electron-shared interaction. And when $\nabla^2(\rho(r)) > 0$, the electron density is depleted towards each nucleus. Due to the parallel gradient and the curvature of electron density being large, net forces of repulsion act on the nuclei in this case, which indicates closed shell interaction. The

relationship of the energetic topological parameters and $\nabla^2(\rho(r))$ can be written by the expression as

$$\frac{1}{4}\nabla^2\rho(r) = 2G(r) + V(r) \qquad (1.48)$$

Where $G(r)$ is kinetic electronic energy density and $V(r)$ is potential electronic energy density. Therefore, total electronic energy density $H(r)$ is the sum of kinetic and potential energy densities. Bond ellipticity is defined as $\varepsilon = (\lambda_1/\lambda_2 - 1)$ in terms of two negative curvatures, which reflect the deviation of the charge distribution of a bond path from axial symmetry, thus providing a sensitive measure of the sensitivity of a system to structural changes. The dissociation energy of the interaction ($D.E_{int}$) is one measure of the strength of the interaction and can be estimated from the equation $D.E_{int} = -\frac{1}{2} V(r)$, more precisely $D.E_{int}$ (kcal.mol^{-1}) = $-313.754 \times V(r)$ (au) [205]. Therefore QTAIM theory serves as a bridge between the quantum chemical methods and experimental methods for a quantitative understanding of chemical concepts.

1.11. Non-Covalent Interaction (NCI) Plot Index

Non-Covalent Interaction (NCI) plot [206] provides a visualization index based on the electron density and its derivatives. NCI plot enables the identification of non-covalent interactions such as van der Walls interactions, hydrogen bonds, and steric clashes. NCI analysis depends on electron density and reduced density gradient (RDG) to plot local bonding properties. The two-dimensional plot between RDG and ρ is used to index non-covalent interactions. The reduced density gradient is a dimensionless function, used to describe the deviation from a homogeneous electron distribution and can be defined as,

$$RDG = \frac{1}{2(3\pi^2)^{1/3}} \frac{|\nabla\rho(r)|}{\rho(r)^{4/3}} \qquad (1.49)$$

In the regions far from the molecule, where the density decays exponentially to zero, a very large positive value of the reduced density gradient (RDG) is observed. In the region of covalent bonds and non-covalent interactions, the reduced density gradient (RDG) has very small values and tends to zero. To study non-covalent interactions, the reduced density gradient (RDG) versus electron density ($\rho(r)$) plot is examined in the low-density gradient region. A significant change in the reduced gradient between the interacting atoms occurs when a weak inter or intramolecular interaction is present between the interacting fragments, producing the density critical point. Three types of downward spikes are evident in the RDG graph of attractive interactions and can be distinguished by the value of the second eigenvalue of the

Hessian matrix which is λ_2. The value of λ_2 is negative for hydrogen bond interactions whereas λ_2 is positive for repulsive interactions. The value of λ_2 approaches zero for weak van der Waal interactions.

Isosurfaces instead of critical points represent non-covalent interactions in NCI Plot. Different colors of isosurfaces indicate different natures of the interaction. For example, blue and red colors on the isosurface represent ρ^-cut (attractive) and ρ^+cut (repulsive) interactions, respectively, while yellow and green colors represent weak repulsive and weak attractive interactions [207].

1.12. PIXEL Calculation

Lattice energy and interaction energies for molecular pairs were calculated using the PIXEL approach (developed by Gavezzotti) present in the CLP module [208–210]. This method provides quantitative analysis of crystal lattice energies and pairwise intermolecular interaction energies. In this method, the total interaction energy of molecular pairs can be divided into coulombic, polarization, dispersion, and repulsion energy terms. All hydrogen atoms in the structure should be set to the standard neutron distances according to the default method in the PIXELC program. The contribution (in %) of dispersion energy (E_{Disp}) and electrostatic (Coulombic + polarization) energy (E_{Elec}) to the total interaction energy can be determine by using the following equations.

$$\%E_{Disp} = \left[\frac{E_{Disp}}{E_{Coul} + E_{Pol} + E_{Disp}}\right] \times 100\% \tag{1.50}$$

$$\%E_{Elec} = 100 - \%E_{Disp} \tag{1.51}$$

1.13. References

[1] M.M. Woolfson, M.M. Woolfson, An introduction to X-ray crystallography, Cambridge University Press, 1997.

[2] A.A. Bunaciu, E.G. UdriŞTioiu, H.Y. Aboul-Enein, X-Ray Diffraction: Instrumentation and Applications, Crit Rev Anal Chem. 45 (2015) 289–299.

[3] R.H. Blessing, Phasing in Crystallography: A Modern Perspective, Acta Crystallogr. A 70 (2014) 518–519.

[4] A.L. Patterson, A Fourier Series Method for the Determination of the Components of Interatomic Distances in Crystals, Phys. Rev. 46 (1934) 372–376.

[5] P. Müller, Practical suggestions for better crystal structures, Crystallogr. Rev. 15 (2009) 57–83.

[6] D. Harker, J.S. Kasper, Phases of Fourier coefficients directly from crystal diffraction data, Acta Cryst. 1 (1948) 70–75.

[7] H.T. Hauptman, J. Karle, The calculation of phases from the Patterson function, Acta Cryst. 15 (1962) 547–550.

[8] A.J.C Wilson, Determination of Absolute from Relative X-Ray Intensity Data, Nature (London) 150 (1942) 151–152.

[9] J.A. Goedkoop, Remarks on the theory of phase limiting inequalities and equalities, Acta Cryst. 3 (1950) 374–378.

[10] J.T. Karle, H. Hauptman, The phases and magnitudes of the structure factors, Acta Cryst. 3 (1950) 181–187.

[11] W.T. Cochran, Cochran, Relations between the phases of structure factors, Acta Cryst. 8 (1955) 473–478.

[12] J.T. Karle, H. Hauptman, A theory of phase determination for the four types of non-centrosymmetric space groups 1*P222*, 2*P22*, 3P_1*2*, 3P_2*2*, Acta Cryst. 9 (1956) 635–651.

[13] D. Sayre, The squaring method: a new method for phase determination, Acta Cryst. 5 (1952) 60–65.

[14] G.M. Sheldrick, SHELXS-97: Program for crystal structure solution, University of Göttingen, Germany, 1997.

[15] M.C. Burla, R. Caliandro, B. Carrozzini, G.L. Cascarano, C. Cuocci, C. Giacovazzo, M. Mallamo, A. Mazzone, G. Polidori, Crystal structure determination and refinement *via SIR2014*, J. of Appl. Cryst. 48 (2015) 306–309.

[16] G. Sheldrick, Crystal Structure Refinement with SHELXL. Acta Crystallogr. Sect. C 71 (2015) 3–8.

[17] Bruker APEX2, SAINT and SADABS, Bruker AXS Inc., Madison, Wisconsin, USA, 2011.

[18] R.I. Cooper, A.L. Thompson, D.J. Watkin, *CRYSTALS* enhancements: dealing with hydrogen atoms in refinement, J. Appl. Cryst. 43 (2010) 1100–1107.

[19] L.J. Farrugia, *WinGX* and *ORTEP for Windows*: an update, J. Appl. Crystallogr. 45 (2012) 849–854.

[20] A.L. Spek, Structure Validation in Chemical Crystallography, Acta Crystallogr. Sect. D 65 (2009) 148–155.

[21] A.L. Spek, *checkCIF* validation ALERTS: what they mean and how to respond, Acta Crystallogr. Sect. E 76 (2020) 1–11.

[22] E. Wu, *POWD*, an interactive program for powder diffraction data interpretation and indexing, J. Appl. Crystallogr. 22 (1989) 506–510.

[23] S. Islam, P. Dey, S.K. Seth, A combined experimental and theoretical studies of two new Co(II)–PDA complexes: unusual 2D and 3D supramolecular networks [PDA= 2, 6-pyridinedicarboxylic acid], Polyhedron 242 (2023) 116514.

[24] J. Tauc, R. Grigorovici, A. Vancu, Optical Properties and Electronic Structure of Amorphous Germanium, Phys. Status Solidi B 15 (1966) 627–637.

[25] J. H. Edgar, Prospects for device implementation of wide band gap semiconductors, J. Mater. Res. 7 (1992) 235–252.

[26] G.R. Desiraju, Crystal Engineering: A Holistic View, Angew. Chem. Int. Ed. 46 (2007) 8342–8356.

[27] G.R. Desiraju, Crystal Engineering: The Design of Organic Solids, Materials Science Monographs, Elsevier, Amsterdam 54, 1989.

[28] R. Pepinsky, Crystal engineering-new concept in crystallography, Phys. Rev. 100 (1955) 971–971.

[29] G.M.J. Schmidt, Photodimerization in the solid state, Pure Appl. Chem. 27 (1971) 647–678.

[30] M. Lusi, Engineering Crystal Properties through Solid Solutions, Cryst. Growth Des. 18 (2018) 3704−3712.

[31] G.R. Desiraju, Crystal engineering: A brief overview. J. Chem. Sci. 122 (2010) 667−675.

[32] P. Ganguly, G.R. Desiraju, Long-range synthon Aufbau modules (LSAM) in crystal structures: systematic changes in $C_6H_{6-n}F_n$ ($0 \leq n \leq 6$) fluorobenzenes, CrystEngComm 12 (2010) 817−833.

[33] C. O'Dowd, J.D. Kennedy, M. Thornton-Pett, The use of Kitaigorodskii's Aufbau principle in the solid-state study of crystalline borane compounds. A preliminary account, J. Organomet. Chem. 657 (2002) 20−39.

[34] G. R. Desiraju, Crystal Engineering: From Molecule to Crystal, J. Am. Chem. Soc. 135 (2013) 9952−9967.

[35] O.V. Shishkin, R.I. Zubatyuk, S.V. Shishkina, V.V. Dyakonenko, V.V. Medviediev, Role of supramolecular synthons in the formation of the supramolecular architecture of molecular crystals revisited from an energetic viewpoint†, Phys. Chem. Chem. Phys. 16 (2014) 6773−6786.

[36] M. Waller, S. Grimme, Weak Intermolecular Interactions: A Supermolecular Approach, in: J. Leszczynski, A. Kaczmarek-Kedziera, T. Puzyn, M. G. Papadopoulos, H. Reis, M. K. Shukla, (Eds.), Handbook of Computational Chemistry, Springer International Publishing, Switzerland, 2017.

[37] P. Hobza, J. Rezac, Introduction: Noncovalent Interactions, Chem. Rev. 116 (2016) 4911–4912.

[38] S. Scheiner, Noncovalent Forces; Springer, 2015.

[39] P. Manna, S. K. Seth, Antonio Bauzá, M. Mitra, S. R. Choudhury, A. Frontera, S. Mukhopadhyay, pH Dependent Formation of Unprecedented Water–Bromide Cluster in the Bromide Salts of PTP Assisted by Anion−π Interactions: Synthesis, Structure, and DFT Study, Cryst. Growth Des. 14 (2014) 747–755.

[40] P. Manna, S. K. Seth, M. Mitra, S. R. Choudhury, Antonio Bauzá, A. Frontera, S. Mukhopadhyay, Experimental and Computational Study of Counterintuitive $ClO_4^-\cdots ClO_4^-$ Interactions and the Interplay between π^+–π and Anion$\cdots\pi^+$ Interactions, Cryst. Growth Des. 14 (2014) 5812–5821.

[41] S. K. Seth, A. Bauzá, A. Frontera, Bipolar behaviour of salt-bridges: a combined theoretical and crystallographic study†, New J. Chem. 42 (2018) 12134–12142.

[42] S. Tripathi, S. Islam, S. K. Seth, A. Bauzá, A. Frontera, S. Mukhopadhyay, Supramolecular assemblies involving salt bridges: DFT and X-ray evidence of bipolarity†, CrystEngComm 22 (2020) 8171–8181.

[43] J. J. Novoa, Intermolecular Interactions in Crystals: Fundamentals of Crystal Engineering, Royal Society of Chemistry, 2017.

[44] R. Breslow, Molecular recognition, Proc. Nati. Acad. Sci. 90 (1993) 1139.

[45] A. Kumar, S.S. Sun, A.J. Lees, Directed assembly metallocyclic supramolecular systems for molecular recognition and chemical sensing. Coord. Chem. Rev. 252 (2008) 922–939.

[46] J. Rebek Jr, Introduction to the Molecular Recognition and Self-Assembly Special Feature, Proc. Nati. Acad. Sci. 106 (2009) 10423–10424.

[47] C.J. Pedersen, Cyclic Polyethers and Their Complexes with Metal Salts, J. Am. Chem. Soc. 89 (1967) 7017–7036.

[48] D.J. Cram, The Design of Molecular Hosts, Guests, and Their Complexes (Nobel Lecture)†, Angew. Chem. Int. Ed. 27 (1988) 1009–1020.

[49] J.M. Lehn, Supramolecular Chemistry—Scope and Perspectives Molecules, Supermolecules, and Molecular Devices (Nobel Lecture)†, Angew. Chem. Int. Ed. 27 (1988) 89–112.

[50] K. Ariga, T. Kunitake, Supramolecular Chemistry-Fundamentals and Applications: Advanced Textbook. Springer Science & Business Media, 2006.

[51] C.A. Schalley, Molecular recognition and supramolecular chemistry in the gas phase, Mass Spectrum. Rev. 20 (2001) 253–309.

[52] L.R. Nassimbeni, Physicochemical Aspects of Host−Guest Compounds, Acc. Chem. Res. 36 (2003) 631–637.

[53] M.J. Hannon, Supramolecular DNA recognition†‡, Chem. Soc. Rev. 36 (2007) 280–295.

[54] E. Kimura, Model Studies for Molecular Recognition of Carbonic Anhydrase and Carboxypeptidase, Acc. Chem. Res. 34 (2001) 171–179.

[55] J.M. Thomas, Design, Synthesis, and In Situ Characterization of New Solid Catalysts, Angew. Chem., Int. Ed. 38 (1999) 3588–3628.

[56] I. Yoshimura, Y. Miyahara, N. Kasagi, H. Yamane, A. Ojida, I. Hamachi, Molecular Recognition in a Supramolecular Hydrogel to Afford a Semi-Wet Sensor Chip, J. Am. Chem. Soc. 126 (2004) 12204–12205.

[57] L.M. Perdigão, N.R. Champness, P.H. Beton, Surface self-assembly of the cyanuric acid–melamine hydrogen bonded network, ChemComm (2006) 538–540.

[58] A. Mulder, J. Huskens, D.N. Reinhoudt, Multivalency in supramolecular chemistry and nanofabrication, Org. Biomol. Chem. 2 (2004) 3409–3424.

[59] K. Nørgaard, T. Bjørnholm, Supramolecular chemistry on water – towards self-assembling molecular electronic circuitry, ChemComm (2005) 1812–1823.

[60] C.J. Kepert, Advanced functional properties in nanoporous coordination framework materials, ChemComm (2006) 695–700.

[61] S. Parveen, R.J. Davey, G. Dent, R.G. Pritchard, Linking solution chemistry to crystal nucleation: the case of tetrolic acid, ChemComm (2005) 1531–1533.

[62] J. Vicens, Q. Vicens, Emergences of supramolecular chemistry: from supramolecular chemistry to supramolecular science, J. Incl. Phenom. Macrocycl. Chem. 71 (2011) 251–274.

[63] R. Chakrabarty, P.S. Mukherjee, P.J., Stang, Supramolecular Coordination: Self-Assembly of Finite Two- and Three-Dimensional Ensembles, Chem. Rev. 111 (2011) 6810–6918.

[64] M. Muthukumar, C.K. Ober, E.L. Thomas, Competing Interactions and Levels of Ordering in Self-Organizing Polymeric Materials, Science 277 (1997) 1225–1232.

[65] R. Kramer, J.M. Lehn, A. Marquis-Rigault, Self-recognition in helicate self-assembly: spontaneous formation of helical metal complexes from mixtures of ligands and metal ions, Proc. Natl. Acad. Sci. 90 (1993) 5394–5398.

[66] P. Espinet, M.A. Esteruelas, L.A. Oro, J.L. Serrano, E. Sola, Transition metal liquid crystals: advanced materials within the reach of the coordination chemist, Coord. Chem. Rev. 117 (1992) 215–274.

[67] M.N. Jones, D. Chapman, Micelles, monolayers, and biomembranes; Wiley-Liss, 1995.

[68] J.P. Collin, P. Gaviña, V. Heitz, J.P. Sauvage, Construction of One-Dimensional Multicomponent Molecular Arrays: Control of Electronic and Molecular Motions Eur. J. Inorg. Chem. 1998 (1998) 1–14.

[69] C.J. Jones, Transition metals as structural components in the construction of molecular containers, Chem. Soc. Rev. 27 (1998) 289–300.

[70] G. Férey, C. Mellot-Draznieks, C. Serre, F. Millange, J. Dutour, S. Surblé, I. Margiolaki, A Chromium Terephthalate-Based Solid with Unusually Large Pore Volumes and Surface Area, Science 309 (2005) 2040–2042.

[71] H. Abourahma, B. Moulton, V. Kravtsov, M.J. Zaworotko, Supramolecular Isomerism in Coordination Compounds: Nanoscale Molecular Hexagons and Chains, J. Am. Chem. Soc. 124 (2002) 9990–9991.

[72] X.L. Wang, C. Qin, E.B. Wang, Polythreading of Infinite 1D Chains into Different Structural Motifs: Two Poly(Pseudo-Rotaxane) Architectures Constructed by Concomitant Coordinative and Hydrogen Bonds, Cryst Growth Des. 6 (2006) 439–443.

[73] R. Kitaura, S. Kitagawa, Y. Kubota, T.C. Kobayashi, K. Kindo, Y. Mita, A. Matsuo, M. Kobayashi, H.C. Chang, T.C. Ozawa, M. Suzuki, Formation of a One-Dimensional Array of Oxygen in a Microporous Metal-Organic Solid, Science 298 (2002) 2358–2361.

[74] K. Koch, H.J. Ensikat, The hydrophobic coatings of plant surfaces: Epicuticular wax crystals and their morphologies, crystallinity and molecular self-assembly, Micron 39 (2008) 759–772.

[75] G.M. Whitesides, B. Grzybowski, Self-Assembly at All Scales, Science 295 (2002) 2418–2421.

[76] R. Custelcean, C. Afloroaei, M. Vlassa, M. Polverejan, Formation of Extended Tapes of Cyclic Water Hexamers in an Organic Molecular Crystal Host, Angew. Chem. Int. Ed. 112 (2000) 3224–3226.

[77] H. Yin, G. Hummer, J.C. Rasaiah, Metastable Water Clusters in the Nonpolar Cavities of the Thermostable Protein Tetrabrachion, J. Am. Chem. Soc. 129 (2007) 7369–7377.

[78] C. Meier, U. Ziener, K. Landfester, P. Weihrich, Weak Hydrogen Bonds as a Structural Motif for Two-Dimensional Assemblies of Oligopyridines on Highly Oriented Pyrolytic Graphite: An STM Investigation, J. Phys. Chem. B 109 (2005) 21015–21027.

[79] B. K. Saha, A. Nangia, Helical water chains in aquapores of organic hexahost: remarkable halogen-substitution effect on the handedness of water helix†, Chem. Commun. (2005) 3024–3026.

[80] S. Islam, S. Tripathi, A. Hossain, S.K. Seth, S. Mukhopadhyay, pH-induced structural variations of two new Mg(II)-PDA complexes: experimental and theoretical studies, J. Mol. Struct. 1262 (2022) 133373.

[81] H. M. Jr. Schmeck, "Chemistry and Physics Nobels Hail Discoveries on Life and Superconductors; Three Share Prize for Synthesis of Vital Enzymes" New York Times, October 15, 1987.

[82] G.R. Desiraju, Supramolecular Synthons in Crystal Engineering—A New Organic Synthesis†, Angew. Chem. Int. Ed. Engl. 34 (1995) 2311–2327.

[83] E. Corey, General methods for the construction of complex molecules, J. Pure Appl. Chem. 14 (1967) 19−38.

[84] O.V. Shishkin, R.I. Zubatyuk, S.V. Shishkina, V.V. Dyakonenko, and V.V. Medviediev, Role of supramolecular synthons in the formation of the supramolecular architecture of molecular crystals revisited from an energetic viewpoint†, Phys. Chem. Chem. Phys. 16 (2014) 6773−6786.

[85] R.D. Bailey Walsh, M.W. Bradner, S. Fleischman, L.A. Morales, B. Moulton, N. Rodríguez-Hornedob, M. J. Zaworotko, Crystal engineering of the composition of pharmaceutical phases, Chem. Commun. (2003) 186−187.

[86] M. Mohana, P.T. Muthiah, C.D. McMillen, Supramolecular hydrogen-bonding patterns in 1: 1 cocrystals of 5-fluorouracil with 4-methylbenzoic acid and 3-nitrobenzoic acid, Acta Crystallogr. C Struct. Chem. 73 (2017) 259−263.

[87] C. Chen, K. Zhang, Y. Sun, S. Xiang, Y. Geng, K. Liu, L. Wang, Supramolecular structural motifs in compounds of acetoguanamine and various carboxylic acids: N-H···O heterosynthons and N-H···N homosynthons, J. Mol. Struct. 1170 (2018) 60−69.

[88] T.K. Adalder, R. Sankolli, P. Dastidar, Homo- or Heterosynthon? A Crystallographic Study on a Series of New Cocrystals Derived from Pyrazinecarboxamide and Various Carboxylic Acids Equipped with Additional Hydrogen Bonding Sites, Cryst. Growth Des. 12 (2012) 2533−2542.

[89] S.G. Fleischman, S.S. Kuduva, J.A. McMahon, B. Moulton, R.D. Bailey Walsh, N. Rodríguez-Hornedo, M.J. Zaworotko, Crystal Engineering of the Composition of Pharmaceutical Phases: Multiple-Component Crystalline Solids Involving Carbamazepine, Cryst. Growth Des. 3 (2003) 909−919.

[90] J.A. McMahon, J.A. Bis, P. Vishweshwar, T.R. Shattock, O.L. McLaughlin, M.J. Zaworotko, Crystal engineering of the composition of pharmaceutical phases. 3. Primary amide supramolecular heterosynthons and their role in the design of pharmaceutical co-crystals, Z. Krystallog. 220 (2005) 340−350.

[91] O.V. Shishkin, Evaluation of true energy of halogen bonding in the crystals of halogen derivatives of trityl alcohol, Chem. Phys. Lett. 458 (2008) 96−100.

[92] K. Merz, V. Vasylyeva, Development and boundaries in the field of supramolecular synthons†, CrystEngComm 12 (2010) 3989−4002.

[93] J.L. Atwood, J.E.D. Davies, D.D. MacNicol, F. Vögtle, J.M. Lehn, Comprehensive Supramolecular Chemistry; Pergamon: Oxford, 1996.

[94] G. R. Desiraju, C. V. K. Perspectives in Supramolecular Chemistry: The Crystal as a Supramolecular Entity; Wiley: Chichester, 1995.

[95] J. Steed, J. L. Atwood, J. L. Supramolecular Chemistry; Wiley, New York, 2000.

[96] L. Lindoy, F.I.M. Atkinson, Self-Assembly in Supramolecular Systems; Royal Society of Chemistry, Cambridge, 2000.

[97] J.M. Lehn, Toward complex matter: Supramolecular chemistry and self-organization, Proc. Natl. Acad. Sci. U. S. A. 99 (2002) 4763–4768.

[98] T. Steiner, The Hydrogen Bond in the Solid State, Angew. Chem. Int. Ed. 41(2002) 48–76.

[99] E. Arunan, G. R. Desiraju, R. A. Klein, J. Sadlej, S. Scheiner, I. Alkorta, D. C. Clary, R. H. Crabtree, J. J. Dannenberg and P. Hobza, Defining the hydrogen bond: An account (IUPAC Technical Report), Pure Appl. Chem. 83 (2011) 1619–1636.

[100] L. Pauling, The Nature of the Chemical Bond—1992, J. Chem. Educ. 69 (1992) 519.

[101] G.R. Desiraju, T. Steiner, The Weak Hydrogen Bond: In Structural Chemistry and Biology (Vol. 9), IUCr, 2001.

[102] A.V. Bondi, van der Waals Volumes and Radii, J. Phys. Chem. 68 (1964) 441–451.

[103] R.S. Rowland, R. Taylor Intermolecular Nonbonded Contact Distances in Organic Crystal Structures: Comparison with Distances Expected from van der Waals Radii, J. Phys. Chem. 100 (1996) 7384–7391.

[104] R. Preißner, U. Egner, W. Saenger, Occurrence of bifurcated three-center hydrogen bonds in protpins, FEBS Lett. 288 (1991) 192–196.

[105] F.O. Tzul, K.L. Schweiker G.I. Makhatadze, Modulation of folding energy landscape by charge–charge interactions: Linking experiments with computational modeling, Proc. Natl. Acad. Sci. U. S. A., 112 (2015) E259–E266.

[106] M.P. Williamson, A.M. Hounslow, J. Ford, K. Fowler, M. Hebditch, P.E. Hansen, Detection of salt bridges to lysines in solution in barnase†, Chem. Commun. 49 (2013) 9824–9826.

[107] I. Gitlin, J.D. Carbeck, G. M. Whitesides, Why Are Proteins Charged? Networks of Charge–Charge Interactions in Proteins Measured by Charge Ladders and Capillary Electrophoresis, Angew. Chem. Int. Ed. 45 (2006) 3022–3060.

[108] S. Kumar, R. Nussinov, Salt bridge stability in monomeric proteins, J. Mol. Biol. 293 (1999) 1241–1255.

[109] S Kumar, R. Nussinov, Relationship between Ion Pair Geometries and Electrostatic Strengths in Proteins, Biophys. J. 83 (2002) 1595–1612.

[110] V. Ferretti, V. Bertolasi, L. Pretto, Supramolecular aggregation by means of charge-assisted hydrogen bonds in acid-base adducts containing amidinium cations, New J. Chem. 28 (2004) 646–651.

[111] E. Yashima, K. Maeda, Y. Furusho, Single- and Double-Stranded Helical Polymers: Synthesis, Structures, and Functions, Acc. Chem. Res. 41 (2008) 1166–1180.

[112] H. Katagiri, Y. Tanaka, Y. Furusho and E. Yashima, Multicomponent cylindrical assemblies driven by amidinium-carboxylate salt-bridge formation, Angew. Chem. Int. Ed. 46 (2007) 2435–2439.

[113] Q. Xu, H. Guo, A. Wlodawer, H. Guo, The Importance of Dynamics in Substrate-Assisted Catalysis and Specificity, J. Am. Chem. Soc. 128 (2006) 5994–5995.

[114] S. Tripathi, S. Islam, S.K. Seth, A. Bauzá, A. Frontera, S. Mukhopadhyay, Supramolecular assemblies involving salt bridges: DFT and X-ray evidence of bipolarity, CrystEngComm 22 (2020) 8171–8181.

[115] G.R. Desiraju, T. Steiner, The Weak Hydrogen Bond in Structural Chemistry and Biology; Oxford University Press, Oxford, 1999.

[116] D. Sadhukhan, M. Maiti, G. Pilet, A. Bauzá, A. Frontera, S. Mitra, Hydrogen Bond, π–π, and CH–π Interactions Governing the Supramolecular Assembly of Some Hydrazone Ligands and Their Mn^{II} Complexes – Structural and Theoretical Interpretation, Eur. J. Inorg. Chem. 2015 (2015) 1958−1972.

[117] M. Kaufmann, M. Gisler, C.J. Leumann, Stable Cyclohexyl–Phenyl Recognition in the Center of a DNA Duplex†, Angew. Chem. Int. Ed. 121 (2009) 3868−3871.

[118] M. Majumder, B.K. Mishra, N. Sathyamurthy, CH···π and π···π interaction in benzene–acetylene clusters, Chem. Phys. Lett. 557 (2013) 59−65.

[119] L. Berg, M.S. Niemiec, W. Qian, C.D. Andersson, P. Wittung- Stafshede, F. Ekström, A. Linusson, Similar but Different: Thermodynamic and Structural Characterization of a Pair of Enantiomers Binding to Acetylcholinesterase†, Angew. Chem. Int. Ed. 51 (2012) 12716−12720.

[120] J. Černyý, M. Kabeláč, P. Hobza, Double-Helical → Ladder Structural Transition in the B-DNA is Induced by a Loss of Dispersion Energy, J. Am. Chem. Soc. 130 (2008) 16055−16059.

[121] R.K. Raju, N.A. Burton, I.H. Hillier, Modelling the binding of HIV-reverse transcriptase and nevirapine: an assessment of quantum mechanical and force field approaches and predictions of the effect of mutations on binding†, Phys. Chem. Chem. Phys. 12 (2010) 7117−7125.

[122] Y. Umezawa, S. Tsuboyama, K. Honda, J. Uzawa, M. Nishio, CH/π Interaction in the Crystal Structure of Organic Compounds. A Database Study, Bull. Chem. Soc. Jpn. 71 (1998) 1207−1213.

[123] S.K. Seth, The Importance of CH···X (X = O, π) Interaction of a New Mixed Ligand Cu(II) Coordination Polymer: Structure, Hirshfeld Surface and Theoretical Studies, Crystals 8 (2018) 455.

[124] P. Chakraborty, S. Purkait, S. Mondal, A. Bauzá, A. Frontera, C. Massera, and D. Das, Exploration of CH···π interactions involving the π-system of pseudohalide coligands in metal complexes of a Schiff-base ligand†, CrystEngComm 17 (2015) 4680−4690.

[125] M. Brandl, M.S. Weiss, A. Jabs, J. Sühnel, R. Hilgenfeld, CH···π-interactions in proteins, J. Mol. Biol. 307 (2001) 357−377.

[126] L.L. Kiessling, R.C. Diehl, CH−π Interactions in Glycan Recognition, ACS Chem. Biol. 16 (2021) 1884−1893.

[127] D. Scuderi, K. Le Barbu-Debus, A. Zehnacker, The role of weak hydrogen bonds in chiral recognition†‡, Phys. Chem. Chem. Phys. 13 (2011) 17916−17929.

[128] M. Nishio, M. Hirota, Y. Umezawa, The CH/π Interaction: Evidence, Nature, and Consequences (Vol. 21), John Wiley & Sons, 1998.

[129] H. Suezawa, T. Yoshida, Y. Umezawa, S. Tsuboyama, M. Nishio, CH/π Interactions Implicated in the Crystal Structure of Transition Metal Compounds − A Database Study, Eur. J. Inorg. Chem. 2002 (2002) 3148−3155.

[130] P. Das, S. Islam, D. Das, P.P. Ray, S.K. Seth, Intriguing π-interactions involving aromatic neutrals, aromatic cations and semiconducting behavior in a pyridinium-carboxylate salt, J. Mol. Struct. 1284 (2023) 135326.

[131] H. Zhang, Y. Fang, F. Yang, X. Liu, X. Lu, Aromatic organic molecular crystal with enhanced π–π stacking interaction for ultrafast Zn-ion storage†, Energy Environ. Sci. 13 (2020) 2515−2523.

[132] C.D. Churchill, S.D. Wetmore, Noncovalent Interactions Involving Histidine: The Effect of Charge on π−π Stacking and T-Shaped Interactions with the DNA Nucleobases, J. Phys. Chem. B 113 (2009) 16046−16058.

[133] C. Zeng, Y. Chen, K. Kirschbaum, K.J. Lambright, R. Jin, Emergence of hierarchical structural complexities in nanoparticles and their assembly, Science 354 (2016) 1580−1584.

[134] C. Chipot, R. Jaffe, B. Maigret, D.A. Pearlman, P.A. Kollman, Benzene Dimer: A Good Model for π−π Interactions in Proteins? A Comparison between the Benzene and the Toluene Dimers in the Gas Phase and in an Aqueous Solution, J. Am. Chem. Soc. 118 (1996) 11217−11224.

[135] Y. Zhao, D.G. Truhlar, Computational characterization and modeling of buckyball tweezers: density functional study of concave–convex π···π interactions†, Phys. Chem. Chem. Phys. 10 (2008) 2813−2818.

[136] M. Kertesz, Pancake bonding: Pancake Bonding: An Unusual Pi-Stacking Interaction. Chem. Eur. J. 25 (2019) 400−416.

[137] C.A. Hunter, MELDOLA LECTURE. The Role of Aromatic Interactions in Molecular Recog n it ion, Chem. Soc. Rev. 23 (1994) 101−109.

[138] K.M. Guckian, B.A. Schweitzer, R.X.F. Ren, C.J. Sheils, D.C. Tahmassebi, E.T. Kool, Factors Contributing to Aromatic Stacking in Water: Evaluation in the Context of DNA, J. Am. Chem. Soc. 122 (2000) 2213−2222.

[139] S. Burattini, B.W. Greenland, D.H. Merino, W. Weng, J. Seppala, H.M. Colquhoun, W. Hayes, M.E. Mackay, I.W. Hamley, S.J. Rowan, A Healable Supramolecular Polymer Blend Based on Aromatic π−π Stacking and Hydrogen-Bonding Interactions, J. Am. Chem. Soc. 132 (2010) 12051−12058.

[140] Z. Zhang, H. Huang, X. Yang, L. Zang, Tailoring Electronic Properties of Graphene by π–π Stacking with Aromatic Molecules, J. Phys. Chem. Lett. 2 (2011) 2897−2905.

[141] C. Janiak, S. Temizdemir, S. Dechert, Hydrotris(indazolyl)borate, Tp^{4Bo}, a surprisingly effective Tp ligand for supramolecular assembly [1], Inorg. Chem. Commun. 3 (2000) 271−275.

[142] C. Janiak, A critical account on π–π stacking in metal complexes with aromatic nitrogen-containing ligands†, J. Chem. Soc., Dalton Trans. (2000) 3885−3896.

[143] C.A. Hunter, J.K. Sanders, The Nature of π−π Interactions, J. Am. Chem. Soc. 112 (1990) 5525−5534.

[144] P. Atkins, P.W. Atkins, J. de Paula, Atkins' Physical Chemistry, Oxford university press, 2014.

[145] F. Cozzi, M. Cinquini, R. Annuziata, J.S. Siegel, Dominance of Polar/π over Charge-Transfer Effects in Stacked Phenyl Interactions, J. Am. Chem. Soc. 115 (1993) 5330−5331.

[146] D.B. Amabilino, J.F. Stoddart, Interlocked and Intertwined Structures and Superstructures, Chem. Rev. 95 (1995) 2725−2828.

[147] N.J. Singh, S.K. Min, D.Y. Kim, K.S. Kim, Comprehensive Energy Analysis for Various Types of π-Interaction, J. Chem. Theory Comput. 5 (2009) 515−529.

[148] I. Geronimo, N.J. Singh, K.S. Kim, Nature of anion-templated π^+–π^+ interactions†, Phys. Chem. Chem. Phys. 13 (2011) 11841−11845.

[149] H.M. Lee, S.B. Suh, J.Y. Lee, P. Tarakeshwar, K.S. Kim, Structures, energies, vibrational spectra, and electronic properties of water monomer to decamer, J. Chem. Phys. 112 (2000) 9759−9772.

[150] B.L. Schottel, H.T. Chifotides, K.R. Dunbar, Anion-π interactions, Chem. Soc. Rev. 37 (2008) 68–83.

[151] C. Estarellas, A. Frontera, D. Quiñonero, P.M. Deyà, Relevant Anion–p Interactions in Biological Systems: The Case of Urate Oxidase**, Angew. Chem. Int. Ed. 50 (2011) 415–418.

[152] A. Hossain, A. Dey, S.K. Seth, P.P. Ray, J. Ortega-Castro, A. Frontera, S. Mukhopadhyay, Anion-dependent structural variations and charge transport property

analysis of 4′-(3-pyridyl)-4,2′:6′,4″-terpyridinium salts†, CrystEngComm 23 (2021) 3569–3581.

[153] R. Robson, B.F. Abrahams, S.R. Batten, R.W. Gable, B.F. Hoskins, B. F.; Liu, J. Supramolecular Architecture, ACS Publications, Washington, DC,1992.

[154] D. Quiñonero, C. Garau, C. Rotger, A. Frontera, P. Ballester, A. Costa, P.M. Deyà, Anion–π Interactions: Do They Exist?†, Angew. Chem. Int. Ed. 41 (2002) 3389–3392.

[155] I. Alkorta, I. Rozas, J. Elguero, Interaction of Anions with Perfluoro Aromatic Compounds, J. Am. Chem. Soc.124 (2002) 8593–8598.

[156] M. Mascal, A. Armstrong, M.D. Bartberger, Anion−Aromatic Bonding: A Case for Anion Recognition by π-Acidic Rings, J. Am. Chem. Soc. 124 (2002) 6274–6276.

[157] C.A. Black, L.R. Hanton, M.D. Spicer, A coordination polymer strategy for anion encapsulation: anion–π interactions in (4,4) nets formed from Ag(I) salts and a flexible pyrimidine ligand†, Chem. Commun. (2007) 3171–3173.

[158] S.R. Choudhury, P. Gamez, A. Robertazzi, C.-Y. Chen, H.M. Lee, S. Mukhopadhyay, Experimental Observation of Supramolecular Carbonyl-π/π-π/π-carbonyl and Carbonyl-π/π-π/π-anion Assemblies Supported by Theoretical Studies, Cryst. Growth Des. 8 (2008) 3773–3784.

[159] Z.F. Tian, H.B. Duan, H. Zhou, X.-M. Ren, H. Zhang, Q.J. Meng, An intriguing $NO_2\cdots\pi$ and $CN\cdots\pi$ interactions in [1-(4′-nitrobenzyl) pyrazinium][$Ni(mnt)_2$]: Crystal structure, magnetic property and DFT calculation, Inorg. Chem. Commun. 12 (2009) 148–150.

[160] S. Ghosh, S. Islam, S. Pramanik, S.K. Seth, Structural elucidation of phenoxybenzaldehyde derivatives from laboratory powder X-ray diffraction: A combined experimental and theoretical quantum mechanical study, J. Mol. Struct. 1268 (2022) 133697.

[161] T.J. Mooibroek, P. Gamez, J. Reedijk, Lone pair–π interactions: a new supramolecular bond?†, CrystEngComm 10 (2008) 1501−1515.

[162] S.K. Seth, I. Saha, C. Estarellas, A. Frontera, T. Kar, S. Mukhopadhyay, Supramolecular Self-Assembly of M-IDA Complexes Involving Lone-Pair$\cdots\pi$ Interactions: Crystal Structures, Hirshfeld Surface Analysis, and DFT Calculations [H_2IDA = iminodiacetic acid, M = Cu(II), Ni(II)], Cryst. Growth Des. 11 (2011) 3250−3265.

[163] M. Egli, S. Sarkhel, Lone Pair−Aromatic Interactions: To Stabilize or Not to Stabilize, Acc. Chem. Res. 40 (2007) 197−205.

[164] S. Sarkhel, A. Rich, M. Egli, Water−Nucleobase "Stacking": H−π and Lone Pair−π Interactions in the Atomic Resolution Crystal Structure of an RNA Pseudoknot, J. Am. Chem. Soc. 125 (2003) 8998−8999.

[165] J.C. Calabrese, D.B. Jordan, A. Boodhoo, S. Sariaslani, T. Vannelli, Crystal Structure of Phenylalanine Ammonia Lyase: Multiple Helix Dipoles Implicated in Catalysis†,‡, Biochemistry 43 (2004) 11403−11416.

[166] E.J. Stollar, J.L. Gelpi, S. Velankar, A. Golovin, M. Orozco, B.F. Luisi, Unconventional interactions between water and heterocyclic nitrogens in protein structures, Proteins 57 (2004) 1−8.

[167] J. Li, J. Zhang, J. Chen, X. Luo, W. Zhu, J. Shen, H. Liu, X. Shen, H. Jiang, Strategy for Discovering Chemical Inhibitors of Human Cyclophilin A: Focused Library Design, Virtual Screening, Chemical Synthesis and Bioassay, J. Comb. Chem. 8 (2006) 326−337.

[168] A. Jain, C.S. Purohit, S. Verma, R. Sankararamakrishnan, Close Contacts between Carbonyl Oxygen Atoms and Aromatic Centers in Protein Structures: π···π or Lone-Pair···π Interactions?, J. Phys. Chem. B 111 (2007) 8680−8683.

[169] P. Manna, S.K. Seth, A. Das, J. Hemming, R. Prendergast, M. Helliwell, S.R. Choudhury, A. Frontera, S. Mukhopadhyay, Anion Induced Formation of Supramolecular Associations Involving Lone pair−π and Anion−π Interactions in Co(II) Malonate Complexes: Experimental Observations, Hirshfeld Surface Analyses and DFT Studies, Inorg. Chem. 51 (2012) 3557−3571.

[170] M. Mitra, P. Manna, A. Das, S.K. Seth, M. Helliwell, A. Bauzá, S.R. Choudhury, A. Frontera, S. Mukhopadhyay, On the Importance of Unprecedented Lone Pair–Salt Bridge Interactions in Cu(II)–Malonate–2-Amino-5-Chloropyridine–Perchlorate Ternary System, J. Phys. Chem. A 117 (2013) 5802−5811.

[171] S.K. Seth, Tuning the formation of MOFs by pH influence: X-ray structural variations and Hirshfeld surface analyses of 2-amino-5-nitropyridine with cadmium chloride†, CrystEngComm 15 (2013) 1772−1781.

[172] B.W. Gung, X.W. Xue, H.J. Reich, Off-Center Oxygen−Arene Interactions in Solution: A Quantitative Study, J. Org. Chem. 70 (2005) 7232−7237.

[173] B.W. Gung, Y. Zou, Z.G. Xu, J.C. Amicangelo, D.G. Irwin, S.Q. Ma, H.C. Zhou, Quantitative Study of Interactions between Oxygen Lone Pair and Aromatic Rings: Substituent Effect and the Importance of Closeness of Contact, J. Org. Chem. 73 (2008) 689−693.

[174] J.C. Amicangelo, B.W. Gung, D.G. Irwin, N.C. Romano, *Ab initio* study of substituent effects in the interactions of dimethyl ether with aromatic rings†, Phys. Chem. Chem. Phys. 10 (2008) 2695−2705.

[175] F.L. Hirshfeld, Bonded-atom fragments for describing molecular charge densities, Theor. Chim. Acta. 44 (1977) 129−138.

[176] M.A. Spackman, J.J. McKinnon, Fingerprinting intermolecular interactions in molecular crystals†, CrystEngComm 4 (2002) 378–392.

[177] J.J. McKinnon, D. Jayatilaka, M.A. Spackman, Towards quantitative analysis of intermolecular interactions with Hirshfeld surfaces, Chem. Commun. (2007) 3814–3816.

[178] M.A. Spackman, J.J. McKinnon, D. Jayatilaka, Electrostatic potentials mapped on Hirshfeld surfaces provide direct insight into intermolecular interactions in crystals, CrystEngComm 10 (2008) 377–388.

[179] M.A. Spackman, D. Jayatilaka, Hirshfeld surface analysis, CrystEngComm 11 (2009) 19–32.

[180] H.F. Clausen, M.S. Chevallier, M.A. Spackman, B.B. Iversen, Three new co-crystals of hydroquinone: crystal structures and Hirshfeld surface analysis of intermolecular interactions†, New. J. Chem. 34 (2010) 193–199.

[181] M. J. Turner, J. J. McKinnon, S. K. Wolff, D. J. Grimwood, P. R. Spackman, D. Jayatilaka, M. A. Spackman, CrystalExplorer17, University of Western Australia, 2017.

[182] P.R. Spackman, M.J. Turner, J.J. McKinnon, S.K. Wolff, D.J. Grimwood, D. Jayatilaka, M.A. Spackman, *CrystalExplorer*: a program for Hirshfeld surface analysis, visualization and quantitative analysis of molecular crystals, J. Appl. Crystallogr. 54 (2021) 1006–1011.

[183] I. J. Bruno, J. C. Cole, P. R. Edgington, M. Kessler, C. F. Macrae, P. McCabe, J. Pearson and R. Taylor, New software for searching the Cambridge Structural Database and visualizing crystal structures, Acta. Crystallogr. B. Struct. Sci. 58 (2002) 389–397.

[184] M.A. Spackman, P.G. Byrom, A novel definition of a molecule in a crystal, Chem. Phys. Lett. 267 (1997) 215–220.

[185] J. J. McKinnon, M. A. Spackman, A. S. Mitchell, Novel tools for visualizing and exploring intermolecular interactions in molecular crystals, Acta. Crystallogr. B. Struct. Sci. 60 (2004) 627–668.

[186] E. Clementi, C. Roetti, Roothaan-Hartree-Fock atomic wavefunctions: Basis functions and their coefficients for ground and certain excited states of neutral and ionized atoms, Z≤54, At. Data Nucl. Data Tables 14 (1974) 177–478.

[187] A. L. Rohl, M. Moret, W. Kaminsky, K. Claborn, J. J. Mckinnon, B. Kahr, Hirshfeld Surfaces Identify Inadequacies in Computations of Intermolecular Interactions in Crystals: Pentamorphic 1,8-Dihydroxyanthraquinone, Cryst. Growth Des. 8 (2008) 4517–4525.

[188] S. K. Seth, Structural characterization and Hirshfeld surface analysis of a Co^{II} complex with imidazo[1,2-*a*]pyridine, Acta. Crystallogr. E: Crystallogr. Commun. 74 (2018) 600–606.

[189] S. Islam, P. Das, S. Tripathi, S. Mukhopadhyay, S.K. Seth, Exploring Solid-State Supramolecular Architectures of Penta (carboxymethyl) diethylenetriamine: Experimental Observation and Theoretical Studies, ChemistrySelect 7 (2022) e202203396.

[190] L. H. Thomas, The production of characteristic X-rays by electronic impact. In Mathematical Proceedings of the Cambridge Philosophical Society, Cambridge University Press, 23 (1927) 829–831.

[191] E. Fermi, Statistical method to determine some properties of atoms, Rend. Accad. Naz. Lincei. 6 (1927) 602–607.

[192] R. Parr and W. Yang, Density-Functional Theory of Atoms and Molecules, Oxford: Oxford Univ. Press, 1989.

[193] P. Hohenberg, W. Kohn, Inhomogeneous Electron Gas, Phys. Rev. 136 (1964) B864.

[194] W. Kohn and L. J. Sham, S Self-Consistent Equations Including Exchange and Correlation Effects, Phys. Rev. 140 (1965) A1133.

[195] C. Lee, W. Yang, R.G. Parr, Development of the Colle-Salvetti correlation-energy formula into a functional of the electron density, Phys. Rev. B 37 (1988) 785.

[196] J.P. Perdew, Y. Wang, Accurate and simple analytic representation of the electron-gas correlation energy, Phys. Rev. B 45 (1992) 13244.

[197] S.F. Boys, F.J.M.P. Bernardi, The calculation of small molecular interactions by the differences of separate total energies. Some procedures with reduced errors, Mol. Phys. 19 (1970) 553–566.

[198] R.F. Bader, Atoms in Molecules, Acc. Chem. Res., 18 (1985) 9–15.

[199] R.F. Bader, A Quantum Theory of Molecular Structure and Its Applications, Chem. Rev., 91 (1991) 893–928.

[200] R.F.W. Bader, From Schrodinger to atoms in molecules, Pure Appl. Chem., 60 (1988) 145–155.

[201] T.A. Keith, AIMAll (version 13.05.06), TK Gristmill Software, Overland Park, KS, USA, 2013.

[202] R. Hilal, S.G. Aziz, A.O. Alyoubi, S. Elroby, Quantum Topology of the Charge density of Chemical Bonds. QTAIM analysis of the C-Br and O-Br bonds, Procedia Comput. Sci. 51 (2015) 1872–1877.

[203] A. Kazachenko, F. Akman, M. Medimagh, N. Issaoui, N. Vasilieva, Y.N. Malyar, I.G. Sudakova, A. Karacharov, A. Miroshnikova, O.M. Al-Dossary, Sulfation of Diethylaminoethyl-Cellulose: QTAIM Topological Analysis and Experimental and DFT Studies of the Properties, ACS Omega 6 (2021) 22603–22615.

[204] P. Dey, S. Islam, S.K. Seth, Quantitative analysis of the interplay of hydrogen bonds in M(II)-hexaaqua complexes with HMTA [M(II) = Co(II), Mg(II); HMTA = hexamethylenetetramine], J. Mol. Struct. 1284 (2023) 135448.

[205] C. Lepetit, M.L. Kahn, QTAIM and ELF topological analyses of zinc-amido complexes, Res. Chem. Intermed. 47 (2021) 377–395.

[206] J. Contreras-García, E.R. Johnson, S. Keinan, R. Chaudret, J.P. Piquemal, D.N. Beratan, W. Yang, NCIPLOT: A Program for Plotting Noncovalent Interaction Regions, J. Chem. Theory Comput. 7 (2011) 625–632.

[207] E.R. Johnson, S. Keinan, P. Mori-Sanchez, J. Contreras-Garcia, A.J. Cohen, W. Yang, Revealing Noncovalent Interactions, J. Am. Chem. Soc. 132 (2010) 6498–6506.

[208] A. Gavezzotti, Efficient computer modeling of organic materials. The atom–atom, Coulomb–London–Pauli (AA-CLP) model for intermolecular electrostatic-polarization, dispersion and repulsion energies†, New J. Chem. 35 (2011) 1360.

[209] A. Gavezzotti, Calculation of Intermolecular Interaction Energies by Direct Numerical Integration over Electron Densities. I. Electrostatic and Polarization Energies in Molecular Crystals, J. Phys. Chem. B 106 (2002) 4145–4154.

[210] A. Gavezzotti, Calculation of Intermolecular Interaction Energies by Direct Numerical Integration over Electron Densities. 2. An Improved Polarization Model and the Evaluation of Dispersion and Repulsion Energies, J. Phys. Chem. B 107 (2003) 2344–2353.

CHAPTER 2

pH-induced structural variations of two new Mg(II)-PDA complexes: experimental and theoretical studies

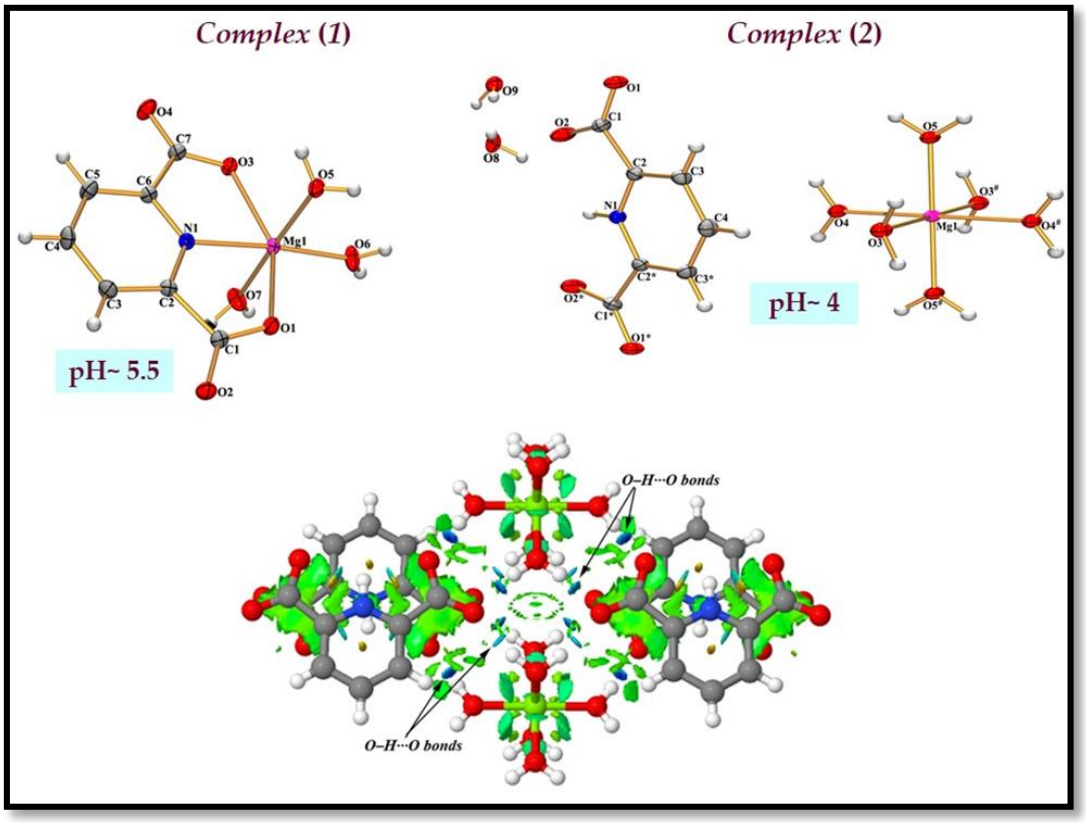

Published in: ***Journal of Molecular Structure*** **1265 (2022) 133373**

2.1. Introduction

The modern research of coordination chemistry is progressing at an explosive pace in crystal engineering because of the self-assembly phenomenon of small building units to complicated architectures, fascinating structural topologies, and potentiality as functional materials in the fields of magnetism, gas absorption, catalysis, luminescence, optoelectronic devices and nonlinear optics [1–5]. In recent years, careful exploration of various noncovalent interactions, namely, intra and intermolecular hydrogen bonding, hydrophobic interactions, dispersion interactions, halogen bonding, cation···π, N–H···π, C–H···π, S–H···π, π···π, lone pair···π, salt bridge···π, etc. interactions gain great attention due to their crucial role in controlling crystal structures and properties of metal complexes [6–12]. However, there is a state of infancy in developing coordination compounds with the desired topologies and properties as many factors affect the molecular architectures. These controlling factors are metal ions, ligands, metal-ligand ratio, counterions, pH value, solvents, and temperature [13–15]. Moreover, nucleophilic activity, positions of donor atoms of ligands, and intrinsic geometric preferences of the central metal atom also play a pivotal role in determining the self-assembled structure of coordination complexes [16].

Being one of the essential controlling factors, an important role is played by pH of the reaction medium in determining coordination mode of the ligands and hence the geometry of the complexes. [17, 18]. It has adverse effects on complex formation such as pH helps in determining the specific binding modes of ligands by protonation/deprotonation, maintaining the metal-to-ligand ratio in the products [19, 20], maintaining the concentration of OH^- ligand [21], in situ formation, and conversion of ligands [22, 23], and control of reaction kinetics by modulation of pH values [24, 25]. Therefore, it is clear that metal-ligand complexation and their packing in the solid-state are significantly controlled by pH [26]. In general, the higher the pH, the deprotonation will lead to greater connectivity (μ) of ligands to the metal ion based on acid-base chemistry and hard and soft acid-base (HSAB) principle *i.e.*, high dimensional self-assembled structure. Therefore, at higher pH, i.e., in an alkaline or weakly acidic medium, coordination of water to the metal centers becomes difficult, resulting in complexes having a lower metal-to-water (coordinated water) ratio. In contrast, at lower pH, alkaline earth metal shows a higher tendency to coordinate with water molecules to satisfy the coordination sphere, which causes a higher metal-to-water (coordinated water) ratio, leading to low dimensional architecture formation [27]. From the above discussion, it is thus evident that the solid-state

structure of metal complexes is greatly influenced by reaction acidity, and it plays a crucial role in determining the dimensionality of the self-assembly structure.

Coordination modes of multicarboxylic acid can be manipulated by changing the pH value as protonated and deprotonated forms of carboxylate moiety depend on their following pK_a values [28]. Thus, the binding of pyridine-2,6-dicarboxylic acid (pK_{a1} and pK_{a2} are 1.4 and 3.1, respectively) to metal ions can be varied by changing the pH value of the reaction medium [29]. Its dicarboxylic acid plays an essential role in producing multidimensional self-assembled complexes. They generally exhibit a variety of binding modes, for example, terminal monodentate, chelating, bridging bidentate in a *syn-syn*, *syn-anti*, and *anti-anti* configuration to two metal centers and bridging tridentate to two metal centers [30] because of having rigid 120° angle between the central pyridine ring and two carboxylate groups [31]. Besides, such ligand causes involvement of hydrogen bonding, π–π, anion–π, cation–π, lone pair–π, *etc.* supramolecular interactions that may lead to the formation of one-dimensional chains and ladders, two-dimensional grids, three-dimensional microporous networks, interpenetrated modes, and helical staircase networks and so on in their complexes [32].

This paper reports the pH-dependent variation of coordination modes of 2,6-pyridine dicarboxylic acid towards Mg(II) metal ion and their structural features in the solid state. The non-covalent interactions are further characterized through Bader's theory of "atoms in molecules" (AIM) and the "noncovalent interaction" (NCI) plot index.

2.2. Experimental Sections

2.2.1. Materials and Measurements

The chemicals used were of reagent-grade quality and purchased from Sigma Aldrich Chemical Company. All reactions were carried out in an aqueous medium under aerobic conditions. During the whole experiment, doubly distilled water was used. Elemental analyses (C, H, and N) of the investigating complexes were performed on a Perkin-Elmer 240C elemental analyzer.

2.2.2. Syntheses

2.2.2a. Synthesis of Complex [Mg(dipic)(H_2O)$_3$].2H_2O (1)

$Mg(NO_3)_2.6H_2O$ (0.512 g, 2.0 mmol) was dissolved in 50 mL of water. The water mixture was then allowed to react with pyridine-2,6-dicarboxylic acid (0.336 g, 2.0 mmol) at 60 °C, which results in a colorless solution (Scheme 2.1). The pH of the reaction mixture was adjusted to ~5.5 by adding a freshly prepared solution of triethylamine in methanol. The

resulting reaction mixture was stirred at 60 °C for two hours, then cooled to room temperature, filtered, and kept undisturbed for crystallization. After four weeks, block-shaped, colorless single crystals suitable for X-ray analysis were obtained. The crystals were collected by filtration, washed with cold water, and dried in the air (yield: 65%). Anal. calcd. for $C_7H_{13}MgNO_9$: C, 30.08; H, 4.69; N, 5.01%. Found: C, 30.10; H, 4.73; N, 4.98%.

2.2.2b. Synthesis of Complex [Mg(H₂O)₆].2dipicH (2)

Taking complex (**1**) as the precursor, we have planned to synthesize complex **2**. For the synthesis, a solid crystal of complex (**1**) (0.279 gm, 1.0 mmol) was first dissolved in 40 mL of distilled water, and then nitric acid was added (HNO_3: H_2O = 1: 20). That results in the reaction medium having pH ~ 4, further stirred at 60°C for two hours. The final reaction mixture was then cooled to room temperature, filtered, and kept undisturbed for slow evaporation. After five weeks, block-shaped, colorless single crystals suitable for X-ray analysis were obtained. The crystals were collected by filtration, washed with cold water, and dried in the air (yield: 62%). Anal. calcd. for $C_{14}H_{20}MgN_2O_{14}$: C, 36.19; H, 4.34; N, 6.03%. Found: C, 36.16; H, 4.32; N, 6.06%.

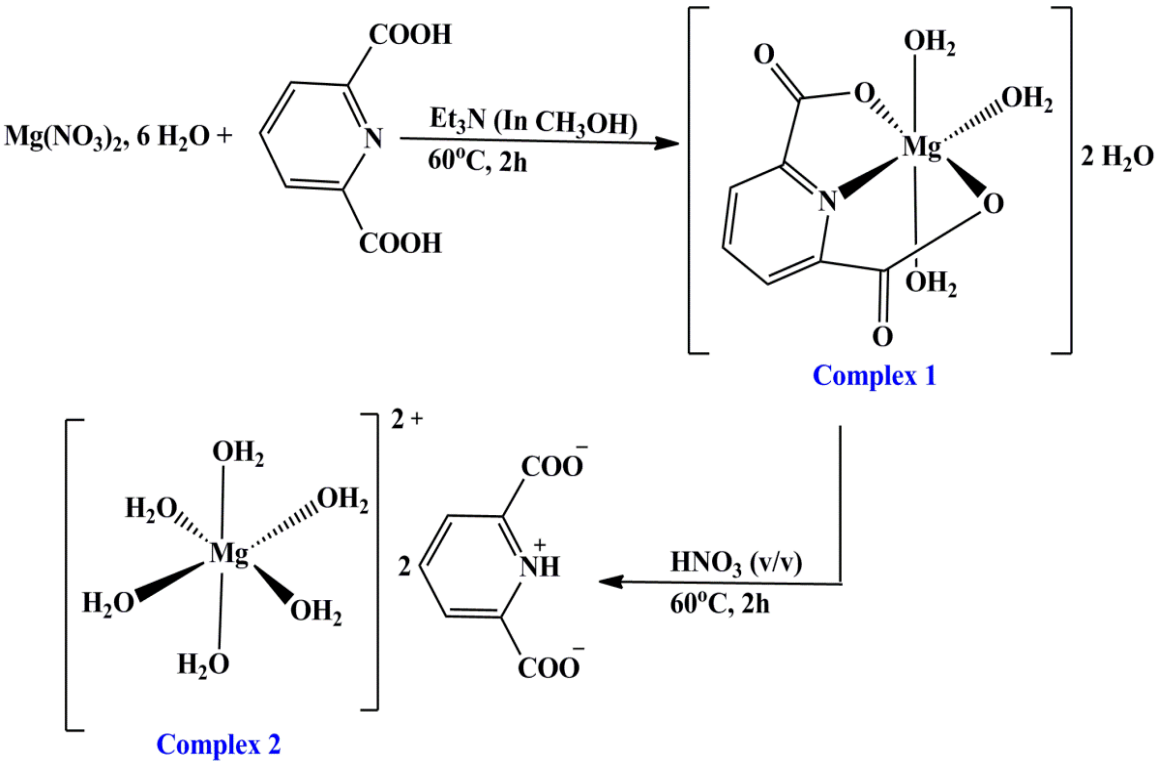

Scheme 2.1. Schematic representation for the synthesis of both the complexes.

2.2.3. X-ray Crystal Structure Determination

Single crystal X-ray diffraction intensity data was collected using Bruker APEX-II CCD diffractometer with MoKα radiation (λ = 0.71073 Å) at 120(2)K. The data was reduced

by performing the program Bruker SAINT [33], and an empirical absorption correction based on the multi-scan method [34] was applied. The title structures were solved using the direct method (SHELXS-14) [35] and refined (SHELXL-18) [36] using the full-matrix least-squares method on F^2. We have used difference fourier electron density map to locate all the atom's positions. Difference maps are calculated using coefficients of ($|F_o|$ - $|F_c|$) with the calculated phase angles, where F_o is the observed structure factor, and F_c is the calculated structure factor. Difference maps tend to produce peaks where low electron density has been included in the model and produce negative holes where too much electron density has been included in the model. All the non-hydrogen atoms are assigned accordingly. A difference in electron density synthesis was calculated around the circle representing possible hydrogen positions' loci. The maximum electron density is then taken as the starting position for the hydrogen atom(s). The distinct peaks corresponding to the hydrogen atoms are observed in the difference Fourier map and assigned accordingly. The OH H-atom positions obtained from a difference Fourier map was refined freely, while the C-bound H atoms were placed in idealized positions using the riding method, with bond distances ranging from 0.93 to 0.98 Å and U_{iso}(H) values set at 1.5U_{eq} of the parent atoms. The structure solution was performed using the WinGX program V2014.1 [37] and analyzed by the program PLATON [38]. The crystal data and structure refinement parameters of the title complexes are summarized in Table 2.1. CCDC 2144365–2144366 contains the supplementary crystallographic data of complexes (**1**) and (**2**), respectively.

Table 2.1. Crystal data and structure refinement parameters for the title complexes (**1**–**2**).

Crystal data	Complex (**1**)	Complex (**2**)
Chemical formula	$C_7H_{13}Mg_1N_1O_9$	$C_{14}H_{20}Mg_1N_2O_{14}$
Formula weight	279.49	464.63
Temperature (K)	120(2)	120(2)
Wavelength (Å)	0.71073	0.71073
Crystal system, space group	Monoclinic, $P2_1/n$	Monoclinic, C2/m
a, *b*, *c* (Å)	8.8884(9), 9.8998(10), 13.1928(14)	13.1412(15), 11.0501(15), 6.5214(8)
β (°)	97.290(2)	93.798(3)
V (Å^3)	1151.5(2)	944.9(2)
Z, Calculated density (Mg/m^3)	4, 1.612	2, 1.633
μ (mm^{-1})	0.197	0.176
F(000)	584	484
Crystal size (mm)	0.21 × 0.13 × 0.08	0.21 × 0.14 × 0.09

θ range for data collection (º)	2.58 to 25.00	2.41 to 24.99
Limiting indices	$-10 \le h \le 10$, $-11 \le k \le 11$, $-15 \le l \le 15$	$-15 \le h \le 15$, $-13 \le k \le 12$, $-7 \le l \le 7$
Reflections collected / unique	10563 / 2028 [R(int) = 0.0248]	4383 / 877 [R(int) = 0.0238]
Completeness to θ	100.0 %	99.9 %
Absorption correction	Semi-empirical from equivalents	Semi-empirical from equivalents
Max. and min. transmission	0.98 and 0.97	0.98 and 0.97
Refinement method	Full-matrix least-squares on F^2	Full-matrix least-squares on F^2
Data/parameters	2028/163	877/80
Goodness-of-fit on F^2	1.046	1.115
Final R indices [I>2sigma(I)]	$R_1 = 0.0268$, $wR_2 = 0.0709$	$R_1 = 0.0251$, $wR_2 = 0.0722$
R indices (all data)	$R_1 = 0.0285$, $wR_2 = 0.0722$	$R_1 = 0.0257$, $wR_2 = 0.0726$
Largest diff. peak and hole (e $Å^{-3}$)	0.214, −0.316	0.251, −0.177

$R_1 = \sum||F_o|-|F_c||/\sum|F_o|$, $wR_2 = [\sum\{(F_o^2-F_c^2)^2\}/\sum\{w(F_o^2)^2\}]^{1/2}$, $w = 1/\{\sigma^2(F_o^2) + (aP)^2 + bP\}$, where, a = 0.0378 and b = 0.5748 for (**1**); a = 0.0330 and b = 0.9319 for (**2**).

2.2.4. Theoretical Methods

The quantum chemical computations of both complexes are achieved with the support of MP2/ B3LYP /6–311++ G (d,p) basis set available in Gaussian 09 w calculation package [39]. Theoretical calculations have been performed considering the crystallographic coordinates as input. Theoretical models have been developed from supramolecular networks. We have used Bader's "Atoms in molecules" theory [40] to analyze the weak noncovalent interactions by the AIMall calculation package [41]. Non-covalent interactions are characterized at their bond critical points (BCPs) using the Atoms in Molecules (AIM) theory [42]. According to the topological properties, electron density is concentrated over $\nabla^2(\rho(r)) < 0$ and is depleted for $\nabla^2(\rho(r)) > 0$. Selected topological parameters such as electron density, $\rho(r)$, Laplacian of the electron density, $\nabla^2(\rho(r))$, potential electronic energy density V(r), kinetic electronic energy density, G(r), and total electronic energy density [H(r) = V(r) + G(r)] were used at their bond critical points (BCPs) to characterize the nature and strength of intermolecular interactions. The theoretical NCI plot [43] is a visualization index that has been used for the characterization of noncovalent interactions. Isosurfaces instead of critical points

represent the noncovalent interactions. These isosurfaces represent favorable and unfavorable interactions and are differentiated by the isosurface color scheme with a red-yellow-green-blue scale. The red and blue surfaces represent ρ^{+}cut (repulsive) and ρ^{-}cut (attractive) interactions [44], respectively. However, weak repulsive and weak attractive interactions are represented by the yellow and green colors, respectively.

2.3. Results and Discussion

2.3.1. Structural Description of Complex (1)

Complex (**1**) crystallizes in a monoclinic system with space group $P2_1/n$. The coordination geometry around the Mg(II) ion is distorted octahedral. The equatorial sites are occupied by one nitrogen N1, two carboxylate oxygen O1, O3 atoms from dipic ligand, and one oxygen atom O6 of the water molecule (Figure 2.1). Two oxygen O5 and O7 atoms from the solvent water molecules occupy the axial sites. There are two more solvent water molecules in the asymmetric unit (Figure 2.1). The N(1)–Mg(1)–O(7) angle is 89.05º, showing that O(7) atom lies cis to ring nitrogen atom N(1) (Table 2.2). The bite angles around the Mg(II) ion are N(1)–Mg(1)–O(1) = 74.27(4)°; N(1)–Mg(1)–O(3) = 73.96(4)°; O(1)–Mg(1)–O(6) = 101.40(4)° and O(3)–Mg(1)–O(6) = 110.39(4)°, summing up the in-plane angle to be exactly 360.02°. That shows the high planarity of one solvent water oxygen atom and O, N, O donor atoms of the dipic ligand. In the five-membered chelate rings, Mg(1)–O(1)–C(1)–C(2)–N(1) and Mg(1)–O(3)–C(7)–C(6)–N(1), all atoms are almost coplanar with O1 and C1 have the largest deviation [+0.054(1); –0.074(1)] in the opposite directions from the least-square mean plane of the chelate rings. The dihedral angle between two chelate rings is 1.49(3)°.

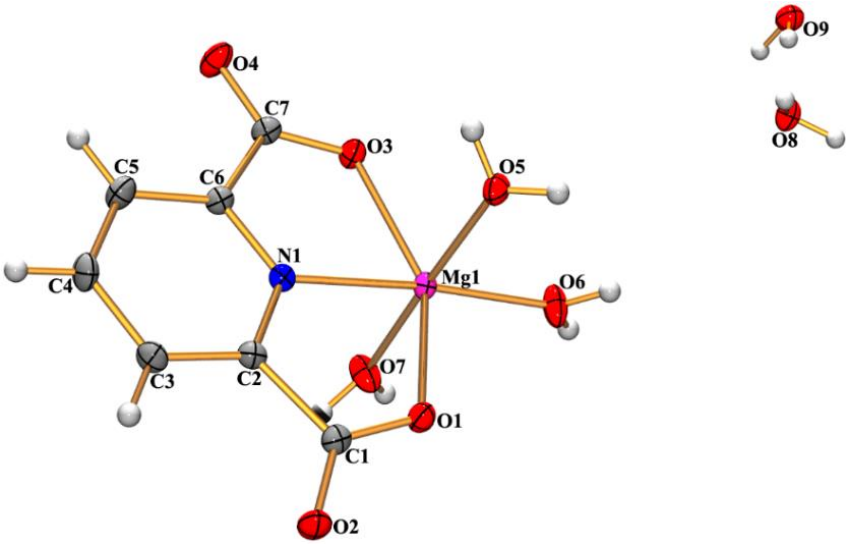

Figure 2.1. An ORTEP view of complex (**1**) with the atom-numbering scheme. Thermal ellipsoids are drawn at 30% probability.

The solid-state structure of the complex (**1**) is stabilized through multiple O–H···O hydrogen bonds and lone-pair(l.p)···π interactions (Table 2.3). In the first sub-structure, two metal-coordinating water oxygen atoms O(5) and O(6), play the role of donors to the carboxylate oxygen atoms O(3) and O(4) of the partner molecule at (3/2–x, –1/2+y, 1/2–z) by generating an $R_2^2(8)$ motif (Figure 2.2). Due to the self-complementarity, another water oxygen atom O(7), play the role of donor to the carboxylate oxygen atom at (5/2–x, 1/2+y, 1/2–z) to build a two-dimensional supramolecular framework in (110) plane (Figure 2.2). In another substructure, the carbonyl oxygen atoms O(2) and O(4) in the molecules at (2–x, –y, –z) and (2–x, 1–y, –z) are juxtaposed towards the centroid of the pyridine ring. The separation distance between the carbonyl oxygen atoms and the centroid of the sandwiched pyridine ring are 3.405(2)Å and 3.633(2)Å respectively, suggesting lone-pair(l.p)···π interactions (Figure 2.3a). The combination of the hydrogen bonding contacts among coordinating water oxygen atoms O(5) and O(6) with the carboxylate oxygen atoms and the (l.p)···π/π···(l.p) network leads the molecules to build a supramolecular layered assembly (Figure 2.3b).

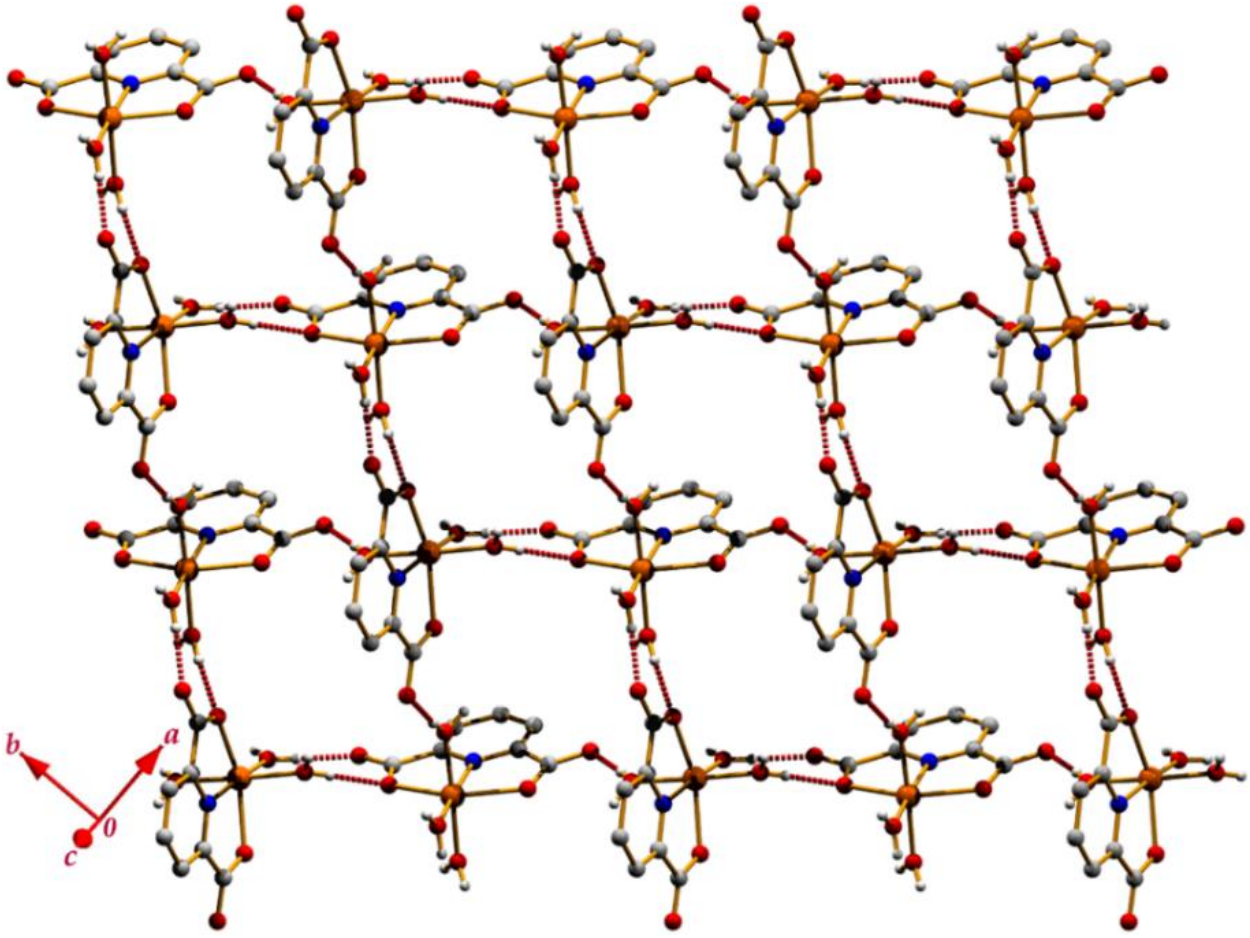

Figure 2.2. Supramolecular framework in (**1**) through O–H···O hydrogen bonds.

Table 2.2. Selected bond lengths (Å) and bond angles (°) of the title complexes.

Complex (**1**)				Complex (**2**)	
Mg(1)–O(6)	1.9962(11)	Mg(1)–N(1)	2.0972(12)	Mg(1)–O(5)	2.0054(12)
Mg(1)–O(7)	2.0233(10)	Mg(1)–O(1)	2.1451(10)	Mg(1)–O(4)	2.0462(12)
Mg(1)–O(5)	2.0413(10)	Mg(1)–O(3)	2.1624(10)	Mg(1)–O(3)	2.1170(12)
O(6)–Mg(1)–O(7)	88.61(4)	O(5)–Mg(1)–O(1)	92.25(4)	O(5)–Mg(1)–O(4)	90.0
O(6)–Mg(1)–O(5)	88.22(4)	N(1)–Mg(1)–O(1)	74.27(4)	O(5)–Mg(1)–O(3)	90.0
O(7)–Mg(1)–O(5)	176.48(5)	O(6)–Mg(1)–O(3)	110.39(4)	O(4)–Mg(1)–O(3)	91.56(5)
O(6)–Mg(1)–N(1)	175.08(5)	O(7)–Mg(1)–O(3)	90.73(4)	O(5)–Mg(1)–O(5)$^{\#1}$	180.0
O(7)–Mg(1)–N(1)	89.05(4)	O(5)–Mg(1)–O(3)	88.93(4)	C(3)–C(4)–C(3)$^{\#2}$	121.03(16)
O(5)–Mg(1)–N(1)	94.22(4)	N(1)–Mg(1)–O(3)	73.96(4)	C(2)–N(1)–C(2)$^{\#2}$	125.54(15)
O(6)–Mg(1)–O(1)	101.40(4)	O(1)–Mg(1)–O(3)	148.21(4)		
O(7)–Mg(1)–O(1)	89.89(4)				

Symmetry transformations used to generate equivalent atoms: #1: (–x, –y, –z+2) and #2: (x, –y, z).

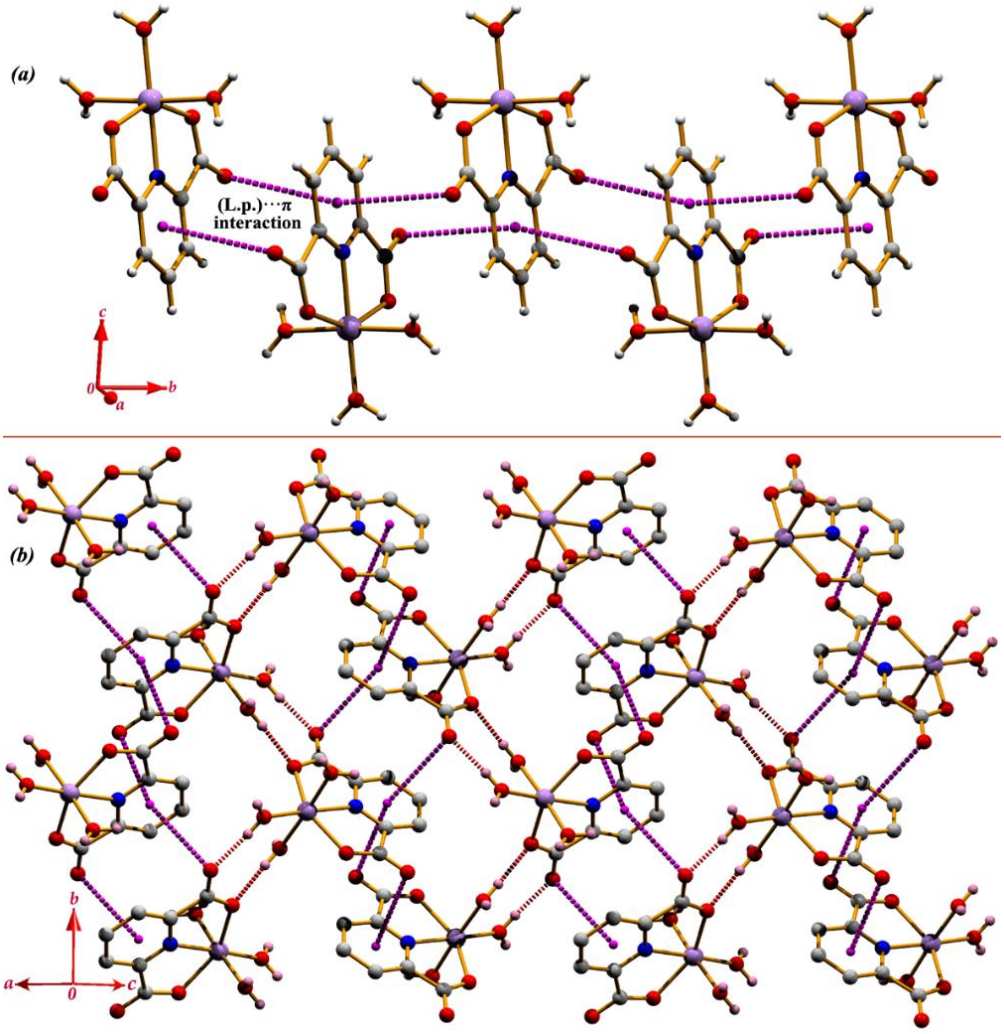

Figure 2.3. (a) Perspective view of the (l.p)···π/π···(l.p) network in (**1**); (b) Supramolecular layered framework generated through O–H···O hydrogen bonds and (l.p)···π interaction in (**1**).

2.3.2. Structural Description of Complex (2)

Complex (**2**) is crystallized in the monoclinic crystal system with C2/m space group. In complex (**2**), as illustrated in the ORTEP (Figure 2.4), the molecular view consists of one-half of the aquated cation and two halves of the ligand molecule. The remaining portion of cationic and anionic moieties is generated via a centre of inversion. The metal ion is positioned in the inversion center (–x, –y, –z+2) and is situated in a perfect octahedral environment constructed from six water molecules (Figure 2.4). The dipic ligand is not bound to the metal ions, remaining outside the coordination shell. The N(1) and C(4) atoms of the pyridine ring of the dipic ligand are in the inversion center (x, –y, z) (see Figure 2.4). The Mg–O bond lengths vary in the range 2.048–2.118Å and are comparable to those of the similar complexes reported earlier [45, 46].

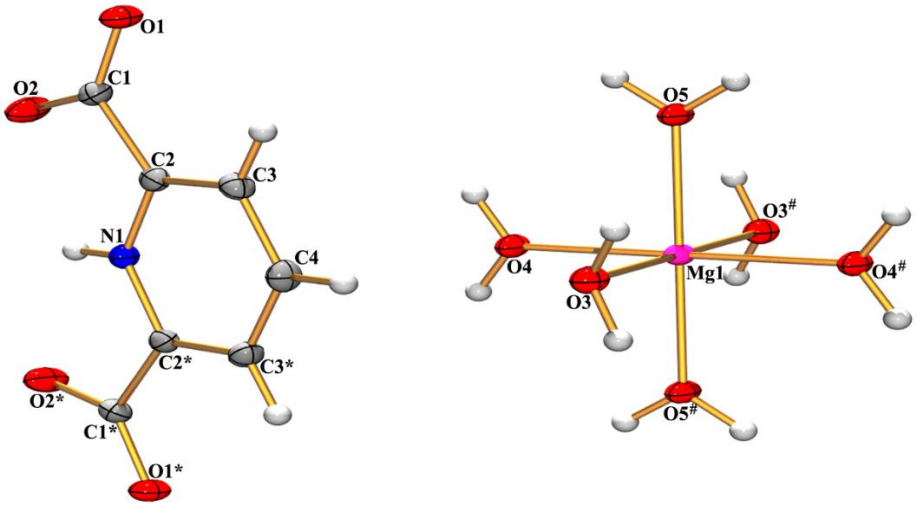

Figure 2.4. An ORTEP view of complex (**2**) with the atom-numbering scheme. Thermal ellipsoids are drawn at 30% probability.

Complex (**2**) is stabilized through N–H···O, O–H···O and intramolecular C–H···O hydrogen bonds (Table 2.3). The supramolecular structures generated via hydrogen bonds between the $[Mg(H_2O)_6]^{2+}$ and anionic dipic ligand are illustrated separately. In the first substructure, the carboxylate oxygen atom O(1) acts as a double acceptor for the donor water oxygen atoms O(3) and O(4) in the molecules at (1/2–x, 1/2–y, 2–z), and (1/2–x, 1/2–y, 1–z) respectively. Moreover, another water oxygen atom O(5) at (1/2–x, 1/2–y, 1–z) acts as a donor to another carboxylate oxygen atom O(2) to build a supramolecular framework in the (011) plane (Figure 2.5).

Table 2.3. Hydrogen-bond geometry (Å, °).

D*–H···*A	***D*–H**	**H···*A***	***D*···*A***	***D*–H···*A***	***Symmetry***
*Complex (**1**)*					
O5–H5A···O9	0.82	1.96	2.7821(14)	174	1–x, 1–y, 1–z
O5–H5B···O3	0.82	1.91	2.7277(14)	177	3/2–x, –1/2+y, 1/2–z
O6–H6A···O4	0.83	1.83	2.6574(14)	177	3/2–x, –1/2+y, 1/2–z
O6–H6B···O9	0.83	2.06	2.8574(14)	161	3/2–x, –1/2+y, 3/2–z
O7–H7A···O2	0.83	1.83	2.6586(14)	173	5/2–x, 1/2+y, 1/2–z
O7–H7B···O8	0.83	1.99	2.7972(14)	167	2–x, 1–y, 1–z
O8–H8A···O1	0.83	1.98	2.7809(14)	162	–1/2+x, 1/2–y, 1/2+z
O8–H8B···O4	0.83	1.89	2.7063(13)	171	x, y, 1+z
O9–H9A···O8	0.82	1.96	2.7696(15)	167	---
O9–H9B···O2	0.82	2.03	2.8342(15)	166	2–x, 1–y, 1–z
*Complex (**2**)*					
N1–H1···O2	0.86	2.16	2.5643(12)	108	x, –y, z
O3–H3A···O1	0.83	1.95	2.7701(13)	169	1/2–x, 1/2–y, 2–z
O4–H4A···O1	0.83	1.94	2.7571(13)	170	1/2–x, 1/2–y, 1–z
O5–H5A···O2	0.83	1.86	2.6811(12)	176	1/2–x, 1/2–y, 1–z
C4–H4···O3	0.93	2.51	3.251(2)	137	---

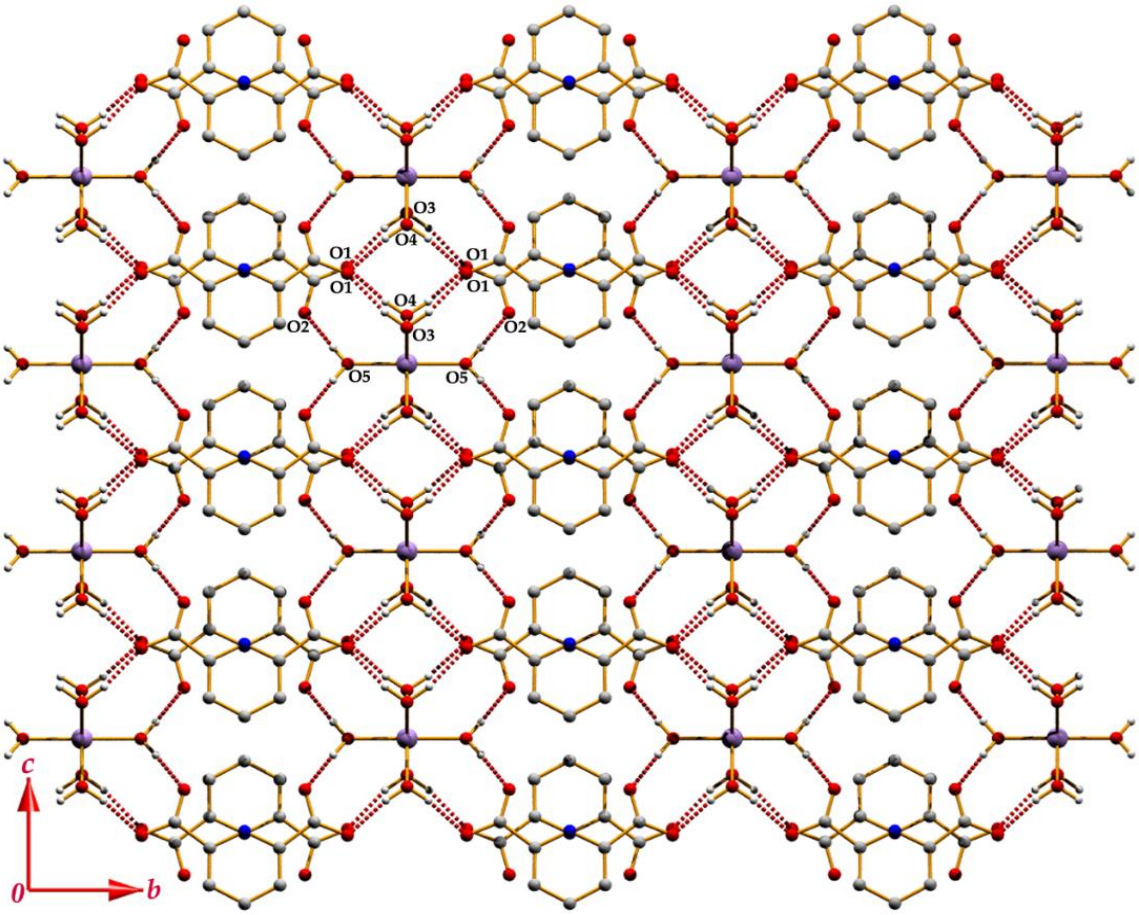

Figure 2.5. Supramolecular framework generated through O–H···O hydrogen bonds in (**2**).

2.3.3. Theoretical Analysis

Bader's theory of "atoms in molecules"(AIM) has been used for title complexes (**1**–**2**) to characterize different interactions that are exhibited by the structures. We have used various models that are generated from the X-ray structures. Here, the bond path and a bond critical point (CP) that interconnects two atoms of the molecule [40, 42] characterize the noncovalent interactions. For complex (**1**), a part of the self-assembled structure (see Figure 2.3a) has been used as a model for AIM analysis. Here, the bond critical point (ρ_{BCP} = 0.0042 a.u.) (see Table 2.4) and a bond path interconnecting the carboxylate carbonyl oxygen atom and a carbon atom of the pyridine ring characterized the lone-pair(l.p)···π interaction in (**1**) (see Figure 2.6a). In another model (see Figure 2.6b), we have used a part of the packing of Figure 2.3b for characterization of O–H···O hydrogen bonds. The bond critical points (ρ_{BCP} = 0.0313 and 0.0271 a.u.) and the bond paths between two water oxygen and carboxylate oxygen atoms represent strong O–H···O hydrogen bonds in (**1**) (Figure 2.6b). For complex (**2**), the model has been used from the packing diagram (see Figure 2.5). The hydrogen bonds in between the water oxygen atoms and carboxylate oxygen atoms are characterized by the bond path and BCPs (Figure 2.6b). The $\rho(r)$ values (0.0300 a.u. and 0.0266 a.u.) at the bond CPs designate the bonds where O(1) acts as a double donor to the water oxygen atoms O(3) and O(4). Moreover, the most robust hydrogen bonding contact is also evidenced by the bond critical point (ρ_{BCP} = 0.0321 a.u.) that agrees well with the experimental observations (see Table 2.3).

The topological and energetic properties of the noncovalent interactions at the bond critical points (BCPs) in the observed dimers of the crystal structures of (**1**-**2)** were analyzed by comparing selected topological properties, including the electron density ($\rho(r)$), the Laplacian of electron density ($\nabla^2\rho(r)$), the potential electronic energy density (V(r)), the kinetic electronic energy density (G(r)), the total electronic energy density (H(r)=V(r)+G(r)) and $\left|-\frac{V(r)}{G(r)}\right|$ value. The lone-pair(l.p) ···π interaction in (**1**) and O–H···O hydrogen bonds in both complexes have been involved in the stabilization of observed molecular dimers (Table 2.4 and Figure 2.6). According to Gatti's assignment, all these interactions are classified as closed-shell interactions [47] using the values of $\left|-\frac{V(r)}{G(r)}\right| < 1$, H(r) > 0 and the positive value of the Laplacian $\nabla^2\rho(r) > 0$.

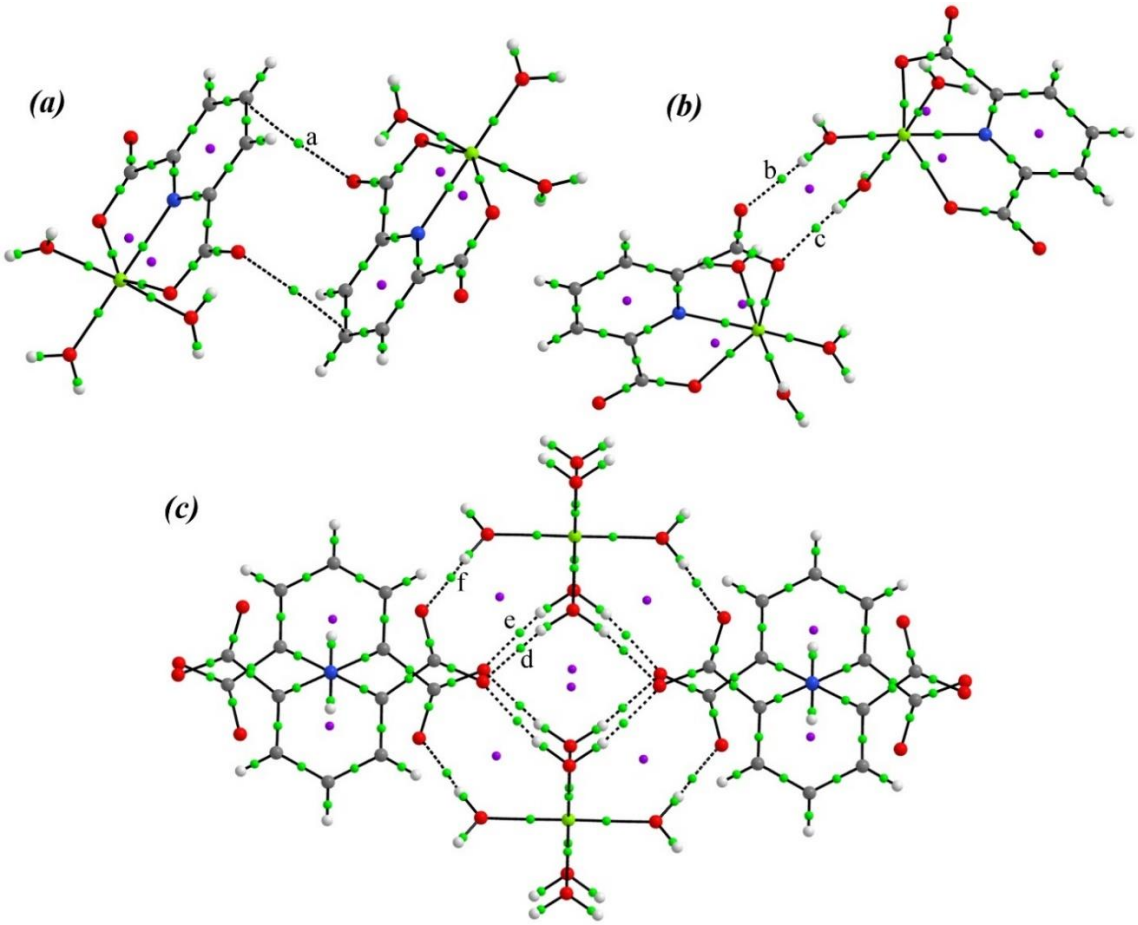

Figure 2.6. AIM analyses of complexes (**1**)(a,b) and (**2**)(c). Green and violet spheres represent bond and ring critical points, respectively.

Table 2.4. Topological parameters for intermolecular interactions [in different dimers of (**1**) and (**2**)] at their (3, –1) BCPs. [$\rho(r)$: electron density (eÅ^{-3}); $\nabla^2\rho(r)$: Laplacian of electron density (eÅ^{-5}); **ε**: ellipticity; $V(r)$: potential energy density; $G(r)$: kinetic energy density; $H(r)$: total electronic density; $V(r)$, $G(r)$ and $H(r)$ values in a.u.

	Interaction	$\boldsymbol{\rho}$	$\boldsymbol{\nabla^2\rho}$	**ε**	$\boldsymbol{V(r)}$	$\boldsymbol{G(r)}$	$\boldsymbol{H(r)}$	$\left\lvert-\frac{\boldsymbol{V(r)}}{\boldsymbol{G(r)}}\right\rvert$
Complex (1)	C7–O4···π (a)	0.0042	0.0136	1.5669	–0.0022	0.0028	0.0006	0.7857
	O6–H6A···O4 (b)	0.0313	0.1518	0.0372	–0.0330	0.0355	0.0025	0.9290
	O5–H5B···O3 (c)	0.0271	0.1297	0.0435	–0.0275	0.0300	0.0025	0.9166
Complex (2)	O4–H4A···O1 (d)	0.0300	0.1285	0.0420	–0.0299	0.0310	0.0011	0.9645
	O3–H3A···O1 (e)	0.0266	0.1302	0.0214	–0.0271	0.0298	0.0027	0.9093
	O5–H5A···O2 (f)	0.0321	0.1446	0.0374	–0.0334	0.0348	0.0014	0.9597

Furthermore, the noncovalent interactions that are involved within the structures of the title complexes are characterized through the 'noncovalent interaction' (NCI) plot index. Herein, we have used a part of the packing diagrams for both complexes that are shown in Figures 2.3a, 2.3b and 2.5, respectively. Different noncovalent interactions are evident by the green and blue isosurfaces. In Figure 2.7a, the cooperativity of the (l.p)···π interaction has been characterized by the dual large green isosurfaces in between the carboxylate oxygen atom and the centroid of the pyridine ring. The large flattened greenish isosurface represents the dual interplay of the (l.p)···π interaction (Figure 2.7a). The deep blue colored isosurfaces (see Figure 2.7b) that are evident in between the water and carboxylate oxygen atoms represent strong O–H···O hydrogen bonds in (**1**). The representation of the NCI plot of complex (**2**) highlights the presence of multi O–H···O hydrogen bonds (Figure 2.7c). The dark blue colored isosurfaces that are evidenced in the map and are located in between water oxygen atoms and carboxylate oxygen atoms characterize the O–H···O hydrogen-bonding contacts in (**2**). As discussed in the AIM calculation, the most favorable O–H···O contact can also be identified by close examination of the blue patches of the isosurface (Figure 2.7c). Subsequently, all the evident isosurfaces agree well with the AIM study and structural observation of both complexes.

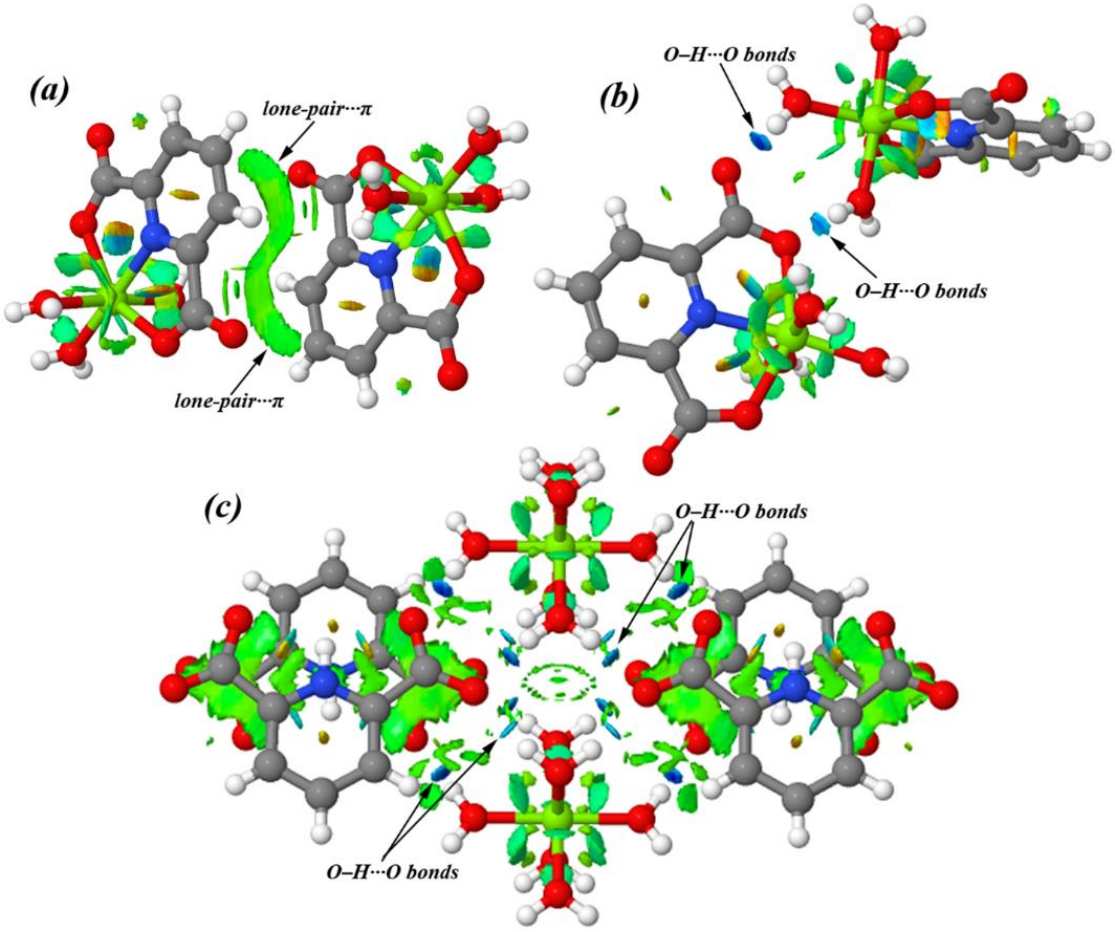

Figure 2.7. NCI plot index of the modeled structure of compounds (**1)**(a,b) and (**2)**(c).

2.4. Conclusions

Two new pH-dependent Mg(II)-PDA complexes have been synthesized and structurally characterized. The cooperativity of the noncovalent interactions has been explored in detail by examining the supramolecular behavior of the complexes. How a minor tuning of the pH value affects the solid-state structural assemblies has been explored herein. Theoretical AIM and NCI plot analyses have further characterized the non-covalent interactions and, consequently, the self-assemblies. Topological analysis at bond critical points of intermolecular interactions revealed that all of the interactions are closed-shell interactions. The theoretical investigations agree well with the experimental findings. The findings reported herein are expected to be beneficial in understanding the pH dependency and the cooperative outcome of the noncovalent interactions in building supramolecular assemblies.

2.5. References

[1] G. Ferey, Hybrid porous solids: past, present, future, Chem. Soc. Rev. 37 (2008) 191–214.

[2] Y.L. Liu, J.F. Eubank, A.J. Cairns, J. Eckert, V.C. Kravtsov, R. Luebke, M. Eddaoudi, Assembly of Metal–Organic Frameworks (MOFs) Based on Indium-Trimer Building Blocks: A Porous MOF with soc Topology and High Hydrogen Storage†, Angew. Chem. Int. Ed. 119 (2007) 3342–3347.

[3] Y.B. Zhang, W.X. Zhang, F.Y. Feng, J.P. Zhang, X.M. Chen, A Highly Connected Porous Coordination Polymer with Unusual Channel Structure and Sorption Properties†, Angew. Chem. Int. Ed. 48 (2009) 5287–5290.

[4] L.Q. Ma, A. Jin, Z.G. Xie, W.B. Lin, Freeze Drying Significantly Increases Permanent Porosity and Hydrogen Uptake in 4,4-Connected Metal–Organic Frameworks†, Angew. Chem. Int. Ed. 48 (2009) 9905–9908.

[5] L. Qin, J.S. Hu, L.F. Huang, Y.Z. Li, Z.J. Guo, H. G. Zheng, Syntheses, Syntheses, Characterizations, and Properties of Six Metal−Organic Complexes Based on Flexible Ligand 5-(4-Pyridyl)-methoxyl Isophthalic Acid, Cryst. Growth Des. 10 (2010) 4176–4183.

[6] M. Waller, S. Grimme, Weak intermolecular interactions: a supermolecular approach; 2012.

[7] P. Hobza, J. Rezac, Introduction: Noncovalent Interactions, Chem. Rev. 116 (2016) 4911–4912.

[8] S. Scheiner, Noncovalent Forces, Springer, 2015.

[9] P. Manna, S.K. Seth, Antonio Bauzá, M. Mitra, S.R. Choudhury, A. Frontera, S. Mukhopadhyay, pH Dependent Formation of Unprecedented Water–Bromide Cluster in the Bromide Salts of PTP Assisted by Anion−π Interactions: Synthesis, Structure, and DFT Study, Cryst. Growth Des. 14 (2014) 747–755.

[10] P. Manna, S.K. Seth, M. Mitra, S.R. Choudhury, Antonio Bauzá, A. Frontera, S. Mukhopadhyay, Experimental and Computational Study of Counterintuitive ClO_4^- $\cdots ClO_4^-$ Interactions and the Interplay between π^+–π and Anion$\cdots\pi^+$ Interactions, Cryst. Growth Des. 14 (2014) 5812–5821.

[11] S.K. Seth, A. Bauzá, A. Frontera, Bipolar behaviour of salt-bridges: a combined theoretical and crystallographic study†, New J. Chem. 42 (2018) 12134–12142.

[12] S. Tripathi, S. Islam, S.K. Seth, A. Bauzá, A. Frontera, S. Mukhopadhyay, Supramolecular assemblies involving salt bridges: DFT and X-ray evidence of bipolarity†, CrystEngComm 22 (2020) 8171–8181.

[13] S.K. Seth, Tuning the formation of MOFs by pH influence: X-ray structural variations and Hirshfeld surface analyses of 2-amino-5-nitropyridine with cadmium chloride†, CrystEngComm 15 (2013) 1772–1781.

[14] F. Yuan, J. Xie, H.M. Hu, C.M. Yuan, B. Xu, M.L. Yang, F.X. Dong, G.L. Xue, Effect of pH/metal ion on the structure of metal–organic frameworks based on novel bifunctionalized ligand 4′-carboxy-4,2′:6′,4″-terpyridine†, CrystEngComm 15 (2013) 1460–1467.

[15] H.R. Khavasi, B.M.M. Sadegh, Temperature-Dependent Supramolecular Motif in Coordination Compounds, Inorg. Chem. 49 (2010) 5356–5358.

[16] Q.Y. Li, G.W. Yang, L. Shen, M.H. He, W. Shen, K. Gu, J.N. Jin, Magnesium(II), Calcium(II), and Barium(II) Coordination Compounds Constructed by 1H-Tetrazolate-5-acetic Acid Ligand†, Z. Anorg. Allg. Chem. 638 (2012) 826–831.

[17] M. Chen, S.S. Chen, T.A. Okamura, Z. Su, M.S. Chen, Y. Zhao, W.Y. Sun, N. Ueyama, pH Dependent Structural Diversity of Metal Complexes with 5-(4*H*-1,2,4-Triazol-4-yl)benzene-1,3-dicarboxylic Acid, Cryst. Growth Des. 11 (2011) 1901–1912.

[18] H.C. Fang, J.Q. Zhu, L.J. Zhou, H.Y. Jia, S.S. Li, X. Gong, S.B. Li, Y.P. Cai, P.K. Thallapally, J. Liu, G.J. Exarhos, pH-Dependent Assembly and Conversions of Six Cadmium(II)-Based Coordination Complexes, Cryst. Growth Des. 10 (2010) 3277–3284.

[19] S.T. Wu, L.S. Long, R.B. Huang, L.S. Zheng, pH-Dependent Assembly of Supramolecular Architectures from 0D to 2D Networks, Cryst. Growth Des. 7 (2007) 1746–1752.

[20] H. Wang, Y.Y. Wang, G.P. Yang, C.J. Wang, G.L. Wen, Q.Z. Shia, S.R. Batten, A series of intriguing metal–organic frameworks with 3,3′,4,4′- benzophenonetetracarboxylic acid: structural adjustment and pH-dependence†, CrystEngComm 10 (2008) 1583–1594.

[21] W.X. Chen, S.T. Wu, L.S. Long, R.B. Huang, L.S. Zheng, Construction of a Three-fold Parallel Interpenetration Network and Bilayer Structure Based on Copper(II) and Trimesic Acid, Cryst. Growth Des. 7 (2007) 1171–1175.

[22] X.J. Kong, G.L. Zhuang, Y.P. Ren, L.S. Long, R.B. Huang, L.S. Zheng, *In situ* cyclodehydration of iminodiacetic acid into 2,5-diketopiperazine-1,4-diacetate in lanthanide-based coordination polymers†, Dalton Trans. (2009) 1707–1709.

[23] X.J. Kong, Y.P. Ren, L.S. Long, R.B. Huang, L.S. Zheng, M. Kurmoo, Influence of reaction conditions on the channel shape of 3d-4f heterometallic metal–organic framework†‡, CrystEngComm 10 (2008) 1309–1314.

[24] S.T. Wu, Y.R. Wu, Q.Q. Kang, H. Zhang, L.S. Long, Z.P. Zheng, R.B. Huang, L.S. Zheng, Chiral Symmetry Breaking by Chemically Manipulating Statistical Fluctuation in Crystallization†, Angew. Chem., Int. Ed. 46 (2007) 8475–8479.

[25] I. Katsuki, Y. Motoda, Y. Sunatsuki, N. Matsumoto, T. Nakashima, M. Kojima, Spontaneous Resolution Induced by Self-Organization of Chiral Self-Complementary Cobalt(III) Complexes with Achiral Tripod-Type Ligands Containing Three Imidazole Groups, J. Am. Chem. Soc. 124 (2002) 629–640.

[26] D. Sun, Z.H. Wei, C.F. Yang, D.F. Wang, N. Zhang, R.B. Huang, L.S. Zheng, pH-Dependent Ag(I) coordination architectures constructed from 4-cyanopyridine and phthalic acid: from discrete structure to 2D sheet†, CrystEngComm 13 (2011) 1591–1601.

[27] L. Pan, T. Frydel, M.B. Sander, X. Huang, J. Li, The Effect of pH on the Dimensionality of Coordination Polymers, Inorg. Chem. 40 (2001) 1271–1283.

[28] J.X. Yang, X. Zhang, J.K. Cheng, J. Zhang, Y.G. Yao, pH Influence on the Structural Variations of 4, 4′-Oxydiphthalate Coordination Polymers, Cryst. Growth Des. 12 (2012) 333–345.

[29] E. Norkus, I. Stalnionienė, D.C. Crans, Interaction of pyridine- and 4-hydroxypyridine-2, 6-dicarboxylic acids with heavy metal ions in aqueous solutions, Heteroat. Chem. 14 (2003) 625–632.

[30] H.L. Gao, L. Yi, B. Zhao, X.Q. Zhao, P. Cheng, D.Z. Liao, S.P. Yan, Synthesis and Characterization of Metal−Organic Frameworks Based on 4-Hydroxypyridine-2, 6-dicarboxylic Acid and Pyridine-2, 6-dicarboxylic Acid Ligands, Inorg. Chem. 45 (2006) 5980–5988.

[31] B. Zhao, L. Yi, Y. Dai, X. Y. Chen, P. Cheng, D. Z. Liao, S. P. Yan, Z. H. Jiang, Systematic Investigation of the Hydrothermal Syntheses of Pr(III)−PDA (PDA= Pyridine-2, 6-dicarboxylate Anion) Metal−Organic Frameworks, Inorg. Chem. 44 (2005) 911–920.

[32] M.S. Liu, Q.Y. Yu, Y.P. Cai, C.Y. Su, X.M. Lin, X.X. Zhou, J.W. Cai, One-, Two-, and Three-Dimensional Lanthanide Complexes Constructed from Pyridine-2, 6-dicarboxylic Acid and Oxalic Acid Ligands, Cryst. Growth Des. 8 (2008) 4083–4091.

[33] Bruker, SAINT, Version 6.36a, Bruker AXS Inc., Madison, Wisconsin, USA, 2002.

[34] Bruker, SMART, Version 5.625 and SADABS, Version 2.03a, Bruker AXS Inc., Madison, Wisconsin, USA, 2001.

[35] G.M. Sheldrick, A short history of *SHELX*, Acta Cryst. A 64 (2008) 112–122.

[36] G.M. Sheldrick, Crystal structure refinement with *SHELXL*, Acta Cryst. C 71 (2015) 3–8.

[37] L.J. Farrugia, *WinGX* and *ORTEP* for Windows: an update, J. Appl. Cryst. 45 (2012) 849−854.

[38] A.L. Spek, Single-crystal structure validation with the program PLATON, J. Appl. Crystallogr. 36 (2003) 7–13.

[39] M.J. Frisch, G.W. Trucks, H.B. Schlegel, G.E. Scuseria, M.A. Robb, J.R. Cheeseman, G. Scalmani, V. Barone, G.A. Petersson, H. Nakatsuji, et al. Gaussian 09, Revision C.01; Gaussian, Inc.: Wallingford, CT, USA, 2009.

[40] R.F.W. Bader, A Quantum Theory of Molecular Structure and Its Applications, Chem. Rev. 91 (1991) 893–928.

[41] T.A. Keith, AIMAll, Version 13.05.06; TK Gristmill Software: Overland Park, KS, USA, 2013.

[42] R.F.W. Bader, Atoms in Molecules, a Quantum Theory; Oxford University Press: New York, NY, USA, 1990.

[43] J. Contreras-García, E.R. Johnson, S. Keinan, R. Chaudret, J.P. Piquemal, D.N. Beratan, W. Yang, NCIPLOT: A Program for Plotting Noncovalent Interaction Regions, J. Chem. Theory Comput. 7 (2011) 625–632.

[44] E.R. Johnson, S. Keinan, P. Mori-Sanchez, J. Contreras-Garcia, A.J. Cohen, W. Yang, Revealing Noncovalent Interactions, J. Am. Chem. Soc. 132 (2010) 6498–6506.

[45] A. Das, S. R. Choudhury, B. Dey, S. K. Yalamanchili, M. Helliwell, P. Gamez, A. Frontera, Supramolecular Assembly of Mg(II) Complexes Directed by Associative Lone Pair−π/π− π/π−Anion−π/π−Lone Pair Interactions, J. Phys. Chem. B 114 (2010) 4998–5009.

[46] R. K. Mudsainiyan, A. K. Jassal, N. Islam, Self-assembled H-bonded supramolecular interactions in monomeric complex $[Mg(H_2O)_6].L_2.2bipy.H_2O$;[LH = 2-amino-5-nitrobenzoic acid, bipy = 4,4′-bipyridine]: Joint theoretical calculations and Hirshfeld surface analysis, J. Mol. Struct. 1232 (2021) 130073.

[47] C. Gatti, Chemical Bonding in Crystals: New Directions. Zeitschrift für Krist. - Cryst. Mater. 220 (2005) 399–457

CHAPTER 3

Exploring Solid-State Supramolecular Architectures of Penta(carboxymethyl)diethylenetriamine: Experimental Observation and Theoretical Studies

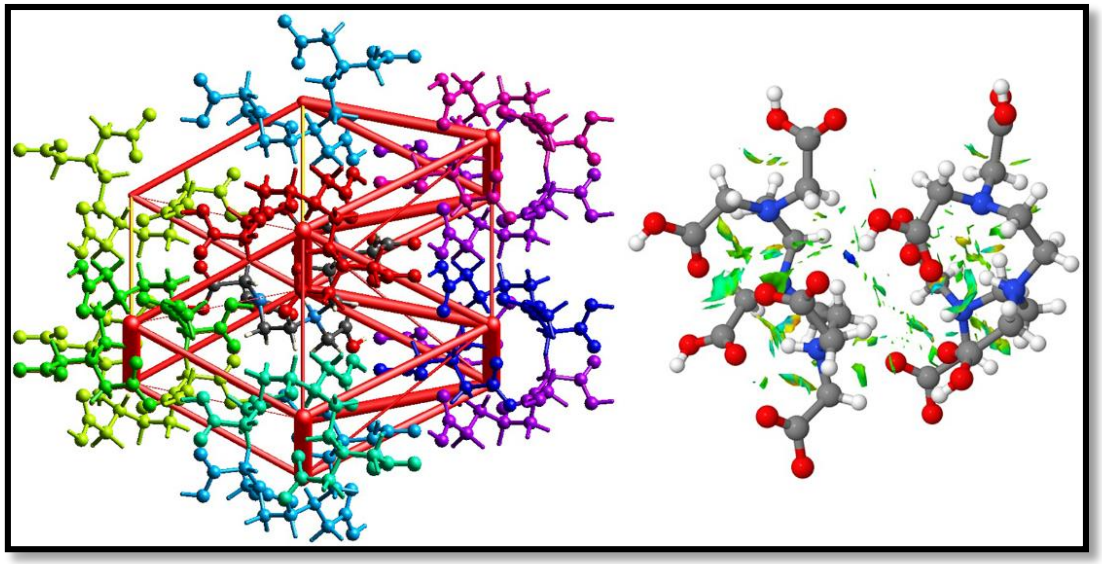

Published in: ***ChemistrySelect*** **7 (2022) e202203396**

3.1. Introduction

Diethylenetriaminepentaacetic acid (DTPA) [1, 2] is comprised of five carboxylate groups that are bound to three nitrogen atoms [3]. Due to the high reactivity of the carboxylic group [4], DTPA behaves as a bridging agent [5, 6]. So it has been recognized in the world of research as a polycarboxylic acid chelator [7]. The conjugate base of DTPA is potentially an octadentate ligand [3, 8]. DTPA forms eight bonds and wraps around a metallic ion [9]. Its complexes may also contain an additional water molecule that coordinates the metal ion [10]. However, transition metals usually form less than eight coordination bonds [11]. DTPA can still bind to other reagents even after creating a metal complex. Given these comprehensive coordinating abilities, DTPA is approved for its use in medical imaging and decontaminating internally deposited radionuclides [12, 13], such as plutonium, curium, and americium [14].

In the past two decades, great attention has been paid to understanding nature and the roles of non-covalent interactions, for example, halogen bonding, π–π^+, π^+–π^+, anion···π, anion···π^+, lone-pair(l.p)···π, N–H···π, C–H···π(chelate), metal···π, salt bridge(SB)···(SB), C–H···(SB), (SB)···π^+, (l.p)···(SB), N–H···SB···lone pair, σ–hole interaction, π–hole interaction, etc. [15–25]. Non-covalent interactions significantly determine the structure and macroscopic properties that would further help fabricate materials with desired parameters. The non-covalent interactions such as Hydrogen bonding, π···π, C–H···π, cation···π, anion···π, and lone-pair···π are mainly responsible for the generation and stabilization of supramolecular structures [18–21, 26–29]. These interactions are omnipresent in macromolecular compounds like proteins [30, 31] polysaccharides [32, 33] and are directly secondary to quaternary structures. Conventional hydrogen bonding (such as N–H···O and O–H···O) remains the most reliable and widely used in chemical, biological, and material science due to specific, highly directive, and relatively strong interactions [22]. The non-covalent interactions have emerged as a novel conception in the field of anion transport, anion-sensing and anion-recognition chemistry, trans-membrane anion transport, and catalysis [34–36].

We have structurally characterized compound (**1**) and analyzed non-covalent interactions that help govern self-assembly. Hirshfeld surface analysis and corresponding fingerprint plots have been presented to explore the nature of intermolecular interactions within the title crystal structure. The characteristics of the non-covalent interactions are theoretically studied using Bader's quantum theory of "atoms-in-molecules" (QTAIM), and we have also performed topological analysis of QTAIM [37–46] to characterize the bond critical points and

calculated the dissociation energy of the interactions. Further, we have studied "Non-covalent Interaction" (NCI) plot index.

3.2. Experimental Sections

3.2.1. Crystallization

The reagents were purchased from a commercial source and used without further purification. Diethylenetriaminepentaacetic acid (Aldrich, St. Louis, Missouri, United States) was used as received. Double distilled and then freshly boiled water was used throughout. Diethylenetriaminepentaacetic acid (2.0 mmol, 0.786 g) was taken into a 100 mL flask and dissolved in water/methanol in 2:1 molar ratio. Thus, the solution mixture was heated at 323 K for 1h and then kept for crystallization at room temperature (295 K). The resulting solution was kept undisturbed at ambient temperature and covered with paraffin film. A few small holes were made using a needle to let the solvent evaporate slowly. After a few weeks, testable colorless crystals were filtrated, washed with water, and dried in the air. The CHN elemental analyses were performed on a PerkinElmer 2400 Series-II CHN analyzer, USA, elemental analyzer. A Perkin-Elmer LX-1 FT-IR spectrophotometer was used to record the infrared spectrum with a modern diamond attenuated total reflectance (ATR) accessory method in the range 4000–400 cm^{-1}. Anal. Calcd. for $C_{14}H_{23}N_3O_{10}$ (MW = 393.35 for **1**): C, 42.75; H, 5.89; N, 10.68%. Found: C, 42.73; H, 5.91; N, 10.65%. Main IR absorption bands observed for **1** (in cm^{-1}) are 3205 (w), 3061 (s), 3011 (s), 2910 (w), 1732 (s), 1685 (s), 1631 (vs), 1545 (s), 1441 (s), 1395 (s), 1044 (s), 773 (vs) (Figure 3.1).

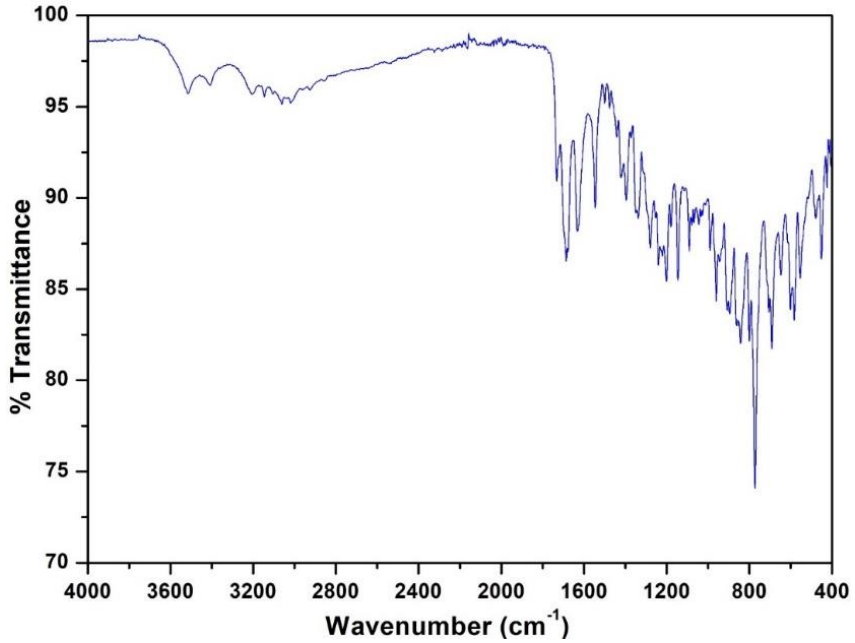

Figure 3.1. The IR spectrum of (**1**).

3.2.2. X-ray Crystal Structure Determination

Single crystal X-ray data of compound (**1**) was collected at 120(2)K on the Bruker SMART APEX-II single-crystal X-ray CCD diffractometer having graphite monochromator (Mo–Kα, λ = 0.71073 Å) radiation. Data reduction was executed using the program Brukar SAINT [47]. An empirical absorption correction was performed using the SADABS program based on the multi-scan method [48]. The structure of the title compound was solved by the direct method and refined by the full-matrix least-square technique on F^2 using the programs (SHELXS-14) [49] and (SHELXL-18) [50], respectively. All the non-H atoms were refined anisotropically, whereas the H atoms were placed at geometrically idealized positions. The structure was solved using the WinGX system V2014.1 [51] and geometrically analyzed by PLATON [52]. A summarized list of crystal data and relevant refinement parameters of compound (**1**) are given in Table 3.1.

Table 3.1. Crystal data and structure refinement parameters for compound (**1**).

Empirical formula	$C_{14}H_{23}N_3O_{10}$
Formula weight	393.35
Temperature	120(2) K
Wavelength (Mo Kα)	0.71073 Å
Crystal system, space group	Monoclinic, $P2_1/c$
Unit cell parameters	a = 17.8462(14)Å
	b = 8.9381(7)Å
	c = 10.7308(9)Å
	α = 90°
	β = 105.238(2)°
	γ = 90°
Volume	1651.5(2)$Å^3$
Crystal size	0.15× 0.09× 0.05 mm
Z / Density (clac.)	**4** / 1.582 Mg/m^3
Absorption coefficient	0.135 mm^{-1}
F(000)	832
θ-range for data collection	2.567– 24.994°
Limiting indices	$–21 \leq h \leq 21$; $–10 \leq k \leq 10$; $–12 \leq l \leq 12$
Reflections collected/unique	14999/2864 [R(int) =0.0284]
Completeness to theta	98.1 %

Absorption correction	Semi-empirical from equivalents
Max. and min. transmission	0.99 and 0.98
Refinement method	full-matrix least-squares on F^2
Data / restraints / parameters	2864 / 0 / 247
Goodness-of-fit on F^2	1.049
Final R indices [$I > 2\sigma(I)$]	$R_1 = 0.0303$, $wR_2 = 0.0714$
R indices (all data)	$R_1 = 0.0330$, $wR_2 = 0.0734$
Largest diff. peak and hole	0.241 and –0.218 e·Å^{-3}
CCDC number	2132357

$R_1 = \Sigma||F_o|-|F_c||/\Sigma|F_o|$, $wR_2 = [\Sigma\{(F_o^2-F_c^2)^2\}/\Sigma\{w(F_o^2)^2\}]^{1/2}$, $w = 1/\{\sigma^2(F_o^2) + (aP)^2 + bP\}$, where a = 0.0324 and b = 0.7774 and $P= (F_o^2 + 2F_c^2)/3$ for the title structure.

3.2.3. Hirshfeld Surface Analysis

The molecular Hirshfeld surface [53–55] of the title compound is generated based on the electron distribution of the molecules evaluated as the sum of spherical atom electron densities [56, 57]. For the given crystal structure and a set of spherical atomic electron densities, the Hirshfeld surface is unique [58]. The normalized contact distance (d_{norm}) is generated based on d_e, d_i, and the *vdW* radii of the atom. d_e is defined as the distance from the Hirshfeld surface to the closest nucleus external to the surface, whereas d_i is the distance from the Hirshfeld surface to the closest nucleus internal to the surface. The 2D fingerprint plot generated for the crystal structure (based on d_e and d_i) summarizes intermolecular contacts within the crystal [15, 59]. We have performed the "energy framework analysis" using the *CrystalExplorer17* program [60] to explore the intermolecular interaction topology. The individual energy components of the energy framework are signified as cylinders, where the radius of the cylinders is proportional to the magnitude of the interaction energy. The energy components corresponding to electrostatic (E_{ele}), dispersion (E_{dis}), and total energy (E_{tot}) are depicted in red, green, and blue color codes, respectively.

3.2.4. Theoretical Methods

The non-covalent interactions and the wave function analysis were calculated using the *Gaussian16* calculation package [61] at the B3LYP level with a basis set 6-311++G(d,p). The crystallographic coordinates have been used in the theoretical calculations. We have used Bader's quantum theory of "Atoms in molecules" (QTAIM) [62] to analyze the weak non-covalent interactions that have been computed at the same level of theory using the AIMall calculation package [63]. Topological analysis of the Laplacian of electron charge density

provides a powerful tool for investigating the electronic and conformational properties of the molecules and hence allows for much better insights into the interatomic interactions [64]. The topological properties of the charge density ($\rho(r)$) are characterized by their critical points (CPs), and its Laplacian which is expressed in terms of $L(r) = -\nabla^2(\rho(r))$ and is calculated using the Atoms In Molecules (AIM) theory [65]. It has been noted that electron density is depleted where $\nabla^2(\rho(r)) > 0$, and it is concentrated where $\nabla^2(\rho(r)) < 0$. Selected topological parameters such as electron density, $\rho(r)$, Laplacian of the electron density, $\nabla^2\rho(r)$, potential electronic energy density $V(r)$, kinetic electronic energy density, $G(r)$, and total electronic energy density ($H(r) = V(r) + G(r)$) were used at their bond critical points (BCPs) to characterize the nature and strength of intermolecular interactions.

The theoretical non-covalent interactions (NCI) plot index [66] is used to assess the nature of interactions as attractive or repulsive and reveal them in real space. This is the method for plotting non-covalent interaction regions based on the NCI visualization index derived from the electron density. The density cubes needed to generate the NCIplot surfaces have been computed at the same level of theory using the Gaussian program. Instead of critical points, the non-covalent interactions are represented by isosurfaces that illustrate both favorable and unfavorable interactions and are differentiated by the sign of the second-density Hessian eigenvalue and defined by isosurface color scheme with a red-yellow-green-blue scale. The blue and red surfaces represent ρ^-cut (attractive) and ρ^+cut (repulsive) interactions [67], respectively. However, the green and yellow colors represent weak attractive, and repulsive interactions [68].

3.3. Results and Discussion

3.3.1. Structural Description

The title compound DTPA is a polycarboxylic amino acid comprised of diethylene triamine as the backbone consisting of five carboxylic acid groups. The title compound crystallized in monoclinic space group $P2_1/c$ (Table 3.1). The solid-state structure at 120 K with the highest precision [69] with an R-value of 0.03 has been reported herein. The molecular ORTEP [51] view of compound (**1**) is appended in Figure 3.2 with the atom numbering scheme. Extended supramolecular networks of compound (**1**) are stabilized through O–H···O and C–H···O interactions (Table 3.2).

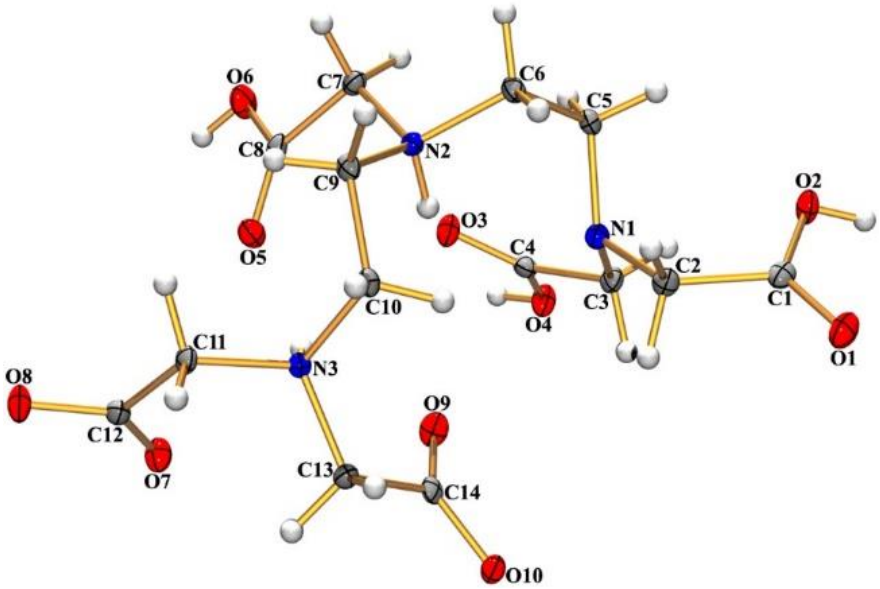

Figure 3.2. ORTEP view with atom numbering scheme of compound (**1**) with displacement ellipsoids at the 30% probability level.

In the first substructure, carboxylate oxygen atom O(2) interacts with another carboxylate oxygen atom O(10) of the molecules at (–x, –1/2+y, 3/2–z), whereas another oxygen atom O(6) of the molecule at (x, y, z) acts as a donor to the carboxylate oxygen O(8) of the molecule at (1–x, –1/2+y, 3/2–z). These two O–H···O interactions lead the molecules to generate a self-assembled structure in the (110) plane (see Figure 3.3). Again O(4) atom of the molecule at (x, y, z) interacts with carboxylate oxygen O(10) of the molecules at (x, 3/2–y, –1/2+z). All these three O–H···O interactions are responsible for the formation of another supramolecular network in the (101) plane (see Figure 3.4).

Table 3.2. Relevant hydrogen bonding parameters (Å, °).

D–H···A	**D–H**	**H···A**	**D···A**	**D–H···A**	**Symmetry**
O2–H2···O10	0.82	1.83	2.6381(13)	167	–x, –1/2+y, 3/2–z
O4–H4···O10	0.82	1.88	2.6668(13)	159	x, 3/2–y, –1/2+z
O6–H6···O8	0.82	1.66	2.4457(13)	159	1–x, –1/2+y, 3/2-z
C2–H2A···O4	0.97	2.57	3.3604(16)	138	x, 3/2–y, 1/2+z
C3–H3B···O1	0.97	2.57	3.1777(16)	121	–x, –1/2+y, 3/2–z
C3–H3B···O4	0.97	2.57	3.3876(16)	142	–x, 1–y, 1–z
C5–H5A···O1	0.97	2.58	3.3356(16)	134	–x, –1/2+y, 3/2–z
C5–H5B···O1	0.97	2.44	3.2726(16)	143	–x, 1–y, 2–z
C7–H7A···O10	0.97	2.54	3.4092(15)	149	x, –1+y, z

C7–H7B···O8	0.97	2.30	3.2243(16)	159	1–x, 1–y, 2–z
C10–H10B···O7	0.97	2.36	3.0291(15)	126	x, 3/2–y, 1/2+z
C10–H10B···O9	0.97	2.55	3.0108(15)	109	x, 3/2–y, 1/2+z
C11–H11B···O8	0.97	2.58	3.3400(16)	135	1–x, 2–y, 2–z

In another substructure, C(3) acts as a donor to the carboxylate oxygen O(4) of the molecules at (–x, 1–y, 1–z). This C3–H3B···O4 interaction and its centrosymmetric analog generate an $R_2^2(8)$ dimeric ring (P) centered at (0, 1/2, 1/2) (Figure 3.5). Another carbon atom C(5), interacts with O(1) of the molecule at (–x, 1–y, 2–z), and a centrosymmetric dimeric $R_2^2(12)$ ring (Q) centered at (0, 1/2, 1) is formed (Figure 3.5). Again another centrosymmetric dimeric ring $R_2^2(16)$ (R) centered at (1/2, 1/2, 1) is created when C(7) is involved in the interaction with O(8) of the molecule at (1–x, 1–y, 2–z) (Figure 3.5). Thus, these three centrosymmetric dimeric rings (P, Q, R) are alternately linked to generating a supramolecular compound network (**1**) in the (101) plane (Figure 3.5). Further, the carbon atoms C(7) and C(10) act as donors to the carboxyl oxygen atoms O(10) and O(7) at (x, –1+y, z) and (x, 3/2–y, 1/2+z) respectively. The combination of two C–H···O interactions leads to the generation of another supramolecular architecture in the (011) plane (Figure 3.6).

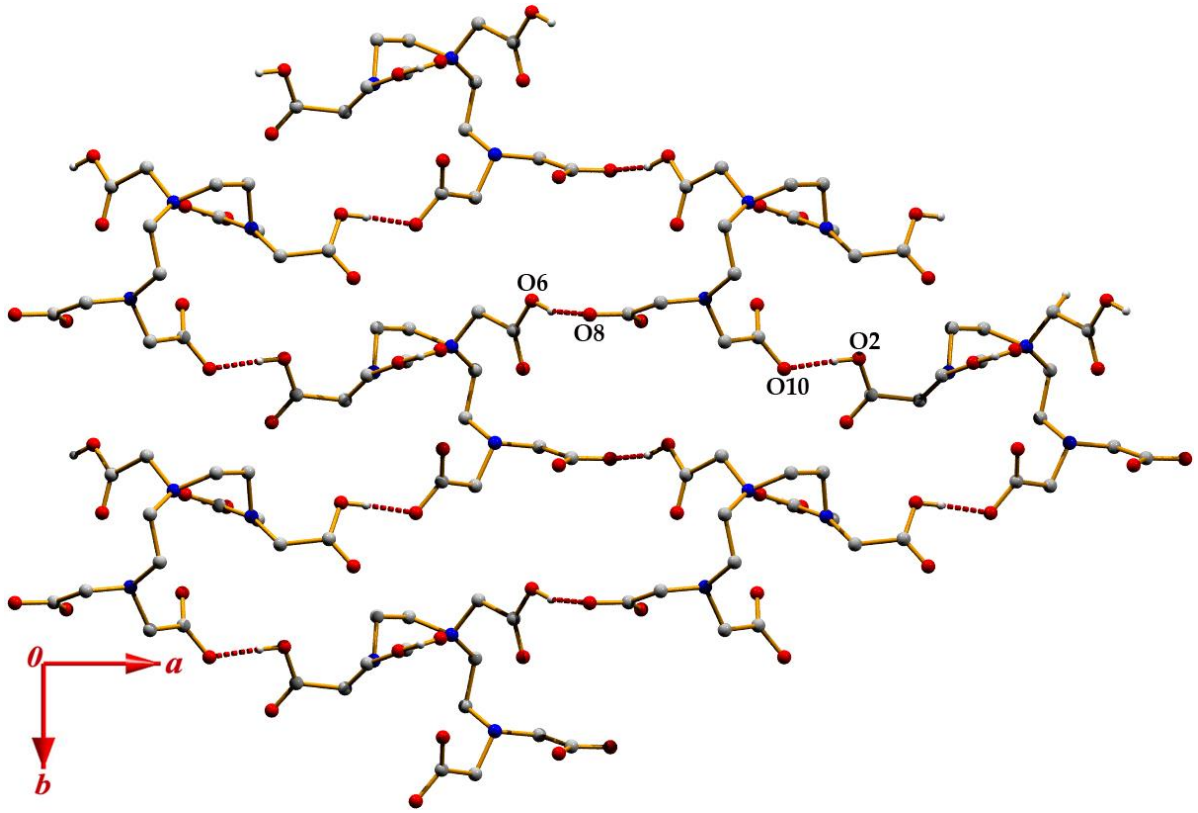

Figure 3.3. Supramolecular networks are generated through O–H···O bonds in the (110) plane.

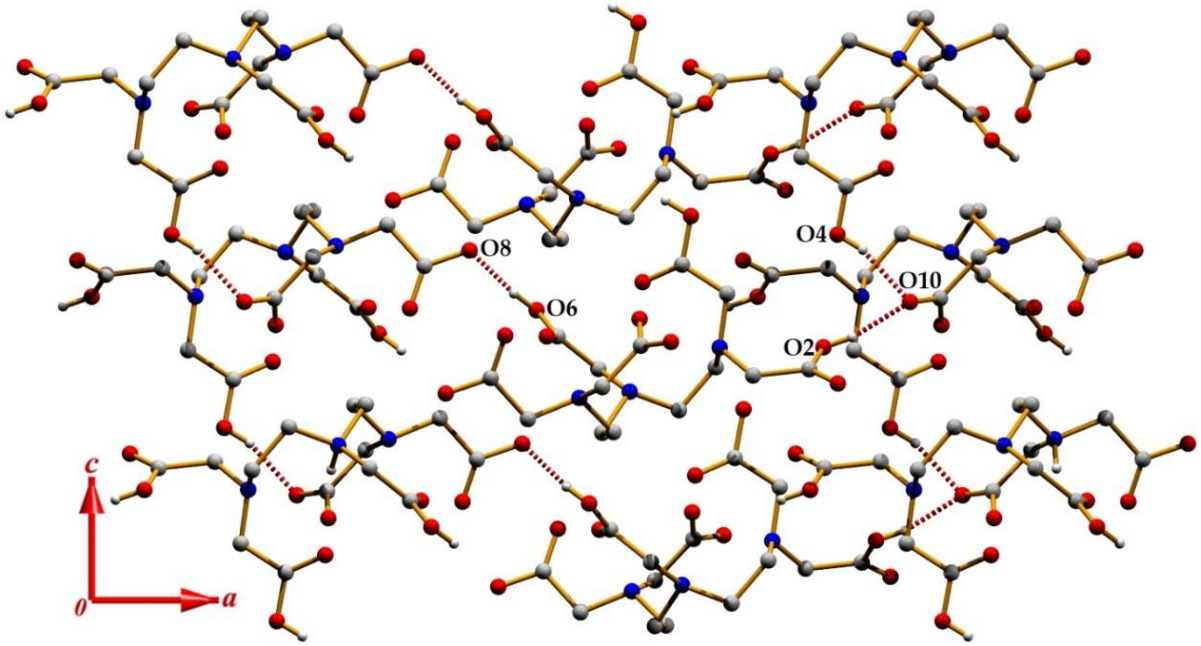

Figure 3.4. Supramolecular networks generated through O–H···O bonds in the (101) plane.

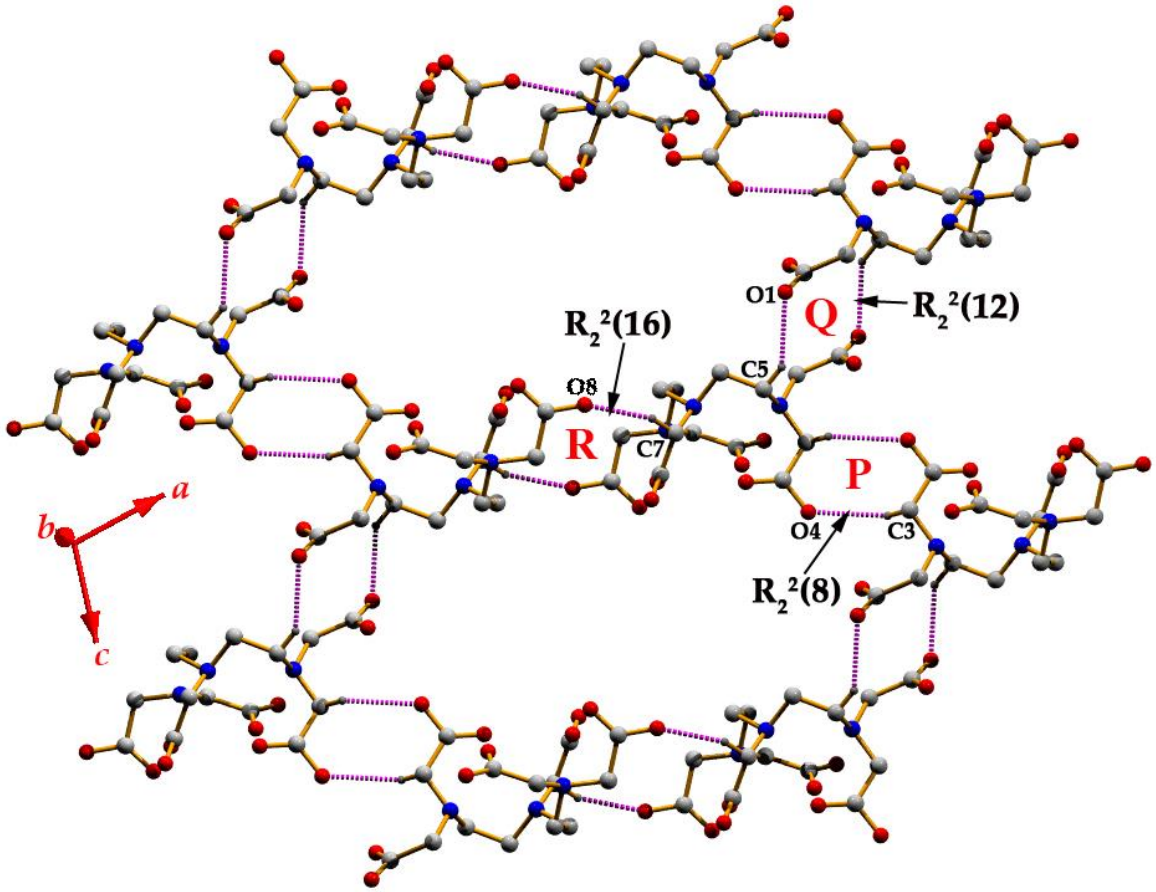

Figure 3.5. Three different centrosymmetric dimeric rings lead to forming a 2D supramolecular network.

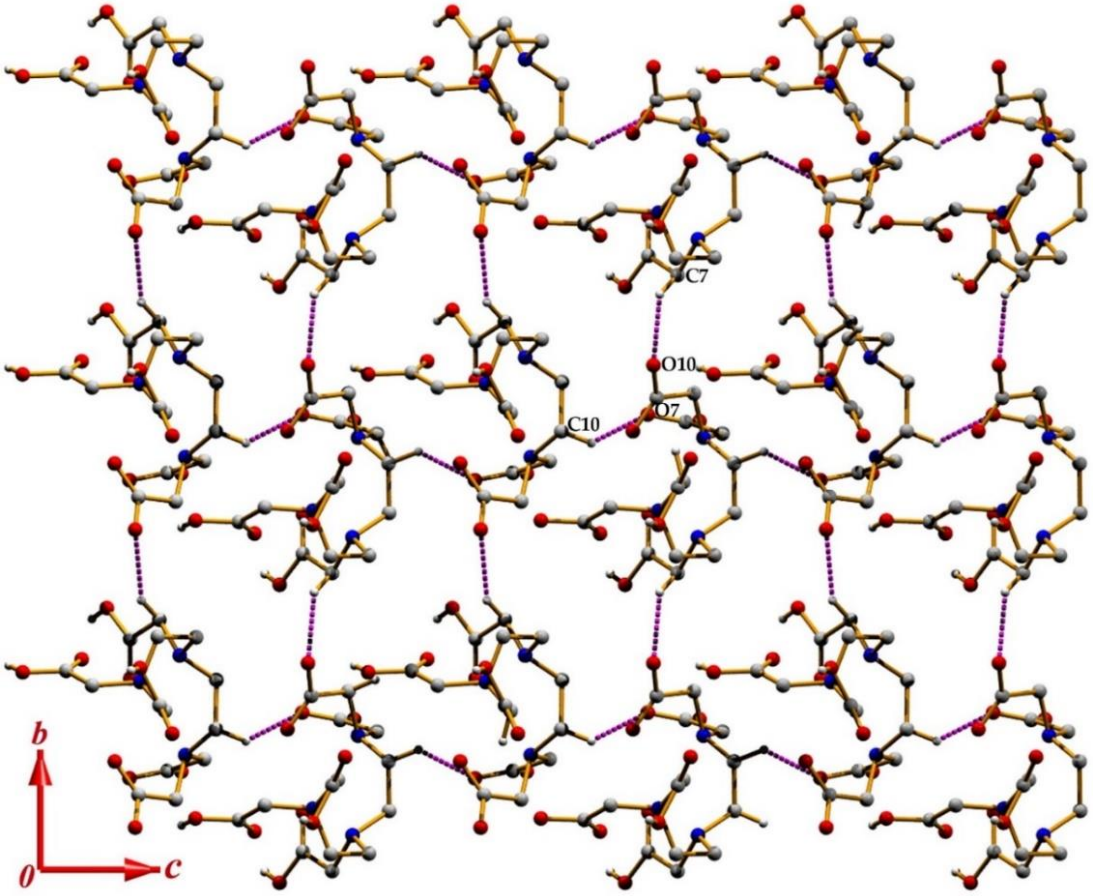

Figure 3.6. C–H···O bonds lead to a 2D supramolecular network for compound (**1**).

3.3.2. Hirshfeld Surface

The Hirshfeld surface was calculated to evaluate the contribution of intermolecular interactions that are involved within the structure. The calculated d_{norm} and fragment patch surfaces are illustrated in Figure 3.7 that have been mapped in the range of (–0.855Å to 1.452Å) and (0.0Å to 13.00Å), respectively. The d_{norm} surface reveals all interactions among donors, acceptors, and other close contacts. The large circular depressions in the d_{norm} surface designate the strong O–H···O hydrogen bonds (Figure 3.7a). The visual illustration of the fragment patches (Figure 3.7b) signifies the identification of their closeness to adjacent molecules. The dominant O···H/H···O interactions appear in the fingerprint plot as two distinct spikes (Figure 3.8) in the region of (d_i = 0.936Å; d_e = 0.570Å). The O···H/H···O interactions comprise 66.9% of the total Hirshfeld surface area of the compound (**1**). The C···H/H···C contacts in the region of (d_i = 1.718 Å; d_e = 1.147 Å) contributed 3.1% of the total Hirshfeld surface area (See Figure 3.8). Other close contacts C···O/O···C, C···C, and O···O are evident in the fingerprint plot in region of (d_i = 1.633 Å; d_e = 1.392 Å), d_i = d_e = 1.683 Å and d_i = d_e = 1.513 Å respectively. Moreover, a significant contribution (27.7%) comes from H···H contact, reproduced in the

scattered points of the fingerprint plot in the region of d_i=d_e=1.162 Å. This analysis quantifies all the interactions in the structure in a novel visual manner.

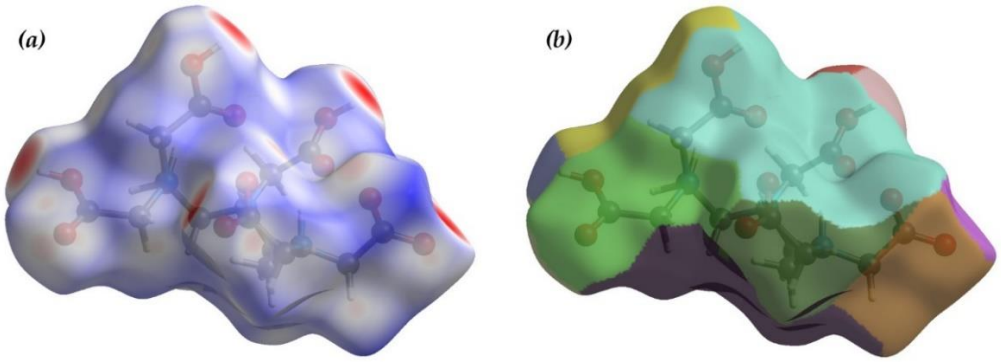

Figure 3.7. Hirshfeld surfaces mapped with d_{norm} (a) and fragment patches (b) for compound (**1**).

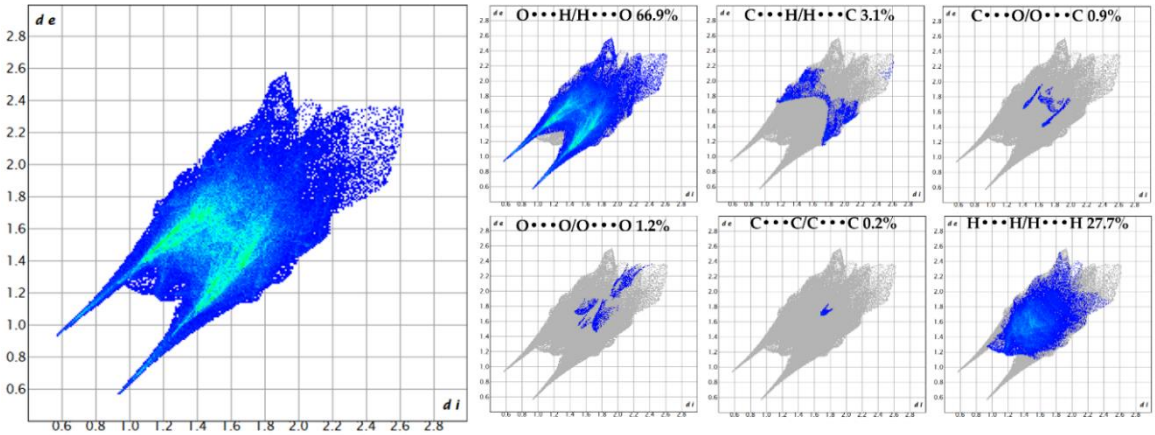

Figure 3.8. Fingerprint plots (Full) and decomposed plots.

We have calculated the energy frameworks regarding interaction energies (Figure 3.9), where the structure cluster is mapped within 3.8Å. Figure 3.9 also illustrates the energy components (E_{ele}, E_{pol}, $E_{dis,}$ and E_{rep}) of the interaction energies and the sum of the energy components (E_{tot}) relative to the reference molecule. Other parameters related to lattice energy calculations have been included in Figure 3.9. The topology of the energy distribution was analyzed using energy frameworks. In this calculation, the cylindrical radii are proportional to the relative strength of the corresponding energies. They are adjusted to the scale factors of K_{ele}= 1.057, K_{pol} = 0.740, K_{dis} = 0.871, K_{rep} = 0.618 [70] with a cut-off value of 5 kJ/mol within 3 ×3 ×3 unit cells (Figure 3.10). The energy framework calculation discloses the different energy modules as follows, i.e., electrostatic energy (E_{ele}) –586.8 kJ/mol, polarization energy (E_{pol}) –292.1 kJ/mol, dispersion energy (E_{dis}) –251.2 kJ/mol, repulsion energy (E_{rep}) 464.9 kJ/mol and total energy (E_{tot}) –767.9 kJ/mol. Among the individual energy components generated, the electrostatic force accredited to the hydrogen bonds dominates the dispersion

forces, which are clearly revealed by the relatively large size of the red cylinders in the energy framework diagrams compared to the green-colored cylinders (see Figure 3.10). The energy framework calculation thus provides their overall self-association in the supramolecular network.

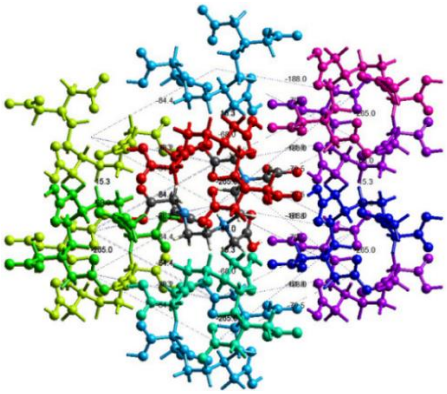

	N	Symop	R	E_ele	E_pol	E_dis	E_rep	E_tot
	2	x, -y+1/2, z+1/2	5.84	-205.1	-81.3	-70.5	118.8	-265.0
	1	-x, -y, -z	9.83	3.1	-7.4	-21.7	20.7	-8.3
	2	-x, y+1/2, -z+1/2	9.40	-80.8	-38.1	-30.3	89.9	-84.4
	1	-x, -y, -z	10.34	-10.9	-11.5	-30.8	30.3	-28.2
	2	x, -y+1/2, z+1/2	8.52	35.1	-11.6	-23.4	11.5	15.3
	2	x, y, z	8.94	-43.6	-18.4	-20.6	15.6	-68.0
	1	-x, -y, -z	9.29	-145.8	-44.5	-23.0	30.8	-188.0
	2	-x, y+1/2, -z+1/2	10.86	-106.1	-48.9	-9.4	124.7	-79.5
	1	-x, -y, -z	11.30	-32.7	-30.4	-21.5	22.6	-61.8

Figure 3.9. The color-coded interaction mapping (left) and the parameters for lattice energy calculations (right) for compound (**1**).

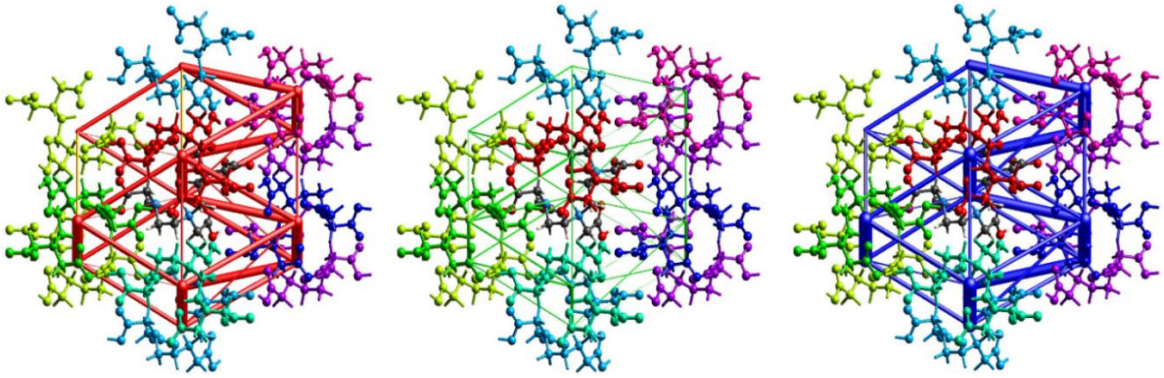

Figure 3.10. Energy framework of the titled compound, the electrostatic potential force (left column), dispersion force (middle column), and total energy (right column) diagrams.

3.3.3. Theoretical Calculations

We have performed DFT/B3LYP/6311++G(d, p) level of theoretical calculations to analyze and characterize the hydrogen bonding contacts. First, Bader's theory of "atoms-in-molecules" (AIM) has been performed, where the crystallographic coordinates and the molecular fragments are used from the X-ray packing diagrams. According to this calculation, the existence of a bond critical point (BCP) and the bond path connecting two atoms designate the interaction between two atoms [55]. Each and every BCP includes well-to-do chemical information that indicates the nature of the chemical bond. To characterize a chemical bond at BCP, parameters like electron density (ρ_{BCP}), Laplacian of electron density ($\nabla^2\rho_{BCP}$), kinetic energy density (G_{BCP}), potential energy density (V_{BCP}), and total energy density ($H_{BCP} = V_{BCP} + G_{BCP}$) are usually used. The dissociation energy of the interaction ($D.E_{int}$) can be estimated

from the equation $D.E_{int} = -\frac{1}{2} V_{BCP}$, more precisely $D.E_{int}$ (kcal mol^{-1}) = − 313.754 × V_{BCP} (au) [71]. Detailed AIM parameters at the BCPs are listed in Table 3.3 for selected intermolecular interactions. The electron localization function (ELF) measures the excess as shown in Figure 3.11; the small green spheres represent the bond critical points (BCP), the small violet spheres represent the ring critical point (RCP), and the dashed lines represent the bond path connecting the atoms. The bond path connecting O–H and O atoms in the first and second models (see Figures 3.11 a, b) represents O–H···O interactions in (**1**). The ρ(r) values of O(2)–H(2)···O(10) and O(4)–H(4)···O(10) are 0.0326 a.u. and 0.0286 a.u. respectively, it may be noted that the O(2)–H(2)···O(10) bonding contact is more favorable compared to the O(4)–H(4)···O(10) bond due to large ρ(r) value, which is in agreement with X-ray structural findings (see Table 3.2). In another model (Figure 3.11 c), the weak C(7)–H(7A)···O(10) bond is characterized by the bond path, and the corresponding ρ(r) value is 0.0087 a.u. Further in the dimeric ring model (Figure 3.11 d), the ρ(r) values of C(3)–H(3B)···O(4), C(5)–H(5B)···O(1), and C(7)–H(7B)···O(8) are 0.0075 a.u., 0.0094 a.u., and 0.0122 a.u. respectively. All these interactions have a positive value of $\nabla^2\rho_{BCP,}$ which indicates closed-shell interactions [72, 73]. These closed-shell interactions dominate $G_{BCP,}$ which is slightly greater than $|V_{BCP}|$ resulting in a positive value of H_{BCP} but close to zero, and the ratio $\frac{|V_{BCP}|}{G_{BCP}}$ is less than unity [73]. It can be noted that the strength of O–H···O contacts is greater than that of C–H···O contacts (Table 3.3). Therefore, the inspection of the AIM calculation indicates that the $\rho(r)$ values, $D.E_{int}$, and corresponding bond CPs agree with the experimental findings.

Table 3.3. Detailed AIM parameters at the BCPs.

Intermolecular Interaction	$\boldsymbol{\rho_{BCP}}$ $(\mathbf{e}.\text{Å}^{-3})$	$\boldsymbol{\nabla^2\rho_{BCP}}$ $(\mathbf{e}.\text{Å}^{-5})$	$\mathbf{V_{BCP}}$ $(\mathbf{a.u})$	$\mathbf{G_{BCP}}$ $(\mathbf{a.u})$	$\mathbf{H_{BCP}}$ $(\mathbf{a.u})$	$\left\lvert\frac{-V_{BCP}}{G_{BCP}}\right\rvert$	**D.E$_{int}$ (kcal. mol^{-1})**
O2–H2···O10 (a)	0.0326	0.1284	–0.0295	0.0308	0.0013	0.9578	9.256
O4–H4···O10 (b)	0.0286	0.1128	–0.0242	0.0262	0.0020	0.9236	7.593
C7–H7A···O10 (c)	0.0087	0.0264	–0.0047	0.0057	0.0010	0.8245	1.475
C3–H3B···O4 (d)	0.0075	0.0258	–0.0044	0.0054	0.0010	0.8148	1.380
C5–H5B···O1 (e)	0.0094	0.0328	–0.0056	0.0069	0.0013	0.8116	1.757
C7–H7B···O8 (f)	0.0122	0.0440	–0.0071	0.0091	0.0020	0.7809	2.227

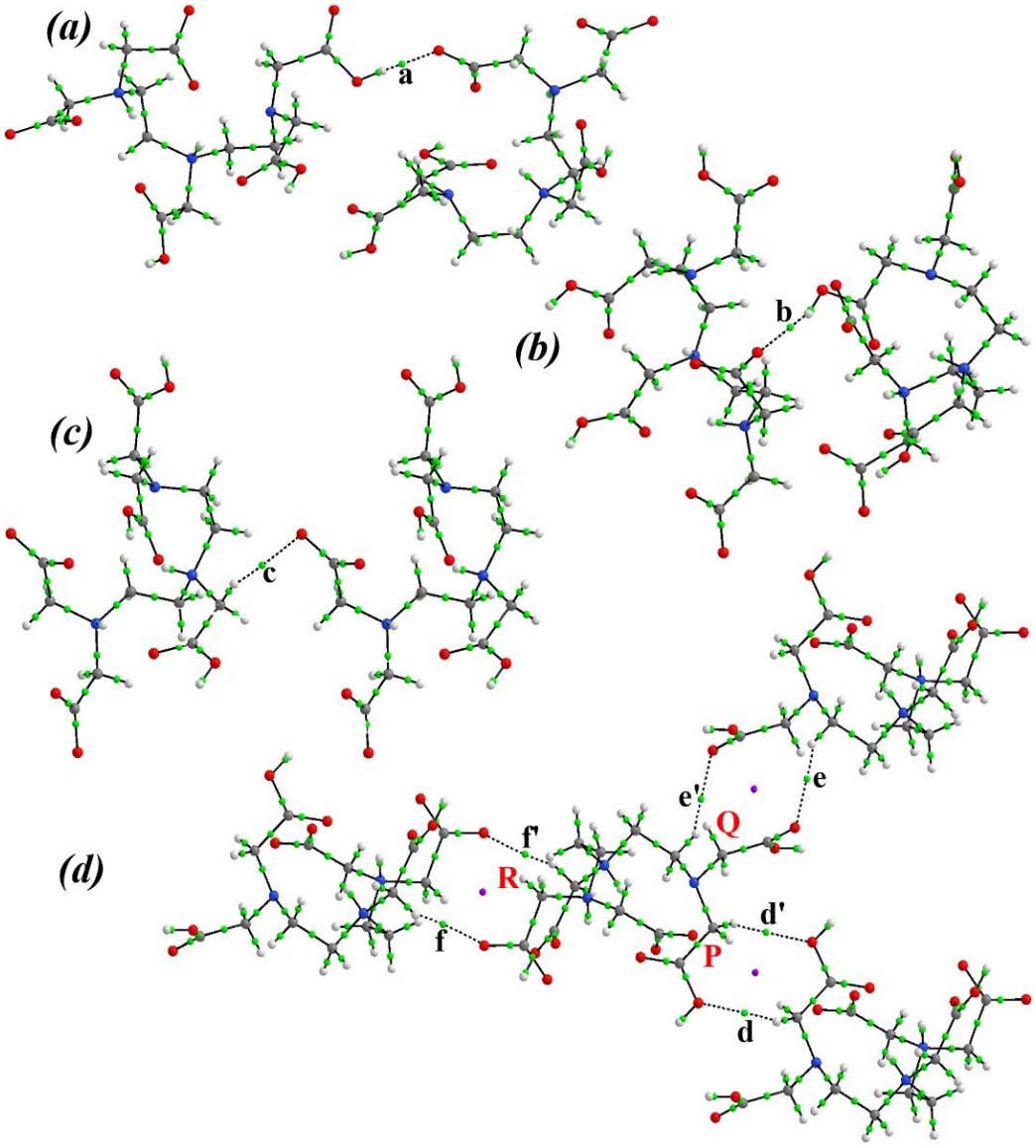

Figure 3.11. AIM analysis of the self-assembled dimers (*a–c*) and tetramer (*d*) retrieved from the X-ray structure of the titled compound. Green and violet spheres represent the bond and ring critical points, respectively. The bond path connecting the bond critical points are denoted by the dashed lines.

Again, we have used the 'non-covalent interaction' (NCI) plot computational tool to characterize the self-assembled structures generated through hydrogen bonding interaction (Figure 3.12 a–d). We have used the same structural models that are used in AIM calculation. The presence of blue isosurface in Figures 3.12 a, b indicates the existence of strong O–H···O bonds in between the carboxylate oxygen atoms. A critical analysis of the O–H···O bonds among the carboxylate groups can be identified and characterized by the dense blue-colored patches (see Figures 3.12 a, b). The theoretical NCI analysis of the O–H···O hydrogen bonds shows consistencies with the theoretical AIM analysis (see Table 3.3) and agrees well with the

experimental findings (see Table 3.2). The green isosurfaces that are evident in between the C–H donors and the carboxylate oxygen atoms represent the weak C–H···O bonding contact in (**1**) (see Figures 3.12 c, d). The C7–H7B···O8 bond has the lowest H···A value (Table 3.2) and highest ρ(r) value in AIM analysis (see Table 3.3) among four C–H···O bonds that are depicted in Figure 10. As expected, the C7–H7B···O8 displays a larger and dense green patch in comparison to the other three C–H···O bonds (Figures 3.12 c, d) which is again consistent with the AIM analysis and experimental evidence. All the isosurfaces presented here in the theoretical NCI calculation agree with the experimental findings.

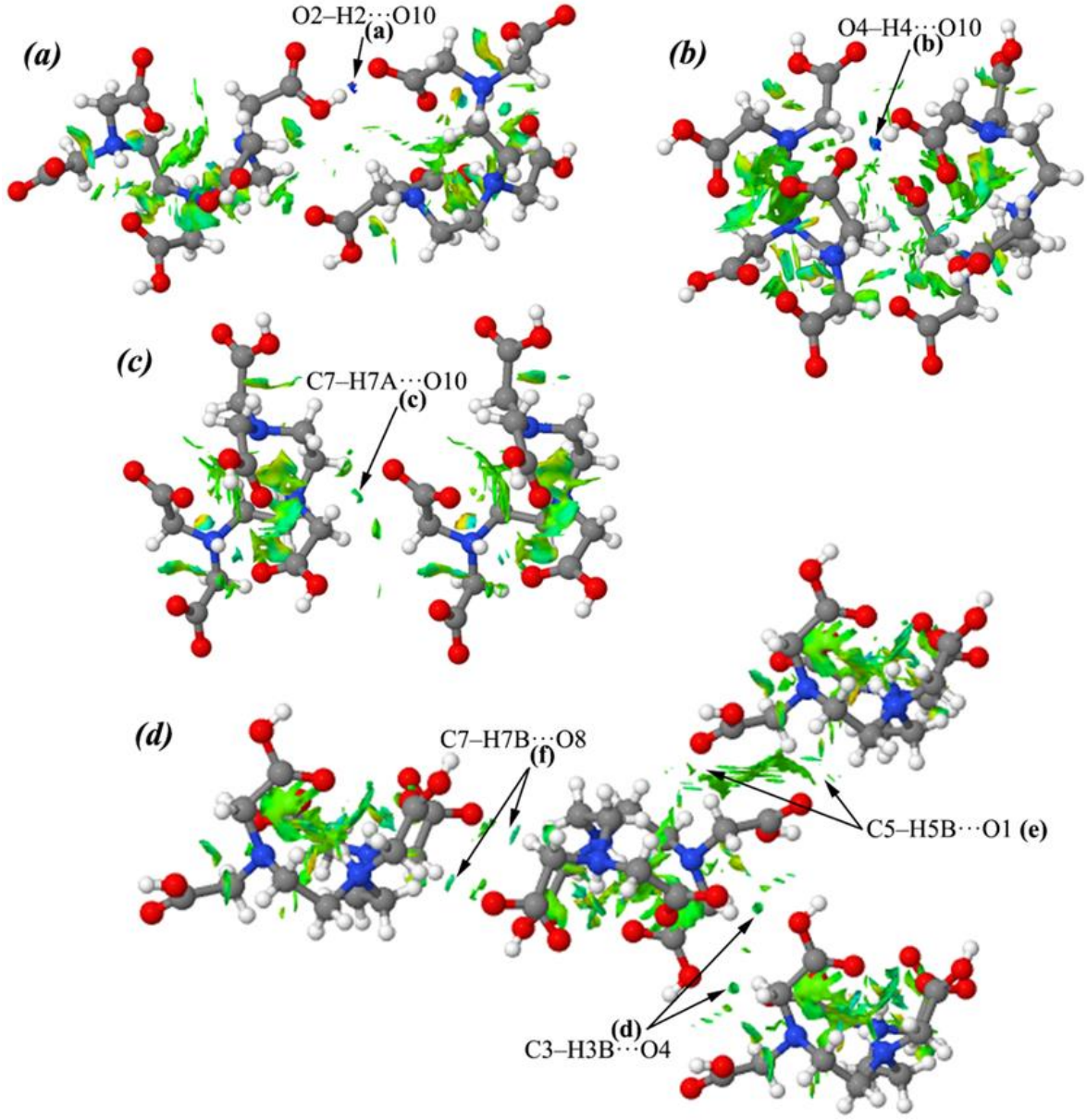

Fig. 3.12. NCI plot of the self-assembled structures of compound (**1**). A perspective view of the self-assembled dimers (*a–c*) and tetramer (*d*) has been illustrated. The gradient cut-off is s = 0.35 a.u., and the color scale is $-0.04 < \rho < 0.04$ a.u.

3.4. Conclusions

The supramolecular structure of the title compound has been scrutinized in detail. The cooperativity of the non-covalent interactions has been studied by exploring the supramolecular behavior in the solid-state. The molecular energy framework calculation revealed that the electrostatic force accredited to the hydrogen bonds dominates the dispersion forces. Bader's theory of 'atoms-in-molecules' (AIM) characterizes the non-covalent interactions and self-assemblies. QTAIM topological analysis revealed that all interactions are closed-shell interactions at their bond critical point. Furthermore, the theoretical NCI plot index also characterizes the self-assemblies and corresponding interactions. The theoretical investigations are in agreement with the experimental findings. The results reported herein might help understand the supramolecular aggregation in accordance with intermolecular hydrogen bonds and the quantification of non-covalent interactions. The detailed theoretical studies might be helpful to future research work relating to this ligand and its metal complexes.

3.5. References

[1] R.E. Sievers, J.C. Bailar Jr, Some Metal Chelates of Ethylenediaminetetraacetic Acid, Diethylenetriaminepentaacetic Acid, and Triethylenetetraminehexaacetic Acid, Inorg. Chem. 1 (1962) 174–182.

[2] R.A. Guilmette, J.E. Parks, A. Lindenbaum, Synthesis And Therapeutic Testing of Mono- and Dialkyl Esters of Pentetic (Diethylenetriaminepentaacetic) Acid for Decorporation of Polymeric Plutonium, J. Pharm. Sci. 68 (1979) 194–196.

[3] H.R. Maecke, A. Riesen, W. Ritter, The Molecular Structure of Indium-DTPA, J. Nucl. Med. 30 (1989) 1235–1239.

[4] N.C. Liu, Q.H. Xie, W.E. Baker, Comparison of the effectiveness of different basic functional groups for the reactive compatibilization of polymer blends, Polymer 34 (1993) 4680–4687.

[5] D.J. Hnatowich, W.W. Layne, R.L. Childs, The preparation and labeling of DTPA-coupled albumin, Int. J Appl. Radiat. Isot. 33 (1982) 327–332.

[6] M. Mahmoud, B.B. Geri, K. Abdelgawad, M.S. Kamal, I. Hussein, S. Elkatatny, R. Shawabkeh, Evaluation of the Reaction Kinetics of Diethylenetriaminepentaacetic Acid Chelating Agent and a Converter with Barium Sulfate (Barite) Using a Rotating Disk Apparatus, Energy Fuels 32 (2018) 9813–9821.

[7] X. Zhao, L. Song, Z. Zhang, R. Wang, J. Fu, Adsorption investigation of MA-DTPA chelating resin for Ni (II) and Cu (II) using experimental and DFT methods, J. Mol. Struct. 986 (2011) 68–74.

[8] P. Thakur, J.L. Conca, C.J. Dodge, A.J. Francis, G.R. Choppin, Complexation thermodynamics and structural studies of trivalent actinide and lanthanide complexes with DTPA, MS-325 and HMDTPA, Radiochim. Acta 101 (2013) 221–232.

[9] A.A.B. Moghal, S.A.S. Mohammed, A. Almajed, M.A. Al-Shamrani, Desorption of Heavy Metals from Lime-Stabilized Arid-Soils using Different Extractants, Int. J. Civ. Eng. 18 (2020) 449–461.

[10] A.T. Onawole, I.A. Hussein, A. Sultan, S. Abdel-Azeim, M. Mahmoud, M.A. Saad, Molecular and electronic structure elucidation of $Fe^{2+/}Fe^{3+}$ complexed chelators used in iron sulphide scale removal in oil and gas wells, Can. J. Chem. Eng. 97 (2019) 2021–2027.

[11] G.J., Kubas, Molecular Hydrogen Complexes: Coordination of a σ Bond to Transition Metals, Acc. Chem. Res. 21 (1988) 120–128.

[12] A.E. Gorden, J. Xu, K.N. Raymond, P. Durbin, Rational Design of Sequestering Agents for Plutonium and Other Actinides, Chem. Rev. 103 (2003) 4207–4282.

[13] V.K. Singh, P.L. Romaine, T.M. Seed, Medical Countermeasures for Radiation Exposure and Related Injuries: Characterization of Medicines, FDA-Approval Status and Inclusion into the Strategic National Stockpile, Health Phys. 108 (2015) 607.

[14] D. Poudel, L. Bertelli, J.A. Klumpp, T.L. Waters, Some Considerations for Chelation Treatment and Surgical Excision Following Incorporation of Plutonium in Wounds, Health Phys. 114 (2018) 307–318.

[15] S.K. Seth, Structural characterization and Hirshfeld surface analysis of a CoII complex with imidazo [1, 2-a] pyridine, Acta Crystallogr. E: Crystallogr. Commun. 74 (2018) 600–606.

[16] A. Hossain, A. Dey, S.K. Seth, P.P. Ray, J. Ortega-Castro, A. Frontera, S. Mukhopadhyay, Anion-dependent structural variations and charge transport property analysis of 4′-(3-pyridyl)-4, 2′: 6′, 4″-terpyridinium salts, CrystEngComm 23 (2021) 3569–3581.

[17] A. Das, A.D. Jana, S.K. Seth, B. Dey, S.R. Choudhury, T. Kar, S. Mukhopadhyay, N.J. Singh, I.C. Hwang, K.S. Kim, Intriguing π^{+}–π Interaction in Crystal Packing, J. Phys. Chem. B 114 (2010) 4166–4170.

[18] S. Ghosh, S. Islam, S. Pramanik, S.K. Seth, Structural elucidation of phenoxybenzaldehyde derivatives from laboratory powder X-ray diffraction: A combined experimental and theoretical quantum mechanical study, J. Mol. Struct. 1268 (2022) 133697.

[19] S.K. Seth, I. Saha, C. Estarellas, A. Frontera, T. Kar, S. Mukhopadhyay, Supramolecular Self-Assembly of M-IDA Complexes Involving Lone-Pair···π Interactions: Crystal Structures, Hirshfeld Surface Analysis, and DFT Calculations [H_2IDA= iminodiacetic acid, M= Cu (II), Ni (II)], Cryst. Growth Des. 11 (2011) 3250–3265.

[20] T. Maity, H. Mandal, A. Bauzá, B.C. Samanta, A. Frontera, S.K. Seth, Quantifying conventional C–H···π (aryl) and unconventional C–H···π (chelate) interactions in dinuclear Cu(II) complexes: experimental observations, Hirshfeld surface and theoretical DFT study, New J. Chem. 42 (2018) 10202–10213.

[21] S.K. Seth, A. Bauzá, A. Frontera, Bipolar behaviour of salt-bridges: a combined theoretical and crystallographic study†, New J. Chem. 42 (2018) 12134–12142.

[22] S. Tripathi, S. Islam, S.K. Seth, A. Bauzá, A. Frontera, S. Mukhopadhyay, Supramolecular assemblies involving salt bridges: DFT and X-ray evidence of bipolarity†, CrystEngComm 22 (2020) 8171–8181.

[23] M. Mitra, P. Manna, A. Das, S.K. Seth, M. Helliwell, A. Bauzá, S.R. Choudhury, A. Frontera, S. Mukhopadhyay, On The Importance of Unprecedented Lone Pair–Salt Bridge Interactions in Cu (II)–Malonate–2-Amino-5-Chloropyridine–Perchlorate Ternary System, J. Phys. Chem. A 117 (2013) 5802–5811.

[24] S. K. Seth, A. Bauzá, A. Frontera, Quantitative Analysis of Weak Non-covalent σ-Hole and π-Hole Interactions, in Understanding Intermolecular Interactions in the Solid State: Approaches and Techniques, ed. D. Chopra, Royal Society of Chemistry, London, 2019.

[25] A. Bauzá, S.K. Seth, A. Frontera, Molecular electrostatic potential and "atoms-in-molecules" analyses of the interplay between π-hole and lone pair···π/X–H···π/metal···π interactions, J. Comput. Chem. 39 (2018) 458–463.

[26] S. Tripathi, A. Hossain, S.K. Seth, S. Mukhopadhyay, Supramolecular association and quantification of intermolecular interactions of 4′-functionalized 2, 2′: 6′, 2 ″-terpyridines: Experimental observation and theoretical studies, J. Mol. Struct. 1226 (2021) 129254.

[27] S.K. Seth, D. Sarkar, T. Kar, Use of π–π forces to steer the assembly of chromone derivatives into hydrogen bonded supramolecular layers: crystal structures and Hirshfeld surface analyses†, CrystEngComm 13 (2011) 4528–4535.

[28] S.K. Seth, P. Manna, N.J. Singh, M. Mitra, A.D. Jana, A. Das, S.R. Choudhury, T. Kar, S. Mukhopadhyay, K.S. Kim, Molecular architecture using novel types of non-covalent π-interactions involving aromatic neutrals, aromatic cations and π-anions†, CrystEngComm 15 (2013) 1285–1288.

[29] P. Manna, S.K. Seth, M. Mitra, S.R. Choudhury, A. Bauzá, A. Frontera, S. Mukhopadhyay, Experimental and Computational Study of Counterintuitive $ClO_4^-\cdots ClO_4^-$ Interactions and the Interplay between π^+–π and Anion$\cdots\pi^+$ Interactions, Cryst. Growth Des. 14 (2014) 5812–5821.

[30] L. Pauling, R.B. Corey, The Pleated Sheet, A New Layer Configuration of Polypeptide Chains, Proc. Natl. Acad. Sci. U.S.A. 37 (1951) 251–256.

[31] L. Pauling, R.B. Corey, H.R. Branson, The structure of proteins. Two hydrogen-bonded helical configurations of the polypeptide chain, Proc. Natl. Acad. Sci. U.S.A. 37 (1951) 205–211.

[32] B. Casu, M. Reggiani, G.G. Gallo, A. Vigevani, Hydrogen bonding and conformation of glucose and polyglucoses in dimethyl-sulphoxide solution*, Tetrahedron 22 (1966) 3061–3083.

[33] W. Banks, C.T. Greenwood, On hydrogen bonding in amylose, Biopolymers 11 (1972) 315–318.

[34] Y. Zhao, Y. Cotelle, N. Sakai, S. Matile, Unorthodox Interactions at Work, J. Am. Chem. Soc. 138 (2016) 4270–4277.

[35] C. Parthiban, K.P. Elango, Selective colorimetric sensing of fluoride ion via H-bonding in 80% aqueous solution by transition metal chelates, Sens. Actuators B 245 (2017) 321–333.

[36] M. Raynal, P. Ballester, A. Vidal-Ferran, P.W.N.M.V. Leeuwen, Supramolecular catalysis. Part 1: non-covalent interactions as a tool for building and modifying homogeneous catalysts, Chem. Soc. Rev. 43 (2014) 1660–1733.

[37] K.I. Kulish, A.S. Novikov, P.M. Tolstoy, D.S. Bolotin, N.A. Bokach, A.A. Zolotarev, V.Y. Kukushkin, Solid state and dynamic solution structures of O-carbamidine amidoximes gives further insight into the mechanism of zinc (II)-mediated generation of 1, 2, 4-oxadiazoles, J. Mol. Struct. 1111 (2016) 142–150.

[38] S. A. Katkova, A. S. Mikherdov, M. A. Kinzhalov, A. S. Novikov, A. A. Zolotarev, V.P. Boyarskiy, V.Y. Kukushkin, (Isocyano Group pi-Hole)....[dz2-M-II] Interactions of (Isocyanide)[M-II] Complexes, in which Positively Charged Metal Centers (d (8)-M= Pt, Pd) Act as Nucleophiles, Chem. Eur. J. 25 (2019) 8590–8598.

[39] A.A. Eliseeva, D.M. Ivanov, A.S. Novikov, A.V. Rozhkov, I.V. Kornyakov, A.Y. Dubovtsev, V.Y. Kukushkin, Hexaiododiplatinate (ii) as a useful supramolecular synthon for halogen bond involving crystal engineering†, Dalton Trans. 49 (2020) 356–367.

[40] A.S. Mikherdov, A.S. Novikov, M.A. Kinzhalov, A.A. Zolotarev, V.P. Boyarskiy, Intra-/Intermolecular Bifurcated Chalcogen Bonding in Crystal Structure of Thiazole/Thiadiazole Derived Binuclear (Diaminocarbene) Pd^{II} Complexes, Crystals 8 (2018) 112.

[41] A.G. Tskhovrebov, A.S. Novikov, O.V. Odintsova, V.N. Mikhaylov, V.N. Sorokoumov, T.V. Serebryanskaya, G.L. Starova, Supramolecular polymers derived from the Pt^{II} and Pd^{II} schiff base complexes via C (sp^2)–H… Hal hydrogen bonding: Combined experimental and theoretical study, J. Organomet. Chem. 886 (2019) 71–75.

[42] O.V. Repina, A.S. Novikov, O.V. Khoroshilova, A.S. Kritchenkov, A.A. Vasin, A.G. Tskhovrebov, Lasagna-like supramolecular polymers derived from the Pd^{II} osazone complexes via C (sp^2)–H···Hal hydrogen bonding, Inorganica Chim. Acta. 502 (2020) 119378.

[43] M.A. Kryukova, A.V. Sapegin, A.S. Novikov, M. Krasavin, D.M. Ivanov, New Crystal Forms for Biologically Active Compounds. Part 1: Noncovalent Interactions in Adducts of Nevirapine with XB Donors, Crystals 9 (2019) 71.

[44] A.S. Mikherdov, A.S. Novikov, M.A. Kinzhalov, V.P. Boyarskiy, G.L. Starova, A.Y. Ivanov, V.Y. Kukushkin, Halides Held by Bifurcated Chalcogen–Hydrogen Bonds. Effect of μ (S, N–H) Cl Contacts on Dimerization of Cl (carbene) Pd^{II} Species, Inorg. Chem. 57 (2018) 3420–3433.

[45] A.M. Afanasenko, M.S. Avdontceva, A.S. Novikovand, T.G. Chulkova, Halogen and hydrogen bonding in cis-dichlorobis(propionitrile)platinum(II) chloroform monosolvate, Z. Kristallogr. Cryst. Mater. 231 (2016) 435–440.

[46] L.E. Zelenkov, D.M. Ivanov, M.S. Avdontceva, A.S. Novikov, N.A. Bokach, Tetrachloromethane as halogen bond donor toward metal-bound halides, Z. Kristallogr. Cryst. Mater. 234 (2019) 9–17.

[47] BrukerSAINT, Version 6.36a, Bruker AXS Inc., Madison, Wisconsin, USA, 2002.

[48] Bruker SMART, Version 5.625 and SADABS, Version 2.03a, Bruker AXS Inc., Madison, Wisconsin, USA, 2001.

[49] G.M. Sheldrick, A short history of SHELX, Acta Crystallogr., Sect. A 64 (2008) 112–122.

[50] G.M. Sheldrick, Crystal structure refinement with SHELXL, Acta Crystallogr., Sect. C 71 (2015) 3–8.

[51] L.J. Farrugia, WinGX and ORTEP for Windows: an update, J. Appl. Cryst. 45 (2012) 849–854.

[52] A.L. Spek, Single-crystal structure validation with the program PLATON, J. Appl. Crystallogr. 36 (2003) 7–13.

[53] M.A. Spackman, J.J. McKinnon, Fingerprinting intermolecular interactions in molecular crystals, CrystEngComm 4 (2002) 378–392.

[54] J.J. McKinnon, D. Jayatilaka, M.A. Spackman, Towards quantitative analysis of intermolecular interactions with Hirshfeld surfaces, Chem. Commun. (2007) 3814–3816.

[55] S.K. Seth, The Importance of CH···X (X = O, π) Interaction of a New Mixed Ligand Cu(II) Coordination Polymer: Structure, Hirshfeld Surface and Theoretical Studies, Crystals 8 (2018) 455.

[56] M.A. Spackman, P.G. Byrom, A novel definition of a molecule in a crystal, Chem. Phys. Lett. 267 (1997) 215–220.

[57] J.J. McKinnon, A.S. Mitchell, M.A. Spackman, Hirshfeld Surfaces, A New Tool for Visualising and Exploring Molecular Crystals, Chem. Eur. J. 4 (1998) 2136–2141.

[58] J.J. McKinnon, M.A. Spackman, A.S. Mitchell, Novel tools for visualizing and exploring intermolecular interactions in molecular crystals, Acta Crystallogr. B. 60 (2004) 627–668.

[59] A.L. Rohl, M. Moret, W. Kaminsky, K. Claborn, J.J. Mckinnon, B. Kahr, Hirshfeld Surfaces Identify Inadequacies in Computations of Intermolecular Interactions in Crystals: Pentamorphic 1,8-Dihydroxyanthraquinone, Cryst. Growth Des. 8 (2008) 4517–4525.

[60] M.J. Turner, J.J. McKinnon, S.K. Wolff, D.J. Grimwood, P.R. Spackman, D. Jayatilaka, M.A. Spackman, CrystalExplorer17, University of Western Australia, 2017.

[61] M. J. Frisch, G. W. Trucks, H. B. Schlegel, G. E. Scuseria, M. A. Robb, J. R. Cheeseman, G. Scalmani, V. Barone, G. A. Petersson, H. Nakatsuji, X. Li, M. Caricato, A. V. Marenich, J. Bloino, B. G. Janesko, R. Gomperts, B. Mennucci, H. P. Hratchian, J. V. Ortiz, A. F. Izmaylov, J. L. Sonnenberg, D. Williams-Young, F. Ding, F. Lipparini, F. Egidi, J. Goings, B. Peng, A. Petrone, T. Henderson, D. Ranasinghe, V. G. Zakrzewski, J. Gao, N. Rega, G. Zheng, W. Liang, M. Hada, M. Ehara, K. Toyota, R. Fukuda, J. Hasegawa, M. Ishida, T. Nakajima, Y. Honda, O. Kitao, H. Nakai, T. Vreven, K. Throssell, J. A. Montgomery Jr., J. E. Peralta, F. Ogliaro, M. J. Bearpark, J. J. Heyd, E. N. Brothers, K. N. Kudin, V. N. Staroverov, T. A. Keith, R. Kobayashi, J. Normand, K. Raghavachari, A. P. Rendell, J. C. Burant, S. S. Iyengar, J. Tomasi, M. Cossi, J. M. Millam, M. Klene, C. Adamo, R. Cammi, J. W. Ochterski, R. L. Martin, K. Morokuma, O. Farkas, J. B. Foresman, D. J. Fox, Gaussian 16, Revision C.01, Gaussian, Inc., Wallingford, CT, 2016.

[62] R.F.W. Bader, A Quantum Theory of Molecular Structure and Its Applications, Chem. Rev. 91 (1991) 893–928.

[63] T.A. Keith, AIMAll (version 13.05.06), TK Gristmill Software, Overland Park, KS, USA, 2013.

[64] R. Hilal, S.G. Aziz, A.O. Alyoubi, S. Elroby, Quantum Topology of the Charge Density of Chemical Bonds. QTAIM Analysis of the C-Br and O-Br bonds*, Procedia Comput. Sci. 51 (2015) 1872–1877.

[65] R.F.W. Bader, Atoms in Molecules, A Quantum Theory, Oxford University Press, New York, 1990.

[66] J. Contreras-García, E.R. Johnson, S. Keinan, R. Chaudret, J.P. Piquemal, D.N. Beratan, W. Yang, NCIPLOT: A Program for Plotting Noncovalent Interaction Regions, J. Chem. Theory Comput. 7 (2011) 625–632.

[67] E.R. Johnson, S. Keinan , P. Mori-Sanchez, J. Contreras-Garcia, A.J. Cohen, W. Yang, Revealing Non-covalent Interactions, J. Am. Chem. Soc. 132 (2010) 6498–6506.

[68] S. Tripathi, A. Hossain, S.K. Seth, S. Mukhopadhyay, Quantitative insights into the crystal structure of a mixed-ligand Co(III) complex: Experimental and theoretical studies, J. Mol. Struct. 1216 (2020) 128207.

[69] L.M. Shkol'nikova, G.V. Polyanchuk, N.M. Dyatlova, I.A. Polyakova, X-ray structural investigation of organic ligands of the complex one type. VI. Crystal and molecular structure of diethylenetriamine-N, N, N′, N″, N″-pentaacetic acid, J. Struct. Chem. 25 (1984) 264–272.

[70] T. Vishwanath, A. Ashish, C.R. Shankar, K.D. Amar, Single-crystal XRD, Hirshfeld surfaces, 3D energy framework calculations, and DFT studies of 4, 5-diphenyl-1, 3, 4-thiadiazole-2-thiolate: a mesoionic compound, Journal of Molecular Structure, 1264 (2022) 133290.

[71] C. Lepetit, M.L. Kahn, QTAIM and ELF topological analyses of zinc-amido complexes, Res. Chem. Intermed. 47 (2021) 377–395.

[72] S. Islam, S. Tripathi, A. Hossain, S.K. Seth, S. Mukhopadhyay, pH-induced structural variations of two new Mg (II)-PDA complexes: experimental and theoretical studies, J. Mol. Struct. 1265 (2022) 133373.

[73] C. Gatti, Chemical bonding in crystals: new directions, Z. Kristallogr. Cryst. Mater. 220 (2005) 399–457.

CHAPTER 4

A combined experimental and theoretical studies of two new Co(II)–PDA complexes: unusual 2D and 3D supramolecular networks [PDA = 2,6-pyridinedicarboxylic acid]

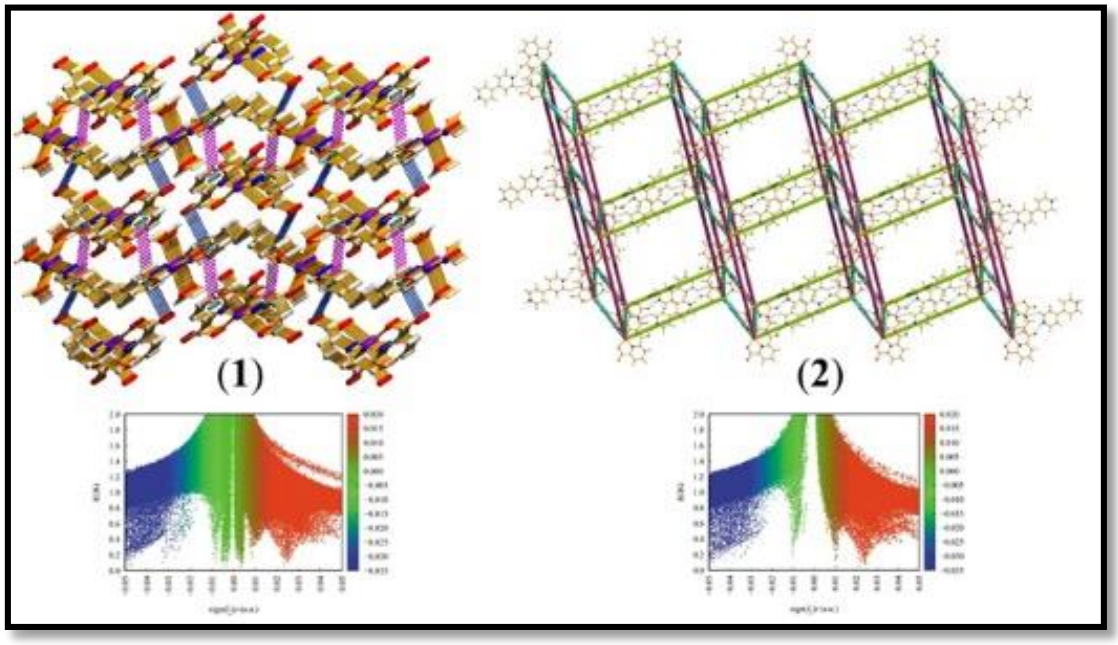

Published in: ***Polyhedron*** **242 (2023) 116514**

4.1. Introduction

The design, synthesis, and development of metal–organic complexes have attracted considerable attention from researchers, not only because of their countless potential applications in various fields but also because of their interesting structural topologies [1–4]. In synthesizing metal-organic complexes, transition metals have always been proven to be the most crucial class of atoms because of their potent ability to bind to one or more ligands through coordination bonds [5, 6]. Thus metal ions play a pivotal role in controlling the coordination geometry and properties of metal-organic complexes. The versatile nature of metal-ligand coordinative bonding allows chemists to control molecular assemblies. However, many factors can effectively influence the design and synthesis of the desired structural topologies, such as metal-ligand ratio, counterions, pH value, solvents, and temperature [7–10].

The selectivity of ligands is vital for designing and synthesizing metal-organic complexes. The 2,6-Pyridinedicarboxylic acid (2,6-pydc) is a frequently used ligand that coordinates to metal ions with tridentate mode [9]. The donor sites of 2,6-pydc are occupied by one pyridine nitrogen atom and two carboxylate oxygen atoms. 2,6-pydc is able to form stable coordination complexes with most transition metal centers, thereby occupying a prominent place as a building block in coordination chemistry [11]. Bridging dipyridine ligands, such as 4,4′-trimethylenedipyridine (4,4'-tmdpy), 4,4'-bipyridine (4,4′-bpy), etc., have been used for the construction of various hybrid solids [12, 13]. 4,4'-tmdpy is a flexible N-donor to construct several coordination polymers with different structural topologies among the N-donor bridging ligands [14, 15].

The comprehensive study of noncovalent interactions is necessary to develop new supramolecular chemistry applications. Molecular recognition events occur spontaneously in crystalline solids due to mutual interactions through various forces. One can design a crystal with desired properties with a clear idea of how molecular recognition involves various noncovalent interactions [16, 17]. Though hydrogen bonding has been extensively employed in crystal packing, other kinds of weak interactions establish their contributions to the building of supramolecular architectures. For example, the interactions incorporating aromatic π-ring such as π···π^+, π^+···π^+, anion···π, anion···π^+, lone-pair(l.p)···π, C–H···π, metal···π, salt-bridge (SB)···π^+, etc. are also very crucial to incarnate the crystal structure in solid state [18–24]. Other than the interactions involving the aryl ring, C–H···O, O–H···O, N–H···O, etc. belonging to the hydrogen bond category is also vital to form solid-state structure [18, 19, 25]. Thus, these

interactions are considered for rationalizing supramolecular crystals and stabilizing their intricate structure in the solid state.

We have synthesized and structurally characterized two new Co(II) coordinated metal-organic complexes, and analyzed noncovalent interactions in constructing supramolecular frameworks. Exploration of supramolecular packing diagrams of both complexes (**1** and **2**) reveals unusual types of structural networks, such as $(l.p\cdots\pi/\pi\cdots\pi^{+}/\pi^{+}\cdots\pi/\pi\cdots\pi/\pi\cdots\pi^{+}/\pi^{+}\cdots\pi/\pi\cdots l.p)_n$. We have further characterized the noncovalent interactions using Bader's quantum theory of "atoms-in-molecules" (QTAIM) [26, 27] and analyzed topological parameters, and calculated the dissociation energy of interactions. Further, we have performed the "Noncovalent Interaction" (NCI) plot index [28, 29] for analyzing noncovalent interactions. Also, we have calculated the optical band gap from UV-Vis spectroscopy using Tauc's equation [30] for both complexes.

4.2. Experimental Sections

4.2.1. Materials and Measurements

All chemicals used were of reagent-grade quality and purchased from Sigma Aldrich Chemical Co. All reactions were carried out in an aqueous medium under aerobic conditions. During the whole experiment, doubly distilled water was used. The CHN elemental analyses of both complexes were performed on a PerkinElmer 2400 Series-II CHN analyzer, USA, elemental analyzer. We have used a Perkin-Elmer LX-1 FT-IR spectrophotometer with a modern diamond attenuated total reflectance (ATR) accessory method to record the infrared spectrum in the range of 4000–400 cm^{-1}. The absorbance spectrum of the title complexes was recorded in the wavelength range of 190 nm–1100 nm using a UV-vis spectrophotometer (UV/Vis Lamda 365, PerkinElmer). To analyze the phase purity of the samples, powder X-ray diffraction (PXRD) data were recorded in the 2θ range of 5°–40° on a Bruker D8 Advance X-ray diffractometer using Cu Kα radiation (λ = 1.548 Å) generated at 35 kV and 35 mA.

4.2.2. Syntheses of The Title Complexes

4.2.2a. Synthesis of Complex (1)

Cobalt(II) nitrate hexahydrate (0.291 g, 1.0 mmol) dissolved in 25 ml of water was allowed to react with pyridine-2,6-dicarboxylic acid (0.334 g, 2.0 mmol) in water (25 ml) at 50°C, resulting a pink solution. A warm aqueous solution (25 ml) of 4,4'-trimethylenedipyridine (0.396 g, 2 mmol) was added dropwise to the above solution with continuous stirring. The reaction mixture thus obtained was further heated at 50°C for two

hours with continuous stirring. The solution was then cooled to room temperature and filtered, and the filtrate was left unperturbed. After a few weeks, block-shaped, pink crystals, suitable for X-ray diffraction analysis were obtained. The crystals were collected by filtration, washed with cold water, and dried in air. Anal. Calcd. for $C_{27}H_{32}Co_2N_4O_{14}$ (**1**): C, 42.98%; H, 4.27%; N, 7.42% and found: C, 42.95%; H, 4.29%; N, 7.40%. The PXRD patterns of complex (**1**) are shown in Figure 4.1a. The main IR absorption bands observed (in cm^{-1}) for complex (**1**) are 3151 (w), 3095 (s), 2862 (s), 1622 (vs), 1589 (vs), 1502 (vs), 1431 (vs), 1365 (vs), 1282 (vs), 1220 (s), 1188 (vs), 1076 (vs), 767 (vs) (Figure 4.2).

4.2.2b. Synthesis of Complex (2)

Cobalt(II) nitrate hexahydrate (0.291 g, 1.0 mmol) was reacted with pyridine-2,6-dicarboxylic acid (0.334 g, 2.0 mmol) in water (50mL) at 60 °C. A warm aqueous solution (20 mL) of 4,4'-Bipyridine (0.624 g, 4.0 mmol) was then added dropwise to the above solution with continuous stirring for about an hour at normal laboratory temperature (~32 °C). The solution mixture was left undisturbed for a few days when block-shaped, pink crystals suitable for X-ray diffraction analysis were obtained. The crystals were collected by filtration, washed with cold water, and dried in air. Anal. Calcd. for $C_{48}H_{52}Co_2N_8O_{27}$ (**2**): C, 44.66%; H, 4.06%; N, 8.68% and found: C, 44.63%; H, 4.07%; N, 8.70%. The PXRD patterns of complex (**2**) are shown in Figure 4.1b. The main IR absorption bands observed (in cm^{-1}) for complex (**2**) are 3100 (s), 3007 (w), 2598 (w), 1583 (vs), 1492 (vs), 1365 (vs), 1282 (vs), 1214 (s), 1188 (vs), 1075 (s), 990 (s), 813 (s), 777 (vs), 729 (s) (Figure 4.3).

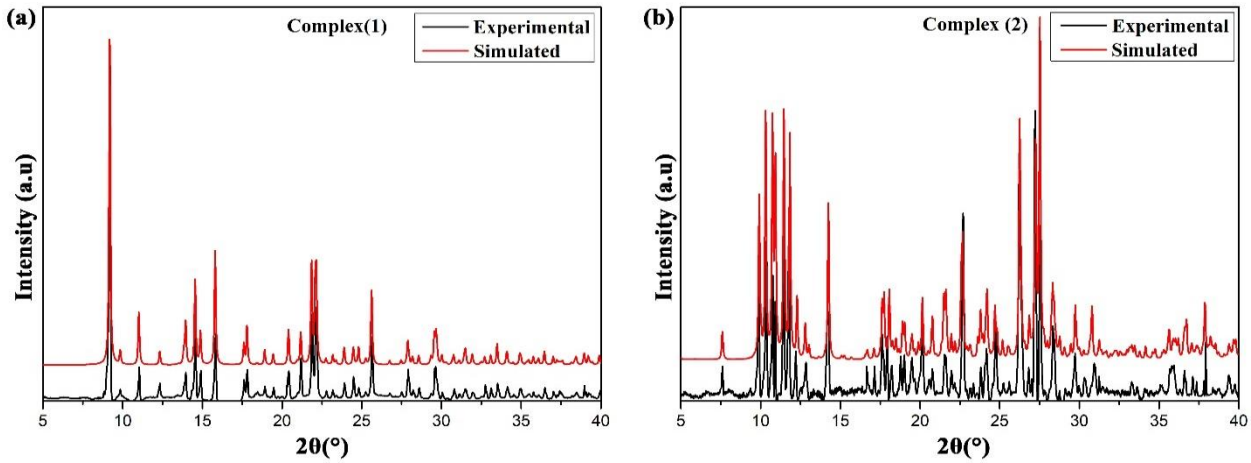

Figure 4.1. PXRD patterns of (a) complex (**1);** and (b) complex (**2**).

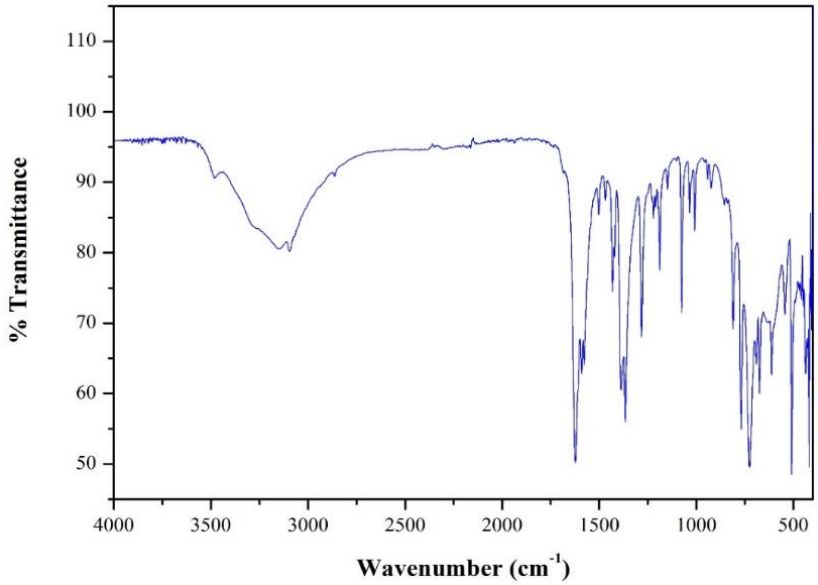

Figure 4.2. IR spectra of complex (**1**).

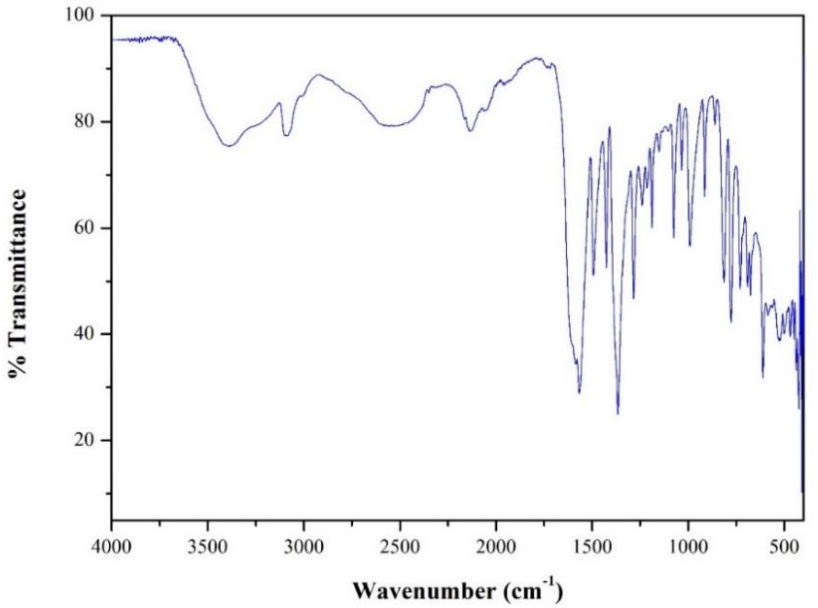

Figure 4.3. IR spectra of complex (**2**).

4.2.3. X-ray Crystal Structure Determination

Optically transparent, good single crystals were selected for single-crystal X-ray diffraction (SCXRD) to determine crystal structure. Intensity data collection was performed by using Bruker APEX-II CCD diffractometer having a fine-focus sealed tube as diffraction source of MoKα radiation (λ = 0.71073 Å) at 273(2) K and 120(2) K for (**1**) and (**2**) respectively. Collected intensity data were reduced using the Bruker SAINT v8.34A program [31], and an empirical absorption correction based on the multi-scan method was applied using the process SADABS [32]. The structure solution of both complexes was carried out using SHELXT-14 [33] and then refined by the full-matrix least-squares technique on F^2 using

SHELXL-18 [34] for (**1**) and SHELXL-14 [34] for (**2**). The hydrogen atoms were placed at their geometrically idealized positions and refined isotropically. The structure solution of (**1**) was performed using the WinGX program V2014.1 [35], whereas Olex2 1.5 program [36] was used for the structure solution of (**2**). For analyzing the crystal information files (CIFs) of both complexes, the program PLATON [37] was used. The crystal information and structure refinement parameters are summarized in Table 4.1. CCDC 2238424–2238425 contains the supplementary crystallographic data of complexes (**1**)–(**2**), respectively.

Table 4.1. Crystal data and structure refinement parameters for (**1**) and (**2**).

	Complex (**1**)	Complex (**2**)
Empirical formula	$C_{27}H_{32}Co_2N_4O_{14}$	$C_{48}H_{52}Co_2N_8O_{27}$
Formula weight	754.42	1290.83
Temperature	273(2)K	120 K
Wavelength (Mo Kα)	0.71073Å	0.71073Å
Crystal system, space group	Monoclinic, P2/c	Triclinic, P –1
Unit cell parameters	a = 9.748(1) Å	a = 10.252(3) Å
	b = 8.965(1)Å	b = 15.232(5) Å
	c = 18.197(2)Å	c = 17.640(6) Å
	α = 90°	α = 91.647(4)°
	β = 99.431(2)°	β = 92.314(4)°
	γ = 90°	γ = 100.921(4)°
Volume	1568.8(2)Å^3	2700.7(15) Å^3
Crystal size	0.21 × 0.13 × 0.08mm	0.15 × 0.12 × 0.1 mm
Crystal shape	Block	Block
Crystal color	Dark pink	Metallic dark red
Z /Density (clac.)	2, 1.597Mg/m^3	2, 1.587 Mg/m^3
Absorption coefficient	1.133mm^{-1}	0.714 mm^{-1}
F(000)	776	1332
θ-range for data collection	2.269–24.997°	1.156–25°
Limiting indices	–11≤ h ≤ 11;	–12≤ h ≤ 12;
	–10≤ k ≤ 10;	–18≤ k ≤ 18;
	–21≤ l ≤ 21	–20≤ l ≤ 20

Reflections collected/unique	18943/2764 [R(int) =0.0526]	25247/ 9357 [R(int) =0.0686]
Completeness to theta	99.7%	98.5%
Absorption correction	Semi-empirical from equivalents	Semi-empirical from equivalents
Max. and min. transmission	0.92 and 0.84	0.932 and 0.90
Refinement method	full-matrix least-squares on F^2	full-matrix least-squares on F^2
Data/ parameters	2764/ 215	9357/ 861
Goodness-of-fit on F^2	1.078	1.034
Final R indices [$I > 2\sigma(I)$]	$R_1 = 0.0281$, $wR_2 = 0.0795$	$R_1 = 0.0777$, $wR_2 = 0.2104$
R indices (all data)	$R_1 = 0.0310$, $wR_2 = 0.0819$	$R_1 = 0.1091$, $wR_2 = 0.2326$
Largest diff. peak and hole	0.301 and –0.435 e·Å^{-3}	1.929 and –0.745 e·Å^{-3}

$R_1 = \Sigma||F_o|-|F_c||/\Sigma|F_o|$, $wR_2 = [\Sigma\{(F_o^2-F_c^2)^2\}/\Sigma\{w(F_o^2)^2\}]^{1/2}$, $w = 1/\{\sigma^2(F_o^2) + (aP)^2 + bP\}$, where $P= (F_o^2 + 2F_c^2)/3$ for both complexes, a = 0.0420 and b = 0.8374 for (**1**) and a = 0.1305 and b = 6.6104 for (**2**).

4.2.4. Theoretical Methods

Both complexes' quantum chemical computations are performed using *Gaussian 16w* calculation package [38] at the DFT/B3LYP level with 6311G basis set. We have used the models generated from supramolecular architectures to perform theoretical calculations. For the characterization of weak noncovalent interactions, we have used Bader's quantum theory of "Atoms in Molecules" (QTAIM) [26, 27] using the AIMall calculation package [39]. The topological parameters derived from QTAIM [40] allow for much better insights into the interatomic interactions, and it can be used as a powerful tool for investigating the electronic and conformational properties of the molecules [41]. There are some notable points named critical points where the gradient of electron density (ρ_{BCP}) vanishes. The critical points of bonds are known as bond critical points (BCPs), lying in the bond path connecting two atoms. Every BCP contains well-to-do chemical information, reflecting the bond's nature. The topological parameters like electron density (ρ_{BCP}), Laplacian of the electron density ($\nabla^2(\rho_{BCP})$), and potential energy density (V_{BCP}) are mainly used for characterizing noncovalent interactions. Electron density concentrated towards the interaction line when $\nabla^2(\rho_{BCP}) < 0$ and depleted towards the nucleus when $\nabla^2(\rho_{BCP}) > 0$. Employing potential energy density (V_{BCP}), dissociation energy of interaction can be obtained using the formula $D.E_{int} = –½ V_{BCP}$, more

accurately $D.E_{int}$ (Kcal.mol^{-1}) = –313.754 × V_{BCP} (au) [42]. The NCI Plot Index is a visualization index for analyzing noncovalent interactions. We have used Multiwfn [43] and visual molecular dynamics (VMD) [44] for indexing NCI Plot [28, 29]. Isosurfaces represent noncovalent interactions in NCI Plot. Different colors of isosurfaces indicate different natures of the interaction. For example, the blue and red color of the isosurface represents ρ^{-}cut (attractive) and ρ^{+}cut (repulsive) interactions, respectively, whereas yellow and green colors indicate weak repulsive and weak attractive interactions [29].

4.3. Results and Discussion

4.3.1. Structural Description of Complex (1)

Complex (**1**) crystallizes in a monoclinic crystal system with a P2/c space group which is quite unusual, and it is here justified by the intrinsic molecular symmetry of the cation, and the ORTEP [35] diagram depicted in Figure 4.4. Complex (**1**) is composed of an anionic moiety made up of a Co(1) center and two $(2,6\text{-pydc})^{2-}$ anions, as well as a one-dimensional polymeric cationic chain in which the 4,4'-tmdpy ligands connect the Co(2) sites and lattice water molecules (see Figure 4.4). Two pydc ligands operate in a tridentate mode toward the Co(1) ion to create the anionic unit, resulting an octahedral geometry. The Co(2) center also adopts an octahedral environment in the cationic portion, where the CoN_2O_4 core adopts a *trans* arrangement and is coordinated by two nitrogen atoms from a 4,4'-tmdpy ligand and four oxygen atoms from lattice water molecules. In each cation chain of $[Co(4,4'\text{-tmdpy})(H_2O)_4]^{2+}{}_n$ unit, the nitrogen atoms of the 4,4'-tmdpy ligand bridge the Co(2) sites by generating a cationic polymeric zigzag chain. In contrast to the Co(1) site, it is noted that Co(2)–O bond distances are shorter than Co(2)–N (see Table 4.2). It is apparent that Co(1)–O distances are longer than Co(1)–N distances. In the cationic unit, the O(5) and O(6) atoms occupy the axial positions and are nearly perpendicular with an angle of 93.96(6)º, as well as N(2) also occupying an axial position with O(5)–Co(2)–N(2) and O(6)–Co(2)–N(2) angles of 91.58(6)º and 91.08(6)º respectively (see Table 4.2). Noting that two pyridine rings of the polymeric cationic unit are not coplanar, the dihedral angle between them is 56.75º. Two rigid $(2,6\text{-pydc})^{2-}$ have a dihedral angle of 83.82º, deviating 6.18 degrees from the perpendicular.

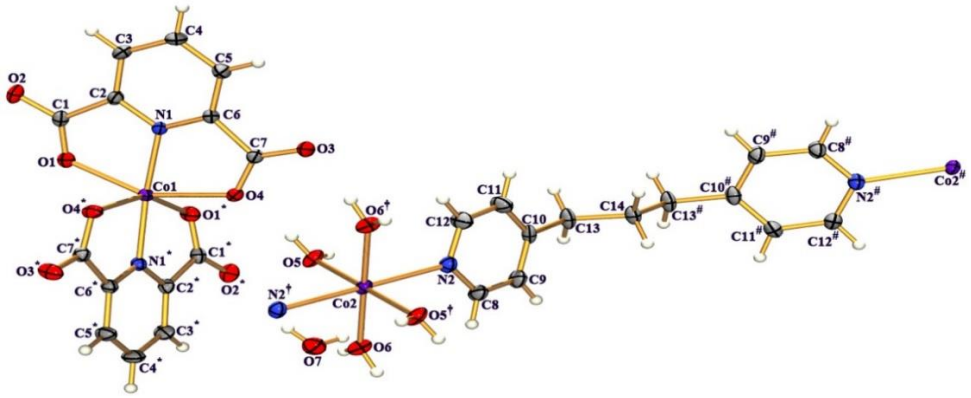

Figure 4.4. An ORTEP view of the asymmetric unit of complex (**1**) with the atom-numbering scheme. Thermal ellipsoids are drawn at 30% probability. Symmetry codes: * = 1–x, y, 1/2–z; # = –x, y, 3/2–z; † = 1–x, –y, 1–z.

Table 4.2. Selected bond lengths (Å) and bond angles (°) around the metal centers in complex (**1**) and (**2**).

Complex(1)		***Complex(2)***	
Co1–N1	2.0342(17)	Co1–O11	2.123(4)
Co1–O1*	2.1756(15)	Co1–O14	2.151(4)
Co1–O4*	2.1478(15)	Co1–O15	2.152(4)
Co1–N1*	2.0342(17)	Co1–N7	2.019(5)
Co1–O1	2.1756(15)	Co1–N8	2.024(5)
Co1–O4	2.1478(15)	Co1–O10	2.196(4)
Co2–O5	2.0469(14)	Co2–O2	2.201(4)
Co2–O6	2.0893(16)	Co2–O3	2.141(4)
Co2–N2	2.2457(19)	Co2–O6	2.166(4)
Co2–O5†	2.0469(14)	Co2–O7	2.225(4)
Co2–O6†	2.0893(16)	Co2–N3	2.019(5)
Co2–N2†	2.2457(19)	Co2–N4	2.016(5)
O4a–Co1–N1*	94.72(6)	O14–Co1–N8	76.78(16)
N1–Co1–N1*	165.73(7)	O15–Co1–N7	103.41(17)
O1a–Co1–O4*	151.33(6)	O15–Co1–N8	76.49(16)
O1a–Co1–N1*	75.70(6)	N7–Co1–N8	174.14(16)
O4a–Co1–N1*	75.75(6)	O11–Co1–O14	93.64(15)
O1–Co1–O4	151.33(6)	O11–Co1–O15	89.20(15)
O1–Co1–N1	75.70(6)	O10–Co1–O11	153.56(17)

O1–Co1–O1*	101.60(6)	O10–Co–O14	91.94(15)
O1–Co1–O4*	87.49(6)	O10–Co1–O15	97.56(15)
O1–Co1–N1*	113.83(6)	O10–Co1–N7	76.27(16)
O4–Co1–N1	75.75(6)	O10–Co1–N8	97.91(16)
O1a–Co1–O4	87.49(6)	O11–Co1–N8	108.53(16)
O4–Co1–O4*	97.48(6)	O14–Co1–O15	152.60(17)
O4–Co1–N1*	94.72(6)	O11–Co1–N7	77.30(16)
O1a–Co1–N1	113.83(6)	O14–Co1–N7	103.80(17)
O5–Co2–O6	86.04(6)	O2–Co2–O3	151.14(17)
O5–Co2–N2	88.42(6)	O2–Co2–O6	89.97(15)
O5–Co2–O5†	180.00	O2–Co2–O7	95.90(15)
O5–Co2–O6†	93.96(6)	O2–Co2–N3	75.41(17)
O5–Co2–N2†	91.58(6)	O2–Co2–N4	107.51(16)
O6–Co2–N2	91.08(6)	O3–Co2–O6	100.48(15)
O5c–Co2–O6	93.96(6)	O3–Co2–O7	87.33(15)
O6–Co2–O6†	180.00	O3–Co2–N3	76.79(18)
O6–Co2–N2†	88.92(6)	O3–Co2–N4	101.09(17)
O5c–Co2–N2	91.58(6)	O6–Co2–O7	152.18(17)
O6c–Co2–N2	88.92(6)	O6–Co2–N3	95.93(17)
N2–Co2–N2†	180.00	O6–Co2–N4	76.65(16)
O5c–Co2–O6†	86.04(6)	O7–Co2–N3	111.87(17)
O5c–Co2–N2†	88.42(6)	O7–Co2–N4	75.65(16)
O6c–Co2–N2†	91.08(6)	N3–Co2–N4	171.88(15)

The noncovalent interactions such as hydrogen bonding (O–H···O and C–H···O), π···π, and lone pair (l.p)···π interactions are responsible for the generation and stabilization of supramolecular structures for (**1**) in solid-state (Table 4.3, 4.4, 4.5). The water oxygen O(7) acts as a donor to carboxylate oxygen atom O(1) and carbonyl oxygen atom O(2) of the acid moiety at (x, 1–y, 1/2+z) and (1–x, y, 1/2–z) respectively, hence a centrosymmetric tetrameric ring $R_4^4(12)$ is formed. Again the carbonyl oxygen O(3) at (–x, y, 1/2–z) interacts through H-bonding interaction when C(5) plays the role of donor, forming a centrosymmetric dimeric ring $R_2^2(10)$. The combination of these $R_4^4(12)$ and $R_2^2(10)$ ring motifs leads to the formation of a two-dimensional framework in the (101) plane (Figure 4.5). The $R_2^2(10)$ dimeric ring in

another substructure mentioned above forms a one-dimensional chain of acid moieties. Parallel 1D polymeric chains are connected to the chains of acid moieties through the O(6)–H(6A)···O(3) interactions, resulting in the formation of a two-dimensional supramolecular framework in the (101) plane (Figure 4.6).

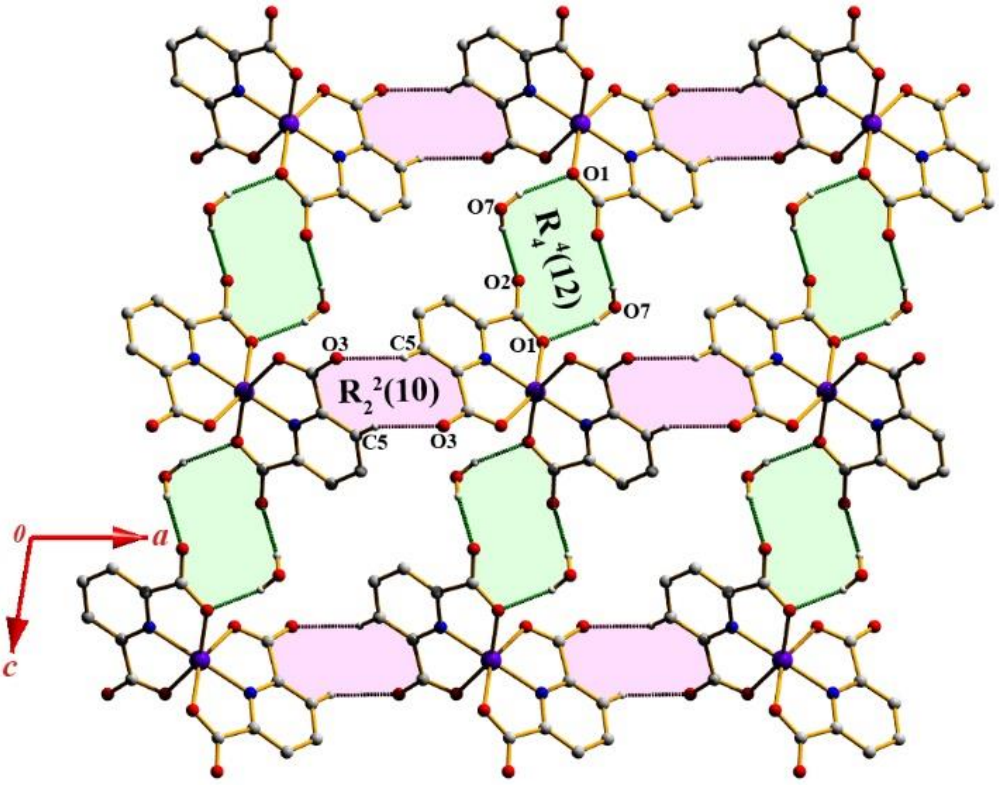

Figure 4.5. $R_2^2(10)$ and $R_4^4(12)$ ring motifs generate 2D supramolecular assembly in the (101) plane.

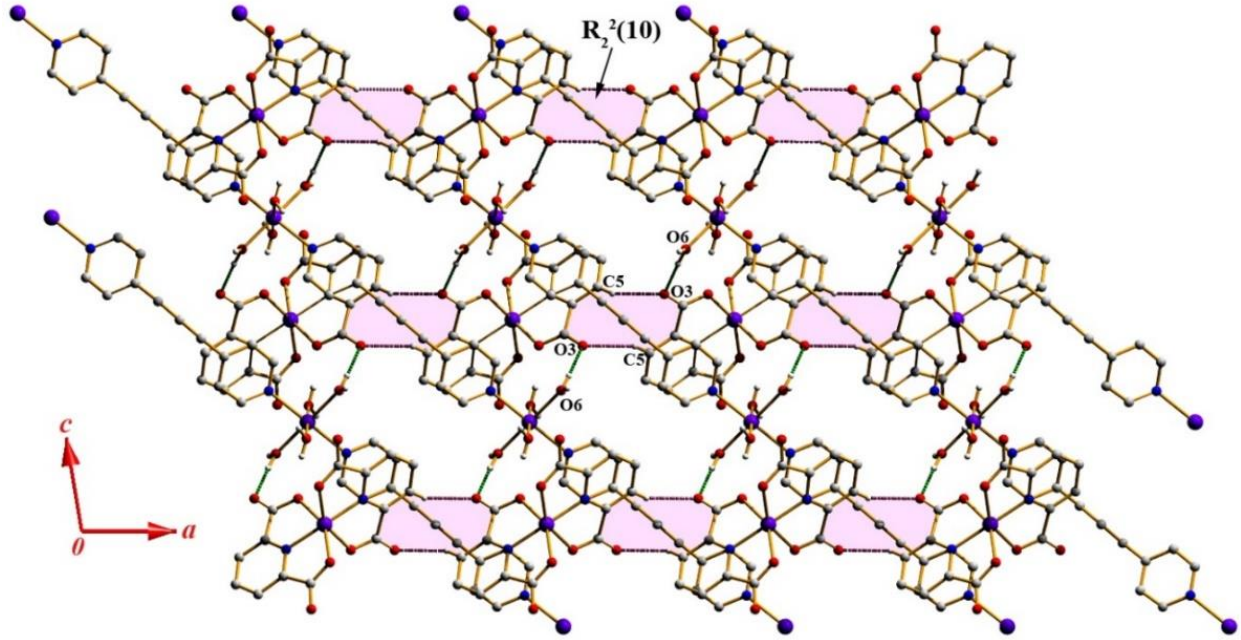

Figure 4.6. Parallel cationic polymeric zigzag chains are connected to the acid moieties in the (101) plane.

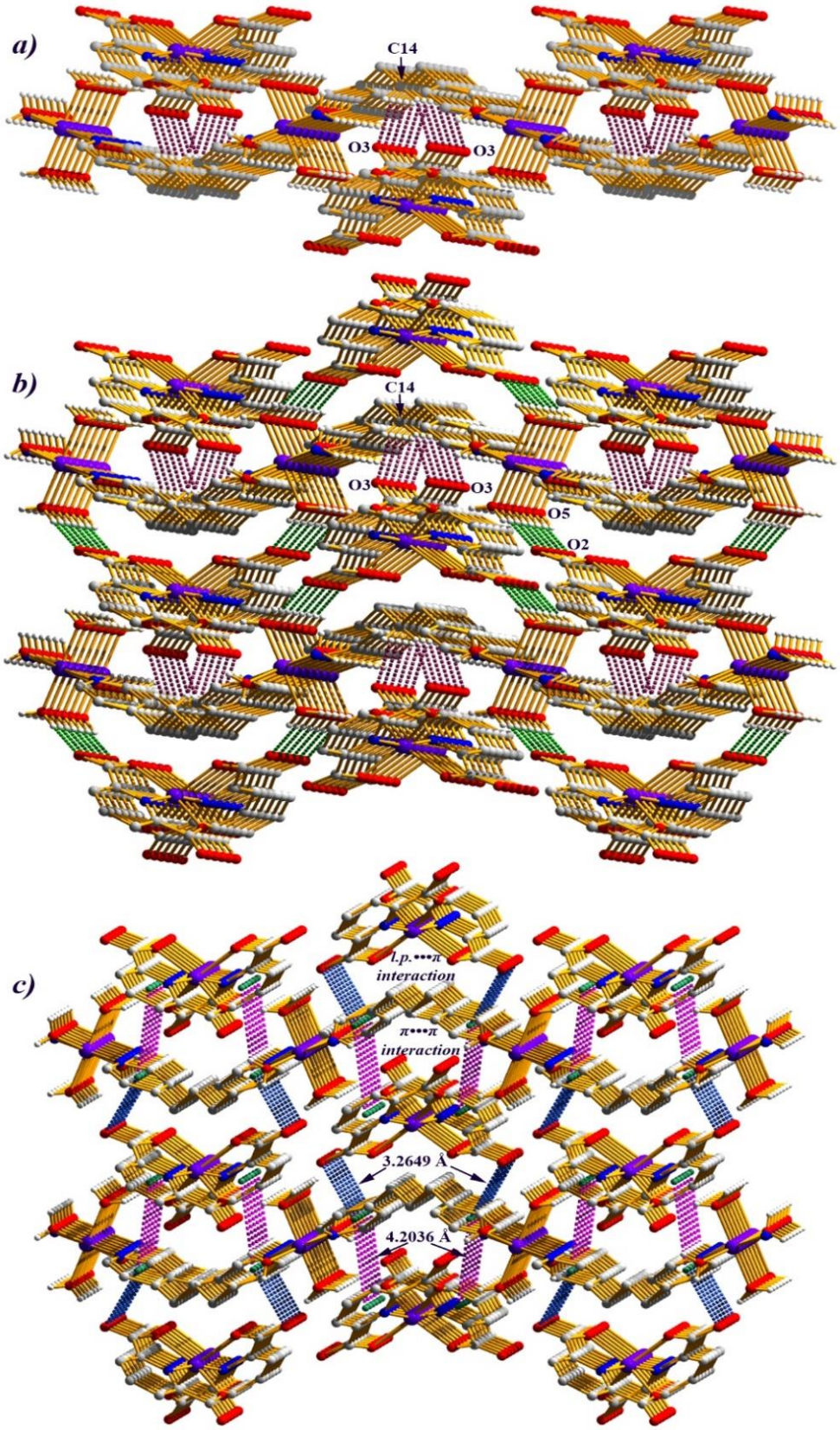

Figure 4.7. (a) Multi-layered braid-like chain formed through C–H···O hydrogen bonding interactions; (b) Parallel multi-layered braid-like chains connected by using O–H···O hydrogen bonding interactions leads to three-dimensional supramolecular self-assembly in (**1**); (c) Same three-dimensional supramolecular self-assembly generated through l.p···π/ π···π interactions.

Further in another substructure, the carbon atom C(14), located at the inversion center of the polymeric chain, acts as a donor to the carbonyl oxygen atoms O(3) of two parallel acid moieties of the molecules at (–x, –y, 1–z) and (x, –y, 1/2+z) (see Table 4.3). Now the carbonyl oxygen atoms O(3) of the symmetric part of acid moieties again interact with C(14) of the polymeric chain, which leads to the formation of another polymeric chain parallel to the former. Thus multiple layers of polymeric chains and acid moieties are formed involving C(14)–H(14A)···O(3) interactions forming a multi-layered braid-like chain as shown in Figure 4.7a. Parallel multi-layered braid-like chains are connected through O(5)–H(5B)···O(2) interaction as shown in Figure 4.7b. Combination of C(14)–H(14A)···O(3) and O(5)–H(5B)···O(2) interactions forms a three-dimensional supramolecular architecture for (**1**) (Figure 4.7b).

This same 3D supramolecular architecture can also be explained by l.p···π/ π···π interactions. The lone pair oxygen O(2) of the acid moiety interacts with the π-rings of the polymeric chain through l.p···π interaction having lone pair and centroid separation distance of 3.265(2) Å (see Table 4.5). In the symmetric unit, there are two lone pairs of oxygen O(2); one O(2) interacts with the π-ring of layer-A of the polymeric chain, whereas another O(2) interacts with the π-ring of layer-B formed by another polymeric chain. Thus the layers are generated in the [100] direction. For generated layers, the π-rings of the polymeric chain interact with the π-rings of the acid moieties having a centroid to centroid distance of 4.204(2) Å (see Table 4.4). Thus three-dimensional supramolecular architecture associated with l.p···π/ π···π interactions is depicted in Figure 4.7c. Both hydrogen bonding interactions (O–H···O and C–H···O) and the interactions involving the pyridine rings (l.p···π and π···π) are responsible for the stabilization of the supramolecular network of Figure 4.7 (b or c) in complex (**1**).

Table 4.3. Relevant hydrogen bonding parameters (Å, °).

D–H···A	D–H	H···A	D···A	D–H···A	Symmetry
Complex (1)					
O(5)–H(5B)···O(2)	0.82	1.91	2.731(2)	174	x, 1–y, 1/2+z
O(6)–H(6A)···O(3)	0.82	1.86	2.674(2)	169	1–x, –y, 1–z
O(7)–H(7A)···O(2)	0.83	2.19	3.013(2)	170	1–x, y, 1/2–z
O(7)–H(7B)···O(1)	0.82	1.99	2.792(2)	163	x, 1–y, 1/2+z
C(5)–H(5)···O(3)	0.93	2.36	3.169(3)	146	–x, y, 1/2–z
C(12)–H(12)···O(6)	0.93	2.55	3.128(3)	121	1–x, –y, 1–z
C(14)–H(14A)···O(3)	0.97	2.50	3.392(3)	153	–x, –y, 1–z

C(14)–H(14A)···O(3)	0.97	2.50	3.392(3)	153	x, –y, 1/2+z
Complex (2)					
N(2)–H(2)···O(1)	0.88	1.75	2.621(7)	167	–
N(5)–H(5)···O(8)	0.88	1.76	2.622(7)	166	–
N(6)–H(6)···O(9)	0.88	1.83	2.624(7)	149	–
O(19)–H(19A)···O(20)	0.83	1.80	2.488(2)	139	–
O(20)–H(20A)···O(4)	0.81	1.99	2.751(8)	156	–
O(22)–H(22A)···O(7)	0.83	2.17	2.989(6)	170	2–x, 1–y, 1–z
O(23)–H(23A)···O(2)	0.83	2.04	2.858(6)	170	–
O(26)–H(26B)···O(25)	0.83	1.97	2.727(7)	152	–
C(1)–H(1A)···O(27)	0.95	2.46	3.170(8)	131	–
C(6)–H(6A)···O(23)	0.95	2.54	3.262(8)	133	–
C(14)–H(14)···O(22)	0.95	2.44	3.197(8)	137	–
C(15)–H(15)···O(13)	0.95	2.38	3.197(7)	144	1+x, 1+y, 1+z
C(20)–H(20)···O(12)	0.95	2.27	3.103(8)	146	2+x, y, 1+z
C(25)–H(25)···O(21)	0.95	2.48	3.329(2)	149	–
C(34)–H(34)···O(25)	0.95	2.58	3.296(8)	132	2–x, –y, –z
C(37)–H(37)···O(18)	0.95	2.40	3.329(8)	165	–
C(44)–H(44)···O(4)	0.95	2.38	3.166(7)	140	–1+x, –1+y, –1+z
C(45)–H(45)···O(17)	0.95	2.45	3.156(8)	131	–

Table 4.4. Geometrical parameters (Å, °) for π-stacking interaction.

Rings i–j	**Rc[b]**	**R1v[c]**	**R2v[d]**	**α[e]**	**β[f]**	**γ[g]**	**Slippage**
Complex (1)							
Cg(1)–Cg(6)	4.204(2)	–3.677(1)	–4.051(1)	13.5(2)	15.50	28.98	–
Complex (2)							
Cg(5)–Cg(13)	3.715(3)	3.393(2)	3.465(2)	7.8(3)	21.17	24.02	–
Cg(11)–Cg(11)	3.749(3)	3.398(2)	3.399(2)	0	24.98	24.98	1.583
Cg(11)–Cg(16)	3.722(4)	–3.435(2)	–3.443(2)	3.1(3)	22.30	22.62	–
Cg(12)–Cg(14)	3.826(3)	–3.412(2)	–3.467(2)	2.1(3)	25.05	26.91	–

[a]In complex (**1**), Cg(1) and Cg(6) are the centroids of (N2, C8–C12), and (N1, C2–C6), respectively. In complex (**2**), Cg(5), Cg(6) Cg(11), Cg(12), Cg(13), Cg(14), and Cg(16) are the centroids of (N3, C12–C16), (N4, C19–C23), (N7, C36–C40), (N8, C43–C47), (N1, C1–C5), (N2, C6–C10), and (N6, C30–C34), respectively. [b] Centroid distance between ring i and ring j. [c]Vertical distance from ring centroid i to ring j. [d] Vertical distance from ring centroid j

to ring i. [e] Dihedral angle between the first ring mean plane and the second ring mean plane of the partner molecule. [f] Angle between centroids of the first and second ring mean planes. [g]Angle between the centroid of the first ring and normal to the second ring mean plane of the partner molecule.

Table 4.5. Geometrical parameters (Å, °) for lone pair (l.p)···π interactions.

Y–X···Cg	X···Cg	X···Perp	Y–X···Cg	Symmetry
Complex (1)				
C(1)–O(2)···Cg(1)	3.265(2)	3.233	86.2(2)	x, 1–y, –1/2+z
Complex (2)				
C(11)–O(1)···Cg(5)	3.702(5)	–3.302	80.1(3)	2–x, 1–y, 1–z
C(11)–O(1)···Cg(14)	3.521(5)	3.220	95.4(3)	3–x, 1–y, 1–z
C(24)–O(8)···Cg(6)	3.851(5)	–3.388	91.8(3)	2–x, –y, 1–z
C(24)–O(8)···Cg(15)	3.373(5)	3.327	97.5(3)	1–x, –y, 1–z
C(41)–O(12)···Cg(15)	3.239(5)	–3.107	88.0(4)	–x, –y, –z
C(48)–O(16)···Cg(13)	3.514(5)	–3.278	82.5(3)	1–x, –y, –z

In complex (**1**), Cg(1) and Cg(6) are the centroids of (N2, C8–C12), and (N1, C2–C6), respectively. In complex (**2**), Cg(5), Cg(6) Cg(11), Cg(12), Cg(13), Cg(14), Cg(15), and Cg(16) are the centroids of (N3, C12–C16), (N4, C19–C23), (N7, C36–C40), (N8, C43–C47), (N1, C1–C5), (N2, C6–C10), (N5, C25–C29), and (N6, C30–C34), respectively.

4.3.2. Structural Description of Complex (2)

Complex (**2**) is crystallized in a triclinic crystal system with P–1 space group. The asymmetric unit of (**2**) consists of two discrete mononuclear cobalt (II)-dipicolinate unit $[Co(2,6\text{-}pydc)_2]^{2-}$ (moiety A and moiety B) associated with two doubly protonated 4,4'-bipyridine counter ions (moiety C and moiety D) for neutralization of charge, and eleven uncoordinated solvent water molecules. One solvent water molecule is found as disordered, and the corresponding oxygen atom has an occupancy of 0.6 and 0.4 (see Figure 4.8). The cationic portion of the asymmetric unit consists of a doubly protonated bipyridine molecule (bipyridinium cation), and the anionic portion is the $[Co(2,6\text{-}pydc)_2]^{2-}$ complex. Each Co^{II} atom is coordinated by four oxygen atoms and two nitrogen atoms from two dipicolinate ligands in a tridentate fashion and is at the centre of a distorted octahedral environment formed by the CoO_4N_2 bonding set. In anionic moiety A, the angles O(2)–Co(2)–O(6) [89.97(15)º], O(3)–Co(2)–O(7) [87.33(15)º] and N(3)–Co(2)–N(4) [171.88(15)º] indicate that the coordination environment around Co(II) ion is a distorted octahedron. As expected, the Co–O distances are longer than the Co-N distances in both moieties of A and B (see Table 4.2). Indeed, in an

anionic fragment two rigid (2,6-pydc)$^{2-}$ are almost perpendicular to each other, having dihedral angles of 83.39º and 85.45º in moieties A and B, respectively.

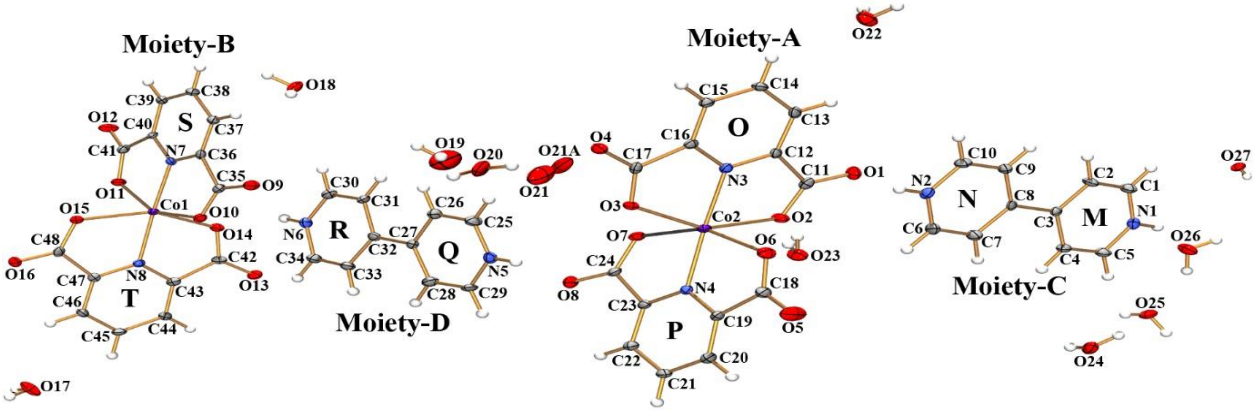

Figure 4.8. An ORTEP view of complex (**2**) with the atom-numbering scheme. Thermal ellipsoids are drawn at 30% probability.

In the solid state, the supramolecular structure of the complex (**2**) is stabilized through hydrogen bonding interactions (such as N–H···O, O–H···O, and C–H···O) and the interactions involving pyridine rings (such as π···π, π···π$^+$, π$^+$···π, lone pair···π). In the first substructure of complex (**2**), the oxygen atom O(8) is oriented towards the π-face of ring-P with a distance of 3.851Å, suggesting l.p···π interaction. Due to its self-complementary nature, this ring-P is further juxtaposed to ring-R through π···π$^+$ interaction having a ring centroid separation of 3.690Å. Further, the ring-R is connected to ring-S through π$^+$···π interaction with the centroid to the centroid separation distance of 3.722Å. Again, ring-S is juxtaposed to ring-S of the partner molecule due to its self-complementary nature and exhibits π···π stacking interaction having a ring centroid separation of 3.749Å and ring offset of 1.583 Å. The combination of l.p···π and different π-interactions constitutes a network chain, l.p···π/π···π$^+$/π$^+$···π/π···π. The sequence of these interactions is reversed from π···π stacking interaction, thus forming a rare combination of an extended 1D network (l.p···π/π···π$^+$/π$^+$···π/π···π/π···π$^+$/π$^+$···π/π···l.p)$_n$. The parallel 1D extended networks are connected through a combination of lone pair···π and C–H···O interactions where the oxygen atom O(1) orients towards ring-O, suggesting l.p···π interaction having a ring to the lone-pair separation distance of 3.702 Å. The carbon atoms C(15) and C(44) act as a donor to the carbonyl oxygen O(13) and O(4), hence forming $R_2^2(10)$ dimeric ring (Figure 4.9).

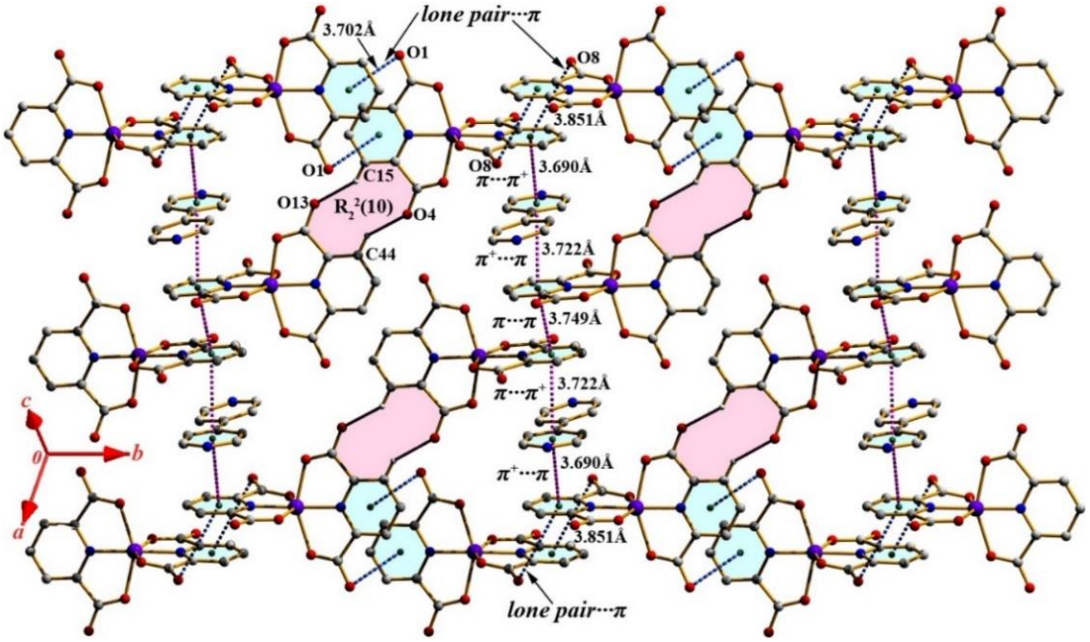

Figure 4.9. Two-dimensional supramolecular self-assembly of complex (**2**) generated with a rare combination of the extended (lone pair···π/π···π^+/π^+···π/π···π/π···π^+/π^+···π/π···lone pair)$_n$ network.

In another substructure of complex (**2**), again the oxygen atoms O(1) and O(8) of the acid moiety-A orient towards the π-face of the ring-O and ring-P of partner molecules, having oxygen and ring centroid separation distance 3.702 Å and 3.851Å respectively, suggesting l.p···π interactions, forming a 1D chain of acid moiety-A which propagates along [010] direction. Two parallel 1D chains of acid moiety-A are connected through C(20)–H(20)···O(12) interaction and π···π stacking interaction (above mentioned), which leads to the formation of another two-dimensional supramolecular structure in (011) plane for complex (**2**) depicted in Figure 4.10.

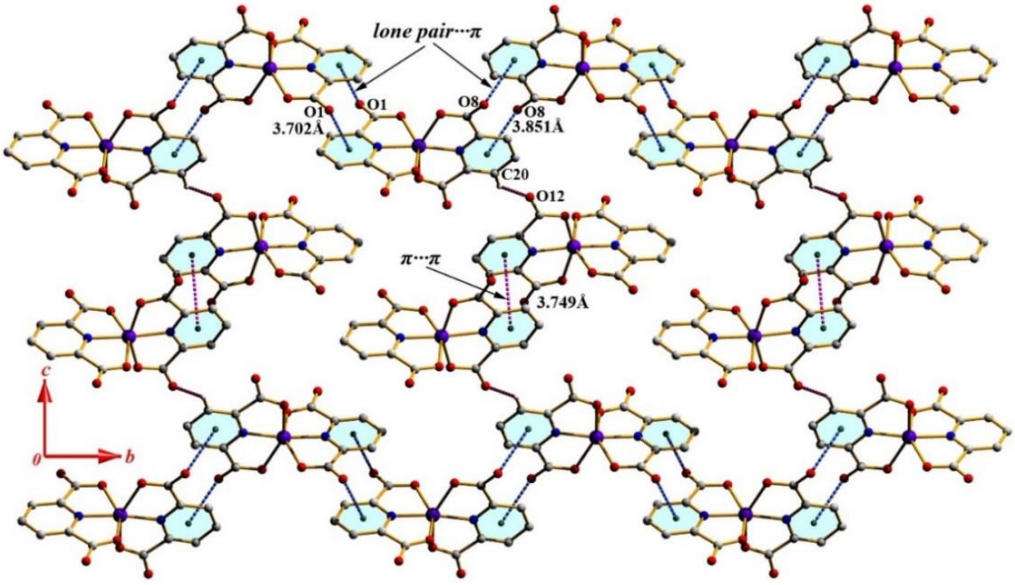

Figure 4.10. Two-dimensional supramolecular structure in (011) plane for complex (**2**).

We have explored unique supramolecular self-assembly for complex (2), where 3D boxes are assembled in a 2D plane. In this complex (2) substructure, above mentioned $R_2^2(10)$ dimeric ring is formed between moiety-A and B. Now the moiety-B's carbonyl oxygen O(9) interacts with the moiety-D's nitrogen atom N(6). Then the carbon atom C(34) of the moiety-D acts as a donor to the solvent water oxygen O(25). Again O(25) interacts with another solvent, water oxygen O(26), and the nitrogen N(1) of the moiety-C acts as a donor to O(26). Another pyridine nitrogen N(2) of moiety-C acts as a donor to the carbonyl oxygen O(1) of moiety-A. Again a $R_2^2(10)$ dimeric ring is formed, and the repetition of mentioned interactions generates a loop-like structure (Figure 4.11). The bipyridine moiety-D connects two loops through N(5)–H(5)···O(8) interaction, forming a 2D box-like structure (Figure 4.12). Further, these 2D boxes are connected through C(20)–H(20)···O(12) interaction to generate a 3D box-like structure (Figure 4.12). Hence a sequential combination of these interactions helps to assemble 3D boxes propagating in the 2D plane for complex (**2**) (Figure 4.13).

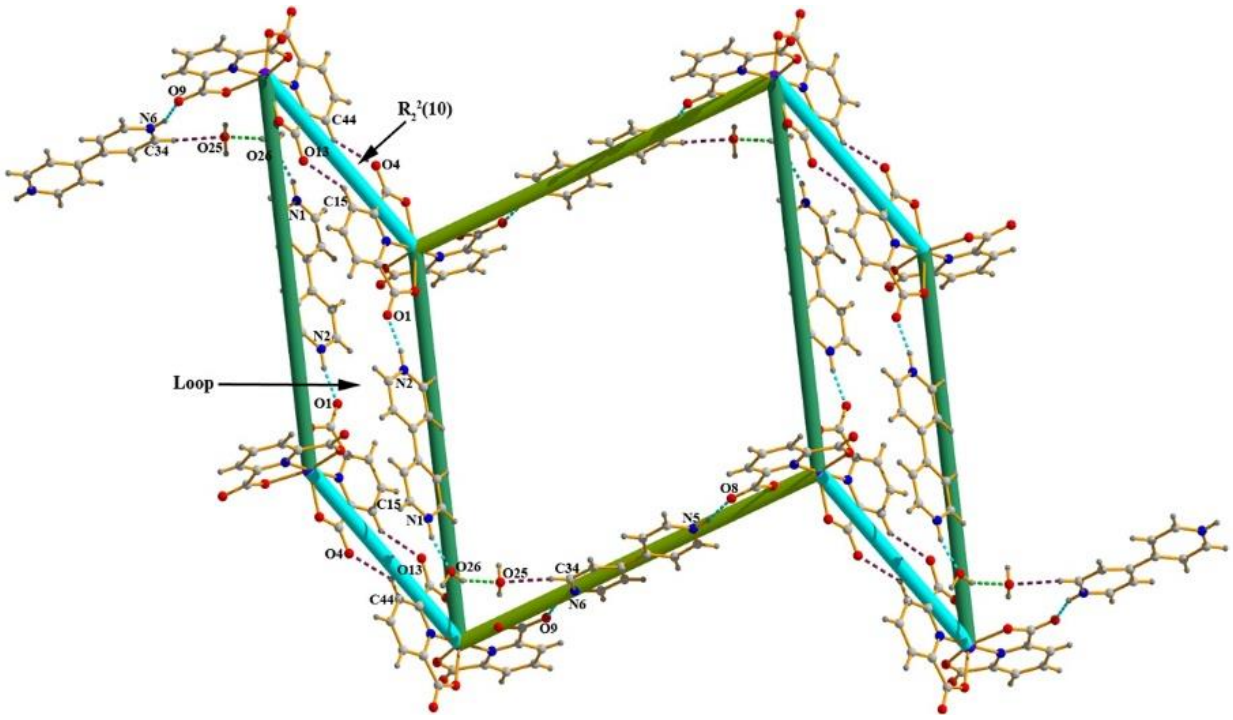

Figure 4.11. Two loops are connected through N–H···O interaction, forming 2D boxes.

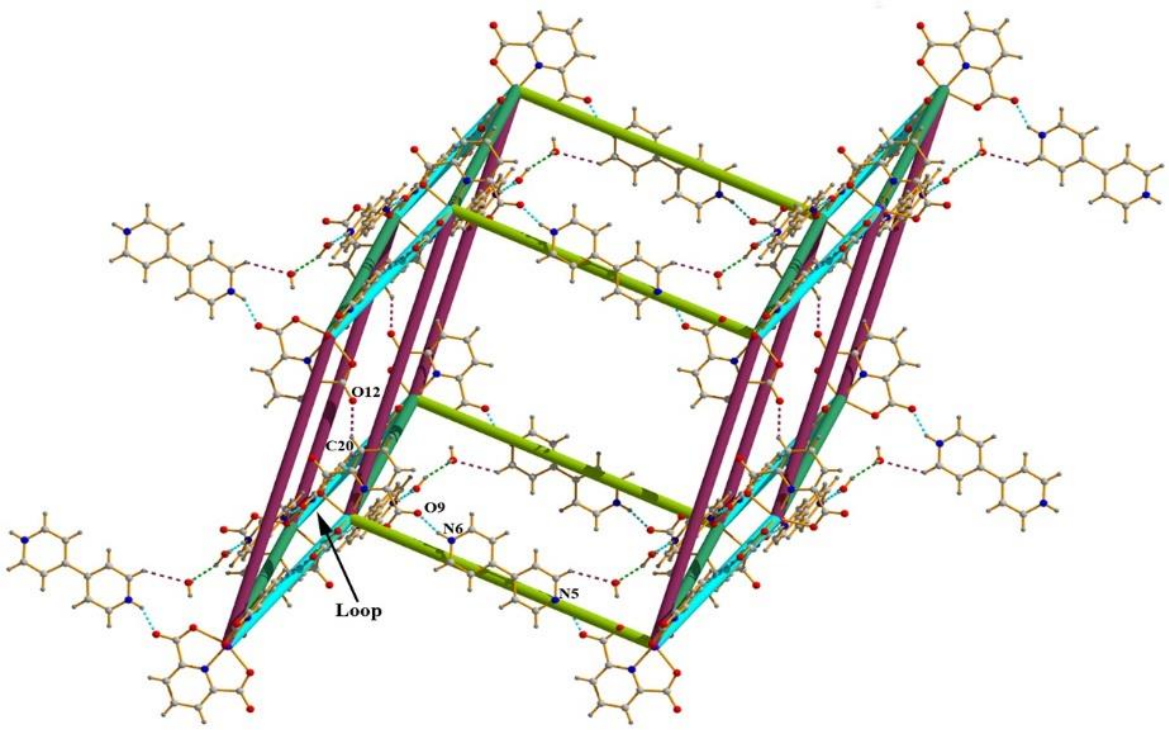

Figure 4.12. 2D boxes are connected through C–H···O interaction, forming 3D boxes.

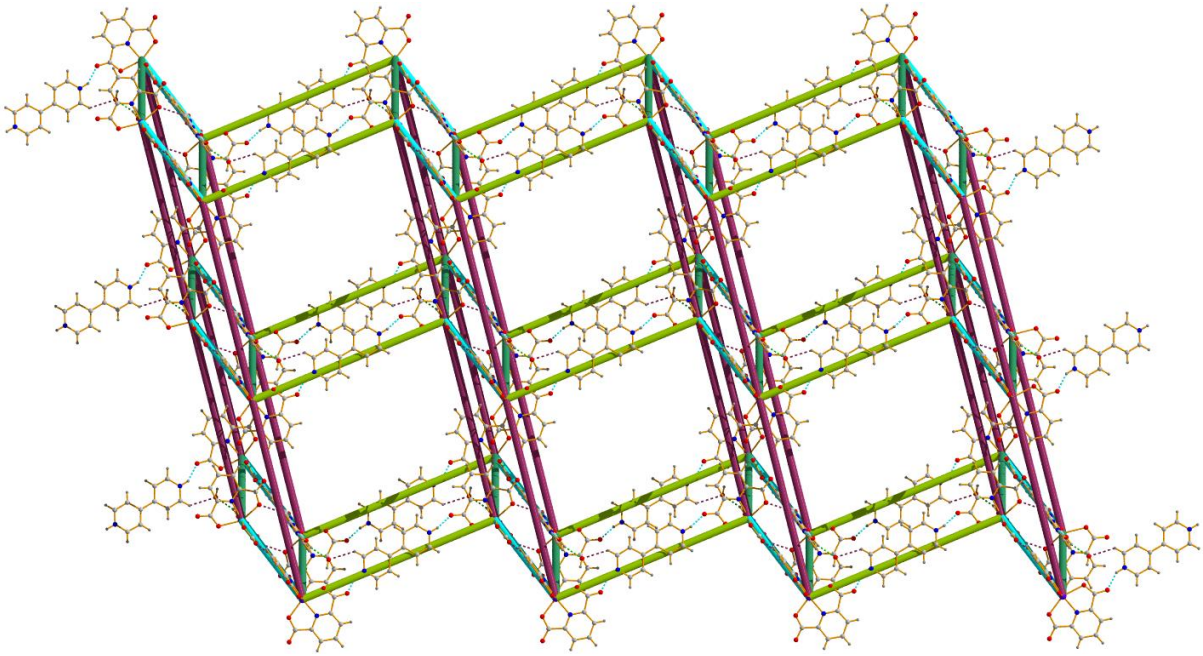

Figure 4.13. 3D boxes are propagating in the 2D plane for complex (**2**).

In another substructure of complex (2), the carbonyl oxygen O(12) of the acid moiety B interacts with the carbon atom C(20) through hydrogen bonding interaction, and again above mentioned $R_2^2(10)$ dimeric ring is formed. A combination of these interactions leads to the 1D chain of acid moieties. Two parallel chains of acid moiety are connected with the help of bi-pyridine moiety-D as the nitrogen atoms N(5) and N(6) of the bipyridine moiety-D act as a donor to the carbonyl oxygen O(8) of the acid moiety-A and O(9) of the acid moiety-B

respectively and generates the two-dimensional supramolecular structure of the complex (**2**) in (110) plane as shown in Figure 4.14.

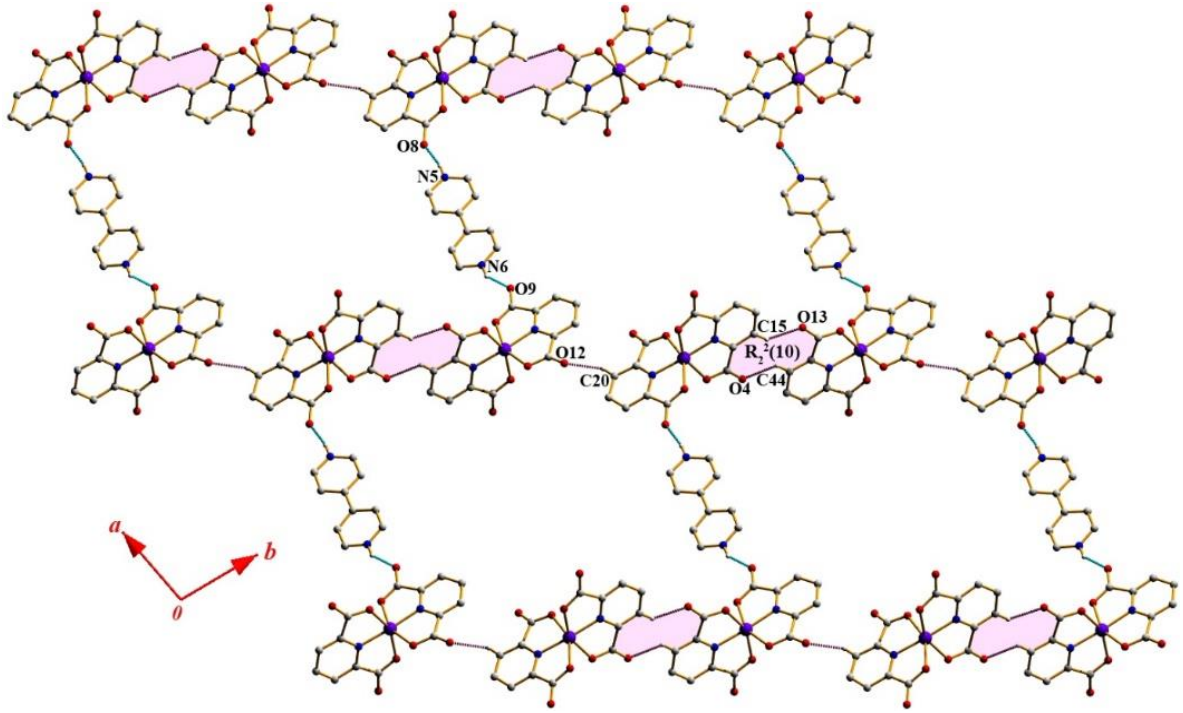

Figure 4.14. Two-dimensional supramolecular self-assembly for complex (**2**) generated through Hydrogen bonding interactions in (110) plane.

4.3.3. Theoretical Calculations

Bader's quantum theory of "Atoms in Molecules" (QTAIM) characterizes the noncovalent interactions involved in building supramolecular architectures. The models used herein are derived from the supramolecular assemblies. The topological parameters' values determine the nature of the interactions. The QTAIM models for complex (**1**) are depicted in Figure 4.15 (a, b, and c). A part of the self-assembled structure of Figure 4.7 (b or c) is used as a theoretical model to characterize both hydrogen bonding interactions and the interactions involving the pyridine rings in complex (**1**), which is depicted in Figure 4.15a. As expected, the calculated dissociation energy for O(5)–H(5B)···O(2) interaction (d, ρ_{BCP} = 0.0279 a.u) is maximum whereas, for the π···π interaction (a, ρ_{BCP} = 0.0027 a.u) it is minimum. From Table 4.6, it can be seen that lone pair···π interaction (c, ρ_{BCP} = 0.0049 a.u) is more favorable among the interactions involving the pyridine rings in complex (**1**), which is in agreement with X-ray structural studies. We have used a part of the self-assembled structure of Figure 4.6 as a theoretical model to characterize O–H···O hydrogen bonding interaction in complex (**1**) which is depicted in Figure 4.15b. This O(6)–H(6A)···O(3) hydrogen bonding interaction (e, ρ_{BCP} = 0.0336 a.u) has the highest dissociation energy among the noncovalent interactions involving in complex (**1**) (see Table 4.6). We have used a part of the self-assembled structure of the

centrosymmetric dimeric and tetrameric ring from Figure 4.5 as a theoretical model to characterize both C–H···O and O–H···O hydrogen bonding interactions in complex (**1**), which is shown in Figure 4.15c. It can be seen from Table 4.6 that O(7)–H(7A)···O(1) interaction (f, f′, ρ_{BCP} = 0.0247 a.u) is more favorable than O(7)–H(7B)···O(2) interaction (g, g′, ρ_{BCP} = 0.0154 a.u) for the construction of centrosymmetric tetrameric ring (Figure 4.15c). The C(5)–H(5)···O(3) interaction (h, h′, ρ_{BCP} = 0.0122 a.u) which is responsible for the generation of the centrosymmetric dimeric ring, is less favorable than O–H···O hydrogen bonding interactions, which is in agreement with X-ray structural studies. For complex (**2**), the QTAIM models are depicted in Figure 4.15(d–g). To characterize the extended (lone-pair···π/π···π^+/π^+···π/π···π/π···π^+/π^+···π/π···lone-pair)$_n$ network in complex (**2**), we have used a part of the self-assembled structure from Figure 4.9 as a theoretical model, which is depicted in Figure 4.15d. In this extended network model, the bond critical points and bond paths interconnecting the lone pair oxygen and the carbon atom of the pyridine ring represent and characterizes lone pair···π interactions (i, i′, ρ_{BCP} = 0.0045 a.u). Again, the bond critical points and bond paths denoted by (j, j′) and (k, k′) represents and characterizes π···π^+ interactions (ρ_{BCP} = 0.0044 a.u) and π^+···π interactions (ρ_{BCP} = 0.0047 a.u) respectively. In the middle portion of this model, the bond paths interconnecting the carbon atoms of the pyridine rings of acid moieties represent and characterize π···π interactions (l, l′, ρ_{BCP} = 0.0052 a.u). For complex (**2**), among the interactions involving aryl ring π···π staking interaction (l, l′) is more favorable due to higher ρ_{BCP} value (ρ_{BCP} = 0.0052 a.u) and hence higher dissociation energy (Table 4.6). Parts of the self-assembled structure of Figure 4.14 are used as theoretical models to characterize both C–H···O and N–H···O hydrogen bonding interactions in complex (**2**), which are depicted in Figure 4.15(e–g). For complex (**2**), C–H···O hydrogen bonding interactions are designated by m, n, and o, and C(20)–H(20)···O(12) (m) interaction (ρ_{BCP} = 0.0135 a.u) is more favorable among C–H···O interactions. The ρ_{BCP} value for N(5)–H(5)···O(8) (p) and N(6)–H(5)···O(9) is 0.0399 a.u and 0.0350 a.u respectively, indicating the former one is more favorable N–H···O hydrogen bonding interaction for complex (**2**).

Thus, by analyzing the topological parameters at (3, –1) BCPs of the noncovalent interactions, it is evident that N–H···O hydrogen bonding interactions are stronger as compared to O–H···O than C–H···O than the interactions involving aryl rings (Table 4.6), which also agree with the X-ray crystallographic study (Table 4.3, 4.4 and 4.5). Further, $\nabla^2(\rho_{BCP})$ is positive for all the interactions, which indicates that all the interactions are closed-shell type [45, 46].

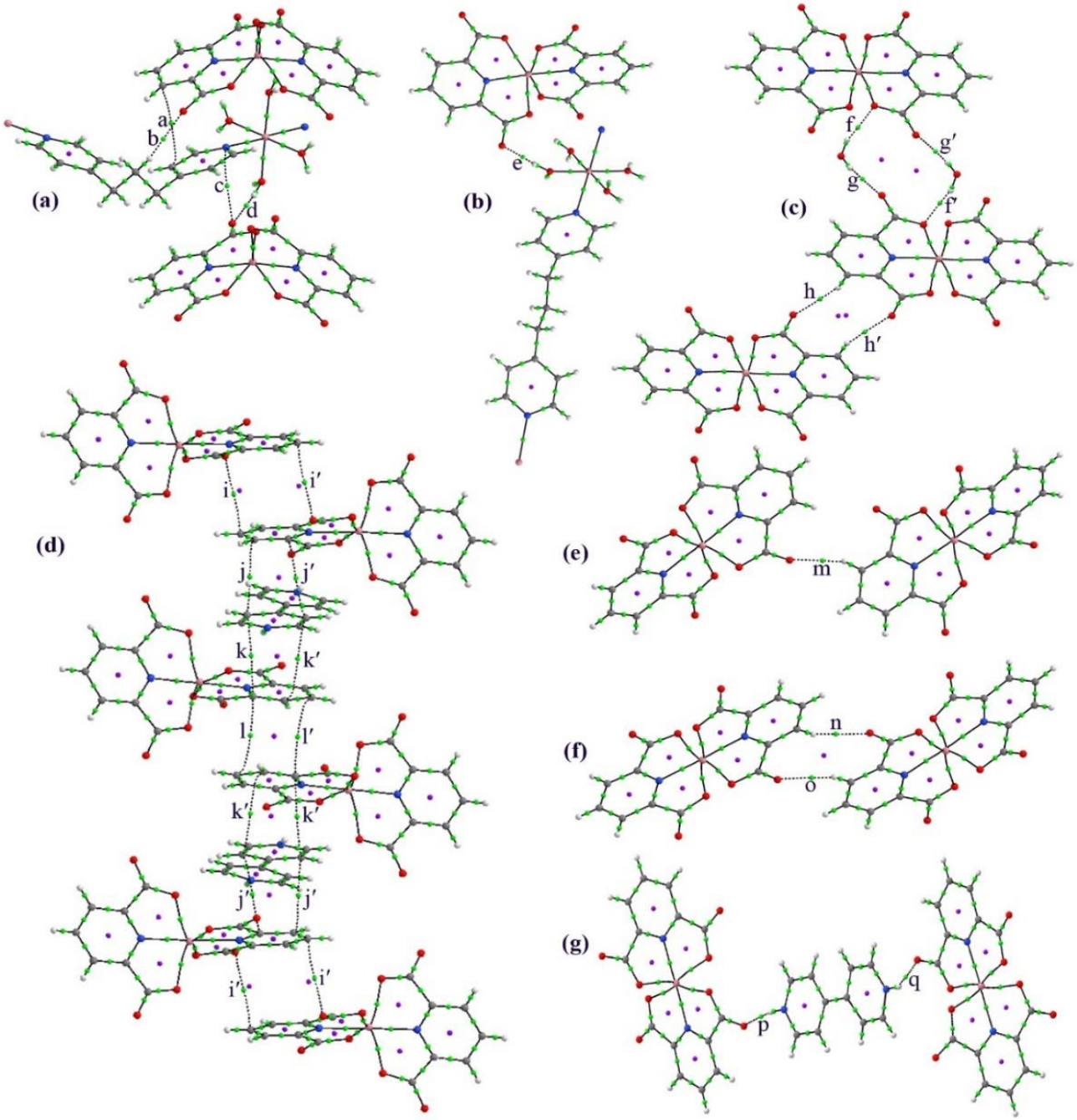

Figure 4.15. QTAIM analyses of (**1**) (a, b, and c) and (**2**) (d, e, f, and g). Green and violet spheres are bond critical points (BCPs) and ring critical points (RCPs), respectively.

Table 4.6. Detailed QTAIM topological parameters at BCPs.

Interaction	$\boldsymbol{\rho_{BCP}}$**(a.u)**	$\boldsymbol{\nabla^2\rho_{BCP}}$**(a.u**	$\boldsymbol{V_{BCP}}$**(a.u)**	$\boldsymbol{D.E_{int}}$ **(kcal/mol)**
Complex (1)				
(a) π···π	0.0027	0.0079	–0.0012	0.376
(b) C(14)–H(14A)···O(3)	0.0085	0.0321	–0.0057	1.788
(c) lone pair···π	0.0049	0.0182	–0.0033	1.035

(d) O(5)–H(5B)···O(2)	0.0279	0.1056	–0.0259	8.126
(e) O(6)–H(6A)···O(3)	0.0336	0.1231	–0.0316	9.915
(f, f′) O(7)–H(7A)···O(1)	0.0247	0.0937	–0.0235	7.373
(g, g′) O(7)–H(7B)···O(2)	0.0154	0.0574	–0.0134	4.204
(h, h′) C(5)–H(5)···O(3)	0.0122	0.0456	–0.0091	2.855
Complex (2)				
(i, i′) lone pair···π	0.0045	0.0152	-0.0023	0.722
(j, j′) $\pi\cdots\pi^{+}$	0.0044	0.0132	–0.0021	0.659
(k, k′) $\pi^{+}\cdots\pi$	0.0047	0.0127	–0.0020	0.628
(l, l′) π···π	0.0052	0.0152	–0.0024	0.753
(m) C(20)–H(20)···O(12)	0.0135	0.0525	–0.0028	3.294
(n) C(15)–H(15)···O(13)	0.0114	0.0420	–0.0083	2.604
(o) C(44)–H(44)···O(4)	0.0114	0.0431	–0.0083	2.604
(p) N(5)–H(5)···O(8)	0.0399	0.1623	–0.0379	11.891
(q) N(6)–H(5)···O(9)	0.0350	0.1401	–0.0327	10.259

Further, the noncovalent interactions that are involved in forming supramolecular frameworks are analyzed through NCI Plot Index. NCI Plot generally exhibits blue-green isosurfaces for indicating noncovalent interactions. Blue isosurfaces indicate strong noncovalent interactions, whereas green isosurfaces indicate comparatively weak noncovalent interactions. We have used the same theoretical models for NCI Plot Index. For complex (**1**), weak π···π and lone pair···π interactions are indicated by flat green isosurfaces (Figure 4.16a), C–H···O interactions are indicated by small green isosurfaces (Figure 4.16 a, c), and O–H···O interactions are indicated by both green and blue isosurfaces, as O–H···O interactions are comparatively strong hydrogen bond interaction (Figure 4.16 a, b and c). For complex (**2**), noncovalent interactions involving aryl rings are indicated by flat green isosurfaces (Figure 4.16d). As expected, small green isosurfaces indicate C–H···O interactions (Figure 4.16 e, f). Strong N–H···O interactions are indicated by small blue isosurfaces (Figure 4.16g).

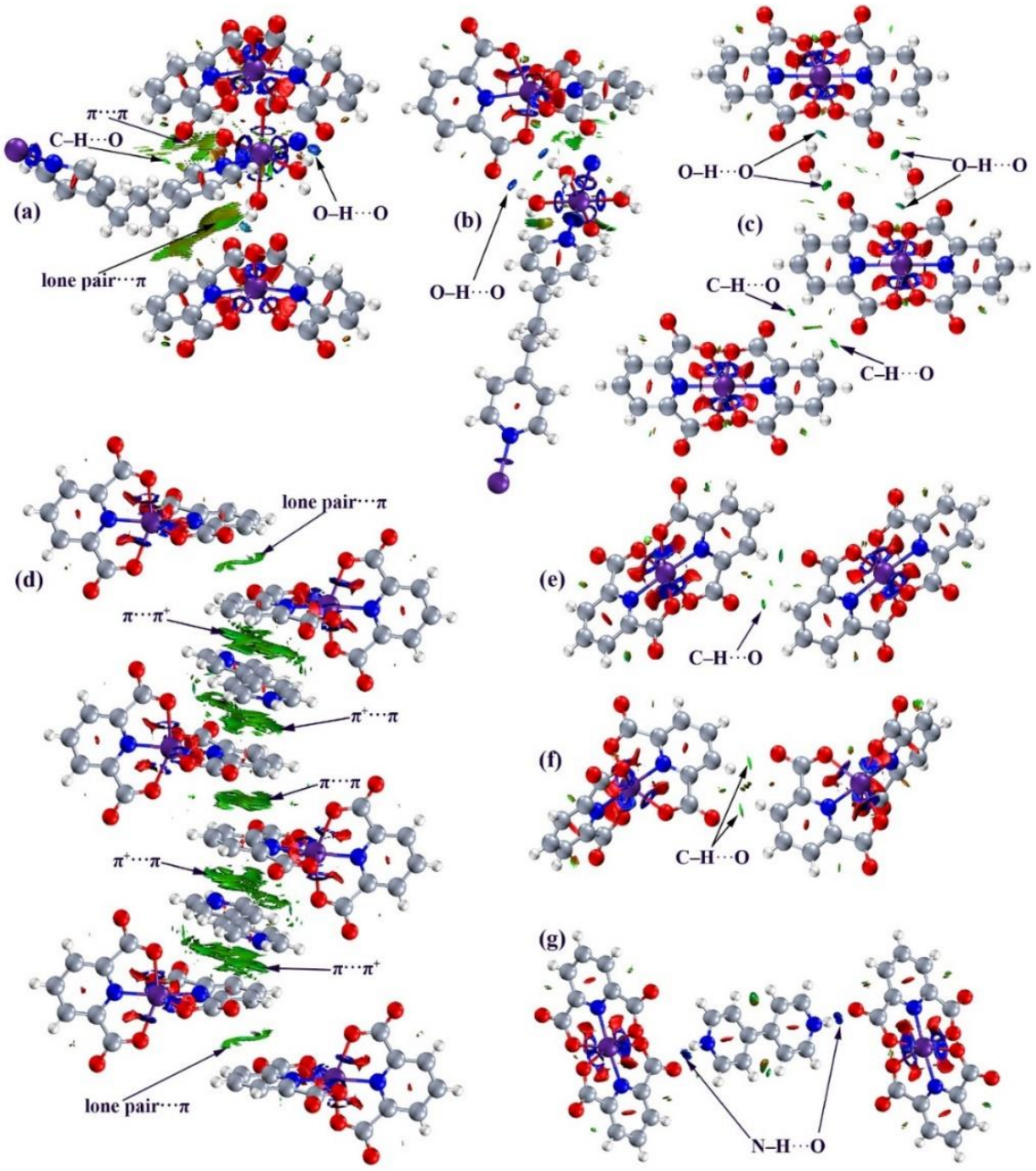

Figure 4.16. NCI plot index of the modeled structure of (**1**) (a, b, and c) and (**2**) (d, e, f, and g).

In RDG (Reduced Density Gradient) vs. sign (λ_2)ρ scatter plots (where λ_2 is the second eigenvalue of third-ordered Hessian's matrix), the blue and green downward spikes indicate strong and weak noncovalent interactions, respectively (Figure 4.17). We have used the same models also for scatter plots (models a, b, and c for (**1**) whereas d, e, f, and g for (**2**)). For example, in Figure 4.17a, the greenish blue spike indicates O–H···O hydrogen bonding interactions, while other green spikes are because of C–H···O and the weak aryl ring interactions. In Figures 4.17b and g, the deep blue spikes indicate strong hydrogen bonding interactions (N–H···O and O–H···O). Other green spikes indicate lone pair···π, π···π^+, π^+···π,

π···π, etc. interactions (Figure 4.17). The isosurfaces in NCI plots and the spikes in RDG scatter plots agree with X-ray structural studies and QTAIM Studies.

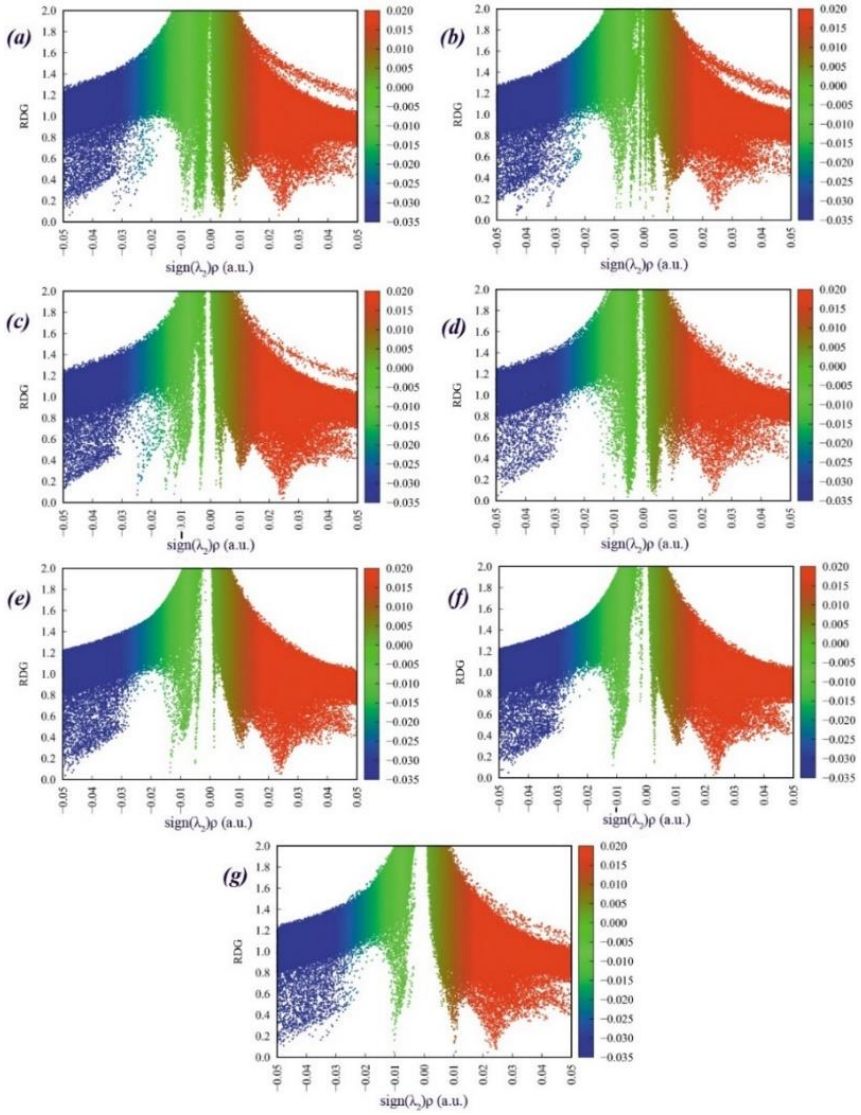

Figure 4.17. RDG vs. sign (λ_2)ρ scatter plots of (**1**) (a, b and c) and (**2**) (d, e, f and g).

4.3.4. Optical Characterization

The optical properties of our synthesized complexes were determined by UV−Vis spectroscopy. We prepared 10 ml of 10^{-4}(M) solution for each complex by dissolving both complexes separately in N,N–dimethylformamide (purity 99.8%). From optical absorption spectra, the optical band gap can be calculated by the famous Tauc's equation:

$$(\alpha h\nu) = A(h\nu - E_g)^n, \qquad (1)$$

Where α is the absorption coefficient, h is Planck's constant, ν is the frequency of incident radiation, E_g is band gap energy, and A is an arbitrary constant and is considered as 1 for the ideal case (depends on temperature, photo energy, and phonon energy). Here for the allowed direct band gap, n=1/2, and the allowed indirect band gap, n=2.

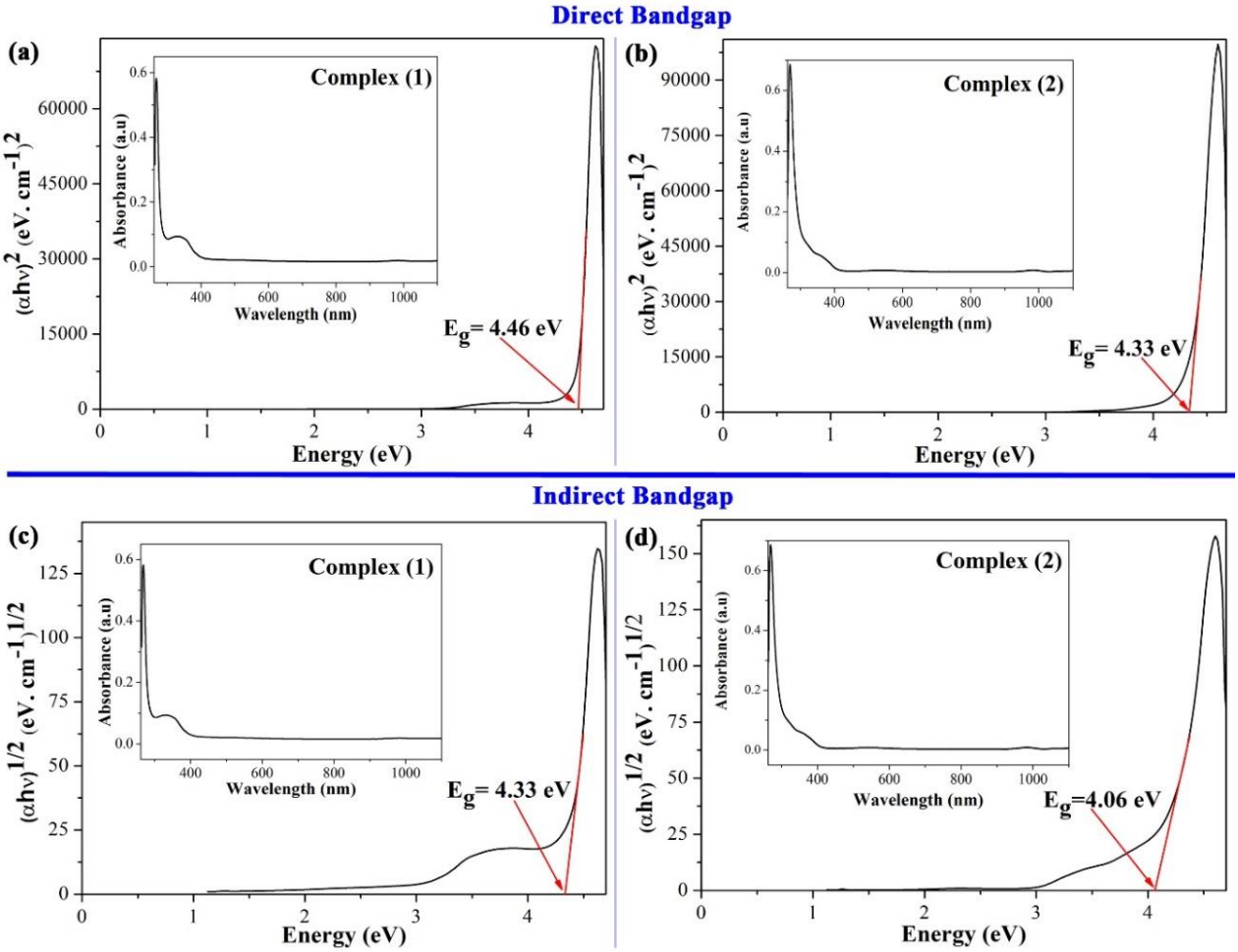

Figure 4.18. Tauc's plots to estimate the band gap of the title complexes. (a) Direct band gap of **1**; (b) Direct band gap of **2**; (c) Indirect band gap of **1**; (d) Indirect band gap of **2**.

Tauc's equation (1) shows that when α becomes zero, the band gap energy is hν. Allowed direct band gap can be obtained from $(\alpha h\nu)^2$ vs energy graph, and for complex (**1**) and (**2**) calculated allowed direct band gap energy is 4.46 eV and 4.33 eV, respectively (Figure 4.18 a and b). Allowed indirect band gap can be obtained from $(\alpha h\nu)^{1/2}$ vs. energy graph, and for complex (**1**) and (**2**), calculated allowed indirect band gap energy is 4.33 eV and 4.06 eV, respectively (Figure 4.18 c and d). Therefore, it is expected from the results that complex (**2**) shows better semiconducting behavior than complex (**1**), and their band gaps are within the range of wide band gap semiconductors [47].

4.4. Conclusions

The crystal structures of two new Co(II)-PDA complexes (**1**-**2**) have been determined by solving the structures from single crystal X-ray diffraction data. We have explored a three-dimensional network for (**1**) constructed by weak lone pair···π/π···π interactions. In the case of complex (**2**), we have explored a rare extended (lone

pair···π/π···π^+/π^+···π/π···π/π···π^+/π^+···π/π···lone pair)$_n$ self-assembled network. Bader's quantum theory of atoms in molecules (QTAIM) further characterizes noncovalent interactions from single-crystal X-ray diffraction data. Topological analysis of QTAIM revealed that all the interactions involved in constructing self-assembled networks are closed-shell interactions. Furthermore, the theoretical NCI plot index and scatter plots characterize noncovalent interactions. All the theoretical results agree well with the experimental findings. The results reported herein might help in understanding the supramolecular aggregation in accordance with hydrogen bonds, lone pair···π, π···π, π···π^+, π^+···π, etc. Optical characterization of the compounds revealed that their band gaps are within the range of wide band gap semiconductors. Electrical properties need to be studied to establish the structure-property relationship.

4.5. References

[1] X.Y. Li, Q.P. Kang, L.Z. Liu, J.C. Ma, W.K. Dong, Trinuclear Co(II) and Mononuclear Ni(II) Salamo-Type Bisoxime Coordination Compounds, Crystals 8 (2018) 43.

[2] L.P. Tang, L.M. Tang, D. Wang, H.X. Deng, K.Q. Chen, Metal and ligand effects on the stability and electronic properties of crystalline two-dimensional metal-benzenehexathiolate coordination compounds, J. Phys. Condens. Matter. 30 (2018) 465301.

[3] J. Gu, M. Wen, Y. Cai, Z. Shi, D.S. Nesterov, M.V. Kirillova, A.M. Kirillov, Cobalt(II) Coordination Polymers Assembled from Unexplored Pyridine-Carboxylic Acids: Structural Diversity and Catalytic Oxidation of Alcohols, Inorg. Chem. 58 (2019) 5875–5885.

[4] L.H. Abdel-Rahman, A.A. Abdelhamid, A.M. Abu-Dief, M.R. Shehata, M.A. Bakheet, Facile synthesis, X-Ray structure of new multi-substituted aryl imidazole ligand, biological screening and DNA binding of its Cr (III), Fe (III) and Cu (II) coordination compounds as potential antibiotic and anticancer drugs, J. Mol. Struct. 1200 (2020) 127034.

[5] T.R. Cook, Y.R. Zheng, P.J. Stang, Metal–Organic Frameworks and Self-Assembled Supramolecular Coordination Complexes: Comparing and Contrasting the Design, Synthesis, and Functionality of Metal–Organic Materials, Chem. Rev. 113 (2013) 734–777.

[6] S. Tripathi, A. Hossain, S.K. Seth, S. Mukhopadhyay, Quantitative insights into the crystal structure of a mixed-ligand Co (III) complex: Experimental and theoretical studies, J. Mol. Struct. 1216 (2020) 128207.

[7] S.K. Seth, Tuning the formation of MOFs by pH influence: X-ray structural variations and Hirshfeld surface analyses of 2-amino-5-nitropyridine with cadmium chloride†, CrystEngComm 15 (2013) 1772–1781.

[8] F. Yuan, J. Xie, H.M. Hu, C.M. Yuan, B. Xu, M.L. Yang, F.X. Dong, G.L. Xue, Effect of pH/metal ion on the structure of metal–organic frameworks based on novel bifunctionalized ligand 4′-carboxy-4,2′:6′,4″-terpyridine†, CrystEngComm 15 (2013) 1460–1467.

[9] S. Islam, S. Tripathi, A. Hossain, S.K. Seth, S. Mukhopadhyay, pH-induced structural variations of two new Mg (II)-PDA complexes: experimental and theoretical studies, J. Mol. Struct. 1262 (2022) 133373.

[10] H.R. Khavasi, B.M. Mohammad Sadegh, Temperature-Dependent Supramolecular Motif in Coordination Compounds, Inorg. Chem. 49 (2010) 5356–5358.

[11] C. Yenikaya, M. Poyraz, M. Sarı, F. Demirci, H. İlkimen, O. Büyükgüngör, Synthesis, characterization and biological evaluation of a novel Cu (II) complex with the mixed ligands 2, 6-pyridinedicarboxylic acid and 2-aminopyridine, Polyhedron 28 (2009) 3526–3532.

[12] L. Wang, M. Yang, G. Li, Z. Shi, S. Feng, Hydrothermal synthesis and characterization of a new three-dimensional hybrid zinc phosphate $[Zn_2(HPO_4)_2(4,4'\text{-bipy})]\cdot 3H_2O$ with neutral porous framework, J. Solid State Chem. 179 (2006) 156–160.

[13] L. Hu, J. Fan, C. Slebodnick, B.E. Hanson, Structural Diversity in 4,4‘-Trimethylenedipyridine−zinc phosphite Hybrids: Incorporation of Neutral Guest Molecules in Hybrid Materials, Inorg. Chem. 45 (2006) 7681–7688.

[14] F.A. Almeida Paz, J. Klinowski, Two- and Three-Dimensional Cadmium−Organic Frameworks with Trimesic Acid and 4,4‘-Trimethylenedipyridine, Inorg. Chem. 43 (2004) 3882–3893.

[15] D. Kong, J. Zoñ, J. McBee, A. Clearfield, Rational Design and Synthesis of Porous Organic−Inorganic Hybrid Frameworks Constructed by 1,3,5-Benzenetriphosphonic Acid and Pyridine Synthons, Inorg. Chem. 45 (2006) 977–986.

[16] G.R. Desiraju, Crystal Engineering: From Molecule to Crystal, J. Am. Chem. Soc. 135 (2013) 9952–9967.

[17] S.K. Seth, D. Sarkar, T. Kar, Use of π–π forces to steer the assembly of chromone derivatives into hydrogen bonded supramolecular layers: crystal structures and Hirshfeld surface analyses†, CrystEngComm 13 (2011) 4528–4535.

[18] A. Hossain, A. Dey, S. K. Seth, P. P. Ray, J. Ortega-Castro, A. Frontera, S. Mukhopadhyay, Anion-dependent structural variations and charge transport property analysis of 4′-(3-pyridyl)-4,2′:6′,4″-terpyridinium salts†, CrystEngComm 23 (2021) 3569–3581.

[19] S. Ghosh, S. Islam, S. Pramanik, S.K. Seth, Structural elucidation of phenoxybenzaldehyde derivatives from laboratory powder X-ray diffraction: A combined experimental and theoretical quantum mechanical study, J. Mol. Struct. 1268 (2022) 133697.

[20] S.K. Seth, I. Saha, C. Estarellas, A. Frontera, T. Kar, S. Mukhopadhyay, Supramolecular Self-Assembly of M-IDA Complexes Involving Lone-Pair···π Interactions: Crystal Structures, Hirshfeld Surface Analysis, and DFT Calculations [H_2IDA = iminodiacetic acid, M = Cu(II), Ni(II)], Cryst. Growth Des. 11 (2011) 3250–3265.

[21] S.K. Seth, The Importance of CH···X (X = O, π) Interaction of a New Mixed Ligand Cu(II) Coordination Polymer: Structure, Hirshfeld Surface and Theoretical Studies, Crystals 8 (2018) 455.

[22] P. Das, S. Islam, D. Das, P.P. Ray, S.K. Seth, Intriguing π-interactions involving aromatic neutrals, aromatic cations and semiconducting behavior in a pyridinium-carboxylate salt, J. Mol. Struct. 1284 (2023) 135326.

[23] A. Bauzá, S.K. Seth, A. Frontera, Molecular electrostatic potential and "atoms-in-molecules" analyses of the interplay between π-hole and lone pair···π/X–H···π/metal···π interactions, J. Comput. Chem. 39 (2018) 458–463.

[24] S. Tripathi, S. Islam, S.K. Seth, A. Bauzá, A. Frontera, S. Mukhopadhyay, Supramolecular assemblies involving salt bridges: DFT and X-ray evidence of bipolarity†, CrystEngComm 22 (2020) 8171–8181.

[25] S. Islam, P. Das, S. Tripathi, S. Mukhopadhyay, S.K. Seth, Exploring Solid-State Supramolecular Architectures of Penta (carboxymethyl) diethylenetriamine: Experimental Observation and Theoretical Studies, ChemistrySelect 7 (2022) e202203396.

[26] R.F.W. Bader, A Quantum Theory of Molecular Structure and Its Applications, Chem. Rev. 91 (1991) 893–928.

[27] R.F.W. Bader, Atoms in Molecules, a Quantum Theory; Oxford University Press: New York, NY, USA, 1990.

[28] J. Contreras-García, E.R. Johnson, S. Keinan, R. Chaudret, J.P. Piquemal, D.N. Beratan, W. Yang, NCIPLOT: A Program for Plotting Noncovalent Interaction Regions, J. Chem. Theory Comput. 7 (2011) 625–632.

[29] E.R. Johnson, S. Keinan, P. Mori-Sanchez, J. Contreras-Garcia, A.J. Cohen, W. Yang, Revealing Noncovalent Interactions, J. Am. Chem. Soc. 132 (2010) 6498–6506.

[30] J. Tauc, R. Grigorovici, A. Vancu, Optical properties and electronic structure of amorphous germanium, Phys. Status Solidi B 15 (1966) 627–637.

[31] BrukerSAINT, version 8.34A, Bruker AXS Inc., Madison, Wisconsin, USA, 2013.

[32] BrukerSMART, Version 5.625 and SADABS, Version 2.03a, Bruker AXS Inc., Madison, Wisconsin, USA, 2001.

[33] G.M. Sheldrick, SHELXT–Integrated space-group and crystal-structure determination, Acta Crystallogr. A 71 (2015) 3–8.

[34] G.M. Sheldrick, Crystal structure refinement with *SHELXL*, Acta Cryst. C 71 (2015) 3–8.

[35] L.J. Farrugia, *WinGX* and *ORTEP* for Windows: An Update, J. Appl. Cryst. 45 (2012) 849−854.

[36] O.V. Dolomanov, L.J. Bourhis, R.J. Gildea, J.A. Howard, H. Puschmann, OLEX2: a complete structure solution, refinement and analysis program, J. Appl. Crystallogr. 42 (2009) 339−341.

[37] A.L. Spek, Single-crystal structure validation with the program PLATON, J. Appl. Crystallogr. 36 (2003) 7–13.

[38] M. J. Frisch, G. W. Trucks, H. B. Schlegel, G. E. Scuseria, M. A. Robb, J. R. Cheeseman, G. Scalmani, V. Barone, G. A. Petersson, H. Nakatsuji, X. Li, M. Caricato, A. V. Marenich, J. Bloino, B. G. Janesko, R. Gomperts, B. Mennucci, H. P. Hratchian, J. V. Ortiz, A. F. Izmaylov, J. L. Sonnenberg, D. Williams-Young, F. Ding, F. Lipparini, F. Egidi, J. Goings, B. Peng, A. Petrone, T. Henderson, D. Ranasinghe, V. G. Zakrzewski, J. Gao, N. Rega, G. Zheng, W. Liang, M. Hada, M. Ehara, K. Toyota, R. Fukuda, J. Hasegawa, M. Ishida, T. Nakajima, Y. Honda, O. Kitao, H. Nakai, T. Vreven, K. Throssell, J. A. Montgomery Jr., J. E. Peralta, F. Ogliaro, M. J. Bearpark, J. J. Heyd, E. N. Brothers, K. N. Kudin, V. N. Staroverov, T. A. Keith, R. Kobayashi, J. Normand, K. Raghavachari, A. P. Rendell, J. C. Burant, S. S. Iyengar, J. Tomasi, M. Cossi, J. M. Millam, M. Klene, C. Adamo, R. Cammi, J. W. Ochterski, R. L. Martin, K. Morokuma, O. Farkas, J. B. Foresman, D. J. Fox, Gaussian 16, Revision C.01, Gaussian, Inc., Wallingford, CT, 2016.

[39] T.A. Keith, AIMAll (version 13.05.06), TK Gristmill Software, Overland Park, KS, USA, 2013.

[40] R. Hilal, S.G. Aziz, A.O.Alyoubi, S. Elroby, Quantum topology of the charge density of chemical bonds. QTAIM analysis of the C-Br and O-Br bonds, Procedia Comput. Sci. 51 (2015) 1872–1877.

[41] A. Hocquet, Intramolecular hydrogen bonding in 2′-deoxyribonucleosides: an AIM topological study of the electronic density, Phys. Chem. Chem. Phys. 3 (2001) 3192–3199.

[42] C. Lepetit, M.L. Kahn, QTAIM and ELF topological analyses of zinc-amido complexes, Res. Chem. Intermed. 47 (2021) 377–395.

[43] T. Lu, F. Chen, Multiwfn: a multifunctional wavefunction analyser, J. Comput. Chem. 33 (2012) 580–592.

[44] W. Humphrey, A. Dalke, K. Schulten, VMD: visual molecular dynamics, J. Mol. Graph. 14 (1996) 33–38.

[45] C. Gatti, Chemical bonding in crystals: new directions, Z. Kristallogr. Cryst. Mater. 220 (2005) 399–457.

[46] P. Dhanishta, S.K. Mishra, N. Suryaprakash,. Intramolecular HB interactions evidenced in dibenzoyl oxalamide derivatives: NMR, QTAIM, and NCI Studies, J. Phys. Chem. A, 122 (2018) 199–208.

[47] J. H. Edgar, Prospects for device implementation of wide band gap semiconductors, J. Mater. Res. 7 (1992) 235–252.

CHAPTER 5

Quantitative investigations of intermolecular interactions in 2-amino-3-nitropyridine polymorphs: Inputs from quantum mechanical calculations

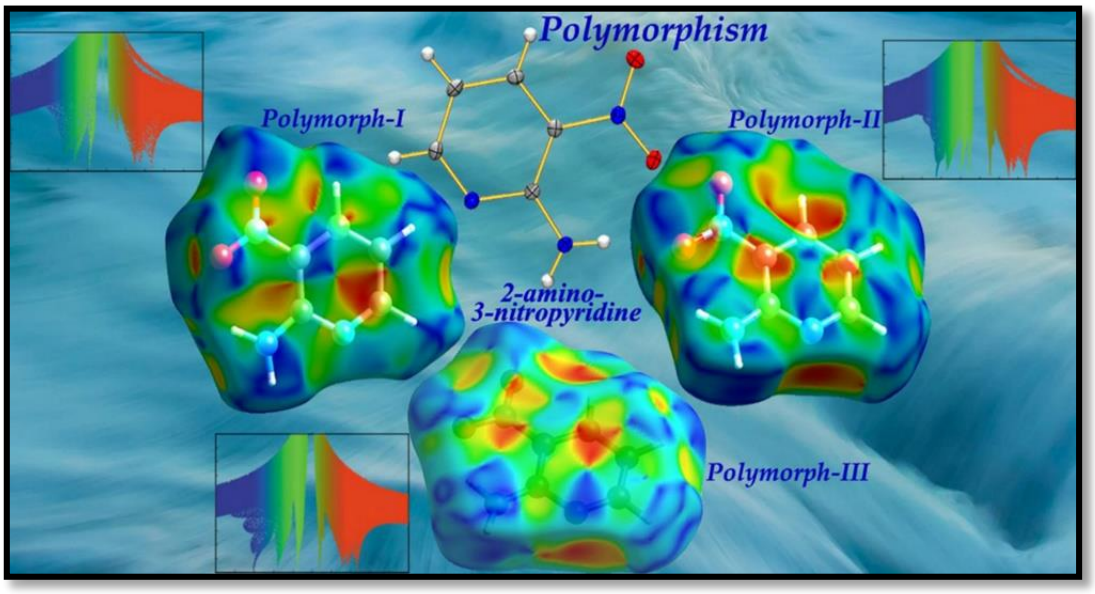

Published in: ***Journal of Molecular Structure*** **1293 (2023) 136253**

5.1. Introduction

Polymorphism [1, 2] has attracted intense attention, and significant progress has been achieved in the last decades in understanding their fascinating structures and valuable properties, such as solubility, stability, dissolution rates, mechanical strength, bioactivity etc [1, 3−5]. Polymorphism is the ability of a compound to exist in at least two or more crystalline forms, resulting from various packing arrangements of its molecules in the crystal; therefore, studies concerning polymorphism are crucial for developing any solid material [6]. Polymorphism mainly attracts greater attention in chemistry, pharmaceutical, and material science [4, 5] mainly due to two reasons [7−9] – (i) their physiochemical properties and (ii) polymorphs can often be protected by a patent and therefore are crucial economic importance [10]. The polymorphs are classified into two categories depending on the geometry of molecular assembly – (i) conformational polymorphism [11] and (ii) packing polymorphism [12]. In the case of conformational polymorphism, identical molecular moieties may be packed in different molecular conformations with different modifications. In packing polymorphism, identical molecular moieties might be packed in different periodic structures, which provides an opportunity to investigate and understand the intermolecular interactions in building solid-state structures.

The subject of why we do not witness more polymorphs has frequently been raised with the development of crystal structure prediction (CSP) with a specific application [13–14]. Studies using CSP have been very effective in determining the organic structures with the lowest energy forms [14]. Understanding the nature of intermolecular interactions during the formation of molecular packing can be done owing to the existence of polymorphs. In recent years, robust synthons, advocates for supramolecular synthons developed by Desiraju, and energetically-favored patterns of hydrogen bonds have been used to address the understanding of polymorphism in terms of molecular organization [2]. When functional groups are present in a molecule, they are utilized for crystallization processes such as molecular recognition and self-assembly. In a recent review, Cruz-Cabeza et al. showed that there may be no relationship at all between polymorphism and molecular structural components [15]. Therefore, it is still unclear how polymorphism and molecular structure are related [16–18]. More specifically, it is currently unclear how and why non-hydrogen bonding compounds crystallize as polymorphic forms.

In this context, a variety of attempts have been used to understand and envisage the final crystal structure, such as – (a) the model to reduce structure into small molecular clusters

and calculation of lattice energies [19]; (b) another model for the formation of a molecular structure depending on strong hydrogen bonds [20]; (c) next model based on supramolecular synthons based on a particular type of interactions [21]; (d) another method based on molecular electrostatic potentials to quantify intermolecular interactions through the estimation of relative hydrogen bonding parameters of the functional groups [22] and (e) Hirshfeld surface [23−25] based tools which represents a novel approach to quantify all intermolecular interactions involved within the crystal in a novel visual manner. The derivation of the Hirshfeld surface is an interpretable visualizing plot of the investigated molecule within its environment, and the decomposition of the surface provides a 2D fingerprint plot [26] to analyze the entire distribution of intermolecular interactions involved in the structure.

Pyridinamines act as important intermediates with several applications in the chemical industry and pharmaceutical products [27]. Pyridine also serves as the building block of polymers with unique physical properties [28]. The nitrogen atom of the pyridine ring in 2-Amino-3-Nitropyridine acts as a cationic binding site where the nitro group acts as a hydrogen acceptor and the amino group as a donor. This electron donating and accepting moieties attached to a conjugated system often induce non-linear optical NLO character [29].

In this paper, we have explored the polymorphs of "2-amino-3-nitropyridine" by comparing their molecular packing, including a detailed assessment of intermolecular interactions through Hirshfeld surface analysis [23−26] as well as various theoretical studies such as theoretical DFT calculation [30], PIXEL method [31], Bader's theory of "Atoms in molecule" [32], and 'Noncovalent interaction' (NCI) plot index [33]. The quantitative analysis of the strength and nature of noncovalent interactions, including the lattice energies have been explored through PIXEL calculation.

5.2. Experimental Sections

5.2.1. Crystallization of Form–I and Form-II

Crystals of **Form–I** suitable for single-crystal X-ray diffraction were obtained upon co-crystallizing 2,6-pyridine-dicarboxylic acid (PDA) with 2-amino-3-nitropyridine. The equivalent amount of PDA and conformer 2-amino-3-nitropyridine were taken into a 50 mL flask and dissolved in methanol/water in a 2:1 molar ratio. Then, the mixture was refluxed for 1 h. The resulting homogeneous solution was kept undisturbed at ambient temperature and covered with paraffin film, and a few small holes were made to evaporate the solvent slowly. The two different forms of the conformer were crystallized with two distinctly different crystal habits, *viz*., colorless needles in bunches and yellow plates along the sides that were separated

manually. The majority of the crystals in the flask (colorless needles) matched with the PDA molecule [34], while very few crystals (yellow plates) were designated as polymorphic **Form–I** of 2-amino-3-nitropyridine. Due to insufficient samples, current studies on **Form–I** was limited to only single-crystal X-ray diffraction and theoretical calculations. The same procedure was followed to grow single crystals of 2-amino-3-nitropyridine (**Form–II**) by using malonic acid as a conformer.

5.2.2. Crystallographic Analysis

Single crystal X-ray diffraction intensity data of the title compounds were collected at 120(2) K using a Bruker APEX-II CCD diffractometer equipped with graphite monochromated MoKα radiation (λ = 0.71073 Å). Data reduction was carried out using the program Bruker SAINT [35]. An absorption correction based on the multi-scan method [36] was applied. The structures of the title compounds were solved by direct methods and refined by the full-matrix least-square technique on F^2 with anisotropic thermal parameters to describe the thermal motions of all nonhydrogen atoms using the programs SHELXS97 and SHELXL97 [37], respectively. All hydrogen atoms were located from difference Fourier maps and treated as riding. All the calculations were performed using the PLATON [38] program of the WinGX suite [39]. Crystallographic data (excluding structure factors) for the structures reported in this article have been deposited with the Cambridge Crystallographic Data Centre as supplementary publication numbers CCDC 1033932 and 1033933 for the polymorphic **Form–I** and **Form–II** respectively. Table 5.1 contains the crystal data and refinement parameters of grown polymorphs (**Form–I** and **Form–II)** along with previously reported **Form–I (**CSD ref code AMNTPY) [40] and **Form–II (**CSD ref code AMNTPY01) [41] as well as **Form–III (**CSD ref code AMNTPY02) [41]. The simulated PXRD peak of the polymorphs is included in Figure 5.1.

Table 5.1. Crystal data and structure refinement parameters for the title polymorphs.

Structure	**Form−I***	**Form−I[#1]**	**Form−II***	**Form−II[#2]**	**Form−III [#3]**
Empirical formula	$C_5H_5N_3O_2$	$C_5H_5N_3O_2$	$C_5H_5N_3O_2$	$C_5H_5N_3O_2$	$C_5H_5N_3O_2$
Formula Weight	139.12	139.12	139.12	139.12	139.12
Temperature (K)	120(2)	295	120(2)	153	173
Wavelength (Å)	0.71073	–	0.71073	–	–
Crystal system	Monoclinic	Monoclinic	Monoclinic	Monoclinic	Monoclinic
space group	$P2_1/c$	$P2_1/n$	$P2_1/c$	$P2_1/c$	$P2_1/n$

a, b, c (Å)	8.518(2), 4.928(2), 14.429(3)	8.743(1) 4.898(1) 14.473(1)	4.9026(6), 6.9198(7), 17.412(2)	4.917(1) 6.940(2) 17.507(3)	3.737(2) 7.445(2) 20.974(6)
α, β, γ (°)	107.098(3)	106.57(1)	95.584(2)	95.63(2)	90.52(3)
Volume ($Å^3$)	578.9(3)	594.042	587.90(12)	594.527	583.514
Z / Density (calc.) (Mg/m^3)	4 / 1.596	–/1.555	4 / 1.572	–/1.554	–/1.584
Absorption coefficient (mm^{-1})	0.127	–	0.125	–	–
F(000)	288	–	288	–	–
Crystal size (mm^3)	0.21 × 0.13 × 0.07	–	0.15 × 0.11 × 0.07	–	–
θ range (°)	2.50 – 24.99	–	2.35 – 25.00	–	–
Limiting indices	$-10 \le h \le 10$, $-5 \le k \le 5$, $-17 \le l \le 17$	–	$-5 \le h \le 5$, $-8 \le k \le 8$, $-20 \le l \le 20$	–	–
Reflections collected / unique	4807 / 1001 [R(int) = 0.0254]	–	5166 / 1021 [R(int) = 0.0295]	–	–
Completeness to θ (%)	98.6	–	98.6	–	–
Absorption correction	Semi-empirical from equivalents	–	Semi-empirical from equivalents	–	–
Max. and min. transmission	0.99 and 0.98	–	0.99 and 0.98	–	–
Refinement method	Full-matrix least-squares on F^2	–	Full-matrix least-squares on F^2	–	–
Data/restraints/parameters	1001 / 0 / 91	–	1021 / 0 / 92	–	–
Goodness-of-fit on F^2	1.065	–	1.035	–	–
Final R indices [$I > 2\sigma(I)$]	R_1 = 0.0317, wR_2 = 0.0838	R_1 = 0.0570	R_1 = 0.0304, wR_2 = 0.0845	R_1 = 0.0575	R_1 = 0.0716
R indices (all data)	R_1 = 0.0351, wR_2 = 0.0874	–	R_1 = 0.0319, wR_2 = 0.0861	–	–
Largest diff. peak and hole ($e.Å^{-3}$)	0.135 and −0.229	–	0.212 and −0.170	–	–

*Present work; [#1] previous work, CSD ref code: AMNTPY [40]; [#2] previous work, CSD ref code AMNTPY01 [41], [#3] previous work, CSD ref code AMNTPY02 [41]. $R_1 = \sum||F_o|-|F_c||/\sum|F_o|$, $wR_2 = [\sum\{(F_o^2-F_c^2)^2\}/\sum\{w(F_o^2)^2\}]^{1/2}$, $w = 1/\{\sigma^2(F_o^2) + (aP)^2 + bP\}$, where a = 0.0547 and b = 0.0822 for (**Form–I**) and a = 0.0537 and b = 0.1200 for (**Form–II**). $P = (F_o^2 + 2F_c^2)/3$ for all structures.

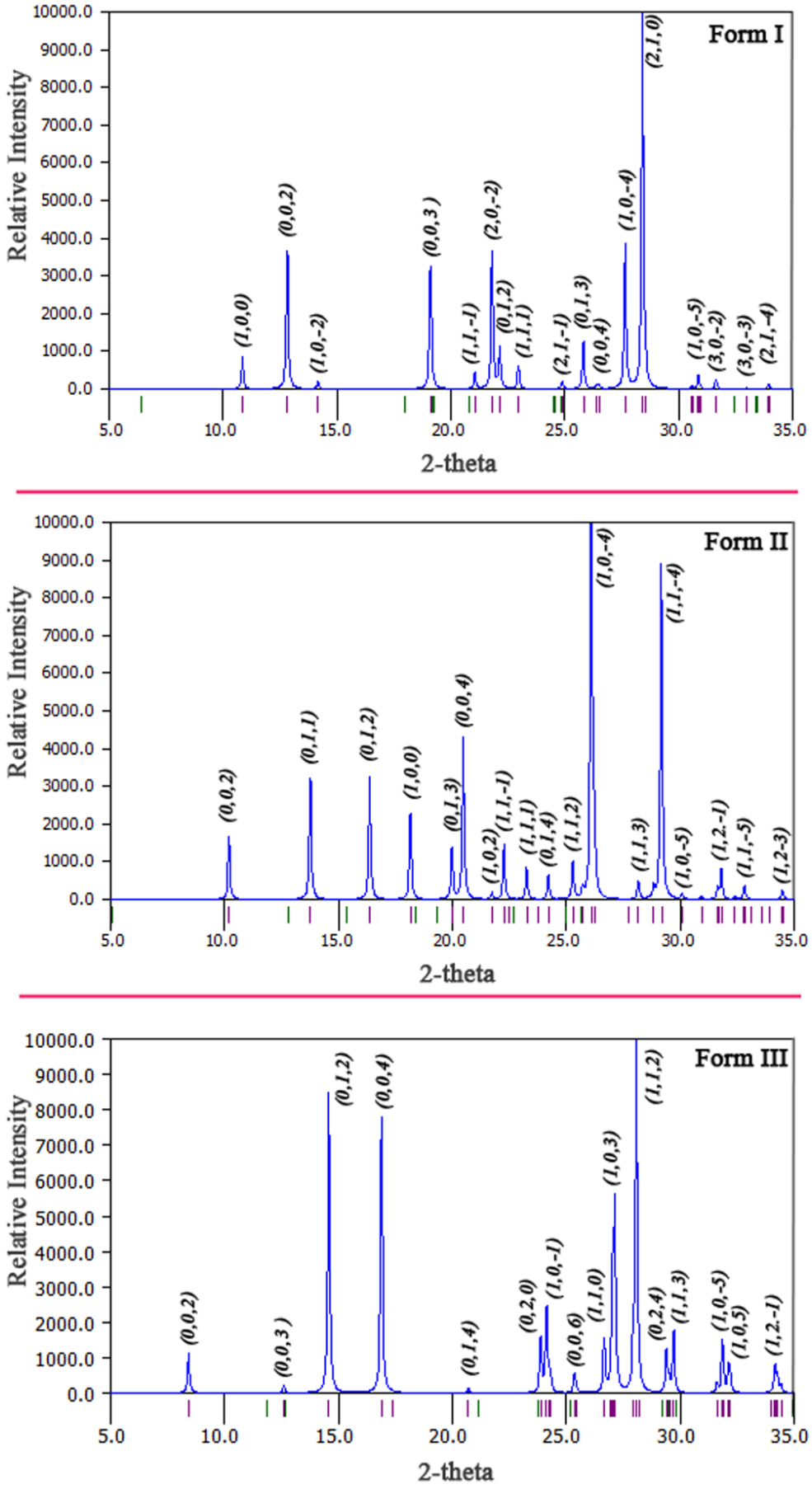

Figure 5.1. Simulated PXRD patterns of **Form−I, Form−II,** and **Form−III.**

Table 5.2. Selected bond lengths (Å).

Bond	Form−I*	Form−I[#1]	Form−II*	Form−II[#2]	Form−III[#3]
C(1)−N(2)	1.331(2)	1.336	1.328(2)	1.331(5)	1.334(6)
C(2)−N(3)	1.436(2)	1.440	1.435(2)	1.438(5)	1.427(6)
N(3)−O(1)	1.238 (2)	1.235	1.235(2)	1.240(4)	1.232(6)
N(3)−O(2)	1.233(2)	1.229	1.228(2)	1.242(4)	1.237(6)

*Present work; [#1] previous work, CSD ref code: AMNTPY [40]; [#2] previous work, CSD ref code AMNTPY01 [41], [#3] previous work, CSD ref code AMNTPY02 [41]

Table 5.3. Selected bond angles (°).

Bond	Form−I*	Form−I[#1]	Form−II*	Form−II[#2]	Form−III[#3]
N(1)−C(1)−N(2)	115	114	115	115	115
C(2)−C(1)−N(2)	126	126	126	119	127
C(1)−C(2)−N(3)	122	120	122	122	120
C(2)−N(3)−O(1)	119	119	119	119	118
C(2)−N(3)−O(2)	119	119	119	119	120
O(1)−N(3)−O(2)	122	122	122	122	121

*Present work; [#1] previous work, CSD ref code: AMNTPY [40]; [#2] previous work, CSD ref code AMNTPY01 [41], [#3] previous work, CSD ref code AMNTPY02 [41]

5.2.3. Hirshfeld Surface Analysis

Single molecular Hirshfeld surfaces [23−25] in the crystal structures are constructed based on the electron distribution calculated as the sum of spherical atom electron densities. For a given crystal structure and set of spherical atomic electron densities, the Hirshfeld surface is unique [42], and it is the property that suggests the possibility of gaining additional insight into the intermolecular interaction of molecular crystals. The normalized contact distance (d_{norm}) based on both d_e (distance from the point to the nearest nucleus external to the surface) and d_i (distance to the nearest nucleus internal to the surface) and the vdW radii of the atom, given by the equation (1) enables identification of the regions of particular importance to intermolecular interactions [23]. The combination of d_e and d_i in the form of a 2D fingerprint plot [23−26] summarizes intermolecular contacts in the crystal [23]. The Hirshfeld surfaces are mapped with d_{norm}, and 2D fingerprint plots presented in this paper were generated using CrystalExplorer 2.1 [43].

$$d_{norm} = \frac{d_i - r_i^{vdw}}{r_i^{vdw}} + \frac{d_e - r_e^{vdw}}{r_e^{vdw}} \qquad (1)$$

5.2.4. Theoretical Methods

The wavefunction analyses have been carried out by using the Gaussian16 calculation package [44] with DFT/B3LYP/6311++G(d,p) basis set. The interaction energies are calculated using specific dimer models derived from the supramolecular network.

Lattice energy and intermolecular interaction energies for molecular pairs of the polymorphs were decomposed into coulombic, polarization, dispersion, and repulsion energy terms which are evaluated using the PIXELC method in the CLP module [45]. In this calculation, all the hydrogen atoms were moved to their neutron distances, and B3LYP/ 6–311++G(d, p) basis set was used for the calculations of accurate electron density [31].

We have used Bader's theory of "Atoms in molecules" [46] to analyze the noncovalent by AIMALL calculation package [47]. The charge density ρ(r), and its Laplacian L(r) = $\nabla^2\rho(r)$ are calculated using the "Atom in molecule" (QTAIM) theory at the (3, –1) bond critical point (BCPs). According to topological properties, the electron density is depleted where $\nabla^2\rho(r)$ is positive for closed-shell interaction [48]. Other topological parameters such as kinetic electronic energy density G(r), potential electronic energy density V(r), and total electronic energy density H(r) [H(r) = V(r) + G(r)] were obtained at BCPs for characterizing the intermolecular interactions [49]. At the bond critical point, the dissociation energy can be calculated as −V(r)/2 in the Hartree unit which can be converted in kcal/mol unit by 313.7545×(−V(r)). For noncovalent interactions, kinetic electronic energy density G(r) is greater than potential electronic energy density V(r), so that $\frac{|V(r)|}{G(r)}$ is always less than 1 [50]. The relatively low value of charge density (ρ), the small positive value of the Laplacian ($\nabla^2\rho(r)$), and energy density (H(r)) at BCPs and the relationship $\left|\frac{V}{G}\right| < 1$ indicate that all noncovalent interactions are "closed–shell" interactions where the noncovalent interactions are dominated by the charge contraction away from the interatomic surface toward each nucleus [51]. Using the NCI plot index [52], we can further characterize the noncovalent interactions by visualizing the isosurfaces instead of the bond critical points. A blue-green-yellow-red color scheme represents these isosurfaces. Red and blue isosurfaces represent the repulsive ($\rho^{+)}$ and attractive (ρ^{-}) interactions [53] while yellow and green isosurfaces represent the weak repulsive and weak attractive interactions.

5.3. Results and Discussion

5.3.1. Structural Comparision

The molecular view of the polymorphic forms of 2-amino-3-nitropyridine has been depicted in Figure 5.2 using ORTEP-III [54]. The solid-state structure of the polymorphs **Form–I** and **Form–II** at 120 K with the highest precision compared to the previously reported forms [40, 41] with an R-value of 0.0317 and 0.0304 have been reported herein. **Form–III** has been collected from CCDC (AMNTPY02) [41] which has no anisotropic parameter. So, the molecular view of **Form–III** is in ball & stick format (Figure 5.2c). The comparison between the unit cell dimensions for the polymorphs (Table 5.1) shows they are entirely different. Some selected bond lengths and bond angles are given in Tables 5.2 and 5.3. The morphologies of the polymorphic forms of 2-amino-3-nitropyridine have been depicted in Figure 5.3. X-ray crystallography reveals that the polymorphs are stabilized through a combination of N–H···N, O–H···O, and C–H···O hydrogen bonding interactions; however, polymorphic **Form–I** exhibits weak π···π and carbonyl (L.P)···π interactions. In the solid state, the polymorphs interlink themselves to generate different structures through strong N–H···N and O–H···O hydrogen bonds (Table 5.4).

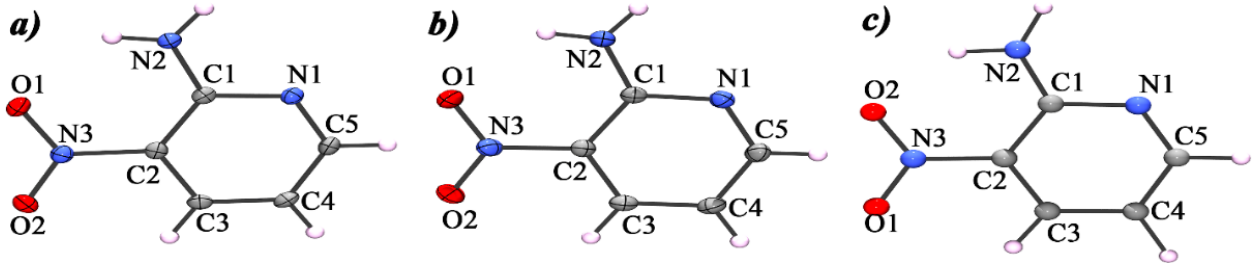

Figure 5.2. ORTEP view and atom numbering scheme of the polymorphs a) **Form–I,** and b) **Form–II,** with displacement ellipsoid at 30% probability, and **c) Form–III** in ball & stick format.

Table 5.4. Hydrogen bonding geometry of polymorphic forms of the title polymorphs (Å, °).

D–H···A	d(D–H)	d(H···A)	d(D···A)	∠D–H···A	Symmetry
Form–I*					
N(2)–H(2A)···N(1)	0.86	2.13	2.991(2)	177	1–x, –1–y, –z
N(2)–H(2B)···O(1)	0.86	2.07	2.666(2)	126	---
N(2)–H(2B)···O(1)	0.86	2.41	2.999(2)	127	1–x, –1/2+y, 1/2–z
C(3)–H(3)···O(2)	0.93	2.44	3.279(2)	150	–x, 1–y, –z
Form–I$^{\#1}$					
N(2)–H(2A)···N(1)	0.97	2.04	3.009(2)	176	1–x, –1–y, –z
N(2)–H(2B)···O(1)	0.88	2.03	2.671(2)	129	---
N(2)–H(2B)···O(1)	0.88	2.47	3.045(2)	124	1/2–x, 1/2+y, 1/2–z

C(3)–H(3)···O(2)	0.99	2.47	3.345(2)	148	–x, 1–y, –z
Form–II*					
N(2)–H(2A)···N(1)	0.86	2.10	2.963(2)	176	–1–x, 1–y, –z
N(2)–H(2B)···O(1)	0.86	2.06	2.659(2)	126	---
N(2)–H(2B)···O(1)	0.86	2.30	3.032(2)	143	–x, 2–y, –z
C(3)–H(3)···O(2)	0.93	2.49	3.167(2)	130	1–x, –1/2+y, 1/2–z
Form–II[#2]					
N(2)–H(2A)···N(1)	0.92	2.07	2.972(5)	166	2–x, 1–y, 2–z
N(2)–H(2B)···O(1)	0.95	2.08	2.662(4)	117	---
N(2)–H(2B)···O(1)	0.95	2.19	3.044(4)	147	2–x,1–y, 2–z
C(3)–H(3)···O(2)	1.04	2.41	3.178(4)	129	–x, 1/2+y, 3/2–z
Form–III[#3]					
N(2)–H(1)···O(2)	0.95	2.49	2.965(6)	119	–x, 1–y, 1–z
N(2)–H(1)···O(2)	0.95	1.91	2.672(5)	136	---
N(2)–H(1)···N(3)	0.95	2.53	2.966(6)	108	---
N(2)–H(2)···N(1)	1.05	1.97	2.679(6)	157	1–x, 2–y, 1–z
C(4)–H(4)···O(1)	1.17	2.45	3.277(6)	126	–1/2–x, 1/2+y, 3/2–z
C(3)–H(3)···O(1)	0.97	2.33	2.679(6)	101	---

*Present work; [#1] previous work, CSD ref code: AMNTPY [40]; [#2] previous work, CSD ref code AMNTPY01 [41], [#3] previous work, CSD ref code AMNTPY02 [41].

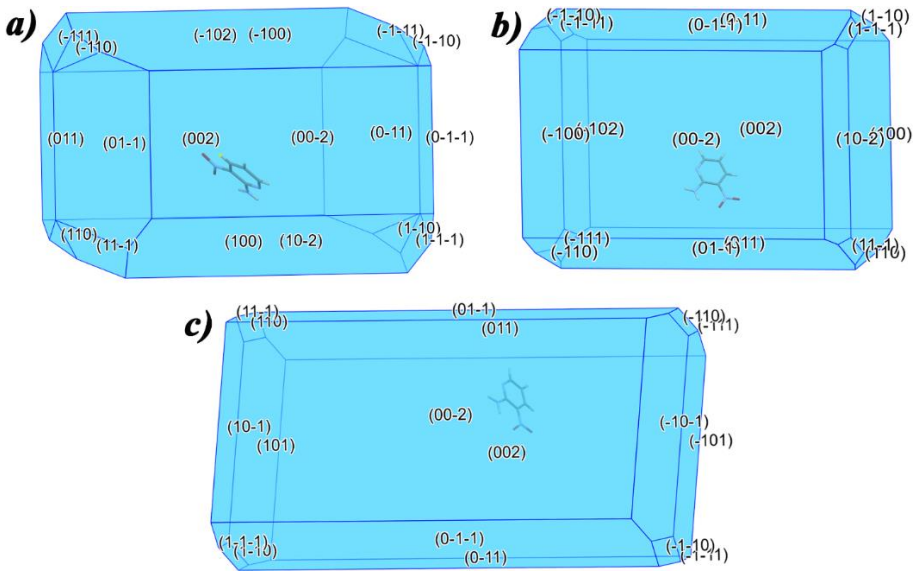

Figure 5.3. The BFDH morphology of the polymorphic (a) **Form−I,** (b) **Form−II,** and (c) **Form−III**.

In **Form–I**, the amine nitrogen atom N2 in the molecule at (x, y, z) acts as a donor to the pyridine ring nitrogen atom N1 in the molecule at (1–x, –1–y, –z), so generating a centrosymmetric $R_2^2(8)$ dimeric ring (A) centered at (½, ½, 0) (Figure 5.4a). Additional reinforcement with the amine nitrogen N2 and oxygen atom O1 of the nitro group in the

molecule at (x, y, z) and (1–x, –1/2+y, 1/2–z) leads the molecules to generate a supramolecular network structure in (011) plane (Figure 5.4a).

In case of **Form–II**, the amine nitrogen atom N2 at (x, y, z) acts as a donor to the pyridine nitrogen atom N1 at (–1–x, 1–y, –z), generating a centrosymmetric $R_2^2(8)$ dimeric ring (A) centred at (½, ½, 0) (Figure 5.4b). Again this amine nitrogen atom N2 acts as a donor to the oxygen atom O1 of the nitro group at (–x, 2–y, –z), thus generating a centrosymmetric $R_2^2(12)$ dimeric ring (B) centred at [010] (Figure 5.4b). These two types of centrosymmetric dimeric rings (A) and (B) in **Form–II** are alternately linked into infinite zigzag ABABAB…. chain along [010] direction (Figure 5.4b).

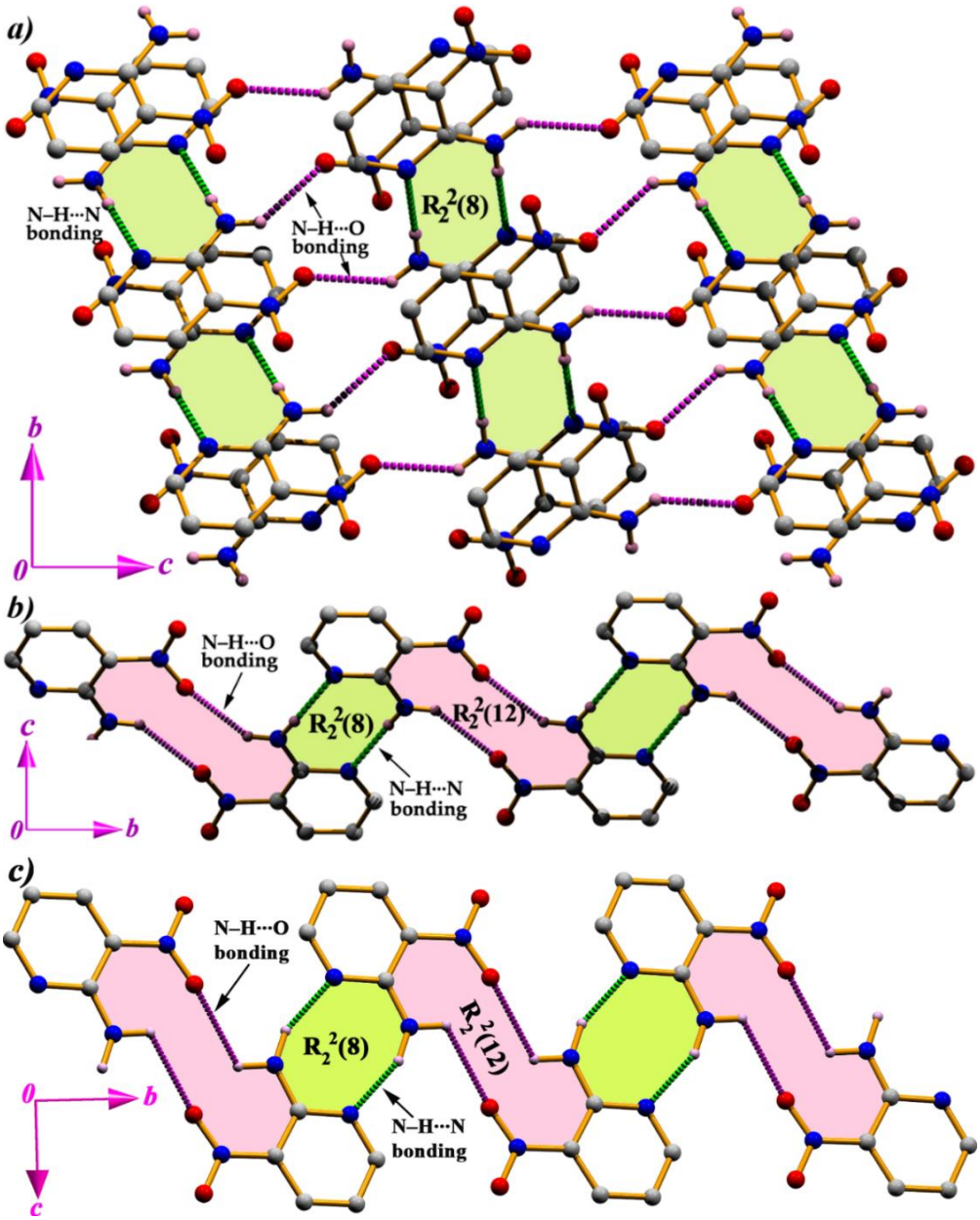

Figure 5.4. Formation of different supramolecular network structures for **Form–I (a), Form–II (b),** and **Form–III (c)** through N–H···N and N–H···O hydrogen bonding interactions.

In **Form–III**, the amine nitrogen atom N2 in the molecule at (x, y, z) acts as a donor to the pyridine ring nitrogen atom N1 in the molecule at (1–x, 2–y, 1–z). Thus, N–H···N interactions generate centrosymmetric $R_2^2(8)$ dimeric ring (A) centered at (½, 1, ½) (Figure 5.4c). Moreover, the amine nitrogen N2 and oxygen atom O2 of the nitro group in the molecule at (x, y, z) and (–x, 1–y, 1–z) leads the molecules to generate another centrosymmetric $R_2^2(12)$ dimeric ring (B) centered at (0, ½, ½) (Figure 5.4c). These two types of centrosymmetric dimeric rings (A) and (B) are linked alternatively into infinite zigzag ABABAB…. chain along [010] direction (Figure 5.4c).

Again the reinforcement between the strong N–H···N and weak C–H···O hydrogen bonding interactions in both the polymorphic forms exhibit new assembly in the solid state. In **Form–I**, the pyridine ring carbon atom C3 in the molecule at (x, y, z) acts as a donor to the oxygen atom O2 of the nitro group in the molecule at (–x, 1–y, –z), so generating a centrosymmetric $R_2^2(10)$ dimeric ring (M) centred at (0, ½, 0) (Figure 5.5a). The molecules of **Form–I** generate $R_2^2(8)$ dimeric ring (A) through N–H···N bond and these two types of dimeric rings are alternately linked into infinite AMAM… chain along [010] direction. Parallel layers of AMAM... chains are interconnected through the N–H···O hydrogen bond due to the self-complementary nature of the molecules of **Form–I**. The amine nitrogen acts as a donor to the nitro oxygen atom to interlink the parallel AMAM… chain, thus generating a two-dimensional network structure in the (011) plane (Figure 5.5a). In **Form–II**, layers of centrosymmetric $R_2^2(8)$ dimeric ring (A) motifs are in parallel orientation and propagating along [010] direction. These parallel layers are interconnected through weak C–H···O bonds to form a network. The pyridine ring carbon atom C3 at (x, y, z) acts as a donor to the oxygen atom of the nitro group in the molecule at (1–x, –1/2+y, 1/2–z), thus generating an $R_6^6(32)$ ring motif (N) in **Form–II** (Figure 5.5b). The two types of ring motifs (A) and (N) in **Form–II** are alternately linked into a network structure in the (011) plane (Figure 5.5b). In the case of **Form–III**, the layers of centrosymmetric $R_2^2(8)$ dimeric ring (A) motifs are in anti-parallel orientation along the [010] direction. These anti-parallel layers are interconnected through C–H···O hydrogen bond interaction. The carbon atom C4 in the pyridine ring at (x, y, z) acts as a donor to the oxygen atom O1 of the nitro group in the molecule at (–1/2–x, 1/2+y, 3/2–z) which generates an $R_6^6(32)$ ring motif (N) (Figure 5.5c). The alternative propagation of the ring motifs (A) and (N) in **Form–III** form a two-dimensional network structure in the (011) plane (Figure 5.5c).

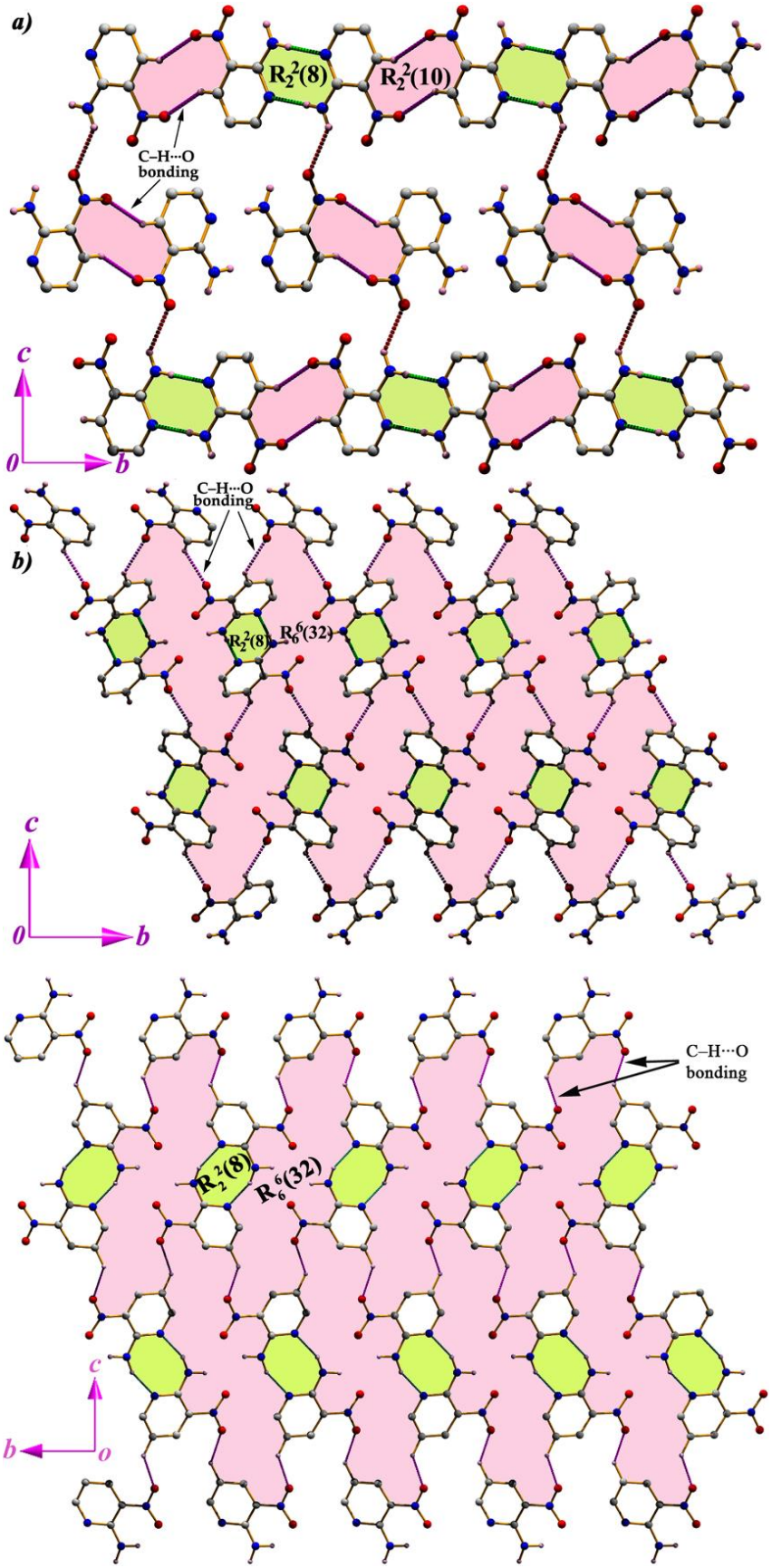

Figure 5.5. (a) Propagation of centrosymmetric R_2^2 (8) and R_2^2 (10) rings and formation of 2D network structure in **Form–I**; (b) Generation of the 2D network in **Form–II**; (c) Formation of the 2D network in **Form–III**.

A close examination concerning the intermolecular interactions involved within the polymorphic forms of 2-amino-3-nitropyridine displays that the **Form–I** exhibits face-to-face π···π and carbonyl(L.P)···π type weak noncovalent interactions in the solid-state. The molecular packing in **Form–I** is such that the π···π stacking interactions between the pyridine rings are optimized [55–57]. The pyridine rings (N1/C1–C5) of the molecules at (x, y, z) and (1–x, –y, –z) are strictly parallel, with an interplanar spacing of 3.367 Å, and a ring centroid separation of 4.255(2) Å, corresponding to a ring offset of 2.77 Å (Figure 5.6). Moreover, an unusual contact between the carbonyl oxygen atom and the π-cloud of the pyridine ring is observed, which is responsible for forming the new molecular assembly (Figure 5.6). The carbonyl oxygen atom O2 at (x, y, z) is oriented toward the centroid of the pyridine ring (N1/C1-C5) in the molecule at (–x, –y, –z). The distance between O2 and the centroid of the pyridine ring is 3.567(2) Å [angle N3–O2···Cg(1) = 103.62(7)º, N3···Cg(1) = 4.039(2) Å, where Cg(1) is the centroid of the pyridine ring], suggesting a significant lone pair···π interaction [58,59]. This dual recognition of π···π and carbonyl(L.P)···π which can be designated as cooperative lone pair···π/π···π/π···lone pair network generates a unique supramolecular self-assembly, where weak noncovalent interactions are responsible for the formation and strengthening of assembly in **Form–I** (Figure 5.6). Significantly, **Form–II** and **Form–III** do not exhibit π···π or lone pair···π interactions in the solid-state.

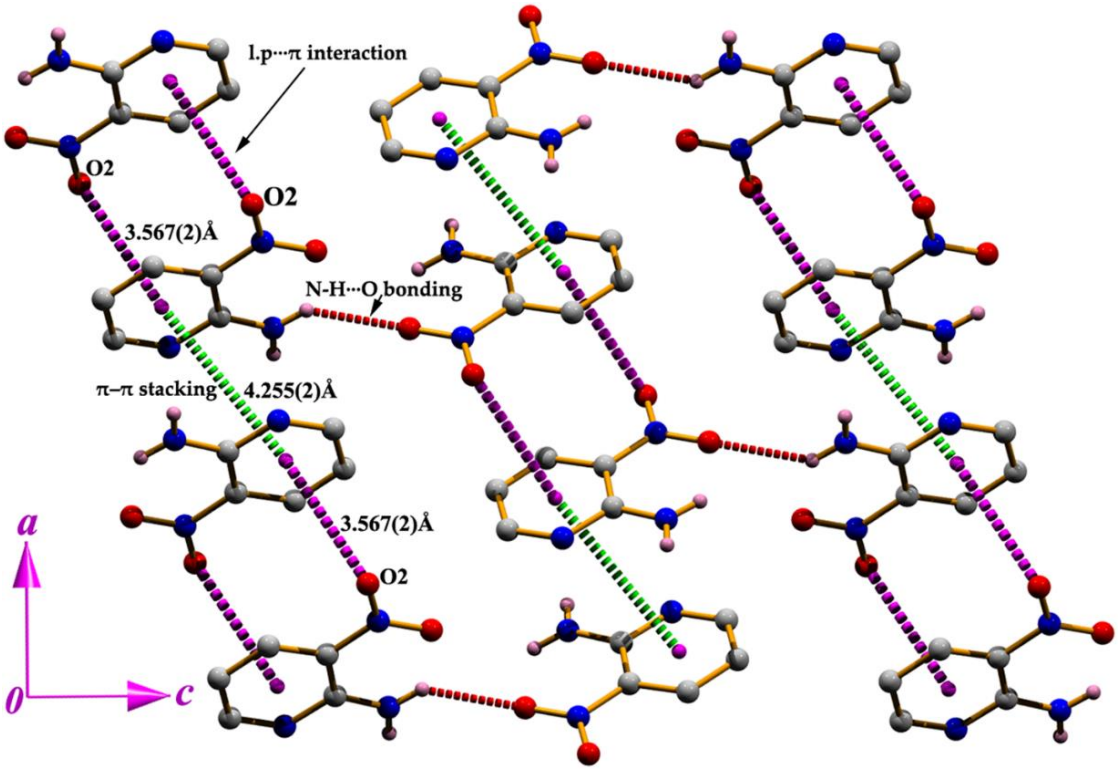

Figure 5.6. Perspective view of cooperative pair···π/π···π/π···lone pair network in **Form–I**.

5.3.2. Hirshfeld Surface

The Hirshfeld surfaces of the polymorphic forms of 2-amino-3-nitropyridine are illustrated in Figure 5.7, showing the surfaces that have been mapped over d_{norm} and shape-index. Referring to Figure 5.7, the dominant interactions between the amine nitrogen atom and the nitrogen atom of the pyridine ring in the polymorphs can be seen in the Hirshfeld surface area by the bright red encircles. The dominant interactions between the amine nitrogen atom and the oxygen atom of the nitro group are also evident in the d_{norm} surface of both the polymorphic forms by the large circular depressions (Figure 5.7). The light red spots are due to weak C–H···O interactions, other spots on the d_{norm} surfaces correspond to C···O, and H···H close contacts. The small extent of the visible area and very light-colored regions on the surfaces indicate weaker and longer contacts other than hydrogen bonds. The dominant N–H···N interaction appears as two distinct spikes in the fingerprint plot (Figure 5.8) with almost equal lengths for both the polymorphic forms of 2-amino-3-nitropyridine. For the N···H/H···N interactions, complementary regions are visible in the fingerprint plots where one molecule acts as a donor ($d_e > d_i$) and the other as an acceptor ($d_e < d_i$). The upper spikes correspond to the donor spike (amine nitrogen atom interacting with pyridine ring nitrogen atom), with the lower spike being an acceptor spike (pyridine ring nitrogen atom acts as acceptor to the amine nitrogen atom); these two spikes in the fingerprint plot designates the formation of a centrosymmetric $R_2^2(8)$ dimeric ring (A) motif for all the polymorphs (Figure 5.8). The fingerprint plots can be decomposed to highlight particular atom pair close contacts. The decomposed plot concerning N–H···N interaction has been depicted in Figures 5.9–5.11 for **Form–I, Form–II,** and **Form–III** respectively. The Hirshfeld surface analysis does not show similar proportions to the N···H (7.7% in **Form–I** and **Form–III** whereas 8.2% in **Form–II**) and H···N (6.3% in **Form–I**, 6.8% in **Form–II**, and 5.5% in **Form–III**) interactions for the three polymorphic forms. Therefore, N–H···N interaction proportions comprise 14.0% (d_i = 1.182 Å; d_e = 0.796 Å) in **Form-I,** whereas **Form–II,** and **Form–III** comprise 15.0% (d_i = 1.162 Å; d_e = 0.781 Å), and 13.2% (d_i = 1.192 Å; d_e = 0.806 Å) of the molecules' total surface area respectively (Figures 5.9–5.11).

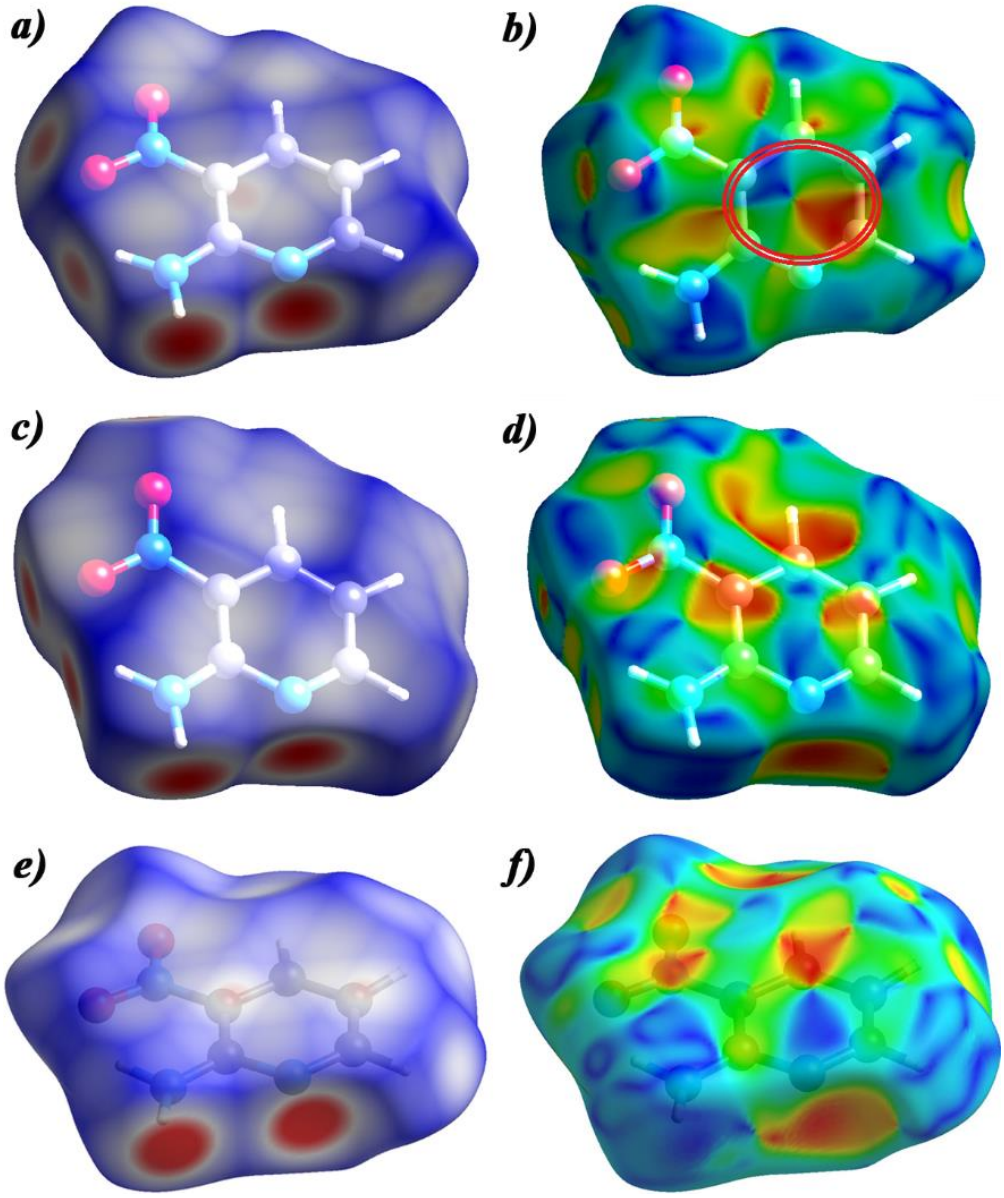

Figure 5.7. Hirshfeld surfaces mapped with d_{norm} (left) and shape-index (right) for **Form–I** (top) and **Form–II** (middle) and **Form–III** (bottom).

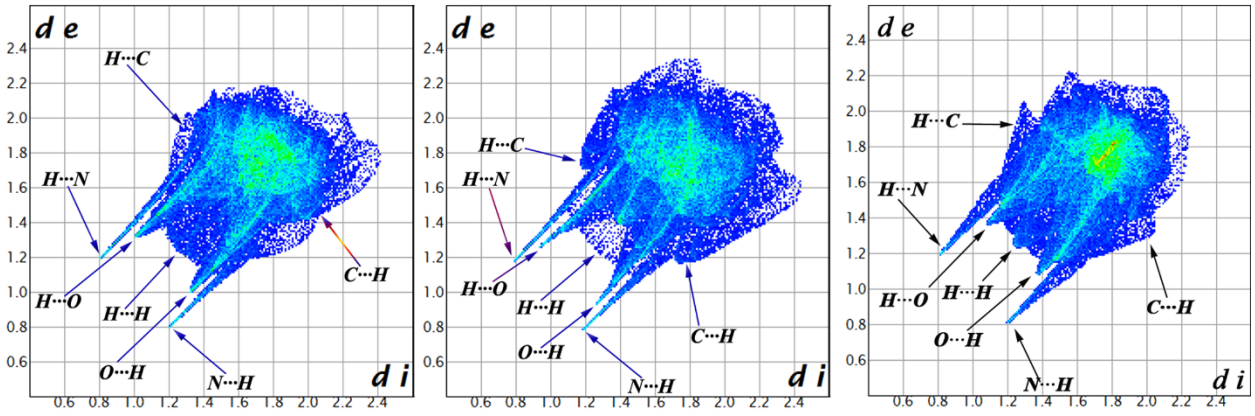

Figure 5.8. Fingerprint plot (Full) for the polymorphic **Form–I** (left), **Form–II** (middle), and **Form–III** (right).

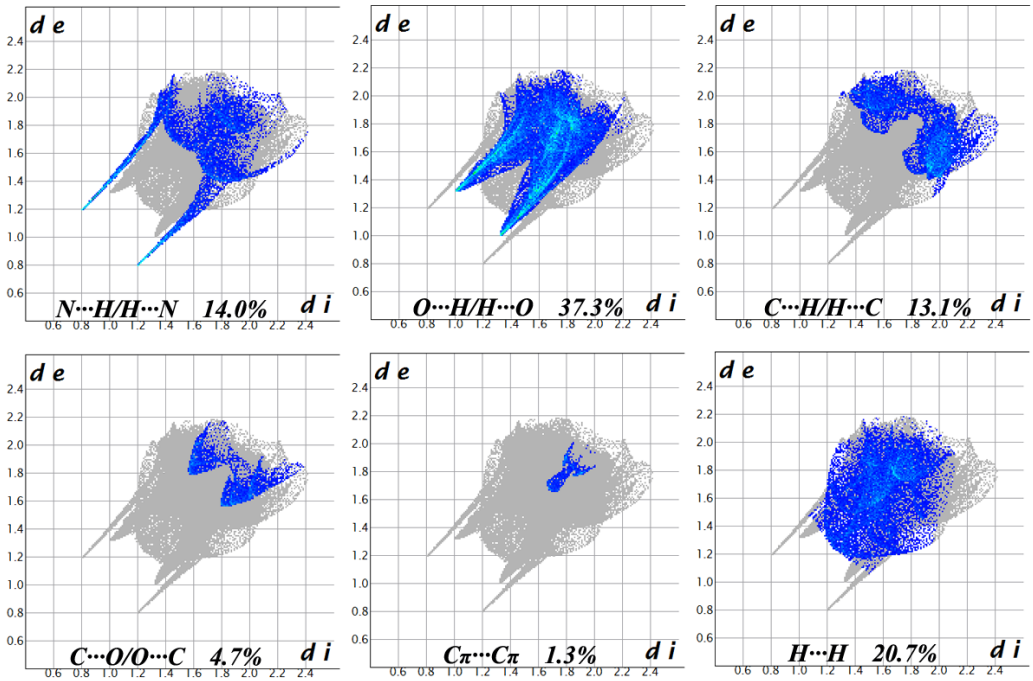

Figure 5.9. Fingerprint plots resolved into different intermolecular interactions in **Form−I** showing percentages of contacts that contributed to the total Hirshfeld surface area of the molecules.

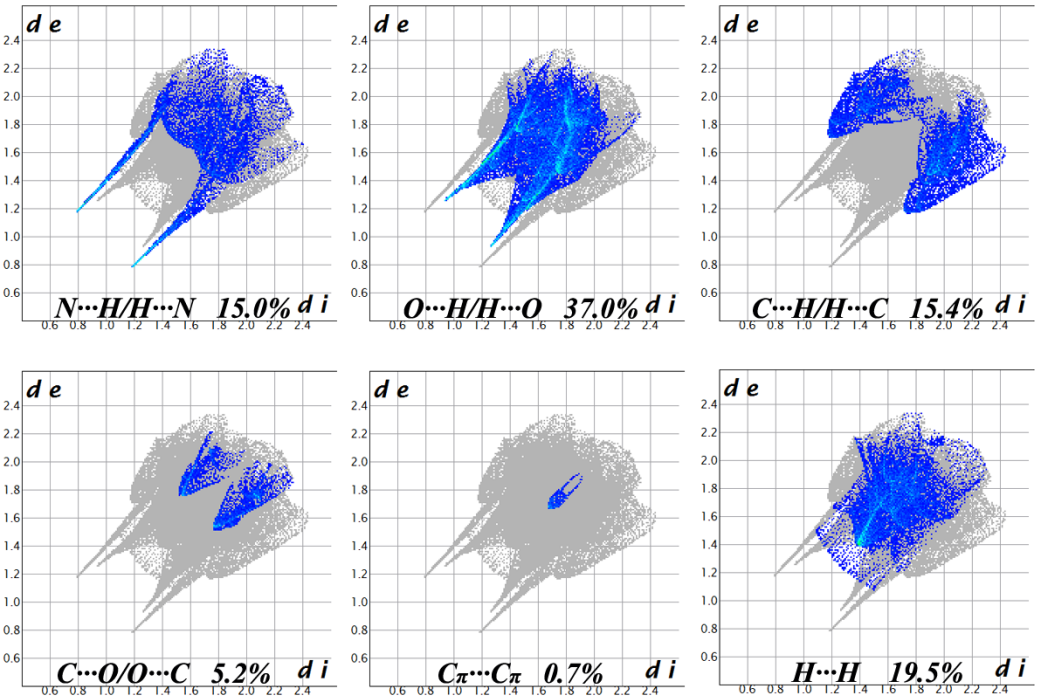

Figure 5.10. Fingerprint plots resolved into different intermolecular interactions in **Form–II** showing percentages of contacts contributed to the total Hirshfeld surface area of the molecules.

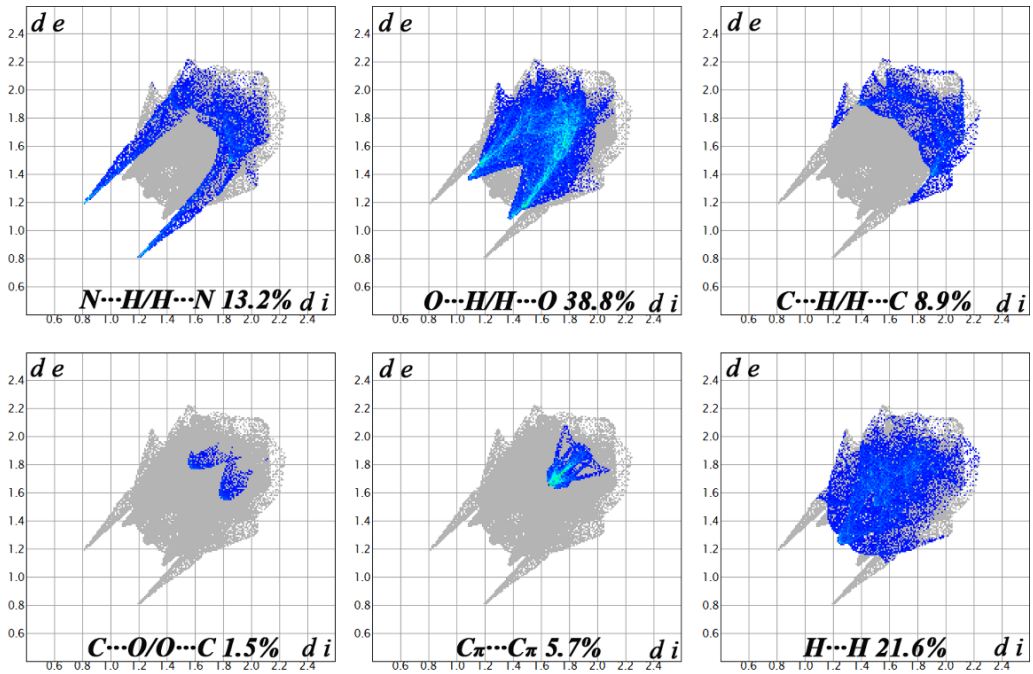

Figure 5.11. Fingerprint plots resolved into different intermolecular interactions in **Form–III** showing percentages of contacts contributed to the total Hirshfeld surface area of the molecules.

Another dominant N–H···O and weak C–H···O intermolecular interactions appear as two distinct spikes of almost equal lengths in the two-dimensional fingerprint plots (Figure 5.8). Where the donor spike designates that the amine nitrogen atom or the pyridine ring carbon atom is interacting with the oxygen atom of the nitro group whereas the acceptor spike designates that the oxygen atom is in contact with the amine nitrogen atom or the pyridine ring carbon atom. This O···H/H···O interaction leads the molecules to generate the centrosymmetric dimeric rings and the proportions of O···H/H···O interactions comprising 37.3% (d_i = 1.307 Å; d_e = 0.996 Å), 37.0% (d_i = 1.242 Å; d_e = 0.921 Å), and 38.8% (d_i = 1.362 Å; d_e = 1.086 Å) of the total Hirshfeld surface for each molecule of **Form–I, Form–II,** and **Form–III** respectively. No significant C–H···π interactions are observed in all polymorphic forms, with C···H/H···C close contacts varying from 13.1% in **Form–I** to 8.9% in **Form–III**. From the Hirshfeld surface of **Form–I**, it is clear that the pyridine rings are related to one another through face-to-face π···π stacking interaction since a large flat region across the molecule is evident. This is also clearly evident by the adjacent red and blue triangles on the shape index surface (Figure 5.7). The polymorphic **Form–II** and **Form–III** do not exhibit π···π stacking interactions which is also clearly evident by the shape-index figure since there is no signature of red and blue triangles (Figure 5.7). The contribution to the total Hirshfeld surface area due to $C_\pi\cdots C_\pi$ stacking interaction is 1.3% ($d_i = d_e$ = 1.648 Å) in **Form–I** whereas **Form–II** exhibits 0.7% ($d_i = d_e$ = 1.653 Å) due to C···C short contacts. The C···C interaction in **Form–III** comprises 5.7%

($d_i = d_e$ = 1.647 Å) of the total Hirshfeld surface area. A significant difference between the molecular interactions in the polymorphs in terms of H···H interactions is reflected in the distribution of scattered points in the fingerprint plots, which spread only up to $d_i = d_e$ = 1.232 Å in **Form–I**, $d_i = d_e$ = 1.367 Å in **Form–II** and $d_i = d_e$ = 1.237 Å in **Form–III**. The percentages of different types of interactions exhibited by the polymorphs have been included in the decomposed fingerprint plots of the structures (Figure 5.9–5.11). The Hirshfeld surfaces mapped with d_{norm} corresponding to N···H/H···N, O···H/H···O, C···H/H···C, C···O/O···C, C_π···C_π and H···H interactions for the polymorphic forms of 2-Amino-3-nitropyridine have been included in Figure 5.12, Figure 5.13, and Figure 5.14.

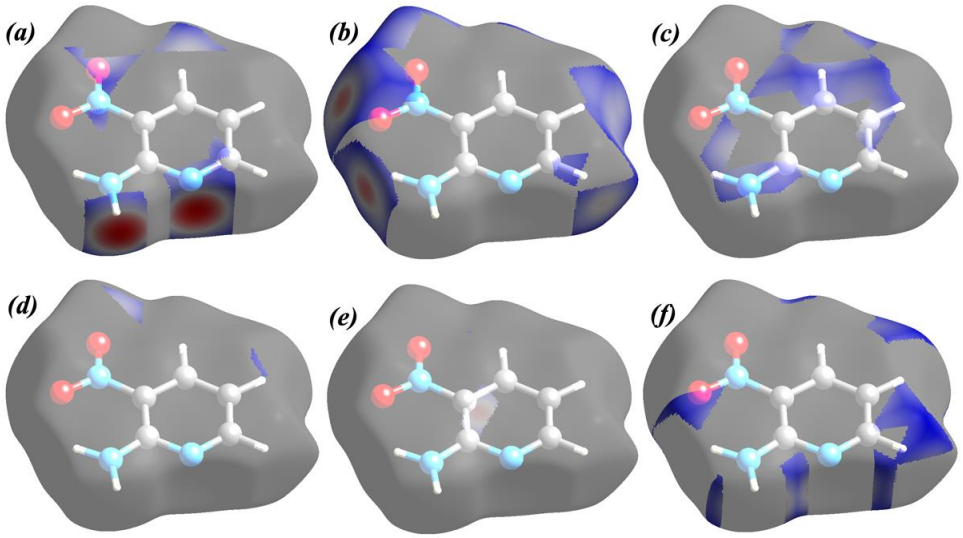

Figure 5.12. d_{norm} surfaces mapped for (a) N···H/H···N; (b) O···H/H···O (c) C···H/H···C; (d) C···O/O···C; (e) C_π···C_π and (f) H···H interactions in **Form–I** showing the contribution to the total Hirshfeld surface area of the molecules.

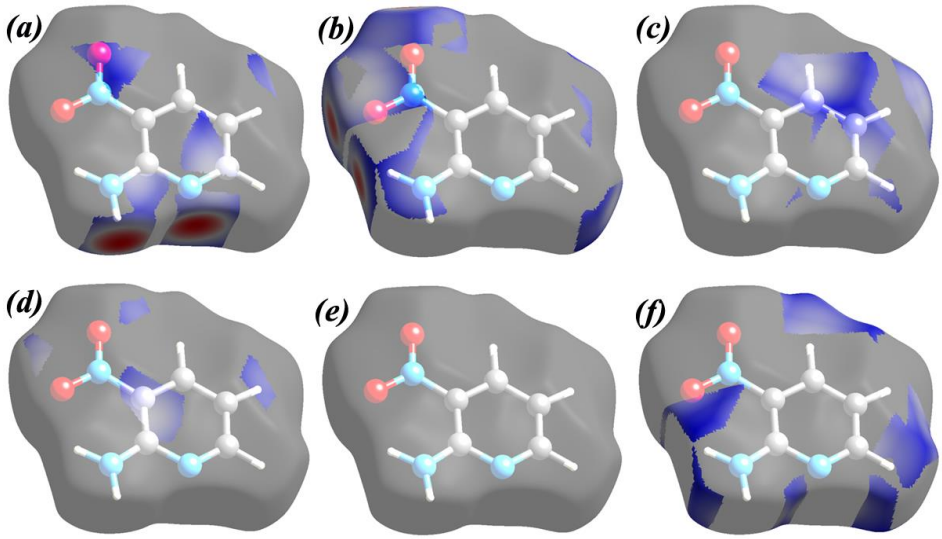

Figure 5.13. d_{norm} surfaces mapped for (a) N···H/H···N; (b) O···H/H···O (c) C···H/H···C; (d) C···O/O···C; (e) C_π···C_π and (f) H···H interactions in **Form–II** showing the contribution to the total Hirshfeld surface area of the molecules.

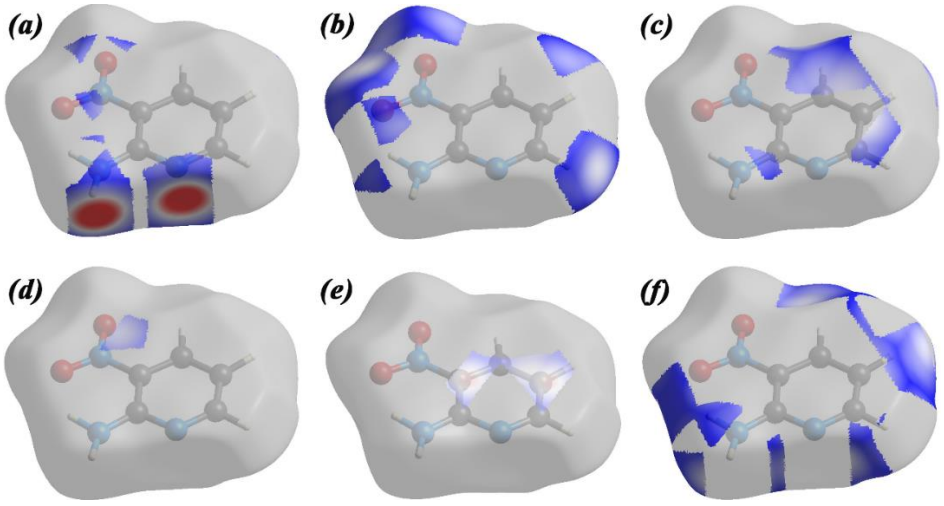

Figure 5.14. d_{norm} surfaces mapped for (a) N···H/H···N; (b) O···H/H···O (c) C···H/H···C; (d) C···O/O···C; (e) C_{π}···C_{π} and (f) H···H interactions in **Form–III** showing the contribution to the total Hirshfeld surface area of the molecules.

5.3.3. Theoretical Analysis

5.3.3.1.Energetic Features

We have analyzed the noncovalent interactions involved in the supramolecular packing by executing a computational study using DFT calculations. Studying the energetic properties of noncovalent interactions is our main focus. We have prepared some dimer models of **Form–I**, **Form–II**, and **Form–III** to evaluate the formation energies of noncovalent interactions. Each monomer unit consists of intramolecular hydrogen bond interaction(s), (N(2)–H(2B)···O(1) for **Form–I** and **Form–II**, and N(2)–H(1)···O(2), C(3)–H(3)···O(1), and N(2)–H(1)···N(3) for **Form–III**. The modification of the monomer is not required to omit the intramolecular interaction(s) as the difference between the energy of dimer and monomers calculates the formation energy. In Figure 5.15a, the formation energy of N–H···N in **Form–I** is ΔE_1= –5.6 kcal/mol while **Form–II** has ΔE_1= –5.4 kcal/mol (Figure 5.15e). The highest formation energy of N–H···N is –9.3 kcal/mol in **Form–III** (Figure 5.15h). So, the interaction energies of N–H···N interaction in **Form–III** is –4.7 kcal/mol which is higher compared to **Form–I** (–2.7 kcal/mol), and **Form–II** (–2.7 kcal/mol). The formation energy of N–H···O of **Form–II** is ΔE_1= –5.1 kcal/mol as shown in Figure 5.15f. So, the evaluated binding energy is –2.55 kcal/mol. For the same interaction, the binding energy of **Form–I** is ΔE_2= –2.3 kcal/mol (Figure 5.15b) which is lower than **Form–II**. However, the interaction energy (–2.1 kcal/mol) due to N–H···O (Formation energy of dimer is –4.2 kcal/mol) in **Form–III** (Figure 5.15i) is in between **Form–I** and **Form–II**. Following Figure 5.15c, we have computed the formation energy of C–H···O interactions that is –4.0 kcal/mol for **Form–I**. The interaction energy of this interaction is –2.0

kcal/mol for **Form–I** whereas **Form–II** has weaker interaction energy (ΔE_7= –1.1 kcal/mol) (Figure 5.15g). C–H···O interaction in **Form–III (**Figure 5.15j**)** has the least interaction energy (–0.9 kcal/mol) compared to the others. Finally, the formation energy of **Form–I** due to lone pair···π interaction has been calculated. The formation energy is ΔE_4= –0.4 kcal/mol. So, the interaction energy of lone pair···π interaction is –0.2 kcal/mol.

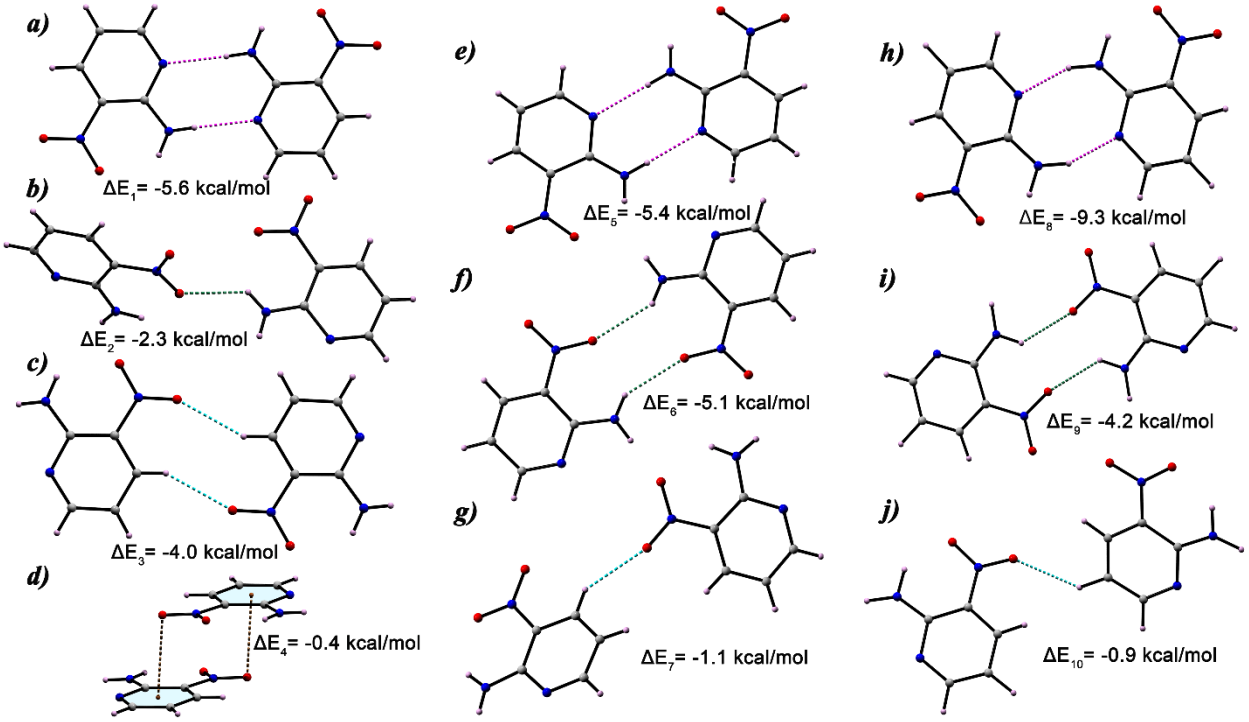

Figure 5.15. Different theoretical models were used to analyze the energy of noncovalent interactions observed in the supramolecular networks in **Form–I** (a–d), **Form–II** (e–g), and **Form–III**.

5.3.3.2.Energy Decomposition Analysis of Dimeric Molecular Pairs

5.3.3.2a. Molecular Pairs in Form–I

For investigating the significant interactions to stabilize the crystal structure in **Form–I**, seven molecular pairs (MPs) have been obtained. The MPs are depicted in Fig. 5.16, whose interaction energies vary from –47.6 kJ/mol to –2.3 kJ/mol (Table 5.5). The most stable dimeric unit (MP1) is stabilized through N–H···N, N–H···C and H···H interactions which have interaction energy –47.6 kJ/mol. This dimeric unit MP1 is predominantly electrostatic in nature with an 82% contribution towards stabilization. In MP2, the interaction energy corresponding to C–H···O and H···H interactions is –23.9 kJ/mol. The intermolecular interaction involved in MP3 is N–H···O interaction which has interaction energy –12.5 kJ/mol. In MP4, the interaction energy of C–H···O has interaction energy –10.9 kJ/mol. The MP2 MP3, and MP4 also show electrostatic in nature with the contribution of 69%, 68%, and 64% respectively. The C···C and

C···N contacts stabilize MP5 with interaction energy –9.6 kJ/mol. The electrostatic and dispersion energy contribute around 54% and 46% towards stabilizing MP5. The MP6 and MP7 exhibit dispersion energies of 66% and 72% corresponding to total interaction energies of –3.7 kJ/mol and –2.3 kJ/mol respectively.

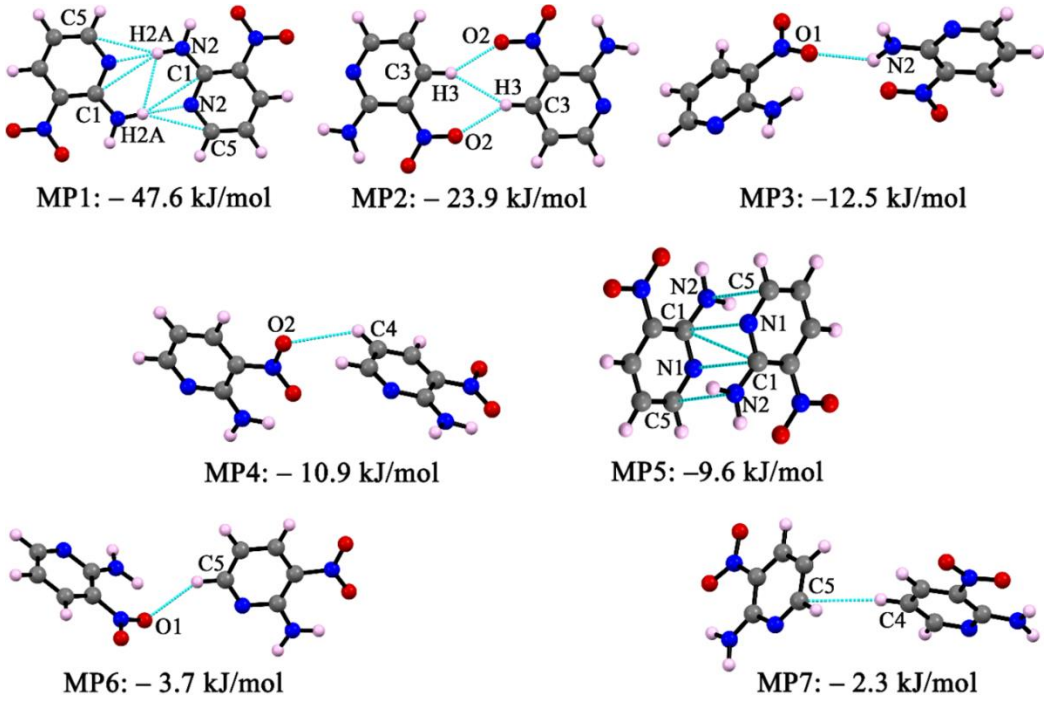

Fig. 5.16 Molecular dimers observed in the crystal structure in **Form–I**.

Table 5.5. Interaction energy (kJ/mol) of the molecular pairs of **Form–I**, **Form–II,** and **Form–III.**

MP(s)	Symmetry Code	Cg··Cg (Å)	E_{Coul}	E_{Pol}	E_{Disp}	E_{Rep}	E_{Total}	Involved Interactions	Geometry (Å, °)
Form–I									
1	1–x, –1–y, –z	6.195	–88.5	–38.6	–27.6	107.2	–47.6	N(2)–H(2A)···N(1) N(2)–H(2A)···C(1) N(2)–H(2A)···C(2)	1.976, 177 2.950, 159 2.832, 154
2	–x, 1–y, –z	6.833	–24.3	–5.9	–13.5	19.8	–23.9	C(3)–H(3)···O(2) H(3)···H(3)	2.307, 148 2.471
3	1–x, 1/2+y, 1/2–z	7.586	–12.5	–3.5	–7.5	11.0	–12.5	N(2)–H(2B)···O(1)	2.316, 124
4	x, 1/2–y, –1/2+z	7.687	–9.5	–2.7	–7.0	8.2	–10.9	C(4)–H(4)···O(2)	2.775, 120
5	1–x, –y, –z	3.995	–18.3	–5.5	–32.3	46.5	–9.6	C(5)···N(2) C(1)···N(1) C(1)··· C(1)	3.301 3.308 3.316

6	x, –1/2–y, –1/2+z	7.565	–1.5	–1.5	–5.9	5.2	–3.7	C(5)–H(5)···O(1)	2.549, 146
7	–x, –1/2+y, –1/2–z	7.680	–1.1	–1.5	–6.6	4.7	–2.3	C(4)–H(4)···C(5)	2.963, 162
Form–II									
1	–1–x, 1–y, –z	6.157	–91.1	–40.2	–28.3	117.9	–41.6	N(2)–H(2A)···N(1) N(2)–H(2A)···C(5) N(2)–H(2A)···C(1) H(2A)··· H(2A)	1.949, 176 2.797, 154 2.932, 158 2.483
2	–x, 2–y, –z	7.286	–32	–8.1	–13.6	25.4	–28.2	N(2)–H(2B)···O(1) O(1)···O(1)	2.175, 141 3.056
3	1–x, 1/2+y, 1/2–z	7.257	–8.3	–3.4	–9.1	11.3	–9.5	C(3)–H(3)···O(2) C(4)–H(4)···O(2)	2.395, 127 2.729, 113
4	1+x, 1+y, z	8.481	–6.0	–1.5	–4.0	3.0	–8.5	C(5)–H(5)···O(2)	2.685, 170
5	–1+x, y, z	4.903	–8.7	–3.8	–20.5	27.0	–6.0	N(1)···C(3) C(1)···O(2)	3.298 3.272
6	x, 1+y, z	6.920	–4.4	–2.1	–8.4	9.8	–5.1	C(5)···O(1)	3.245
7	–x, –1/2+y, 1/2–z	5.787	–1.5	–2.4	–13.1	12.5	–4.4	C(4)–H(4)···C(2) C(4)–H(4)···C(3)	2.990 2.875
Form–III									
1	1–x, 2–y, 1–z	6.197	–82.2	–36.4	–26.5	101.2	–43.9	N(2)–H(2)···C(5) N(2)–H(2)···N(1)	2.016, 169 2.767, 160
2	–x, 1–y, 1–z	7.229	–23.2	–4.5	–12.1	18.8	–20.9	N(2)–H(1)···O(2)	2.460, 118
3	–1/2–x, –1/2+y, 3/2–z	7.241	–7.4	–3.1	–9.5	9.7	–10.3	C(4)–H(4)···O(1) H(4)···H(1)	2.505, 128 2.498
4	–1+x, –1+y, z	8.330	–6.1	–1.9	–4.6	4.5	–8.1	C(5)–H(5)···O(1)	2.652, 153
5	x, –1+y, z	7.445	–3.5	–2.0	–7.0	7.8	–4.8	C(5)–H(5)···O(2)	2.631, 122
6	1+x, y, z	3.737	–10.2	–6.0	–34.2	47.1	–3.3	C(1)··· C(2) C(5)··· C(3) C(5)··· C(4)	3.322 3.396 3.338

5.3.3.2b. Molecular Pairs in Form–II

The investigation of interaction energies for the molecular pairs (MPs) revealed seven dimeric units (Figure 5.17) for the structure of **Form–II**. The interaction energies range from –41.6 kJ/mol to –4.4 kJ/mol, as summarized in Table 5.5. The first molecular pair MP1 is generated through N–H···N, N–H···C and H···H interactions (E_{Total}= –41.6 kJ/mol) with a

significant contribution of electrostatic energy (82%). This dimeric unit MP2 is also predominantly electrostatic in nature with a 75% contribution toward stabilization. The total interaction energy due to N–H···O and O···O interactions in MP2 is –28.2 kJ/mol. The dimeric unit MP3 and MP are also electrostatic in nature with 56% and 65% contribution respectively. Both dimeric units (MP3 and MP4) are stabilized through C–H···O interactions which have interaction energies – 9.5 kJ/mol and –8.5 kJ /mol respectively. The N···C and C···O contacts stabilize MP5 with interaction energy –6.0 kJ/mol. The dispersion energy contributes 62% towards the stabilization of MP5. The interaction energies of MP6 and MP7 are –5.1 kJ/mol and –4.4kJ/mol respectively which are dispersive (57% and 77% respectively) in nature.

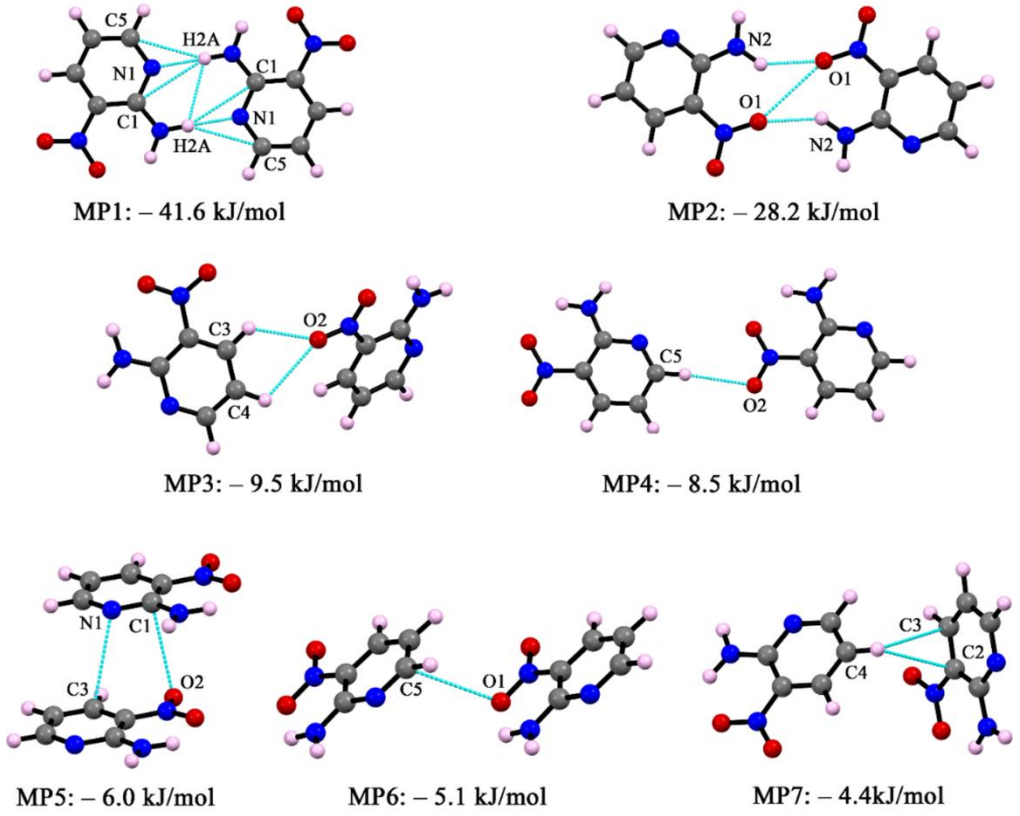

Figure 5.17. Molecular dimers observed in the crystal structure in **Form–II**.

5.3.3.2c. Molecular Pairs in Form–III

Six dimeric molecular pairs (MPs) (Figure 5.18) are extracted to investigate the interaction energies ranging from –43.9 kJ/mol to –3.3 kJ/mol (Table 5.5) in **Form–III**. The first molecular pair MP1 is generated through N–H···N, N–H···C interactions (E_{Total}= –43.9 kJ/mol) with significant electrostatic energy (82%) contribution. This second molecular pair (MP2) is stabilized through N–H···O interaction (E_{Total}= –20.9 kJ/mol) which is also predominantly electrostatic (75%) in nature. The dimeric units MP3 and MP4 are also

electrostatic in nature with 53% and 58% contribution respectively whereas MP4 and MP5 are dispersive in nature with 57% and 68% respectively. The C–H···O and H···H contact exhibits –10.3 kJ/mol while the C–H···O interactions in MP4 and MP5 obtain –8.1 kJ/mol and –4.8 kJ/mol respectively. The molecular pair MP6 is stabilized through C···C interactions which contribute –10.3 kJ/mol.

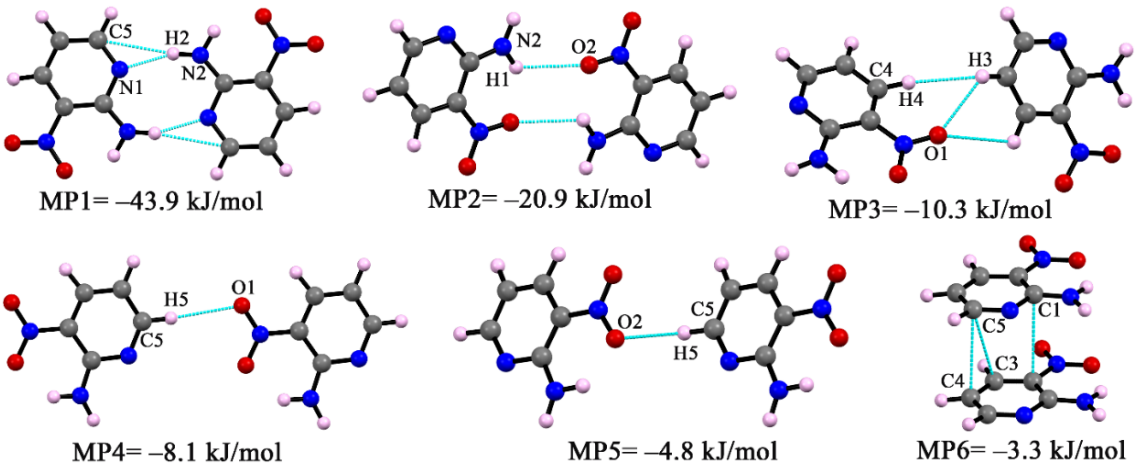

Figure 5.18. Molecular dimers observed in the crystal structure in **Form–III**.

5.3.3.3. Lattice Energies

The lattice energies for the crystal structure of all the polymorphs have been calculated (Table 5.6), showing the overall contribution of electrostatic and dispersion energy components towards stabilizing the structures. Both polymorphs show higher electrostatic energy compared to dispersion energy. The percentage of electrostatic energies of **Form–I, Form–II,** and **Form–III** are 58.4%, 58.9%, and 55.0% respectively.

Table 5.6. Calculated lattice energy (kJ/mol) for **Form–I** and **Form–II**.

Polymorphs	E_{Coul}	E_{Pol}	E_{Disp}	E_{Rep}	E_{Total}
Form–I	–102.9	–35.5	–98.6	156.6	–80.4
Form–II	–100.6	–35.7	–95.2	153.7	–77.7
Form–III	–85.0	–32.2	–96.0	141.5	–71.7

5.3.3.4.QTAIM Calculation

The fragments from molecular assemblies (Figure 5.19) used in theoretical DFT calculation (Figure 5.15) are again considered to analyze the noncovalent interactions by Bader's theory of "atoms in molecules". Application of QTAIM approach to **Form–I** & **Form–II** results in the bond paths between two atoms involved in the interaction along with (3, –1) bond critical points. Evaluation of topological parameters at BCPs reveals the dissociation energy of the individual interaction (Table 5.7). In **Form–I**, the centrosymmetric dimeric ring generated through N–H···N interaction shows the highest electron density (ρ_{BCP} = 0.0200 a.u.)

and dissociation energy (D_E = 4.016 kcal/mol) at the bond critical points (denoted as 'A' in Fig. 11a) among all other intermolecular interactions. The electron density and dissociation energy corresponding to the intermolecular N–H···O interaction (denoted as 'C' in Figure 5.19b) are ρ_{BCP} = 0.0087 a.u. and D_E = 1.802 kcal/mol. Again, the lower value of ρ_{BCP} and D_E corresponding to the C–H···O bond (denoted as 'D' in Figure 5.19c) signifies the interaction to be less favorable than other hydrogen bond interactions. The contributions of all three intermolecular bonds analyzed by QTAIM theory are in the same order of robustness as derived in DFT calculation. The connecting bond path between oxygen and aryl ring carbon atom characterizes lone-pair···π interaction. In **Form–I**, lone-pair···π interaction can be considered as more favorable than π···π interaction as the former has the higher electron density and dissociation energy at the bond critical point (see Table 5.7). Eventually, the small positive values of electron density (ρ(r)), Laplacian of electron density ($\nabla^2\rho(r)$) and H(r), and $\frac{|V(r)|}{G(r)} < 1$ classify the interaction as "closed-shell" in nature according to Gatti's assignment [60].

Again, in **Form–II**, N–H···N (denoted as 'H' in Figure 5.19f) interaction contributes significantly in stabilizing the crystal structure as it has the highest electron density (ρ_{BCP} = 0.0212 a.u.) and dissociation energy (D_E = 4.361 kcal/mol) at its bond critical point out of all intermolecular interactions. The ρ(r) and D_E value of N–H···O (denoted as 'J' in Figure 5.19g) forming a dimeric ring signifies that N–H···N is more favorable than N–H···O interaction which agrees well with the result of DFT study. Besides, C–H···O interaction shows the least value of ρ(r) (0.0075 a.u.) and D_E (1.506 kcal/mol) as anticipated from interaction energy calculation. Moreover, all interactions in **Form-II** are closed-shell interactions considering (ρ(r))>0, $\nabla^2(r)$>0, H(r) >O and $\frac{|V(r)|}{G(r)} < 1$.

Similarly, in **Form–III**, a centrosymmetric dimeric ring is generated through N–H···N interaction having the highest electron density (ρ_{BCP} = 0.0288 a.u., denoted as 'M') which is also greater than that of **Form–I** and **Form–II**. Again, likely in **Form–II**, **Form–III** exhibits a centrosymmetric dimer through N–H···O interaction. The electron density and dissociation energy at the BCP (denoted by 'O') of N–H···O interaction are 0.0078 a.u. and 1.663 kcal/mol. Lastly, C–H···O interaction exhibits a greater value of electron density (0.0092 a.u., denoted by 'P') and dissociation energy (2.102 kcal/mol) than N–H···O interaction. This is because of larger bond length of C–H (1.142 Å) from normal C–H (0.93 Å) bond length (collected from CCDC (AMNTPY02) [41]) Moreover, all interactions in **Form–III** are closed-shell interactions considering (ρ(r))>0, $\nabla^2(r)$>0, H(r) >0, and $\frac{|V(r)|}{G(r)} < 1$.

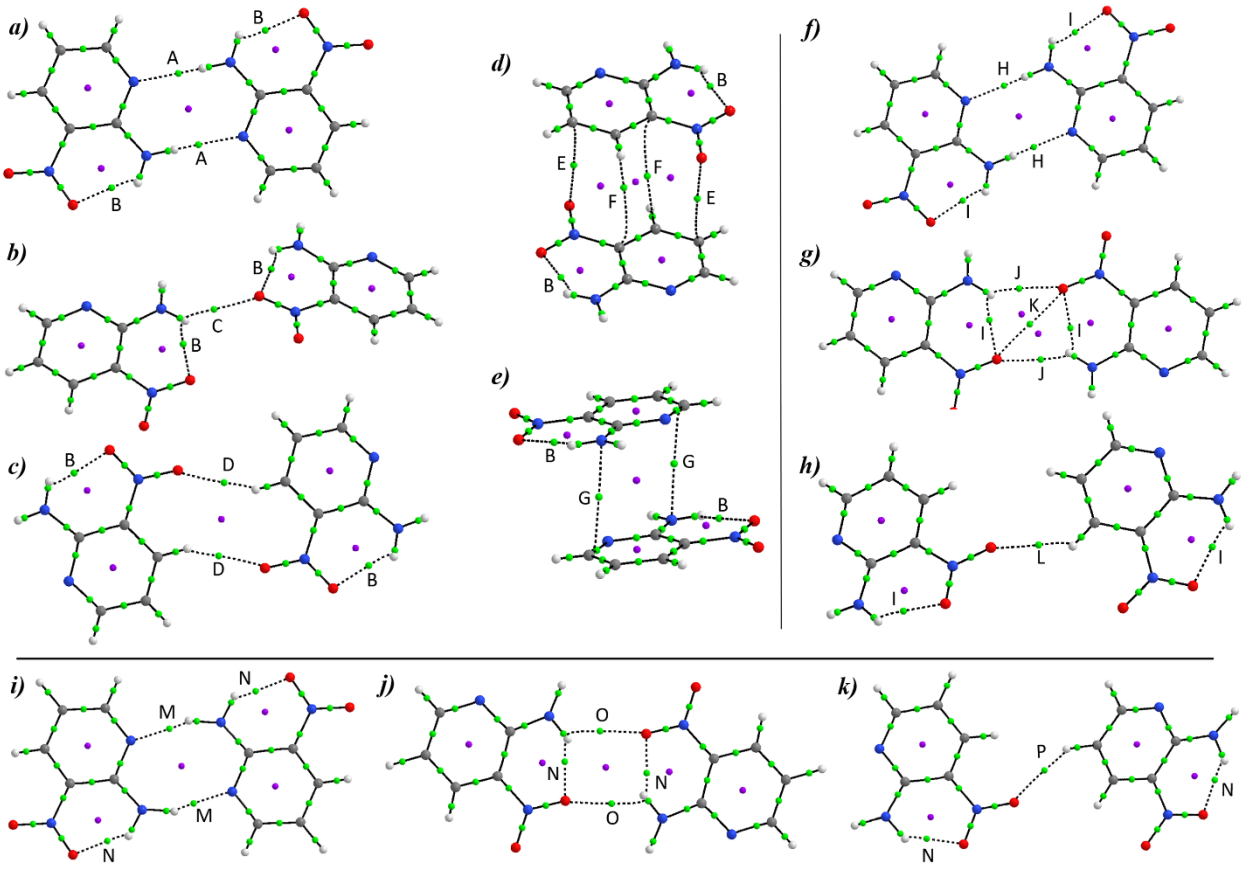

Figure 5.19. Distribution of bond critical points in different dimers in **Form–I** (a-e), **Form–II** (f-h), and **Form–III** (i-k). Green dots indicate bond critical points (BCPs).

Table 5.7. Topological parameters for noncovalent interactions (in different dimers of **Form–I, Form–II,** and **Form–III**) at their (3, -1) BCPs. [$\rho(r)$: electron density (a.u); $\nabla^2\rho(r)$: Laplacian of electron density (a.u); $V(r)$: potential energy density; $G(r)$: kinetic energy density; $H(r)$: total electronic density; $V(r)$, $G(r)$ and $H(r)$ values in a.u. and D_E in kcal/mol].

Interactions	**BCPs**	$\boldsymbol{\rho(r)}$	$\boldsymbol{\nabla^2\rho(r)}$	$\boldsymbol{V(r)}$	$\boldsymbol{G(r)}$	$\boldsymbol{\frac{\lvert V(r)\rvert}{G(r)}}$	$\boldsymbol{H(r)}$	$\boldsymbol{D_E}$
Form–I								
N(2)–H(2A)···N(1)	A	0.0200	0.0741	–0.0128	0.0156	0.8205	0.0028	4.016
	A	0.0200	0.0741	–0.0128	0.0156	0.8205	0.0028	4.016
Intra (N–H···O)	B	0.0224	0.1021	–0.0174	0.0215	0.8093	0.0041	5.459
	B	0.0224	0.1021	–0.0174	0.0215	0.8093	0.0041	5.459
N(2)–H(2B)···O(1)	C	0.0087	0.0380	–0.0058	0.0076	0.7632	0.0018	1.820
C(3)–H(3)···O(2)	D	0.0078	0.0309	–0.0047	0.0062	0.7581	0.0015	1.475
	D	0.0078	0.0309	–0.0047	0.0062	0.7581	0.0015	1.475
lone-pair···π	E	0.0052	0.0156	–0.0028	0.0034	0.8235	0.0006	0.879

	E	0.0052	0.0156	–0.0028	0.0034	0.8235	0.0006	0.879
π···π	F	0.0040	0.0115	–0.0017	0.0023	0.7391	0.0006	0.533
	F	0.0040	0.0115	–0.0017	0.0023	0.7391	0.0006	0.533
π···π	G	0.0065	0.0188	–0.0034	0.0041	0.8293	0.0007	1.067
	G	0.0065	0.0188	–0.0034	0.0041	0.8293	0.0007	1.067
Form–II								
N(2)–H(2A)···N(1)	H	0.0212	0.0788	–0.0139	0.0168	0.8274	0.0029	4.361
	H	0.0212	0.0788	–0.0139	0.0168	0.8274	0.0029	4.361
Intra (N–H···O)	I	0.0228	0.1046	–0.0179	0.0220	0.8136	0.0041	5.616
	I	0.0228	0.1046	–0.0179	0.0220	0.8136	0.0041	5.616
N(2)–H(2B) ···O(1)	J	0.0094	0.0438	–0.0063	0.0086	0.7326	0.0023	1.977
	J	0.0094	0.0438	–0.0063	0.0086	0.7326	0.0023	1.977
Intra (O···O)	K	0.0057	0.0245	–0.0043	0.0052	0.8269	0.0009	1.349
C(3)–H(3)···O(2)	L	0.0075	0.0310	–0.0048	0.0063	0.7619	0.0015	1.506
Form–III								
N(2)–H(1)···N(1)	M	0.0288	0.0820	–0.0196	0.0200	0.9800	0.0004	6.150
	M	0.0288	0.0820	–0.0196	0.0200	0.9800	0.0004	6.150
Intra (N–H···O)	N	0.0308	0.1253	–0.0259	0.0286	0.9056	0.0027	8.126
	N	0.0308	0.1253	–0.0259	0.0286	0.9056	0.0027	8.126
N(2)–H(1)···O(2)	O	0.0078	0.0325	–0.0053	0.0067	0.7910	0.0014	1.663
	O	0.0078	0.0325	–0.0053	0.0067	0.7910	0.0014	1.663
Intra (N–H···O)	N	0.0305	0.1250	–0.0257	0.0285	0.9018	0.0028	8.063
	N	0.0305	0.1250	–0.0257	0.0285	0.9018	0.0028	8.063
C(4)–H(4)···O(1)	P	0.0092	0.0317	–0.0067	0.0068	0.9853	0.0001	2.102
Intra (N–H···O)	N	0.0306	0.1245	–0.0256	0.0284	0.9014	0.0028	8.032
	N	0.0306	0.1245	–0.0256	0.0284	0.9014	0.0028	8.032

5.3.3.5.NCI Plot Index

Furthermore, we have analyzed and characterized the noncovalent interactions involved in the supramolecular assemblies by the "noncovalent interaction" (NCI) plot index. The same models have been used in QTAIM calculation. The interactions are represented by the isosurfaces which are differentiated by a color scheme with a red-yellow-green-blue scale. For **Form-I**, and **Form–II,** N–H···N interactions are represented by two greenish-blue isosurfaces (indicated by arrows) and greenish-blue spike in RDG vs sign($\lambda_2\rho$) graph in Figure 5.20a, f

respectively. The blue isosurfaces, as well as the blue spike in the scattered graph (in Figure 5.20i) confirm the presence of strong hydrogen bond (N–H···N) interactions in **Form–III**. Again, N–H···O interaction in **Form–I** is shown by a small green isosurface in Figure 5.20b.

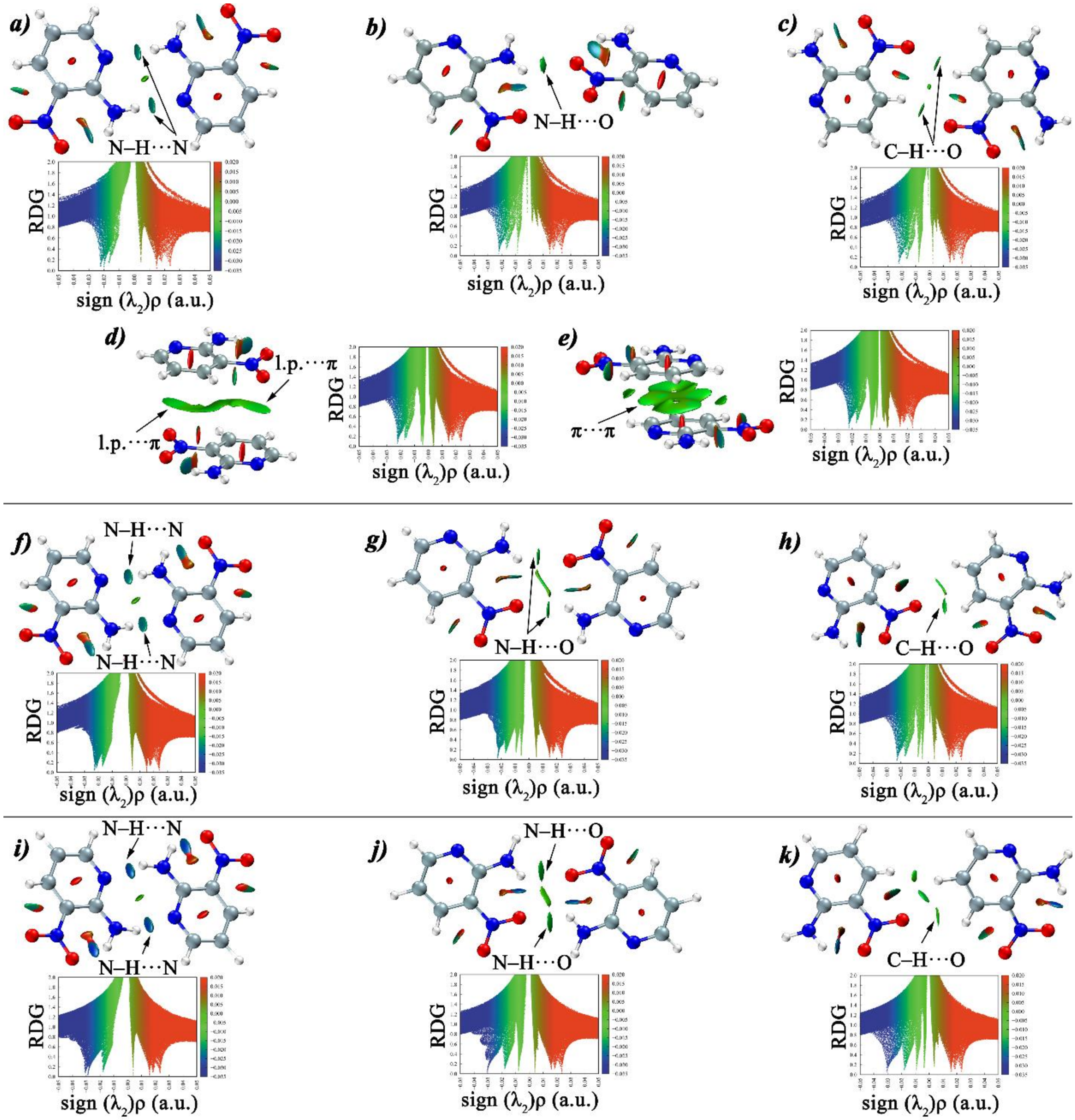

Figure 5.20. NCI plot of different noncovalent interactions observed in **Form–I** (a-e), **Form–II** (f-h), and **Form–III** (i-k).

As N–H···O interaction forms a dimeric ring in **Form–II**, and **Form–III,** two green isosurfaces illustrate the N–H···O interactions in the mentioned form (Figure 5.20g, j). Similarly, C–H···O interactions constituting a dimeric ring in **Form–I** are depicted as small green isosurfaces (Figure 5.20c) whereas a single C–H···O interaction in **Form–II,** and **Form–**

III is represented by just one small green isosurface (Figure 5.20h, k). All N–H···O and C–H···O interactions are also represented by green spikes in the respective RDG vs sign($\lambda_2\rho$) scattered graph. In **Form–I**, lone pair···π interaction is represented by an extended isosurface in Figure 5.20d. In Figure 5.20e, π···π interaction is characterized by the stretched green isosurface in **Form–I**. The green spikes in the scattered plots in Figure 5.20d and Figure 5.20e further confirm the presence of weak noncovalent interactions. Lastly, all the prominent isosurfaces and their respective spikes in RDG vs sign($\lambda_2\rho$) graph analyzed by the NCI plot index verified the existence of these noncovalent interactions observed in structural and other theoretical studies.

5.4. Conclusions

In conclusion, the polymorphic forms of 2-amino-3-nitropyridine have been reported in the context of an interesting case study of packing polymorphism. The present study highlights the importance of exploring intermolecular interactions through the Hirshfeld surface to screen polymorphs. The Hirshfeld surface analyses indicated a cooperative understanding at the intermolecular level; two crystalline forms are indicated to stabilize through the diverse contribution from intermolecular interactions. The interaction energies of non-covalent interactions are analyzed through theoretical DFT calculations and further analyzed through the PIXEL method. The PIXEL method obtains more precise interaction energy with detailed energy decomposition. From energy decomposition analysis, it is found that high interaction energy is due to electrostatic interaction where the higher dispersive interaction leads to lower interaction energy. The lattice energies of the polymorphs are also analyzed through the PIXEL method. The noncovalent interactions are further analyzed through Bader's theory of 'Atoms in molecule' (QTAIM) and 'Noncovalent Interaction' (NCI) plot index. The topological parameters and energetic features at the (3, −1) bond critical point suggest that all interactions are "close shell" interactions. Theoretical analyses of noncovalent interactions are in good agreement with the experimental findings. This approach can be helpful in crystal engineering to explore rapid quantitative insight into the intermolecular interactions and designing of novel organic materials.

5.5. References

[1] J. Bernstein, Polymorphism in Molecular Crystals; Clarendon Press, Oxford UK, 2002.

[2] G.R. Desiraju, Crystal Engineering: A Holistic View, Angew. Chem. Int. Ed. 46 (2007) 8342–8356.

[3] R. Hilfiker, Polymorphism in the Pharmaceutical Industry; Wiley-VCH, Weinheim, 2006.

[4] J. Bernstein, Polymorphism − A Perspective, Cryst. Growth Des. 11 (2011) 632–650.

[5] R. J. Davey, Pizzas, polymorphs and pills, Chem. Commun. (2003) 1463–1467.

[6] J. Bernstein, Polymorphism in Molecular Crystals; International Union of Crystal, Oxford UK, 2010.

[7] D. Braga, F. Grepioni, L. Maini, The growing world of crystal forms, Chem. Commun. 46 (2010) 6232–6242.

[8] J. Wouters, L. Quere, Pharmaceutical Salts and Co-crystals; Royal Society of Chemistry, Cambridge UK, 2011.

[9] H. G. Brittain, Polymorphism and Solvatomorphism 2006, J. Pharm. Sci. 97 (2008) 3611–3636.

[10] J.O. Henck, U.J. Griesser, A. Burger, Polymorphie von Arzneistoffen. Eine wirtschaftliche Herausforderung, Pharm. Ind. 59 (1997) 165–169.

[11] A.J. Cruz-Cabeza, J. Bernstein, Conformational Polymorphism, Chem. Rev. 114 (2014) 2170–2191.

[12] K. Fucke, N. Qureshi, D.S. Yufit, J.A.K. Howard, J.W. Steed, Hydrogen Bonding Is Not Everything: Extensive Polymorphism in a System with Conserved Hydrogen Bonded Synthons Cryst. Growth Des. 10 (2010) 880–886.

[13] S.L. Price, Why don't we find more polymorphs? Acta. Crystallogr. B. Struct. Sci. Cryst. Eng. Mater. 69 (2013) 313–328.

[14] S.L. Price, From crystal structure prediction to polymorph prediction: interpreting the crystal energy landscape, Phys. Chem. Chem. Phys. 10 (2008) 1996–2009.

[15] A.J. Cruz-Cabeza, S.M. Reutzel-Edens, J. Bernstein, 2015. Facts and fictions about polymorphism†, Chem. Soc. Rev. 44 (2015) 8619–8635.

[16] J.M. Lehn, Perspectives in Chemistry—Steps towards Complex Matter, Angew. Chem. Int. Ed. 52 (2013) 2836–2850.

[17] R.F. Ludlow, S. Otto, Systems chemistry, Chem. Soc. Rev. 37 (2008) 101–108.

[18] J. Vicens, Q. Vicens, Origins and emergences of supramolecular chemistry, J. Incl. Phenom. Macrocycl. Chem. 65 (2009) 221–235.

[19] J.D. Dunitz, A. Gavezzotti, How molecules stick together in organic crystals: weak intermolecular interactions, Chem. Soc. Rev. 38 (2009) 2622–2633.

[20] M.C. Etter, Encoding and Decoding Hydrogen-Bond Patterns of Organic Compounds, Acc. Chem. Res. 23 (1990) 120–126.

[21] G.R. Desiraju, Supramolecular Synthons in Crystal Engineering—A New Organic Synthesis†, Angew. Chem. Int. Ed. Engl. 34 (1995) 2311–2327.

[22] C.A. Hunter, Quantifying Intermolecular Interactions: Guidelines for the Molecular Recognition Toolbox, Angew. Chem. Int. Ed. 43 (2004) 5310–5324.

[23] M.A. Spackman, J.J. McKinnon, Fingerprinting intermolecular interactions in molecular crystals†, CrystEngComm 4 (2002) 378–392.

[24] M.A. Spackman, J.J. McKinnon, D. Jayatilaka, Electrostatic potentials mapped on Hirshfeld surfaces provide direct insight into intermolecular interactions in crystals, CrystEngComm 10 (2008) 377–388.

[25] S.K. Seth, D. Sarkar, A.D. Jana, On the Possibility of Tuning Molecular Edges To Direct Supramolecular Self-Assembly in Coumarin Derivatives through Cooperative Weak Forces: Crystallographic and Hirshfeld Surface Analyses, Cryst. Growth Des. 11 (2011) 4837–4849.

[26] A.L. Rohl, M. Moret, W. Kaminsky, K. Claborn, J.J. Mckinnon, B. Kahr, Hirshfeld Surfaces Identify Inadequacies in Computations of Intermolecular Interactions in Crystals: Pentamorphic 1,8-Dihydroxyanthraquinone, Cryst. Growth Des. 8 (2008) 4517–4525.

[27] A. Siddiqui-Jain, J.P. Hoj, D.W. Cescon, M.D. Hansen, Pharmacology and in vivo efficacy of pyridine-pyrimidine amides that inhibit microtubule polymerization. Bioorg. Med. Chem.28 (2018) 934-941.

[28] J. Stankevičiūtė, J. Vaitekūnas, V. Petkevičius, R. Gasparavičiūtė, D. Tauraitė, R. Meškys, Oxyfunctionalization of pyridine derivatives using whole cells of *Burkholderia* sp. MAK1, Sci. Rep. 6 (2016) 39129.

[29] H. Koshima, M. Hamada, I. Yagi, K. Uosaki, Synthesis, Structure, and Second-Harmonic Generation of Noncentrosymmetric Cocrystals of 2-Amino-5-nitropyridine with Achiral Benzenesulfonic Acids, Cryst Growth Des. 1 (2001) 467-471.

[30] P. Dey, S. Islam, S.K. Seth, Quantitative analysis of the interplay of hydrogen bonds in M(II)-hexaaqua complexes with HMTA [M(II) = Co(II), Mg(II); HMTA = hexamethylenetetramine], J. Mol. Struct. 1284 (2023) 135448.

[31] D. Dey, S.K. Seth, T.P. Mohan, D. Chopra, Quantitative analysis of intermolecular interactions in crystalline substituted triazoles. J. Mol. Struct. 1273 (2023) 134380.

[32] R.F. Bader, Atoms in Molecules, Acc. Chem. Res. 18 (1985) 9-15.

[33] S. Islam, P. Dey, S.K. Seth, A combined experimental and theoretical studies of two new Co(II)–PDA complexes: Unusual 2D and 3D supramolecular networks [PDA = 2,6-pyridinedicarboxylic acid], Polyhedron 242 (2023) 116514.

[34] V.C. Tellez, B.S. Gaytan, S. Bernes, E.G. Vergara, The supramolecular structure of pyridine-2,6-dicarboxylic acid, Acta Crystallogr. Sect.C: Cryst. Struct. Commun. 58 (2002) o228–o230.

[35] BrukerSAINT, Version 6.36a, Bruker AXS Inc., Madison, Wisconsin, USA, 2002.

[36] BrukerSMART, Version 5.625 and SADABS, Version 2.03a, Bruker AXS Inc., Madison, Wisconsin, USA, 2001.

[37] G. M. Sheldrick, SHELXS97 and SHELXL97: programs for crystal structure solution and refinement, University of Göttingen, Germany, 1997.

[38] A. L. Spek, PLATON, a multipurpose crystallographic tool, Utrecht University, Utrecht, The Netherlands, 2000.

[39] L.J. Farrugia, WinGX suite for small-molecule single-crystal crystallography, J. Appl. Cryst. 32 (1999) 837–838.

[40] R. Destro, T. Pilati, M. Simonetta, 2-Amino-3-nitropyridine, Acta. Crystallogr. B. Struct. Sci. Cryst. Eng. Mater. 31 (1975) 2883–2885.

[41] C.B. Aakeröy, A.M. Beatty, M. Nieuwenhuyzen, M. Zou, A structural study of 2-amino-5-nitropyridine and 2-amino-3-nitropyridine: intermolecular forces and polymorphism, J. Mater. Chem. 8 (1998) 1385–1389.

[42] J.J. McKinnon, M.A. Spackman, A.S. Mitchell, Novel tools for visualizing and exploring intermolecular interactions in molecular crystals, Acta Crystallogr. Sect. B: Struct. Sci. 60 (2004) 627–668.

[43] S.K. Wolff, D.J. Grimwood, J.J. McKinnon, D. Jayatilaka, M.A. Spackman, CrystalExplorer 2.1, University of Western Australia, Perth, Australia, 2007.

[44] M.J. Frisch, G.W. Trucks, H.B. Schlegel, G.E. Scuseria, M.A. Robb, J.R. Cheeseman, G. Scalmani, V. Barone, G.A. Petersson, H. Nakatsuji, X. Li, M. Caricato, A.V. Marenich, J. Bloino, B.G. Janesko, R. Gomperts, B. Mennucci, H.P. Hratchian, J.V. Ortiz, A.F. Izmaylov, J.L. Sonnenberg, D. Williams-Young, F. Ding, F. Lipparini, F. Egidi, J. Goings, B. Peng, A. Petrone, T. Henderson, D. Ranasinghe, V.G. Zakrzewski, J. Gao, N. Rega, G. Zheng, W. Liang, M. Hada, M. Ehara, K. Toyota, R. Fukuda, J. Hasegawa, M. Ishida, T. Nakajima, Y. Honda, O. Kitao, H. Nakai, T. Vreven, K. Throssell, J.A. Montgomery Jr., J.E. Peralta, F. Ogliaro, M.J. Bearpark, J.J. Heyd, E. N. Brothers, K.N. Kudin, V.N. Staroverov, T.A. Keith, R. Kobayashi, J. Normand, K. Raghavachari, A.P. Rendell, J.C. Burant, S.S. Iyengar, J. Tomasi, M. Cossi, J.M. Millam, M. Klene, C. Adamo, R. Cammi, J. W. Ochterski, R.L. Martin, K. Morokuma, O. Farkas, J. B. Foresman, D.J. Fox, Gaussian 16, Revision C.01, Gaussian, Inc., Wallingford, CT, 2016.

[45] A. Gavezzotti, Efficient computer modeling of organic materials. The atom-atom, Coulomb–London–Pauli (AA-CLP) model for intermolecular electrostatic-polarization, dispersion and repulsion energies†, New J. Chem. 35 (2011) 1360.

[46] R.F. Bader, A Quantum Theory of Molecular Structure and Its Applications, Chem. Rev. 91 (1991) 893–928.

[47] T.A. Keith, AIMAll, Version 13.05.06, TK Gristmill Software, Overland Park, KS, USA, 2013.

[48] P. Dhanishta, S.K. Mishra, N. Suryaprakash, Intramolecular HB Interactions Evidenced in Dibenzoyl Oxalamide Derivatives: NMR, QTAIM, and NCI Studies, J. Phys. Chem. A 122 (2018) 199–208.

[49] N.S. Venkataramanan, A. Suvitha, Nature of bonding and cooperativity in linear DMSO clusters: A DFT, AIM and NCI analysis, J. Mol. Graph. Model 81 (2018) 50–59.

[50] N. Kumar, S. Saha, G.N. Sastry, Towards developing a criterion to characterize noncovalent bonds: a quantum mechanical study†, Phys. Chem. Chem. Phys. 23 (2021) 8478–8488.

[51] C.S. Liu, P.Q. Chen, E.C. Yang, J.L. Tian, X.H. Bu, Z.M. Li, H.W. Sun, Z. Lin, Z., Silver(I) Complexes in Coordination Supramolecular System with Bulky Acridine-

Based Ligands: Syntheses, Crystal Structures, and Theoretical Investigations on C−H···Ag Close Interaction, Inorg. chem. 45 (2006) 5812–5821.

[52] J. Contreras-García, E.R. Johnson, S. Keinan, R. Chaudret, J.P. Piquemal, D.N. Beratan, W. Yang, NCIPLOT: A Program for Plotting Noncovalent Interaction Regions, J. Chem. Theory Comput. 7 (2011) 625–632.

[53] E.R. Johnson, S. Keinan, P. Mori-Sánchez, J. Contreras-García, A.J. Cohen, W. Yang, Revealing Noncovalent Interactions, J. Am. Chem. Soc. 132 (2010) 6498–6506.

[54] L.J. Farrugia, ORTEP-III (Version 1.06), Department of Chemistry, University of Glasgow, Scotland, UK.

[55] S.K. Seth, D. Sarkar, T. Kar, Use of π–π forces to steer the assembly of chromone derivatives into hydrogen bonded supramolecular layers: crystal structures and Hirshfeld surface analyses†, CrystEngComm 13 (2011) 4528–4535.

[56] S.K. Seth, P. Manna, N.J. Singh, M. Mitra, A.D. Jana, A. Das, S.R. Choudhury, T. Kar, S. Mukhopadhyay, K.S. Kim, Molecular architecture using novel types of noncovalent π-interactions involving aromatic neutrals, aromatic cations and π-anions†, CrystEngComm 15 (2013) 1285–1288.

[57] P. Manna, S.K. Seth, M. Mitra, A. Das, N.J. Singh, S.R. Choudhury, T. Kar, S. Mukhopadhyay, A successive layer-by-layer assembly of supramolecular frameworks driven by a novel type of face-to-face π^+–π^+ interactions†, CrystEngComm 15 (2013) 7879–7886.

[58] S.K. Seth, I. Saha, C. Estarellas, A. Frontera, T. Kar, S. Mukhopadhyay, Supramolecular Self-Assembly of M-IDA Complexes Involving Lone-Pair···π Interactions: Crystal Structures, Hirshfeld Surface Analysis, and DFT Calculations [H_2IDA = iminodiacetic acid, M = Cu(II), Ni(II)], Cryst. Growth Des. 11 (2011) 3250–3265.

[59] S.K. Seth, B. Dey, T. Kar, S. Mukhopadhyay, Experimental observation of supramolecular carbonyl–π/π–π/π–carbonyl assemblies of Cu^{II} complex of iminodiacetate and dipyridylamine, J. Mol. Struct. 973 (2010) 81–88.

[60] C. Gatti, Chemical Bonding in Crystals: New directions, Z. fur Krist. - Cryst. Mater. 132 (2010) 6498–6506.

SUMMARY AND FUTURE PLAN

SUMMARY

The present research aims to synthesize and analyze various functional organic and hybrid inorganic-organic materials through experimental and theoretical X-ray structural studies. Therefore, it makes perfect sense to investigate molecular structures in the context of crystal engineering as it deals with problems related to intermolecular interactions. Predicting the supramolecular aggregation of a specific set of molecules in a crystal is very difficult and essentially impossible because predicting the crystal structure is a challenging task still far from being solved. Consequently, the prediction problem often applies only to supramolecular synthons of different functional groups or recognition patterns. One of the primary objectives of crystal engineering is to control the topology of crystal packing for functional solids through covalent and non-covalent interactions. Thus the successful incorporation of suitable structural units into a crystal can lead to the development of novel materials.

The aim of the research program described in the thesis is to systematically examine the various non-covalent bonding interactions observed in the new crystal structures. This proposed research work examines the fact that apart from strong hydrogen bonding interactions, various weak interactions play an important role in the formation of supramolecular architecture. Exploration of supramolecular structures can help identify supramolecular synthons of significance in crystal engineering. Based on this concept I have focused my research on the study of non-covalent interactions for creating crystal structures of the compounds under investigation. In this thesis, it is revealed that hydrogen bonds act as the driving force behind the primary supramolecular aggregation, while weak forces govern the final packing of molecules in the solid state.

Non-covalent interactions are not the only controlling factor, the molecular architectures can be affected by various factors, e.g., pH value, metal ions, ligands, metal-ligand ratio, solvents, temperature, etc. To understand the relevance of this point, pH-dependent, and ligand-dependent structural variations are investigated and included in this thesis. In addition, the proposed research work included a detailed study of packing polymorphism in the context of crystal engineering.

SUMMARY

In solid state, the formation of extensive supramolecular networks through non-covalent interactions are very interesting. In this context, our serendipitous discovery of extensive (lone pair···π/π···π$^+$/π$^+$···π/π···π/π···π$^+$/π$^+$···π/π···lone pair)$_n$ network in the solid state structures sheds light on the importance of such newly discovered supramolecular forces in organizing and stabilizing molecular components in crystals. In addition, this thesis also included several articulated supramolecular structures through the unique combination of weak non-covalent forces, for example, a unique 3D supramolecular architecture generated through π···π and lone pair···π interactions, 3D supramolecular boxes propagating in 2D plane, etc.

Crystal engineers are more interested in the individual potentiality of non-covalent forces. Several theoretical methods are used to explore non-covalent forces both qualitatively and quantitatively. Properties of the Hirshfeld surfaces provide visual interpretation of non-covalent forces, while the corresponding 2D fingerprint plots reveals the percentage contribution of each contacts. Interaction energies of a dimer can be evaluated using the DFT calculation, whereas the contribution of dispersion as well as electrostatic part to the total interaction energy can be obtained by using PIXEL calculations. PIXEL calculations also provide the lattice energies of the crystal structures. The QTAIM is used to further characterize the non-covalent interactions. The topological analysis at the bond critical points (BCPs) reveals the closed-shell nature of the non-covalent interaction and also dissociation energy can be calculated. The colored isosurfaces in the NCI Plot also reveals the strong or weak nature of interactions.

FUTURE PLAN

Currently, I am trying to design and synthesize new organic compounds as well as metal organic complexes and analyze them through experimental and theoretical methods in the near future. In the continuation of my research, efforts will be made to explore new non-covalent interactions and unique self-assemblies in the solid state. Also, attempts will be made to synthesize novel polymorphs, co-crystals, salts, etc., and establish correlations between the structures and properties of the synthesized compounds. In addition, extended networks will be characterized by high-performance theoretical methods. Efforts will also be made to investigate the non-linear optical properties in the near future.

LIST OF PUBLICATIONS

1. **pH-induced structural variations of two new Mg (II)-PDA complexes: experimental and theoretical studies**

   Samiul Islam, Suparna Tripathi, Anower Hossain, Saikat Kumar Seth, Subrata Mukhopadhyay

   Journal of Molecular Structure 1265 (2022) 133373

2. **Exploring Solid-State Supramolecular Architectures of Penta (carboxymethyl) diethylenetriamine: Experimental Observation and Theoretical Studies**

   Samiul Islam, Prantika Das, Suparna Tripathi, Saikat Kumar Seth, Subrata Mukhopadhyay

   ChemistrySelect 7 (2022) e202203396

3. **A combined experimental and theoretical studies of two new Co (II)–PDA complexes: unusual 2D and 3D supramolecular networks [PDA= 2, 6-pyridinedicarboxylic acid]**

   Samiul Islam, Pratik Dey, Saikat Kumar Seth

   Polyhedron 242 (2023) 116514

4. **Quantitative investigations of intermolecular interactions in 2-amino-3-nitropyridine polymorphs: Inputs from quantum mechanical calculations**

   Samiul Islam, Pratik Dey, Prantika Das, Saikat Kumar Seth,

   Journal of Molecular Structure 1293 (2023) 136253

Publications not included in this thesis

5. **Supramolecular assemblies involving salt bridges: DFT and X-ray evidence of bipolarity**

   Suparna Tripathi, **Samiul Islam**, Saikat Kumar Seth, Antonio Bauzá, Antonio Frontera, Subrata Mukhopadhyay,

   CrystEngComm 22 (2020) 8171–8181 (Published as Front Cover Page)

6. **Structural elucidation of phenoxybenzaldehyde derivatives from laboratory powder X-ray diffraction: A combined experimental and theoretical quantum mechanical study**

   Soumen Ghosh, **Samiul Islam**, Samiran Pramanik, Saikat Kumar Seth

   Journal of Molecular Structure 1268 (2022) 133697

7. **Intriguing π-interactions involving aromatic neutrals, aromatic cations and semiconducting behavior in a pyridinium-carboxylate salt**

   Prantika Das, **Samiul Islam**, Dhananjoy Das, Partha Pratim Ray, Saikat Kumar Seth

   Journal of Molecular Structure 1284 (2023) 135326

8. **Quantitative analysis of the interplay of hydrogen bonds in M (II)-hexaaqua complexes with HMTA [M (II)= Co (II), Mg (II); HMTA= hexamethylenetetramine]**

Pratik Dey, **Samiul Islam**, Saikat Kumar Seth

Journal of Molecular Structure 1284 (2023) 135448

9. **Structural and computational insights into two trimethylenedipyridine co-crystals: Inputs from X-ray diffraction, Hirshfeld surface, PIXEL, QTAIM and NCI plots**

Pratik Dey, **Samiul Islam**, Prantika Das, Saikat Kumar Seth

Journal of Molecular Structure 1296 (2024) 136820

10. **Insights into the structural investigation of metal-complexes with 1,3-diamino-2-hydroxypropanetetraacetic acid: Inputs from X-ray and computational studies**

Prantika Das, **Samiul Islam**, Saikat Kumar Seth

Polyhedron 248 (2024) 116732

11. **2D–3D supramolecular assemblies featuring lone-pair⋯π interaction in two Cu(II)–PDA complexes: Experimental and computational assessment**

Prantika Das, **Samiul Islam**, Saikat Kumar Seth

Manuscript Under Review in Polyhedron
(Manuscript Number: POLYH-D-24-00007)

12. **Structural elucidation and various computational studies for quantitative investigation of intermolecular interactions in pyridine-2,6-dicarboxylic acid and its di-hydrate**

Samiul Islam, Pratik Dey, Saikat Kumar Seth

Manuscript Under Review in Journal of Molecular Structure
(Manuscript Number: MOLSTRUC-D-23-08445)

13. **Trimorphic forms of iminodiacetic acid: an energetic and topological approach to understand the supramolecular structures**

Pratik Dey, **Samiul Islam**, Saikat Kumar Seth

Manuscript Submitted in ChemistrySelect
(Manuscript Number: slct.202400059)

Journal of Molecular Structure 1265 (2022) 133373

Contents lists available at ScienceDirect

Journal of Molecular Structure

journal homepage: www.elsevier.com/locate/molstr

pH-induced structural variations of two new Mg(II)-PDA complexes: experimental and theoretical studies

Samiul Islam[a], Suparna Tripathi[a,b], Anowar Hossain[b], Saikat Kumar Seth[a,*], Subrata Mukhopadhyay[b]

[a] Department of Physics, Jadavpur University, Kolkata 700032, India
[b] Department of Chemistry, Jadavpur University, Kolkata 700032, India

ARTICLE INFO

Article history:
Received 9 February 2022
Revised 19 May 2022
Accepted 23 May 2022
Available online 25 May 2022

Keywords:
PH-dependent Mg(II) complexes
Supramolecular structure
Bader's theory of 'atoms-in-molecules' (AIM)
Theoretical 'Noncovalent interaction' (NCI) plot index

ABSTRACT

PH-dependent reaction between 2,6-pyridine dicarboxylic acid (PDA) and $Mg(NO_3)_2$ in water results in the formation of two new complexes (**1**) and (**2**). The grown complexes are characterized through single-crystal X-ray diffraction analyses. The structural investigations exhibit that the hydrogen bonds and lone-pair$\cdots\pi$ interactions stabilize the crystal structure of the complex (1) whereas complex (2) is stabilized through hydrogen bonds only. The noncovalent interactions have been characterized using Bader's theory of "atoms in molecules" (AIM). The nature of these interactions have been studied using atoms in molecules topological analysis. Topological analysis of intermolecular interactions at their bond critical points revealed that all of the interactions are of closed-shell interactions. The "noncovalent interaction" (NCI) plot index has been performed to characterize the noncovalent interactions of the structures discussed in this study.

1. Introduction

The modern research of coordination chemistry is progressing at an explosive pace in crystal engineering because of the self-assembly phenomenon of small building units to complicated architectures, fascinating structural topologies, and potentiality as functional materials in the fields of magnetism, gas absorption, catalysis, luminescence, optoelectronic devices and nonlinear optics [1–5]. In recent years, careful exploration of various noncovalent interactions, namely, intra and intermolecular hydrogen bonding, hydrophobic interactions, dispersion interactions, halogen bonding, cation$\cdots\pi$, N–H$\cdots\pi$, C–H$\cdots\pi$, S–H$\cdots\pi$, $\pi\cdots\pi$, lone pair$\cdots\pi$, salt bridge$\cdots\pi$, etc. interactions gain great attention due to their crucial role in controlling crystal structures and properties of metal complexes [6–12]. However, there is a state of infancy in developing coordination compounds with the desired topologies and properties as many factors affect the molecular architectures. These controlling factors are metal ions, ligands, metal-ligand ratio, counterions, pH value, solvents, and temperature [13–15]. Moreover, nucleophilic activity, positions of donor atoms of ligands, and intrinsic geometric preferences of the central metal atom also play a pivotal role in determining the self-assembled structure of coordination complexes [16].

Being one of the essential regulating factors, the pH of the reaction medium plays a pivotal role in determining coordination modes of the ligand and hence geometry of the complexes [17,18]. It has adverse effects on complex formation such as pH helps in determining the specific binding modes of ligand by protonation/deprotonation, maintaining the metal-to-ligand ratio in the products [19,20], maintaining the concentration of OH^- ligand [21], in situ formation, and conversion of ligands [22,23], and control of reaction kinetics by modulation of pH values [24,25]. Therefore, it is clear that metal-ligand complexation and their packing in the solid-state are significantly controlled by pH [26]. In general, the higher the pH, the deprotonation will lead to greater connectivity (μ) of ligands to the metal ion based on acid-base chemistry and hard and soft acid-base (HSAB) principle i.e., high dimensional self-assembled structure. Therefore, at higher pH, i.e., in alkaline or weakly acidic medium, coordination of water to the metal centers becomes difficult, resulting in complexes having a lower metal-to-water (coordinated water) ratio. In contrast, at lower pH, alkaline earth metal shows a higher tendency to coordinate with water molecules to satisfy the coordination sphere, which causes a higher metal-to-water (coordinated water) ratio, leading to low dimensional architecture formation [27]. From the above discussion, it is thus evident that the solid-state structure of metal complexes

* Corresponding author:
E-mail address: saikatk.seth@jadavpuruniversity.in (S.K. Seth).

https://doi.org/10.1016/j.molstruc.2022.133373
0022-2860/

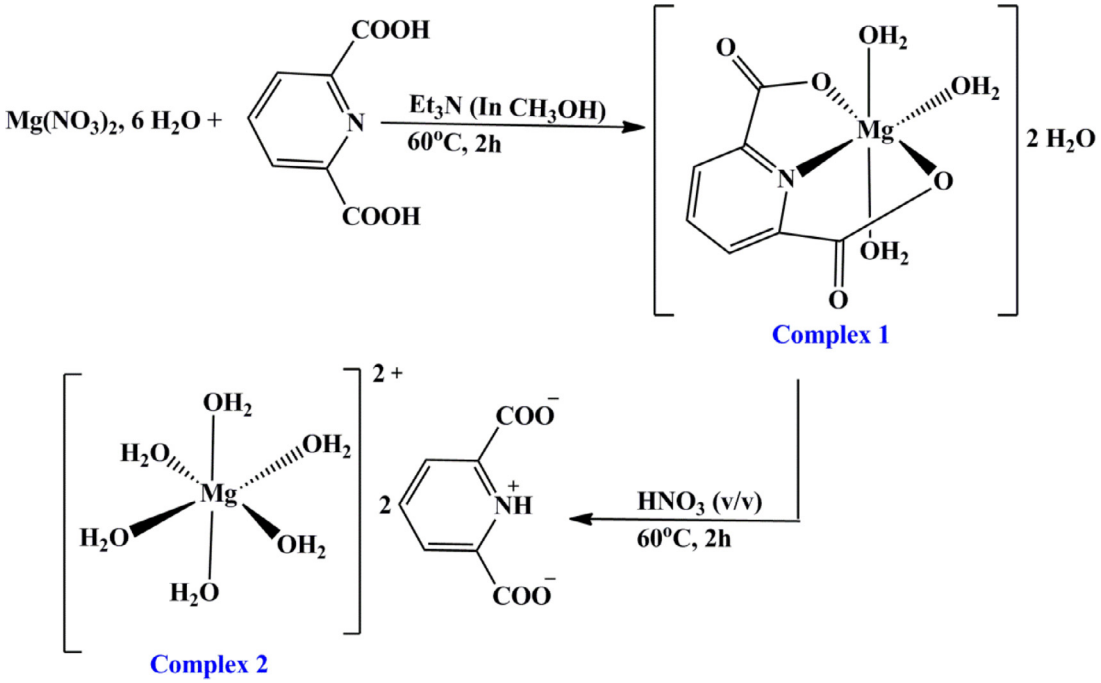

Scheme 1. Schematic representation for the synthesis of both the complexes.

is greatly influenced by reaction acidity, and it plays a crucial role in determining the dimensionality of the self-assembly structure.

Coordination modes of multicarboxylic acid can be manipulated by changing the pH value as protonated, and deprotonated forms of carboxylate moiety depend on their following pK_a values [28]. Thus, the binding of pyridine-2,6-dicarboxylic acid (pK_{a1} and pK_{a2} are 1.4 and 3.1, respectively) to metal ions can be varied by changing the pH value of the reaction medium [29]. Its dicarboxylic acid plays an essential role in producing multidimensional self-assembled complexes. They generally display a variety of binding modes such as terminal monodentate, chelating, bridging bidentate in a syn-syn, syn-anti, and anti-anti configuration to two metal centers and bridging tridentate to two metal centers [30] because of having rigid 120° angle between the central pyridine ring and two carboxylate groups [31]. Besides, such ligand causes involvement of hydrogen bonding, π–π, anion–π, cation–π, lone pair–π, etc. supramolecular interactions that may lead to the formation of one-dimensional chains and ladders, two-dimensional grids, three-dimensional microporous networks, interpenetrated modes, and helical staircase networks and so on in their complexes [32].

This paper reports the pH-dependent variation of coordination modes of 2,6-pyridine dicarboxylic acid towards Mg(II) metal ion and their structural features in the solid state. The noncovalent interactions are further characterized through Bader's theory of "atoms in molecules" (AIM) and the "noncovalent interaction" (NCI) plot index.

2. Experimental sections

2.1. Materials and Measurements

All chemicals used were of reagent grade quality and purchased from Sigma Aldrich Chemical Co. All reactions were carried out in an aqueous medium under aerobic conditions. During the whole experiment, doubly distilled water was used. Elemental analyses (C, H, and N) were performed on a Perkin-Elmer 240C elemental analyzer.

2.2. Syntheses

Synthesis of Complex [Mg(dipic)(H_2O)$_3$].2H_2O (**1**).

$Mg(NO_3)_2.6H_2O$ (0.512 g, 2.0 mmol) dissolved in 50 mL of water was allowed to react with pyridine-2,6-dicarboxylic acid (0.336 g, 2.0 mmol) at 60°C, which results in a colorless solution (Scheme 1). The pH of the reaction mixture was adjusted to ~5.5 by adding a freshly prepared solution of triethylamine in methanol. The reaction mixture thus obtained was stirred at 60°C for two hours, then cooled to room temperature, filtered, and kept undisturbed for crystallization. After four weeks, block-shaped, colorless single crystals suitable for X-ray analysis were obtained. The crystals were collected by filtration, washed with cold water, and dried in the air (yield: 65%). Anal. calcd. for $C_7H_{13}MgNO_9$: C, 30.08; H, 4.69; N, 5.01%. Found: C, 30.10; H, 4.73; N, 4.98%.

Synthesis of Complex [Mg(H_2O)$_6$].2dipicH (**2**).

Taking complex (**1**) as the precursor, we have planned to synthesize complex **2**. For the synthesis, a solid crystal of complex (**1**) (0.279 gm, 1.0 mmol) was first dissolved in 40 mL of distilled water, and then nitric acid was added (HNO_3: H_2O = 1: 20). That results in the reaction medium having pH ~ 4, further stirred at 60°C for two hours. The final reaction mixture was then cooled to room temperature, filtered, and kept undisturbed for slow evaporation. After five weeks, block-shaped, colorless single crystals suitable for X-ray analysis were obtained. The crystals were collected by filtration, washed with cold water, and dried in the air (yield: 62%). Anal. calcd. for $C_{14}H_{20}MgN_2O_{14}$: C, 36.19; H, 4.34; N, 6.03%. Found: C, 36.16; H, 4.32; N, 6.06%.

2.3. X-ray crystal structure determination

Single crystal X-ray diffraction intensity data was collected using Bruker APEX-II CCD diffractometer with Mo$K\alpha$ radiation (λ = 0.71073 Å) at 120(2)K. The data reduction was performed using the program Bruker SAINT [33], and an empirical absorption correction was applied based on the multi-scan method [34]. The title structures were solved by the direct method (SHELXS-14) [35] and refined (SHELXL-18) [36] by the full-matrix least-squares

Table 1
Crystal data and structure refinement parameters for the title complexes (1–2).

Crystal data	Complex (1)	Complex (2)
Chemical formula	$C_7H_{13}Mg_1\ N_1O_9$	$C_{14}H_{20}Mg_1\ N_2O_{14}$
Formula weight	279.49	464.63
Temperature (K)	120(2)	120(2)
Wavelength (Å)	0.71073	0.71073
Crystal system, space group	Monoclinic, $P2_1/n$	Monoclinic, C2/m
a, b, c (Å)	8.8884(9), 9.8998(10), 13.1928(14)	13.1412(15), 11.0501(15), 6.5214(8)
β (°)	97.290(2)	93.798(3)
V (Å^3)	1151.5(2)	944.9(2)
Z, Calculated density (Mg/m^3)	4, 1.612	2, 1.633
μ (mm^{-1})	0.197	0.176
F(000)	584	484
Crystal size (mm)	0.21 × 0.13 × 0.08	0.21 × 0.14 × 0.09
θ range for data collection (°)	2.58 to 25.00	2.41 to 24.99
Limiting indices	-10<=h<=10, -11<=k<=11, -15<=l<=15	-15<=h<=15, -13<=k<=12, -7<=l<=7
Reflections collected / unique	10563 / 2028 [R(int) = 0.0248]	4383 / 877 [R(int) = 0.0238]
Completeness to θ	100.0 %	99.9 %
Absorption correction	Semi-empirical from equivalents	Semi-empirical from equivalents
Max. and min. transmission	0.98 and 0.97	0.98 and 0.97
Refinement method	Full-matrix least-squares on F^2	Full-matrix least-squares on F^2
Data/parameters	2028/163	877/80
Goodness-of-fit on F^2	1.046	1.115
Final R indices [I>2sigma(I)]	R_1 = 0.0268, wR_2 = 0.0709	R_1 = 0.0251, wR_2 = 0.0722
R indices (all data)	R_1 = 0.0285, wR_2 = 0.0722	R_1 = 0.0257, wR_2 = 0.0726
Largest diff. peak and hole (e Å^{-3})	0.214, −0.316	0.251, −0.177

$R_1 = \Sigma||F_o|-|F_c||/\Sigma|F_o|$, $wR_2 = [\Sigma\{(F_o^2-F_c^2)^2\}/\Sigma\{w(F_o^2)^2\}]^{1/2}$, $w = 1/\{\sigma^2(F_o^2) + (aP)^2 + bP\}$, where, a = 0.0378 and b = 0.5748 for (**1**); a = 0.0330 and b = 0.9319 for (**2**).

technique on F^2. We have used difference fourier electron density map to locate all the atom's positions. Difference maps are calculated using coefficients of ($|F_o|$ - $|F_c|$) with the calculated phase angles, where F_o is the observed structure factor, and F_c is the calculated structure factor. Difference maps tend to produce peaks where low electron density has been included in the model and produce negative holes where too much electron density has been included in the model. All the non-hydrogen atoms are assigned accordingly. A difference electron density synthesis was calculated around the circle representing possible hydrogen positions' loci. The maximum electron density is then taken as the starting position for the hydrogen atom(s). The distinct peaks corresponding to the hydrogen atoms are observed in the difference Fourier map and assigned accordingly. The OH H-atom positions obtained from a difference Fourier map was refined freely, while the C-bound H atoms were placed in idealized positions using the riding method, with bond distances ranging from 0.93 to 0.98 Å and $U_{iso}(H)$ values set at $1.5U_{eq}$ of the parent atoms. The structure solution was performed using the WinGX program V2014.1 [37] and analyzed by the program PLATON [38]. The crystal data and structure refinement parameters of the title compounds are summarized in Table 1. CCDC 2144365–2144366 contains the supplementary crystallographic data of complexes (**1**) and (**2**), respectively.

2.4. Theoretical methods

The quantum chemical computations of both complexes are achieved with the support of MP2/ B3LYP /6–311++ G (d,p) basis set available in Gaussian 09 w calculation package [39]. We have used the crystallographic coordinates for the theoretical calculations by using the models that are generated from the supramolecular networks. We have used Bader's "Atoms in molecules" theory [40] to analyze the weak noncovalent interactions by the AIMall calculation package [41]. The charge density (ρ(r)) is characterized by their critical points (CPs), and it's Laplacian that is expressed in terms of $L(r) = -\nabla^2(\rho(r))$ and is calculated using the Atom In Molecule (AIM) theory [42]. According to the topological properties, electron density is concentrated over $\nabla^2(\rho(r)) < 0$ and is depleted for $\nabla^2(\rho(r)) > 0$. Selected topological parameters such as electron density, ρ(r), Laplacian of the electron density, $\nabla^2\rho(r)$, potential electronic energy density V(r), kinetic electronic energy density, G(r), and total electronic energy density [H(r) = V(r) + G(r)] were used at their bond critical points (BCPs) to characterize the nature and strength of intermolecular interactions. The theoretical NCI plot [43] is a visualization index that has been used for the characterization of noncovalent interactions. Isosurfaces instead of critical points represent the noncovalent interactions. These isosurfaces represent favorable and unfavorable interactions and are differentiated by the isosurface color scheme with a red-yellow-green-blue scale. The red and blue surfaces represent ρ^+cut (repulsive) and ρ^-cut (attractive) interactions [44], respectively. However, weak repulsive and weak attractive interactions are represented by the yellow and green colors, respectively.

3. Results and discussion

3.1. Structural description of complex (1)

Complex (**1**) crystallizes in a monoclinic system with space group $P2_1/n$. The coordination geometry around the Mg(II) ion is distorted octahedral. The equatorial sites are occupied by one nitrogen N1, two carboxylate oxygen O1, O3 atoms from dipic ligand, and one oxygen atom O6 of the water molecule (Fig. 1). Two oxygen O5 and O7 atoms from the solvent water molecules occupy the axial sites. There are two more solvent water molecules in the asymmetric unit (Fig. 1). The N(1)–Mg(1)–O(7) angle is 89.05°, showing that O(7) atom lies cis to ring nitrogen atom N(1) (Table 2). The bite angles around the Mg(II) ion are N(1)–Mg(1)–O(1) = 74.27(4)°; N(1)–Mg(1)–O(3) = 73.96(4)°; O(1)–Mg(1)–O(6) = 101.40(4)° and O(3)–Mg(1)–O(6) = 110.39(4)°, summing up the in-plane angle to be exactly 360.02°. That shows the high planarity of one solvent water oxygen atom and O, N, O donor atoms of the dipic ligand. In the five-membered chelate rings, Mg(1)–O(1)–C(1)–C(2)–N(1) and Mg(1)–O(3)–C(7)–C(6)–N(1), all atoms are almost coplanar with O1 and C1 have the largest deviation [+0.054(1); -0.074(1)] in the opposite directions from the least-square mean plane of the chelate rings. The dihedral angle between two chelate rings is 1.49(3)°.

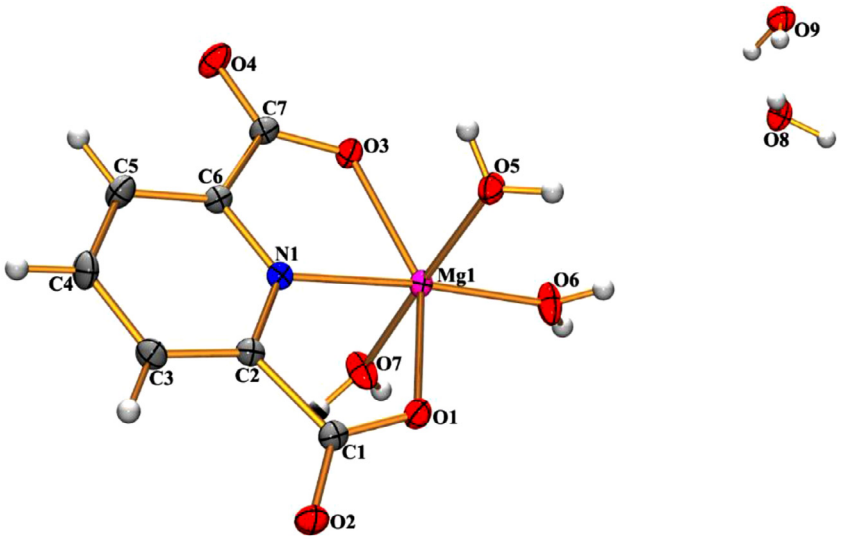

Fig. 1. An ORTEP view of complex (**1**) with the atom-numbering scheme. Thermal ellipsoids are drawn at 30% probability.

Table 2
Selected bond lengths (Å) and bond angles (°) of the title complexes.

Complex (1)				Complex (2)	
Mg(1)-O(6)	1.9962(11)	Mg(1)-N(1)	2.0972(12)	Mg(1)-O(5)	2.0054(12)
Mg(1)-O(7)	2.0233(10)	Mg(1)-O(1)	2.1451(10)	Mg(1)-O(4)	2.0462(12)
Mg(1)-O(5)	2.0413(10)	Mg(1)-O(3)	2.1624(10)	Mg(1)-O(3)	2.1170(12)
O(6)-Mg(1)-O(7)	88.61(4)	O(5)-Mg(1)-O(1)	92.25(4)	O(5)-Mg(1)-O(4)	90.0
O(6)-Mg(1)-O(5)	88.22(4)	N(1)-Mg(1)-O(1)	74.27(4)	O(5)-Mg(1)-O(3)	90.0
O(7)-Mg(1)-O(5)	176.48(5)	O(6)-Mg(1)-O(3)	110.39(4)	O(4)-Mg(1)-O(3)	91.56(5)
O(6)-Mg(1)-N(1)	175.08(5)	O(7)-Mg(1)-O(3)	90.73(4)	O(5)-Mg(1)-O(5)$^{\#1}$	180.0
O(7)-Mg(1)-N(1)	89.05(4)	O(5)-Mg(1)-O(3)	88.93(4)	C(3)-C(4)-C(3)$^{\#2}$	121.03(16)
O(5)-Mg(1)-N(1)	94.22(4)	N(1)-Mg(1)-O(3)	73.96(4)	C(2)-N(1)-C(2)$^{\#2}$	125.54(15)
O(6)-Mg(1)-O(1)	101.40(4)	O(1)-Mg(1)-O(3)	148.21(4)		
O(7)-Mg(1)-O(1)	89.89(4)				

Symmetry transformations used to generate equivalent atoms: #1: (-x, -y, -z+2) and #2: (x, -y, z).

Table 3
Hydrogen-bond geometry (Å, °).

D–H···A	D–H	H···A	D···A	D–H···A	Symmetry
Complex (**1**)					
O5–H5A···O9	0.82	1.96	2.7821(14)	174	1-x, 1-y, 1-z
O5–H5B···O3	0.82	1.91	2.7277(14)	177	3/2-x, -1/2+y, 1/2-z
O6–H6A···O4	0.83	1.83	2.6574(14)	177	3/2-x, -1/2+y, 1/2-z
O6–H6B···O9	0.83	2.06	2.8574(14)	161	3/2-x, -1/2+y, 3/2-z
O7–H7A···O2	0.83	1.83	2.6586(14)	173	5/2-x, 1/2+y, 1/2-z
O7–H7B···O8	0.83	1.99	2.7972(14)	167	2-x, 1-y, 1-z
O8–H8A···O1	0.83	1.98	2.7809(14)	162	-1/2+x, 1/2-y, 1/2+z
O8–H8B···O4	0.83	1.89	2.7063(13)	171	x, y, 1+z
O9–H9A···O8	0.82	1.96	2.7696(15)	167	—
O9–H9B···O2	0.82	2.03	2.8342(15)	166	2-x, 1-y, 1-z
Complex (**2**)					
N1–H1···O2	0.86	2.16	2.5643(12)	108	x, -y, z
O3–H3A···O1	0.83	1.95	2.7701(13)	169	1/2-x, 1/2-y, 2-z
O4–H4A···O1	0.83	1.94	2.7571(13)	170	1/2-x, 1/2-y, 1-z
O5–H5A···O2	0.83	1.86	2.6811(12)	176	1/2-x, 1/2-y, 1-z
C4–H4···O3	0.93	2.51	3.251(2)	137	—

The solid-state structure of the complex (**1**) is stabilized through multiple O–H···O hydrogen bonds and lone-pair(l.p)···π interactions (Table 3). In the first sub-structure, two metal-coordinating water oxygen atoms O(5) and O(6), acts as a donor to the carboxylate oxygen atoms O(3) and O(4) of the partner molecule at (3/2-x, -1/2+y, 1/2-z) by generating an $R_2^2(8)$ motif (Fig. 2). Due to the self-complementarity, another water oxygen atom O(7), acts as a donor to the carboxylate oxygen atom at (5/2-x, 1/2+y, 1/2-z) to build a two-dimensional supramolecular framework in (110) plane (Fig. 2). In another substructure, the carbonyl oxygen atoms O(2) and O(4) in the molecules at (2-x, -y, -z) and (2-x, 1-y, -z) are juxtaposed towards the centroid of the pyridine ring. The separation distance between the carbonyl oxygen atoms and the centroid of the sandwiched pyridine ring are 3.405(2)Å and 3.633(2)Å respectively, suggesting lone-pair(l.p)···π interactions (Fig. 3a). The combination of the hydrogen bonding contacts among coordinating water oxygen atoms O(5) and O(6) with the carboxylate oxygen atoms and the (l.p)···π/π···(l.p) network leads the molecules to build a supramolecular layered assembly (Fig. 3b).

3.2. Structural description of complex (2)

Complex (**2**) is crystallized in the monoclinic crystal system with C2/m space group. In complex (**2**), as illustrated in the ORTEP (Fig. 4), the molecular view consists of one-half of the aquated cation and two halves of the ligand molecule. The remaining portion of cationic and anionic moieties is generated via a centre of inversion. The metal ion is positioned in the inversion center (-x, -y, -z+2) and is situated in a perfect octahedral environment constructed from six water molecules (Fig. 4). The dipic ligand is not bound to the metal ions, remaining outside the coordination shell. The N(1) and C(4) atoms of the pyridine ring of the dipic ligand are in the inversion center (x, -y, z) (see Fig. 4). The Mg–O bond lengths vary in the range 2.048–2.118Å and are comparable to those of the similar complexes reported earlier [45, 46].

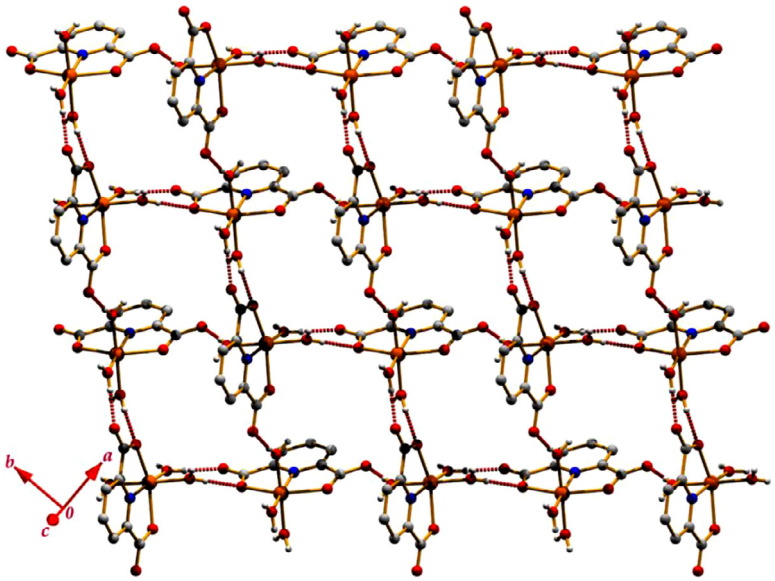

Fig. 2. Supramolecular framework in (**1**) through O–H···O hydrogen bonds.

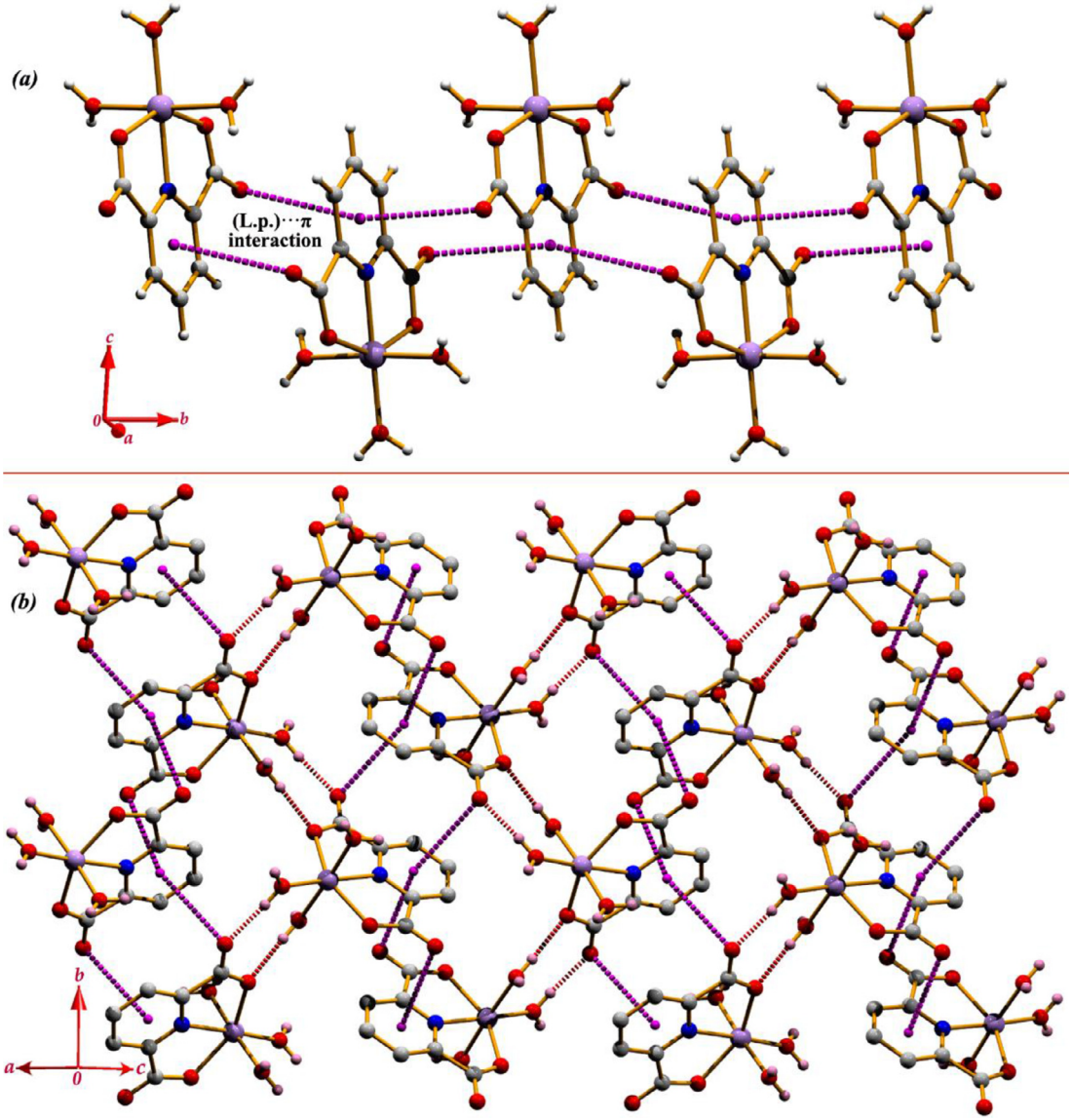

Fig. 3. (a) Perspective view of the (l.p)···π/π···(l.p) network in (**1**); (b) Supramolecular layered framework generated through O–H···O hydrogen bonds and (l.p)···π interaction in (**1**).

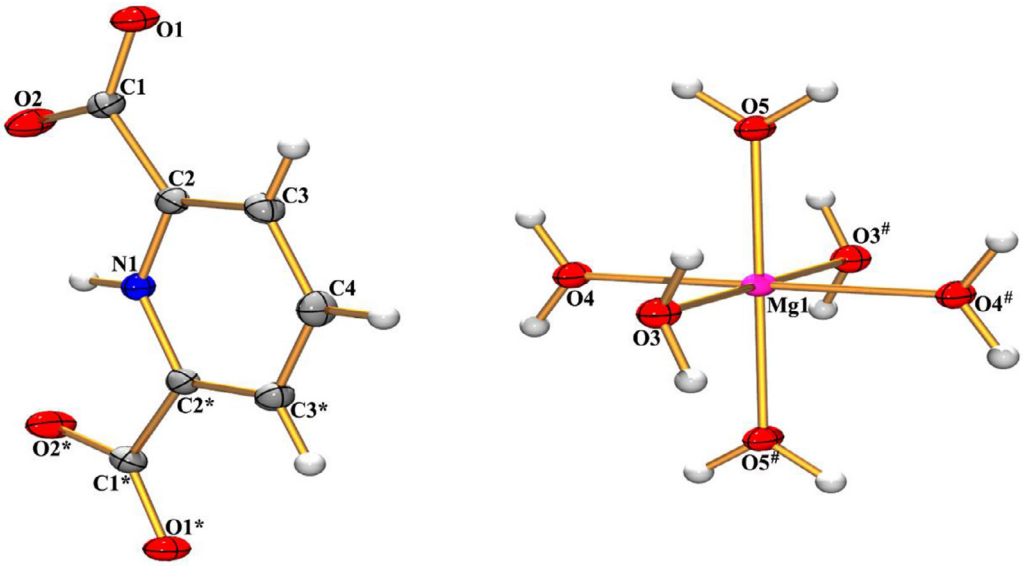

Fig. 4. An ORTEP view of complex (**2**) with the atom-numbering scheme. Thermal ellipsoids are drawn at 30% probability.

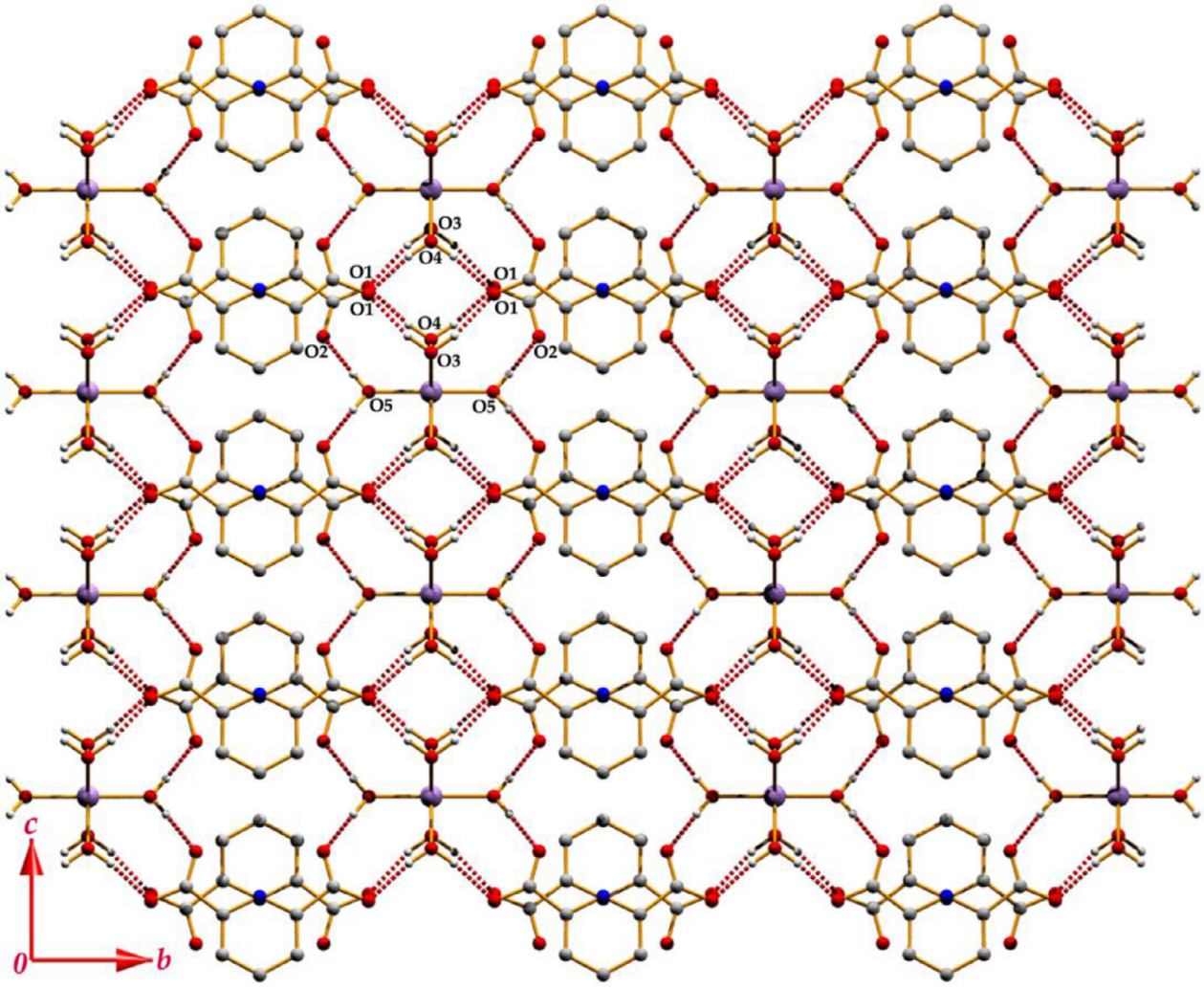

Fig. 5. Supramolecular framework generated through O–H···O hydrogen bonds in (**2**).

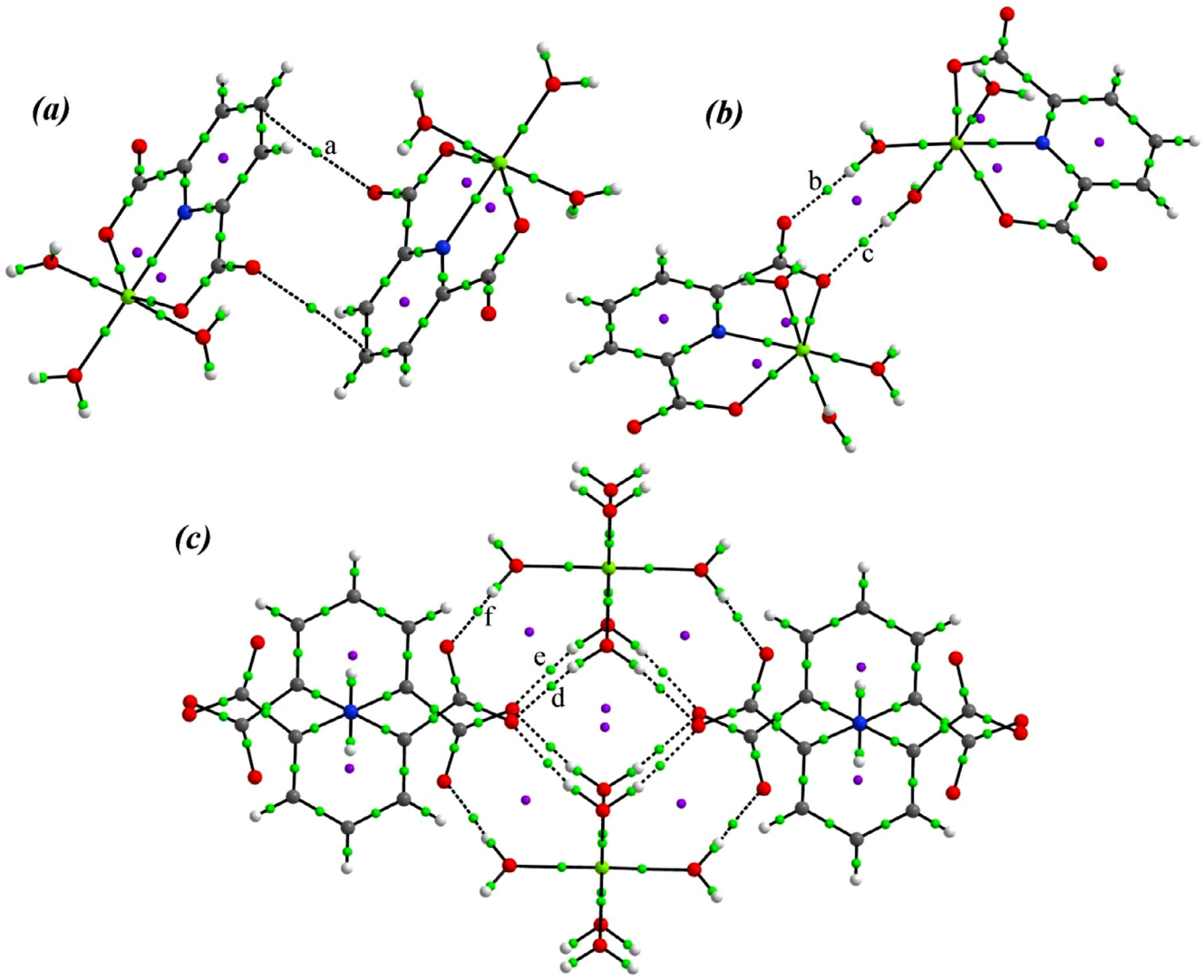

Fig. 6. AIM analyses of complexes (**1**)(*a,b*) and (**2**)(*c*). Green and violet spheres represent bond and ring critical points, respectively.

Complex (**2**) is stabilized through N–H···O, O–H···O and intramolecular C–H···O hydrogen bonds (Table 3). The supramolecular structures generated via hydrogen bonds between the $[Mg(H_2O)_6]^{2+}$ and anionic dipic ligand are illustrated separately. In the first substructure, the carboxylate oxygen atom O(1) acts as a double acceptor for the donor water oxygen atoms O(3) and O(4) in the molecules at (1/2-x, 1/2-y, 2-z), and (1/2-x, 1/2-y, 1-z) respectively. Moreover, another water oxygen atom O(5) at (1/2-x, 1/2-y, 1-z) acts as a donor to another carboxylate oxygen atom O(2) to build a supramolecular framework in the (011) plane (Fig. 5).

3.3. Theoretical analysis

Bader's theory of "atoms in molecules"(AIM) has been used for title complexes (**1–2**) to characterize different interactions that are exhibited by the structures. We have used various models that are generated from the X-ray structures. Here, the bond path and a bond critical point (CP) that interconnects two atoms of the molecule [40, 42] characterize the noncovalent interactions. For complex (**1**), a part of the self-assembled structure (see Fig. 3a) has been used as a model for AIM analysis. Here, the bond critical point (ρ_{BCP} = 0.0042 a.u.) (see Table 4) and a bond path interconnecting the carboxylate carbonyl oxygen atom and a carbon atom of the pyridine ring characterized the lone-pair(l.p)···π interaction in (**1**) (see Fig. 6a). In another model (see Fig. 6b), we have used a part of the packing of Fig. 3b for characterization of O–H···O hydrogen bonds. The bond critical points (ρ_{BCP} = 0.0313 and 0.0271 a.u.) and the bond paths between two water oxygen and carboxylate oxygen atoms represent strong O–H···O hydrogen bonds in (**1**) (Fig. 6b). For complex (**2**), the model has been used from the packing diagram (see Fig. 5). The hydrogen bonds in between the water oxygen atoms and carboxylate oxygen atoms are characterized by the bond path and BCPs (Fig. 6b). The ρ(r) values (0.0300 a.u. and 0.0266 a.u.) at the bond CPs designate the bonds where O(1) acts as a double donor to the water oxygen atoms O(3) and O(4). Moreover, the most robust hydrogen bonding contact is also evidenced by the bond critical point (ρ_{BCP} = 0.0321 a.u.) that agrees well with the experimental observations (see Table 3).

The topological and energetic properties of the noncovalent interactions at the bond critical points (BCPs) in the observed dimers of the crystal structures of (**1-2**) were analyzed by comparing selected topological properties, including the electron density (ρ(r)), the Laplacian of electron density ($\nabla^2\rho$(r)), the potential electronic energy density (V(r)), the kinetic electronic energy density (G(r)), the total electronic energy density (H(r)=V(r)+G(r)) and $|-\frac{V(r)}{G(r)}|$

Table 4
Topological parameters for intermolecular interactions [in different dimers of (1) and (2)] at their (3, –1) BCPs. [ρ(r): electron density (eÅ^{-3}); $\nabla^2\rho$(r): Laplacian of electron density (eÅ^{-5}); ε: ellipticity; V(r): potential energy density; G(r): kinetic energy density; H(r): total electronic density; V(r), G(r) and H(r) values in a.u.

	Interaction	ρ	$\nabla^2\rho$	ε	V(r)	G(r)	H(r)	$\lvert-\frac{V(r)}{G(r)}\rvert$
Complex-**1**	C7–O4···π (a)	0.0042	0.0136	1.5669	-0.0022	0.0028	0.0006	0.7857
	O6–H6A···O4 (b)	0.0313	0.1518	0.0372	-0.0330	0.0355	0.0025	0.9290
	O5–H5B···O3 (c)	0.0271	0.1297	0.0435	-0.0275	0.0300	0.0025	0.9166
Complex-**2**	O4–H4A···O1 (d)	0.0300	0.1285	0.0420	-0.0299	0.0310	0.0011	0.9645
	O3–H3A···O1 (e)	0.0266	0.1302	0.0214	-0.0271	0.0298	0.0027	0.9093
	O5–H5A···O2 (f)	0.0321	0.1446	0.0374	-0.0334	0.0348	0.0014	0.9597

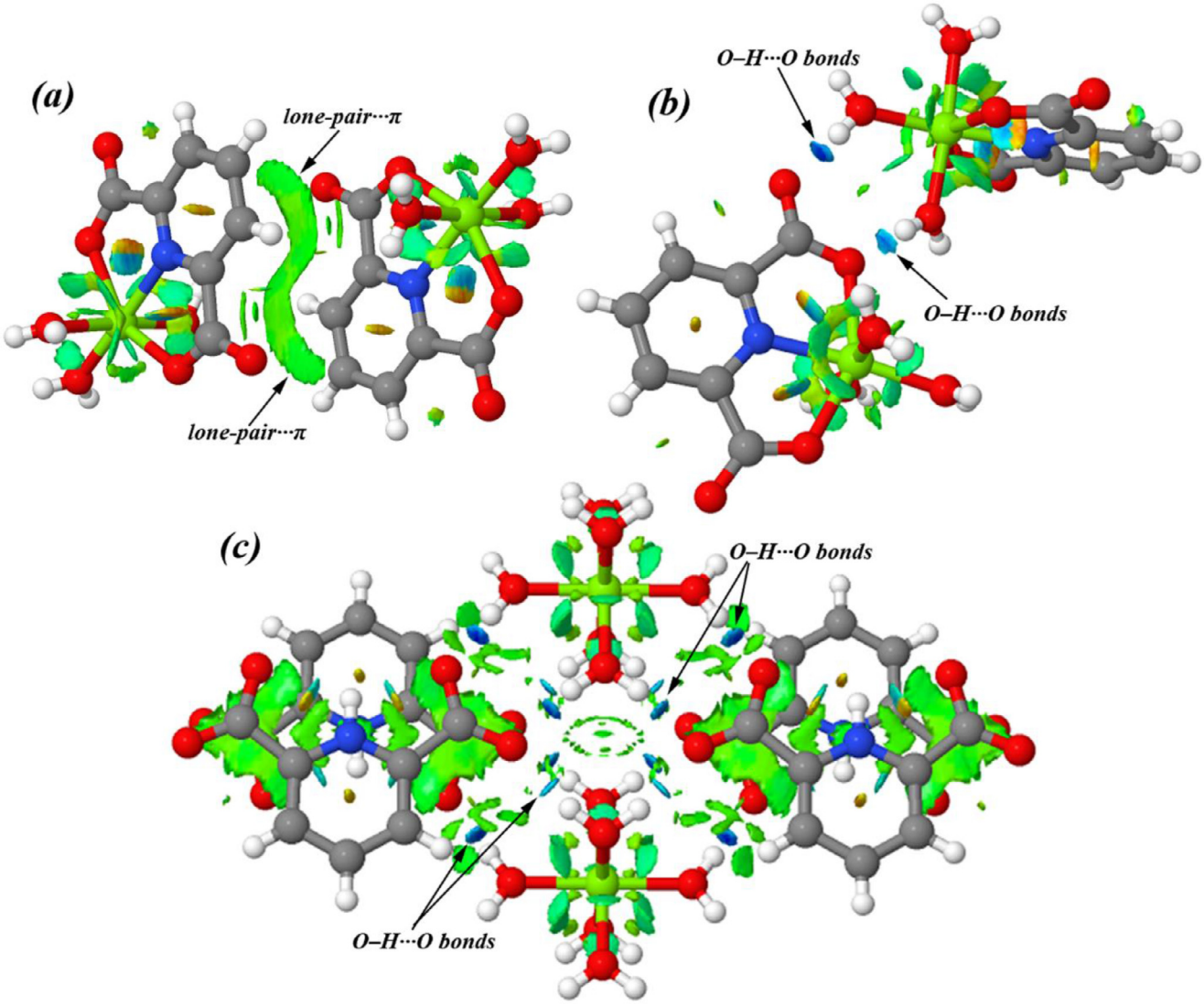

Fig. 7. NCI plot index of the modeled structure of compounds (**1**)(*a,b*) and (**2**)(*c*).

value. The lone-pair(l.p.)···π interaction in (1) and O–H···O hydrogen bonds in both complexes have been involved in the stabilization of observed molecular dimers (Table 4 and Fig. 6). According to Gatti's assignment, all these interactions are classified as closed-shell interactions [47] using the values of $\lvert-\frac{V(r)}{G(r)}\rvert < 1$, H(r) > 0 and the positive value of the Laplacian $\nabla^2\rho(r) > 0$.

Furthermore, the noncovalent interactions that are involved within the structures of the title complexes are characterized through the 'noncovalent interaction' (NCI) plot index. Herein, we have used a part of the packing diagrams for both complexes that are shown in Figs. 3a, 3b and 5, respectively. Different noncovalent interactions are evident by the green and blue isosurfaces. In Fig. 7a, the cooperativity of the (l.p)···π interaction has been characterized by the dual large green isosurfaces in between the carboxylate oxygen atom and the centroid of the pyridine ring. The large flattened greenish isosurface represents the dual interplay of the (l.p)···π interaction (Fig. 7a). The deep blue colored isosurfaces (see Fig. 7b) that are evident in between the water and carboxylate oxygen atoms represent strong O–H···O hydrogen bonds in (**1**). The representation of the NCI plot of complex (**2**) highlights the presence of multi O–H···O hydrogen bonds (Fig. 7c). The dark blue colored isosurfaces that are evidenced in the map and are located

in between water oxygen atoms and carboxylate oxygen atoms characterize the O–H···O hydrogen-bonding contacts in (**2**). As discussed in the AIM calculation, the most favorable O–H···O contact can also be identified by close examination of the blue patches of the isosurface (Fig. 7c). Subsequently, all the evident isosurfaces agree well with the AIM study and structural observation of both complexes.

4. Conclusions

Two new pH-dependent Mg(II)-PDA complexes have been synthesized and structurally characterized. The cooperativity of the noncovalent interactions has been explored in detail by examining the supramolecular behavior of the complexes. How a minor tuning of the pH value affects the solid-state structural assemblies has been explored herein. Theoretical AIM and NCI plot analyses have further characterized the noncovalent interactions and, consequently, the self-assemblies. Topological analysis of intermolecular interactions at their bond critical points revealed that all of the interactions are closed-shell interactions. The theoretical investigations agree well with the experimental findings. The findings reported herein are expected to be beneficial in understanding the pH dependency and the cooperative outcome of the noncovalent interactions in building supramolecular assemblies.

Credit Author Statement

Samiul Islam and Suparna Tripathi: Synthesis, X-ray structural characterization and exploration of self-assembled structures and analysis of the X-ray data; Anowar Hossain: Synthesis write-up; Saikat Kumar Seth: Theoretical calculation, investigation, writing, reviewing and editing; Subrata Mukhopadhyay: Reviewing and editing.

Supplementary information

CCDC 2144365–2144366 contains the supplementary crystallographic data for complexes (**1–2**). These data can be obtained free of charge via http://www.ccdc.cam.ac.uk/conts/retrieving.html, or from the Cambridge Crystallographic Data Centre, 12Union Road, Cambridge CB21EZ, UK; fax: (+44)1223-336-033; or e-mail:deposit@ccdc.cam.ac.uk. The full and breakdown fingerprint plots are included as supplementary data.

Declaration of Competing Interest

There are no conflicts to declare.

Acknowledgments

S. K. Seth gratefully acknowledges the financial support from SERB (New Delhi) India for Research Project (EEQ/2019/000384).

Supplementary materials

Supplementary material associated with this article can be found, in the online version, at doi:10.1016/j.molstruc.2022.133373.

References

[1] G. Ferey, Hybrid porous solids: past, present, future, Chem. Soc. Rev. 37 (2008) 191–214.
[2] Y.L. Liu, J.F. Eubank, A.J. Cairns, J. Eckert, V.C. Kravtsov, R. Luebke, M. Eddaoudi, Assembly of metal–organic frameworks (MOFs) based on indium-trimer building blocks: a porous MOF with soc topology and high hydrogen storage, Angew. Chem. Int. Ed. 119 (2007) 3342–3347.
[3] Y.B. Zhang, W.X. Zhang, F.Y. Feng, J.P. Zhang, X.M. Chen, A highly connected porous coordination polymer with unusual channel structure and sorption properties, Angew. Chem. Int. Ed. 48 (2009) 5287–5290.
[4] L.Q. Ma, A. Jin, Z.G. Xie, W.B. Lin, Freeze drying significantly increases permanent porosity and hydrogen uptake in 4, 4-connected metal–organic frameworks, Angew. Chem. Int. Ed. 48 (2009) 9905–9908.
[5] L. Qin, J.S. Hu, L.F. Huang, Y.Z. Li, Z.J. Guo, H.G. Zheng, Syntheses, Characterizations, and Properties of Six Metal– Organic Complexes Based on Flexible Ligand 5-(4-Pyridyl)-methoxyl Isophthalic Acid, Cryst. Growth Des. 10 (2010) 4176–4183.
[6] M. Waller, S. Grimme, Weak intermolecular interactions: a supermolecular approach, in: J. Leszczynski (Ed.), Handbook of Computational Chemistry, Springer International Publishing, Switzerland, 2017, pp. 593–619.
[7] P. Hobza, J. Rezac, Introduction: noncovalent interactions, Chem. Rev. 116 (2016) 4911–4912.
[8] S. Scheiner, Noncovalent forces; Springer; 2015.
[9] P. Manna, S.K. Seth, Antonio Bauzá, M. Mitra, S.R. Choudhury, A. Frontera, S. Mukhopadhyay, pH dependent formation of unprecedented water–bromide cluster in the bromide salts of PTP assisted by anion– π interactions: synthesis, structure, and DFT Study, Cryst. Growth Des. 14 (2014) 747–755.
[10] P. Manna, S.K. Seth, M. Mitra, S.R. Choudhury, Antonio Bauzá, A. Frontera, S. Mukhopadhyay, Experimental and computational study of counterintuitive $ClO_4^-\cdots ClO_4^-$interactions and the interplay between π^+–π and Anion$\cdots\pi^+$ interactions, Cryst. Growth Des. 14 (2014) 5812–5821.
[11] S.K. Seth, A. Bauzá, A. Frontera, Bipolar behaviour of salt-bridges: a combined theoretical and crystallographic study, New J. Chem. 42 (2018) 12134–12142.
[12] S. Tripathi, S. Islam, S.K. Seth, A. Bauzá, A. Frontera, S. Mukhopadhyay, Supramolecular assemblies involving salt bridges: DFT and X-ray evidence of bipolarity, CrystEngComm 22 (2020) 8171–8181.
[13] S.K. Seth, Tuning the formation of MOFs by pH influence: X-ray structural variations and Hirshfeld surface analyses of 2-amino-5-nitropyridine with cadmium chloride, CrystEngComm 15 (2013) 1772–1781.
[14] F. Yuan, J. Xie, H.M. Hu, C.M. Yuan, B. Xu, M.L. Yang, F.X. Dong, G.L. Xue, Effect of pH/metal ion on the structure of metal–organic frameworks based on novel bifunctionalized ligand 4′-carboxy-4, 2′: 6′, 4′′-terpyridine, CrystEngComm 15 (2013) 1460–1467.
[15] H.R. Khavasi, B.M.M. Sadegh, Temperature-dependent supramolecular motif in coordination compounds, Inorg. Chem. 49 (2010) 5356–5358.
[16] QY Li, G.W. Yang, L. Shen, M.H. He, W. Shen, K. Gu, J.N. Jin, Calcium (II), and Barium (II) Coordination Compounds Constructed by 1H-Tetrazolate-5-acetic Acid Ligand, Z. Anorg. Allg. Chem. 638 (2012) 826–831.
[17] M. Chen, S.S. Chen, T.A. Okamura, Z. Su, M.S. Chen, Y. Zhao, W.Y. Sun, N. Ueyama, pH dependent structural diversity of metal complexes with 5-(4 H-1, 2, 4-triazol-4-yl) benzene-1, 3-dicarboxylic acid, Cryst. Growth Des. 11 (2011) 1901–1912.
[18] H.C. Fang, J.Q. Zhu, L.J. Zhou, H.Y. Jia, S.S. Li, X. Gong, S.B. Li, Y.P. Cai, P.K. Thallapally, J. Liu, J G, Exarhos, pH-dependent assembly and conversions of six cadmium (II)-based coordination complexes, Cryst. Growth Des. 10 (2010) 3277–3284.
[19] S.T. Wu, L.S. Long, R.B. Huang, L.S. Zheng, pH-dependent assembly of supramolecular architectures from 0D to 2D networks, Cryst. Growth Des. 7 (2007) 1746–1752.
[20] H. Wang, Y.-Y. Wang, G.-P. Yang, C.-J. Wang, G.-L. Wen, Q.-Z. Shia, S.R. Batten, A series of intriguing metal–organic frameworks with 3, 3′, 4, 4′-benzophenonetetracarboxylic acid: structural adjustment and pH-dependence, CrystEngComm 10 (2008) 1583–1594.
[21] W.X. Chen, S.T. Wu, L.S. Long, R.B. Huang, L.S. Zheng, Construction of a three--fold parallel interpenetration network and bilayer structure based on copper (II) and trimesic acid, Cryst. Growth Des. 7 (2007) 1171–1175.
[22] X.J. Kong, G.L. Zhuang, Y.P. Ren, L.S. Long, R.B. Huang, L.S. Zheng, in: In situ cyclodehydration of iminodiacetic acid into 2, 5-diketopiperazine-1, 4-diacetate in lanthanide-based coordination polymers, Dalton Trans, 2009, pp. 1707–1709.
[23] X.J. Kong, Y.P. Ren, L.S. Long, R.B. Huang, L.S. Zheng, M. Kurmoo, Influence of reaction conditions on the channel shape of 3d-4f heterometallic metal–organic framework, CrystEngComm 10 (2008) 1309–1314.
[24] S.T. Wu, Y.R. Wu, Q.Q. Kang, H. Zhang, L.S. Long, Z.P. Zheng, R.B. Huang, L.S. Zheng, Chiral symmetry breaking by chemically manipulating statistical fluctuation in crystallization, Angew. Chem., Int. Ed. 46 (2007) 8475–8479.
[25] I. Katsuki, Y. Motoda, Y. Sunatsuki, N. Matsumoto, T. Nakashima, M. Kojima, Spontaneous resolution induced by self-organization of chiral self-complementary cobalt (III) complexes with achiral tripod-type ligands containing three imidazole groups, J. Am. Chem. Soc. 124 (2002) 629–640.
[26] D. Sun, Z.H. Wei, C.F. Yang, D.F. Wang, N. Zhang, R.B. Huang, L.S. Zheng, pH-Dependent Ag (I) coordination architectures constructed from 4-cyanopyridine and phthalic acid: from discrete structure to 2D sheet, CrystEngComm 13 (2011) 1591–1601.
[27] L. Pan, T. Frydel, M.B. Sander, X. Huang, J. Li, The effect of pH on the dimensionality of coordination polymers, Inorg. Chem. 40 (2001) 1271–1283.
[28] J.X. Yang, X. Zhang, J.K. Cheng, J. Zhang, Y.G. Yao, pH influence on the structural variations of 4, 4′-oxydiphthalate coordination polymers, Cryst. Growth Des. 12 (2012) 333–345.
[29] E. Norkus, I. Stalnionienė, D.C. Crans, Interaction of pyridine-and 4-hydroxypyridine-2, 6-dicarboxylic acids with heavy metal ions in aqueous solutions, Heteroat. Chem. 14 (2003) 625–632.
[30] H.L. Gao, L. Yi, B. Zhao, X.Q. Zhao, P. Cheng, D.Z. Liao, S.P. Yan, Synthesis and characterization of metal– organic frameworks based on 4-hydroxypyridine-2, 6-dicarboxylic acid and pyridine-2, 6-dicarboxylic acid ligands, Inorg. Chem. 45 (2006) 5980–5988.

[31] B. Zhao, L. Yi, Y. Dai, X.Y. Chen, P. Cheng, D.Z. Liao, S.P. Yan, Z.H. Jiang, Systematic investigation of the hydrothermal syntheses of Pr (III)– PDA (PDA= Pyridine-2, 6-dicarboxylate anion) metal– organic frameworks, Inorg. Chem. 44 (2005) 911–920.
[32] M.S. Liu, Q.Y. Yu, Y.P. Cai, C.Y. Su, X.M. Lin, X.X. Zhou, J.W. Cai, One-, two-, and three-dimensional lanthanide complexes constructed from pyridine-2, 6-dicarboxylic acid and oxalic acid ligands, Cryst. Growth Des. 8 (2008) 4083–4091.
[33] SAINT Bruker, Version 6.36a, Bruker AXS Inc., Madison, Wisconsin, USA (2002).
[34] SMART Bruker, Version 5.625 and SADABS, Version 2.03a, Bruker AXS Inc., Madison, Wisconsin, USA (2001).
[35] G.M. Sheldrick, A short history of SHELX, Acta Cryst. A 64 (2008) 112–122.
[36] G.M. Sheldrick, Crystal structure refinement with SHELXL, Acta Cryst. C 71 (2015) 3–8.
[37] L.J. Farrugia, WinGX and ORTEP for Windows: an update, J. Appl. Cryst. 45 (2012) 849–854.
[38] A.L. Spek, Single-crystal structure validation with the program PLATON, J. Appl. Crystallogr. 36 (2003) 7–13.
[39] M.J. Frisch, G.W. Trucks, H.B. Schlegel, G.E. Scuseria, M.A. Robb, J.R. Cheeseman, G. Scalmani, V. Barone, G.A. Petersson, H. Nakatsuji, et al., Gaussian 09, Revision C.01; Gaussian, Inc, Wallingford, CT, USA, 2009.
[40] R.F.W. Bader, A quantum theory of molecular structure and its applications, Chem. Rev. 91 (1991) 893–928.
[41] T.A. Keith, AIMAll, Version 13.05.06, TK Gristmill Software, Overland Park, KS, USA, 2013.
[42] R.F.W. Bader, Atoms in Molecules, a Quantum Theory, Oxford University Press, New York, NY, USA, 1990.
[43] J. Contreras-García, E.R. Johnson, S. Keinan, R. Chaudret, J.P. Piquemal, D.N. Beratan, W. Yang, NCIPLOT: A Program for Plotting Noncovalent Interaction Regions, J. Chem. Theory Comput. 7 (2011) 625–632.
[44] E.R. Johnson, S. Keinan, P. Mori-Sanchez, J. Contreras-Garcia, A.J. Cohen, W. Yang, Revealing Noncovalent Interactions, J. Am. Chem. Soc. 132 (2010) 6498–6506.
[45] A. Das, S.R. Choudhury, B. Dey, S.K. Yalamanchili, M. Helliwell, P. Gamez, A. Frontera, Supramolecular assembly of Mg (II) complexes directed by associative lone Pair– π/π– π/π– Anion– π/π– Lone pair interactions, J. Phys. Chem. B 114 (2010) 4998–5009.
[46] R.K. Mudsainiyan, A.K. Jassal, N. Islam, Self-assembled H-bonded supramolecular interactions in monomeric complex [Mg $(H_2O)_6$].L_2.2bipy.H_2O;[LH= 2-amino-5-nitrobenzoic acid, bipy= 4, 4′-bipyridine]: Joint theoretical calculations and Hirshfeld surface analysis, J. Mol. Struct 1232 (2021) 130073.
[47] C. Gatti, Chemical Bonding in Crystals: New Directions, Zeitschrift für Krist. - Cryst. Mater. 220 (2005) 399–457.

ChemistrySelect

Research Article
doi.org/10.1002/slct.202203396

Chemistry Europe
European Chemical Societies Publishing

www.chemistryselect.org

Exploring Solid-State Supramolecular Architectures of Penta(carboxymethyl)diethylenetriamine: Experimental Observation and Theoretical Studies

Samiul Islam,[a] Prantika Das,[a] Suparna Tripathi,[a, b] Subrata Mukhopadhyay,[b] and Saikat Kumar Seth*[a]

Crystals of penta(carboxymethyl)diethylenetriamine have been structurally characterized through single-crystal X-ray diffraction analysis. X-ray diffraction analysis reveals that various non-covalent interactions combine to determine the crystal packing and final solid-state supramolecular assembling behavior. The title compound exhibited various 2D supramolecular networks generated through O–H···O and C–H···O interactions. The C–H···O interactions are pivotal in building a two-dimensional framework, whose formation is readily analyzed with zero-dimensional centrosymmetric dimeric rings as building blocks within the structure. All the intermolecular interactions are quantified through Hirshfeld surface analysis and fingerprint plots. Energy frameworks are constructed to analyze the dominant interaction energy involved in molecular packing strength. Bader's quantum theory of "atoms-in-molecules" (QTAIM) has been used to analyze and characterize non-covalent interactions. The QTAIM analysis validates the existence of hydrogen bonding contacts, and the topological properties of bond critical points (BCPs), such as the electron density $\rho(r)$ and its Laplacian $\nabla^2\rho(r)$, are presented to correlate with the interaction energy. The topological analysis revealed that all of the interactions are closed-shell interactions. Finally, the "Non-covalent Interaction" (NCI) plot index illustrates the solid-state supramolecular networks.

Introduction

Diethylenetriaminepentaacetic acid (DTPA)[1,2] is comprised of five carboxylate groups that are bound to three nitrogen atoms.[3] Due to the high reactivity of the carboxylic group,[4] DTPA behaves as a bridging agent.[5,6] So it has been recognized in the world of research as a polycarboxylic acid chelator.[7] The conjugate base of DTPA is potentially an octadentate ligand.[3,8] DTPA forms eight bonds and wraps around a metallic ion.[9] Its complexes may also contain an additional water molecule that coordinates the metal ion.[10] However, transition metals usually form less than eight coordination bonds.[11] DTPA can still bind to other reagents even after creating a metal complex. Given these comprehensive coordinating abilities, DTPA is approved for its use in medical imaging and decontaminating internally deposited radionuclides,[12,13] such as plutonium, curium, and americium.[14]

In the past two decades, great attention has been paid to understanding nature and the roles of non-covalent interactions, for example, halogen bonding, π–π^+, π^+–π^+, anion···π, anion···π^+, lone-pair(l.p)···π, N–H···π, C–H···π(chelate), metal···π, salt bridge(SB)···(SB), C–H···(SB), (SB)···π^+, (l.p)···(SB), N–H···SB···lone pair, σ–hole interaction, π–hole interaction, etc..[15–25] Non-covalent interactions play a significant role in determining the structure and macroscopic properties that would further help to fabricate materials possessing desired parameters. The non-covalent interactions such as Hydrogen bonding, π-π, C–H···π, cation···π, anion···π, and lone-pair···π are mainly responsible for the generation and stabilization of supramolecular structures.[18–21,26–29] These interactions are omnipresent in macromolecular compounds like proteins[30,31] polysaccharides[32,33] and are directly secondary to quaternary structures. Conventional hydrogen bonding (such as N–H···O and O–H···O) remains the most reliable and widely used in the field of chemical, biological, and material science due to specific, highly directive, and relatively strong interactions.[22] The non-covalent interactions have emerged as a novel conception in the field of anion transport, anion-sensing and anion-recognition chemistry, trans-membrane anion transport, and catalysis.[34–36]

We have structurally characterized compound (**1**) (Figure 1) and analyzed non-covalent interactions that help govern self-assembly. Hirshfeld surface analysis and corresponding fingerprint plots have been presented to explore the nature of intermolecular interactions within the title crystal structure. The characteristics of the non-covalent interactions are theoretically studied using Bader's quantum theory of "atoms-in-molecules" (QTAIM) and we have also performed topological analysis of QTAIM[37–46] to characterize the bond critical points and calculated the dissociation energy of the interactions. Further we have studied "Non-covalent Interaction" (NCI) plot index.

[a] S. Islam, P. Das, S. Tripathi, Dr. S. Kumar Seth
Department of Physics
Jadavpur University
Kolkata 700032, India
E-mail: saikatk.seth@jadavpuruniversity.in
[b] S. Tripathi, Prof. S. Mukhopadhyay
Department of Chemistry
Jadavpur University
Kolkata 700032, India

Supporting information for this article is available on the WWW under https://doi.org/10.1002/slct.202203396

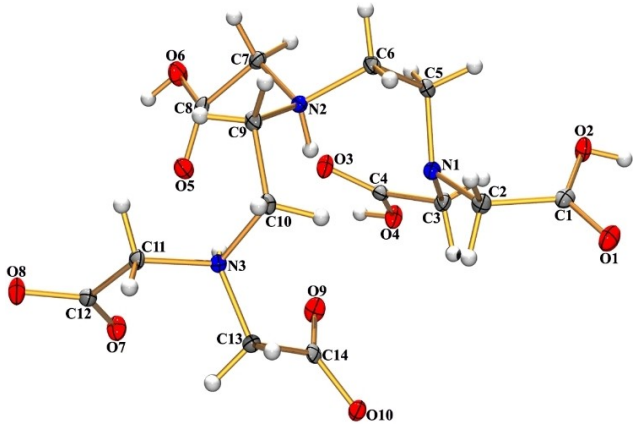

Figure 1. ORTEP view with atom numbering scheme of compound (**1**) with displacement ellipsoids at the 30% probability level.

Table 1. Relevant hydrogen bonding parameters (Å, °).

D–H···A	D–H	H···A	D···A	D–H···A	Symmetry
O2–H2···O10	0.82	1.83	2.6381(13)	167	−x,−1/2+y,3/2-z
O4–H4···O10	0.82	1.88	2.6668(13)	159	x,3/2-y,−1/2+z
O6–H6···O8	0.82	1.66	2.4457(13)	159	1-x,−1/2+y,3/2-z
C2–H2A···O4	0.97	2.57	3.3604(16)	138	x,3/2-y,1/2+z
C3–H3B···O1	0.97	2.57	3.1777(16)	121	−x,−1/2+y,3/2-z
C3–H3B···O4	0.97	2.57	3.3876(16)	142	−x,1-y,1-z
C5–H5A···O1	0.97	2.58	3.3356(16)	134	−x,−1/2+y,3/2-z
C5–H5B···O1	0.97	2.44	3.2726(16)	143	−x,1-y,2-z
C7–H7A···O10	0.97	2.54	3.4092(15)	149	x,−1+y,z
C7–H7B···O8	0.97	2.30	3.2243(16)	159	1-x,1-y,2-z
C10–H10B···O7	0.97	2.36	3.0291(15)	126	x,3/2-y,1/2+z
C10–H10B···O9	0.97	2.55	3.0108(15)	109	x,3/2-y,1/2+z
C11–H11B···O8	0.97	2.58	3.3400(16)	135	1-x,2-y,2-z

Results and Discussion

Structural Description

The title compound DTPA is a polycarboxylic amino acid comprised of diethylene triamine as the backbone consisting of five carboxylic acid groups. The title compound crystallized in monoclinic space group $P2_1/c$. The solid-state structure at 120 K with the highest precision[47] with an R-value of 0.03 has been reported herein. The molecular ORTEP[48] view of compound (**1**) is appended in Figure 1 with the atom numbering scheme. Extended supramolecular networks of compound (**1**) are stabilized through O–H···O and C–H···O interactions (Table 1).

In the first substructure, carboxylate oxygen atom O(2) interacts with another carboxylate oxygen atom O(10) of the molecules at (−x, −1/2+y, 3/2-z), whereas another oxygen atom O(6) of the molecule at (x, y, z) acts as a donor to the carboxylate oxygen O(8) of the molecule at (1-x, −1/2+y, 3/2-z). These two O–H···O interactions lead the molecules to generate a self-assembled structure in the (110) plane (see Figure 2). Again O(4) atom of the molecule at (x, y, z) interacts with carboxylate oxygen O(10) of the molecules at (x, 3/2-y, −1/2+z). All these three O–H···O interactions are responsible for the formation of another supramolecular network in the (101) plane (see Figure 3).

In another substructure, C(3) acts as a donor to the carboxylate oxygen O(4) of the molecules at (−x, 1-y, 1-z). This C3-H3B···O4 interaction and its centrosymmetric analog generate an $R_2^2(8)$ dimeric ring (P) centered at (0, 1/2, 1/2) (Figure 4). Another carbon atom C(5), interacts with O(1) of the molecule at (−x, 1-y, 2-z), and a centrosymmetric dimeric $R_2^2(12)$ ring (Q) centered at (0, 1/2, 1) is formed (Figure 4). Again another centrosymmetric dimeric ring $R_2^2(16)$ (R) centered at (1/2, 1/2, 1) is created when C(7) is involved in the interaction with O(8) of the molecule at (1-x, 1-y, 2-z) (Figure 4). Thus, these three centrosymmetric dimeric rings (P, Q, R) are

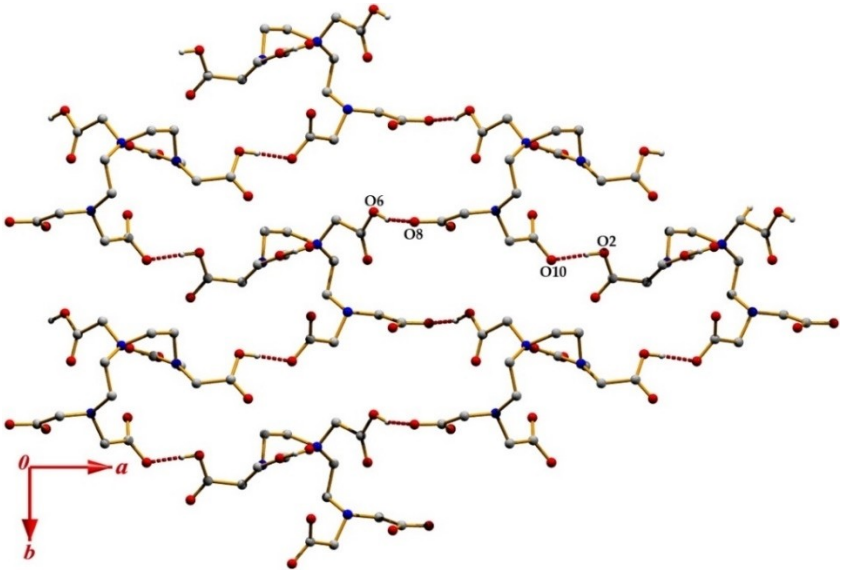

Figure 2. Supramolecular networks generated through O–H···O bonds in (110) plane.

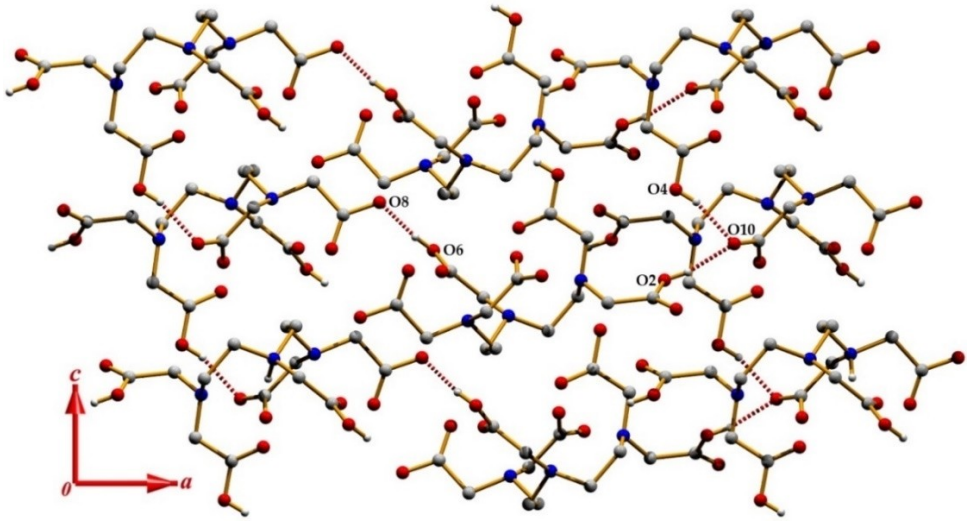

Figure 3. Supramolecular networks generated through O–H···O bonds in (101) plane.

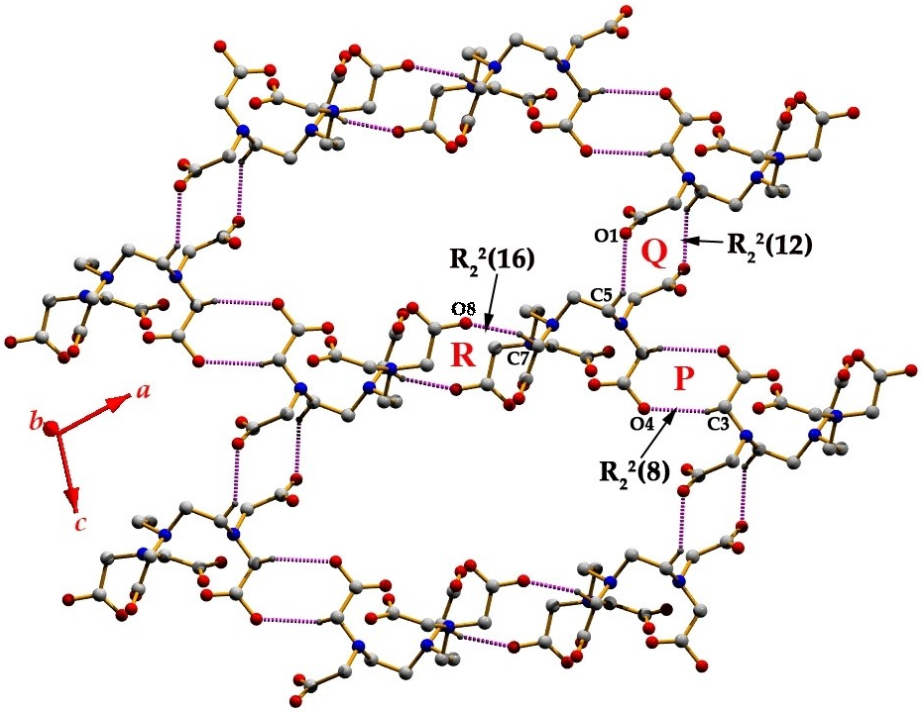

Figure 4. Three different centrosymmetric dimeric rings lead to forming a 2D supramolecular network.

alternately linked to generating a supramolecular compound network (**1**) in (101) plane (Figure 4). Further, the carbon atoms C(7) and C(10) act as donors to the carboxyl oxygen atoms O(10) and O(7) at (x, −1+y, z) and (x, 3/2-y, 1/2+z) respectively. The combination of another two C–H···O interactions leads to the generation of another supramolecular architecture in the (011) plane (Figure S1).

Hirshfeld Surface

The Hirshfeld surface was calculated to evaluate the contribution of intermolecular interactions that are involved within the structure. The calculated d_{norm} and fragment patch surfaces are illustrated in Figure 5 that have been mapped in the range of (−0.855 Å to 1.452 Å) and (0.0 Å to 13.00 Å), respectively. The d_{norm} surface reveals all interactions among donors, acceptors, and other close contacts. The large circular depressions in the d_{norm} surface designate the strong O–H···O hydrogen bonds

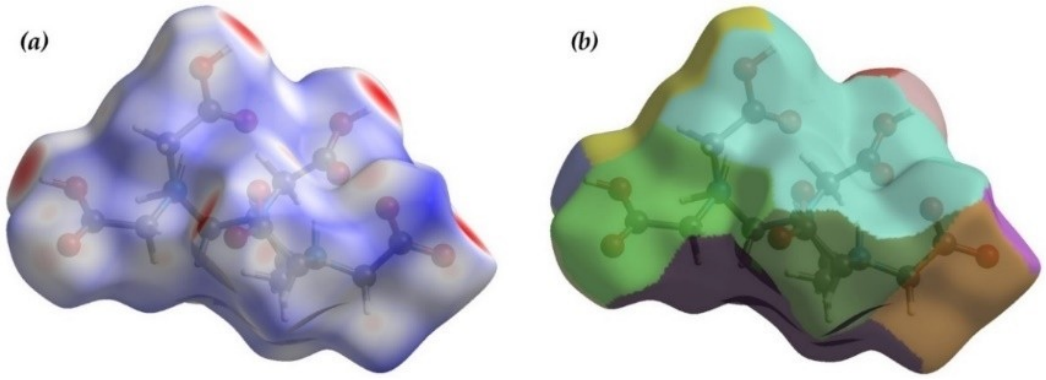

Figure 5. Hirshfeld surfaces mapped with d_{norm} (a) and fragment patches (b) for compound (**1**).

(Figure 5a). The visual illustration of the fragment patches (Figure 5b) signifies the identification of their closeness to adjacent molecules. The dominant O···H/H···O interactions appear in the fingerprint plot as two distinct spikes (Figure 6) in the region of (d_i = 0.936 Å; d_e = 0.570 Å). The O···H/H···O interactions comprise 66.9% of the total Hirshfeld surface area of the compound (**1**). The C···H/H···C contacts in the region of (d_i = 1.718 Å; d_e = 1.147 Å) contributed 3.1% of the total Hirshfeld surface area (See Figure 6). Other close contacts C···O/O···C, C···C, and O···O are evident in the fingerprint plot in region of (d_i = 1.633 Å; d_e = 1.392 Å), $d_i = d_e$ = 1.683 Å and $d_i = d_e$ = 1.513 Å respectively. Moreover, a significant contribution (27.7%) comes from H···H contact that is reproduced in the scattered points of the fingerprint plot in the region of $d_i = d_e$ = 1.162 Å. This analysis quantifies all the interactions in the structure in a novel visual manner.

We have calculated the energy frameworks regarding interaction energies (Figure 7), where the structure cluster is mapped within 3.8 Å. Figure 7 also illustrates the energy components (E_{ele}, E_{pol}, E_{dis}, and E_{rep}) of the interaction energies and the sum of the energy components (E_{tot}) relative to the reference molecule. Other parameters related to lattice energy calculations have been included in Figure 7. The topology of the energy distribution was analyzed using energy frameworks. In this calculation, the cylindrical radii are proportional to the relative strength of the corresponding energies. They are adjusted to the scale factors of K_{ele} = 1.057, K_{pol} = 0.740, K_{dis} = 0.871, K_{rep} = 0.618[49] with a cut-off value of 5 kJ/mol within 3 × 3 × 3 unit cells (Figure 8). The energy framework calculation discloses the different energy modules as follows, i.e., electrostatic energy (E_{ele}) −586.8 kJ/mol, polarization energy (E_{pol}) −292.1 kJ/mol, dispersion energy (E_{dis}) −251.2 kJ/mol, repulsion energy (E_{rep}) 464.9 kJ/mol and total energy (E_{tot}) −767.9 kJ/mol. Among the individual energy components generated, the electrostatic force accredited to the hydrogen bonds dominates the dispersion forces, which are clearly revealed by the relatively large size of the red cylinders in the energy framework diagrams compared to the green-colored cylinders (see Figure 8). The energy framework calculation thus provides their overall self-association in the supramolecular network.

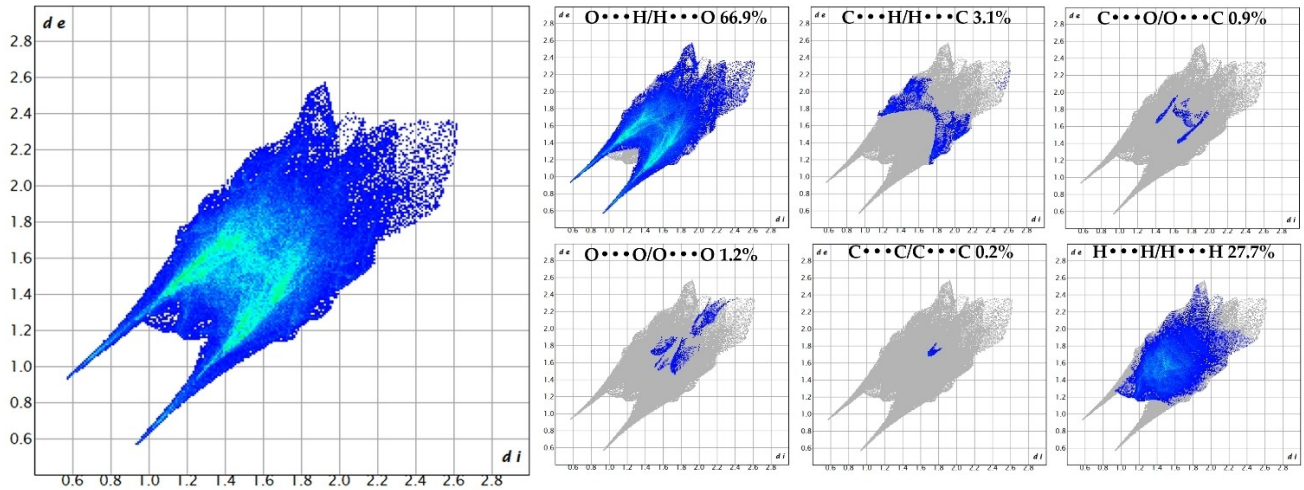

Figure 6. Fingerprint plots (Full) and decomposed plots.

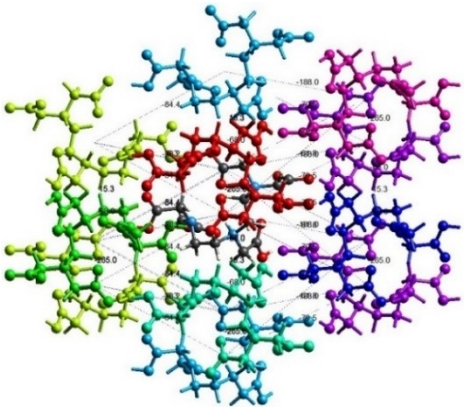

	N	Symop	R	E_ele	E_pol	E_dis	E_rep	E_tot
	2	x, -y+1/2, z+1/2	5.84	-205.1	-81.3	-70.5	118.8	-265.0
	1	-x, -y, -z	9.83	3.1	-7.4	-21.7	20.7	-8.3
	2	-x, y+1/2, -z+1/2	9.40	-80.8	-38.1	-30.3	89.9	-84.4
	1	-x, -y, -z	10.34	-10.9	-11.5	-30.8	30.3	-28.2
	2	x, -y+1/2, z+1/2	8.52	35.1	-11.6	-23.4	11.5	15.3
	2	x, y, z	8.94	-43.6	-18.4	-20.6	15.6	-68.0
	1	-x, -y, -z	9.29	-145.8	-44.5	-23.0	30.8	-188.0
	2	-x, y+1/2, -z+1/2	10.86	-106.1	-48.9	-9.4	124.7	-79.5
	1	-x, -y, -z	11.30	-32.7	-30.4	-21.5	22.6	-61.8

Figure 7. The color-coded interaction mapping (left) and the parameters for lattice energy calculations (right) for compound (**1**).

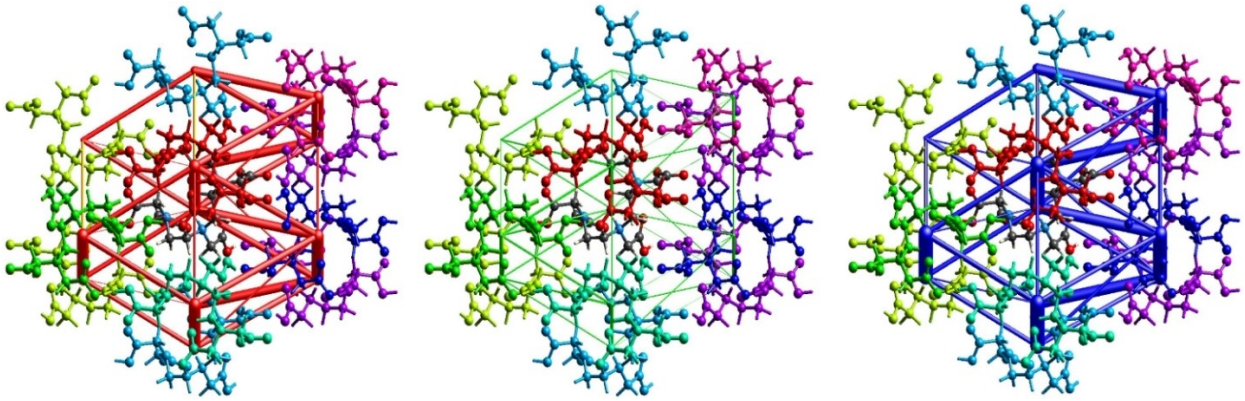

Figure 8. Energy framework of compound (**1**), the electrostatic potential force (left column), dispersion force (middle column), and total energy (right column) diagrams.

Theoretical Calculations

We have performed DFT/B3LYP/6311G++(d, p) level of theoretical calculations to analyze and characterize the hydrogen bonding contacts. First, Bader's theory of "atoms-in-molecules" (AIM) has been performed, where the crystallographic coordinates and the molecular fragments are used from the X-ray packing diagrams. According to this calculation, the existence of a bond critical point (BCP) and the bond path connecting two atoms designate the interaction between two atoms.[50] Each and every BCP includes well-to-do chemical information that indicates the nature of the chemical bond. To characterize a chemical bond at BCP, parameters like electron density (ρ_{BCP}), Laplacian of electron density ($\nabla^2\rho_{BCP}$), kinetic energy density (G_{BCP}), potential energy density (V_{BCP}), and total energy density ($H_{BCP} = V_{BCP} + G_{BCP}$) are usually used. The dissociation energy of the interaction ($D.E_{int}$) can be estimated from the equation $D.E_{int} = -{}^1/_2\ V_{BCP}$, more precisely $D.E_{int}$ (kcal mol^{-1}) $= -313.754 \times V_{BCP}$ (au).[51] Detailed AIM parameters at the BCPs are listed in Table 3S for selected intermolecular interactions. The electron localization function (ELF) measures the excess as shown in Figure 9; the small green spheres represent the bond critical points (BCP), the small violet spheres represent the ring critical point (RCP), and the dashed lines represent the bond path connecting the atoms. The bond path connecting O–H and O atoms in the first and second model (see Figures 9a,b) represents O–H···O interactions in (**1**). The ρ(r) values of O(2)–H(2)···O(10) and O(4)–H(4)···O(10) are 0.0326 a.u. and 0.0286 a.u. respectively, it may be noted that the O(2)–H(2)···O(10) bonding contact is more favorable compared to the O(4)–H(4)···O(10) bond due to large ρ(r) value, which is in agreement with X-ray structural findings (see Table 1). In another model (Figure 9c), the weak C(7)–H(7 A)···O-(10) bond is characterized by the bond path, and the corresponding ρ(r) value is 0.0087 a.u. Further in dimeric ring model (Figure 9d), the ρ(r) values of C(3)–H(3B)···O(4), C(5)–H(5B)···O(1), and C(7)–H(7B)···O(8) are 0.0075 a.u., 0.0094 a.u., and 0.0122 a.u. respectively. All these interactions have a positive value of $\nabla^2\rho_{BCP,}$ which indicates closed-shell interactions.[52,53] These closed-shell interactions have dominating $G_{BCP,}$ which is slightly greater than $|V_{BCP}|$ results in a positive value of H_{BCP} but closed to zero, and the ratio $\frac{|V_{BCP}|}{G_{BCP}}$ is less than unity.[53] It can be noted that the strength of O–H···O contacts are greater than that of C–H···O contacts (Table 2). Therefore,

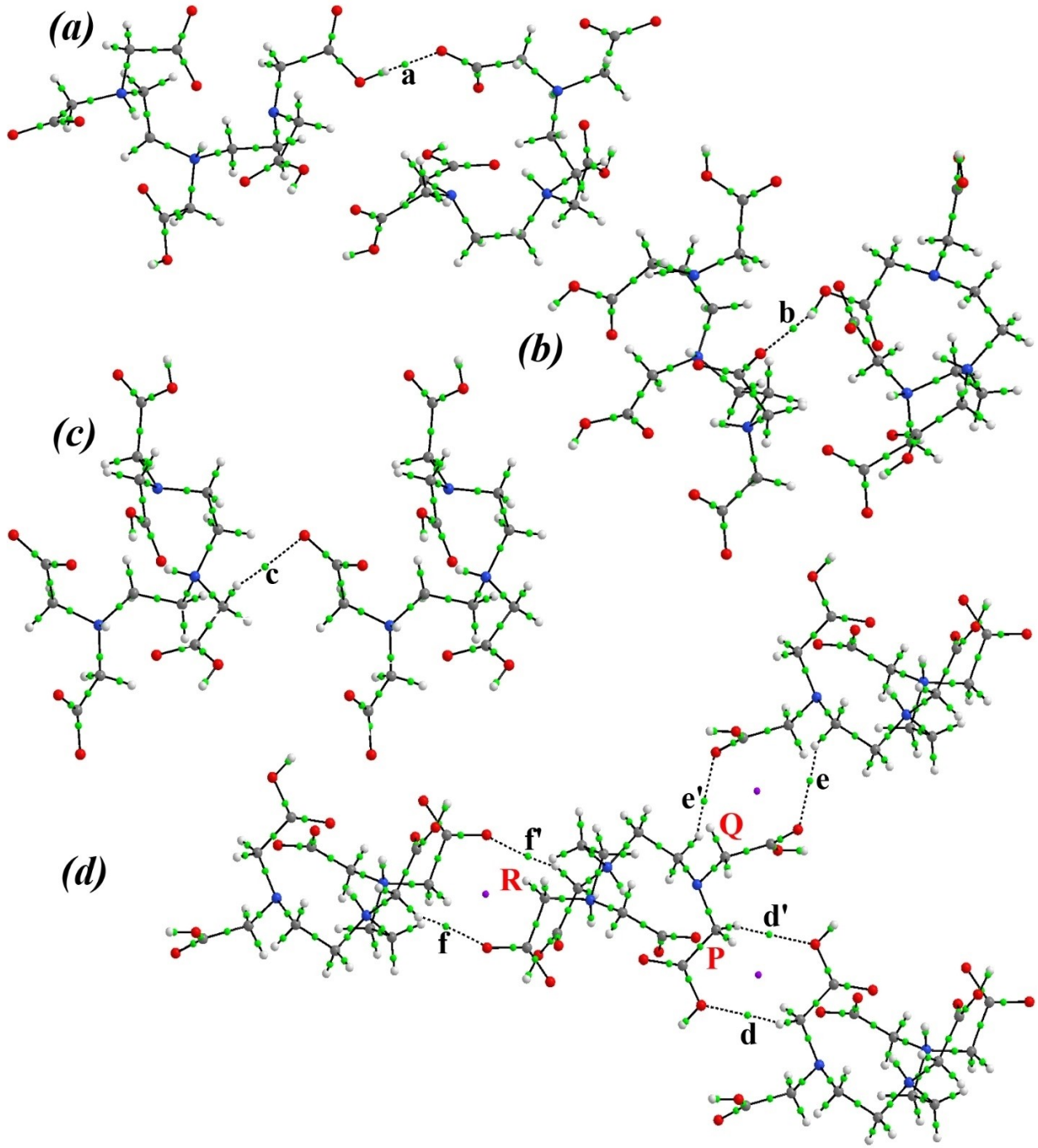

Figure 9. AIM analysis of the self-assembled dimers (*a–c*) and tetramer (*d*) retrieved from the X-ray structure of the titled compound. Green and violet spheres represent the bond and ring critical points, respectively. The bond path connecting the bond critical points are denoted by dashed line.

Table 2. Detailed AIM parameters at the BCPs.

Intermolecular Interaction	ρ_{BCP} (**e**.Å^{-3})	$\nabla^2\rho_{BCP}$ (**e**.Å^{-5})	V_{BCP} (**a**.**u**)	G_{BCP} (**a**.**u**)	H_{BCP} (**a**.**u**)	$\frac{\lvert V_{BCP}\rvert}{G_{BCP}}$	$D.E_{int}$ (kcal. mol^{-1})
O2–H2···O10 (a)	0.0326	0.1284	−0.0295	0.0308	0.0013	0.9578	9.256
O4–H4···O10 (b)	0.0286	0.1128	−0.0242	0.0262	0.0020	0.9236	7.593
C7–H7A···O10 (c)	0.0087	0.0264	−0.0047	0.0057	0.0010	0.8245	1.475
C3–H3B···O4 (d, d′)	0.0075	0.0258	−0.0044	0.0054	0.0010	0.8148	1.380
C5–H5B···O1 (e, e′)	0.0094	0.0328	−0.0056	0.0069	0.0013	0.8116	1.757
C7–H7B···O8 (f, f′)	0.0122	0.0440	−0.0071	0.0091	0.0020	0.7809	2.227

the inspection of the AIM calculation indicates that the ρ(r) values, $D.E_{int}$, and corresponding bond CPs are in agreement with the experimental findings.

Again, we have used the 'non-covalent interaction' (NCI) plot computational tool to characterize the self-assembled structures generated through hydrogen bonding interaction (Figure 10 a–d). We have used the same structural models that are used in AIM calculation. The presence of blue isosurface in Figures 10a,b indicates the existence of strong O–H···O bonds in between the carboxylate oxygen atoms. A critical analysis of the O–H···O bonds among the carboxylate groups can be identified and characterized by the dense blue-colored patches (see Figures 10a,b). The theoretical NCI analysis of the O–H···O hydrogen bonds shows consistencies with the theoretical AIM analysis (see Table 2) and agrees well with the experimental findings (see Table 1). The green isosurfaces that are evident in between the C–H donors and the carboxylate oxygen atoms represent the weak C–H···O bonding contact in (**1**) (see Figures 10c,d). The C7–H7B···O8 bond has the lowest H···A value (Table 1) and highest ρ(r) value in AIM analysis (see Table 2) among four C–H···O bonds that are depicted in Figure 10. As expected, the C7–H7B···O8 displays a larger and dense green patch in comparison to the other three C–H···O bonds (Figures 10c,d) which is again consistent with the AIM analysis and experimental evidence. All the isosurfaces presented here

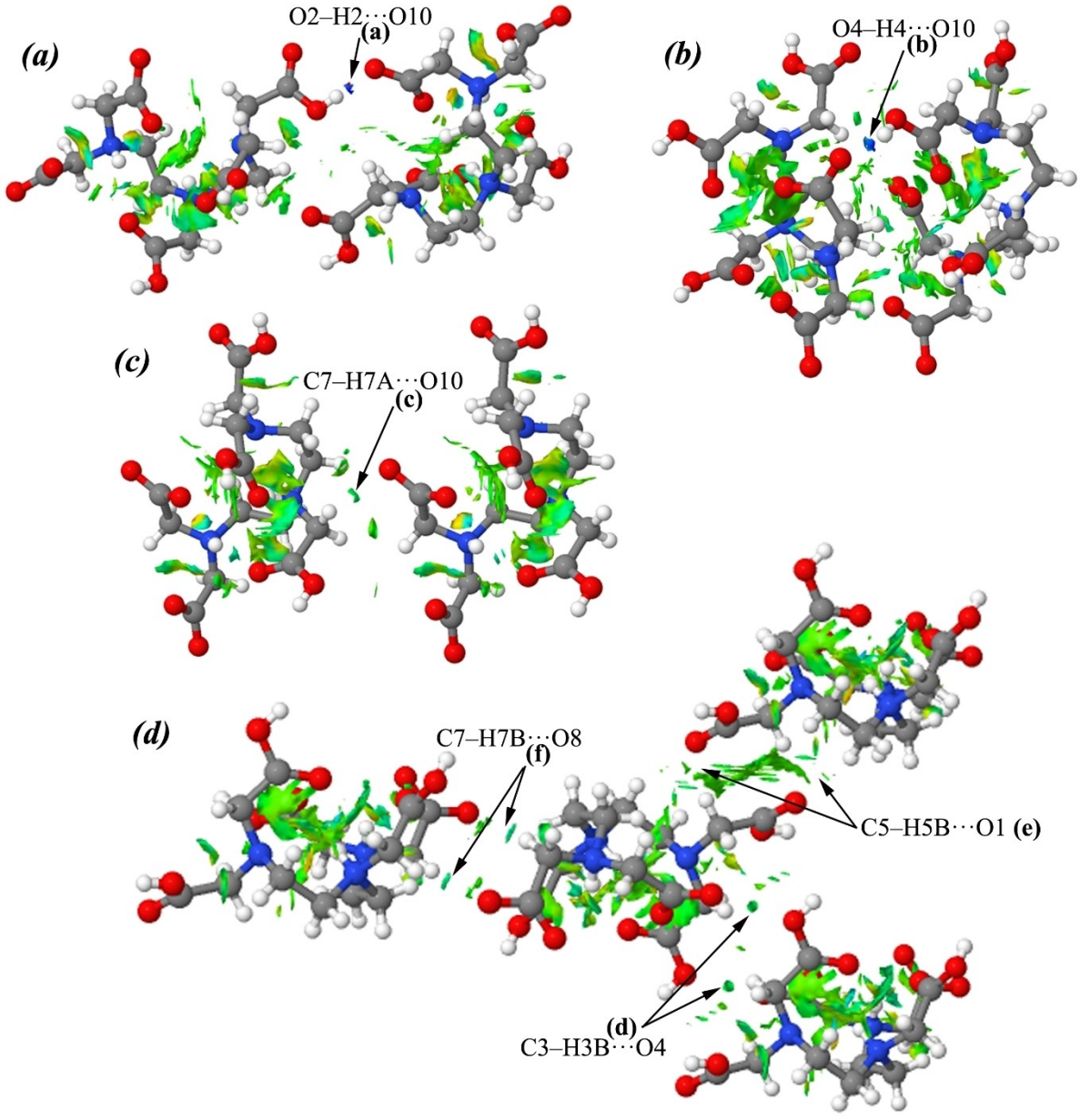

Figure 10. NCI plot of the self-assembled structures of compound (**1**). A perspective view of the self-assembled dimers (*a–c*) and tetramer (*d*) has been illustrated. The gradient cut-off is s = 0.35 a.u., and the color scale is $-0.04 < \rho < 0.04$ a.u.

in the theoretical NCI calculation agree with the experimental findings.

Conclusion

The supramolecular structure of the title compound has been scrutinized in detail. The cooperativity of the non-covalent interactions has been studied by exploring the supramolecular behavior in the solid-state. The molecular energy framework calculation revealed that the electrostatic force accredited to the hydrogen bonds dominates the dispersion forces. Bader's theory of 'atoms-in-molecules' (AIM) characterizes the non-covalent interactions and self-assemblies. QTAIM topological analysis revealed that all of the interactions are closed-shell interactions at their bond critical point. Furthermore, the theoretical NCI plot index also characterizes the self-assemblies and corresponding interactions. The theoretical investigations are in agreement with the experimental findings. The results reported herein might help in understanding the supramolecular aggregation in accordance with intermolecular hydrogen bonds and the quantification of non-covalent interactions. The detail theoretical studies might be helpful to the future research work relating to this ligand and its metal complexes.

Experimental Sections

Crystallization

The reagents were purchased from a commercial source and used without further purification. Diethylenetriaminepentaacetic acid (Aldrich, St. Louis, Missouri, United States) was used as received. Double distilled and then freshly boiled water was used throughout. Diethylenetriaminepentaacetic acid (2.0 mmol, 0.786 g) was taken into a 100 mL flask and dissolved in water/methanol in 2:1 molar ratio. Thus, the solution mixture was heated at 323 K for 1 h and then kept for crystallization at room temperature (295 K). The resulting solution was kept undisturbed at ambient temperature and covered with paraffin film. A few small holes were made using a needle to allow the solvent to evaporate slowly. After a few weeks, testable colorless crystals were collected by filtration, washed with water, and dried in the air. The CHN elemental analyses were performed on a PerkinElmer 2400 Series-II CHN analyzer, USA, elemental analyzer. A Perkin-Elmer LX-1 FT-IR spectrophotometer was used to record the infrared spectrum with a modern diamond attenuated total reflectance (ATR) accessory method in the range 4000–400 cm^{-1}. Anal. Calcd. for $C_{14}H_{23}N_3O_{10}$ (MW = 393.35 for **1**): C, 42.75; H, 5.89; N, 10.68 %. Found: C, 42.73; H, 5.91; N, 10.65 %. Main IR absorption bands observed for **1** (in cm^{-1}) are 3205 (w), 3061 (s), 3011 (s), 2910 (w), 1732 (s), 1685 (s), 1631 (vs), 1545 (s), 1441 (s), 1395 (s), 1044 (s), 773 (vs) (Figure S2).

X-ray Crystal Structure Determination

Single crystal X-ray data of compound (**1**) was collected at 120(2)K on the Bruker SMART APEX-II single-crystal X-ray CCD diffractometer having graphite monochromator (Mo-Kα, $\lambda = 0.71073$ Å) radiation. Data reduction was executed using the program Brukar SAINT.[54] An empirical absorption correction was performed using the SADABS program based on the multi-scan method.[55] The structure of the title compound was solved by the direct method and refined by the full-matrix least-square technique on F^2 using the programs (SHELXS-14)[56] and (SHELXL-18),[57] respectively. All the non-H atoms were refined anisotropically, whereas the H atoms were placed at their geometrically idealized positions. The structure was solved using the WinGX system V2014.1[48] and geometrically analyzed by PLATON.[58] A summarized list of crystal data and relevant refinement parameters of compound (**1**) are given below.

Crystal data for (1). $C_{14}H_{23}N_3O_{10}$, $M = 393.35$, colorless needle, 0.15× 0.09× 0.05 mm, monoclinic, space group $P2_1/c$. $a = 17.8462(14)$Å, $b = 8.9381(7)$Å, $c = 10.7308(9)$Å, $\alpha = \gamma = 90°$, $\beta = 105.238(2)°$, $V = 1651.5(2)$Å^3, $Z = 4$, $D_c = 1.582$ Mg/m^3, $\mu = 0.135$ mm^{-1}, *F(000)* = 832, Mo K_α radiation, $\lambda = 0.71073$ Å, $T = 120(2)$ K, θ range = 2.567– 24.994°, limiting indices = $-21 \le h \le 21$; $-10 \le k \le 10$; $-12 \le l \le 12$, reflections collected/unique = 14999/2864 [*R(int)* = 0.0284], Completeness to $\theta = 98.1$ %, absorption correction = semi-empirical from equivalents, max. and min. transmission = 0.99 and 0.98, data/restraints/parameters = 2864/0/247, final GOF = 1.049, $R_1 = 0.0303$, $wR_2 = 0.0714$, *R* indices based on $I > 2\sigma(I)$ (refinement on F^2), $R_1 = 0.0330$, $wR_2 = 0.0734$, *R* indices based on all data, largest diffraction peak and hole = 0.241 and −0.218 e Å^{-3}.

Deposition number CCDC 2132357 (for **1**) contain the supplementary crystallographic data for this paper. These data are provided free of charge by the joint Cambridge Crystallographic Data Centre and Fachinformationszentrum Karlsruhe Access Structures service www.ccdc.cam.ac.uk/structures.

Hirshfeld Surface Analysis

The molecular Hirshfeld surface[50,59, 60] of the title compound is generated based on the electron distribution of the molecules evaluated as the sum of spherical atom electron densities.[61,62] For the given crystal structure and a set of spherical atomic electron densities, the Hirshfeld surface is unique.[63] The normalized contact distance (d_{norm}) is generated based on d_e, d_i and the *vdW* radii of the atom. d_e is defined as the distance from the Hirshfeld surface to the closest nucleus external to the surface, whereas d_i is the distance from the Hirshfeld surface to the closest nucleus internal to the surface. The 2D fingerprint plot generated for the crystal structure (based on d_e and d_i) provides a summary of intermolecular contacts within the crystal.[15,64] We have performed the "energy framework analysis" using the *CrystalExplorer17* program[65] to explore the intermolecular interaction topology. The individual energy components of the energy framework are signified as cylinders, where the radius of the cylinders is proportional to the magnitude of the interaction energy. The energy components corresponding to electrostatic (E_{ele}), dispersion (E_{dis}), and total energy (E_{tot}) are depicted in red, green, and blue color codes, respectively.

Theoretical Methods

The non-covalent interactions and the wave function analysis were calculated using the *Gaussian16* calculation package[66] at the B3LYP level with a basis set 6–311++G(d,p). The crystallographic coordinates have been used in the theoretical calculations. We have used Bader's quantum theory of "Atoms in molecules" (QTAIM)[67] to analyze the weak non-covalent interactions that have been computed at the same level of theory by means of the AIMall calculation package.[68] Topological analysis of the Laplacian of electron charge density provides a powerful tool for investigating the electronic and conformational properties of the molecules and

hence allows for much better insights into the interatomic interactions.[69] The topological properties of the charge density (ρ(r)) are characterized by their critical points (CPs), and its Laplacian which is expressed in terms of $L(r) = -\nabla^2(\rho(r))$ and are calculated using the Atoms In Molecules (AIM) theory.[70] It has been noted that electron density is depleted where $\nabla^2(\rho(r)) > 0$, and it is concentrated where $\nabla^2(\rho(r)) < 0$. Selected topological parameters such as electron density, ρ (r), Laplacian of the electron density, $\nabla^2\rho(r)$, potential electronic energy density V(r), kinetic electronic energy density, G(r), and total electronic energy density ($H(r) = V(r) + G((r))$ were used at their bond critical points (BCPs) to characterize the nature and strength of intermolecular interactions.

The theoretical non-covalent interactions (NCI) plot index[71] is used to assess the nature of interactions in terms of being attractive or repulsive and revealed them in real space. This is the method for plotting non-covalent interaction regions based on the NCI visualization index derived from the electron density. The density cubes needed to generate the NCIplot surfaces have been computed at the same level of theory using the Gaussian program. Instead of critical points, the non-covalent interactions are represented by isosurfaces that illustrate both favorable and unfavorable interactions and are differentiated by the sign of the second density Hessian eigenvalue and defined by isosurface color scheme with a red-yellow-green-blue scale. The blue and red surfaces represent ρ^-cut (attractive) and ρ^+cut (repulsive) interactions,[72] respectively. However, the green and yellow colors represent weak attractive, and repulsive interactions.[73]

Supplementary Information

Electronic supporting information (ESI) includes: Figure S1: C–H···O bonds lead to the formation of a 2D supramolecular network for compound (**1**); Figure S2: IR spectrum of (**1**); Table S1. Atomic coordinates ($\times 10^{-4}$ and equivalent isotropic displacement parameters ($Å^2 \times 10^{-3}$) for (**1**). U(eq) is defined as one third of the trace of the orthogonalized U_{ij} tensor; Table S2. Anisotropic displacement parameters ($Å^2 \times 10^{-3}$) for (**1**).

Acknowledgements

S. Islam thankfully acknowledges the University Grants Commission (New Delhi) for a Senior Research Fellowship. P. Das cordially acknowledges Department of Science and Technology for DST-INSPIRE fellowship (Grant no. IF190666). S. K. Seth gratefully acknowledges the financial support from SERB (New Delhi) India, for Research Project (EEQ/2019/000384).

Conflict of Interest

There are no conflicts to declare.

Data Availability Statement

Data sharing is not applicable to this article as no new data were created or analyzed in this study.

Keywords: Bader's theory of 'atoms-in-molecules' (AIM) · Hirshfeld surface and Energy Frameworks · Noncovalent interaction (NCI) plot · Solid-state structure · Topological analysis of QTAIM

[1] R. E. Sievers, J. C. Bailar Jr, *Inorg. Chem.* **1962**, *1*, 174–182.
[2] R. A. Guilmette, J. E. Parks, A. Lindenbaum, *J. Pharm. Sci.* **1979**, *68*, 194–196.
[3] H. R. Maecke, A. Riesen, W. Ritter, *J. Nucl. Med.* **1989**, *30*, 1235–1239.
[4] N. C. Liu, Q. H. Xie, W. E. Baker, *Polymer* **1993**, *34*, 4680–4687.
[5] D. J. Hnatowich, W. W. Layne, R. L. Childs, *Int. J. Appl. Radiat. Isot.* **1982**, *33*, 327–332.
[6] M. Mahmoud, B. B. Geri, K. Abdelgawad, M. S. Kamal, I. Hussein, S. Elkatatny, R. Shawabkeh, *Energy Fuels* **2018**, *32*, 9813–9821.
[7] X. Zhao, L. Song, Z. Zhang, R. Wang, J. Fu, *J. Mol. Struct.* **2011**, *986*, 68–74.
[8] P. Thakur, J. L. Conca, C. J. Dodge, A. J. Francis, G. R. Choppin, *Radiochim. Acta* **2013**, *101*, 221–232.
[9] A. A. B. Moghal, S. A. S. Mohammed, A. Almajed, M. A. Al-Shamrani, *Int. J. Civ. Eng.* **2020**, *18*, 449–461.
[10] A. T. Onawole, I. A. Hussein, A. Sultan, S. Abdel-Azeim, M. Mahmoud, M. A. Saad, *Can. J. Chem. Eng.* **2019**, *97*, 2021–2027.
[11] G. J. Kubas, *Acc. Chem. Res.* **1988**, *21*, 120–128.
[12] A. E. Gorden, J. Xu, K. N. Raymond, P. Durbin, *Chem. Rev.* **2003**, *103*, 4207–4282.
[13] V. K. Singh, P. L. Romaine, T. M. Seed, *Health Phys.* **2015**, *108*, 607.
[14] D. Poudel, L. Bertelli, J. A. Klumpp, T. L. Waters, *Health Phys.* **2018**, *114*, 307–318.
[15] S. K. Seth, *Acta Crystallogr. E: Crystallogr. Commun.* **2018**, *74*, 600–606.
[16] A. Hossain, A. Dey, S. K. Seth, P. P. Ray, J. Ortega-Castro, A. Frontera, S. Mukhopadhyay, *CrystEngComm* **2021**, *23*, 3569–3581.
[17] A. Das, A. D. Jana, S. K. Seth, B. Dey, S. R. Choudhury, T. Kar, S. Mukhopadhyay, N. J. Singh, I. C. Hwang, K. S. Kim, *J. Phys. Chem. B* **2010**, *114*, 4166–4170.
[18] S. Ghosh, S. Islam, S. Pramanik, S. K. Seth, *J. Mol. Struct.* **2022**, *1268*, 133697.
[19] S. K. Seth, I. Saha, C. Estarellas, A. Frontera, T. Kar, S. Mukhopadhyay, *Cryst. Growth Des.* **2011**, *11*, 3250–3265.
[20] T. Maity, H. Mandal, A. Bauzá, B. C. Samanta, A. Frontera, S. K. Seth, *New J. Chem.* **2018**, *42*, 10202–10213.
[21] S. K. Seth, A. Bauzá, A. Frontera, *New J. Chem.* **2018**, *42*, 12134–12142.
[22] S. Tripathi, S. Islam, S. K. Seth, A. Bauzá, A. Frontera, S. Mukhopadhyay, *CrystEngComm* **2020**, *22*, 8171–8181.
[23] M. Mitra, P. Manna, A. Das, S. K. Seth, M. Helliwell, A. Bauzá, S. R. Choudhury, A. Frontera, S. Mukhopadhyay, *J. Phys. Chem. A* **2013**, *117*, 5802–5811.
[24] S. K. Seth, A. Bauzá, A. Frontera, Quantitative Analysis of Weak Non-covalent σ-Hole and π-Hole Interactions, in Understanding Intermolecular Interactions in the Solid State: Approaches and Techniques, ed. D. Chopra, Royal Society of Chemistry, London, **2019**.
[25] A. Bauzá, S. K. Seth, A. Frontera, *J. Comput. Chem.* **2018**, *39*, pp.458–463.
[26] S. Tripathi, A. Hossain, S. K. Seth, S. Mukhopadhyay, *J. Mol. Struct.* **2021**, *1226*, 129254.
[27] S. K. Seth, D. Sarkar, T. Kar, *CrystEngComm* **2011**, *13*, 4528–4535.
[28] S. K. Seth, P. Manna, N. J. Singh, M. Mitra, A. D. Jana, A. Das, S. R. Choudhury, T. Kar, S. Mukhopadhyay, K. S. Kim, *CrystEngComm* **2013**, *15*, 1285–1288.
[29] P. Manna, S. K. Seth, M. Mitra, S. R. Choudhury, A. Bauzá, A. Frontera, S. Mukhopadhyay, *Cryst. Growth Des.* **2014**, *14*, 5812–5821.
[30] L. Pauling, R. B. Corey, *Proc. Natl. Acad. Sci. USA* **1951**, *37*, 251–256.
[31] L. Pauling, R. B. Corey, H. R. Branson, *Proc. Natl. Acad. Sci. USA* **1951**, *37*, 205–211.
[32] B. Casu, M. Reggiani, G. G. Gallo, A. Vigevani, *Tetrahedron* **1966**, *22*, 3061–3083.
[33] W. Banks, C. T. Greenwood, *Biopolymers* **1972**, *11*, 315–318.
[34] Y. Zhao, Y. Cotelle, N. Sakai, S. Matile, *J. Am. Chem. Soc.* **2016**, *138*,4270–4277.
[35] C. Parthiban, K. P. Elango, *Sens. Actuators B* **2017**, *245*, 321–333.
[36] M. Raynal, P. Ballester, A. Vidal-Ferran, P. W. N. M. V. Leeuwen, *Chem. Soc. Rev.* **2014**, *43*, 1660–1733.
[37] K. I. Kulish, A. S. Novikov, P. M. Tolstoy, D. S. Bolotin, N. A. Bokach, A. A. Zolotarev, V. Y. Kukushkin, *J. Mol. Struct.* **2016**, *1111*, 142–150.

[38] S. A. Katkova, A. S. Mikherdov, M. A. Kinzhalov, A. S. Novikov, A. A. Zolotarev, V. P. Boyarskiy, V. Y. Kukushkin, *Chem. Eur. J.* **2019**, *25*, 8590–8598.
[39] A. A. Eliseeva, D. M. Ivanov, A. S. Novikov, A. V. Rozhkov, I. V. Kornyakov, A. Y. Dubovtsev, V. Y. Kukushkin, *Dalton Trans.* **2020**, *49*, 356–367.
[40] A. S. Mikherdov, A. S. Novikov, M. A. Kinzhalov, A. A. Zolotarev, V. P. Boyarskiy, *Crystals* **2018**, *8*, 112.
[41] A. G. Tskhovrebov, A. S. Novikov, O. V. Odintsova, V. N. Mikhaylov, V. N. Sorokoumov, T. V. Serebryanskaya, G. L. Starova, *J. Organomet. Chem.* **2019**, *886*, 71–75.
[42] O. V. Repina, A. S. Novikov, O. V. Khoroshilova, A. S. Kritchenkov, A. A. Vasin, A. G. Tskhovrebov, *Inorg. Chim. Acta* **2020**, *502*, 119378.
[43] M. A. Kryukova, A. V. Sapegin, A. S. Novikov, M. Krasavin, D. M. Ivanov, *Crystals* **2019**, *9*, 71.
[44] A. S. Mikherdov, A. S. Novikov, M. A. Kinzhalov, V. P. Boyarskiy, G. L. Starova, A. Y. Ivanov, V. Y. Kukushkin, *Inorg. Chem.* **2018**, *57*, 3420–3433.
[45] A. M. Afanasenko, M. S. Avdontceva, A. S. Novikovand, T. G. Chulkova, *Z. Kristallogr. Cryst. Mater.* **2016**, *231*,435–440.
[46] L. E. Zelenkov, D. M. Ivanov, M. S. Avdontceva, A. S. Novikov, N. A. Bokach, *Z. Kristallogr. Cryst. Mater.* **2019**, *234*, 9–17.
[47] L. M. Shkol'nikova, G. V. Polyanchuk, N. M. Dyatlova, I. A. Polyakova, *J. Struct. Chem.* **1984**, *25*, 264–272.
[48] L. J. Farrugia, WinGX and ORTEP for Windows: an update, *J. Appl. Crystallogr.* **2012**, *45*, 849–854.
[49] T. Vishwanath, A. Ashish, C. R. Shankar, K. D. Amar, *J. Mol. Struct.* **2022**, *1264*, 133290.
[50] S. K. Seth, *Crystals* **2018**, *8*, 455.
[51] C. Lepetit, M. L. Kahn, *Res. Chem. Intermed.* **2021**, *47*, 377–395.
[52] S. Islam, S. Tripathi, A. Hossain, S. K. Seth, S. Mukhopadhyay, *J. Mol. Struct.* **2022**, *1265*, 133373.
[53] C. Gatti, *Z. Kristallogr. Cryst. Mater.* **2005**, *220*, 399–457.
[54] BrukerSAINT, Version 6.36a, Bruker AXS Inc., Madison, Wisconsin, USA, **2002**.
[55] Bruker SMART, Version 5.625 and SADABS, Version 2.03a, Bruker AXS Inc., Madison, Wisconsin, USA, **2001**.
[56] G. M. Sheldrick, *Acta Crystallogr. Sect. A* **2008**, *64*, 112–122.
[57] G. M. Sheldrick, *Acta Crystallogr. Sect. C* **2015**, *71*, 3–8.
[58] A. L. Spek, *J. Appl. Crystallogr.* **2003**, *36*, 7–13.
[59] M. A. Spackman, J. J. McKinnon, *CrystEngComm* **2002**, *4*, 378–392.
[60] J. J. McKinnon, D. Jayatilaka, M. A. Spackman, *Chem. Commun.* **2007**, 3814–3816.
[61] M. A. Spackman, P. G. Byrom, *Chem. Phys. Lett.* **1997**, *267*, 215–220.
[62] J. J. McKinnon, A. S. Mitchell, M. A. Spackman, *Chem. Eur. J.* **1998**, *4*, 2136–2141.
[63] J. J. McKinnon, M. A. Spackman, A. S. Mitchell, *Acta Crystallogr. B.* **2004**, *60*, 627–668.
[64] A. L. Rohl, M. Moret, W. Kaminsky, K. Claborn, J. J. Mckinnon, B. Kahr, *Cryst. Growth Des.* **2008**, *8*, 4517–4525.
[65] M. J. Turner, J. J. McKinnon, S. K. Wolff, D. J. Grimwood, P. R. Spackman, D. Jayatilaka, M. A. Spackman, CrystalExplorer17, University of Western Australia, **2017**.
[66] M. J. Frisch, G. W. Trucks, H. B. Schlegel, G. E. Scuseria, M. A. Robb, J. R. Cheeseman, G. Scalmani, V. Barone, G. A. Petersson, H. Nakatsuji, X. Li, M. Caricato, A. V. Marenich, J. Bloino, B. G. Janesko, R. Gomperts, B. Mennucci, H. P. Hratchian, J. V. Ortiz, A. F. Izmaylov, J. L. Sonnenberg, D. Williams-Young, F. Ding, F. Lipparini, F. Egidi, J. Goings, B. Peng, A. Petrone, T. Henderson, D. Ranasinghe, V. G. Zakrzewski, J. Gao, N. Rega, G. Zheng, W. Liang, M. Hada, M. Ehara, K. Toyota, R. Fukuda, J. Hasegawa, M. Ishida, T. Nakajima, Y. Honda, O. Kitao, H. Nakai, T. Vreven, K. Throssell, J. A. Montgomery Jr., J. E. Peralta, F. Ogliaro, M. J. Bearpark, J. J. Heyd, E. N. Brothers, K. N. Kudin, V. N. Staroverov, T. A. Keith, R. Kobayashi, J. Normand, K. Raghavachari, A. P. Rendell, J. C. Burant, S. S. Iyengar, J. Tomasi, M. Cossi, J. M. Millam, M. Klene, C. Adamo, R. Cammi, J. W. Ochterski, R. L. Martin, K. Morokuma, O. Farkas, J. B. Foresman, D. J. Fox, Gaussian 16, Revision C.01, Gaussian, Inc., Wallingford, CT, **2016**.
[67] R. F. W. Bader, *Chem. Rev.* **1991**, *91*, 893–928.
[68] T. A. Keith, AIMAll (version 13.05.06), TK Gristmill Software, Overland Park, KS, USA, **2013**.
[69] R. Hilal, S. G. Aziz, A. O. Alyoubi, S. Elroby, *Procedia Comput. Sci.* **2015**, *51*, 1872–1877.
[70] R. F. W. Bader, Atoms in Molecules, A Quantum Theory, Oxford University Press, New York, **1990**.
[71] J. Contreras-García, E. R. Johnson, S. Keinan, R. Chaudret, J. P. Piquemal, D. N. Beratan, W. Yang, *J. Chem. Theory Comput.* **2011**, *7*, 625–632.
[72] E. R. Johnson, S. Keinan, P. Mori-Sanchez, J. Contreras-Garcia, A. J. Cohen, W. Yang, *J. Am. Chem. Soc.* **2010**, *132*, 6498–6506.
[73] S. Tripathi, A. Hossain, S. K. Seth, S. Mukhopadhyay, *J. Mol. Struct.* **2020**, *1216*, 128207.

Submitted: September 1, 2022
Accepted: October 18, 2022

ChemistrySelect

Supporting Information

Exploring Solid-State Supramolecular Architectures of Penta(carboxymethyl)diethylenetriamine: Experimental Observation and Theoretical Studies

Samiul Islam, Prantika Das, Suparna Tripathi, Subrata Mukhopadhyay, and Saikat Kumar Seth*

Contents

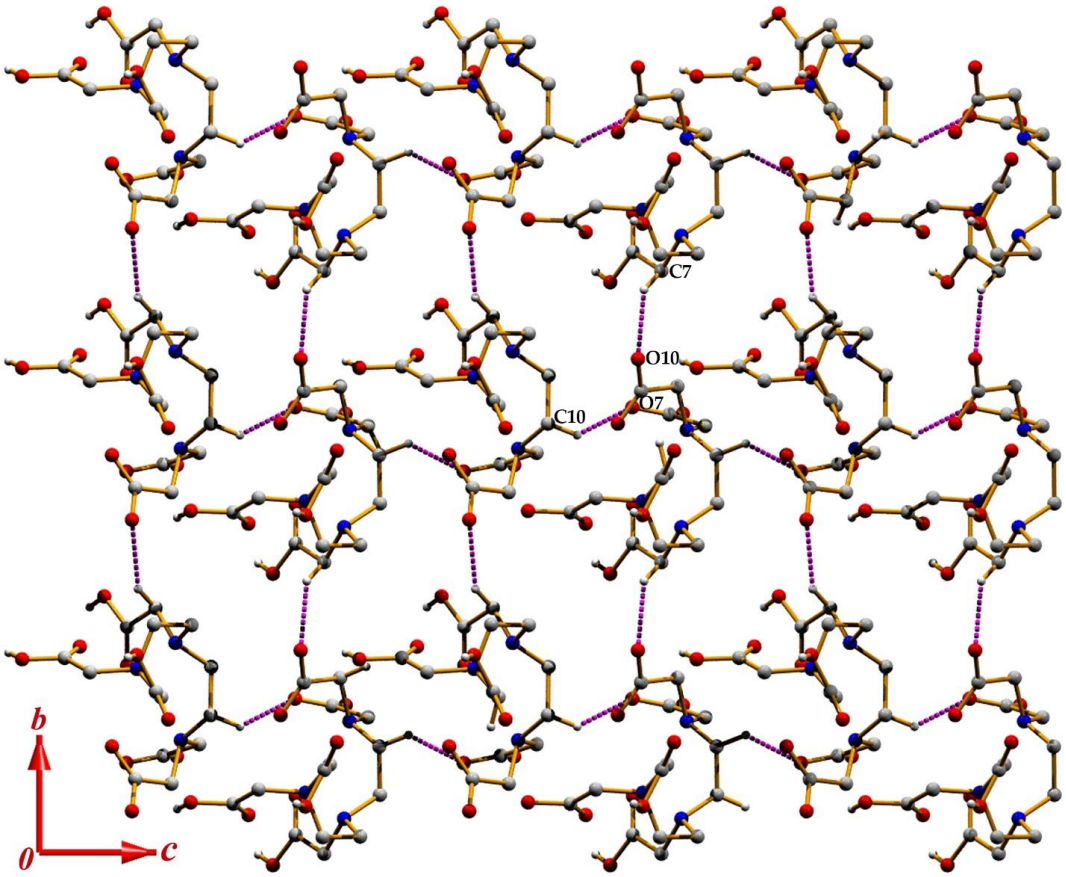

Figure S1. C–H···O bonds lead to the formation of a 2D supramolecular network for compound (**1**).

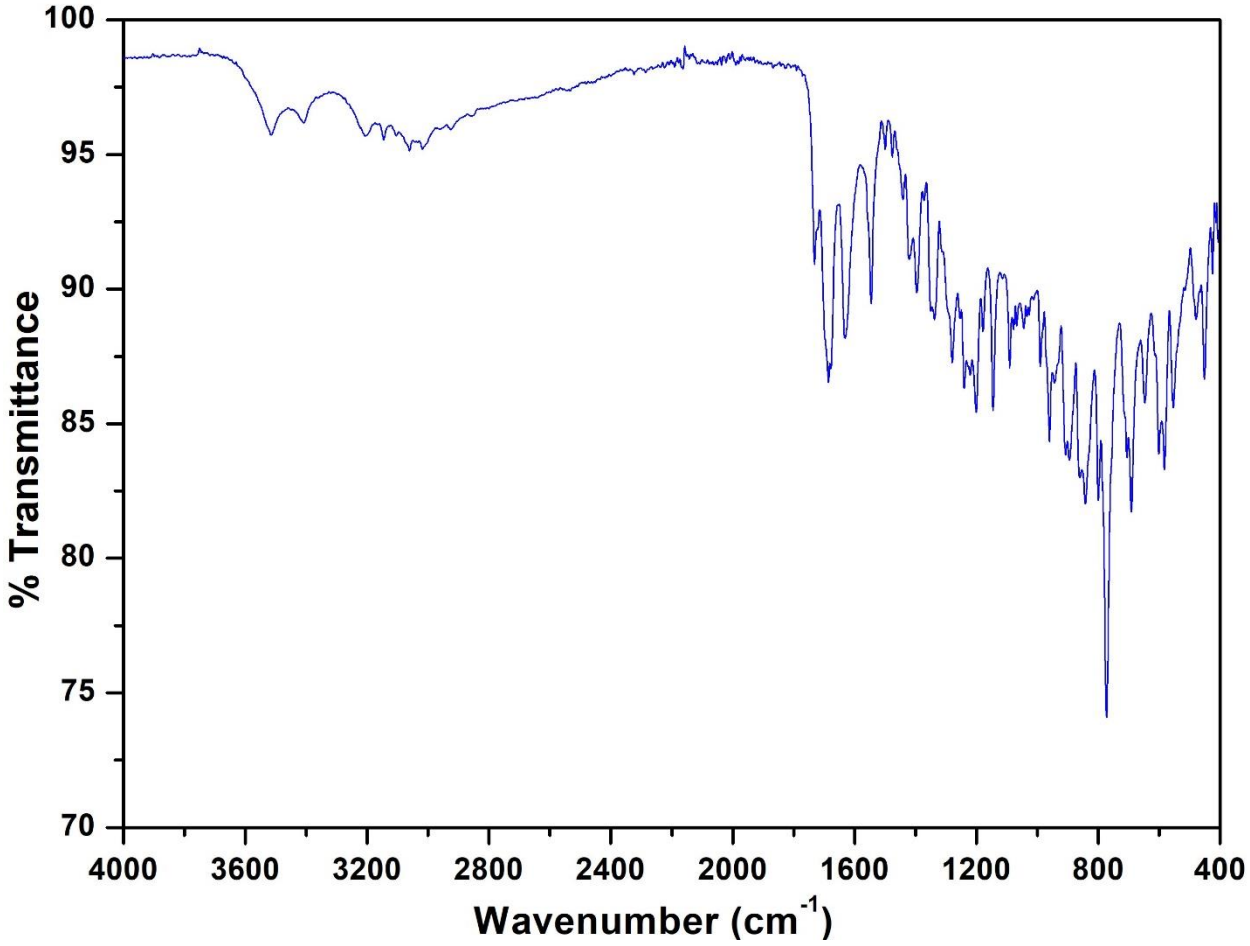

Figure S2. IR spectrum of (**1**).

Table S1. Atomic coordinates (× 10^{-4} and equivalent isotropic displacement parameters (Å^2 × 10^{-3}) for (**1**). U(eq) is defined as one third of the trace of the orthogonalized U_{ij} tensor.

Atom	x	y	z	U(eq)
C(1)	-89(1)	6160(1)	8724(1)	16(1)
O(2)	-391(1)	4901(1)	8153(1)	20(1)
O(1)	-460(1)	7109(1)	9091(1)	24(1)
N(1)	1169(1)	5377(1)	8161(1)	14(1)
N(2)	2701(1)	4484(1)	9304(1)	13(1)
N(3)	3482(1)	7825(1)	9465(1)	12(1)
C(9)	3282(1)	5304(1)	10367(1)	14(1)
C(13)	3095(1)	9315(1)	9186(1)	15(1)
C(12)	4731(1)	8354(1)	8949(1)	15(1)
C(3)	837(1)	5488(2)	6768(1)	16(1)
C(11)	4341(1)	7962(1)	10012(1)	15(1)
C(7)	3077(1)	3284(1)	8715(1)	15(1)
C(6)	2036(1)	3872(1)	9782(1)	15(1)
C(5)	1307(1)	3849(1)	8670(1)	14(1)
C(10)	3110(1)	6962(1)	10350(1)	14(1)
C(2)	782(1)	6344(1)	8883(1)	17(1)
C(14)	2344(1)	9162(1)	8113(1)	14(1)
C(4)	1395(1)	4997(1)	6018(1)	15(1)
C(8)	3558(1)	3927(1)	7871(1)	16(1)
O(4)	1062(1)	5046(1)	4759(1)	21(1)
O(10)	1877(1)	10258(1)	8017(1)	17(1)
O(3)	2060(1)	4611(1)	6470(1)	20(1)
O(6)	3766(1)	2890(1)	7196(1)	24(1)
O(7)	4339(1)	8603(1)	7851(1)	21(1)
O(5)	3720(1)	5254(1)	7874(1)	20(1)
O(8)	5472(1)	8379(1)	9351(1)	22(1)
O(9)	2255(1)	8039(1)	7424(1)	22(1)

Table S2. Anisotropic displacement parameters ($Å^2 \times 10^{-3}$) for (**1**). The anisotropic displacement factor exponent takes the form: $-2\pi^2 [h^2 a^{*2} U_{11} + ... + 2 h k a^* b^* U_{12}]$.

Atom	U_{11}	U_{22}	U_{33}	U_{23}	U_{13}	U_{12}
C(1)	18(1)	19(1)	12(1)	4(1)	4(1)	4(1)
O(2)	12(1)	25(1)	24(1)	-3(1)	4(1)	0(1)
O(1)	23(1)	27(1)	26(1)	-2(1)	10(1)	7(1)
N(1)	14(1)	15(1)	15(1)	0(1)	4(1)	1(1)
N(2)	12(1)	13(1)	12(1)	0(1)	2(1)	0(1)
N(3)	11(1)	13(1)	13(1)	0(1)	3(1)	0(1)
C(9)	12(1)	17(1)	12(1)	0(1)	0(1)	-2(1)
C(13)	14(1)	13(1)	18(1)	0(1)	4(1)	1(1)
C(12)	14(1)	13(1)	18(1)	0(1)	3(1)	0(1)
C(3)	13(1)	19(1)	16(1)	3(1)	2(1)	2(1)
C(11)	10(1)	18(1)	15(1)	1(1)	1(1)	0(1)
C(7)	14(1)	13(1)	17(1)	-1(1)	3(1)	2(1)
C(6)	14(1)	18(1)	15(1)	2(1)	6(1)	-1(1)
C(5)	13(1)	16(1)	15(1)	0(1)	5(1)	-2(1)
C(10)	13(1)	17(1)	14(1)	0(1)	5(1)	-1(1)
C(2)	17(1)	17(1)	18(1)	-3(1)	4(1)	0(1)
C(14)	13(1)	18(1)	14(1)	3(1)	8(1)	-1(1)
C(4)	15(1)	14(1)	16(1)	3(1)	3(1)	-2(1)
C(8)	10(1)	19(1)	17(1)	-2(1)	0(1)	2(1)
O(4)	17(1)	32(1)	15(1)	4(1)	5(1)	4(1)
O(10)	14(1)	19(1)	19(1)	2(1)	5(1)	3(1)
O(3)	14(1)	29(1)	18(1)	2(1)	4(1)	3(1)
O(6)	23(1)	23(1)	31(1)	-7(1)	16(1)	-2(1)
O(7)	16(1)	29(1)	15(1)	3(1)	3(1)	0(1)
O(5)	20(1)	18(1)	23(1)	-2(1)	9(1)	-2(1)
O(8)	12(1)	34(1)	20(1)	5(1)	4(1)	0(1)
O(9)	19(1)	25(1)	20(1)	-6(1)	3(1)	1(1)

checkCIF/PLATON report

Structure factors have been supplied for datablock(s) shelx

THIS REPORT IS FOR GUIDANCE ONLY. IF USED AS PART OF A REVIEW PROCEDURE FOR PUBLICATION, IT SHOULD NOT REPLACE THE EXPERTISE OF AN EXPERIENCED CRYSTALLOGRAPHIC REFEREE.

No syntax errors found. CIF dictionary Interpreting this report

Datablock: shelx

```
Bond precision:   C-C = 0.0018 A          Wavelength=0.71073

Cell:             a=17.8462(14)     b=8.9381(7)          c=10.7308(9)
                  alpha=90          beta=105.238(2)      gamma=90
Temperature:      120 K

                 Calculated                Reported
Volume           1651.5(2)                 1651.5(2)
Space group      P 21/c                    P 21/c
Hall group       -P 2ybc                   -P 2ybc
Moiety formula   C14 H23 N3 O10            ?
Sum formula      C14 H23 N3 O10            C14 H23 N3 O10
Mr               393.35                    393.35
Dx,g cm-3        1.582                     1.582
Z                4                         4
Mu (mm-1)        0.135                     0.135
F000             832.0                     832.0
F000'            832.54
h,k,lmax         21,10,12                  21,10,12
Nref             2919                      2864
Tmin,Tmax        0.986,0.993               0.980,0.990
Tmin'            0.980

Correction method= # Reported T Limits: Tmin=0.980 Tmax=0.990
AbsCorr = MULTI-SCAN

Data completeness= 0.981           Theta(max)= 24.994

R(reflections)= 0.0303( 2635)                    wR2(reflections)=
                                                 0.0734( 2864)
S = 1.049                 Npar= 247
```

The following ALERTS were generated. Each ALERT has the format
test-name_ALERT_alert-type_alert-level.
Click on the hyperlinks for more details of the test.

Alert level C

PLAT911_ALERT_3_C Missing FCF Refl Between Thmin & STh/L= 0.594 53 Report

Alert level G

PLAT007_ALERT_5_G Number of Unrefined Donor-H Atoms ..... 5 Report
PLAT066_ALERT_1_G Predicted and Reported Tmin&Tmax Range Identical ? Check
PLAT432_ALERT_2_G Short Inter X...Y Contact O7 ..C9 3.00 Ang.
x,3/2-y,-1/2+z = 4_575 Check
PLAT432_ALERT_2_G Short Inter X...Y Contact O9 ..C10 3.01 Ang.
x,3/2-y,-1/2+z = 4_575 Check
PLAT793_ALERT_4_G Model has Chirality at N2 (Centro SPGR) S Verify
PLAT883_ALERT_1_G No Info/Value for _atom_sites_solution_primary . Please Do !
PLAT909_ALERT_3_G Percentage of I>2sig(I) Data at Theta(Max) Still 85% Note
PLAT910_ALERT_3_G Missing # of FCF Reflection(s) Below Theta(Min). 2 Note
PLAT913_ALERT_3_G Missing # of Very Strong Reflections in FCF .... 3 Note
PLAT933_ALERT_2_G Number of HKL-OMIT Records in Embedded .res File 54 Note
PLAT965_ALERT_2_G The SHELXL WEIGHT Optimisation has not Converged Please Check
PLAT967_ALERT_5_G Note: Two-Theta Cutoff Value in Embedded .res .. 50.0 Degree
PLAT978_ALERT_2_G Number C-C Bonds with Positive Residual Density. 7 Info

0 **ALERT level A** = Most likely a serious problem - resolve or explain
0 **ALERT level B** = A potentially serious problem, consider carefully
1 **ALERT level C** = Check. Ensure it is not caused by an omission or oversight
13 **ALERT level G** = General information/check it is not something unexpected

2 ALERT type 1 CIF construction/syntax error, inconsistent or missing data
5 ALERT type 2 Indicator that the structure model may be wrong or deficient
4 ALERT type 3 Indicator that the structure quality may be low
1 ALERT type 4 Improvement, methodology, query or suggestion
2 ALERT type 5 Informative message, check

It is advisable to attempt to resolve as many as possible of the alerts in all categories. Often the minor alerts point to easily fixed oversights, errors and omissions in your CIF or refinement strategy, so attention to these fine details can be worthwhile. In order to resolve some of the more serious problems it may be necessary to carry out additional measurements or structure refinements. However, the purpose of your study may justify the reported deviations and the more serious of these should normally be commented upon in the discussion or experimental section of a paper or in the "special_details" fields of the CIF. checkCIF was carefully designed to identify outliers and unusual parameters, but every test has its limitations and alerts that are not important in a particular case may appear. Conversely, the absence of alerts does not guarantee there are no aspects of the results needing attention. It is up to the individual to critically assess their own results and, if necessary, seek expert advice.

Publication of your CIF in IUCr journals

A basic structural check has been run on your CIF. These basic checks will be run on all CIFs submitted for publication in IUCr journals (*Acta Crystallographica*, *Journal of Applied Crystallography*, *Journal of Synchrotron Radiation*); however, if you intend to submit to *Acta Crystallographica Section C* or *E* or *IUCrData*, you should make sure that full publication checks are run on the final version of your CIF prior to submission.

Publication of your CIF in other journals

Please refer to the *Notes for Authors* of the relevant journal for any special instructions relating to CIF submission.

PLATON version of 18/12/2021; check.def file version of 18/12/2021

Datablock shelx - ellipsoid plot

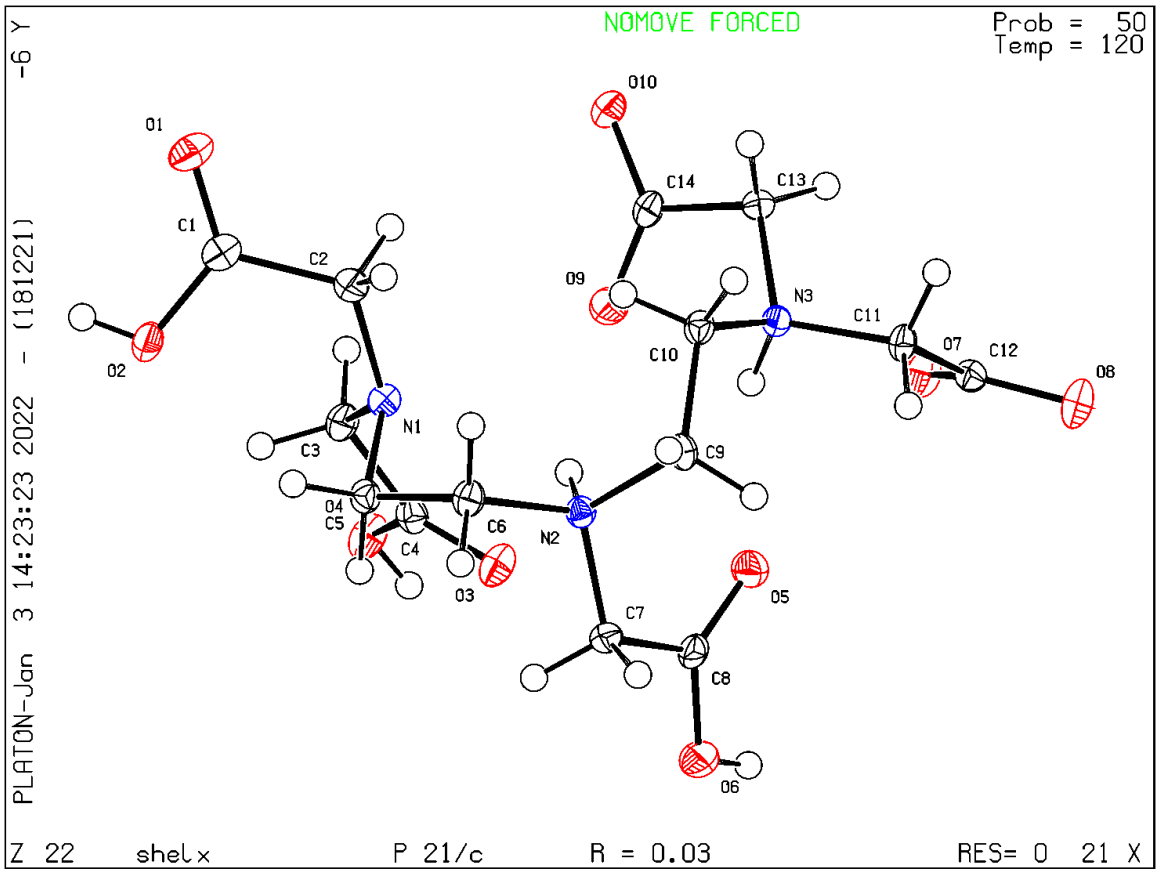

Polyhedron 242 (2023) 116514

Contents lists available at ScienceDirect

Polyhedron

journal homepage: www.elsevier.com/locate/poly

A combined experimental and theoretical studies of two new Co(II)–PDA complexes: Unusual 2D and 3D supramolecular networks [PDA = 2,6-pyridinedicarboxylic acid]

Samiul Islam, Pratik Dey, Saikat Kumar Seth *

Department of Physics, Jadavpur University, Kolkata 700032, India

ARTICLE INFO

Keywords:
Octahedral Co(II) complexes
(Lone pair···π/
π···π^+/π^+···π/π···π/π···π^+/π^+···π/π···lone pair)$_n$ network
Quantum theory of atoms-in-molecules (QTAIM)
Theoretical noncovalent interaction (NCI) plot index

ABSTRACT

Two new Co(II) complexes, {[Co(2,6-pydc)$_2$]·[Co(4,4′-tmdpy)(H$_2$O)$_4$]$_n$·2H$_2$O}(**1**) and {2[*Co*(2,6-*pydc*)$_2$]$^{2-}$·[2(4,4′-bpy]$^{2+}$·10(H$_2$O)·O}(**2**) [2,6-pydc = 2,6-pyridinedicarboxylic acid, 4,4′-tmdpy = 4,4′-trimethylenedipyridine, 4,4′-bpy = 4,4′-Bipyridine] were designed, synthesized, and characterized using elemental analysis, spectroscopic techniques, and single-crystal X-ray diffraction analysis. For complex (**1**), hydrogen bonding, π···π and lone pair (l.p.)···π interactions produce supramolecular assemblies, whereas for complex (**2**), hydrogen bonding, π···π, π···π^+, π^+···π, l.p···π play the pivotal role in building final solid-state structure. Complex (**1**) exhibits a unique 3D supramolecular architecture generated through π···π and l.p···π interactions. Complex (**2**) also exhibits a unique (l.p···π/π···π^+/π^+···π/π···π/π···π^+/π^+···π/π···l.p)$_n$ self-assembly. The noncovalent interactions were characterized through Bader's quantum theory of "Atoms In Molecules" (QTAIM). Evaluation of topological parameters at (3, –1) bond critical points (BCPs) confirmed the 'closed-shell' nature of the intermolecular interactions. Furthermore, the theoretical "Noncovalent Interaction" (NCI) plot index was used to characterize noncovalent interactions.

1. Introduction

The design, synthesis, and development of metal–organic complexes have attracted considerable attention from researchers, not only because of their countless potential applications in various fields but also because of their interesting structural topologies [1–4]. In synthesizing metal–organic complexes, transition metals have always proven to be the most important class of atoms because of their potent ability to bind to one or more ligands through coordination bonds [5,6]. Thus metal ions play a pivotal role in controlling the coordination geometry and properties of metal–organic complexes. The versatile nature of metal–ligand coordinative bonding allows chemists to control molecular assemblies. However, there are many factors that can effectively influence the design and synthesis of the desired structural topologies, such as metal–ligand ratio, counterions, pH value, solvents, and temperature [7–10].

Selectivity of ligand is vital for designing and synthesizing metal–organic complexes. The 2,6-pyridinedicarboxylic acid (2,6-pydc) is a frequently used ligand that coordinates to metal ions with tridentate mode [9]. The donor sites of 2,6-pydc are occupied by one pyridine nitrogen atom and two carboxylate oxygen atoms. 2,6-pydc is able to form stable coordination complexes with most transition metal centers, thereby occupying a prominent place as a building block in coordination chemistry [11]. Bridging dipyridine ligands, such as 4,4′-trimethylenedipyridine (4,4′-tmdpy), 4,4′-bipyridine (4,4′-bpy), etc., have been used for the construction of various hybrid solids [12,13]. 4,4′-tmdpy is used as a flexible *N*-donor to construct several coordination polymers with different structural topologies, among the *N*-donor bridging ligands [14,15].

The comprehensive study of noncovalent interactions is necessary to develop new supramolecular chemistry applications. In crystalline solids, molecular recognition events occur spontaneously due to mutual interactions through various forces. One can design a crystal with desired properties with a clear idea of how molecular recognition involves various noncovalent interactions [16,17]. Though hydrogen bonding has been extensively employed in crystal packing, there are other various kinds of weak interactions establishing their contributions to the building of supramolecular architectures. For example, the interactions incorporating aromatic π-ring such as π···π^+, π^+···π^+, anion···π, anion···π^+, lone-pair(l.p)···π, C–H···π, metal···π, salt-bridge

* Corresponding author.
E-mail address: saikatk.seth@jadavpuruniversity.in (S.K. Seth).

https://doi.org/10.1016/j.poly.2023.116514
Received 26 March 2023; Accepted 14 June 2023
Available online 22 June 2023

(SB)···π^+, etc. are also very crucial to incarnate the crystal structure in solid state [18–24]. Other than the interactions involving the aryl ring, C–H···O, O–H···O, N–H···O, etc. belonging to the hydrogen bond category is also vital to form solid-state structure [18,19,25]. Thus, these interactions are considered for rationalizing supramolecular crystals and stabilizing their intricate structure in the solid state.

We have synthesized and structurally characterized two new Co(II) coordinated metal–organic complexes, and analyzed noncovalent interactions in constructing supramolecular frameworks. Exploration of supramolecular packing diagrams of both complexes (**1** and **2**) reveals unusual types of structural networks, such as $(l.p\cdots\pi/\pi\cdots\pi^+/\pi^+\cdots\pi/\pi\cdots\pi/\pi\cdots\pi^+/\pi^+\cdots\pi/\pi\cdots l.p)_n$. We have further characterized the noncovalent interactions using Bader's quantum theory of "atoms-in-molecules" (QTAIM) [26,27] and analyzed topological parameters, and calculated the dissociation energy of interactions. Further, we have performed the "Noncovalent Interaction" (NCI) plot index [28,29] for analyzing noncovalent interactions. Also, we have calculated the optical band gap from UV–Vis spectroscopy using Tauc's equation [30] for both complexes.

2. Experimental sections

2.1. Materials and measurements

All chemicals used were of reagent-grade quality and purchased from Sigma Aldrich Chemical Co. All reactions were carried out in an aqueous medium under aerobic conditions. During the whole experiment, doubly distilled water was used. The CHN elemental analyses of both complexes were performed on a PerkinElmer 2400 Series-II CHN analyzer, USA, elemental analyzer. We have used a Perkin-Elmer LX-1 FT-IR spectrophotometer with a modern diamond attenuated total reflectance (ATR) accessory method to record the infrared spectrum in the range 4000–400 cm^{-1}. The absorbance spectrum of the title complexes was recorded in the wavelength range of 190 nm-1100 nm using a UV–vis spectrophotometer (UV/Vis Lamda 365, PerkinElmer). To analyze the phase purity of the samples, powder X-ray diffraction (PXRD) data were recorded in the 2θ range of 5°–40° on a Bruker D8 Advance X-ray diffractometer using Cu Kα radiation (λ = 1.548 Å) generated at 35 kV and 35 mA.

2.2. Syntheses of the title complexes

2.2.1. Synthesis of complex (1)

Cobalt(II) nitrate hexahydrate (0.291 g, 1.0 mmol) dissolved in 25 ml of water was allowed to react with pyridine-2,6-dicarboxylic acid (0.334 g, 2.0 mmol) in water (25 ml) at 50 °C, resulting a pink solution. A warm aqueous solution (25 ml) of 4,4′-trimethylenedipyridine (0.396 g, 2 mmol) was added dropwise to the above solution with continuous stirring. The reaction mixture thus obtained was further heated at 50 °C for two hour with continuous stirring. The solution was then cooled to room temperature and filtered, and the filtrate was left unperturbed. After a few weeks, block-shaped, pink crystals, suitable for X-ray diffraction analysis were obtained. The crystals were collected by filtration, washed with cold water, and dried in air. Anal. Calcd. for $C_{27}H_{32}Co_2N_4O_{14}$ (**1**): C, 42.98%; H, 4.27%; N, 7.42% and found: C, 42.95%; H, 4.29%; N, 7.40%. The PXRD patterns of complex (**1**) are shown in Fig. S1a. The main IR absorption bands observed (in cm^{-1}) for complex (**1**) are 3151 (w), 3095 (s), 2862 (s), 1622 (vs), 1589 (vs), 1502 (vs), 1431 (vs), 1365 (vs), 1282 (vs), 1220 (s), 1188 (vs), 1076 (vs), 767 (vs) (Fig. S2).

2.2.2. Synthesis of complex (2)

Cobalt(II) nitrate hexahydrate (0.291 g, 1.0 mmol) was reacted with pyridine-2,6-dicarboxylic acid (0.334 g, 2.0 mmol) in water (50 ml) at 60 °C. A warm aqueous solution (20 ml) of 4,4′-Bipyridine (0.624 g, 4.0 mmol) was then added dropwise to the above solution with continuous stirring for about an hour at normal laboratory temperature (~32 °C). The solution mixture was left undisturbed for a few days when block-shaped, pink crystals suitable for X-ray diffraction analysis were obtained. The crystals were collected by filtration, washed with cold water, and dried in air. Anal. Calcd. for $C_{48}H_{52}Co_2N_8O_{27}$ (**2**): C, 44.66%; H, 4.06%; N, 8.68% and found: C, 44.63%; H, 4.07%; N, 8.70%. The PXRD patterns of complex (**2**) are shown in Fig. S1b. The main IR absorption bands observed (in cm^{-1}) for complex (**2**) are 3100 (s), 3007 (w), 2598 (w), 1583 (vs), 1492 (vs), 1365 (vs), 1282 (vs), 1214 (s), 1188 (vs), 1075 (s), 990 (s), 813 (s), 777 (vs), 729 (s) (Fig. S3).

2.3. X-ray crystal structure determination

Optically transparent, good single crystals were selected for single-crystal X-ray diffraction (SCXRD) to determine crystal structure. Intensity data collection was performed by using Bruker APEX-II CCD diffractometer having a fine-focus sealed tube as diffraction source of MoKα radiation (λ = 0.71073 Å) at 273(2) K and 120(2) K for (**1**) and (**2**) respectively. Collected intensity data were reduced using the Bruker SAINT v8.34A program [31], and an empirical absorption correction based on the multi-scan method was applied using the process SADABS [32]. The structure solution of both complexes was carried out using SHELXT-14 [33] and then refined by the full-matrix least-squares technique on F^2 using SHELXL-18 [34] for (**1**) and SHELXL-14 [34] for (**2**). The hydrogen atoms were placed at their geometrically idealized positions and refined isotropically. The structure solution of (**1**) was performed using the WinGX program V2014.1 [35], whereas Olex2 1.5 program [36] was used for the structure solution of (**2**). For analyzing the crystal information files (CIFs) of both complexes, the program PLATON [37] was used. The crystal information and structure refinement parameters are summarized in Table 1. CCDC 2238424–2238425 contains the supplementary crystallographic data of complexes (**1**)–(**2**), respectively. Selected bond lengths (Å) and bond angles (°) around the metal centers in complexes (**1**) and (**2**) are given in Table S1.

2.4. Theoretical methods

Both complexes' quantum chemical computations are performed using *Gaussian 16w* calculation package [38] at the DFT/B3LYP level with 6311G basis set. We have used the models generated from supramolecular architectures to perform theoretical calculations. For the characterization of weak noncovalent interactions, we have used Bader's quantum theory of "Atoms in Molecules" (QTAIM) [26,27] using the AIMall calculation package [39]. The topological parameters derived from QTAIM [40] allow for much better insights into the interatomic interactions, and it can be used as a powerful tool for investigating the electronic and conformational properties of the molecules [41]. There are some notable points named critical points where the gradient of electron density (ρ_{BCP}) vanishes. The critical points of bonds are known as bond critical points (BCPs) lying in the bond path connecting two atoms. Every BCP contains well-to-do chemical information, reflecting the bond's nature. The topological parameters like electron density (ρ_{BCP}), Laplacian of the electron density ($\nabla^2(\rho_{BCP})$), and potential energy density (V_{BCP}) are mainly used for characterizing noncovalent interactions. Electron density concentrated towards the interaction line when $\nabla^2(\rho_{BCP}) < 0$ and depleted towards the nucleus when $\nabla^2(\rho_{BCP}) > 0$. Employing potential energy density (V_{BCP}), dissociation energy of interaction can be obtained using the formula $D.E_{int} = -½\ V_{BCP}$, more accurately $D.E_{int}$ (Kcal.mol^{-1}) = –313.754 × V_{BCP} (au) [42]. The NCI Plot Index is a visualization index for analyzing noncovalent interactions. We have used Multiwfn [43] and visual molecular dynamics (VMD) [44] for indexing NCI Plot [28,29]. Isosurfaces represent noncovalent interactions in NCI Plot. Different colors of isosurfaces indicate different natures of the interaction. For example, the blue and red color of the isosurface represents ρ^-cut (attractive) and ρ^+cut (repulsive) interactions, respectively, whereas yellow and green colors indicate weak repulsive and weak attractive interactions [29].

Table 1
Crystal data and structure refinement parameters for (**1**) and (**2**).

	Complex (**1**)	Complex (**2**)
Empirical formula	$C_{27}H_{32}Co_2N_4O_{14}$	$C_{48}H_{52}Co_2N_8O_{27}$
Formula weight	754.42	1290.83
Temperature	273(2)K	120 K
Wavelength (Mo Kα)	0.71073 Å	0.71073 Å
Crystal system, space group	Monoclinic, *P2/c*	Triclinic, P –1
Unit cell parameters	a = 9.748(1) Å	a = 10.252(3) Å
	b = 8.965(1)Å	b = 15.232(5) Å
	c = 18.197(2)Å	c = 17.640(6) Å
	α = 90°	α = 91.647(4)°
	β = 99.431(2)°	β = 92.314(4)°
	γ = 90°	γ = 100.921(4)°
Volume	1568.8(2)Å^3	2700.7(15) Å^3
Crystal size	0.21 × 0.13 × 0.08 mm	0.15 × 0.12 × 0.1 mm
Crystal shape	Block	Block
Crystal colour	Dark pink	Metallic dark red
Z /Density (clac.)	2, 1.597 Mg/m^3	2, 1.587 Mg/m^3
Absorption coefficient	1.133 mm^{-1}	0.714 mm^{-1}
F(000)	776	1332
θ-range for data collection	2.269–24.997°	1.156–25°
Limiting indices	$-11 \le h \le 11$; $-10 \le k \le 10$;	$-12 \le h \le 12$; $-18 \le k \le 18$;
	$-21 \le l \le 21$	$-20 \le l \le 20$
Reflections collected/unique	18943/2764[R	25247/ 9357[R
	(int) = 0.0526]	(int) = 0.0686]
Completeness to theta	99.7%	98.5%
Absorption correction	Semi-empirical from equivalents	Semi-empirical from equivalents
Max. and min. transmission	0.92 and 0.84	0.932 and 0.90
Refinement method	full-matrix least-squares on F^2	full-matrix least-squares on F^2
Data/ parameters	2764/ 215	9357/ 861
Goodness-of-fit on F^2	1.078	1.034
Final R indices [I > 2σ(I)]	$R_1 = 0.0281$, w$R_2 = 0.0795$	$R_1 = 0.0777$, w$R_2 = 0.2104$
R indices (all data)	$R_1 = 0.0310$, w$R_2 = 0.0819$	$R_1 = 0.1091$, w$R_2 = 0.2326$
Largest diff. peak and hole	0.301 and –0.435 e·Å^{-3}	1.929 and –0.745 e·Å^{-3}

$R_1 = \Sigma||F_o|-|F_c||/\Sigma|F_o|$, w$R_2 = [\Sigma\{(F_o^2-F_c^2)^2\}/\Sigma\{w(F_o^2)^2\}]^{1/2}$, $w = 1/\{\sigma^2(F_o^2) + (aP)^2 + bP\}$, where P= $(F_o^2 + 2F_c^2)/3$ for both complexes, a = 0.0420 and b = 0.8374 for (**1**) and a = 0.1305 and b = 6.6104 for (**2**).

3. Results and discussion

3.1. Structural description of complex (1)

Complex (**1**) crystallizes in a monoclinic crystal system with a *P2/c* space group which is quite unusual, and it is here justified by the intrinsic molecular symmetry of the cation, and the ORTEP [35] diagram depicted in Fig. 1. Complex (**1**) is composed of an anionic moiety made up of a Co(1) center and two $(2,6\text{-pydc})^{2-}$ anions, as well as a one-dimensional polymeric cationic chain in which the 4,4′-tmdpy ligands connect the Co(2) sites and lattice water molecules (see Fig. 1). Two pydc ligands operate in a tridentate mode toward the Co(1) ion to create the anionic unit, resulting an octahedral geometry. The Co(2) center also adopts an octahedral environment in the cationic portion,

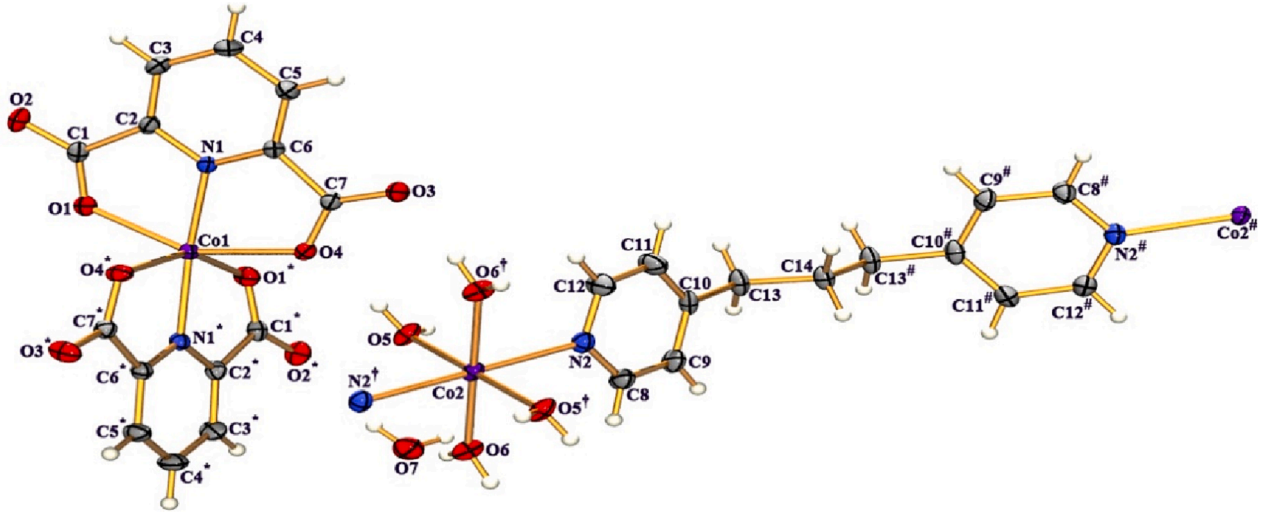

Fig. 1. An ORTEP view of the asymmetric unit of complex (**1**) with the atom-numbering scheme. Thermal ellipsoids are drawn at 30% probability. Symmetry codes: * = 1–x, y, 1/2–z; # = –x, y, 3/2–z; † = 1–x, –y, 1–z.

Table 2
Relevant hydrogen bonding parameters (Å, °).

D–H···A	D–H	H···A	D···A	D–H···A	Symmetry
Complex (1)					
O(5)–H(5B)···O(2)	0.82	1.91	2.731(2)	174	x, 1–y, 1/2 + z
O(6)–H(6A)···O(3)	0.82	1.86	2.674(2)	169	1–x, –y, 1–z
O(7)–H(7A)···O(2)	0.83	2.19	3.013(2)	170	1–x, y, 1/2–z
O(7)–H(7B)···O(1)	0.82	1.99	2.792(2)	163	x, 1–y, 1/2 + z
C(5)–H(5)···O(3)	0.93	2.36	3.169(3)	146	–x, y, 1/2–z
C(12)–H(12)···O(6)	0.93	2.55	3.128(3)	121	1–x, –y, 1–z
C(14)–H(14A)···O(3)	0.97	2.50	3.392(3)	153	–x, –y, 1–z
C(14)–H(14A)···O(3)	0.97	2.50	3.392(3)	153	x, –y, 1/2 + z
Complex (2)					
N(1)–H(1)···O(26)	0.88	1.78	2.617(7)	157	–
N(2)–H(2)···O(1)	0.88	1.75	2.621(7)	167	–
N(5)–H(5)···O(8)	0.88	1.76	2.622(7)	166	–
N(6)–H(6)···O(9)	0.88	1.83	2.624(7)	149	–
O(19)–H(19A)···O(20)	0.83	1.80	2.488(2)	139	–
O(20)–H(20A)···O(4)	0.81	1.99	2.751(8)	156	–
O(22)–H(22A)···O(7)	0.83	2.17	2.989(6)	170	2–x, 1–y, 1–z
O(23)–H(23A)···O(2)	0.83	2.04	2.858(6)	170	–
O(26)–H(26B)···O(25)	0.83	1.97	2.727(7)	152	–
C(1)–H(1A)···O(27)	0.95	2.46	3.170(8)	131	–
C(6)–H(6A)···O(23)	0.95	2.54	3.262(8)	133	–
C(14)–H(14)···O(22)	0.95	2.44	3.197(8)	137	–
C(15)–H(15)···O(13)	0.95	2.38	3.197(7)	144	1 + x, 1 + y, 1 + z
C(20)–H(20)···O(12)	0.95	2.27	3.103(8)	146	2 + x, y, 1 + z
C(25)–H(25)···O(21)	0.95	2.48	3.329	149	–
C(34)–H(34)···O(25)	0.95	2.58	3.296(8)	132	2–x, –y, –z
C(37)–H(37)···O(18)	0.95	2.40	3.329(8)	165	–
C(44)–H(44)···O(4)	0.95	2.38	3.166(7)	140	–1 + x, –1 + y, –1 + z
C(45)–H(45)···O(17)	0.95	2.45	3.156(8)	131	–

where the CoN_2O_4 core adopts a *trans* arrangement and is coordinated by two nitrogen atoms from a 4,4′-tmdpy ligand and four oxygen atoms from lattice water molecules. In each cation chain of $[Co(4,4'\text{-tmdpy})(H_2O)_4]_n^{2+}$ unit, the nitrogen atoms of the 4,4′-tmdpy ligand bridges the Co(2) sites by generating a cationic polymeric zigzag chain. In contrast to the Co(1) site, it is noted that Co(2)–O bond distances are shorter than Co(2)–N (see Table S1). It is apparent that Co(1)–O distances are longer than Co(1)–N distances. In the cationic unit, the O(5) and O(6) atom occupy the axial positions and are nearly perpendicular with an angle of 93.96(6)°, as well as N(2) also occupying axial position with O(5)–Co(2)–N(2) and O(6)–Co(2)–N(2) angles of 91.58(6)° and 91.08(6)° respectively (see Table S1). Noting that two pyridine rings of the polymeric cationic unit are not coplanar, the dihedral angle between them is 56.75°. Two rigid $(2,6\text{-pydc})^{2-}$ have a dihedral angle of 83.82°, deviating 6.18° from perpendicular.

The noncovalent interactions such as hydrogen bonding (O–H···O and C–H···O), π···π, and lone pair (l.p.)···π interactions are responsible for the generation and stabilization of supramolecular structures for (**1**) in solid-state (Tables 2–4). The water oxygen O(7) acts as a donor to carboxylate oxygen atom O(1) and carbonyl oxygen atom O(2) of the acid moiety at (x, 1–y, 1/2 + z) and (1–x, y, 1/2–z) respectively, hence a centrosymmetric tetrameric ring $R_4^4(12)$ is formed. Again the carbonyl oxygen O(3) at (–x, y, 1/2–z) interacts through H-bonding interaction when C(5) plays the role of donor, forming a centrosymmetric dimeric ring $R_2^2(10)$. The combination of these $R_4^4(12)$ and $R_2^2(10)$ ring motifs leads to the formation of a two-dimensional framework in the (1 0 1) plane (Fig. 2). The $R_2^2(10)$ dimeric ring in another substructure mentioned above forms a one-dimensional chain of acid moieties. Parallel 1D polymeric chains are connected to the chains of acid moieties through the O(6)–H(6A)···O(3) interactions, resulting in the formation of a two-dimensional supramolecular framework in the (1 0 1) plane (Fig. 3).

Further in another substructure, the carbon atom C(14), located at the inversion center of the polymeric chain, acts as a donor to the carbonyl oxygen atoms O(3) of two parallel acid moieties of the molecules at (–x, –y, 1–z) and (x, –y, 1/2 + z) (see Table 2). Now the carbonyl oxygen atoms O(3) of the symmetric part of acid moieties again interact with C(14) of the polymeric chain, which leads to the formation of

Table 3
Geometrical parameters (Å, °) for π-stacking interactions[a].

Rings i–j	Rc[b]	R1v[c]	R2v[d]	α[e]	β[f]	γ[g]	Slippage
Complex (1)							
Cg(1)–Cg(6)	4.204(2)	–3.677(1)	–4.051(1)	13.5(2)	15.50	28.98	–
Complex (2)							
Cg(5)–Cg(13)	3.715(3)	3.393(2)	3.465(2)	7.8(3)	21.17	24.02	–
Cg(6)–Cg(16)	3.690(3)	3.395(2)	3.436(2)	4.3(3)	21.42	23.07	–
Cg(11)–Cg(11)	3.749(3)	3.398(2)	3.399(2)	0	24.98	24.98	1.583
Cg(11)–Cg(16)	3.722(4)	–3.435(2)	–3.443(2)	3.1(3)	22.30	22.62	–
Cg(12)–Cg(14)	3.826(3)	–3.412(2)	–3.467(2)	2.1(3)	25.05	26.91	–

[a] In complex (**1**), Cg(1) and Cg(6) are the centroids of (N2, C8–C12), and (N1, *C*2–C6), respectively. In complex (**2**), Cg(5), Cg(6) Cg(11), Cg(12), Cg(13), Cg(14), and Cg(16) are the centroids of (N3, C12–C16), (N4, C19–C23), (N7, C36–C40), (N8, C43–C47), (N1, C1–C5), (N2, C6–C10), and (N6, C30–C34), respectively. [b] Centroid distance between ring i and ring j. [c]Vertical distance from ring centroid i to ring j. [d] Vertical distance from ring centroid j to ring i. [e] Dihedral angle between the first ring mean plane and the second ring mean plane of the partner molecule. [f] Angle between centroids of the first and second ring mean planes. [g]Angle between the centroid of first ring and normal to the second ring mean plane of the partner molecule.

Table 4
Geometrical parameters (Å, °) for lone pair (l.p)···π interactions.

Y–X···Cg	X···Cg	X···Perp	Y–X···Cg	Symmetry
Complex (1)				
C(1)–O(2)···Cg(1)	3.265(2)	3.233	86.2(2)	x, 1–y, –1/2 + z
Complex (2)				
C(11)–O(1)···Cg(5)	3.702(5)	–3.302	80.1(3)	2–x, 1–y, 1–z
C(11)–O(1)···Cg(14)	3.521(5)	3.220	95.4(3)	3–x, 1–y, 1–z
C(24)–O(8)···Cg(6)	3.851(5)	–3.388	91.8(3)	2–x, –y, 1–z
C(24)–O(8)···Cg(15)	3.373(5)	3.327	97.5(3)	1–x, –y, 1–z
C(41)–O(12)···Cg(15)	3.239(5)	–3.107	88.0(4)	–x, –y, –z
C(48)–O(16)···Cg(13)	3.514(5)	–3.278	82.5(3)	1–x, –y, –z

In complex (**1**), Cg(1) and Cg(6) are the centroids of (N2, C8–C12), and (N1, C2–C6), respectively. In complex (**2**), Cg(5), Cg(6) Cg(11), Cg(12), Cg(13), Cg(14), Cg(15), and Cg(16) are the centroids of (N3, C12–C16), (N4, C19–C23), (N7, C36–C40), (N8, C43–C47), (N1, C1–C5), (N2, C6–C10), (N5, C25–C29), and (N6, C30–C34), respectively.

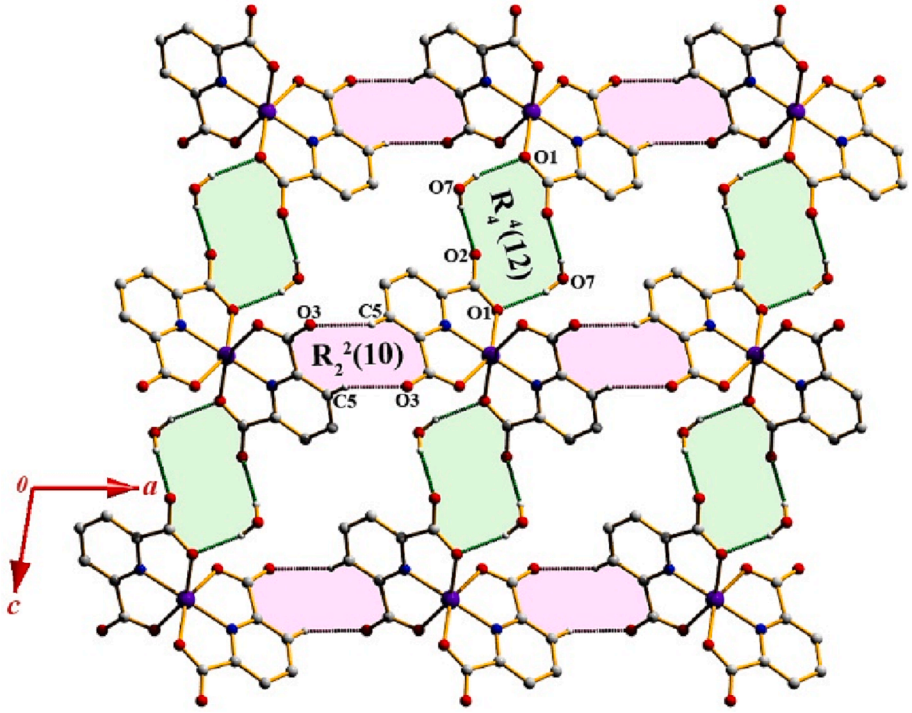

Fig. 2. $R_2^2(10)$ and $R_4^4(12)$ ring motifs generating 2D supramolecular assembly in the (1 0 1) plane.

another polymeric chain parallel to the former. Thus multiple layers of polymeric chains and acid moieties are formed involving C(14)–H(14A)···O(3) interactions forming a multi-layered braid-like chain as shown in Fig. 4a. Parallel multi-layered braid-like chains are connected through O(5)–H(5B)···O(2) interaction as shown in Fig. 4b. Combination of C(14)–H(14A)···O(3) and O(5)–H(5B)···O(2) interactions forms a three-dimensional supramolecular architecture for (**1**) (Fig. 4b).

This same 3D supramolecular architecture can also be explained by l.p.···π/ π···π interactions. The lone pair oxygen O(2) of the acid moiety interacts with the π-rings of the polymeric chain through l.p.···π interaction having lone pair and centroid separation distance of 3.265(2) Å (see Table 4). In the symmetric unit, there are two lone pairs of oxygen O(2); one O(2) interacts with the π-ring of layer-A of the polymeric chain, whereas another O(2) interacts with the π-ring of layer-B formed by another polymeric chain. Thus the layers are generated in the [1 0 0] direction. For generated layers, the π-rings of the polymeric chain interact with the π-rings of the acid moieties having a centroid to centroid distance of 4.204(2) Å (see Table 3). Thus three-dimensional supramolecular architecture associated with l.p.···π/ π···π interactions is depicted in Fig. 4c. Both hydrogen bonding interactions (O–H···O and C–H···O) and the interactions involving the pyridine rings (l.p.···π and π···π) are responsible for the stabilization of the supramolecular network of Fig. 4 (b or c) in complex (**1**).

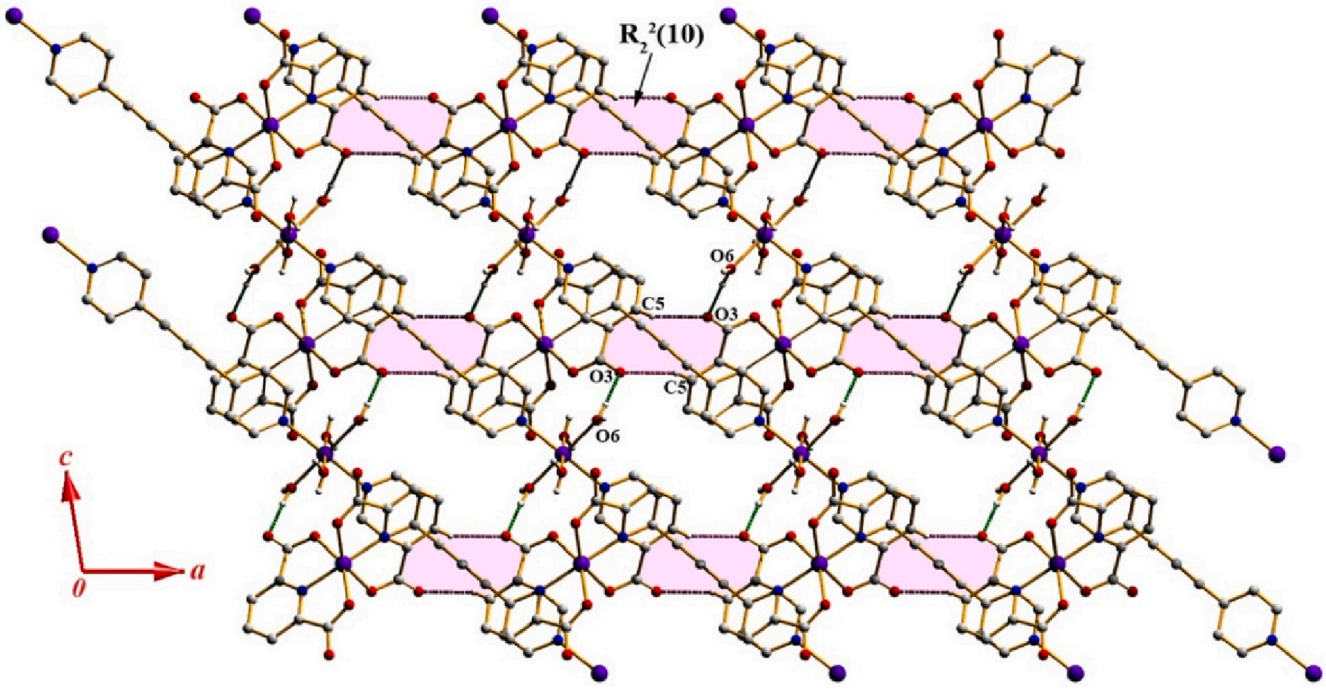

Fig. 3. Parallel cationic polymeric zigzag chains are connected to the acid moieties in the (1 0 1) plane.

3.2. Structural description of complex (2)

Complex (**2**) is crystallized in a triclinic crystal system with P–1 space group. The asymmetric unit of (**2**) consists of two discrete mononuclear cobalt (II)-dipicolinate unit $[Co(2,6\text{-}pydc)_2]^{2-}$ (moiety A and moiety B) associated with two doubly protonated 4,4′-bipyridine counter ions (moiety C and moiety D) for neutralization of charge, and eleven uncoordinated solvent water molecules. One solvent water molecule is found as disordered and the corresponding oxygen atom has the occupancy of 0.6 and 0.4 (see Fig. 5). The cationic portion of the asymmetric unit consists of doubly protonated bipyridine molecule (bipyridinium cation) and the anionic portion is the $[Co(2,6\text{-}pydc)_2]^{2-}$ complex. Each Co^{II} atom is coordinated by four oxygen atoms and two nitrogen atoms from two dipicolinate ligands in a tridentate fashion and are at the centre of distorted octahedral environment formed by the CoO_4N_2 bonding set. In anionic moiety A, the angles O(2)–Co(2)–O(6) [89.97 (15)°], O(3)–Co(2)–O(7) [87.33(15)°] and N(3)–Co(2)–N(4) [171.88 (15)°] indicate that the coordination environment around Co(II) ion is a distorted octahedron. As expected, the Co–O distances are longer than Co-N distances in both moieties of A and B (see Table S1). Indeed, in anionic fragment two rigid $(2,6\text{-}pydc)^{2-}$ are almost perpendicular to each other having dihedral angles of 83.39° and 85.45° in moieties A and B respectively.

In the solid state, the supramolecular structure of the complex (**2**) is stabilized through hydrogen bonding interactions (such as N–H···O, O–H···O, and C–H···O) and the interactions involving pyridine rings (such as π···π, π···π^+, π^+···π, lone pair···π). In the first substructure of complex (**2**), the oxygen atom O(8) is oriented towards the π-face of ring-P with a distance of 3.851 Å, suggesting l.p···π interaction. Due to its self-complementary nature, this ring-P is further juxtaposed to ring-R through π···π^+ interaction having a ring centroid separation of 3.690 Å. Further, the ring-R is connected to ring-S through π^+···π interaction with the centroid to the centroid separation distance of 3.722 Å. Again, ring-S is juxtaposed to ring-S of partner molecule due to its self-complementary nature, and exhibits π···π stacking interaction having a ring centroid separation of 3.749 Å and ring offset of 1.583 Å. The combination of l.p···π and different π-interactions constitutes a network chain, l.p···π/π···π^+/π^+···π/π···π. The sequence of these interactions is reversed from π···π stacking interaction, thus forming a rare combination of an extended 1D network $(l.p\cdots\pi/\pi\cdots\pi^+/\pi^+\cdots\pi/\pi\cdots\pi/\pi\cdots\pi^+/\pi^+\cdots\pi/\pi\cdots l.p)_n$. The parallel 1D extended networks are connected through a combination of lone pair···π and C–H···O interactions where the oxygen atom O (1) orients towards ring-O, suggesting l.p···π interaction having a ring to the lone-pair separation distance of 3.702 Å. The carbon atoms C(15) and C(44) act as a donor to the carbonyl oxygen O(13) and O(4), hence forming $R_2^2(10)$ dimeric ring (Fig. 6).

In another substructure of complex (**2**), again the oxygen atoms O(1) and O(8) of the acid moiety-A orient towards the π-face of the ring-O and ring-P of partner molecules, having oxygen and ring centroid separation distance 3.702 Å and 3.851 Å respectively, suggesting l.p···π interactions, forming 1D chain of acid moiety-A which propagates along [0 1 0] direction. Two parallel 1D chains of acid moiety-A are connected through C(20)–H(20)···O(12) interaction and π···π stacking interaction (above mentioned), which leads to the formation of another two-dimensional supramolecular structure in (0 1 1) plane for complex (**2**) depicted in Fig. 7.

We have explored unique supramolecular self-assembly for complex (**2**), where 3D boxes are assembled in a 2D plane. In this complex (**2**) substructure, above mentioned $R_2^2(10)$ dimeric ring is formed between moiety-A and B. Now the moiety-B's carbonyl oxygen O(9) interacts with the moiety-D's nitrogen atom N(6). Then the carbon atom C(34) of the moiety-D acts as a donor to the solvent water oxygen O(25). Again O

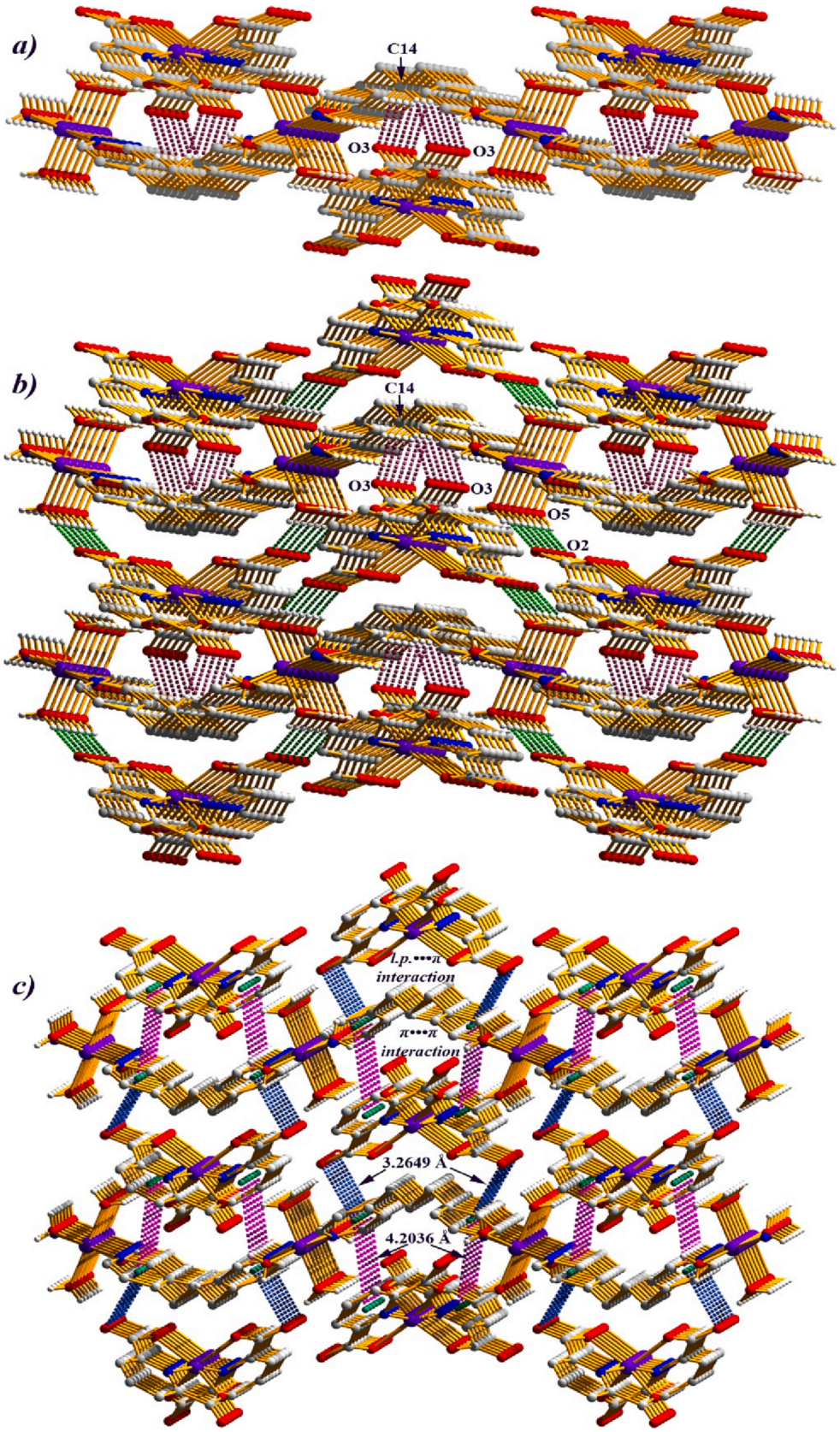

Fig. 4. (a) Multi-layered braid-like chain formed through C–H···O hydrogen bonding interactions; (b) Parallel multi-layered braid-like chains connected by using O–H···O hydrogen bonding interactions leads to three-dimensional supramolecular self-assembly in (**1**); (c) Same three-dimensional supramolecular self-assembly generated through l.p.···π/ π···π interactions.

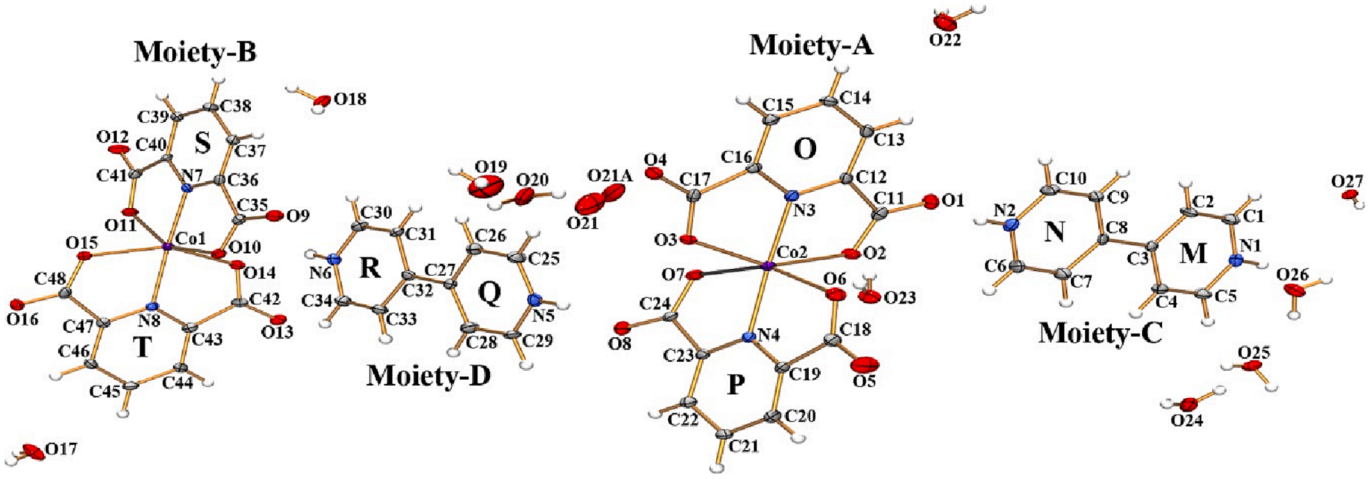

Fig. 5. An ORTEP view of complex (**2**) with the atom-numbering scheme. Thermal ellipsoids are drawn at 30% probability.

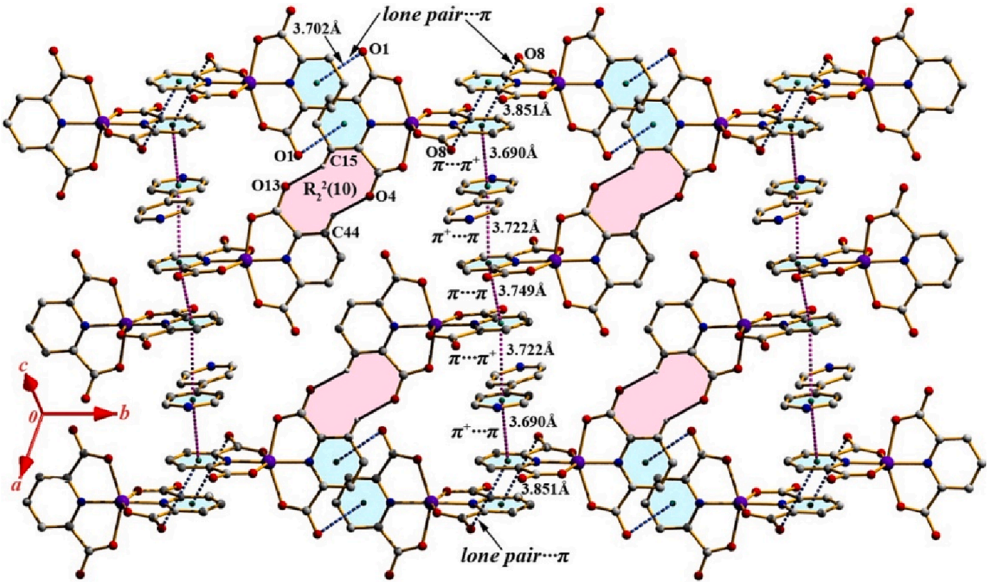

Fig. 6. Two-dimensional supramolecular self-assembly of complex (**2**) generated with a rare combination of the extended (lone pair···π/π···π^+/π^+···π/π···π/π···π^+/π^+···π/π···lone pair)$_n$ network.

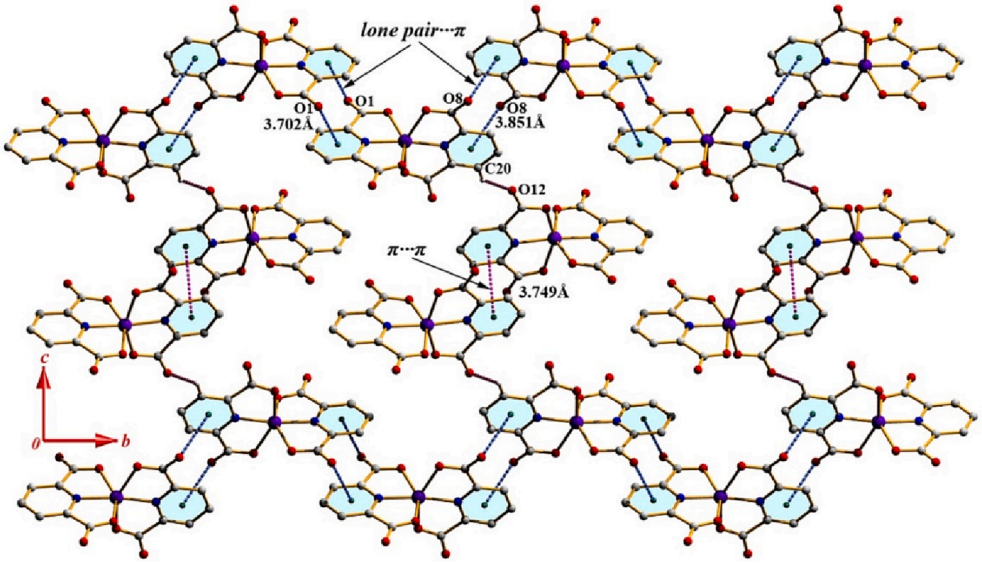

Fig. 7. Two-dimensional supramolecular structure in (0 1 1) plane for complex (**2**).

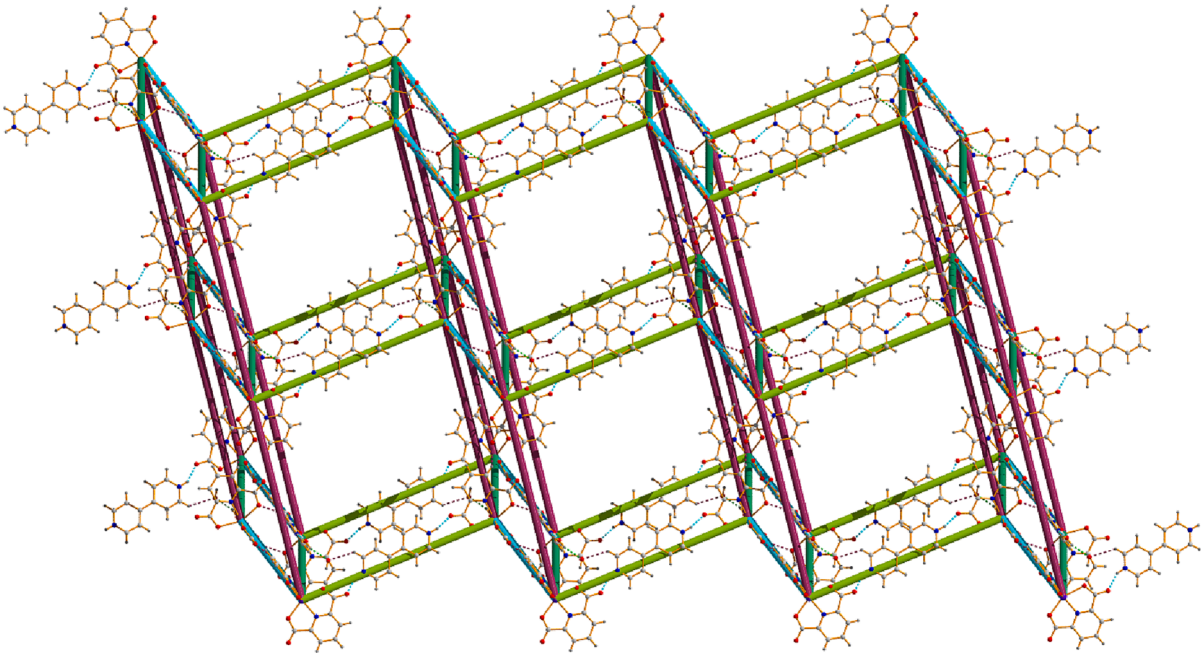

Fig. 8. 3D boxes are propagating in the 2D plane for complex (**2**).

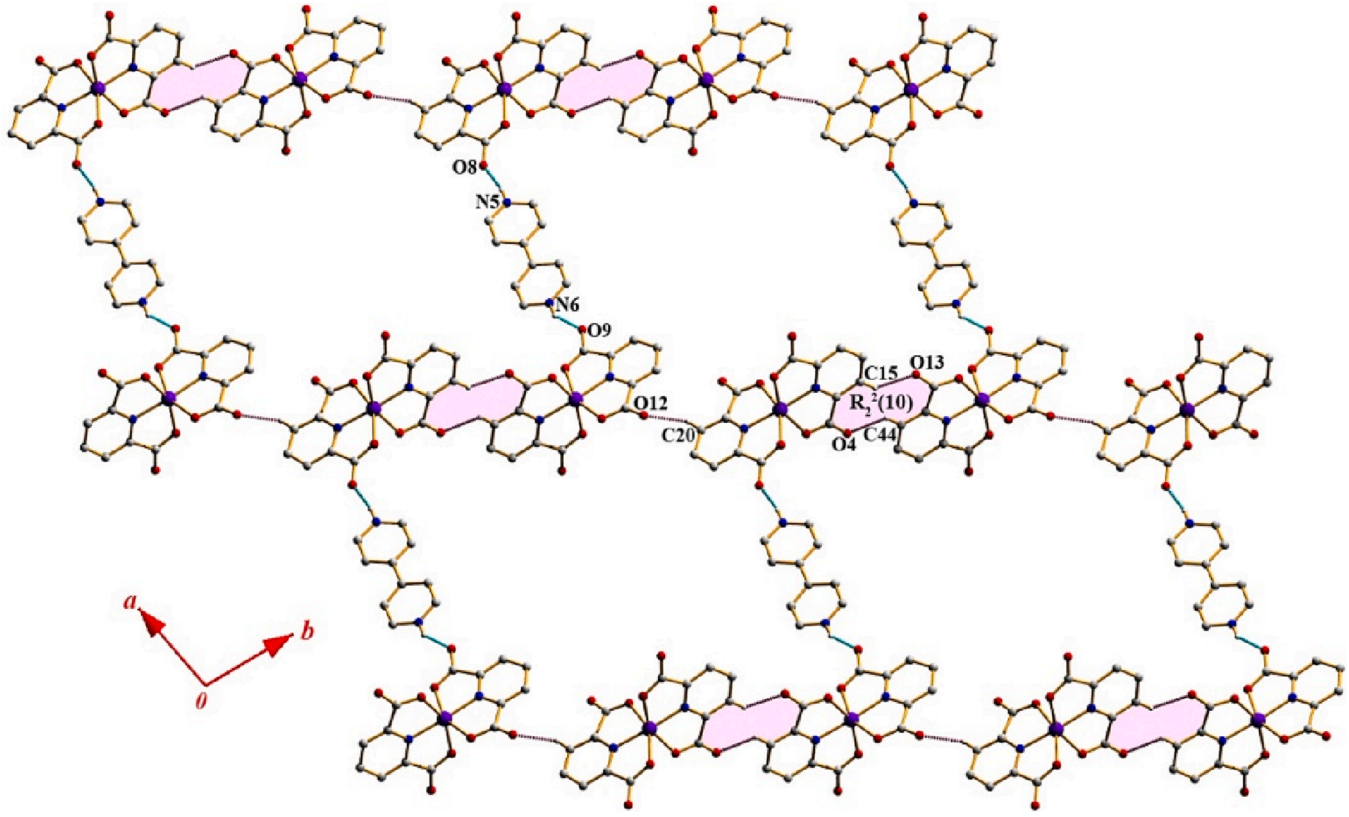

Fig. 9. Two-dimensional supramolecular self-assembly for complex (**2**) generated through Hydrogen bonding interactions in (1 1 0) plane.

(25) interacts with another solvent, water oxygen O(26), and the nitrogen N(1) of the moiety-C acts as a donor to O(26). Another pyridine nitrogen N(2) of moiety-C acts as a donor to the carbonyl oxygen O(1) of moiety-A. Again a $R_2^2(10)$ dimeric ring is formed, and the repetition of mentioned interactions generate a loop-like structure (Fig. S3). The bipyridine moiety-D connects two loops through N(5)–H(5)···O(8) interaction, forming 2D box-like structure (Fig. S4). Further these 2D boxes are connected through C(20)–H(20)···O(12) interaction to generate 3D box-like structure (Fig. S5). Hence a sequential combination of these interactions helps to assemble 3D boxes propagating in the 2D plane for complex (**2**) (Fig. 8).

In another substructure of complex (**2**), the carbonyl oxygen O(12) of the acid moiety B interacts with the carbon atom C(20) through hydrogen bonding interaction, and again above mentioned $R_2^2(10)$ dimeric ring is formed. A combination of these interactions leads to the 1D chain of acid moieties. Two parallel chains of acid moiety are connected with the help of bi-pyridine moiety-D as the nitrogen atoms N(5) and N(6) of the bipyridine moiety-D act as a donor to the carbonyl oxygen O(8) of the acid moiety-A and O(9) of the acid moiety-B respectively, and generates the two-dimensional supramolecular structure of the complex (**2**) in (1 1 0) plane as shown in Fig. 9.

3.3. Theoretical calculations

Bader's quantum theory of "Atoms in Molecules" (QTAIM) characterizes the noncovalent interactions involved in building supramolecular architectures. The models used herein are derived from the supramolecular assemblies. The topological parameters' values determine the nature of the interactions. The QTAIM models for complex (**1**) are depicted in Fig. 10 (a, b, and c). A part of the self-assembled structure of Fig. 4 (b or c) is used as a theoretical model to characterize both hydrogen bonding interactions and the interactions involving the pyridine rings in complex (**1**) which is depicted in Fig. 10a. As expected, the calculated dissociation energy for O(5)–H(5B)···O(2) interaction (d, ρ_{BCP} = 0.0279 a.u) is maximum whereas, for the π···π interaction (a, ρ_{BCP} = 0.0027 a.u), it is minimum. From Table 5 it can be seen that lone pair···π interaction (c, ρ_{BCP} = 0.0049 a.u) is more favourable among the interactions involving the pyridine rings in complex (**1**), which is in agreement with X-ray structural studies. We have used a part of the self-assembled structure of Fig. 3 as a theoretical model to characterize O–H···O hydrogen bonding interaction in complex (**1**) which is depicted in Fig. 10b. This O(6)–H(6A)···O(3) hydrogen bonding interaction (e, ρ_{BCP} = 0.0336 a.u) has the highest dissociation energy among the noncovalent interactions involving in complex (**1**) (see Table 5). We have used a part of the self-assembled structure of centrosymmetric dimeric and tetrameric ring from Fig. 2 as a theoretical model to characterize both C–H···O and O–H···O hydrogen bonding interactions in complex (**1**), which is shown in Fig. 10c. It can be seen from Table 5 that O(7)–H(7A)···O(1) interaction (f, f', ρ_{BCP} = 0.0247 a.u) is more favourable than O(7)–H(7B)···O(2) interaction (g, g', ρ_{BCP} = 0.0154 a.u) for the construction of centrosymmetric tetrameric ring (Fig. 10c). The C(5)–H(5)···O(3) interaction (h, h', ρ_{BCP} = 0.0122 a.u) which is responsible for the generation of centrosymmetric dimeric ring, is less favourable than O–H···O hydrogen bonding interactions, which is in agreement with X-

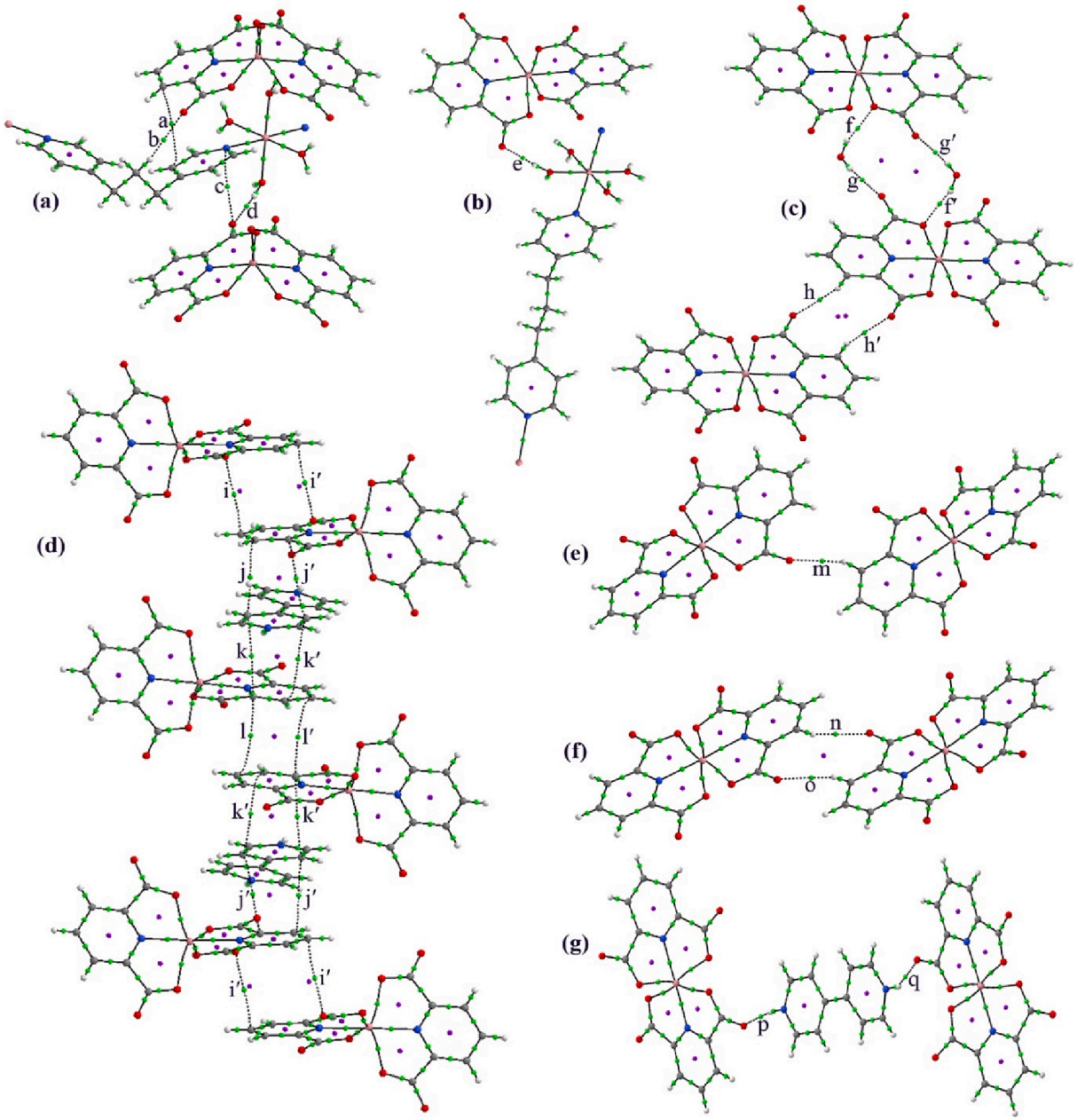

Fig. 10. QTAIM analyses of (**1**) (a, b, and c) and (**2**) (d, e, f and g). Green and violet spheres are bond critical points (BCPs) and ring critical points (RCPs), respectively.

Table 5
Detailed QTAIM topological parameters at BCPs.

Interaction	ρ_{BCP}(a.u)	$\nabla^2\rho_{BCP}$(a.u)	V_{BCP} (a.u)	$D.E_{int}$(kcal/mol)
Complex (1)				
(a) π···π	0.0027	0.0079	–0.0012	0.376
(b) C(14)–H(14A)···O(3)	0.0085	0.0321	–0.0057	1.788
(c) lone pair···π	0.0049	0.0182	–0.0033	1.035
(d) O(5)–H(5B)···O(2)	0.0279	0.1056	–0.0259	8.126
(e) O(6)–H(6A)···O(3)	0.0336	0.1231	–0.0316	9.915
(f, f') O(7)–H(7A)···O(1)	0.0247	0.0937	–0.0235	7.373
(g, g') O(7)–H(7B)···O(2)	0.0154	0.0574	–0.0134	4.204
(h, h') C(5)–H(5)···O(3)	0.0122	0.0456	–0.0091	2.855
Complex (2)				
(i, i') lone pair···π	0.0045	0.0152	–0.0023	0.722
(j, j') π···π^+	0.0044	0.0132	–0.0021	0.659
(k, k') π^+···π	0.0047	0.0127	–0.0020	0.628
(l, l') π···π	0.0052	0.0152	–0.0024	0.753
(m) C(20)–H(20)···O(12)	0.0135	0.0525	–0.0028	3.294
(n) C(15)–H(15)···O(13)	0.0114	0.0420	–0.0083	2.604
(o) C(44)–H(44)···O(4)	0.0114	0.0431	–0.0083	2.604
(p) N(5)–H(5)···O(8)	0.0399	0.1623	–0.0379	11.891
(q) N(6)–H(5)···O(9)	0.0350	0.1401	–0.0327	10.259

ray structural studies. For complex (**2**), the QTAIM models are depicted in Fig. 10(d–g). To characterize the extended (lone-pair···π/π···π^+/π^+···π/π···π/π···π^+/π^+···π/π···lone-pair)$_n$ network in complex (**2**) we have used a part of the self-assembled structure from Fig. 6 as a theoretical model, which is depicted in Fig. 10d. In this extended network model, the bond critical points and bond paths interconnecting the lone pair oxygen and the carbon atom of the pyridine ring represent and characterizes lone pair···π interactions (i, i', ρ_{BCP} = 0.0045 a.u). Again, the bond critical points and bond paths denoted by (j, j') and (k, k') represents and characterizes π···π^+ interactions (ρ_{BCP} = 0.0044 a.u) and π^+···π interactions (ρ_{BCP} = 0.0047 a.u) respectively. In the middle portion of this model, the bond paths interconnecting the carbon atoms of the pyridine rings of acid moieties represent and characterizes π···π interactions (l, l', ρ_{BCP} = 0.0052 a.u). For complex (**2**), among the interactions involving aryl ring π···π staking interaction (l, l') is more favourable due to higher ρ_{BCP} value (ρ_{BCP} = 0.0052 a.u) and hence higher dissociation energy (Table 5). Parts of the self-assembled structure of Fig. 9 are used as theoretical models to characterize both C–H···O and N–H···O hydrogen bonding interactions in complex (**2**), which are depicted in Fig. 10(e–g). For complex (**2**), C–H···O hydrogen bonding interactions are designated by m, n, and o, and, C(20)–H(20)···O(12) (m) interaction (ρ_{BCP} = 0.0135 a.u) is more favourable among C–H···O interactions. The ρ_{BCP} value for N(5)–H(5)···O(8) (p) and N(6)–H(5)···O(9) is 0.0399 a.u and 0.0350 a.u respectively, indicating the former one is more favourable N–H···O hydrogen bonding interaction for complex (**2**).

Thus, by analyzing the topological parameters at (3, –1) BCPs of the noncovalent interactions, it is evident that N–H···O hydrogen bonding interactions are stronger as compared to O–H···O than C–H···O than the interactions involving aryl rings (Table 5), which also agree with the X-ray crystallographic study (Tables 2–4). Further, $\nabla^2(\rho_{BCP})$ is positive for all the interactions, which indicates that all the interactions are closed-shell type [45,46].

Further, the noncovalent interactions that are involved in forming supramolecular frameworks are analyzed through NCI Plot Index. NCI Plot generally exhibits blue-green isosurfaces for indicating noncovalent interactions. Blue isosurfaces indicate strong noncovalent interactions, whereas green isosurfaces indicate comparatively weak noncovalent interactions. We have used the same theoretical models for NCI Plot Index. For complex (**1**), weak π···π and lone pair···π interactions are indicated by flat green isosurfaces (Fig. 11a), C–H···O interactions are indicated by small green isosurfaces (Fig. 11 a, c), and O–H···O interactions are indicated by both green and blue isosurfaces, as O–H···O interactions are comparatively strong hydrogen bond interaction (Fig. 11a, b and c). For complex (**2**), noncovalent interactions involving aryl rings are indicated by flat green isosurfaces (Fig. 11d). As expected, small green isosurfaces indicate C–H···O interactions (Fig. 11 e, f). Strong N–H···O interactions are indicated by small blue isosurfaces (Fig. 11g).

In RDG (Reduced Density Gradient) vs sign (λ_2)ρ scatter plots (where λ_2 is the second eigenvalue of third-ordered Hessian's matrix), the blue and green downward spikes indicate strong and weak noncovalent interactions, respectively (Fig. 12). We have used the same models also for scatter plots (models a, b, and c for (**1**) whereas d, e, f, and g for (**2**)). For example, in Fig. 12a, the greenish blue spike indicates O–H···O hydrogen bonding interactions, while other green spikes are because of C–H···O and the weak aryl ring interactions. In Fig. 12b and g, the deep blue spikes indicate strong hydrogen bonding interactions (N–H···O and O–H···O). Other green spikes indicate lone pair···π, π···π^+, π^+···π, π···π etc. interactions (Fig. 12). The isosurfaces in NCI plots and the spikes in RDG scatter plots agree with X-ray structural studies and QTAIM Studies.

3.4. Optical characterization

The optical properties of our synthesized complexes were determined by UV − Vis spectroscopy. We prepared 10 ml of 10^{-4}(M) solution for each complex by dissolving both complexes separately in N,*N*-dimethylformamide (purity 99.8%). From optical absorption spectra, the optical band gap can be calculated by famous Tauc's equation:

$$(\alpha h\nu) = A\left(h\nu - E_g\right)^n \quad (1)$$

where α is the absorption coefficient, h is Planck's constant, ν is the frequency of incident radiation, E_g is band gap energy, A is an arbitrary constant and is considered as 1 for the ideal case (depends on temperature, photo energy, and phonon energy). Here for the allowed direct band gap, n = 1/2, and the allowed indirect band gap, n = 2.

Tauc's equation (1) shows that when α becomes zero, the band gap energy is hν. Allowed direct band gap can be obtained from $(\alpha h\nu)^2$ vs energy graph, and for complex (**1**) and (**2**) calculated allowed direct band gap energy is 4.46 eV and 4.33 eV, respectively (Fig. 13(a and b)). Allowed indirect band gap can be obtained from $(\alpha h\nu)^{1/2}$ vs. energy

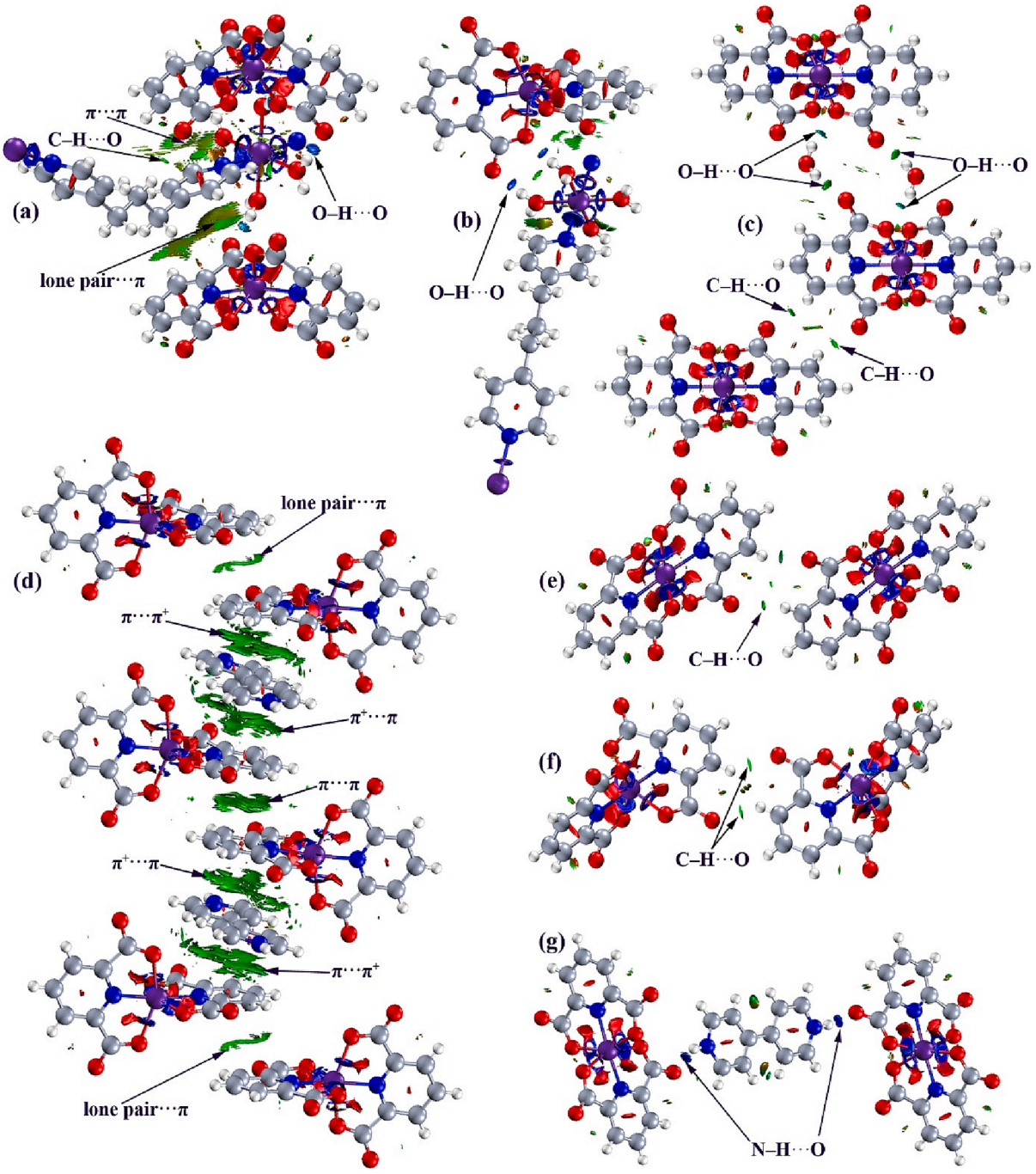

Fig. 11. NCI plot index of the modeled structure of (**1**) (a, b, and c) and (**2**) (d, e, f and g).

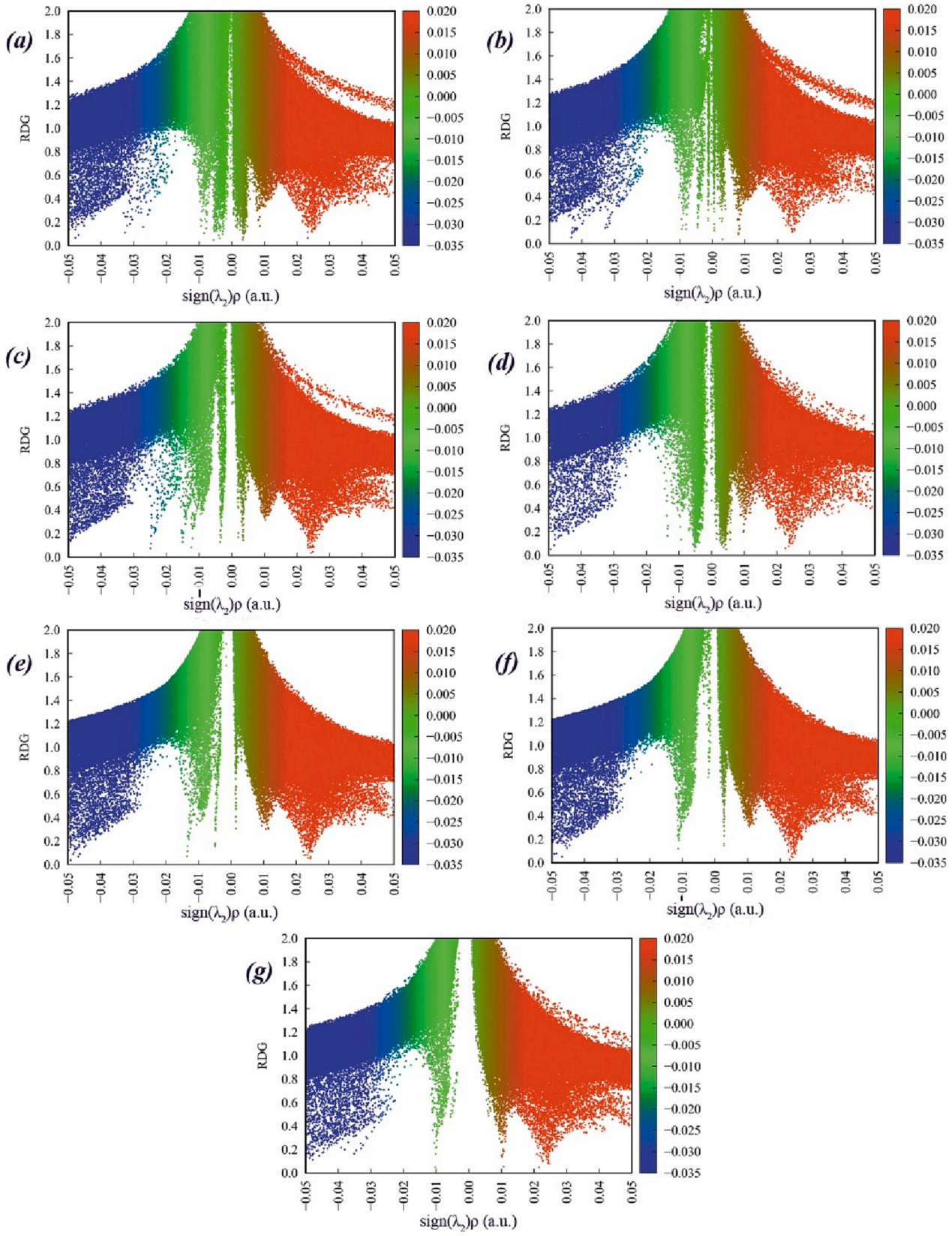

Fig. 12. RDG vs sign $(\lambda_2)\rho$ scatter plots of (**1**) (a, b and c) and (**2**) (d, e, f and g).

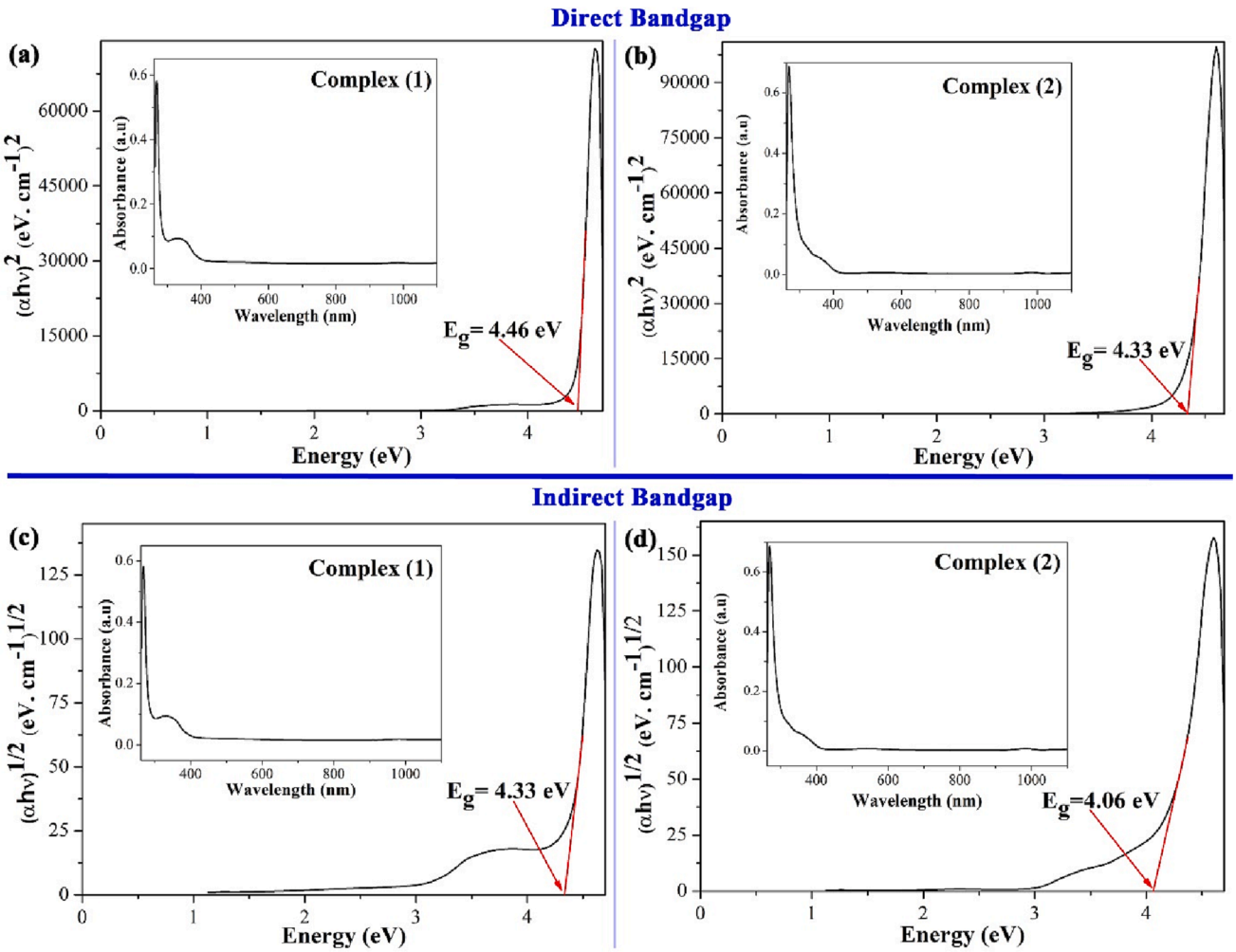

Fig. 13. Tauc's plots to estimate the band gap of the title complexes. (a) Direct band gap of **1**; (b) Direct band gap of **2**; (c) Indirect band gap of **1**; (d) Indirect band gap of **2**.

graph, and for complex (**1**) and (**2**), calculated allowed indirect band gap energy is 4.33 eV and 4.06 eV, respectively (Fig. 13(c and d)). Therefore, it is expected from the results that complex (**2**) shows better semiconducting behavior than complex (**1**), and their band gaps are within the range of wide band gap semiconductors [47].

4. Conclusions

The crystal structures of two new Co(II)-PDA complexes (**1**–**2**) have been determined by solving the structures from single crystal X-ray diffraction data. We have explored a three-dimensional network for (**1**) constructed by weak lone pair···π/π···π interactions. In the case of complex (**2**), we have explored a rare extended (lone pair···π/π···π^+/π^+···π/π···π/π···π^+/π^+···π/π···lone pair)$_n$ self-assembled network. Bader's quantum theory of atoms in molecules (QTAIM) further characterizes noncovalent interactions from single-crystal X-ray diffraction data. Topological analysis of QTAIM revealed that all the interactions involved in constructing self-assembled networks are closed-shell interactions. Furthermore, the theoretical NCI plot index and scatter plots characterize noncovalent interactions. All the theoretical results agree well with the experimental findings. The results reported herein might help in understanding the supramolecular aggregation in accordance with hydrogen bonds, lone pair···π, π···π, π···π^+, π^+···π, etc. Optical characterization of the compounds revealed that their band gaps are within the range of wide band gap semiconductors. Electrical properties need to be studied to establish the structure–property relationship.

Declaration of Competing Interest

The authors declare that they have no known competing financial interests or personal relationships that could have appeared to influence the work reported in this paper.

Data availability

Data will be made available on request.

Acknowledgments

S. Islam thankfully acknowledges the University Grants Commission (Ref. No.: 1528/CSIR-UGC NET JUNE 2019) for a Senior Research Fellowship. Pratik Dey is greatly thankful to the Council of Scientific and Industrial Research (CSIR), New Delhi (CSIR FILE NO.: 09/0096 (11350)/2021-EMR-I) for providing Junior Research Fellowship. S. K. Seth gratefully acknowledges the financial support from SERB (New Delhi) India, for Research Project (EEQ/2019/000384). Authors are grateful to Single Crystal X-ray Diffraction facility at the Department of Chemistry, Jadavpur University, Kolkata, India for data collection.

Appendix A. Supplementary data

CCDC 2238424–2238425 contains the supplementary crystallographic data for complexes (**1**–**2**). Figure S1 includes PXRD patterns of

both complexes. Figures S2 and S3 include the FTIR spectrum of complex (**1**) and (**2**), respectively. Table S1 includes some selected bond lengths and angles around the metal ions of both structures. Figure S4 and S5 depicts hydrogen bonding networks for complex (**2**). Supplementary data to this article can be found online at https://doi.org/10.1016/j.poly.2023.116514.

References:

[1] X.Y. Li, Q.P. Kang, L.Z. Liu, J.C. Ma, W.K. Dong, Trinuclear Co (II) and mononuclear Ni (II) Salamo-type bisoxime coordination compounds, Crystals 8 (2018) 43.

[2] L.P. Tang, L.M. Tang, D. Wang, H.X. Deng, K.Q. Chen, Metal and ligand effects on the stability and electronic properties of crystalline two-dimensional metal-benzenehexathiolate coordination compounds, J. Phys. Condens. Matter. 30 (2018), 465301.

[3] J. Gu, M. Wen, Y. Cai, Z. Shi, D.S. Nesterov, M.V. Kirillova, A.M. Kirillov, Cobalt (II) coordination polymers assembled from unexplored pyridine-carboxylic acids: structural diversity and catalytic oxidation of alcohols, Inorg. Chem. 58 (2019) 5875–5885.

[4] L.H. Abdel-Rahman, A.A. Abdelhamid, A.M. Abu-Dief, M.R. Shehata, M.A. Bakheet, Facile synthesis, X-Ray structure of new multi-substituted aryl imidazole ligand, biological screening and DNA binding of its Cr (III), Fe (III) and Cu (II) coordination compounds as potential antibiotic and anticancer drugs, J. Mol. Struct. 1200 (2020), 127034.

[5] T.R. Cook, Y.R. Zheng, P.J. Stang, Metal–organic frameworks and self-assembled supramolecular coordination complexes: comparing and contrasting the design, synthesis, and functionality of metal–organic materials, Chem. Rev. 113 (2013) 734–777.

[6] S. Tripathi, A. Hossain, S.K. Seth, S. Mukhopadhyay, Quantitative insights into the crystal structure of a mixed-ligand Co (III) complex: experimental and theoretical studies, J. Mol. Struct. 1216 (2020) 128207.

[7] S.K. Seth, Tuning the formation of MOFs by pH influence: X-ray structural variations and Hirshfeld surface analyses of 2-amino-5-nitropyridine with cadmium chloride, CrystEngComm 15 (2013) 1772–1781.

[8] F. Yuan, J. Xie, H.M. Hu, C.M. Yuan, B. Xu, M.L. Yang, F.X. Dong, G.L. Xue, Effect of pH/metal ion on the structure of metal–organic frameworks based on novel bifunctionalized ligand 4′-carboxy-4, 2′: 6′, 4″-terpyridine, CrystEngComm 15 (2013) 1460–1467.

[9] S. Islam, S. Tripathi, A. Hossain, S.K. Seth, S. Mukhopadhyay, pH-induced structural variations of two new Mg (II)-PDA complexes: experimental and theoretical studies, J. Mol. Struct. 1265 (2022) 133373.

[10] H.R. Khavasi, B. Mohammad Sadegh, Temperature-dependent supramolecular motif in coordination compounds, Inorg. Chem. 49 (2010) 5356–5358.

[11] C. Yenikaya, M. Poyraz, M. Sarı, F. Demirci, H. İlkimen, O. Büyükgüngör, Synthesis, characterization and biological evaluation of a novel Cu (II) complex with the mixed ligands 2, 6-pyridinedicarboxylic acid and 2-aminopyridine, Polyhedron 28 (2009) 3526–3532.

[12] L. Wang, M. Yang, G. Li, Z. Shi, S. Feng, Hydrothermal synthesis and characterization of a new three-dimensional hybrid zinc phosphate $[Zn_2(HPO_4)2(4, 4'\text{-bipy})]\cdot 3H_2O$ with neutral porous framework, J. Solid State Chem. 179 (1) (2006) 156–160.

[13] L. Hu, J. Fan, C. Slebodnick, B.E. Hanson, Structural diversity in 4, 4 '-trimethylenedipyridine− zinc phosphite hybrids: incorporation of neutral guest molecules in hybrid materials, Inorg. Chem. 45 (2006) 7681–7688.

[14] F.A. Almeida Paz, J. Klinowski, Two-and Three-dimensional cadmium− organic frameworks with trimesic acid and 4, 4 '-trimethylenedipyridine, Inorg. Chem. 43 (13) (2004) 3882–3893.

[15] D. Kong, J. Zoñ, J. McBee, A. Clearfield, Rational design and synthesis of porous organic− inorganic hybrid frameworks constructed by 1, 3, 5-benzenetriphosphonic acid and pyridine synthons, Inorg. Chem. 45 (3) (2006) 977–986.

[16] G.R. Desiraju, Crystal engineering: from molecule to crystal, J. Am. Chem. Soc. 135 (2013) 9952–9967.

[17] S.K. Seth, D. Sarkar, T. Kar, Use of π–π forces to steer the assembly of chromone derivatives into hydrogen bonded supramolecular layers: crystal structures and Hirshfeld surface analyses, CrystEngComm 13 (2011) 4528–4535.

[18] A. Hossain, A. Dey, S.K. Seth, P.P. Ray, J. Ortega-Castro, A. Frontera, S. Mukhopadhyay, Anion-dependent structural variations and charge transport property analysis of 4′-(3-pyridyl)-4, 2′: 6′, 4″-terpyridinium salts, CrystEngComm 23 (2021) 3569–3581.

[19] S. Ghosh, S. Islam, S. Pramanik, S.K. Seth, Structural elucidation of phenoxybenzaldehyde derivatives from laboratory powder X-ray diffraction: A combined experimental and theoretical quantum mechanical study, J. Mol. Struct. 1268 (2022), 133697.

[20] S.K. Seth, I. Saha, C. Estarellas, A. Frontera, T. Kar, S. Mukhopadhyay, Supramolecular self-assembly of M-IDA complexes involving lone-pair··· π interactions: crystal structures, hirshfeld surface analysis, and DFT calculations [H_2IDA= iminodiacetic acid, M= Cu (II), Ni (II)], Cryst. Growth Des. 11 (2011) 3250–3265.

[21] S.K. Seth, The importance of CH···X (X= O, Π) interaction of a new mixed ligand Cu (II) coordination polymer: structure, hirshfeld surface and theoretical studies, Crystals 8 (2018) 455.

[22] P. Das, S. Islam, D. Das, P.P. Ray, S.K. Seth, Intriguing π-interactions involving aromatic neutrals, aromatic cations and semiconducting behavior in a pyridinium-carboxylate salt, J. Mol. Struct. 1284 (2023), 135326.

[23] A. Bauzá, S.K. Seth, A. Frontera, Molecular electrostatic potential and "atoms-in-molecules" analyses of the interplay between π-hole and lone pair··· π/X–H··· π/metal··· π interactions, J. Comput. Chem. 39 (2018) 458–463.

[24] S. Tripathi, S. Islam, S.K. Seth, A. Bauzá, A. Frontera, S. Mukhopadhyay, Supramolecular assemblies involving salt bridges: DFT and X-ray evidence of bipolarity, CrystEngComm 22 (2020) 8171–8181.

[25] S. Islam, P. Das, S. Tripathi, S. Mukhopadhyay, S.K. Seth, Exploring solid-state supramolecular architectures of penta (carboxymethyl) diethylenetriamine: experimental observation and theoretical studies, ChemistrySelect 7 (2022) e202203396.

[26] R.F.W. Bader, A quantum theory of molecular structure and its applications, Chem. Rev. 91 (5) (1991) 893–928.

[27] R.F.W. Bader, Atoms in Molecules, a Quantum Theory, Oxford University Press, New York, NY, USA, 1990.

[28] J. Contreras-García, E.R. Johnson, S. Keinan, R. Chaudret, J.P. Piquemal, D. N. Beratan, W. Yang, NCIPLOT: a program for plotting noncovalent interaction regions, J. Chem. Theory Comput. 7 (2011) 625–632.

[29] E.R. Johnson, S. Keinan, P. Mori-Sánchez, J. Contreras-García, A.J. Cohen, W. Yang, Revealing noncovalent interactions, J. Am. Chem. Soc. 132 (18) (2010) 6498–6506.

[30] J. Tauc, R. Grigorovici, A. Vancu, Optical properties and electronic structure of amorphous germanium, Phys. Status Solidi B 15 (2) (1966) 627–637.

[31] BrukerSAINT, Version 6.36a, Bruker AXS Inc, Madison, Wisconsin, USA, 2002.

[32] BrukerSMART, Version 5.625 and SADABS, Version 2.03a, Bruker AXS Inc, Madison, Wisconsin, USA, 2001.

[33] G.M. Sheldrick, SHELXT–Integrated space-group and crystal-structure determination, Acta Crystallogr. A 71 (2015) 3–8.

[34] G.M. Sheldrick, Crystal structure refinement with SHELXL, Acta Cryst. C 71 (2015) 3–8.

[35] L.J. Farrugia, WinGX and ORTEP for Windows: an update, J. Appl. Cryst. 45 (4) (2012) 849–854.

[36] O.V. Dolomanov, L.J. Bourhis, R.J. Gildea, J.A. Howard, H. Puschmann, OLEX2: a complete structure solution, refinement and analysis program, J. Appl. Crystallogr. 42 (2009) 339–341.

[37] A.L. Spek, Single-crystal structure validation with the program PLATON, J. Appl. Crystallogr. 36 (1) (2003) 7–13.

[38] M.J. Frisch, G.W. Trucks, H.B. Schlegel, G.E. Scuseria, M.A. Robb, J.R. Cheese-man, G. Scalmani, V. Barone, G.A. Petersson, H. Nakatsuji, X. Li, M. Caricato, A.V. Marenich, J. Bloino, B.G. Janesko, R. Gomperts, B. Mennucci, H.P. Hratchian, J.V. Ortiz, A.F. Izmaylov, J.L. Sonnenberg, D. Williams-Young, F. Ding, F. Lip-parini, F. Egidi, J. Goings, B. Peng, A. Petrone, T. Henderson, D. Ranasinghe, V.G. Zakrzewski, J. Gao, N. Rega, G. Zheng, W. Liang, M. Hada, M. Ehara, K. Toyota, R. Fukuda, J. Hasegawa, M. Ishida, T. Nakajima, Y. Honda, O. Kitao, H. Nakai, T. Vreven, K. Throssell, J.A. Montgomery Jr., J.E. Peralta, F. Ogliaro, M.J. Bearpark, J.J. Heyd, E.N. Brothers, K.N. Kudin, V.N. Staroverov, T.A. Keith, R. Kobayashi, J. Normand, K. Raghavachari, A.P. Rendell, J.C. Burant, S.S. Iyengar, J. Tomasi, M. Cossi, J.M. Millam, M. Klene, C. Adamo, R. Cammi, J.W. Ochterski, R.L. Martin, K. Morokuma, O. Farkas, J.B. Foresman, D.J. Fox, Gaussian 16, Revi-sion C.01, Gaussian, Inc., Wallingford, CT, 2016.

[39] T.A. Keith. AIMAll, Version 13.05.06, TK Gristmill Software, Overland Park, KS, USA, 2013.

[40] R. Hilal, S.G. Aziz, A.O. Alyoubi, S. Elroby, Quantum topology of the charge density of chemical bonds. QTAIM analysis of the C-Br and O-Br bonds, Procedia Comput. Sci. 51 (2015) 1872–1877.

[41] A. Hocquet, Intramolecular hydrogen bonding in 2′-deoxyribonucleosides: an AIM topological study of the electronic density, Phys. Chem. Chem. Phys. 3 (2001) 3192–3199.

[42] C. Lepetit, M.L. Kahn, QTAIM and ELF topological analyses of zinc-amido complexes, Res. Chem. Intermed. 47 (1) (2021) 377–395.

[43] T. Lu, F. Chen, Multiwfn: a multifunctional wavefunction analyser, J. Comput. Chem. 33 (2012) 580–592.

[44] W. Humphrey, A. Dalke, K. Schulten, VMD: visual molecular dynamics, J. Mol. Graph. 14 (1996) 33–38.

[45] C. Gatti, Chemical bonding in crystals: new directions, Z. Kristallogr. Cryst. Mater. 220 (2005) 399–457.

[46] P. Dhanishta, S.K. Mishra, N. Suryaprakash, Intramolecular HB interactions evidenced in dibenzoyl oxalamide derivatives: NMR, QTAIM, and NCI Studies, J. Phys. Chem. A 122 (1) (2018) 199–208.

[47] J.H. Edgar, Prospects for device implementation of wide band gap semiconductors, J. Mater. Res. 7 (1) (1992) 235–252.

Supplementary Information

A combined experimental and theoretical studies of two new Co(II)–PDA complexes: unusual 2D and 3D supramolecular networks [PDA = 2,6-pyridinedicarboxylic acid]

Samiul Islam, Pratik Dey, Saikat Kumar Seth*

Department of Physics, Jadavpur University, Kolkata 700032, India

Corresponding author(s) E-mail: saikatk.seth@jadavpuruniversity.in (S.K.S)

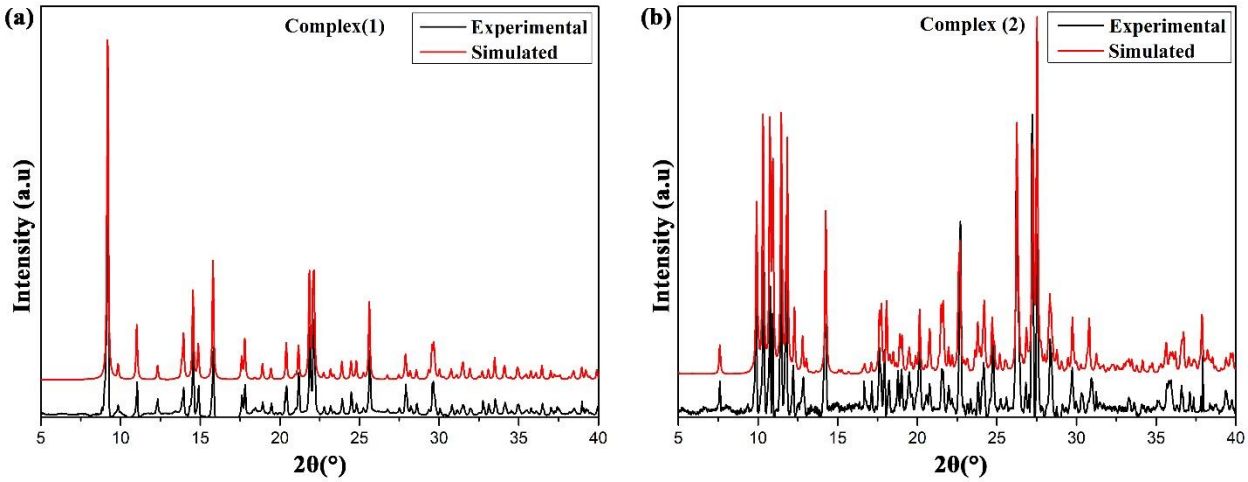

Figure S1. PXRD patterns of (a) complex (**1**)**;** and (b) complex (**2**).

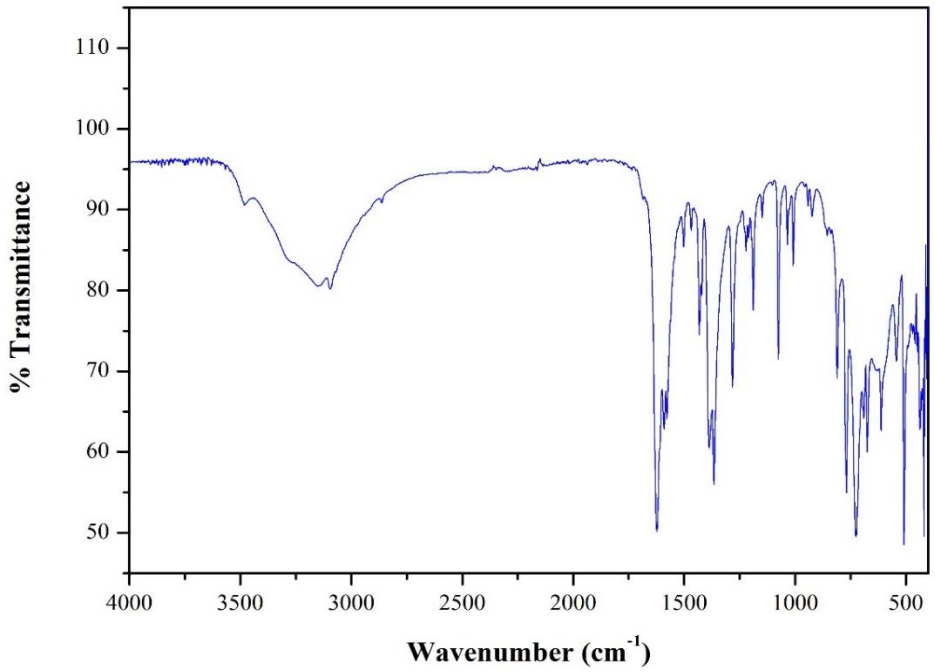

Figure S2. IR spectra of complex (**1**).

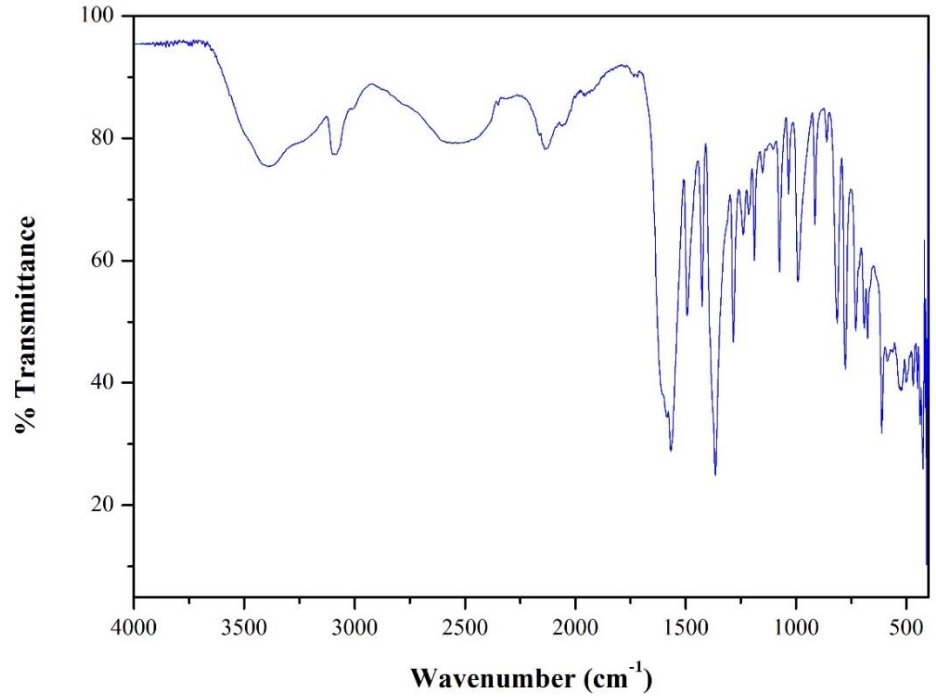

Figure S3. IR spectra of complex (**2**).

Table S1: Selected bond lengths (Å) and bond angles (°) around the metal centers in complex (**1**) and (**2**).

Complex(1)		***Complex(2)***	
Co1–N1	2.0342(17)	Co1–O11	2.123(4)
Co1–O1*	2.1756(15)	Co1–O14	2.151(4)
Co1–O4*	2.1478(15)	Co1–O15	2.152(4)
Co1–N1*	2.0342(17)	Co1–N7	2.019(5)
Co1–O1	2.1756(15)	Co1–N8	2.024(5)
Co1–O4	2.1478(15)	Co1–O10	2.196(4)
Co2–O5	2.0469(14)	Co2–O2	2.201(4)
Co2–O6	2.0893(16)	Co2–O3	2.141(4)
Co2–N2	2.2457(19)	Co2–O6	2.166(4)
Co2–O5†	2.0469(14)	Co2–O7	2.225(4)
Co2–O6†	2.0893(16)	Co2–N3	2.019(5)
Co2–N2†	2.2457(19)	Co2–N4	2.016(5)

O4a–Co1–N1*	94.72(6)	O14–Co1–N8	76.78(16)
N1–Co1–N1*	165.73(7)	O15–Co1–N7	103.41(17)
O1a–Co1–O4*	151.33(6)	O15–Co1–N8	76.49(16)
O1a–Co1–N1*	75.70(6)	N7–Co1–N8	174.14(16)
O4a–Co1–N1*	75.75(6)	O11–Co1–O14	93.64(15)
O1–Co1–O4	151.33(6)	O11–Co1–O15	89.20(15)
O1–Co1–N1	75.70(6)	O10–Co1–O11	153.56(17)
O1–Co1–O1*	101.60(6)	O10–Co–O14	91.94(15)
O1–Co1–O4*	87.49(6)	O10–Co1–O15	97.56(15)
O1–Co1–N1*	113.83(6)	O10–Co1–N7	76.27(16)
O4–Co1–N1	75.75(6)	O10–Co1–N8	97.91(16)
O1a–Co1–O4	87.49(6)	O11–Co1–N8	108.53(16)
O4–Co1–O4*	97.48(6)	O14–Co1–O15	152.60(17)
O4–Co1–N1*	94.72(6)	O11–Co1–N7	77.30(16)
O1a–Co1–N1	113.83(6)	O14–Co1–N7	103.80(17)
O5–Co2–O6	86.04(6)	O2–Co2–O3	151.14(17)
O5–Co2–N2	88.42(6)	O2–Co2–O6	89.97(15)
O5–Co2–O5†	180.00	O2–Co2–O7	95.90(15)
O5–Co2–O6†	93.96(6)	O2–Co2–N3	75.41(17)
O5–Co2–N2†	91.58(6)	O2–Co2–N4	107.51(16)
O6–Co2–N2	91.08(6)	O3–Co2–O6	100.48(15)
O5c–Co2–O6	93.96(6)	O3–Co2–O7	87.33(15)
O6–Co2–O6†	180.00	O3–Co2–N3	76.79(18)
O6–Co2–N2†	88.92(6)	O3–Co2–N4	101.09(17)
O5c–Co2–N2	91.58(6)	O6–Co2–O7	152.18(17)
O6c–Co2–N2	88.92(6)	O6–Co2–N3	95.93(17)
N2–Co2–N2†	180.00	O6–Co2–N4	76.65(16)
O5c–Co2–O6†	86.04(6)	O7–Co2–N3	111.87(17)
O5c–Co2–N2†	88.42(6)	O7–Co2–N4	75.65(16)
O6c–Co2–N2†	91.08(6)	N3–Co2–N4	171.88(15)

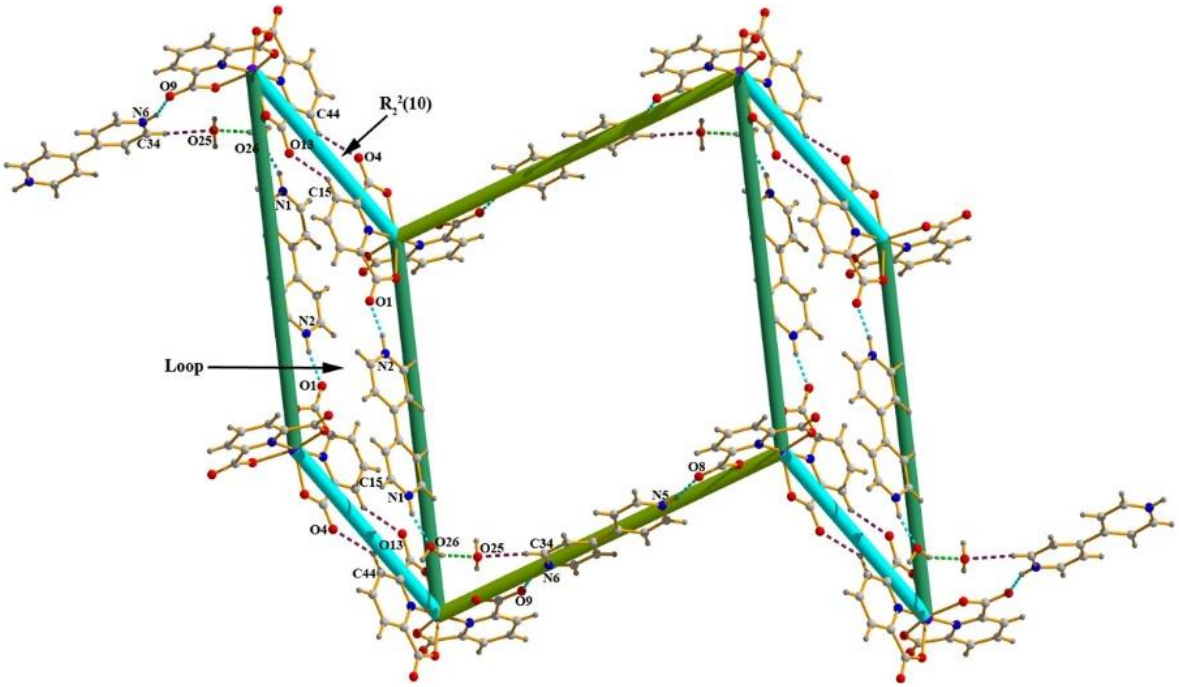

Figure S4. Two loops are connected through N–H···O interaction, forming 2D boxes.

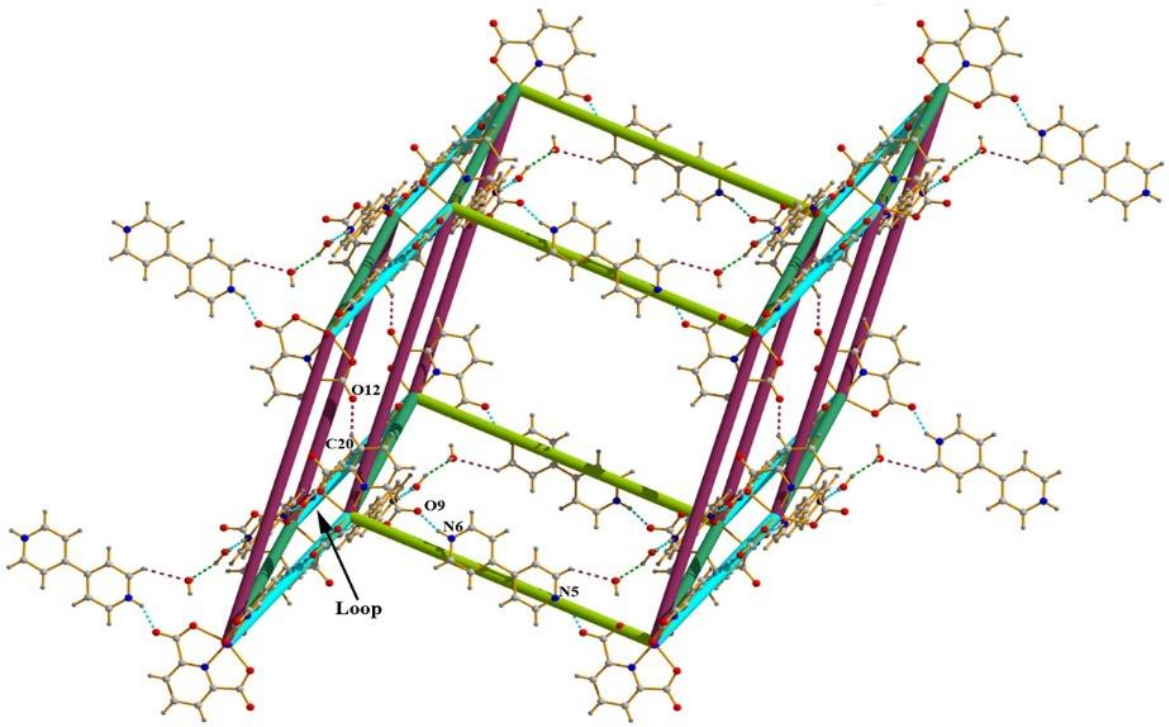

Figure S5. 2D boxes are connected through C–H···O interaction, forming 3D boxes.

Journal of Molecular Structure 1293 (2023) 136253

Contents lists available at ScienceDirect

Journal of Molecular Structure

journal homepage: www.elsevier.com/locate/molstr

Quantitative investigations of intermolecular interactions in 2-amino-3-nitropyridine polymorphs: Inputs from quantum mechanical calculations

Samiul Islam, Pratik Dey, Prantika Das, Saikat Kumar Seth *

Department of Physics, Jadavpur University, Kolkata 700032, India

ARTICLE INFO

Keywords:
Polymorphism in 2-amino-3-nitropyridine
Hirshfeld surface
Interaction energy
PIXEL calculations
QTAIM and NCI plot index

ABSTRACT

Two polymorphic forms (**Form–I** and **Form–II**) of 2-amino-3-nitropyridine are structurally characterized by single crystal X-ray diffraction analysis and compared with another polymorphic form (**Form–III**, retrieved from CSD) with a detailed analysis of the Hirshfeld surfaces and fingerprint plots facilitating a comparison of intermolecular interactions. X-ray crystallography exposes that the polymorphs generate completely different network structures through hydrogen bonding interactions. Polymorphic **Form–I** exhibit a layer assembly through the cooperative face-to-face $\pi\cdots\pi$ and lone pair$\cdots\pi$ interactions, whereas **Form–II,** and **Form–III** displays hydrogen bonds only. A detailed investigation of Hirshfeld surface analysis reveals much more detailed scrutiny of intermolecular interactions experienced by the polymorphic forms of 2-amino-3-nitropyridine. The quantitative analysis of the interaction energies involving various noncovalent interactions was computed and compared to get a deeper insight into the role of such interactions in stabilizing the polymorphs. The interaction energies of non-covalent interactions are calculated through theoretical DFT calculations as well as the PIXEL method. The PIXEL method provides us precise interaction energy calculation with an energy decomposition scheme. Higher electrostatic interaction shows higher interaction energy while the lower interaction energy corresponds to the higher dispersive interaction. The lattice energies of the polymorphs are also obtained *via* the PIXEL method. The nature and strength of these interactions have been studied using Bader's quantum theory of atoms in molecules. The topological analysis unequivocally establishes the presence of (3, −1) bond critical point, suggesting that the intermolecular interactions are closed-shell interactions. The NCI (Non-covalent Interaction) plots are further employed to identify and characterize the non-covalent interactions of the polymorphs.

1. Introduction

Polymorphism [1,2] has attracted intense attention, and significant progress has been achieved in the last decades in understanding their fascinating structures and valuable properties, such as solubility, stability, dissolution rates, mechanical strength, bioactivity etc. [1,3–5]. Polymorphism is the ability of a compound to exist in at least two or more crystalline forms, resulting from various packing arrangements of its molecules in the crystal; therefore, studies concerning polymorphism are crucial for developing any solid material [6]. Polymorphism mainly attracts greater attention in chemistry, pharmaceutical, and material science [4,5] mainly due to two reasons [7–9] – (i) their physiochemical properties and (ii) polymorphs can often be protected by a patent and therefore are crucial economic importance [10]. The polymorphs are classified into two categories depending on the geometry of molecular assembly – (i) conformational polymorphism [11] and (ii) packing polymorphism [12]. In the case of conformational polymorphism, identical molecular moieties may be packed in different molecular conformations with different modifications. In packing polymorphism, identical molecular moieties might be packed in different periodic structures, which provides an opportunity to investigate and understand the intermolecular interactions in building solid-state structures.

The subject of why we do not witness more polymorphs has frequently been raised with the development of crystal structure prediction (CSP) with a specific application [13–14]. Studies using CSP have been very effective in determining the organic structures with the lowest energy forms [14]. Understanding the nature of intermolecular interactions during the formation of molecular packing can be done owing to the existence of polymorphs. In recent years, robust synthons, advocates for supramolecular synthons developed by Desiraju, and energetically-favored patterns of hydrogen bonds have been used to address the understanding of polymorphism in terms of molecular organization [2]. When functional groups are present in a molecule, they are utilized for crystallization processes such as molecular recognition and self-assembly. In a recent review,

* Corresponding author.
E-mail address: saikatk.seth@jadavpuruniversity.in (S.K. Seth).

https://doi.org/10.1016/j.molstruc.2023.136253
Received 29 March 2023; Received in revised form 11 July 2023; Accepted 19 July 2023
Available online 24 July 2023

Cruz-Cabeza et al. showed that there may be no relationship at all between polymorphism and molecular structural components [15]. Therefore, it is still unclear how polymorphism and molecular structure are related [16–18]. More specifically, it is currently unclear how and why non-hydrogen bonding compounds crystallize as polymorphic forms.

In this context, a variety of attempts have been used to understand and envisage the final crystal structure, such as – (a) the model to reduce structure into small molecular clusters and calculation of lattice energies [19]; (b) another model for the formation of a molecular structure depending on strong hydrogen bonds [20]; (c) next model based on supramolecular synthons based on a particular type of interactions [21]; (d) another method based on molecular electrostatic potentials to quantify intermolecular interactions through the estimation of relative hydrogen bonding parameters of the functional groups [22] and (e) Hirshfeld surface [23–25] based tools which represents a novel approach to quantify all intermolecular interactions involved within the crystal in a novel visual manner. The derivation of the Hirshfeld surface is an interpretable visualizing plot of the investigated molecule within its environment, and the decomposition of the surface provides a 2D fingerprint plot [26] to analyze the entire distribution of intermolecular interactions involved in the structure.

Pyridinamines act as important intermediates with several applications in the chemical industry as well as in pharmaceutical products [27]. Pyridine also serves as the building block of polymers with unique physical properties [28]. The nitrogen atom of the pyridine ring in 2-Amino-3-Nitropyridine acts as a cationic binding site where the nitro group act as a hydrogen acceptor and the amino group as a donor. This electron donating and accepting moieties attached to a conjugated system often induce non-linear optical NLO character [29].

In this paper, we have explored the polymorphs of "2-amino-3-nitropyridine" by comparing their molecular packing, including a detailed assessment of intermolecular interactions through Hirshfeld surface analysis [23–26] as well as various theoretical studies such as theoretical DFT calculation [30], PIXEL method [31], Bader's theory of "Atoms in molecule" [32], and 'Noncovalent interaction' (NCI) plot index [33]. The quantitative analysis of the strength and nature of noncovalent interactions, including the lattice energies have been explored through PIXEL calculation.

2. Experimental

2.1. Crystallization of *Form–I* and *Form-II*

Crystals of **Form–I** suitable for single-crystal X-ray diffraction were obtained upon co-crystallization of 2,6-pyridine-dicarboxylic acid (PDA) with 2-amino-3-nitropyridine. The equivalent amount of PDA and conformer 2-amino-3-nitropyridine were taken into a 50 mL flask and dissolved in methanol/water in a 2:1 molar ratio. Then, the mixture was refluxed for 1 h. The resulting homogeneous solution was kept undisturbed at ambient temperature and covered with paraffin film, and a few small holes were made to evaporate the solvent slowly. The two different forms of the conformer were crystallized with two distinctly different crystal habits, *viz.*, colorless needles in bunches and yellow plates along the sides that were separated manually. The majority of the crystals in the flask (colorless needles) matched with the PDA molecule [34], while very few crystals (yellow plates) were designated as polymorphic **Form–I** of 2-amino-3-nitropyridine. Due to the lack of sufficient samples, current studies on **Form–I** was limited to only single-crystal X-ray diffraction and theoretical calculations. The same procedure was followed to grow single crystals of 2-amino-3-nitropyridine (**Form–II**) by using malonic acid as a conformer.

2.2. Crystallographic analysis

Single crystal X-ray diffraction intensity data of the title compounds were collected at 120(2) K using a Bruker APEX-II CCD diffractometer equipped with graphite monochromated MoKα

Table 1
Crystal data and structure refinement parameters for the title polymorphs.

Structure	**Form–I**[*]	**Form–I**[#1]	**Form–II**[*]	**Form–II**[#2]	**Form–III**[#3]
Empirical formula	$C_5H_5N_3O_2$	$C_5H_5N_3O_2$	$C_5H_5N_3O_2$	$C_5H_5N_3O_2$	$C_5H_5N_3O_2$
Formula Weight	139.12	139.12	139.12	139.12	139.12
Temperature (K)	120(2)	295	120(2)	153	173
Wavelength (Å)	0.71073	–	0.71073	–	–
Crystal system	Monoclinic	Monoclinic	Monoclinic	Monoclinic	Monoclinic
space group	$P2_1/c$	$P2_1/n$	$P2_1/c$	$P2_1/c$	$P2_1/n$
a, b, c (Å)	8.518(2), 4.928(2), 14.429 (3)	8.743(1), 4.898(1), 14.473(1)	4.9026(6), 6.9198(7), 17.412(2)	4.917(1), 6.940(2), 17.507(3)	3.737(2), 7.445(2), 20.974(6)
α, β, γ (°)	107.098(3)	106.57(1)	95.584(2)	95.63(2)	90.52(3)
Volume ($Å^3$)	578.9(3)	594.042	587.90(12)	594.527	583.514
Z / Density (calc.) (Mg/m^3)	4 / 1.596	– / 1.555	4 / 1.572	– / 1.554	– / 1.584
Absorption coefficient (mm^{-1})	0.127	–	0.125	–	–
F(000)	288	–	288	–	–
Crystal size (mm^3)	0.21 × 0.13 × 0.07	–	0.15 × 0.11 × 0.07	–	–
θ range (°)	2.50 – 24.99	–	2.35 – 25.00	–	–
Limiting indices	$-10 \le h \le 10$, $-5 \le k \le 5$, $-17 \le l \le 17$	–	$-5 \le h \le 5$, $-8 \le k \le 8$, $-20 \le l \le 20$	–	–
Reflections collected / unique	4807 / 1001 [R(int) = 0.0254]	–	5166 / 1021 [R(int) = 0.0295]	–	–
Completeness to θ (%)	98.6	–	98.6	–	–
Absorption correction	Semi-empirical from equivalents	–	Semi-empirical from equivalents	–	–
Max. and min. transmission	0.99 and 0.98	–	0.99 and 0.98	–	–
Refinement method	Full-matrix least-squares on F^2	–	Full-matrix least-squares on F^2	–	–
Data/restraints/parameters	1001 / 0 / 91	–	1021 / 0 / 92	–	–
Goodness-of-fit on F^2	1.065	–	1.035	–	–
Final R indices [$I > 2\sigma(I)$]	$R_1 = 0.0317$, $wR_2 = 0.0838$	$R_1 = 0.0570$	$R_1 = 0.0304$, $wR_2 = 0.0845$	$R_1 = 0.0575$	$R_1 = 0.0716$
R indices (all data)	$R_1 = 0.0351$, $wR_2 = 0.0874$	–	$R_1 = 0.0319$, $wR_2 = 0.0861$	–	–
Largest diff. peak and hole ($e.Å^{-3}$)	0.135 and −0.229	–	0.212 and −0.170	–	–

[*] Present work with new CIF.
[#1] previous work, CSD ref code: AMNTPY [40].
[#2] previous work, CSD ref code: AMNTPY01 [41].
[#3] previous work, CSD ref code: AMNTPY02 [41].

$R_1 = \sum||F_o|-|F_c||/\sum|F_o|$, $wR_2 = [\sum\{(F_o^2-F_c^2)^2\}/\sum\{w(F_o^2)^2\}]^{1/2}$, $w = 1/\{\sigma^2(F_o^2) + (aP)^2 + bP\}$, where $a = 0.0547$ and $b = 0.0822$ for (**Form–I**) and $a = 0.0537$ and $b = 0.1200$ for (**Form–II**). $P = (F_o^2 + 2F_c^2)/3$ for all structures.

radiation (λ = 0.71073 Å). Data reduction was carried out using the program Bruker SAINT [35]. An absorption correction based on the multi-scan method [36] was applied. The structures of the title compounds were solved by direct methods and refined by the full-matrix least-square technique on F^2 with anisotropic thermal parameters to describe the thermal motions of all nonhydrogen atoms using the programs SHELXS97 and SHELXL97 [37], respectively. All hydrogen atoms were located from difference Fourier maps and treated as riding. All the calculations were performed using the PLATON [38] program of the WinGX suite [39]. Crystallographic data (excluding structure factors) for the structures reported in this article have been deposited with the Cambridge Crystallographic Data Centre as supplementary publication numbers CCDC 1033932 and 1033933 for the polymorphic **Form–I** and **Form–II** respectively. Table 1 contains the crystal data and refinement parameters of grown polymorphs (**Form–I** and **Form–II**) along with previously reported **Form–I** (CSD ref code AMNTPY) [40] and **Form–II** (CSD ref code AMNTPY01) [41] as well as **Form–III** (CSD ref code AMNTPY02) [41]. The simulated PXRD peak of the polymorphs is included in Fig. S1.

2.3. Hirshfeld surface analysis

Molecular Hirshfeld surfaces [23–25] in the crystal structures are constructed based on the electron distribution calculated as the sum of spherical atom electron densities. For a given crystal structure and set of spherical atomic electron densities, the Hirshfeld surface is unique [42], and it is the property that suggests the possibility of gaining additional insight into the intermolecular interaction of molecular crystals. The normalized contact distance (d_{norm}) based on both d_e (distance from the point to the nearest nucleus external to the surface) and d_i (distance to the nearest nucleus internal to the surface) and the *vdW* radii of the atom, given by the Eq. (1) enables identification of the regions of particular importance to intermolecular interactions [23]. The combination of d_e and d_i in the form of a 2D fingerprint plot [23–26] provides a summary of intermolecular contacts in the crystal [23]. The Hirshfeld surfaces are mapped with d_{norm}, and 2D fingerprint plots presented in this paper were generated using CrystalExplorer 2.1 [43].

$$d_{norm} = \frac{d_i - r_i^{vdw}}{r_i^{vdw}} + \frac{d_e - r_e^{vdw}}{r_e^{vdw}} \quad (1)$$

2.4. Theoretical methods

The wavefunction analyses have been carried out by using the Gaussian16 calculation package [44] with DFT/B3LYP/6311++*G*(d,p) basis set. The interaction energies are calculated using specific dimer models derived from the supramolecular network.

Lattice energy and intermolecular interaction energies for molecular pairs of the polymorphs were decomposed into coulombic, polarization, dispersion, and repulsion energy terms which are evaluated using the PIXELC method in the CLP module [45]. In this calculation, all the hydrogen atoms were moved to their neutron distances, and B3LYP/6–311++*G*(d, p) basis set was used for the calculations of accurate electron density [31].

We have used Bader's theory of "Atoms in molecules" [46] to analyze the noncovalent by AIMALL calculation package [47]. The charge density ρ(r), and its Laplacian $L(r) = \nabla^2\rho(r)$ are calculated using the "Atom in molecule" (QTAIM) theory at the (3, –1) bond critical point (BCPs). According to topological properties, the electron density is depleted where $\nabla^2\rho(r)$ is positive for closed-shell interaction [48]. Other topological parameters such as kinetic electronic energy density G(r), potential electronic energy density V(r), and total electronic energy density H(r) [H(r) = V(r) + G(r)] were obtained at BCPs for characterizing the intermolecular interactions [49]. At the bond critical point, the dissociation energy can be calculated as $-V(r)/2$ in the Hartree unit which can be converted in kcal/mol unit by 313.7545 × ($-V(r)$). For noncovalent interactions, kinetic electronic energy density G(r) is greater than potential electronic energy density V(r), so that $\frac{|V(r)|}{G(r)}$ is always less than 1 [50]. The relatively low value of charge density (ρ), the small positive value of the Laplacian ($\nabla^2\rho(r)$), and energy density (H(r)) at BCPs and the relationship $|\frac{V}{G}| < 1$ indicate that all noncovalent interactions are "closed–shell" interactions where the noncovalent interactions are dominated by the charge contraction away from the interatomic surface toward each nucleus [51]. Using the NCI plot index [52], we can further characterize the noncovalent interactions by visualizing the isosurfaces instead of the bond critical points. A blue-green-yellow-red color scheme represents these isosurfaces. Red and blue isosurfaces represent the repulsive (ρ^{+}) and attractive (ρ^{-}) interactions [53] while yellow and green isosurfaces represent the weak repulsive and weak attractive interactions.

3. Result and discussion

3.1. Structural comparison

The molecular view of the polymorphic forms of 2-amino-3-nitropyridine has been depicted in Fig. 1 using ORTEP-III [54]. The solid-state structure of the polymorphs **Form–I** and **Form–II** at 120 K with the highest precision in comparison to the previously reported forms [40, 41] with an R-value of 0.0317 and 0.0304 have been reported herein. The polymorphic **Form–III** that has been retrieved from CSD (AMNTPY02) [41] has no anisotropic thermal parameters. Therefore, the molecular view of **Form–III** has been represented in the ball & stick model (Fig. 1c). The comparison between the unit cell dimensions for the polymorphs (Table 1) shows they are entirely different. Some selected bond lengths and bond angles are given in Tables 2 and 3. The morphologies of the polymorphic forms of 2-amino-3-nitropyridine have been depicted in Fig. S2. X-ray crystallography reveals that the polymorphs are stabilized through a combination of N–H···N, O–H···O, and C–H···O hydrogen bonding interactions; however, polymorphic **Form–I** exhibits weak π···π and carbonyl (l.p)···π interactions. In the solid state, the polymorphs interlink themselves to generate different structures through strong N–H···N and O–H···O hydrogen bonds (Table 4).

In **Form–I**, the amine nitrogen atom N2 in the molecule at (x, y, z)

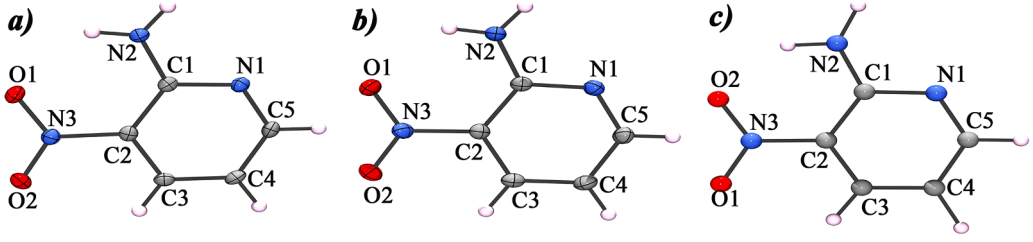

Fig. 1. ORTEP view and atom numbering scheme of the polymorphs (a) **Form–I**, and (b) **Form–II**, with displacement ellipsoid at 30% probability, and (c) **Form–III** in ball & stick format.

Table 2
Selected bond lengths (Å).

Bond	**Form–I**[*]	**Form–I**[#1]	**Form–II**[*]	**Form–II**[#2]	**Form–III**[#3]
C(1)–*N*(2)	1.331(2)	1.336	1.328(2)	1.331(5)	1.334(6)
C(2)–*N*(3)	1.436(2)	1.440	1.435(2)	1.438(5)	1.427(6)
N(3)–*O*(1)	1.238 (2)	1.235	1.235(2)	1.240(4)	1.232(6)
N(3)–*O*(2)	1.233(2)	1.229	1.228(2)	1.242(4)	1.237(6)

[*] Present work with new CIF.
[#1] previous work, CSD ref code: AMNTPY [40].
[#2] previous work, CSD ref code: AMNTPY01 [41].
[#3] previous work, CSD ref code: AMNTPY02 [41].

acts as a donor to the pyridine ring nitrogen atom N1 in the molecule at (1–x, –1–y, –z), so generating a centrosymmetric $R_2^2(8)$ dimeric ring (A) centered at (½, ½, 0) (Fig. 2a). Additional reinforcement with the amine nitrogen N2 and oxygen atom O1 of the nitro group in the molecule at (x, y, z) and (1–x, –1/2+*y*, 1/2–z) leads the molecules to generate a supramolecular network structure in (011) plane (Fig. 2a).

In case of **Form–II**, the amine nitrogen atom N2 at (x, y, z) acts as a donor to the pyridine nitrogen atom N1 at (–1–x, 1–y, –z), generating a centrosymmetric $R_2^2(8)$ dimeric ring (A) centered at (½, ½, 0) (Fig. 2b). Again this amine nitrogen atom N2 acts as a donor to the oxygen atom O1 of the nitro group at (–x, 2–y, –z), thus generating a centrosymmetric $R_2^2(12)$ dimeric ring (B) centered at [010] (Fig. 2b). These two types of centrosymmetric dimeric rings (A) and (B) in **Form–II** are alternately linked into infinite zigzag ABABAB···. chain along [010] direction (Fig. 2b).

In **Form–III**, the amine nitrogen atom N2 in the molecule at (x, y, z) acts as a donor to the pyridine ring nitrogen atom N1 in the molecule at (1–x, 2–y, 1–z). Thus, N–H···N hydrogen bond generates a centrosymmetric $R_2^2(8)$ dimeric ring (A) centered at (½, 1, ½) (Fig. 2c). Moreover, the amine nitrogen N2 and oxygen atom O2 of the nitro group in the molecule at (x, y, z) and (–x, 1–y, 1–z) leads the molecules to generate another centrosymmetric $R_2^2(12)$ dimeric ring (B) centered at (0, ½, ½) (Fig. 2c). These two types of centrosymmetric dimeric rings (A) and (B) are linked alternatively into infinite zigzag ABABAB···. chain along [010] direction (Fig. 2c).

Again the reinforcement between the strong N–H···N and weak C–H···O hydrogen bonding interactions in both the polymorphic forms

Table 3
Selected bond angles (°).

Bond	**Form–I**[*]	**Form–I**[#1]	**Form–II**[*]	**Form–II**[#2]	**Form–III**[#3]
N(1)–C(1)–*N*(2)	115	114	115	115	115
C(2)–C(1)–*N*(2)	126	126	126	119	127
C(1)–C(2)–*N*(3)	122	120	122	122	120
C(2)–*N*(3)–*O*(1)	119	119	119	119	118
C(2)–*N*(3)–*O*(2)	119	119	119	119	120
O(1)–*N*(3)–*O*(2)	122	122	122	122	121

[*] Present work with new CIF.
[#1] previous work, CSD ref code: AMNTPY [40].
[#2] previous work, CSD ref code: AMNTPY01 [41].
[#3] previous work, CSD ref code: AMNTPY02 [41].

Table 4
Hydrogen bonding geometry of polymorphic forms of the title polymorphs (Å, °).

D–H···A	d(D–H)	d(H···A)	d(D···A)	∠D–H···A	Symmetry
Form–I[*]					
N(2)–H(2A)···N(1)	0.86	2.13	2.991(2)	177	1–x, –1–y, –z
N(2)–H(2B)···O(1)	0.86	2.07	2.666(2)	126	—
N(2)–H(2B)···O(1)	0.86	2.41	2.999(2)	127	1–x, –1/2+*y*, 1/2–z
C(3)–H(3)···O(2)	0.93	2.44	3.279(2)	150	–x, 1–y, –z
Form–I[#1]					
N(2)–H(2A)···N(1)	0.97	2.04	3.009(2)	176	1–x, –1–y, –z
N(2)–H(2B)···O(1)	0.88	2.03	2.671(2)	129	—
N(2)–H(2B)···O(1)	0.88	2.47	3.045(2)	124	1/2–x, 1/2+*y*, 1/2–z
C(3)–H(3)···O(2)	0.99	2.47	3.345(2)	148	–x, 1–y, –z
Form–II[*]					
N(2)–H(2A)···N(1)	0.86	2.10	2.963(2)	176	–1–x, 1–y, –z
N(2)–H(2B)···O(1)	0.86	2.06	2.659(2)	126	—
N(2)–H(2B)···O(1)	0.86	2.30	3.032(2)	143	–x, 2–y, –z
C(3)–H(3)···O(2)	0.93	2.49	3.167(2)	130	1–x, –1/2+*y*, 1/2–z
Form–II[#2]					
N(2)–H(2A)···N(1)	0.92	2.07	2.972(5)	166	2–x, 1–y, 2–z
N(2)–H(2B)···O(1)	0.95	2.08	2.662(4)	117	—
N(2)–H(2B)···O(1)	0.95	2.19	3.044(4)	147	2–x,1–y, 2–z
C(3)–H(3)···O(2)	1.04	2.41	3.178(4)	129	–x, 1/2+*y*, 3/2–z
Form–III[#3]					
N(2)–H(1)···O(2)	0.95	2.49	2.965(6)	119	–x, 1–y, 1–z
N(2)–H(1)···O(2)	0.95	1.91	2.672(5)	136	—
N(2)–H(1)···N(3)	0.95	2.53	2.966(6)	108	—
N(2)–H(2)···N(1)	1.05	1.97	2.679(6)	157	1–x, 2–y, 1–z
C(4)–H(4)···O(1)	1.17	2.45	3.277(6)	126	–1/2–x, 1/2+*y*, 3/2–z
C(3)–H(3)···O(1)	0.97	2.33	2.679(6)	101	—

[*] Present work with new CIF.
[#1] previous work, CSD ref code: AMNTPY [40].
[#2] previous work, CSD ref code: AMNTPY01 [41].
[#3] previous work, CSD ref code: AMNTPY02 [41].

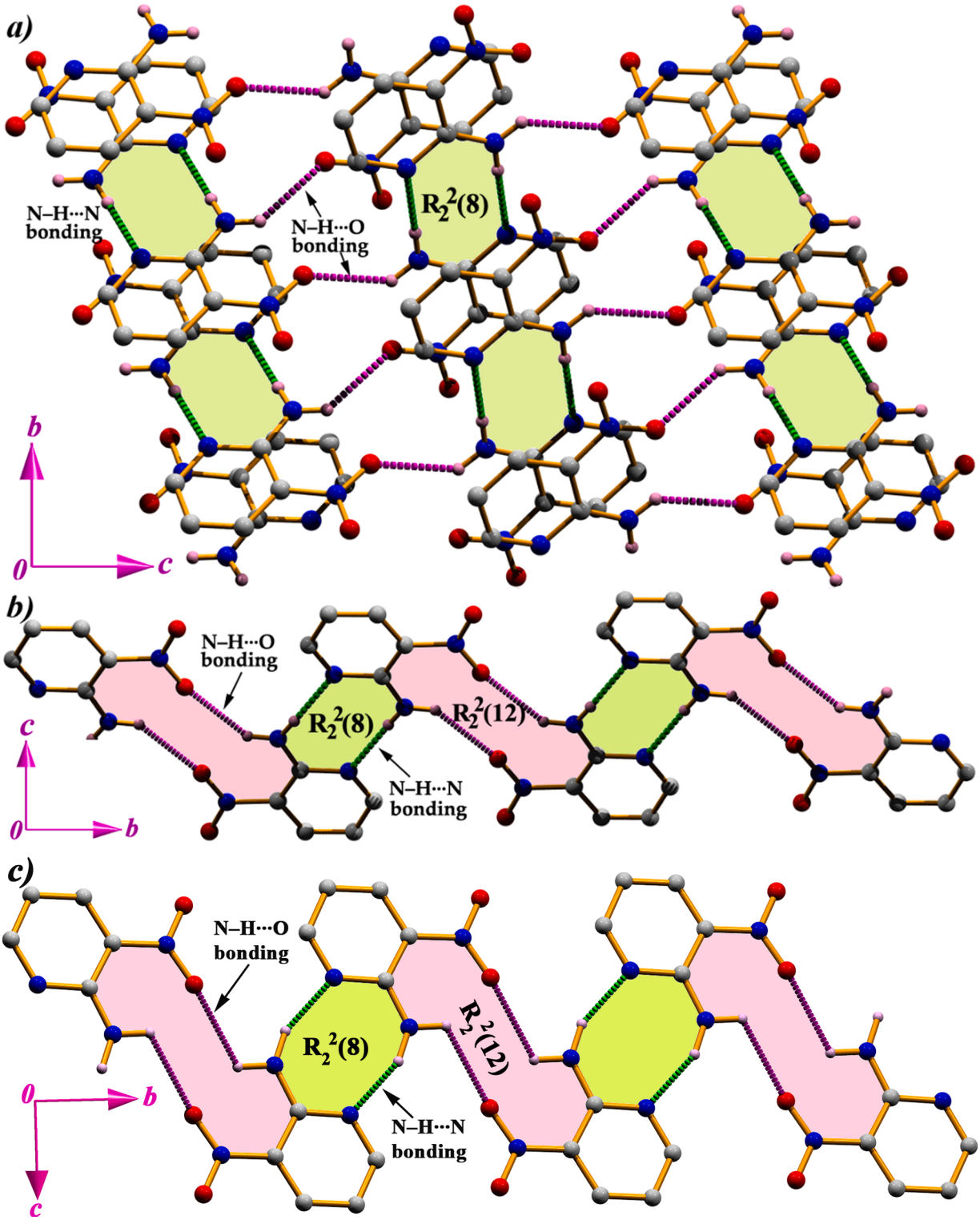

Fig. 2. Formation of different supramolecular network structures for **Form–I** (a), **Form–II** (b), and **Form–III** (c) through N–H···N and N–H···O hydrogen bonding interactions.

exhibit new assembly in the solid state. In **Form–I**, the pyridine ring carbon atom C3 in the molecule at (x, y, z) acts as a donor to the oxygen atom O2 of the nitro group in the molecule at (–x, 1–y, –z), so generating a centrosymmetric $R_2^2(10)$ dimeric ring (M) centered at (0, ½, 0) (Fig. 3a). The molecules of **Form–I** generates $R_2^2(8)$ dimeric ring (A) through N–H···N bond and these two types of dimeric rings are alternately linked into infinite AMAM··· chain along [010] direction. Parallel layers of AMAM··· chains are interconnected through the N–H···O hydrogen bond due to the self-complementary nature of the molecules of **Form–I**. The amine nitrogen acts as a donor to the nitro oxygen atom to interlink the parallel AMAM··· chain, thus generating a two-dimensional network structure in the (011) plane (Fig. 3a). In **Form–II**, layers of centrosymmetric $R_2^2(8)$ dimeric ring (A) motifs are in parallel orientation and propagating along [010] direction. These parallel layers are

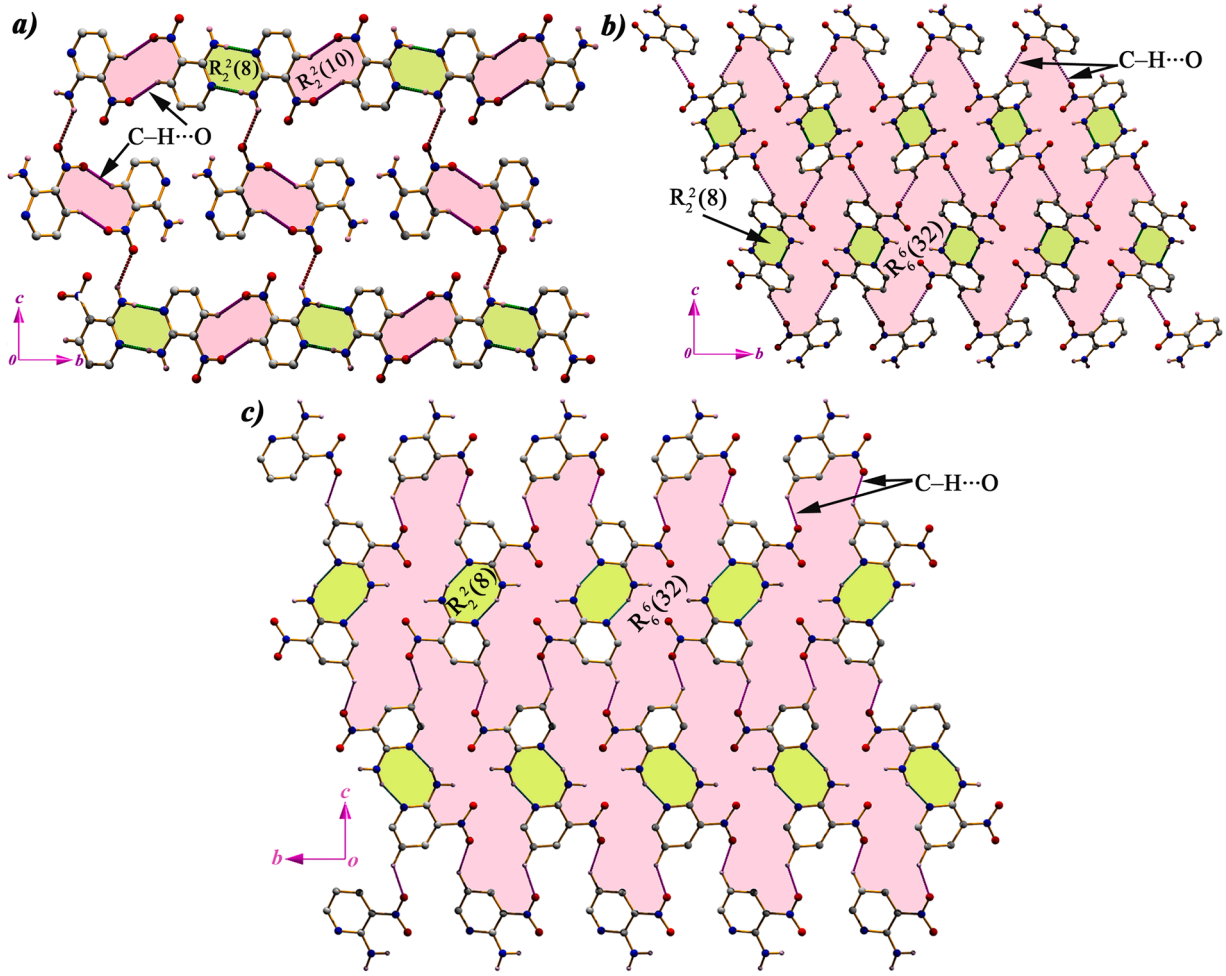

Fig. 3. (a) Propagation of centrosymmetric R_2^2 (8) and R_2^2 (10) rings and formation of 2D network structure in **Form–I**; (b) Generation of the 2D network in **Form–II**; (c) Formation of the 2D network in **Form–III**.

interconnected through weak C–H···O bonds to form a network. The pyridine ring carbon atom C3 at (x, y, z) acts as a donor to the oxygen atom of the nitro group in the molecule at (1–x, –1/2+*y*, 1/2–z), thus generating an $R_6^6(32)$ ring motif (N) in **Form–II** (Fig. 3b). The two types of ring motifs (A) and (N) in **Form–II** are alternately linked into a network structure in (011) plane (Fig. 3b). In the case of **Form–III**, the layers of centrosymmetric $R_2^2(8)$ dimeric ring (A) motifs are in anti-parallel orientation along the [010] direction. These anti-parallel layers are interconnected through C–H···O hydrogen bond interaction. The carbon atom C4 in the pyridine ring at (x, y, z) acts as a donor to the oxygen atom O1 of the nitro group in the molecule at (–1/2–x, 1/2+*y*, 3/2–z) which generates an $R_6^6(32)$ ring motif (N) (Fig. 3c). The alternative propagation of the ring motifs (A) and (N) in **Form–III** form a two-dimensional network structure in (011) plane (Fig. 3c).

A close examination concerning the intermolecular interactions involved within the polymorphic forms of 2-amino-3-nitropyridine displays that the **Form–I** exhibits face-to-face π···π and carbonyl(l.p.)···π type weak noncovalent interactions in the solid-state. The molecular packing in **Form–I** is such that the π···π stacking interactions between the pyridine rings are optimized [55–57]. The pyridine rings (N1/C1–C5) of the molecules at (x, y, z) and (1–x, –y, –z) are strictly parallel, with interplanar spacing of 3.367 Å, and a ring centroid separation of 4.255(2) Å, corresponding to a ring offset of 2.77 Å (Fig. 4). Moreover, an unusual contact between carbonyl oxygen atom and the π-cloud of the pyridine ring is observed, which is responsible for the formation of the new molecular assembly (Fig. 4). The carbonyl oxygen atom O2 at (x, y, z) is oriented toward the centroid of the pyridine ring (N1/C1–C5) in the molecule at (–x, –y, –z). The distance between O2 and the centroid of the pyridine ring is 3.567(2) Å [angle N3–O2···Cg(1) = 103.62(7)°, N3···Cg(1) = 4.039(2) Å, where Cg(1) is the centroid of the pyridine ring], suggesting a significant lone pair···π interaction [58,59]. This dual recognition of π···π and carbonyl(L.P)···π which can be designated as cooperative lone pair···π/π···π/π···lone pair network generates a unique supramolecular self-assembly, where weak non-covalent interactions are responsible for the formation and strengthening of assembly in **Form–I** (Fig. 4). Significantly, **Form–II** and **Form–III** does not exhibit π···π or lone pair···π interactions in the solid-state.

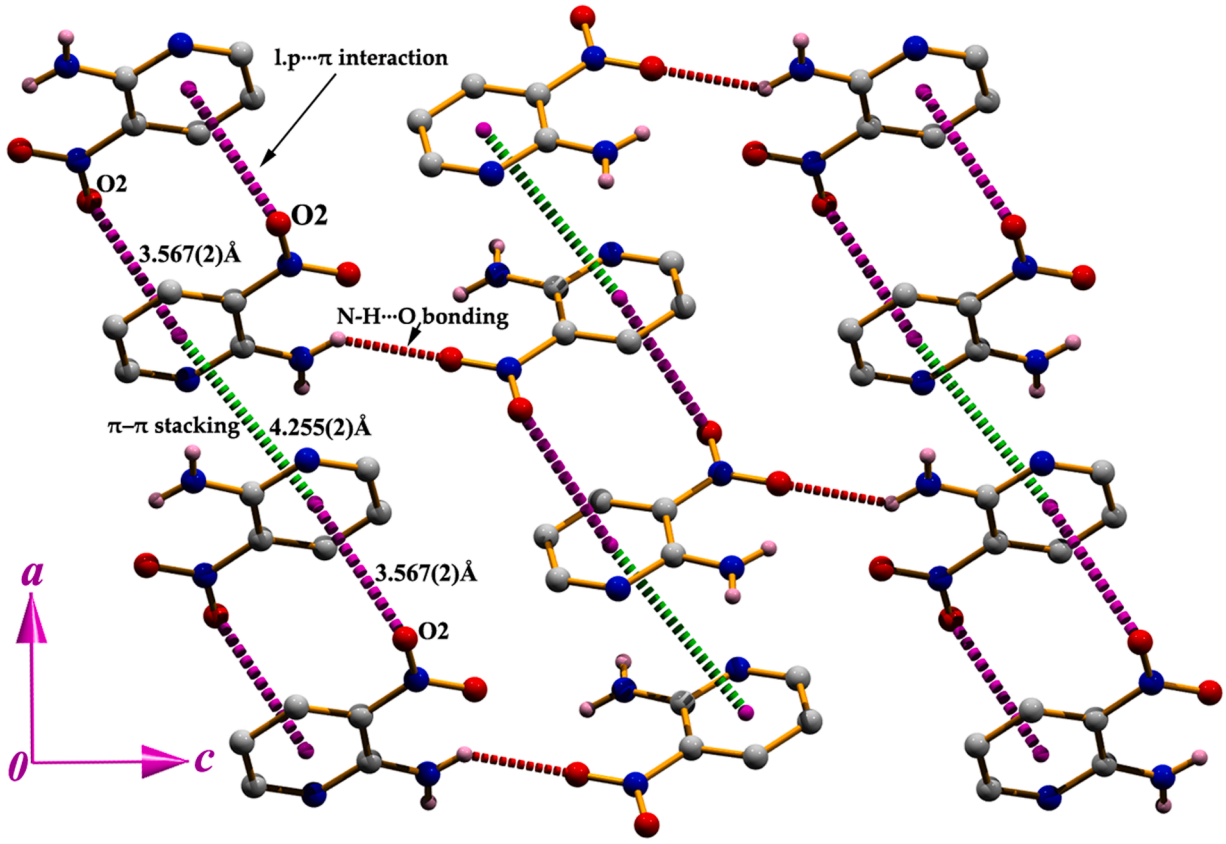

Fig. 4. Perspective view of cooperative pair···π/π···π/π···lone pair network in **Form–I**.

3.2. Hirshfeld surface

The Hirshfeld surfaces of the polymorphic forms of 2-amino-3-nitropyridine are illustrated in Fig. 5, showing the surfaces that have been mapped over d_{norm} and shape-index. Referring to Fig. 5, the dominant interactions between the amine nitrogen atom and the nitrogen atom of the pyridine ring in the polymorphs can be seen in the Hirshfeld surface area by the bright red encircles. The dominant interactions between the amine nitrogen atom and the oxygen atom of the nitro group are also evident in the d_{norm} surface of both the polymorphic forms by the large circular depressions (Fig. 5). The light red spots are due to weak C–H···O interactions, other spots on the d_{norm} surfaces correspond to C···O, and H···H close contacts. The small extents of the visible area and very light-colored regions on the surfaces indicate weaker and longer contacts other than hydrogen bonds. The dominant N–H···N interaction appears as two distinct spikes in the fingerprint plot (Fig. 6) with almost equal lengths for both the polymorphic forms of 2-amino-3-nitropyridine.

For the N···H/H···N interactions, complementary regions are visible in the fingerprint plots where one molecule acts as a donor ($d_e > d_i$) and the other as an acceptor ($d_e < d_i$). The upper spikes correspond to the donor spike (amine nitrogen atom interacting with pyridine ring nitrogen atom), with the lower spike being an acceptor spike (pyridine ring nitrogen atom acts as acceptor to the amine nitrogen atom); these two spikes in the fingerprint plot designates the formation of a centrosymmetric $R_2^2(8)$ dimeric ring (A) motif for all the polymorphs (Fig. 6). The fingerprint plots can be decomposed to highlight particular atom pair close contacts. The decomposed plot concerning N–H···N interaction has been depicted in Figs. S3–S5 for **Form–I, Form–II,** and **Form–III** respectively. The Hirshfeld surface analysis does not show similar proportions to the N···H (7.7% in **Form–I** and **Form–III** whereas 8.2% in **Form–II**) and H···N (6.3% in

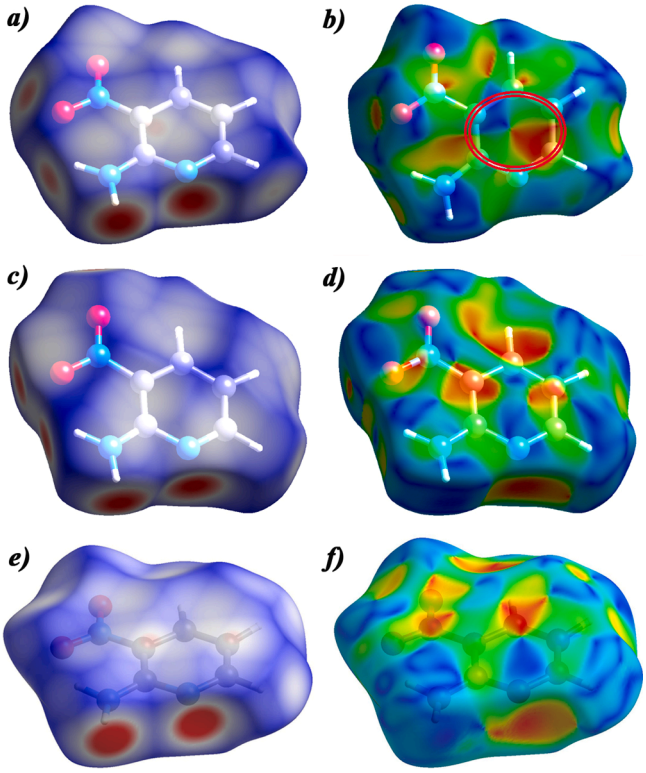

Fig. 5. Hirshfeld surfaces mapped with d_{norm} (left) and shape-index (right) for **Form–I** (top) and **Form–II** (middle) and **Form–III** (bottom).

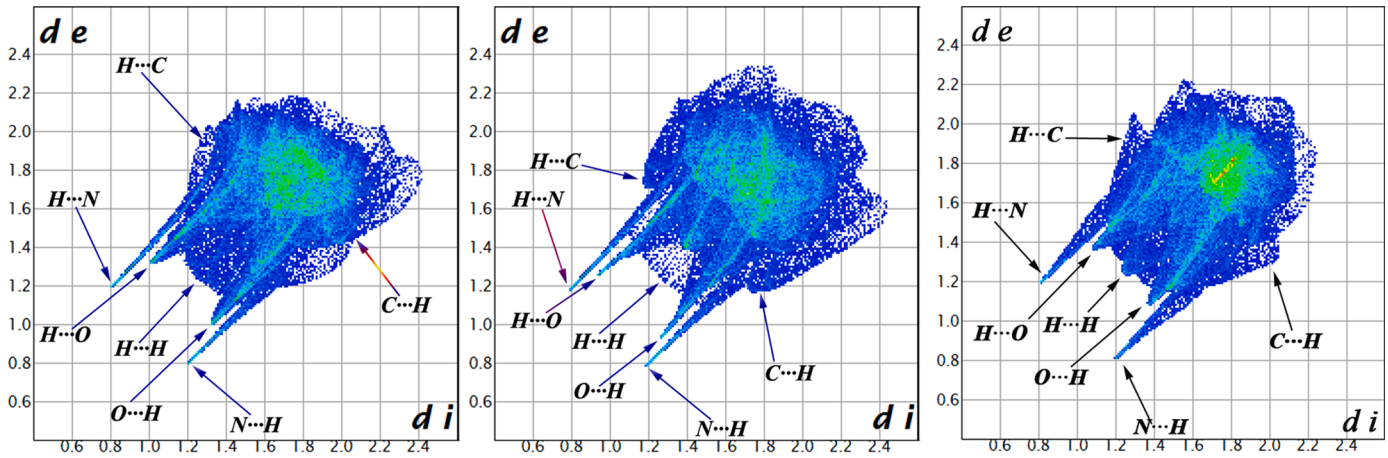

Fig. 6. Fingerprint plot (Full) for the polymorphic **Form–I** (left), **Form–II** (middle), and **Form–III** (right).

Form–I, 6.8% in **Form–II**, and 5.5% in **Form–III**) interactions for the three polymorphic forms. Therefore, N–H···N interaction proportions comprise 14.0% (d_i = 1.182 Å; d_e = 0.796 Å) in **Form–I**, whereas **Form–II,** and **Form–III** comprise 15.0% (d_i = 1.162 Å; d_e = 0.781 Å), and 13.2% (d_i = 1.192 Å; d_e = 0.806 Å) of the molecules' total surface area respectively (Figs. S3–S5).

Another dominant N–H···O and weak C–H···O intermolecular interactions appear as two distinct spikes of almost equal lengths in the two-dimensional fingerprint plots (Fig. 6). Where the donor spike designates that the amine nitrogen atom or the pyridine ring carbon atom interacting with the oxygen atom of the nitro group whereas the acceptor spike designates that the oxygen atom is in contact with the amine nitrogen atom or the pyridine ring carbon atom. This O···H/H···O interaction leads the molecules to generate the centrosymmetric dimeric rings and the proportions of O···H/H···O interactions comprising 37.3% (d_i = 1.307 Å; d_e = 0.996 Å), 37.0% (d_i = 1.242 Å; d_e = 0.921 Å), and 38.8% (d_i = 1.362 Å; d_e = 1.086 Å) of the total Hirshfeld surface for each molecule of **Form–I, Form–II,** and **Form–III** respectively. No significant C–H···π interactions are observed in all polymorphic forms, with C···H/H···C close contacts varying from 13.1% in **Form–I** to 8.9% in **Form–III**. From the Hirshfeld surface of **Form–I**, it is clear that the pyridine rings are related to one another through face-to-face π···π stacking interaction since a large flat region across the molecule is evident. This is also clearly evident by the adjacent red and blue triangles on the shape index surface (Fig. 5). The polymorphic **Form–II** and **Form–III** do not exhibit π···π stacking interactions which is also clearly evident by the shape-index figure since there is no signature of red and blue triangles (Fig. 5). The contribution to the total Hirshfeld surface area due to $C_\pi\cdots C_\pi$ stacking interaction is 1.3% ($d_i = d_e$ = 1.648 Å) in **Form–I** whereas **Form–II** exhibits 0.7% ($d_i = d_e$ = 1.653 Å) due to C···C short contacts. The $C_\pi\cdots C_\pi$ interaction in **Form–III** comprises 5.7% ($d_i = d_e$ = 1.647 Å) of the total Hirshfeld surface area. A significant difference between the molecular interactions in the polymorphs in terms of H···H interactions is reflected in the distribution of scattered points in the fingerprint plots, which spread only up to $d_i = d_e$ = 1.232 Å in **Form–I**, $d_i = d_e$ = 1.367 Å in **Form–II** and $d_i = d_e$ = 1.237 Å in **Form–III**. The percentages of different types of interactions exhibited by the polymorphs have been included in the decomposed fingerprint plots of the structures (Figs. S3–S5). The Hirshfeld surfaces mapped with d_{norm} corresponding to N···H/H···N, O···H/H···O, C···H/H···C, C···O/O···C, $C_\pi\cdots C_\pi$ and H···H interactions for the polymorphic forms of 2-Amino-3-nitropyridine have been included in Figs. S6–S8.

3.3. Theoretical calculations

3.3.1. Energetic features

We have analyzed the noncovalent interactions involved in the supramolecular packing by executing a computational study using DFT calculations. Studying the energetic properties of noncovalent interactions is our main focus. We have prepared some models of **Form–I, Form–II**, and **Form–III** to evaluate the formation energies of noncovalent interactions. Each monomer unit consists of intramolecular hydrogen bond interaction(s), N(2)–H(2B)···O(1) for **Form–I** and **Form–II**, and N(2)–H(1)···O(2), C(3)–H(3)···O(1), and N(2)–H(1)···N(3) for **Form–III**. The modification of the monomer is not required to omit the intramolecular interaction(s) as the difference between the energy of dimer and monomers calculates the formation energy. In Fig. 7a, the formation energy of N–H···N in **Form–I** is ΔE_1= –5.6 kcal/mol while **Form–II** has ΔE_1= –5.4 kcal/mol (Fig. 7e). The highest formation energy of N–H···N is –9.3 kcal/mol in **Form–III** (Fig. 7h). So, the interaction energies of N–H···N interaction in **Form–III** is –4.7 kcal/mol which is higher compared to **Form–I** (–2.7 kcal/mol), and **Form–II** (–2.7 kcal/mol). The formation energy of N–H···O of **Form–II** is ΔE_1= –5.1 kcal/mol as shown in Fig. 7f. So, the evaluated binding energy is –2.55 kcal/mol. For the same interaction, the binding energy of **Form–I** is ΔE_2= –2.3 kcal/mol (Fig. 7b) which is lower than **Form–II**. However, the interaction energy (–2.1 kcal/mol) due to N–H···O bonding (Formation energy of dimer is –4.2 kcal/mol) in **Form–III** (Fig. 7i) is in between **Form–I** and **Form–II**. Following Fig. 7c, we have computed the formation energy of C–H···O interactions that is –4.0 kcal/mol for **Form–I**. The interaction energy of this interaction is –2.0 kcal/mol for **Form–I** whereas **Form–II** has weaker interaction energy (ΔE_7= –1.1 kcal/mol) (Fig. 7g). The C–H···O interaction in **Form–III** (Fig. 7j) has the least interaction energy (–0.9 kcal/mol) compared to the others. Finally, the formation energy of **Form–I** due to lone pair···π interaction has been calculated. The formation energy is ΔE_4= –0.4 kcal/mol. So, the interaction energy of lone pair···π interaction is –0.2 kcal/mol.

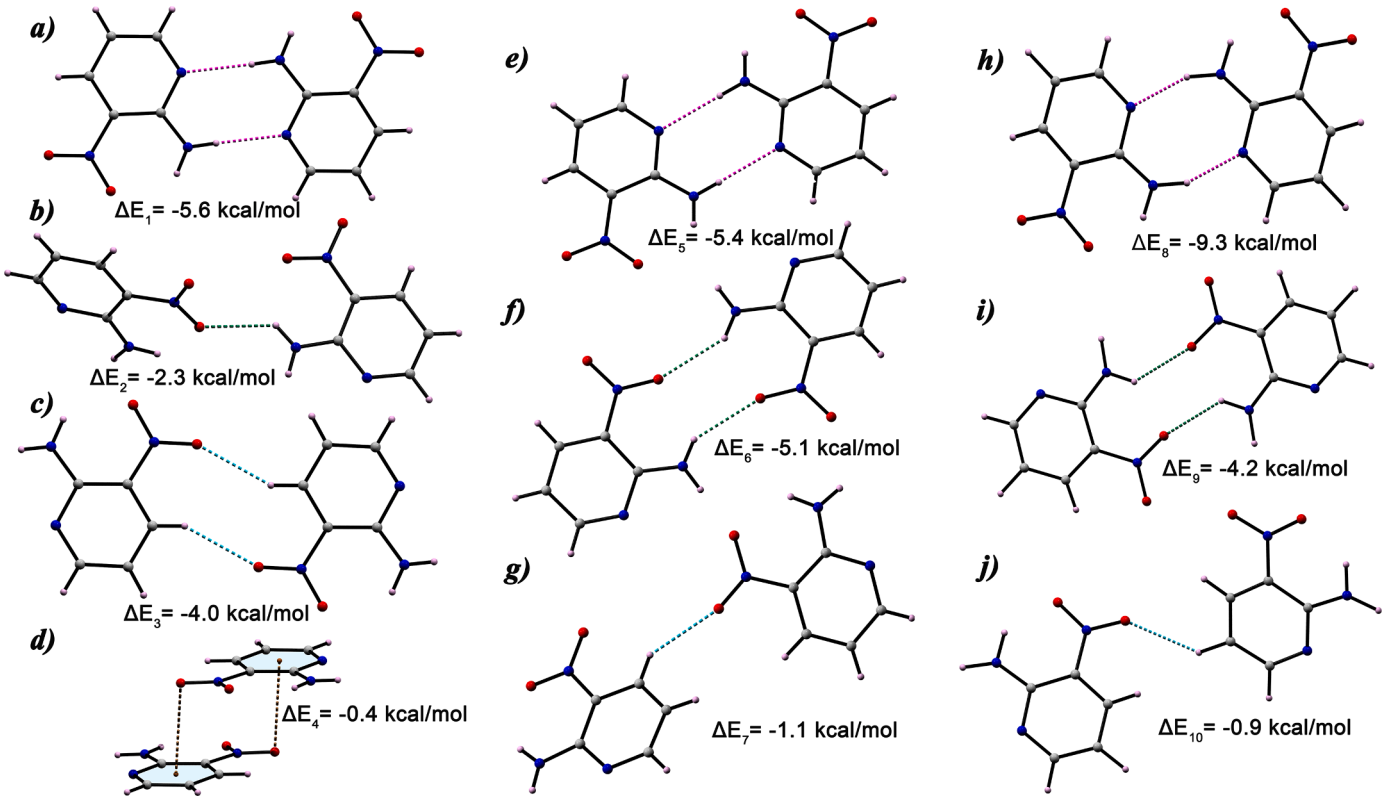

Fig. 7. Different theoretical models used to analyze the energy of noncovalent interactions observed in the supramolecular networks in **Form–I** (a–d), **Form–II** (e–g), and **Form–III**.

3.3.2. Energy decomposition analysis of dimeric molecular pairs in the crystal structures

*3.3.2.1. Molecular pairs in **Form–I**.* For investigating the significant interactions to stabilize the crystal structure in **Form–I**, seven molecular pairs (MPs) have been obtained. The MPs are depicted in Fig. 8, whose interaction energies vary from –47.6 kJ/mol to –2.3 kJ/mol (Table 5). The most stable dimeric unit (MP1) is stabilized through N–H···N, N–H···C and H···H interactions which have interaction energy –47.6 kJ/mol. This dimeric unit MP1 is predominantly electrostatic in nature with an 82% contribution towards stabilization. In MP2, the interaction energy corresponding to C–H···O and H···H interactions is –23.9 kJ/mol.

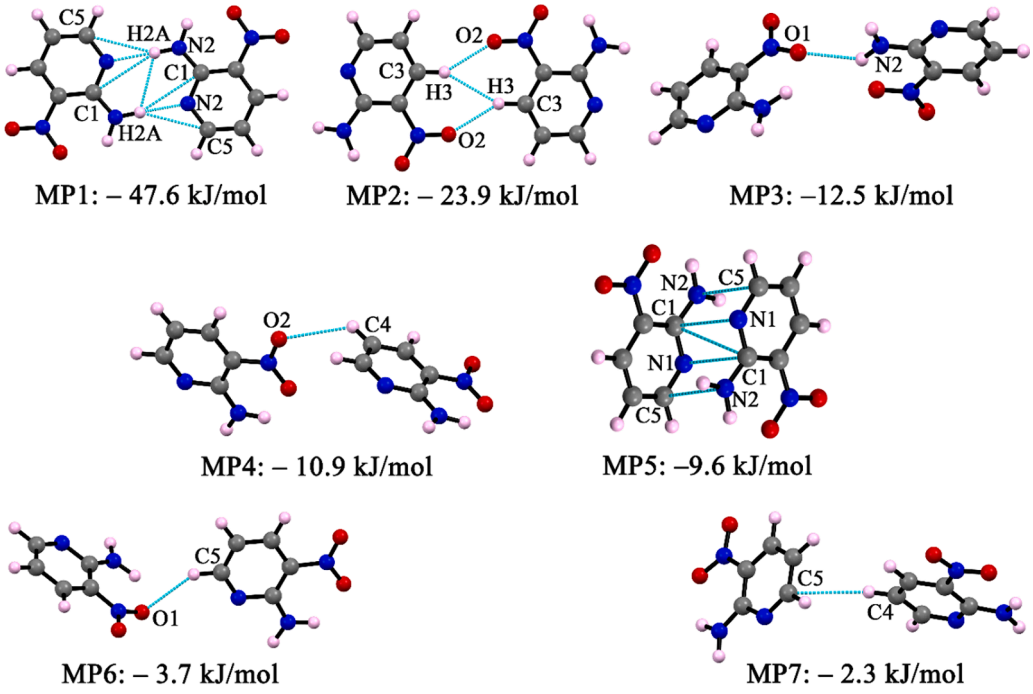

Fig. 8. Molecular dimers observed in the crystal structure in **Form–I**.

Table 5
Interaction energy (kJ/mol) of the molecular pairs of **Form–I, Form–II,** and **Form–III.**

MP(s)	Symmetry Code	Cg··Cg (Å)	E_{Coul}	E_{Pol}	E_{Disp}	E_{Rep}	E_{Total}	Involved Interactions	Geometry (Å, °)
Form–I									
1	1–x, –1–y, –z	6.195	–88.5	–38.6	–27.6	107.2	–47.6	N(2)–H(2A)···N(1)	1.976, 177
								N(2)–H(2A)···C(1)	2.950, 159
								N(2)–H(2A)···C(2)	2.832, 154
2	–x, 1–y, –z	6.833	–24.3	–5.9	–13.5	19.8	–23.9	C(3)–H(3)···O(2)	2.307, 148
								H(3)···H(3)	2.471
3	1–x, 1/2+*y*, 1/2–z	7.586	–12.5	–3.5	–7.5	11.0	–12.5	N(2)–H(2B)···O(1)	2.316, 124
4	x, 1/2–y, –1/2+*z*	7.687	–9.5	–2.7	–7.0	8.2	–10.9	C(4)–H(4)···O(2)	2.775, 120
5	1–x, –y, –z	3.995	–18.3	–5.5	–32.3	46.5	–9.6	C(5)···N(2)	3.301
								C(1)···N(1)	3.308
								C(1)··· C(1)	3.316
6	x, –1/2–y, –1/2+*z*	7.565	–1.5	–1.5	–5.9	5.2	–3.7	C(5)–H(5)···O(1)	2.549, 146
7	–x, –1/2+*y*, –1/2–z	7.680	–1.1	–1.5	–6.6	4.7	–2.3	C(4)–H(4)···C(5)	2.963, 162
Form–II									
1	–1–x, 1–y, –z	6.157	–91.1	–40.2	–28.3	117.9	–41.6	N(2)–H(2A)···N(1)	1.949, 176
								N(2)–H(2A)···C(5)	2.797, 154
								N(2)–H(2A)···C(1)	2.932, 158
								H(2A)··· H(2A)	2.483
2	–x, 2–y, –z	7.286	–32	–8.1	–13.6	25.4	–28.2	N(2)–H(2B)···O(1)	2.175, 141
								O(1)···O(1)	3.056
3	1–x, 1/2+*y*, 1/2–z	7.257	–8.3	–3.4	–9.1	11.3	–9.5	C(3)–H(3)···O(2)	2.395, 127
								C(4)–H(4)···O(2)	2.729, 113
4	1 + *x*, 1+*y*, z	8.481	–6.0	–1.5	–4.0	3.0	–8.5	C(5)–H(5)···O(2)	2.685, 170
5	–1+*x*, y, z	4.903	–8.7	–3.8	–20.5	27.0	–6.0	N(1)···C(3)	3.298
								C(1)···O(2)	3.272
6	x, 1+*y*, z	6.920	–4.4	–2.1	–8.4	9.8	–5.1	C(5)···O(1)	3.245
7	–x, –1/2+*y*, 1/2 –z	5.787	–1.5	–2.4	–13.1	12.5	–4.4	C(4)–H(4)···C(2)	2.990
								C(4)–H(4)···C(3)	2.875
Form–III									
1	1–x, 2–y, 1–z	6.197	–82.2	–36.4	–26.5	101.2	–43.9	N(2)–H(2)···C(5)	2.016, 169
								N(2)–H(2)···N(1)	2.767, 160
2	–x, 1–y, 1–z	7.229	–23.2	–4.5	–12.1	18.8	–20.9	N(2)–H(1)···O(2)	2.460, 118
3	–1/2–x, –1/2+*y*, 3/2–z	7.241	–7.4	–3.1	–9.5	9.7	–10.3	C(4)–H(4)···O(1)	2.505, 128
								H(4)···H(1)	2.498
4	–1 + *x*, –1+*y*, z	8.330	–6.1	–1.9	–4.6	4.5	–8.1	C(5)–H(5)···O(1)	2.652, 153
5	x, –1+*y*, z	7.445	–3.5	–2.0	–7.0	7.8	–4.8	C(5)–H(5)···O(2)	2.631, 122
6	1+*x*, y, z	3.737	–10.2	–6.0	–34.2	47.1	–3.3	C(1)··· C(2)	3.322
								C(5)··· C(3)	3.396
								C(5)··· C(4)	3.338

The intermolecular interaction involved in MP3 is N–H···O interaction which has interaction energy –12.5 kJ/mol. In MP4, the interaction energy of C–H···O has interaction energy –10.9 kJ/mol. The MP2 MP3, and MP4 also show electrostatic in nature with the contribution of 69%, 68%, and 64% respectively. The C···C and C···N contacts stabilize MP5 with interaction energy –9.6 kJ/mol. The electrostatic and dispersion energy contribute around 54% and 46% towards the stabilization of MP5. The MP6 and MP7 exhibit 66% and 72% dispersion energies corresponding to total interaction energies of –3.7 kJ/mol and –2.3 kJ/mol respectively.

*3.3.2.2. Molecular pairs in **Form–II**.* The investigation of interaction energies for the molecular pairs (MPs) revealed seven dimeric units (Fig. 9) for the structure of **Form–II**. The interaction energies range from –41.6 kJ/mol to –4.4 kJ/mol, as summarized in Table 5. The first molecular pair MP1 is generated through N–H···N, N–H···C and H···H interactions (E_{Total}= –41.6 kJ/mol) with a significant contribution of electrostatic energy (82%). This dimeric unit MP2 is also predominantly electrostatic in nature with a 75% contribution toward stabilization. The total interaction energy due to N–H···O and O···O interactions in MP2 is –28.2 kJ/mol. The dimeric unit MP3 and MP are also electrostatic in nature with 56% and 65% contribution respectively. Both dimeric units (MP3 and MP4) are stabilized through C–H···O interactions which have interaction energies – 9.5 kJ/mol and –8.5 kJ /mol, respectively. The N···C and C···O contacts stabilize MP5 with interaction energy –6.0 kJ/mol. The dispersion energy contributes 62% towards the stabilization of MP5. The interaction energies of MP6 and MP7 are –5.1 kJ/mol and –4.4 kJ/mol respectively which are dispersive (57% and 77%, respectively) in nature.

*3.3.2.3. Molecular pairs in **Form–III**.* Six dimeric molecular pairs (MPs) (Fig. 10) are extracted to investigate the interaction energies ranging from –43.9 kJ/mol to –3.3 kJ/mol (Table 5) in **Form–III**. The first

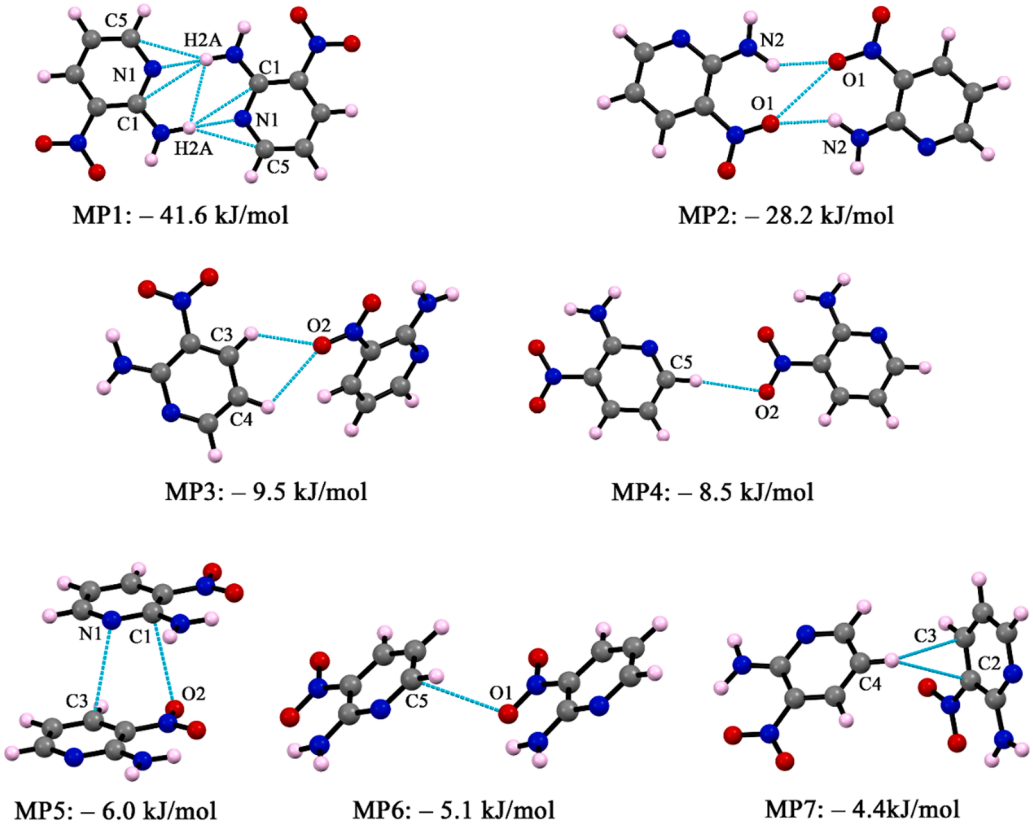

Fig. 9. Molecular dimers observed in the crystal structure in **Form–II**.

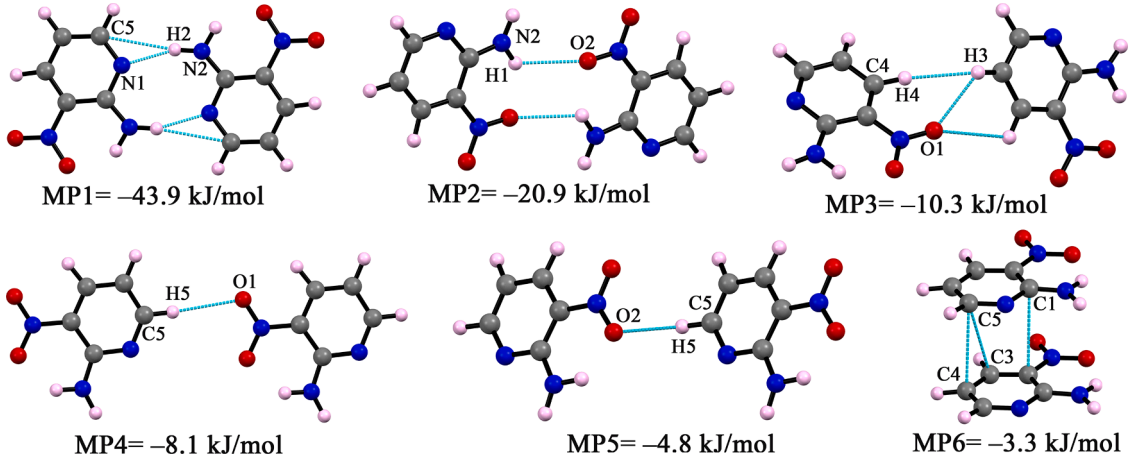

Fig. 10. Molecular dimers observed in the crystal structure in **Form–III**.

molecular pair MP1 is generated through N–H···N, N–H···C interactions (E_{Total} = –43.9 kJ/mol) with significant electrostatic energy (82%) contribution. This second molecular pair (MP2) is stabilized through N–H···O interaction (E_{Total} = –20.9 kJ/mol) which is also predominantly electrostatic (75%) in nature. The dimeric unit MP3 and MP4 are also electrostatic in nature with 53% and 58% contribution respectively whereas MP4 and MP5 are dispersive in nature with 57% and 68% respectively. The C–H···O and H···H contact exhibits –10.3 kJ/mol while the C–H···O interactions in MP4 and MP5 obtain –8.1 kJ/mol and –4.8 kJ/mol, respectively. The molecular pair MP6 is stabilized through C···C interactions which contribute –10.3 kJ/mol.

3.3.3. Lattice energies

The lattice energies for the crystal structure of all the polymorphs have been calculated (Table 6) showing the overall contribution of electrostatic and dispersion energy components towards stabilizing the structures. Both polymorphs show higher electrostatic energy compared to dispersion energy. The percentage of electrostatic energies of **Form–I, Form–II,** and **Form–III** are 58.4%, 58.9%, and 55.0% respectively.

Table 6
Calculated lattice energy (kJ/mol) for **Form–I** and **Form–II**.

Polymorphs	E_{Coul}	E_{Pol}	E_{Disp}	E_{Rep}	E_{Total}
Form–I	–102.9	–35.5	–98.6	156.6	–80.4
Form–II	–100.6	–35.7	–95.2	153.7	–77.7
Form–III	–85.0	–32.2	–96.0	141.5	–71.7

3.3.4. QTAIM calculation

The fragments from molecular assemblies (Fig. 11) used in theoretical DFT calculation (Fig. 7) are again considered to analyze the non-covalent interactions by Bader's theory of "atoms in molecules". Application of QTAIM approach to **Form–I** & **Form–II** results in the bond paths between two atoms involved in the interaction along with (3, –1) bond critical points. Evaluation of topological parameters at BCPs reveals the dissociation energy of the individual interaction (Table 7). In **Form–I**, the centrosymmetric dimeric ring generated through N–H···N interaction shows the highest electron density (ρ_{BCP} = 0.0200 a.u.) and dissociation energy (D_E = 4.016 kcal/mol) at the bond critical points (denoted as 'A' in Fig. 11a) among all other intermolecular interactions. The electron density and dissociation energy corresponding to the intermolecular N–H···O interaction (denoted as 'C' in Fig. 11b) are ρ_{BCP} = 0.0087 a.u. and D_E = 1.802 kcal/mol. Again, the lower value of ρ_{BCP} and D_E corresponding to the C–H···O bond (denoted as 'D' in Fig. 11c) signifies the interaction to be less favorable than other hydrogen bond interactions. The contributions of all three intermolecular bonds analyzed by QTAIM theory are in the same order of robustness as derived in DFT calculation. The connecting bond path between oxygen and aryl ring carbon atom characterizes lone-pair···π interaction. In **Form–I**, lone-pair···π interaction can be considered as more favorable than π···π interaction as the former has the higher electron density and dissociation energy at the bond critical point (see Table 7). Eventually, the small positive values of electron density (ρ(r)), Laplacian of electron

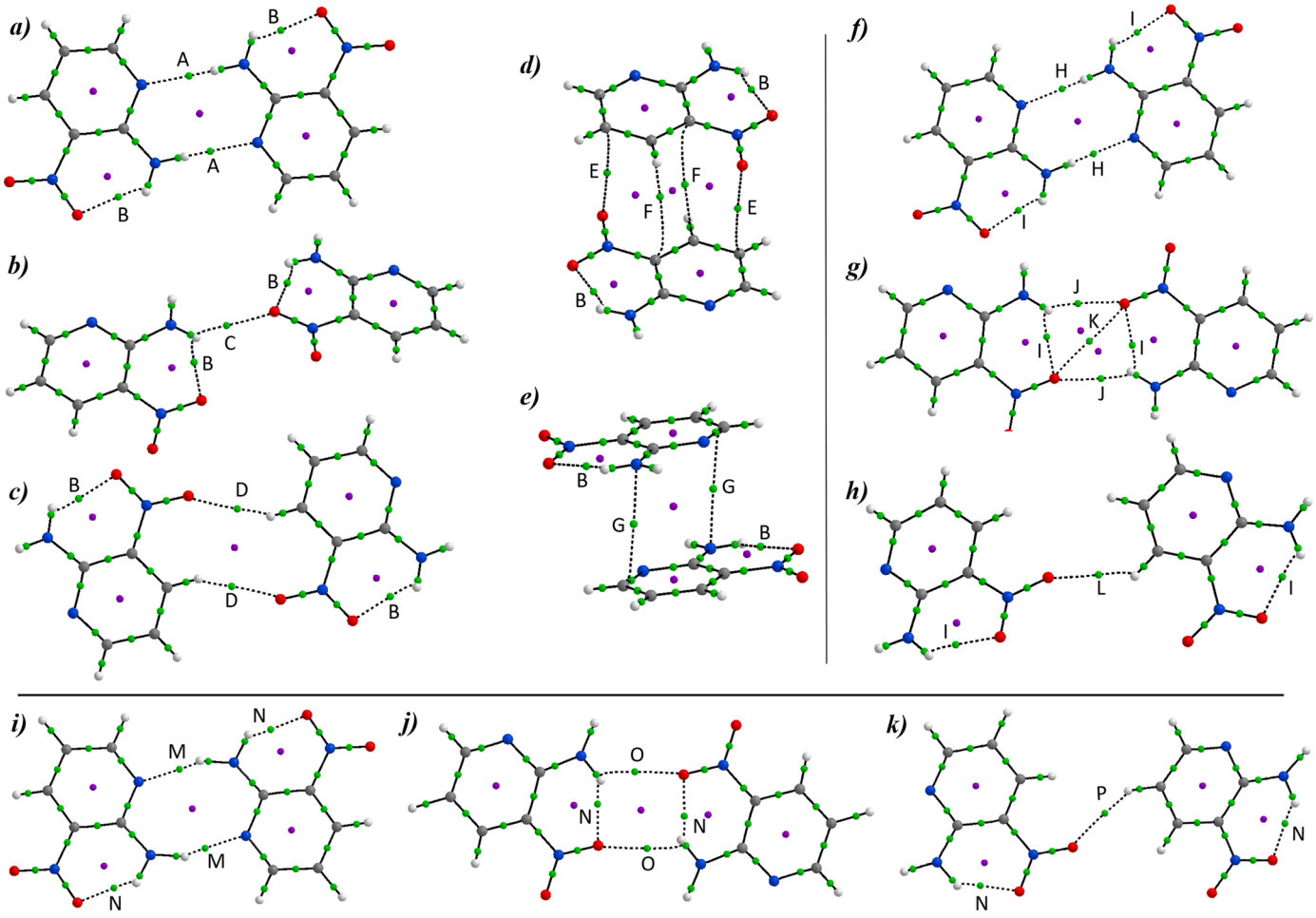

Fig. 11. Distribution of bond critical points in different dimers in **Form–I** (a-e), **Form–II** (f-h), and **Form–III** (i-k). Green dots indicate bond critical points (BCPs).

Table 7
Topological parameters for noncovalent interactions (in different dimers of **Form–I, Form–II,** and **Form–III**) at their (3, −1) BCPs. [$\rho(r)$: electron density (a.u); $\nabla^2\rho(r)$: Laplacian of electron density (a.u); $V(r)$: potential energy density; $G(r)$: kinetic energy density; $H(r)$: total electronic density; $V(r)$, $G(r)$ and $H(r)$ values in a.u. and D_E in kcal/mol].

Interactions	BCPs	$\rho(r)$	$\nabla^2\rho(r)$	$V(r)$	$G(r)$	$\frac{\lvert V(r)\rvert}{G(r)}$	$H(r)$	D_E
Form–I								
N(2)−H(2A)···N(1)	A	0.0200	0.0741	–0.0128	0.0156	0.8205	0.0028	4.016
	A	0.0200	0.0741	–0.0128	0.0156	0.8205	0.0028	4.016
Intra (N−H···O)	B	0.0224	0.1021	–0.0174	0.0215	0.8093	0.0041	5.459
	B	0.0224	0.1021	–0.0174	0.0215	0.8093	0.0041	5.459
N(2)−H(2B)···O(1)	C	0.0087	0.0380	–0.0058	0.0076	0.7632	0.0018	1.820
C(3)−H(3)···O(2)	D	0.0078	0.0309	–0.0047	0.0062	0.7581	0.0015	1.475
	D	0.0078	0.0309	–0.0047	0.0062	0.7581	0.0015	1.475
lone-pair···π	E	0.0052	0.0156	–0.0028	0.0034	0.8235	0.0006	0.879
	E	0.0052	0.0156	–0.0028	0.0034	0.8235	0.0006	0.879
π···π	F	0.0040	0.0115	–0.0017	0.0023	0.7391	0.0006	0.533
	F	0.0040	0.0115	–0.0017	0.0023	0.7391	0.0006	0.533
π···π	G	0.0065	0.0188	–0.0034	0.0041	0.8293	0.0007	1.067
	G	0.0065	0.0188	–0.0034	0.0041	0.8293	0.0007	1.067
Form–II								
N(2)−H(2A)···N(1)	H	0.0212	0.0788	–0.0139	0.0168	0.8274	0.0029	4.361
	H	0.0212	0.0788	–0.0139	0.0168	0.8274	0.0029	4.361
Intra (N−H···O)	I	0.0228	0.1046	–0.0179	0.0220	0.8136	0.0041	5.616
	I	0.0228	0.1046	–0.0179	0.0220	0.8136	0.0041	5.616
N(2)−H(2B)···O(1)	J	0.0094	0.0438	–0.0063	0.0086	0.7326	0.0023	1.977
	J	0.0094	0.0438	–0.0063	0.0086	0.7326	0.0023	1.977
Intra (O···O)	K	0.0057	0.0245	–0.0043	0.0052	0.8269	0.0009	1.349
C(3)−H(3)···O(2)	L	0.0075	0.0310	–0.0048	0.0063	0.7619	0.0015	1.506
Form–III								
N(2)−H(1)···N(1)	M	0.0288	0.0820	–0.0196	0.0200	0.9800	0.0004	6.150
	M	0.0288	0.0820	–0.0196	0.0200	0.9800	0.0004	6.150
Intra (N−H···O)	N	0.0308	0.1253	–0.0259	0.0286	0.9056	0.0027	8.126
	N	0.0308	0.1253	–0.0259	0.0286	0.9056	0.0027	8.126
N(2)−H(1)···O(2)	O	0.0078	0.0325	–0.0053	0.0067	0.7910	0.0014	1.663
	O	0.0078	0.0325	–0.0053	0.0067	0.7910	0.0014	1.663
Intra (N−H···O)	N	0.0305	0.1250	–0.0257	0.0285	0.9018	0.0028	8.063
	N	0.0305	0.1250	–0.0257	0.0285	0.9018	0.0028	8.063
C(4)−H(4)···O(1)	P	0.0092	0.0317	–0.0067	0.0068	0.9853	0.0001	2.102
Intra (N−H···O)	N	0.0306	0.1245	–0.0256	0.0284	0.9014	0.0028	8.032
	N	0.0306	0.1245	–0.0256	0.0284	0.9014	0.0028	8.032

density ($\nabla^2\rho(r)$) and H(r), and $\frac{|V(r)|}{G(r)} < 1$ classify the interaction as "closed-shell" in nature according to Gatti's assignment [60].

Again, in **Form–II**, N−H···N (denoted as 'H' in Fig. 11f) interaction contributes significantly in stabilizing the crystal structure as it has the highest electron density ($\rho_{BCP} = 0.0212$ a.u.) and dissociation energy ($D_E = 4.361$ kcal/mol) at its bond critical point out of all intermolecular interactions. The ρ(r) and D_E value of N−H···O (denoted as 'J' in Fig. 11g) forming a dimeric ring signifies that N−H···N is more favorable than N−H···O interaction which agrees well with the result of the DFT study. Besides, C−H···O interaction shows the least value of ρ(r) (0.0075 a.u.) and D_E (1.506 kcal/mol) as anticipated from interaction energy calculation. Moreover, all interactions in **Form-II** are closed-shell interactions considering (ρ(r))>0, $\nabla^2(r)$>0, H(r) >O and $\frac{|V(r)|}{G(r)} < 1$.

Similarly, in **Form–III**, a centrosymmetric dimeric ring is generated through N−H···N interaction having the highest electron density ($\rho_{BCP} = 0.0288$ a.u., denoted as 'M') which is also greater than that of **Form–I** and **Form–II**. Again, likely in **Form–II, Form–III** exhibits a centrosymmetric dimer through N−H···O interaction. The electron density and dissociation energy at the BCP (denoted by 'O') of N−H···O interaction are 0.0078 a.u. and 1.663 kcal/mol. Lastly, C−H···O interaction exhibits a greater value of electron density (0.0092 a.u., denoted by 'P') and dissociation energy (2.102 kcal/mol) than N−H···O interaction. This is because of larger bond length of C−H (1.142 Å) from normal C−H (0.93 Å) bond length (collected from CCDC (AMNTPY02) [41]) Moreover, all interactions in **Form–III** are closed-shell interactions considering (ρ(r))>0, $\nabla^2(r)$>0, H(r) >0, and $\frac{|V(r)|}{G(r)} < 1$.

3.3.5. *NCI plot index*

Furthermore, we have analyzed and characterized the noncovalent interactions involved in the supramolecular assemblies by the "noncovalent interaction" (NCI) plot index. The same models have been used in QTAIM calculation. The interactions are represented by the isosurfaces which are differentiated by a color scheme with a red-yellow-green-blue scale. For **Form–I**, and **Form–II,** N−H···N interactions are represented by two greenish-blue isosurfaces (indicated by arrows) and greenish-blue spike in RDG vs sign($\lambda_2\rho$) graph in Fig. 12a, 12f, respectively. The blue isosurfaces and the blue spike in the scattered graph (in Fig. 12i) confirm the presence of strong hydrogen bond (N−H···N) interactions in **Form–III**. Again, N−H···O interaction in **Form–I** is shown by a small green isosurface in Fig. 12b. As N−H···O interaction forms a dimeric ring in **Form–II**, and **Form–III,** two green isosurfaces illustrate the N−H···O interactions in the mentioned form (Fig. 12g, j). Similarly, C−H···O interactions constituting a dimeric ring in **Form–I** are depicted as small green isosurfaces (Fig. 12c) whereas a single C−H···O interaction in **Form–II,** and **Form–III** is represented by just one small green isosurface (Fig. 12h, k). All N−H···O and C−H···O interactions are also represented by green spikes in the respective RDG vs sign($\lambda_2\rho$) scattered graph. In **Form–I**, lone pair···π interaction is represented by an extended isosurface in Fig. 12d. In Fig. 12e, π···π interaction is characterized by the stretched green isosurface in **Form–I**. The green spikes in the scattered plots in Fig. 12d and Fig. 12e further confirm the presence of weak noncovalent interactions. Lastly, all the prominent isosurfaces and their respective spikes in RDG vs sign($\lambda_2\rho$) graph analyzed by the NCI plot index verified the existence of these noncovalent interactions observed in structural and other theoretical studies.

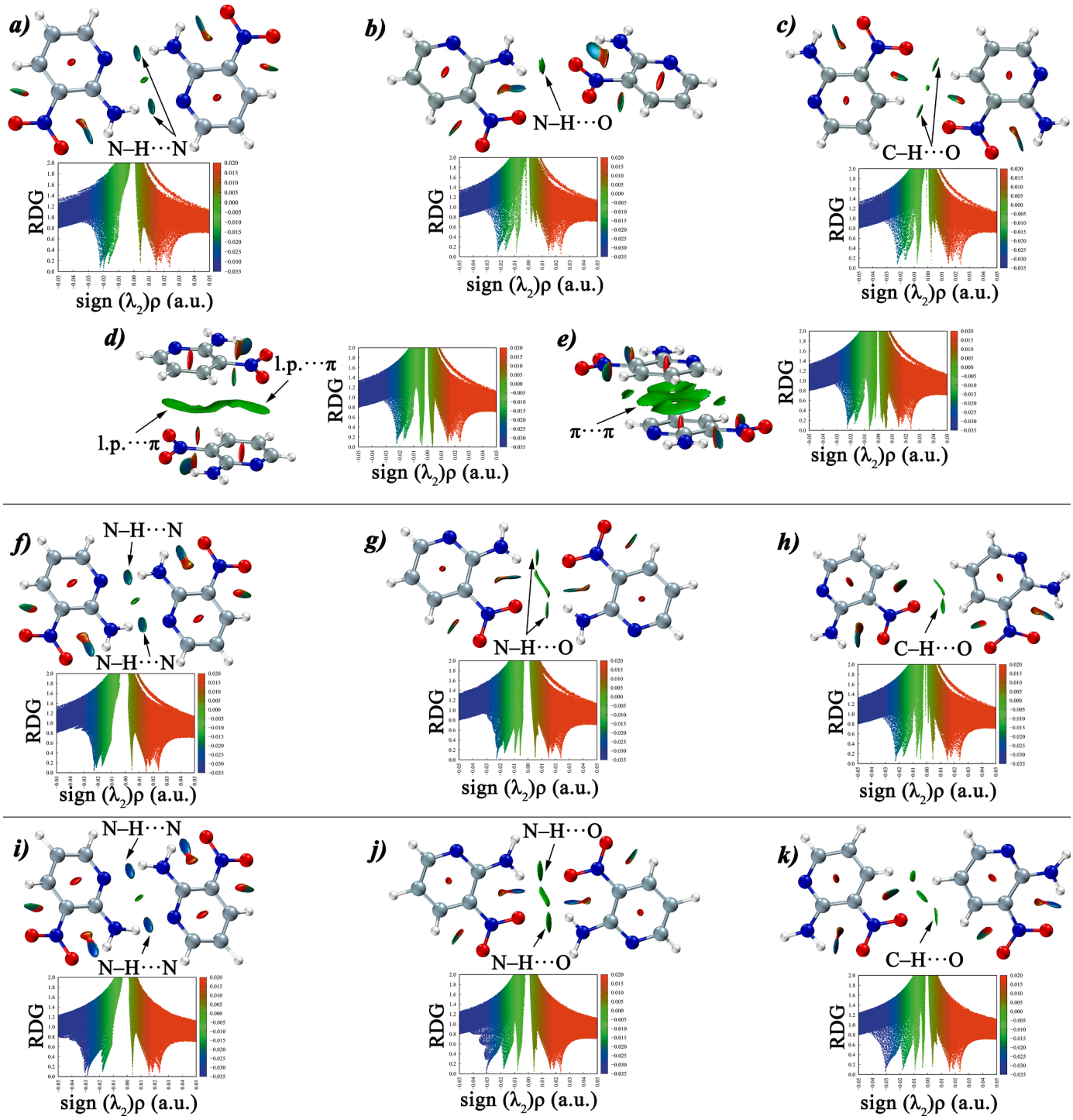

Fig. 12. NCI plot of different noncovalent interactions observed in **Form–I** (a-e), **Form–II** (f-h), and **Form–III** (i-k).

4. Conclusions

In conclusion, the polymorphic forms of 2-amino-3-nitropyridine have been reported in the context of an interesting case study of packing polymorphism. A comparison of polymorphic structures (**Form–I** and **Form–II**) with previously reported **Form–III** that is retrieved from CSD has been presented. The present study highlights the importance of exploring intermolecular interactions through the Hirshfeld surface to screen polymorphs. The Hirshfeld surface analyses indicated a cooperative understanding at the intermolecular level; two crystalline forms are indicated to stabilize through the diverse contribution from intermolecular interactions. The interaction energies of non-covalent interactions are analyzed through theoretical DFT calculations and further analyzed through the PIXEL method. The PIXEL method obtains more precise interaction energy with detailed energy decomposition. From energy decomposition analysis, it is found that high interaction energy is due to electrostatic interaction where the higher dispersive interaction leads to lower interaction energy. The lattice energies of the polymorphs are also analyzed through PIXEL method. The noncovalent interactions are further analyzed through Bader's theory of 'Atoms in molecule' (QTAIM) and 'Noncovalent Interaction' (NCI) plot index. The topological parameters and energetic features at the (3, −1) bond

critical point suggest that all interactions are "closed-shell" interactions. Theoretical analyses of noncovalent interactions are in good agreement with the experimental findings. This approach can be helpful in crystal engineering to explore rapid quantitative insight into the intermolecular interactions and designing of novel organic materials.

CRediT authorship contribution statement

Samiul Islam: Software, Data curation, Methodology, Formal analysis, Investigation, Writing – original draft, Writing – review & editing. **Pratik Dey:** Software, Data curation, Investigation, Validation, Writing – original draft, Writing – review & editing. **Prantika Das:** Software, Investigation. **Saikat Kumar Seth:** Project administration, Conceptualization, Supervision, Writing – review & editing.

Declaration of Competing Interest

The authors declare no competing interest.

Data availability

Data will be made available on request.

Acknowledgments

S. Islam thankfully acknowledges the University Grants Commission (Ref. No.: 1528/CSIR-UGC NET JUNE 2019) for a Senior Research Fellowship. P. Dey is gratefully thankful to the Council of Scientific and Industrial Research (CSIR), New Delhi (CSIR FILE NO.: 09/0096 (11350)/2021-EMR-I) for providing Junior Research Fellowship. P. Das cordially acknowledges the Department of Science and Technology (Govt. of India) for DST-INSPIRE fellowship (DST/INSPIRE Fellowship/2019/IF190666). The financial support from Science and Engineering Research Board (New Delhi, India) for Research Project (EEQ/2019/000384) is gratefully acknowledged by S. K. Seth.

Supplementary materials

Supplementary material associated with this article can be found, in the online version, at doi:10.1016/j.molstruc.2023.136253.

References

[1] J. Bernstein, Polymorphism in Molecular Crystals, Clarendon Press, Oxford UK, 2002.
[2] G.R. Desiraju, Crystal engineering: a holistic view, Angew. Chem. Int. Ed. 46 (2007) 8342–8356.
[3] R. Hilfiker, Polymorphism in the Pharmaceutical Industry, Wiley-VCH, Weinheim, 2006.
[4] J. Bernstein, Polymorphism – a perspective, Cryst. Growth Des. 11 (2011) 632–650.
[5] R.J. Davey, Pizzas, polymorphs and pills, Chem. Commun (2003) 1463–1467.
[6] J. Bernstein, Polymorphism in Molecular Crystals, International Union of Crystal, 2010.
[7] D. Braga, F. Grepioni, L. Maini, The growing world of crystal forms, Chem. Commun. 46 (2010) 6232–6242.
[8] J. Wouters, L. Quere, in: Pharmaceutical Salts and Co-crystals, Royal Society of Chemistry, Cambridge UK, 2011.
[9] H.G. Brittain, Polymorphism and solvatomorphism 2006, J. Pharm. Sci. 97 (2008) 3611–3636.
[10] J.O. Henck, U.J. Griesser, A. Burger, Polymorphie von Arzneistoffen. Eine wirtschaftliche Herausforderung, Pharm. Ind. 59 (1997) 165–169.
[11] A.J. Cruz-Cabeza, J. Bernstein, Conformational polymorphism, Chem. Rev. 114 (2014) 2170–2191.
[12] K. Fucke, N. Qureshi, D.S. Yufit, J.A.K. Howard, J.W. Steed, Hydrogen bonding is not everything: extensive polymorphism in a system with conserved hydrogen bonded synthons, Cryst. Growth Des. 10 (2010) 880–886.
[13] S.L. Price, Why don't we find more polymorphs? Acta Crystallogr. B. Struct. Sci. Cryst. Eng. Mater. 69 (2013) 313–328.
[14] S.L. Price, From crystal structure prediction to polymorph prediction: interpreting the crystal energy landscape, Phys. Chem. Chem. Phys. 10 (2008) 1996–2009.
[15] A.J. Cruz-Cabeza, S.M. Reutzel-Edens, J. Bernstein, Facts and fictions about polymorphism, Chem. Soc. Rev. 44 (2015) 8619–8635.
[16] J.M. Lehn, Perspectives in chemistry—steps towards complex matter, Angew. Chem. Int. Ed. 52 (2013) 2836–2850.
[17] R.F. Ludlow, S. Otto, Systems chemistry, Chem. Soc. Rev. 37 (2008) 101–108.
[18] J. Vicens, Q. Vicens, Origins and emergences of supramolecular chemistry, J. Incl. Phenom. Macrocycl. Chem. 65 (2009) 221–235.
[19] J.D. Dunitz, A. Gavezzotti, How molecules stick together in organic crystals: weak intermolecular interactions, Chem. Soc. Rev. 38 (2009) 2622–2633.
[20] M.C. Etter, Encoding and decoding hydrogen-bond patterns of organic compounds, Acc. Chem. Res. 23 (1990) 120–126.
[21] G.R. Desiraju, Supramolecular synthons in crystal engineering–a new organic synthesis, Angew. Chem. Int. Ed. Engl. 34 (1995) 2311–2327.
[22] C.A. Hunter, Quantifying intermolecular interactions: guidelines for the molecular recognition toolbox, Angew. Chem. Int. Ed. 43 (2004) 5310–5324.
[23] M.A. Spackman, J.J. McKinnon, Fingerprinting intermolecular interactions in molecular crystals, CrystEngComm 4 (2002) 378–392.
[24] S.K. Seth, The importance of CH···X (X = O, π) interaction of a new mixed ligand Cu(II) coordination polymer: structure, Hirshfeld surface and theoretical studies, Crystals 08 (2018) 455.
[25] S.K. Seth, D. Sarkar, A.D. Jana, On the Possibility of tuning molecular edges to direct supramolecular self-assembly in coumarin derivatives through cooperative weak forces: crystallographic and Hirshfeld surface analyses, Cryst. Growth Des. 11 (2011) 4837–4849.
[26] A.L. Rohl, M. Moret, W. Kaminsky, K. Claborn, J.J. Mckinnon, B. Kahr, Hirshfeld surfaces identify inadequacies in computations of intermolecular interactions in crystals: pentamorphic 1,8-Dihydroxyanthraquinone, Cryst. Growth Des. 8 (2008) 4517–4525.
[27] A. Siddiqui-Jain, J.P. Hoj, D.W. Cescon, M.D. Hansen, Pharmacology and *in vivo* efficacy of pyridine-pyrimidine amides that inhibit microtubule polymerization, Bioorg. Med. Chem 28 (2018) 934–941.
[28] J. Stankevičiūtė, J. Vaitekūnas, V. Petkevičius, R. Gasparavičiūtė, D. Tauraitė, R. Meškys, Oxyfunctionalization of pyridine derivatives using whole cells of Burkholderia sp, MAK1, Sci. Rep. 6 (2016) 39129.
[29] H. Koshima, M. Hamada, I. Yagi, K. Uosaki, Synthesis, structure, and second-harmonic generation of noncentrosymmetric cocrystals of 2-amino-5-nitropyridine with achiral benzenesulfonic acids, Cryst Growth Des 1 (2001) 467–471.
[30] P. Dey, S. Islam, S.K. Seth, Quantitative analysis of the interplay of hydrogen bonds in M (II)-hexaaqua complexes with HMTA [M (II)= Co (II), Mg (II); HMTA= hexamethylenetetramine], J. Mol. Struct. 1284 (2023), 135448.
[31] D. Dey, S.K. Seth, T.P. Mohan, D. Chopra, Quantitative analysis of intermolecular interactions in crystalline substituted triazoles, J. Mol. Struct. 1273 (2023), 134380.
[32] R.F. Bader, Atoms in molecules, Acc. Chem. Res. 18 (1985) 9–15.
[33] S. Islam, P. Dey, S.K. Seth, A combined experimental and theoretical studies of two new Co (II)–PDA complexes: unusual 2D and 3D supramolecular networks [PDA= 2, 6-pyridinedicarboxylic acid], Polyhedron 242 (2023), 116514.
[34] V.C. Tellez, B.S. Gaytan, S. Bernes, E.G. Vergara, The supramolecular structure of pyridine-2,6-dicarboxylic acid, Acta Crystallogr. Sect. C Cryst. Struct. Commun. 58 (2002) o228–o230.
[35] BrukerSAINT, Version 6.36a, Bruker AXS Inc., Madison, Wisconsin, USA, 2002.
[36] BrukerSMART, Version 5.625 and SADABS, Version 2.03a, Bruker AXS Inc., Madison, Wisconsin, USA, 2001.
[37] G.M. Sheldrick, SHELXS97 and SHELXL97: Programs For Crystal Structure Solution and Refinement, University of Göttingen, Germany, 1997.
[38] A.L. Spek, PLATON, A Multipurpose Crystallographic Tool, Utrecht University, Utrecht, The Netherlands, 2000.
[39] L.J. Farrugia, WinGX suite for small-molecule single-crystal crystallography, J. Appl. Cryst. 32 (1999) 837–838.
[40] R. Destro, T. Pilati, M. Simonetta, 2-Amino-3-nitropyridine, Acta. Crystallogr. B. Struct. Sci. Cryst. Eng. Mater. 31 (1975) 2883–2885.
[41] C.B. Aakeröy, A.M. Beatty, M. Nieuwenhuyzen, M. Zou, A structural study of 2-amino-5-nitropyridine and 2-amino-3-nitropyridine: intermolecular forces and polymorphism, J. Mater. Chem. 8 (1998) 1385–1389.
[42] J.J. McKinnon, M.A. Spackman, A.S. Mitchell, Novel tools for visualizing and exploring intermolecular interactions in molecular crystals, Acta Crystallogr. Sect. B: Struct. Sci. 60 (2004) 627–668.
[43] S.K. Wolff, D.J. Grimwood, J.J. McKinnon, D. Jayatilaka, M.A. Spackman, CrystalExplorer 2.1, University of Western Australia, Perth, Australia, 2007.
[44] M.J. Frisch, G.W. Trucks, H.B. Schlegel, G.E. Scuseria, M.A. Robb, J.R. Cheeseman, G. Scalmani, V. Barone, G.A. Petersson, H. Nakatsuji, X. Li, M. Caricato, A. V. Marenich, J. Bloino, B.G. Janesko, R. Gomperts, B. Mennucci, H.P. Hratchian, J. V. Ortiz, A.F. Izmaylov, J.L. Sonnenberg, D. Williams-Young, F. Ding, F. Lipparini, F. Egidi, J. Goings, B. Peng, A. Petrone, T. Henderson, D. Ranasinghe, V. G. Zakrzewski, J. Gao, N. Rega, G. Zheng, W. Liang, M. Hada, M. Ehara, K. Toyota, R. Fukuda, J. Hasegawa, M. Ishida, T. Nakajima, Y. Honda, O. Kitao, H. Nakai, T. Vreven, K. Throssell, J.A. Montgomery Jr., J.E. Peralta, F. Ogliaro, M. J. Bearpark, J.J. Heyd, E.N. Brothers, K.N. Kudin, V.N. Staroverov, T.A. Keith, R. Kobayashi, J. Normand, K. Raghavachari, A.P. Rendell, J.C. Burant, S.S. Iyengar, J. Tomasi, M. Cossi, J.M. Millam, M. Klene, C. Adamo, R. Cammi, J.W. Ochterski, R.L. Martin, K. Morokuma, O. Farkas, J.B. Foresman, D.J. Fox, Gaussian 16, Revision C.01, Gaussian, Inc., Wallingford, CT, 2016.
[45] A. Gavezzotti, Efficient computer modeling of organic materials. The atom-atom, Coulomb–London–Pauli (AA-CLP) model for intermolecular electrostatic-polarization, dispersion and repulsion energies, New J. Chem. 35 (2011) 1360.

[46] R.F. Bader, A quantum theory of molecular structure and its applications, Chem. Rev. 91 (1991) 893–928.
[47] T.A. Keith, AIMAll, Version 13.05.06, TK Gristmill Software, Overland Park, KS, USA, 2013.
[48] P. Dhanishta, S.K. Mishra, N. Suryaprakash, Intramolecular HB interactions evidenced in dibenzoyl oxalamide derivatives: NMR, QTAIM, and NCI Studies, J. Phys. Chem. A 122 (2018) 199–208.
[49] N.S. Venkataramanan, A. Suvitha, Nature of bonding and cooperativity in linear DMSO clusters: a DFT, AIM and NCI analysis, J. Mol. Graph. Model. 81 (2018) 50–59.
[50] N. Kumar, S. Saha, G.N. Sastry, Towards developing a criterion to characterize noncovalent bonds: a quantum mechanical study, Phys. Chem. Chem. Phys. 23 (2021) 8478–8488.
[51] C.S. Liu, P.Q. Chen, E.C. Yang, J.L. Tian, X.H. Bu, Z.M. Li, H.W. Sun, Z. Lin, Silver (I) complexes in coordination supramolecular system with bulky acridine-based ligands: syntheses, crystal structures, and theoretical investigations on C−H···Ag close interaction, Inorg. Chem. 45 (2006) 5812–5821.
[52] J. Contreras-García, E.R. Johnson, S. Keinan, R. Chaudret, J.P. Piquemal, D. N. Beratan, W. Yang, NCIPLOT: a program for plotting noncovalent interaction regions, J. Chem. Theory Comput. 7 (2011) 625–632.
[53] E.R. Johnson, S. Keinan, P. Mori-Sánchez, J. Contreras-García, A.J. Cohen, W. Yang, Revealing non-covalent interactions, J. Am. Chem. Soc. 132 (2010) 6498–6506.
[54] L.J. Farrugia, ORTEP-III (Version 1.06), Department of Chemistry, University of Glasgow, Scotland, UK, 2023.
[55] S.K. Seth, D. Sarkar, T. Kar, Use of π–π forces to steer the assembly of chromone derivatives into hydrogen bonded supramolecular layers: crystal structures and Hirshfeld surface analyses, CrystEngComm 13 (2011) 4528–4535.
[56] S.K. Seth, P. Manna, N.J. Singh, M. Mitra, A.D. Jana, A. Das, S.R. Choudhury, T. Kar, S. Mukhopadhyay, K.S. Kim, Molecular architecture using novel types of noncovalent π-interactions involving aromatic neutrals, aromatic cations and π-anions, CrystEngComm 15 (2013) 1285–1288.
[57] P. Manna, S.K. Seth, M. Mitra, A. Das, N.J. Singh, S.R. Choudhury, T. Kar, S. Mukhopadhyay, A successive layer-by-layer assembly of supramolecular frameworks driven by a novel type of face-to-face π^{+}–π^{+} interactions, CrystEngComm 15 (2013) 7879–7886.
[58] S.K. Seth, I. Saha, C. Estarellas, A. Frontera, T. Kar, S. Mukhopadhyay, Supramolecular self-assembly of M-IDA complexes involving lone-pair···π interactions: crystal structures, Hirshfeld surface analysis, and DFT calculations [H_2IDA = iminodiacetic acid, M = Cu(II), Ni(II)], Cryst. Growth Des 11 (2011) 3250–3265.
[59] S.K. Seth, B. Dey, T. Kar, S. Mukhopadhyay, Experimental observation of supramolecular carbonyl–π/π–π/π–carbonyl assemblies of Cu^{II} complex of iminodiacetate and dipyridylamine, J. Mol. Struct. 973 (2010) 81–88.
[60] C. Gatti, Chemical bonding in crystals: new directions, Z. Krist. -Cryst. Mater. 132 (2010) 6498–6506.

Supporting Information

for

Quantitative investigations of intermolecular interactions in 2-Amino-3-nitropyridine polymorphs: Inputs from quantum mechanical calculations

Samiul Islam, Pratik Dey, Prantika Das, Saikat Kumar Seth*

Department of Physics, Jadavpur University, Kolkata 700032, India.

*Corresponding author E-mail: saikatk.seth@jadavpuruniversity.in

*Corresponding author ORCID ID: 0000-0003-4904-6926

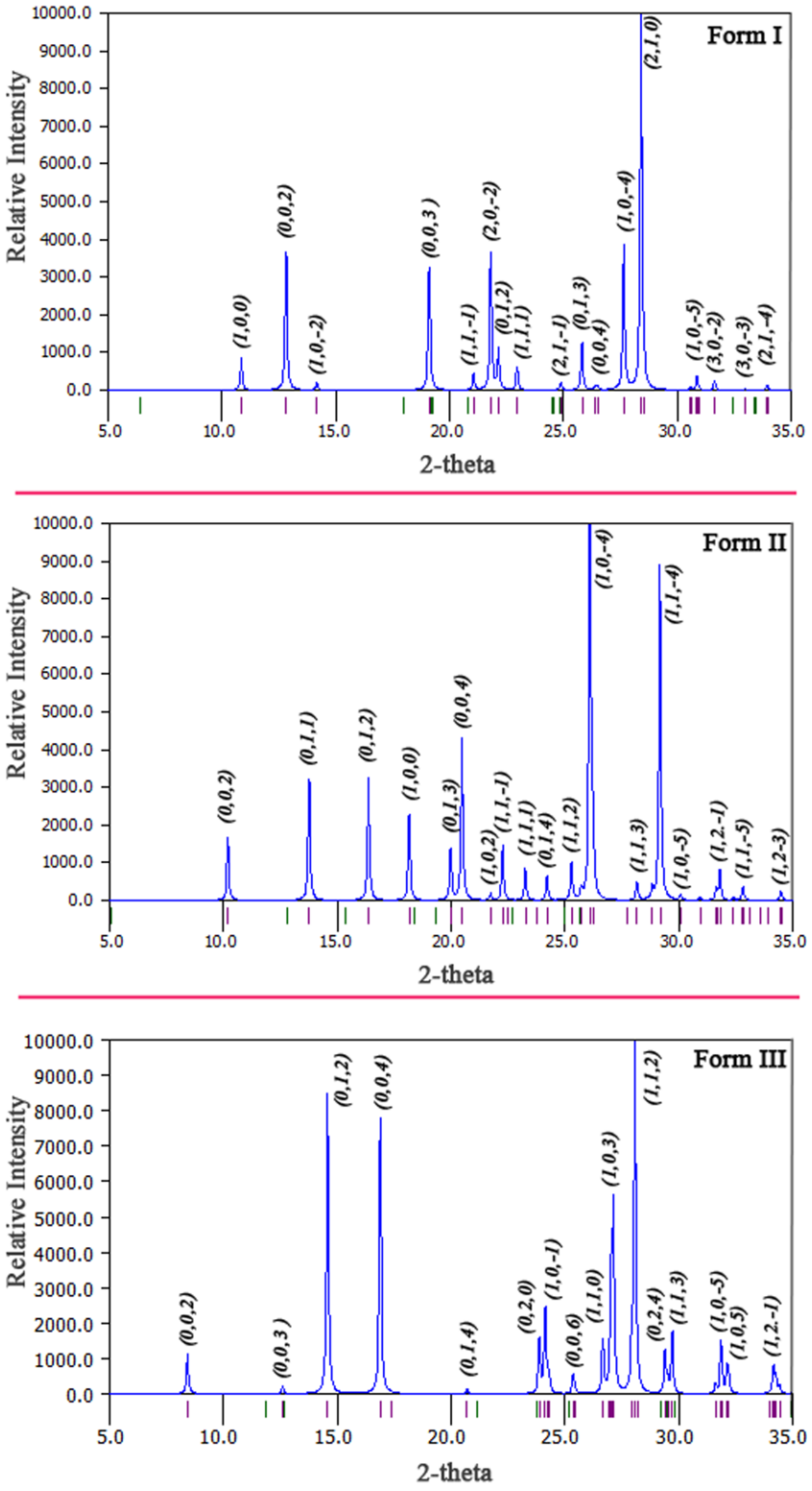

Fig. S1. Simulated PXRD pattern of **Form−I, Form−II,** and **Form−III.**

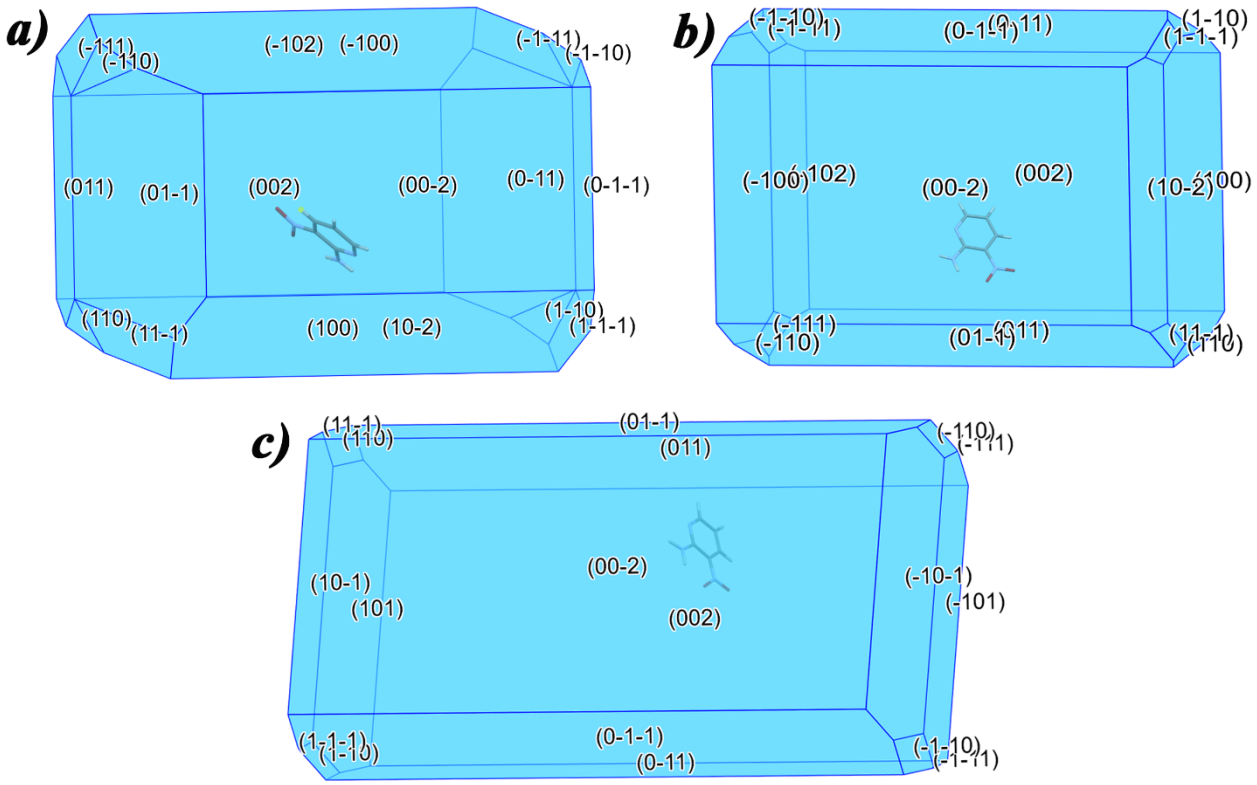

Fig. S2 The BFDH morphology of the polymorphic (a) **Form−I,** (b) **Form−II,** and (c) **Form−III.**

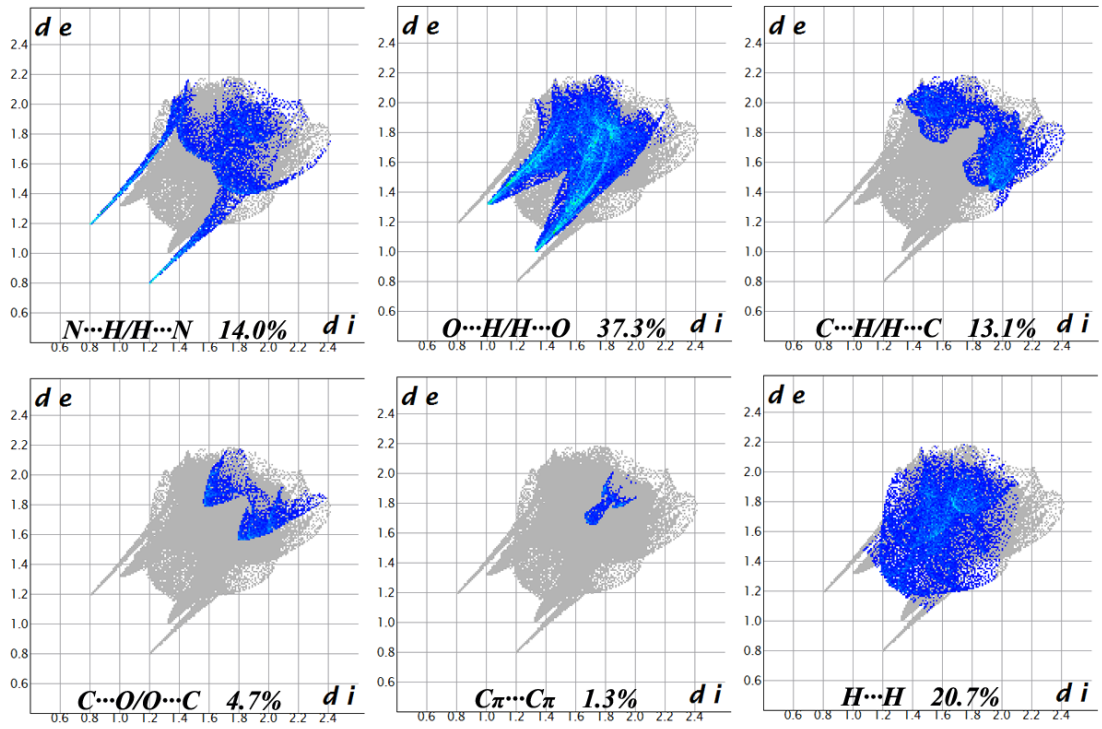

Fig. S3 Fingerprint plots resolved into different intermolecular interactions in **Form−I** showing percentages of contacts contributed to the total Hirshfeld surface area of the molecules.

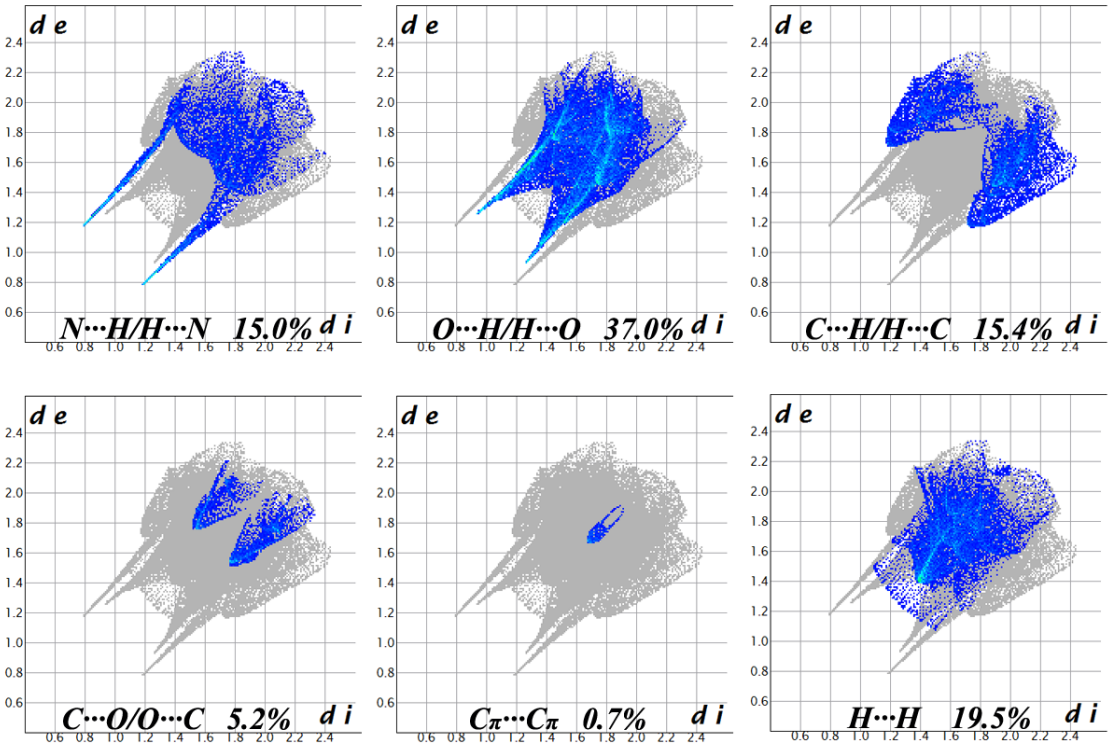

Fig. S4 Fingerprint plots resolved into different intermolecular interactions in **Form**–**II** showing percentages of contacts contributed to the total Hirshfeld surface area of the molecules.

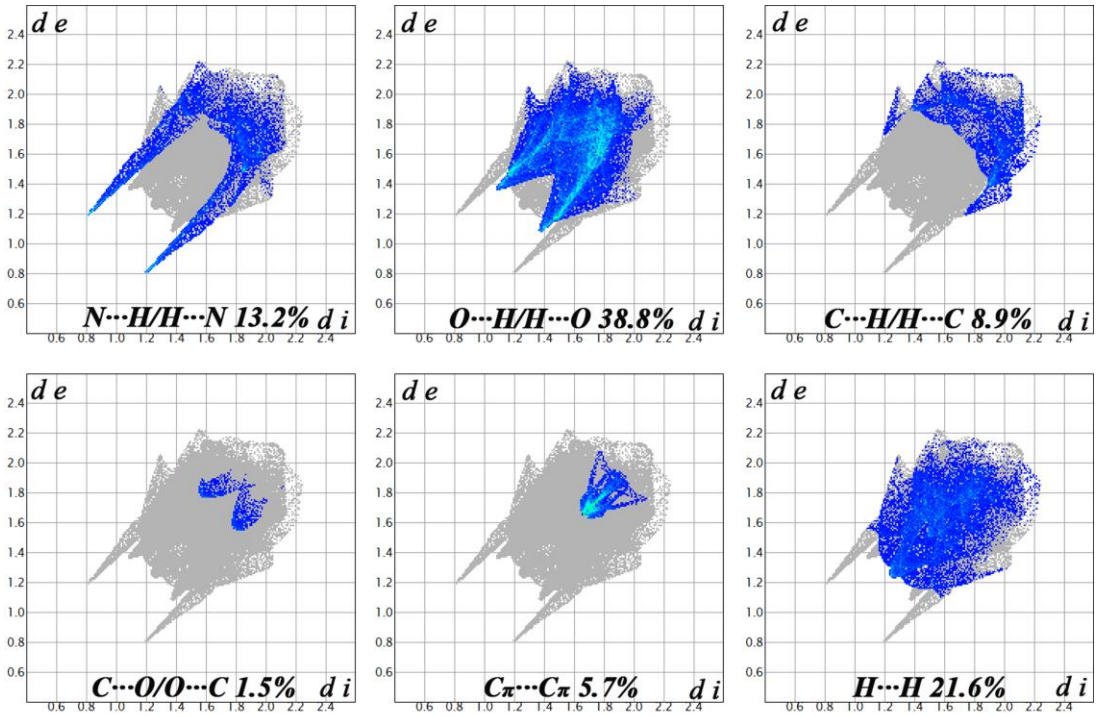

Fig. S5 Fingerprint plots resolved into different intermolecular interactions in **Form**–**III** showing percentages of contacts contributed to the total Hirshfeld surface area of the molecules.

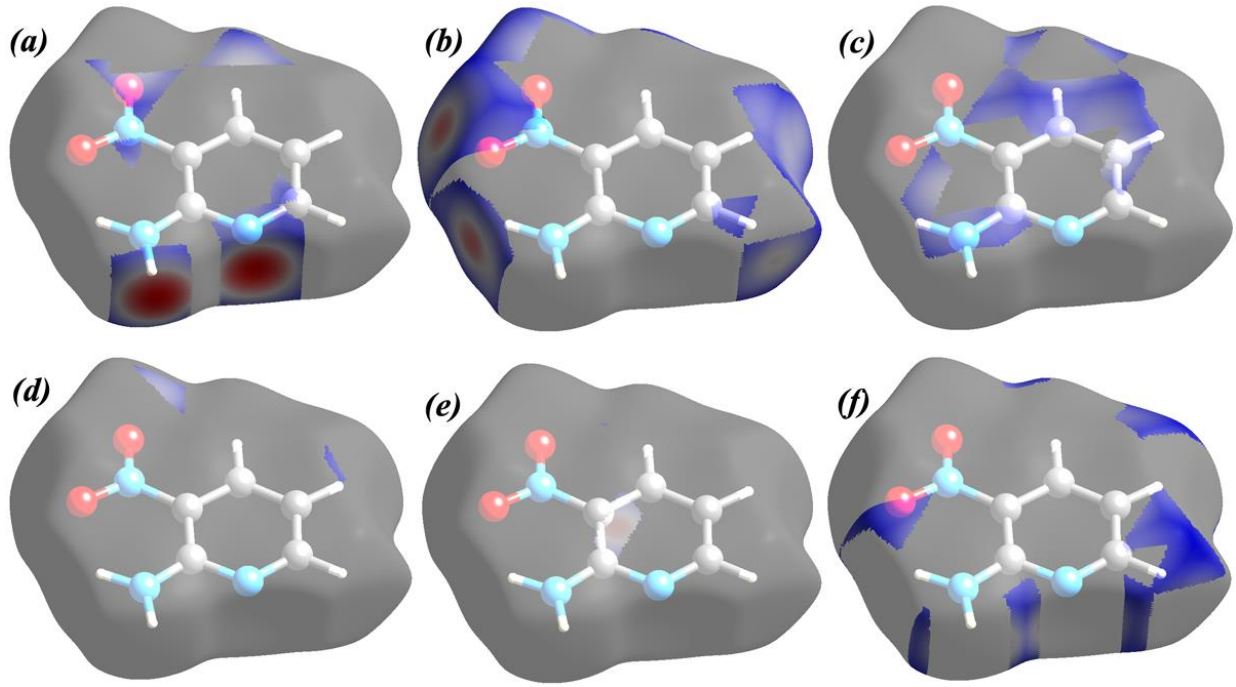

Fig. S6 d_{norm} surfaces mapped for (a) N···H/H···N; (b) O···H/H···O (c) C···H/H···C; (d) C···O/O···C; (e) C_{π}···C_{π} and (f) H···H interactions in **Form−I** showing the contribution to the total Hirshfeld surface area of the molecules.

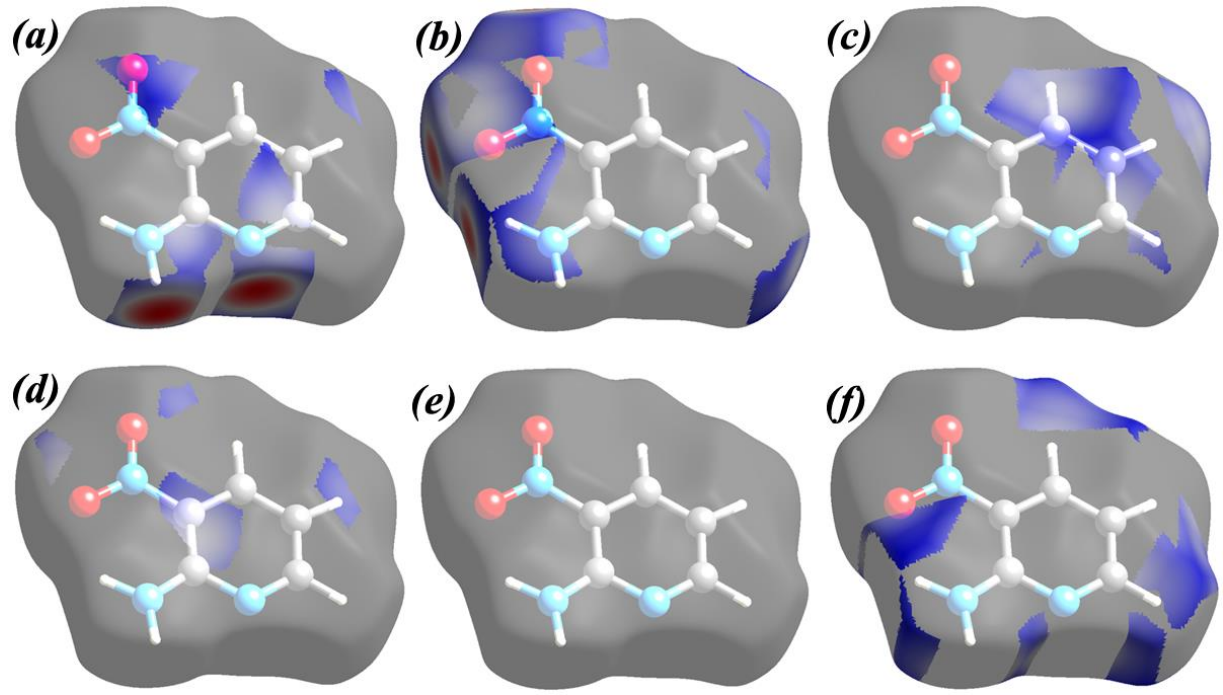

Fig. S7 d_{norm} surfaces mapped for (a) N···H/H···N; (b) O···H/H···O (c) C···H/H···C; (d) C···O/O···C; (e) $C_{\pi}\cdots C_{\pi}$ and (f) H···H interactions in **Form–II** showing the contribution to the total Hirshfeld surface area of the molecules.

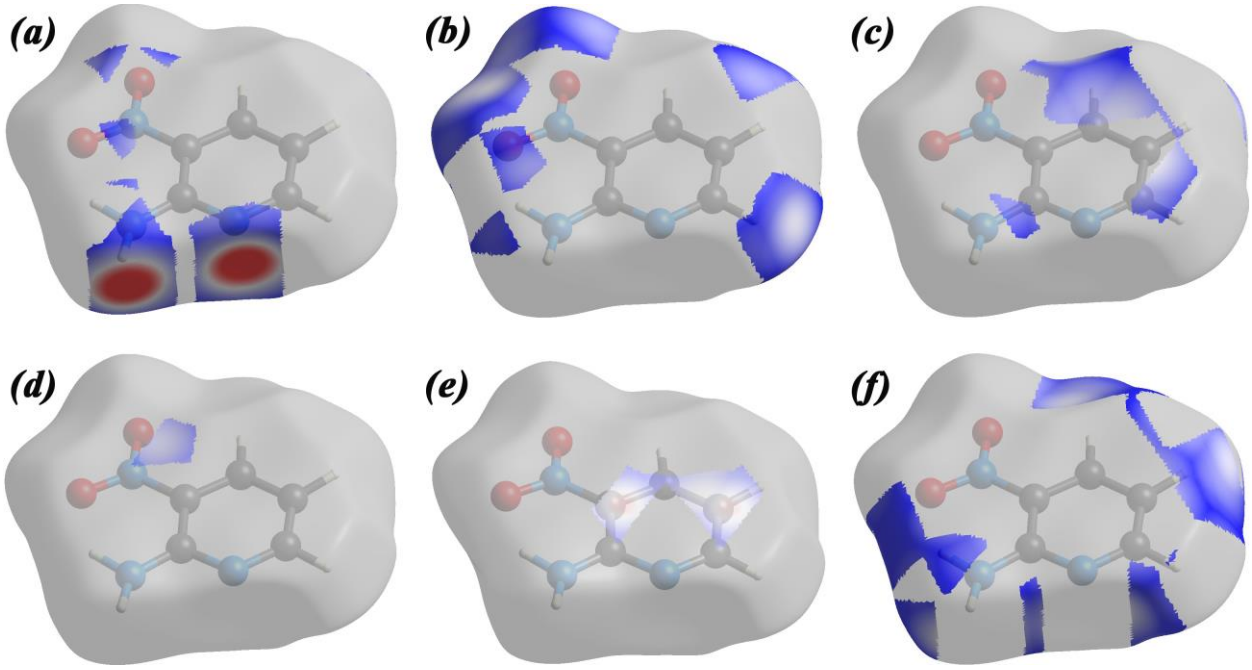

Fig. S8 d_{norm} surfaces mapped for (a) N···H/H···N; (b) O···H/H···O (c) C···H/H···C; (d) C···O/O···C; (e) $C_{\pi}\cdots C_{\pi}$ and (f) H···H interactions in **Form–III** showing the contribution to the total Hirshfeld surface area of the molecules.